Transactions of the ASME®

Journal of Applied Mechanics

Published Bimonthly by The American Society of Mechanical Engineers

VOLUME 68 • NUMBER 4 • JULY 2001

Transactions of the ASME, Journal of Applied Mechanics (ISSN 0021-8936) is published bimonthly (Jan., Mar., May, July, Sept., Nov.) The American Society of Mechanical Engineers, Three Park Avenue, New York, NY 10016. Periodicals postage paid at New York, NY and additional mailing office. POSTMASTER: Send address changes to Transactions of the ASME, Journal of Applied Mechanics, c/o THE AMERICAN SOCIETY OF MECHANICAL ENGINEERS, 22 Law Drive, Box 2300, Fairfield, NJ 07007-2300.
CHANGES OF ADDRESS must be received at Society headquarters seven weeks before they are to be effective. Please send old label and new address.
STATEMENT from By-Laws. The Society shall not be responsible for statements or opinions advanced in papers or . . . printed in its publications (B7.1, Para. 3).
 INDEXED by Applied Mechanics Reviews and Engineering Information, Inc. Canadian Goods & Services Tax Registration #126148048.

(Contents continued on inside back cover)

This journal is printed on acid-free paper, which exceeds the ANSI Z39.48-1992 specification for permanence of paper and library materials. ™
85% recycled content, including 10% post-consumer fibers.

(Contents continued)

Journal of Applied Mechanics Volume 68, Number 4 JULY 2001

BRIEF NOTES

DISCUSSIONS

ERRATA

ANNOUNCEMENTS AND SPECIAL NOTES

Progressive Cracking of a Multilayer System Upon Thermal Cycling

M. R. Begley
Mem. ASME
Department of Civil Engineering,
University of Virginia,
Charlottesville, VA 22904
e-mail: begley@virginia.edu

A. G. Evans
Materials Institute,
Princeton University,
Princeton, NJ 08540

This article considers progressive cracking upon thermal cycling of a thin multilayer on a thick substrate. The prototypical system comprises a thin elastic layer of a dielectric material above another thin metal interconnect layer attached to a silicon substrate. Residual stresses exist because of the thermal expansion misfit and due to deposition. Putative fabrication flaws are presumed to be present in the dielectric. When activated by residual stresses these flaws can induce cracks that channel along the dielectric. Conditions that induce yielding of the metal upon initial cooling are shown to exacerbate this phenomenon. Moreover, subsequent thermal cycling may induce ratcheting, wherein cracks develop progressively due to repeated yielding of the metal layer. The roles of initial stress, cyclic temperature amplitude, and interconnect yield strength in these phenomena are investigated using finite element models which explicitly account for cyclic yielding. The most deleterious situation is found to be that wherein the entire metal layer reaches yield at some stage during the temperature cycle. Several scenarios relevant to semiconductor devices are considered. [DOI: 10.1115/1.1379529]

1 Introduction

Upon thermal cycling during fabrication and qualification testing, multilayers comprised of materials with disparate thermomechanical properties are susceptible to complex mechanical responses. These cyclic phenomena are most pronounced when one of the constituents is susceptible to yielding (such as a metal interconnect) and when there are substantial differences in thermal expansion coefficient among the constituents. One of the most important of these responses, referred to as ratcheting, has been subject to the least analysis. It is characterized by material displacements that increase systematically with each cycle. The phenomenon is dictated by cyclic yielding, biased by an applied or residual stress.

Related behaviors have been found in pressure vessels subject to thermal cycling ([1–7]); this prompted both theoretical and experimental studies on model systems consisting of two bars of unequal length and cross sections. These "two-bar structures" have proven effective in identifying various regimes of behavior, including the unusual phenomenon of "compressive ratcheting," wherein the bars *shorten* during temperature cycling despite the present of a steady *tensile* load. For systems with disparate materials (such as those considered here), a more recent and well-known example of similar behavior occurs in particle-reinforced metals, which elongate along the load axis with each thermal cycle, resulting in large deformations after multiple cycles ([8]). Bree diagrams are used to characterize the behavior (examples of which are provided as Fig. 1), by indicating the combination of thermal expansion misfit, yield strength, and applied stress that activate ratcheting. Outside this domain, the system exhibits benign behavior, designated as shakedown, wherein the cyclic plastic straining is limited to the first few cycles.

The present article explores one manifestation of ratcheting relevant to some electronic devices. It involves plastic deformations that occur in a metal layer (Al or Cu), when encapsulated in a dielectric (such as SiN_x) containing an incipient crack. Once nucleated and upon thermal cycling, the cracks channel along the dielectric, as illustrated schematically in Fig. 2. Such cracks are referred to as steady-state, because the associated energy release rate is independent of their length. They propagate in a manner governed by the opening displacement profile through the film thickness, in the wake of the crack.

To address the problem, the tri-layer model illustrated in Fig. 3 is used. It is comprised of two thin layers on a semi-infinite elastic substrate. The top layer is elastic (representative of a dielectric layer) and the second is elastic/plastic (representative of metal interconnects). Where specific properties are needed for analysis, those summarized on Table 1 are used. Initially, the effect of plasticity in the metal layer on the behavior during the first cycle is addressed and related to effects that occur in thin elastic films deposited on elastic-plastic substrates ([9]). The multilayer scenario differs in two important ways from that for the semi-infinite elastic-plastic substrate: (i) the residual stress in the metal layer enhances plastic deformation, and (ii) the finite thickness of the metal layer (between the dielectric and substrate) provides constraint that limits plastic deformation. The focus of this paper is on the first of these effects. The second will be explored in a companion paper ([10]). It will be shown here that, when the residual stress is sufficiently low such that the plastic zone is small relative to the thickness of the metal layer, the present results for crack opening reduce to those derived by Beuth and Klingbeil [9].

2 Numerical Model

For scenarios where the crack face opens monotonically, the steady-state energy release rate, G_{ss} is related to work done by the residual stress through the crack opening. For uniform film stresses, σ, this may be expressed as

$$G_{ss}=\int_0^{\sigma}\delta(\sigma)d\sigma \tag{1a}$$

where δ is the integral of the crack opening displacements over the crack face, as in

$$\delta=\frac{1}{h}\int_0^{h}u(z)dz \tag{1b}$$

where h is the layer thickness. Note that crack-opening displacements are used here, which are one-half of the total crack opening

Contributed by the Applied Mechanics Division of THE AMERICAN SOCIETY OF MECHANICAL ENGINEERS for publication in the ASME JOURNAL OF APPLIED MECHANICS. Manuscript received by the ASME Applied Mechanics Division, December 22, 1999; final revision, November 7, 2000. Associate Editor: K. Ravi-Chandar. Discussion on the paper should be addressed to the Editor, Professor Lewis T. Wheeler, Department of Mechanical Engineering, University of Houston, Houston, TX 77204-4792, and will be accepted until four months after final publication of the paper itself in the ASME JOURNAL OF APPLIED MECHANICS.

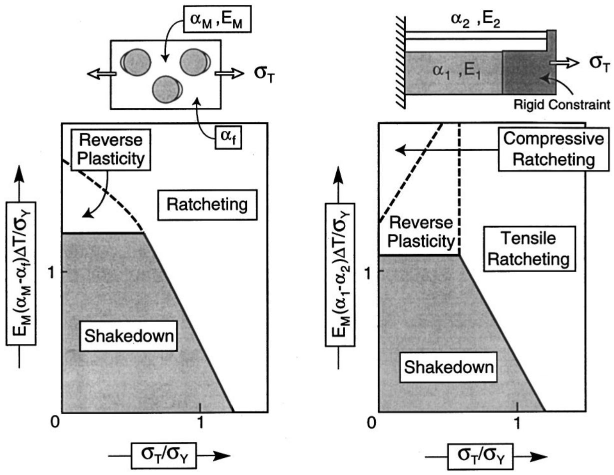

Fig. 1 Bree diagrams for a metal-matrix composite (left) and a two-bar model used for studying pressure vessels (right), illustrating the relationship between thermal loading, applied tensile loading, and regions of ratcheting and shakedown

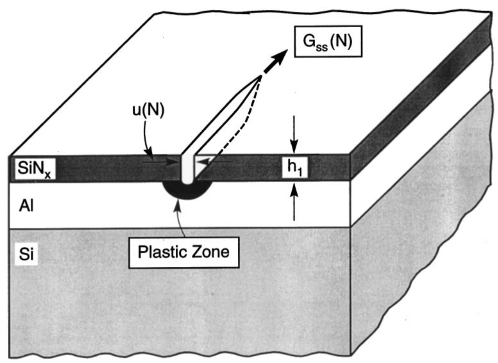

Fig. 2 Schematic of a channeling crack in a multilayer deposited on an elastic substrate. The middle layer represents an elastic-plastic interconnect, while the top layer is representative of an elastic dielectric; *N* is the number of thermal cycles.

Table 1 Properties of the representative system

	E (GPa)	α (ppm/°C)	ν	ε_Y
Top, SiN_x	100	6	0.2	-
Middle, Al	70	25	0.3	0.002
Substrate, Si	200	4	0.2	-

(measured from crack face to crack face). For monotonic opening of channeling cracks, the difficulty in accounting for plastic dissipation can be avoided by considering the work done by an equivalent pressure acting on the crack face ([9]). The key result is that plasticity increases the crack openings, resulting in higher crack driving forces.

Determining the corresponding response upon cyclic loading requires a plasticity flow theory. Simply applying a cyclic pressure to the crack faces does not accurately capture the near-tip deformations. Nevertheless, since the film is elastic, the opening profile of the crack still provides the correct measure of the energy release rate. Moreover, the steady-state opening in the wake, calculated from a plastic analysis, provides a driving force estimate that reveals important trends. This estimate, G_{ss}^{up},

$$G_{ss}^{up} = \sigma\delta, \tag{2}$$

is believed to be an upper bound. (For an elastic system, this expression is exact.) Full three-dimensional calculations of the near-tip deformations for a channeling crack are currently under way to determine the extent to which (2) overestimates the crack driving force ([10]).

While direct evaluation of G_{ss} is not possible using (2), it is still apparent that increases in crack openings correspond to larger crack driving forces. Accordingly, as the opening displacement increases during thermal cycling, the cracks can reach criticality and channel. This happens when G_{ss} reaches the fracture toughness of the dielectric layer, Γ. The ratcheting effect is reflected in increases in δ with thermal cycling, in the presence of a dielectric subject to an initial tension. The focus here is on conditions which cause the crack opening to increase with thermal cycling. *It should be emphasized that, for the present scenarios, the crack*

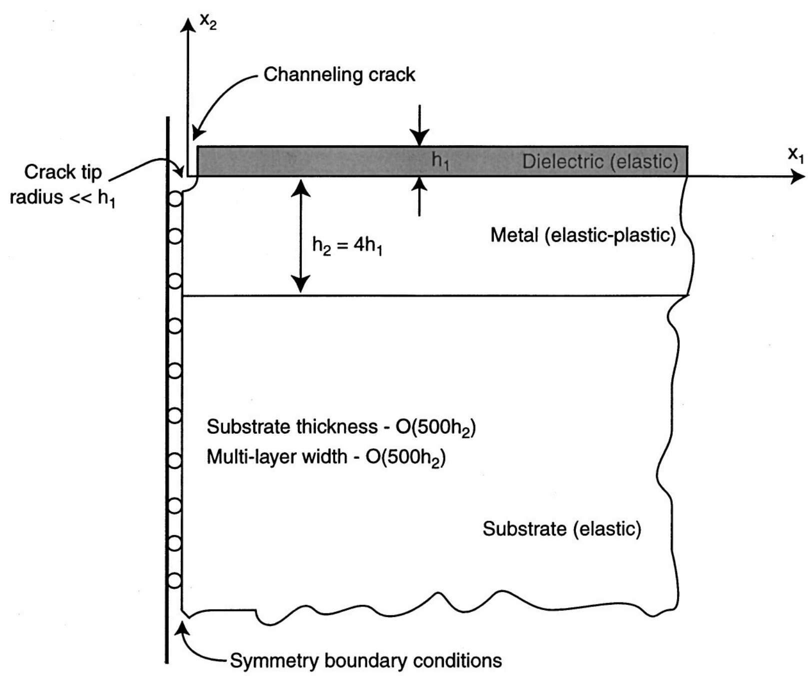

Fig. 3 Schematic of tri-layer system used to define the finite element model

opens systematically and plastic deformation prohibits crack closure. Crack face contact does not occur at any point during the loading cycle. It will be shown in Section 3 that, through proper choice of normalization, the results for crack openings and the upper bound G_{ss}^{up} are identical.

The model characterizes the deformations that occur in a representative slice in the wake of the crack, which is modeled as plane-strain (See Fig. 3.) The substrate is taken to be semi-infinite. The top layer (SiN_x) and substrate (Si) are modeled using isotropic elasticity, while the middle layer (Al) is modeled as elastic-perfectly plastic, using conventional isotropic J_2 flow theory. The finite element models are developed using the commercial code ABAQUS. Plane-strain eight-noded reduced-integration hybrid elements are used; these elements, which include the hydrostatic pressure as an additional elemental variable, are most effective in handling the nearly incompressible behavior of the plastic zone near the crack tip. Convergence tests illustrate that acceptable results are obtained when the dimensions of the outer boundaries are at least 100 times the combined thickness of the top two layers.

Special care has been taken to accurately capture the behavior near the crack tip. Cyclic loading represents a complication from monotonic scenarios, as compressive stresses may develop which act to reduce the crack opening. Furthermore, the large geometry changes at the tip must be accurately accounted for. Singularity elements can lead to numerical difficulties upon load reversal, including ambiguous tip deformations that arise when the elastic layer penetrates the plastically deformed elements. To circumvent this, the crack tip at the interface was modeled as a semi-cylindrical cavity with a tip radius about two orders of magnitude smaller than the thickness of the top elastic layer. Convergence tests have indicated that the crack-opening integrals calculated via (1*b*) (and the energy release rate estimate calculated via (2)) are independent of the initial tip radius. Moreover, the crack opening at the surface is independent of the numerical details. Again, it should be noted that for the problems of present interest, the initial opening experienced during the fabrication/cooling stage is large enough such that the crack does not close at any point during the cycling.

The initial stresses in the layers exert a substantial influence on the behavior. These are introduced into the model by assigning nominal, initial temperature changes to the layers prior to thermal cycling. In all cases, the dielectric is given a temperature input that causes it to be in residual tension prior to cycling (see the Appendix). The metal layer is given a range of initial conditions that simulate most of the expected practical scenarios, as outlined in the Appendix. One extreme, scenario A, allows the metal to have fully yielded in tension before cycling: the most likely scenario. Scenario B permits the metal to be stress-free before cycling: This would happen if the system were cooled below ambient prior to cycling. Scenario C examines an intermediate case wherein the layer is in residual tension at a stress below the yield strength. In the following analyses, initial cooling is first examined, in order to characterize the influence of residual stress in the metal on the initial energy release rate before cycling.

3 The Effect of Residual Stress in the Metal Layer

Cracking of thin elastic films on a *stress-free* semi-infinite elastic-plastic substrate has been previously addressed ([9]). These results are applicable to the initial cooling of the layered system, provided that: (i) the plastic zone is smaller than the thickness of the metal layer, and (ii) the residual stresses in the *metal* layer are too small to significantly enhance plastic deformation. The present calculations explore domains where the prior results are inappropriate.

The calculations are performed to simulate fabrication situations that encompass all practical scenarios, as elaborated upon in the Appendix. These scenarios induce bi-axial misfit stresses in the dielectric and metal layers, designated σ_1^0 for the dielectric layer and σ_2^0 for the metal layer. These misfit stresses can be related to thermal expansions and intrinsic stresses by

$$\sigma_1^0=\frac{E_1(\alpha_1-\alpha_s)\Delta T_1^d}{(1-\nu_1)}+\sigma_1^I \tag{2a}$$

$$\sigma_2^0=\frac{E_2(\alpha_2-\alpha_s)\Delta T_2^d}{(1-\nu_2)}+\sigma_2^I \tag{2b}$$

where α_1, α_2 and α_s are the thermal expansion coefficients for the dielectric, metal and substrate, respectively, ΔT_1^d and ΔT_2^d are the cooling ranges from ''deposition'' to ambient, E_1 and E_2 refer to the respective Young's moduli, ν_1 and ν_2 to the Poisson's ratios, and σ_1^I and σ_2^I to the intrinsic stress in the two layers. Note that in some scenarios σ_2^0 exceeds the yield strength of the metal layer, σ_Y. In such cases, the actual stress in this layer remains at σ_Y, except near the crack tip, where hydrostatic stresses are present.

The results of the calculations are expressed in terms of the following nondimensional quantities. The crack opening is normalized by the value that results from a purely elastic analysis of a system comprised of layers with identical elastic properties, given by ([11])

$$\delta_0=\frac{1.97(1-\nu_1^2)\sigma_1^0 h_1}{E_1} \tag{3}$$

where h_1 is the thickness of the dielectric layer. The factor 1.97 arises from the integration of the corresponding crack opening profile, as in Eq. (1*b*). For such a system, the residual stress in the metal layer has no effect on the crack-opening displacement ([11]). The nondimensional crack opening is thus

$$\Delta\equiv\frac{\delta}{\delta_0}=\frac{E_1\delta}{1.97(1-\nu_1^2)\sigma_1^0 h_1}. \tag{4a}$$

As noted earlier, an upper bound estimate of the crack driving force may be obtained by assuming that the initial misfit stress acts through the current crack opening from the elastic-plastic analysis. Thus, the parameter Δ also represents the normalized upper-bound estimate for the energy release rate, as in

$$\Delta\equiv\frac{G_{ss}^{ub}}{G_0}=\frac{\sigma_1^0\delta}{G_0}=\frac{E_1 G_{ss}^{ub}}{1.97(1-\nu_1^2)(\sigma_1^0)^2 h_1} \tag{4b}$$

where $G_0=\sigma_1^0\delta_0$ and represents the energy release rate for the homogeneous elastic case where the layers have identical elastic properties. In the cases considered here, the adjacent metal layer is less stiff than the dielectric, whereupon the elastic crack opening (and thus the energy release rate) is slightly larger than that for the *homogenous* case. For an elastic system with material properties listed in Table 1 $\Delta\equiv 1.08$. Plastic deformation further increases in this value, as elaborated below. Several normalized stress measures are used to elicit understanding. The first of these is the ratio of the misfit stress in the dielectric to the yield strength of the metal, given as

$$\Sigma_1\equiv\frac{\sigma_1^0}{\sigma_Y}. \tag{5}$$

For a specified metal (given σ_Y), and a dielectric with no intrinsic stress ($\sigma_1^I=0$ in (2*a*)), Σ_1 is explicitly dependent on the temperature change experienced by the dielectric from deposition to ambient. That is

$$\Sigma_1=\frac{E_1(\alpha_1-\alpha_s)\Delta T_1^d}{\sigma_Y(1-\nu_1)}. \tag{6}$$

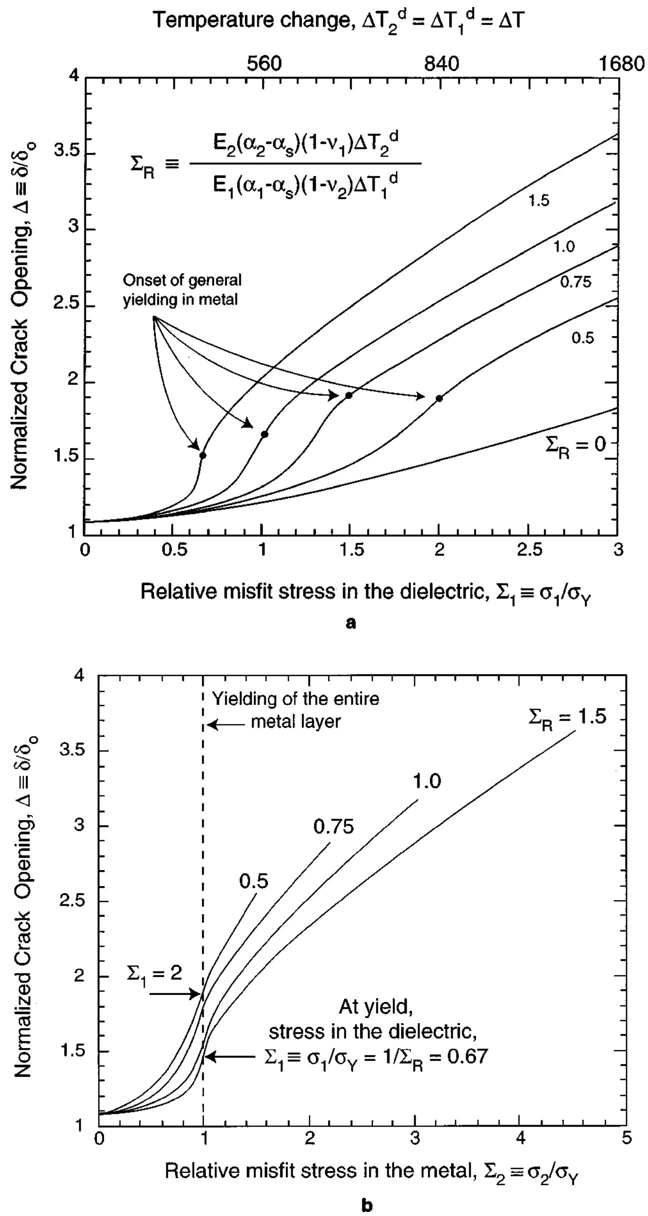

Fig. 4 (*a*) Crack-opening as a function of stress in the dielectric (monotonic loading), for constant ratios of stress in the metal layer to stress in the dielectric. The result is also an upper bound estimate for the energy release rate. (*b*) Crack-opening (or upper bound estimate of the energy release rate) as a function of stress in the metal layer (monotonic loading), for constant ratios of stress in the metal layer to stress in the dielectric.

A second useful measure is the ratio of the misfit stress in the metal layer to its yield strength, given as

$$\Sigma_2 \equiv \frac{\sigma_2^0}{\sigma_Y}. \tag{7}$$

This measure is the normalized magnitude of the stress in the metal layer that would result from a purely elastic analysis. Recall that plasticity limits the actual stress in the metal layer, such that $(\sigma_{xx}/\sigma_Y)_2 \leqslant 1$,[1] even though Σ_2 exceeds unity. Again, for a metal layer with no intrinsic stresses, Σ_2 is explicitly dependent on the temperature change experienced by the metal from deposition to ambient, via an expression identical to (5), with an appropriate change in subscripts.

Somewhat different insight into the role of material properties can be gained by using the ratio of the misfit stresses:

$$\Sigma_R \equiv \frac{\sigma_2^0}{\sigma_1^0} = \frac{\Sigma_2}{\Sigma_1}. \tag{8}$$

This quantity is used primarily to assess the role of the fabrication sequence (or initial cooling), since it reflects the explicit influence of the thermal expansion mismatch. This can be seen by considering a system with no intrinsic stresses, whereupon

$$\Sigma_R = \frac{E_2(\alpha_2-\alpha_s)(1-\nu_1)\Delta T_2^d}{E_1(\alpha_1-\alpha_s)(1-\nu_2)\Delta T_1^d}. \tag{9}$$

For a multilayer wherein both layers experience the same initial temperature change, $(\Delta T_1^d = \Delta T_2^d = \Delta T^d)$, it should be emphasized that Σ_R is purely a function of the elastic properties and the thermal expansion coefficients of the system. In this scenario, the temperature change ΔT^d can be thought of as an alternative independent variable, as it does not enter into the expression for Σ_R.

The first results are obtained for a system cooled from a uniform temperature, such that Σ_R remains constant (8), while Σ_1 is varied (Fig. 4(*a*)). The corresponding misfit stress in the metal layer is dictated by: $\Sigma_2 = \Sigma_R \cdot \Sigma_1$. Absent intrinsic stresses, the abscissa can be re-expressed as the temperature change from "deposition" to ambient for an Al layer, using the properties indicated in Table 2 and Eq. (6). The limit wherein the misfit stress in the metal layer is small, $\Sigma_R \to 0$, corresponds to the case previously considered by Beuth and Klingbeil [9]. Thus, these results express the history of the crack opening as the system is cooled, as well an upper bound estimate for the crack driving force. The critical temperature at which the entire metal layer yields in biaxial tension is labeled in the figure for each Σ_R. Note that when the stress nears this level, the crack opening increases substantially. This effect represents an increase in energy release rate due to plastic deformation enhanced by the misfit stress in the metal layer.

The abrupt increase crack opening when the metal layer becomes fully plastic is illustrated more vividly by Fig. 4(*b*). The results in this figure are generated by converting the abscissa in the previous figure (Σ_1) into the stress in the metal layer (Σ_2) via the misfit stress ratio Σ_R. Since this procedure implies a different scaling for each curve (dictated by the value of Σ_R), the abscissa *cannot* be reinterpreted using a single temperature scale as was done in Fig. 4(*a*). (Put another way, the coefficient that dictates the temperature scale (ΔT^d) depends on Σ_R in Fig. 4(*b*), while in Fig. 4(*a*) it does not.) Nevertheless, a single temperature scale can be determined for each of the curves in Fig. 4(*b*) using the properties outlined in Table 1, Eq. (6), and Eq. (8).

With this in mind, the curves can again be thought of as the history of the crack opening (and the energy release rate estimate) as the system is cooled. It is obvious from Fig. 4(*b*) that general yielding of the metal layer results in a dramatic increase in crack opening, and rationally, the crack driving force. Moreover, the increase is more pronounced when the stress in the dielectric ex-

Table 2 Cyclic loading cases in Fig. 7

Case	Temperature range (°C)	Stress range, $\Delta\Sigma_2$	Initial stress, Σ_2	Σ_1^{max}	Scenario (see Appendix)
a	−40,80	2.1 to 0.3	1	1.07	A
b	−40,100	2.1 to 0.0	1	1.07	A
c	−50,100	0.75 to −1.5	0	1.09	B
d	−50,100	2.25, 0	1	1.09	A
e	−75,150	1.1 to −2.2	0	1.13	C

[1]Hydrostatic stresses cause this inequality to be violated in a small zone near the tip.

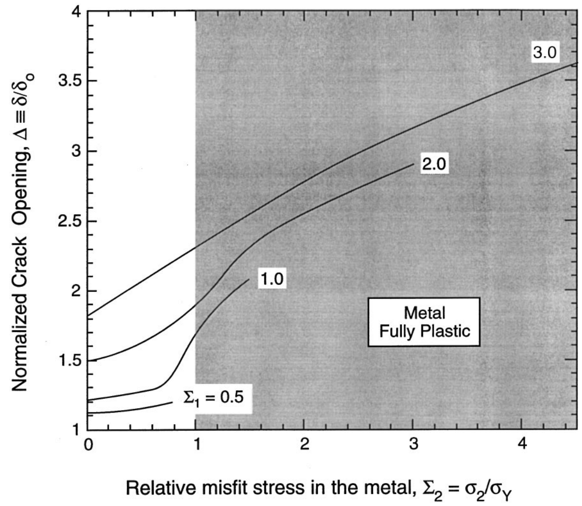

Fig. 5 Crack-opening as a function of stress in the metal layer for several values of stress in the dielectric (monotonic loading). The stress ratio during the loading stage (Σ_R) is dictated by the ratio of Σ_1 and Σ_2.

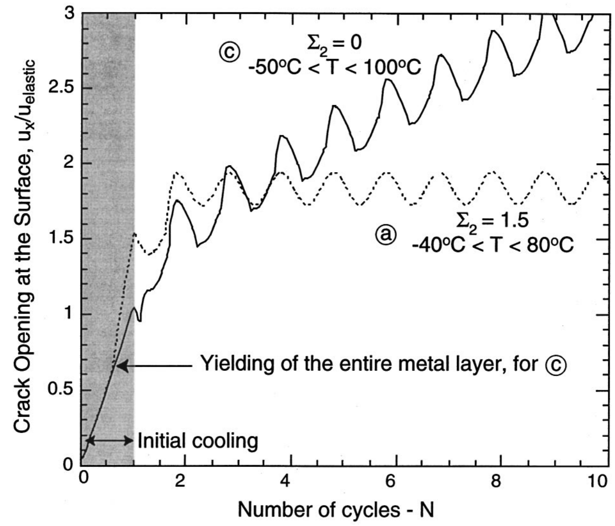

Fig. 6 Crack-opening displacements at the surface of the dielectric as a function of time (or thermal cycles) for two representative cases; the cases are the same as those labeled in Fig. 7 and described in Table 2

ceeds the yield strength of the metal. The curves in Figs. 4(*a*) and 4(*b*) represent a general monotonic loading scenario that highlights the increase in energy release rate due to residual stresses in the metal layer. The results remain valid for nonzero intrinsic stresses and different temperature changes for each layer. For such cases, the figures cannot be interpreted either in terms of a single temperature change, or as the history of the crack driving force as the system is cooled. Rather, each point in Figs. 4(*a*) and 4(*b*) represents the energy release rate at the end of a fabrication sequence characterized by Σ_R and Σ_1.

Alternatively, the fabrication sequence can be characterized by simply specifying the stresses in the layers after cooling. Then, the energy release rate after cooling can be plotted for various final values of Σ_1 and Σ_2, as illustrated in Fig. 5. The curves are terminated at misfit ratios for materials with properties similar to those listed in Table 2: that is $\Sigma_R = 1.5$. When the misfit stress in the metal layer is larger than its yield strength, the stress in this layer plays a more significant role than the misfit stress in the dielectric. The most probable scenarios fall in the shaded region of Fig. 5, dictated by the thermal expansion mismatch between the metal layer and substrate. The limit of no residual stress in the metal layer (i.e., $\Sigma_2 \rightarrow 0$) represents the scenario previous considered by Beuth and Klingbeil [9].

Some fabrication sequences do not correspond to steadily increasing the layer stresses with a fixed ratio (Σ_R). Then, strictly, the energy release rate at the end of the cooling stage is affected by the details of the sequence, since the material behavior is path-dependent. For example, slightly different results are obtained if the stress in one layer is increased in one loading step, and then held fixed while the stress in the second layer is increased to the final value. However, numerical calculations for several scenarios have illustrated that the energy release rate is relatively insensitive to these details. That is, the system behaves in a nearly path-*independent* manner, and acceptable results are obtained for a very wide range of fabrication scenarios merely by specifying the final values of Σ_1 and Σ_2.

4 Cyclic Loading and Ratcheting

All cyclic calculations are conducted using the properties given in Table 1. The effect of constant amplitude temperature cycling on the crack opening at the surface of the dielectric as a function of time is illustrated in Fig. 6. One result is for a metal layer that yields upon initial cooling, and experiences temperature cycling between −40 and 80°C. The other result is for a scenario wherein the metal layer is taken to be stress-free before temperature cycling, with subsequent temperatures ranging between −50 and 100°C. (The two cases also correspond to those considered in Fig. 7.) Both of these temperature ranges are representative of qualification testing. Ratcheting of the crack is obvious for the case involving the larger cyclic temperature range; during cycling, the metal layer experiences yielding in compression at $\Delta T \sim 67°C$, and develops tension (below the yield strength) at the temperature minimum. This case corresponds to Scenario B in the Appendix. For the other case, the metal layer yields repeatedly in tension, but does not experience compression; this case corresponds to Scenario A in the Appendix. These two situations illustrate that yielding of the metal layer prior to cycling influences ratcheting primarily by shifting the stress range experienced by the metal layer. As will be discussed in detail, unidirectional yielding alone, either before or during cycling, is not sufficient to cause ratcheting.

The crack openings and upper-bound energy release rates determined using (2), are summarized on Fig. 7, wherein the maxi-

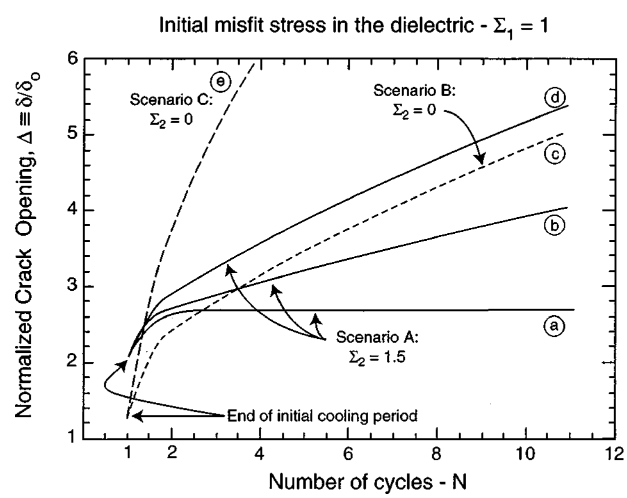

Fig. 7 Crack-opening (or upper bound estimate of the energy release rate) as a function of time (or thermal cycles) for representative cases outlined in Table 2

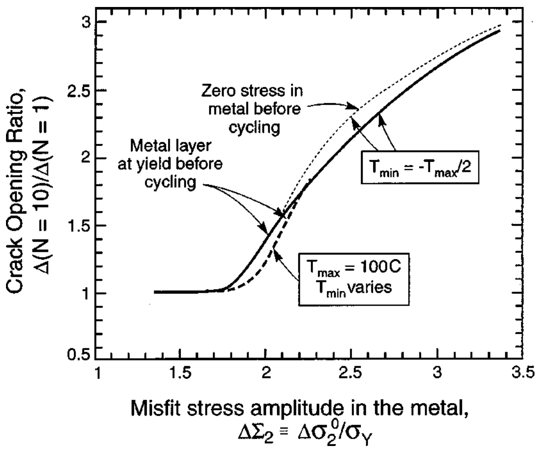

Fig. 8 Fractional increase in crack opening from the first thermal cycle to the tenth thermal cycle, plotted as a function of total stress amplitude range in the metal layer

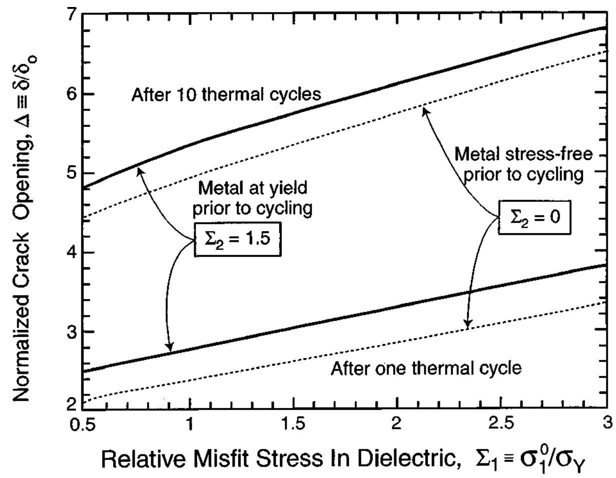

Fig. 9 Crack opening as a function of initial stress in the dielectric layer, for two scenarios. Because of the small difference in thermal expansion between the dielectric and substrate, the mean stress in the dielectric remains close to the initial value.

mum values during each temperature cycle, are normalized by the elastic result. In this manner, the fractional increase in crack opening (or energy release rate) due to plastic deformation is highlighted. The scenarios considered are summarized in Table 2. For each case, the initial misfit stress in the dielectric is equated to the yield strength of the metal (140 MPa). The starting point for each curve ($N=1$) represents the crack opening at the end of the initial cooling period. Note that the cases shown in the figure cover the extreme range of scenarios outlined in the Appendix. Cases (a), (b), and (d) in Fig. 7 represent scenario A, which is characterized by fully yielding the metal layer prior to cycling. Case (c) represents scenario B, which is characterized by an initially stress-free layer; in this case the metal layer experiences unidirectional yielding. Case (e) represents scenario B as well, but with the metal layer experiencing fully reversed yielding. Cases with initial stresses in the metal layer that are below the layer's yield strength (scenario C) show similar behavior.

These cases illustrate that ratcheting is affected most strongly by the temperature amplitude and the corresponding misfit stress *range* in the metal layer. The level of initial misfit has only a small effect, as illustrated by cases (c) and (d), which experience the same temperature range and differ only in the initial stress. Yielding in the metal layer prior to cycling merely serves to increase slightly the overall crack driving force. Moreover, fully reversed yielding causes a dramatic increase in the ratcheting rate (case (e)). The increases in crack opening from the first to the tenth cycle, plotted on Fig. 8, verify that the misfit stress range experienced by the metal layer dominates ratcheting. For two of the lines plotted, the temperature is prescribed such that the minimum temperature was equal to minus one-half of the maximum; this is representative of qualification testing. The third line (appropriately labeled) is for cases wherein the maximum temperature is held fixed at 100°C, and the minimum is adjusted accordingly. The horizontal axis may be reinterpreted as one of the relevant temperatures (mean, minimum or maximum) by using the properties outlined in Table 1, with a different scaling for each curve.

Although the curves correspond to a variety of combinations in the minimum, maximum, and mean misfit stresses, the consistent finding is that ratcheting only becomes significant when the total amplitude of the misfit stress in the metal is approximately twice the yield strength. The calculations presented on these figures, as well as others conducted for a wide range of cases, have demonstrated two necessary criteria for ratcheting: (i) the entire metal layer must yield (or come close to yielding) at some stage during the cycle, and (ii) the misfit stress in the metal layer must become less than or equal to zero at some stage during the cycle.

It had been expected that the misfit stress in the dielectric would play a similar role. However, the predictions (Fig. 9) reveal that, while this stress influences the magnitude of the magnitude of the crack opening, it has relatively little effect on the ratcheting behavior. In the figure, the dashed lines correspond to scenario A and the solid lines to scenario B. In all cases, the temperature ranges from -50°C to 100°C. Because the curves are normalized by δ_0, they would remain constant for a purely elastic system. Thus, the curves represent the growing importance of plastic deformation as the stress in the dielectric increases. Note that ratcheting occurs for *all* values of Σ_1: but the ratcheting *rate* is independent of the mean stress. For the entire range of Σ_1 in Fig. 9, the fractional increase from the first to tenth cycles is between 1.85 and 2.00. This implies that the curves shown in Fig. 8 are valid for a wide range of stresses in the dielectric. Again, yielding in the metal layer prior to cycling is shown to slightly raise the magnitude of the energy release rate, but has almost no effect in on the ratcheting. This weak dependence is consistent with that illustrated in Fig. 8 (which plots results for $\Sigma_1=1$), since all of the cases shown in Fig. 9 correspond to a misfit stress amplitude: $\Delta\Sigma_2 \sim 2.25$.

5 Implications and Conclusions

When the stress amplitudes in the dielectric are on the order of the yield strength in the metal, the preceding conditions for ratcheting and shakedown can be used to construct a modified Bree diagram (Fig. 10(*a*)), where the initial stress in the metal layer and the stress range in the metal are used as coordinates. The shakedown limit is defined by the fact the minimum stress must be less than zero and the maximum stress must exceed yield. The onset of ''strong ratcheting'' is defined by the requirement that the metal layer experience fully reversed yielding. An initial stress in the metal layer affects ratcheting by determining whether a specified temperature change is large enough to satisfy both ratcheting criteria. This diagram may be used for the preliminary design of systems that resist ratcheting. When the stress amplitude in the dielectric are significantly larger than the yield strength of the metal, the diagram must be modified. There is some evidence from the calculations that large stress amplitudes shift the ratcheting boundaries to lower temperature amplitudes, as sketched in Fig. 10(*b*).

It should be noted that the structural ratcheting exhibited in this analysis is not a result of crack face interactions, since the crack opens upon cooling and plastic deformation prohibits crack clo-

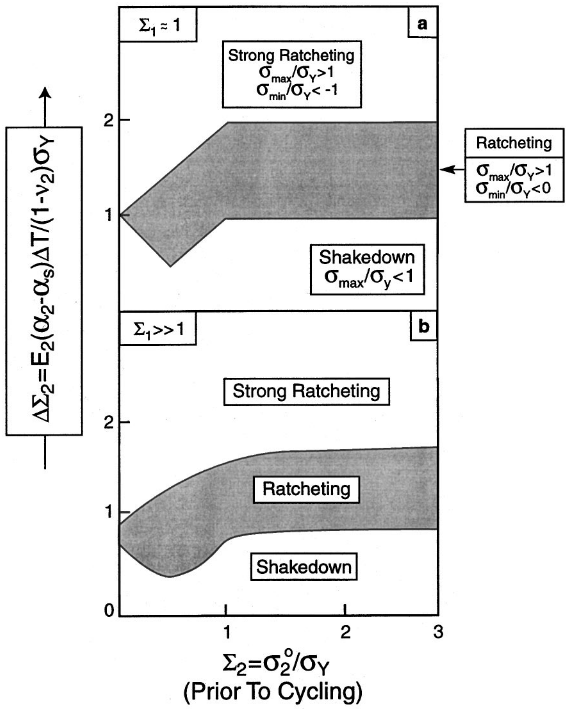

Fig. 10 Modified Bree diagram for a trilayer: (*a*) for moderate values of mean stress in the dielectric, (*b*) for high levels of mean stress in the dielectric

sure. Rather, the ratcheting behavior is a result of repeated plastic straining near the crack tip due to the presence of a biased stress in the top elastic layer. Such ratcheting is generally understood to be dependent on strain-hardening and whether it is kinematic or isotropic. The former is manifest as a Bauschinger effect, wherein the yield strength in compression is reduced by prior yielding in tension. Calculations for the present problem incorporating strain-hardening reveal that such material hardening can limit the magnitude of the crack opening (and hence, energy release rate), but does not eliminate the ratcheting deformation over the first five to ten cycles. Full details of these simulations are available in [10]. A brief summary is given of results obtained for hardening described by a Ramberg-Osgood law, $\varepsilon=\sigma/E+(3/7)(\sigma/\sigma_Y)^n$. With low to moderate hardening ($n\geqslant 10$), the differences between kinematic and isotropic behavior are negligible; moreover, the reduction in energy release rate due to hardening (relative to the elastic-perfectly plastic result) is on the order of ten percent after ten cycles. For stronger hardening ($n\leqslant 5$), the difference between kinematic and isotropic behavior is substantial, with significant reductions in crack driving force. For example, consider case (d) in Fig. 7; using the same loading, modulus and yield strain, and taking $n=5$, the kinematic hardening calculation predicts $\Delta=4.4$ after ten cycles, as opposed to $\Delta=5.4$ for the elastic-perfectly plastic case. The isotropic strain-hardening prediction (with the same properties) yields $\Delta=3.2$. Further calculations for moderate to high levels of strain-hardening demonstrate that shakedown occurs after six or so cycles, wherein the crack opening increases by about 50 percent.

Appendix

Scenarios Chosen to Illustrate the Effects of Initial Stress on Ratcheting

Scenario A: Stress in the Middle Layer at Yield. The metal layer experiences general yielding upon initial cooling if the temperature decrease after deposition, ΔT_2^d, satisfies

$$\Delta T_2^d \geqslant \frac{(1-\nu_2)\varepsilon_Y}{(\alpha_2-\alpha_s)}. \tag{A1}$$

Thereafter, the temperature *amplitude* which would cause fully reversed cyclic yielding is

$$\Delta T_R = 2\,\frac{(1-\nu_2)\varepsilon_Y}{(\alpha_2-\alpha_s)}. \tag{A2}$$

Scenario B: Initially Stress-Free Metal Layer. After initial cooling, the metal layer is taken to be stress free, with the stress in the dielectric given by (2*a*), with the intrinsic stress equal to zero. Then, the entire system is subject to the same temperature cycle, ΔT, such the change in stress in the dielectric is given by

$$\Delta\sigma_i = \frac{E_i(\alpha_i-\alpha_s)\Delta T}{(1-\nu_i)}. \tag{A3}$$

The cyclic temperature amplitude that would cause general yielding of the metal layer is given by

$$\Delta T_Y = \frac{(1-\nu_2)\varepsilon_Y}{(\alpha_2-\alpha_s)}. \tag{A4}$$

For the properties given in Table 1, this critical temperature amplitude is $\Delta T_Y \approx 67°$C. *Since the initial stress in the metal is zero, larger cyclic temperature amplitudes would cause fully reversed yielding.*

Scenario C: Residual Stress in the Both Layers. Both layers experience the same initial cooling from the "deposition" temperature. The initial stresses are then given by (2), with $\Delta T_1^d = \Delta T_2^d$. If this temperature change is greater than that given by (*A*1), the metal would have fully yielded and the behavior is identical to scenario A. The entire system is subject to the same temperature change, ΔT, so that the change in stress in the top layer is again given by (*A*3). The temperature *amplitude* which would cause general yielding upon cycling is then

$$\Delta T_Y = \frac{(1-\nu_2)\varepsilon_Y}{(\alpha_2-\alpha_s)} - \Delta T_1^d. \tag{A5}$$

Fully reversed cyclic yielding occurs if the temperature amplitude is greater than

$$\Delta T_{RY} = \frac{(1-\nu_2)\varepsilon_Y}{(\alpha_2-\alpha_s)} + \Delta T_1^d. \tag{A5}$$

If there is no initial temperature change (i.e., $\Delta T_1^d = \Delta T_2^d = 0$), this scenario is identical to scenario B. Thus, the distinction between the scenarios is whether or not there is an initial stress in the metal layer prior to cycling.

References

[1] Bree, J., 1989, "Plastic Deformation of a Closed Tube due to Interaction of Pressure Stresses and Cyclic Thermal Stresses," Int. J. Mech. Sci., **31**, pp. 865–892.
[2] Ponter, A. R. S., and Cocks, A. C. F., 1984, "The Incremental Strain Growth of an Elastic-Plastic Body Loaded in Excess of the Shakedown Limit," ASME J. Appl. Mech., **51**, pp. 465–470.
[3] Ponter, A. R. S., and Cocks, A. C. F., 1984, "The Incremental Strain Growth of Elastic-Plastic Bodies Subjected to High Levels of Cyclic Thermal Loading," ASME J. Appl. Mech., **51**, pp. 470–474.
[4] Megahed, M. M., Ponter, A. R. S., and Morrison, C. J., 1984, "Experimental Investigations Into the Influence of Cyclic Phenomena of Metals on Structural Ratcheting Behavior," Int. J. Mech. Sci., **26**, pp. 625–638.
[5] Megahed, M. M., 1981, "Influence of Hardening Rule on the Elasto-Plastic Behavior of a Simple Structure Under Cyclic Loading," Int. J. Mech. Sci., **23**, pp. 169–182.
[6] Bree, J., 1968, "Incremental Growth due to Creep and Plastic Yielding of Thin

Tubes Subjected to Internal Pressures and Cyclic Thermal Stresses,'' J. Strain Anal., **3**, pp. 122–127.
[7] Bree, J., 1967, ''Elastic-Plastic Behaviour of Thin Tubes Subjected to Internal Pressure and Intermittent High-Heat Fluxes With Application to Fast-Nuclear-Reaction Fuel Elements,'' J. Strain Anal., **2**, pp. 226–238.
[8] Jansson, S., and Leckie, F. A., 1992, ''Mechanical Behavior of a Continuous Fiber-Reinforced Aluminum Matrix Composite Subjected to Transverse and Thermal Loading,'' J. Mech. Phys. Solids, **40**, pp. 593–612.
[9] Beuth, J. L., and Klingbeil, N. W., 1996, ''Cracking of Thin Films Bonded to Elastic-Plastic Substrates,'' J. Mech. Phys. Solids, **44**, pp. 1411–1428.
[10] Begley, M. R., Evans, A. G., and Ambrico, J. M., 2001, ''Cracking During Thermal Cycling of Thin Multilayers,'' *Proceedings of the International Congress on Fracture*, Honolulu, HI.
[11] Hutchinson, J. W., and Suo, Z., 1994, ''Mixed-Mode Cracking in Layered Materials,'' Adv. Appl. Mech., **29**, pp. 64–191.

G. W. Reich
Aerospace Engineer,
Multidisciplinary Technologies Center,
Air Force Research Laboratory,
AFRL/VASD,
2210 Eighth Street, Building 146,
Wright-Patterson AFB, OH 45433-7531
Mem. ASME

K. C. Park
Professor,
Department of Aerospace Engineering Sciences
and Center for Aerospace Structures,
University of Colorado,
Campus Box 429,
Boulder, CO 80309
Fellow ASME

A Theory for Strain-Based Structural System Identification

A theory for structural system identification which utilizes strains and translational displacements as measured outputs is presented. The state variables of the fundamental first-order form consist of the strains and the elemental or substructural rigid-body motion amplitudes. The theory is applicable to, and to some respects, motivated by the advances and expanded use of embedded piezoelectric sensors and fiber optics. A distinct feature of the present theory is its ability to provide rotational flexibility without having to measure rotational quantities. The theory is illustrated by simple ideal examples.
[DOI: 10.1115/1.1379954]

1 Introduction

The identification of structural models using measured responses plays a fundamental role in vibration and noise controller design, as well as in model-based damage detection or health monitoring of structural systems under service. Most existing identification procedures use the applied excitations or prescribed displacements or accelerations and the measured accelerations or displacements as inputs and outputs, respectively. Consequently, although strain gauges have been extensively used in static testing and strength assessment, very seldom are the outputs of strain gauges incorporated directly into a system realization procedure.

In recent years, new sensors have come of age for structural measurements, including embedded optical fibers, embedded piezoelectric sensors, and laser-based differential kinematic measurements. The outputs from these sensors are difficult to convert into conventional nodal displacements. This calls for the development of a new system identification theory which exploits measurements from these new-generation sensors in construction of the governing equations of motion for vibrating structures, not just for quasi-static properties such as static mode shapes and strength levels.

The other issue in structural system identification is the correlation of system-identified models directly with those generated by the finite element method. With the exception of solid elements, the finite element modeling of beams, plates, and shells usually involve rotational degrees-of-freedom. The installation and accuracy of rotational sensors have been problematic. As a result, rotational sensors have not been widely utilized, which limits the fidelity of identified models. We will show that the use of strain plus translational displacements may be utilized to circumvent the need for measuring rotational motions.

Critical to the use of strains for system identification and their incorporation into theory is the concept of structural partitioning. Strains are typically valid over only a very localized region, and therefore any theory which includes strains as an output or state variable must hold for the local level only. This leads to mathematical substructuring, also known as partitioning or domain decomposition. While typically used for systematic processing on parallel computers, among other uses, substructuring in this context is defined as the separation of dynamics of the system into local regions, plus any interaction dynamics which act between partitions. These subregions can be tied to a reference finite element model, for which one substructure includes one or more finite elements.

This paper covers the basic theory of how a substructural strain-based system identification procedure might be implemented. First we review the equations corresponding to conventional nodal displacement/acceleration based system identification. This is followed by a derivation of the expression of displacement in terms of strain, rather than vice versa. Next, these expressions are utilized to derive the strain-based equations of motion which serve as the foundation of substructural system identification and applications. Finally, several simple examples are presented to demonstrate how this theory may be utilized in practice.

2 Linear Equations of Motion for Vibrating Structures

Before embarking into a derivation of new theory, it is wise to review the mathematics involved with traditional global system identification practices. In particular, we want to remind readers of the origin of the standard second-order system of equations governing the vibrating motion, as well as the related input/output relationship. Once these equations have been recalled, it will be easier for the reader to relate the new theory in the following sections with the more traditional practices represented in this section.

The discrete energy functional $\mathbf{\Pi}$ for a linear damped structure can be expressed as

$$\mathbf{\Pi}(\mathbf{u}_g)=\mathbf{u}_g^T\left(\frac{1}{2}\mathbf{K}_g\mathbf{u}_g-\mathbf{f}_g^D\right),\qquad \mathbf{f}_g^D=\mathbf{f}_g-\mathbf{M}_g\ddot{\mathbf{u}}_g-\mathcal{D}_g\dot{\mathbf{u}}_g \tag{1}$$

where $\mathbf{u}_g$ is the displacement vector of the assembled structure; $\mathbf{f}_g^D$ is the D'Alembert's force vector which consists of the applied force vector $\mathbf{f}_g$, the resisting inertia force $\mathbf{M}_g\ddot{\mathbf{u}}_g$, and the dissipating force $\mathcal{D}_g\dot{\mathbf{u}}_g$. $\mathbf{M}_g$, $\mathcal{D}_g$, and $\mathbf{K}_g$ are the assembled mass, damping, and stiffness matrices, where the subscript g designates "an assembled global structure" to distinguish from "partitioned substructures," and the superscript $(\dot{\ })$ designates time differentiation.

The discrete, damped, time-invariant, linear equations of motion for vibrating structures can be obtained from the stationary value of the preceding discrete energy functional, viz., $\delta\mathbf{\Pi}=0$:

$$\mathbf{M}_g\ddot{\mathbf{u}}_g+\mathcal{D}_g\dot{\mathbf{u}}_g+\mathbf{K}_g\mathbf{u}_g=\mathbf{f}_g. \tag{2}$$

Contributed by the Applied Mechanics Division of THE AMERICAN SOCIETY OF MECHANICAL ENGINEERS for publication in the ASME JOURNAL OF APPLIED MECHANICS. Manuscript received by the ASME Applied Mechanics Division, Feb. 16, 2000; final revision, Feb. 21, 2001. Associate Editor: A. K. Mal. Discussion on the paper should be addressed to the Editor, Professor Lewis T. Wheeler, Department of Mechanical Engineering, University of Houston, Houston, TX 77204-4792, and will be accepted until four months after final publication of the paper itself in the ASME JOURNAL OF APPLIED MECHANICS.

The input-output relation or frequency response function is obtained through a harmonic decomposition of the input-output vectors as

$$\begin{bmatrix} \mathbf{u}_g \\ \mathbf{f}_g \end{bmatrix} = \mathbf{e}^{j\omega t}\begin{bmatrix} \overline{\mathbf{u}_g} \\ \overline{\mathbf{f}_g} \end{bmatrix} \tag{3}$$

with solution for the frequency-domain output $\overline{\mathbf{u}_g}$ as

$$\overline{\mathbf{u}_g} = \mathbf{H}_g(\omega)\overline{\mathbf{f}_g}, \quad \mathbf{H}_g(\omega) = (\mathbf{K}_g + j\omega\mathcal{D}_g - \omega^2\mathbf{M}_g)^{-1} \tag{4}$$

where $\mathbf{H}_g(\omega)$ will be called the "global" frequency response function.

A conventional identification process first obtains the frequency response function (4) by using the measured input force $\mathbf{f}_g$ and the output, usually in terms of the acceleration vector $\ddot{\mathbf{u}}_g$. Once the frequency response function is obtained, the three structural matrices $\mathbf{M}_g$, $\mathcal{D}_g$, and $\mathbf{K}_g$ may be found by a system realization algorithm ([1]) followed by a mass-normalized transformation procedure of Alvin and Park [2].

3 Derivation of Strain-to-Displacement Relation

One difficulty in a systematic derivation of strain-based system identification algorithms has been that while it is trivial to express the strains in terms of displacements, the converse has not been easy. We first note that the displacement $\mathbf{u}$ on an element or substructure can be decomposed into two parts, that is, deformation $\mathbf{d}$ and rigid-body motion $\mathbf{r}$ (see, e.g., [3]):

$$\mathbf{u} = \mathbf{d} + \mathbf{r}. \tag{5}$$

The rigid-body component can be represented by

$$\mathbf{r} = \boldsymbol{\Phi}_\alpha \boldsymbol{\alpha} \tag{6}$$

where $\boldsymbol{\Phi}_\alpha$ represents the elemental rigid-body modes that depend only on the geometry of the element under consideration, and $\boldsymbol{\alpha}$ are the associated generalized coordinates.

In order to make strains available for use in system identification, the deformation vector $\mathbf{d}$ must be expressed in terms of the strains. To this end, we begin with the well-known strain-displacement relation

$$\mathbf{s} = \mathbf{S}^T\mathbf{u} \tag{7}$$

where $\mathbf{s}$ is a general strain variable and $\{\mathbf{S}^T \in \Re^{m\times n}, m \leqslant n\}$ is the discrete strain-displacement relation matrix that can be derived in a variety of ways, e.g., by relying on the finite element shape functions of the assumed element. Substituting $\mathbf{u}$ from (5) yields

$$\mathbf{s} = \mathbf{S}^T(\mathbf{d}+\mathbf{r}) = \mathbf{S}^T(\mathbf{d}+\boldsymbol{\Phi}_\alpha\boldsymbol{\alpha}) = \mathbf{S}^T\mathbf{d} \tag{8}$$

since the rigid-body modes $\boldsymbol{\Phi}_\alpha$ do not incur any strain.

The deformation $\mathbf{d}$ can be obtained from the previous equation as

$$\mathbf{d} = \boldsymbol{\Phi}_s\mathbf{s}, \quad \boldsymbol{\Phi}_s = \mathbf{S}(\mathbf{S}^T\mathbf{S})^{-1}. \tag{9}$$

Substituting (9) and (6) into (5), we arrive at the desired result, a *strain-to-displacement* relation:

$$\mathbf{u} = \boldsymbol{\Phi}_s\mathbf{s} + \boldsymbol{\Phi}_\alpha\boldsymbol{\alpha} = \boldsymbol{\Phi}\begin{Bmatrix} \mathbf{s} \\ \boldsymbol{\alpha} \end{Bmatrix} \quad \boldsymbol{\Phi} = [\boldsymbol{\Phi}_s \quad \boldsymbol{\Phi}_\alpha] \tag{10}$$

where we note that the column size of $\boldsymbol{\Phi}_\alpha$ is at most $6n_s$, in which n_s is the total number of partitioned substructures. Since the preceding expressions are relatively new concepts, we offer some simple examples below.

3.1 Discrete Bar Element. For a planar bar element, the strain in the element is the axial strain ϵ_x caused by elongation of the bar. It is related to the axial displacements (u_1, u_2) at the bar endpoints by the discrete strain-displacement relation given by

$$\epsilon_x = \frac{1}{l}[-1 \quad 1]\begin{Bmatrix} u_1 \\ u_2 \end{Bmatrix} \tag{11}$$

where l is the length of the bar element. From this, one obtains, via (9), that

$$\boldsymbol{\Phi}_s = \frac{l}{2}\begin{bmatrix} -1 \\ 1 \end{bmatrix}. \tag{12}$$

Since the elemental rigid-body mode $\boldsymbol{\Phi}_\alpha$ is given by

$$\boldsymbol{\Phi}_\alpha^T = [1 \quad 1] \tag{13}$$

the displacement-strain relation for a bar element can be written as

$$\begin{Bmatrix} u_1 \\ u_2 \end{Bmatrix} = \frac{l}{2}\begin{bmatrix} -1 \\ 1 \end{bmatrix}\epsilon_x + \begin{bmatrix} 1 \\ 1 \end{bmatrix}\alpha. \tag{14}$$

3.2 Discrete Beam Element. Derivation of the desired displacement-strain relation for a beam element presents both challenges and new insight into the advantages of strain-based system identification. If one employs the Euler-Bernoulli formulation of a plane beam element, it is well known that the bending strains are evaluated at two Barlow points, viz., $\xi = \pm 1/\sqrt{3}$, where the beam axial coordinate x is given by $\{x = l\xi/2, -1 \leqslant \xi \leqslant 1\}$. The bending strain-displacement relation for an element is thus given by ([4])

$$\mathbf{s} = \begin{Bmatrix} \kappa_1(\xi = -1/\sqrt{3}) \\ \kappa_2(\xi = 1/\sqrt{3}) \end{Bmatrix} = \mathbf{S}^T\mathbf{u}, \quad \mathbf{u}^T = \{w_1 \quad \theta_1 \quad w_2 \quad \theta_2\}$$
$$\mathbf{S}^T = \frac{1}{l^2}\begin{bmatrix} -2\sqrt{3} & -(1+\sqrt{3})l & 2\sqrt{3} & (1-\sqrt{3})l \\ 2\sqrt{3} & (-1+\sqrt{3})l & -2\sqrt{3} & (1+\sqrt{3})l \end{bmatrix} \tag{15}$$

where (w_1, w_2) and (θ_1, θ_2) are the vertical and rotational beam displacements at the element endpoints, (κ_1, κ_2) are the bending strains or curvatures at the two Barlow points, and l is the beam length. The elemental rigid-body modes include one translation and one rotation, which can be shown to be

$$\boldsymbol{\Phi}_\alpha^T = \begin{bmatrix} 1 & 0 & 1 & 0 \\ -l & 2 & l & 2 \end{bmatrix}. \tag{16}$$

When the preceding two expressions are substituted into (9) and (10), we obtain the desired strain-to-displacement relation.

$$\begin{bmatrix} w_1 \\ \theta_1 \\ w_2 \\ \theta_2 \end{bmatrix} = \frac{\sqrt{3}}{6(l^2+4)} \times \begin{bmatrix} -l^2 & l^2 \\ 2\sqrt{3}l - \frac{1}{2}(\sqrt{3}+1)l^3 & 2\sqrt{3}l + \frac{1}{2}(-\sqrt{3}+1)l^2 \\ l^2 & -l^2 \\ 2\sqrt{3}l + \frac{1}{2}(\sqrt{3}-1)l^3 & 2\sqrt{3}l + \frac{1}{2}(\sqrt{3}+1)l^3 \end{bmatrix} \times \begin{Bmatrix} \kappa_1 \\ \kappa_2 \end{Bmatrix} + \begin{bmatrix} 1 & -l \\ 0 & 2 \\ 1 & l \\ 0 & 2 \end{bmatrix}\begin{Bmatrix} \alpha_w \\ \alpha_\theta \end{Bmatrix} \tag{17}$$

3.3 Determination of Rotation Degrees-of-Freedom. Observe that the preceding strain-to-displacement relation states that if strain is measured at the two strain sensor locations, along with the two translations (w_1, w_2), the rotations (θ_1, θ_2) and the two rigid-mode amplitudes $(\alpha_w, \alpha_\theta)$ can be obtained for a beam element. This is accomplished in the following manner, as presented by Park and Reich [5]. Equation (10) is partitioned into translation and rotation:

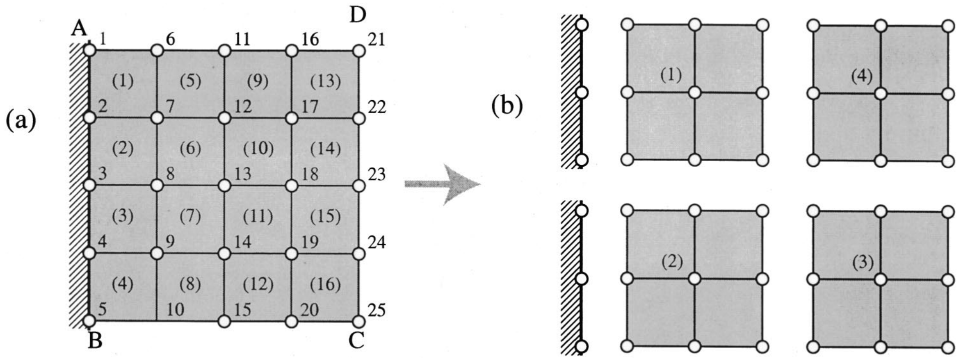

Fig. 1 Example of partitioning into four substructures

$$\begin{Bmatrix} \mathbf{u}_w \\ \mathbf{u}_\theta \end{Bmatrix} = \begin{bmatrix} \mathbf{\Phi}_{s_w} \\ \mathbf{\Phi}_{s_\theta} \end{bmatrix} \mathbf{s} + \begin{bmatrix} \mathbf{\Phi}_{\alpha_w} \\ \mathbf{\Phi}_{\alpha_\theta} \end{bmatrix} \boldsymbol{\alpha} \tag{18}$$

where

$$\mathbf{u}_w = \begin{Bmatrix} w_1 \\ w_2 \end{Bmatrix} \qquad \mathbf{u}_\theta = \begin{Bmatrix} \theta_1 \\ \theta_2 \end{Bmatrix} \tag{19}$$

with similar partitions on $\mathbf{\Phi}_s$ and $\mathbf{\Phi}_\alpha$. This equation is rewritten to solve for the unknown rigid-body amplitudes and rotational degrees-of-freedom

$$\begin{Bmatrix} \boldsymbol{\alpha} \\ \mathbf{u}_\theta \end{Bmatrix} = \mathbf{A}^{-1} \left\{ \begin{bmatrix} \mathbf{\Phi}_{s_w} \\ \mathbf{\Phi}_{s_\theta} \end{bmatrix} \mathbf{s} - \begin{bmatrix} \mathbf{I} \\ \mathbf{0} \end{bmatrix} \mathbf{u}_w \right\}$$
$$\mathbf{A} = \begin{bmatrix} -\mathbf{\Phi}_{\alpha_w} & \mathbf{0} \\ -\mathbf{\Phi}_{\alpha_\theta} & \mathbf{I} \end{bmatrix}. \tag{20}$$

From the last equation, it is clear that the rotations and rigid-body amplitudes can be uniquely determined in this manner. The only assumptions in this exercise are the geometry and element type, so as long as the model chosen is a reasonable match to the physical reality, this estimate of the rotation at the element endpoints should be valid. The results of this procedure can be utilized in several ways. If the global model is desired, then the rotations can be determined and used in a global system identification procedure as in Section 2. Alternatively, the rigid-body amplitudes can be determined and used in a strain-based identification process with applications in damage detection and health monitoring ([6]) or model updating. Both options will be discussed in the following sections.

4 Strain-Based Equations of Motion

As described in the previous section, conventional structural system identification utilizes the excitation forces and the accelerations as the input and output quantities. This practice precludes the use of other sensor output such as strains and deformations, which has hampered the use of piezoelectric strain gauges, optical fibers, and other embedded sensors in the system identification process. In order to more effectively make use of such sensors, we wish to determine the equations of motion in terms of these localized strain quantities.

To this end, consider a structure partitioned into substructures as shown in Fig. 1. Note that, after partitioning, the global nodes that lie on the partition boundaries are co-owned by two or more substructures. For example, global node 13 is co-owned by the four substructures while global node 3 is co-owned by substructures 1 and 2. In other words, partitioning is a disassembly process given by

$$\underset{\substack{\text{Partitioned} \\ \text{displacement}}}{\mathbf{u}} \underset{\Leftarrow}{=} \underset{\substack{\text{Partioning} \\ \text{operator}}}{\mathbf{L}} \cdot \underset{\substack{\text{Assembled} \\ \text{displacement}}}{\mathbf{u}_g} \tag{21}$$

where $\mathbf{L}$ is the assembly Boolean matrix that relates the global and substructural displacements. In addition, the global stiffness matrix $\mathbf{K}_g$ is formed by the assembly of individual substructural stiffnesses via the assembly operator $\mathbf{L}$:

$$\mathbf{K}_g = \mathbf{L}^T \mathbf{K} \mathbf{L}, \quad \mathbf{K} = \begin{bmatrix} \mathbf{K}^{(1)} & & & & \\ & \mathbf{K}^{(2)} & & & \\ & & \mathbf{K}^{(3)} & & \\ & & & \ddots & \\ & & & & \mathbf{K}^{(n_s)} \end{bmatrix} \tag{22}$$

where $\mathbf{K}$ is the block-diagonal collection of unassembled substructural stiffness matrices $\mathbf{K}^{(s)}$. The force vector that is conjugate with the substructural displacement is given by

$$\mathbf{L}^T \mathbf{f} = \mathbf{f}_g \tag{23}$$

where it is noted that $\mathbf{L}^T$ acts as an assembly operator whereas $\mathbf{L}$ is a disassembly operator as shown in (21).

It is important to note that only part of the total substructural displacements $\mathbf{u}$ lie on the substructural boundaries. The substructural boundary displacements, if they are to satisfy the equilibrium state for the global structure, must be constrained so that those displacements that are co-owned by the assembled structure be the same. This can be mathematically stated by using (21) as follows:

$$\mathbf{B}_\lambda^T (\mathbf{u} - \mathbf{L} \mathbf{u}_g) = 0 \tag{24}$$

where $\mathbf{B}_\lambda$ is a Boolean operator which extracts the partition boundary nodes of all the partitioned substructures.

The system energy with constraints can thus be stated as

$$\mathbf{\Pi}(\mathbf{u}, \boldsymbol{\lambda}, \mathbf{u}_g) = \mathbf{u}^T \left(\frac{1}{2} \mathbf{K}\mathbf{u} - \mathbf{f} + \mathbf{M}\ddot{\mathbf{u}} + \mathcal{D}\dot{\mathbf{u}} \right) + \boldsymbol{\lambda}^T \mathbf{B}_\lambda^T (\mathbf{u} - \mathbf{L}\mathbf{u}_g) \tag{25}$$

where $\mathbf{M}$ and $\mathcal{D}$ are the substructural mass and damping matrices, respectively, and $\boldsymbol{\lambda}$ are the localized Lagrangian multipliers or interface forces between respective substructures. The strain-to-displacement relation (10) can now be introduced into the constrained system energy expression (25) to yield

$$\boldsymbol{\Pi}(\mathbf{s},\boldsymbol{\alpha},\boldsymbol{\lambda},\mathbf{u}_g)=(\boldsymbol{\Phi}_s\mathbf{s}+\boldsymbol{\Phi}_\alpha\boldsymbol{\alpha})^T\left\{\frac{1}{2}\mathbf{K}(\boldsymbol{\Phi}_s\mathbf{s}+\boldsymbol{\Phi}_\alpha\boldsymbol{\alpha})-\mathbf{f}+\mathbf{M}(\boldsymbol{\Phi}_s\ddot{\mathbf{s}}+\boldsymbol{\Phi}_\alpha\ddot{\boldsymbol{\alpha}})+\mathcal{D}(\boldsymbol{\Phi}_s\dot{\mathbf{s}}+\boldsymbol{\Phi}_\alpha\dot{\boldsymbol{\alpha}})\right\}+\boldsymbol{\lambda}^T\mathbf{B}_\lambda^T\{(\boldsymbol{\Phi}_s\mathbf{s}+\boldsymbol{\Phi}_\alpha\boldsymbol{\alpha})-\mathbf{L}\mathbf{u}_g\}. \tag{26}$$

The stationary value of $\delta\boldsymbol{\Pi}$ in the previous equation thus yields the following matrix equation set:

$$\begin{bmatrix} \left(\mathbf{M}_s\frac{d^2}{dt^2}+\mathcal{D}_s\frac{d}{dt}+\mathbf{K}_s\right) & \left(\mathbf{M}_{s\alpha}\frac{d^2}{dt^2}+\mathcal{D}_{s\alpha}\frac{d}{dt}\right) & \boldsymbol{\Phi}_s^T\mathbf{B}_\lambda & \mathbf{0} \\ \left(\mathbf{M}_{s\alpha}^T\frac{d^2}{dt^2}+\mathcal{D}_{s\alpha}^T\frac{d}{dt}\right) & \left(\mathbf{M}_\alpha\frac{d^2}{dt^2}+\mathcal{D}_\alpha\frac{d}{dt}\right) & \boldsymbol{\Phi}_\alpha^T\mathbf{B}_\lambda & \mathbf{0} \\ \mathbf{B}_\lambda^T\boldsymbol{\Phi}_s & \mathbf{B}_\lambda^T\boldsymbol{\Phi}_\alpha & \mathbf{0} & -\mathbf{L}_b \\ \mathbf{0} & \mathbf{0} & -\mathbf{L}_b^T & \mathbf{0} \end{bmatrix} \times\begin{Bmatrix}\mathbf{s}\\ \boldsymbol{\alpha}\\ \boldsymbol{\lambda}\\ \mathbf{u}_g\end{Bmatrix}=\begin{Bmatrix}\boldsymbol{\Phi}_s^T\mathbf{f}\\ \boldsymbol{\Phi}_\alpha^T\mathbf{f}\\ \mathbf{0}\\ \mathbf{0}\end{Bmatrix} \tag{27}$$

where $\mathbf{L}_b=\mathbf{B}_\lambda^T\mathbf{L}$. Since the measured output vector consists of the strain $\mathbf{s}$ and the rigid-body amplitude $\boldsymbol{\alpha}$, we eliminate $\boldsymbol{\lambda}$ and $\mathbf{u}_g$ from the preceding equation. This can be accomplished as follows. First, we recast the first two rows in (27) in the form

$$\mathbf{M}_\phi\ddot{\mathbf{q}}=\mathbf{b}-\boldsymbol{\Phi}_b\boldsymbol{\lambda},\quad \boldsymbol{\Phi}_b=\boldsymbol{\Phi}^T\mathbf{B}_\lambda \qquad \mathbf{b}=\boldsymbol{\Phi}^T\mathbf{f}-\mathcal{D}_\phi\dot{\mathbf{q}}-\mathbf{K}_\phi\mathbf{q} \tag{28}$$

where $\mathbf{q}^T=\{\mathbf{s}^T\ \alpha^T\}$ and the strain-based matrices are given by

$$\mathbf{K}_\phi=\boldsymbol{\Phi}^T\mathbf{K}\boldsymbol{\Phi}=\begin{bmatrix}\mathbf{K}_s & \mathbf{0}\\ \mathbf{0} & \mathbf{0}\end{bmatrix} \qquad \mathcal{D}_\phi=\boldsymbol{\Phi}^T\mathcal{D}\boldsymbol{\Phi}=\begin{bmatrix}\mathcal{D}_s & \mathcal{D}_{s\alpha}\\ \mathcal{D}_{s\alpha}^T & \mathcal{D}_\alpha\end{bmatrix},\quad \mathbf{M}_\phi=\boldsymbol{\Phi}^T\mathbf{M}\boldsymbol{\Phi}=\begin{bmatrix}\mathbf{M}_s & \mathbf{M}_{s\alpha}\\ \mathbf{M}_{s\alpha}^T & \mathbf{M}_\alpha\end{bmatrix}. \tag{29}$$

The third row of (27), after time-differentiating twice, can be expressed as

$$\boldsymbol{\Phi}_b^T\ddot{\mathbf{q}}-\mathbf{L}_b\ddot{\mathbf{u}}_g=0 \tag{30}$$

which, upon into substituting (28), becomes

$$\boldsymbol{\Phi}_b^T\mathbf{M}_\phi^{-1}\{\mathbf{b}-\boldsymbol{\Phi}_b\boldsymbol{\lambda}\}-\mathbf{L}_b\ddot{\mathbf{u}}_g=0. \tag{31}$$

Hence, $\boldsymbol{\lambda}$ can be solved to yield

$$\boldsymbol{\lambda}=\mathbf{M}_b\{\boldsymbol{\Phi}_b^T\mathbf{M}_\phi^{-1}\ddot{\mathbf{q}}-\mathbf{L}_b\ddot{\mathbf{u}}_g\},\quad \mathbf{M}_b=(\boldsymbol{\Phi}_b^T\mathbf{M}_\phi^{-1}\boldsymbol{\Phi}_b)^{-1}. \tag{32}$$

Substituting this into the last row of (27), one obtains

$$\ddot{\mathbf{u}}_g=\mathbf{M}_L^{-1}\mathbf{L}_b^T\mathbf{M}_b\boldsymbol{\Phi}_b^T\mathbf{M}_\phi^{-1}\mathbf{b},\quad \mathbf{M}_L=\mathbf{L}_b^T\mathbf{M}_b\mathbf{L}_b \tag{33}$$

Finally, from the preceding two equations, $\boldsymbol{\lambda}$ is obtained as

$$\boldsymbol{\lambda}=\mathbf{P}_b\boldsymbol{\Phi}_b^T\mathbf{M}_\phi^{-1}\mathbf{b},\quad \mathbf{P}_b=\mathbf{M}_b-\mathbf{M}_b\mathbf{L}_b\mathbf{M}_L^{-1}\mathbf{L}_b^T\mathbf{M}_b \tag{34}$$

Eliminating $\boldsymbol{\lambda}$ from (27) and (34), we obtain the desired input-output relation:

$$\mathbf{M}_\phi\ddot{\mathbf{q}}=\mathbf{P}_\phi\mathbf{b}=\mathbf{P}_\phi\{\boldsymbol{\Phi}^T\mathbf{f}-\mathcal{D}_\phi\dot{\mathbf{q}}-\mathbf{K}_\phi\mathbf{q}\} \qquad \mathbf{P}_\phi=\mathbf{I}-\boldsymbol{\Phi}_b\mathbf{P}_b\boldsymbol{\Phi}_b^T\mathbf{M}_\phi^{-1} \tag{35}$$

which can be rearranged in a standard second-order form

$$\mathbf{M}_\phi\ddot{\mathbf{q}}+\mathbf{P}_\phi\mathcal{D}_\phi\dot{\mathbf{q}}+\mathbf{P}_\phi\mathbf{K}_\phi\mathbf{q}=\mathbf{P}_\phi\mathbf{f}_\phi,\quad \mathbf{f}_\phi=\boldsymbol{\Phi}^T\mathbf{f}. \tag{36}$$

This equation is designated as the *strain-based* equation of motion for linear structures. We will employ this equation to develop a strain output-based structural system identification in the next section.

5 System Identification Based on Strain-Based Measured Input and Output Data

System identification based on the strain-based equations of motion (36) is in many respects no different from conventional methods based on the global equations of motion (2). In order for the reader to connect the present method to conventional methods, we first offer their relations by means of coordinate transformation procedures.

First, the strain-to-displacement relation (10) and the global-to-substructural displacement relation (21) can be combined to give

$$\mathbf{q}=\begin{Bmatrix}\mathbf{s}\\ \boldsymbol{\alpha}\end{Bmatrix}=\boldsymbol{\Phi}^{-1}\mathbf{L}\mathbf{u}_g. \tag{37}$$

Second, the external energy invariance condition gives

$$\mathbf{u}_g^T\mathbf{f}_g=\mathbf{u}^T\mathbf{f}=\mathbf{q}^T\mathbf{f}_\phi\Rightarrow\mathbf{f}_g=\mathbf{L}^T\boldsymbol{\Phi}^{-T}\mathbf{f}_\phi. \tag{38}$$

Substituting the global displacement-based frequency response functions (4) into (37) and making use of (38), we obtain the desired frequency response function in terms of strains:

$$\overline{\mathbf{q}}=\mathbf{H}_\phi(\omega)\overline{\mathbf{f}_\phi} \qquad \mathbf{H}_\phi(\omega)=\boldsymbol{\Phi}^{-1}\mathbf{L}\mathbf{H}_g(\omega)\mathbf{L}^T\boldsymbol{\Phi}^{-T}. \tag{39}$$

Note from (36) that the analytical strain-based frequency response functions $\mathbf{H}_\phi(\omega)$ can also be expressed as

$$\mathbf{H}_\phi(\omega)=\{-\omega^2\mathbf{M}_\phi+j\omega\mathbf{P}_\phi\mathcal{D}_\phi+\mathbf{P}_\phi\mathbf{K}_\phi\}^{-1}\mathbf{P}_\phi. \tag{40}$$

Given the information in this and previous sections, we can formulate a logical procedure for strain-based structural system identification. While not unique, these steps outline the most logical path for substructural-based damage detection and model updating ([6]).

Step 1: Using the strains $\mathbf{s}$ and the selected translational displacements (u,v,w), obtain the rigid-body amplitudes $\boldsymbol{\alpha}$ from (10) to determine the strain-based output vector $\mathbf{y}=\mathbf{q}$.

Step 2: Using (38), obtain the strain-based input signal $\mathbf{f}_\phi$.

Step 3: Using the strain-based input and output $\{\mathbf{f}_\phi,\mathbf{y}\}$, obtain the Markov parameters (discrete impulse response) or the frequency response functions (see, e.g., [7]).

Step 4: Perform system realization using the Markov parameters determined from Step 3 to obtain $(\mathbf{A},\mathbf{B},\mathbf{C},\mathbf{D})$ that describe the state space model given by (see, e.g., [1])

$$\dot{\mathbf{x}}(t)=\mathbf{A}\mathbf{x}(t)+\mathbf{B}\mathbf{f}_\phi(t),\quad \mathbf{x}^T=\{\mathbf{s}^T\ \ \boldsymbol{\alpha}^T\ \ \dot{\mathbf{s}}^T\ \ \dot{\boldsymbol{\alpha}}^T\} \qquad \mathbf{y}(t)=\mathbf{C}\mathbf{x}(t)+\mathbf{D}\mathbf{f}_\phi(t) \tag{41}$$

$$\mathbf{A}=\begin{bmatrix}\mathbf{0} & \mathbf{I}\\ -\mathbf{M}_\phi^{-1}\mathbf{P}_\phi\mathbf{K}_\phi & -\mathbf{M}_\phi^{-1}\mathbf{P}_\phi\mathcal{D}_\phi\end{bmatrix},\quad \mathbf{B}=\begin{bmatrix}\mathbf{0}\\ \mathbf{M}_\phi^{-1}\mathbf{P}_\phi\end{bmatrix}$$

where $\mathbf{C}$ and $\mathbf{D}$ are the output and direct transmission operators, respectively.

Step 5: Using the procedure of Alvin and Park [2] obtain the strain-based structural parameters $(\mathbf{M}_\phi,\mathcal{D}_\phi,\mathbf{K}_\phi)$ for damage detection or model updating applications.

Alternatively, Step 5 could be replaced by two steps which result in global structural parameters:

Step 5a: Using (37) and (38), transform the strain-based matrices $(\mathbf{A},\mathbf{B},\mathbf{C},\mathbf{D})$ into the global form.

Step 5b: Obtain global structural parameters $(\mathbf{M}_g,\mathcal{D}_g,\mathbf{K}_g)$ via the procedure of Alvin and Park [2].

6 Illustrative Examples

In order to demonstrate the strain-based system identification procedure outlined in the preceding section, two examples are presented. The first is a simple two-element cantilever beam which illustrates directly the concepts presented in the previous sections. The second example is the identification of a continuum structure, namely a cantilever plate. This second example high-

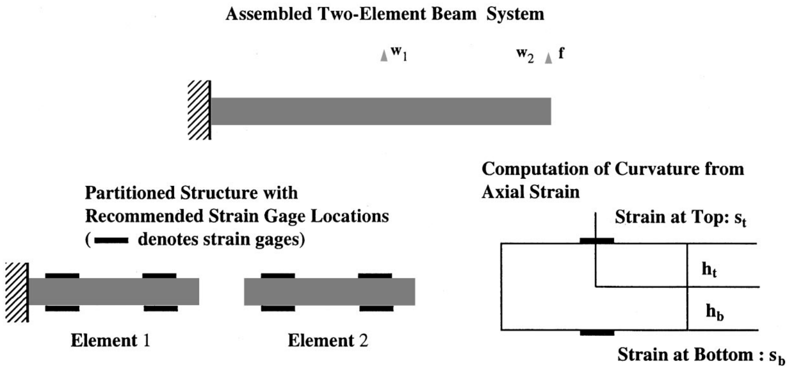

Fig. 2 Partitioned two-beam system

lights some of the advantages of the present procedure when the goal includes localization as well as measurement and identification.

6.1 Cantilever Beam. The first example is a numerical simulation of a simple two-element beam. It is used to demonstrate the ability of the strain-based system identification procedure to determine rotational motion without direct measurements. The dynamics of the global system are reconstructed from the identified mass, damping, and stiffness matrices from a simulated strain-based system realization test. These are compared to the system frequency response functions reconstructed from a global system realization analysis which include the rotation measurements directly.

The cantilever beam is modeled with two Bernoulli beam elements as shown in Fig. 2. In the strain-based numerical evaluation, two transverse displacements (w_1, w_2) and four strains, at the two Barlow points for each element, are measured. The bending strain at a location is computed by placing two axial strain gauges as shown in Fig. 2 according to

$$\mathbf{s} = \frac{1}{2}\left(\frac{\mathbf{s}_t}{h_t} - \frac{\mathbf{s}_b}{h_b}\right). \tag{42}$$

For the global system realization, the transverse displacement and rotation at each node is measured.

A burst random input is applied vertically at the free end and subsequently is transformed into the strain-based force $\mathbf{f}_\phi$. After carrying out the strain-based realization (Steps 2–4), the structural matrices $(\mathbf{M}_g, \mathcal{D}_g, \mathbf{K}_g)$ are obtained as described by Steps 5a and 5b. The global realization is done based on traditional system realization practices. For both sets of analysis, the mass, damping, and stiffness matrices are used to reconstruct the system frequency response functions. Figure 3 shows both sets of reconstructed frequency response functions. Observe that, even though no rotation is measured, the present strain-based realization procedure provides the frequency response function corresponding to rotational degrees of freedom. The strain-based rotational frequency response function lies directly on top of the global rotational frequency response function, which indicates that the strain-based rotations are the same as they would be if they had been measured directly. This information would not be available from most existing system identification procedures without explicit measurement of the rotation degrees-of-freedom.

6.2 Continuum Structure. The second example is a cantilever plate, modeled with 12 elements as shown in Fig. 4. The

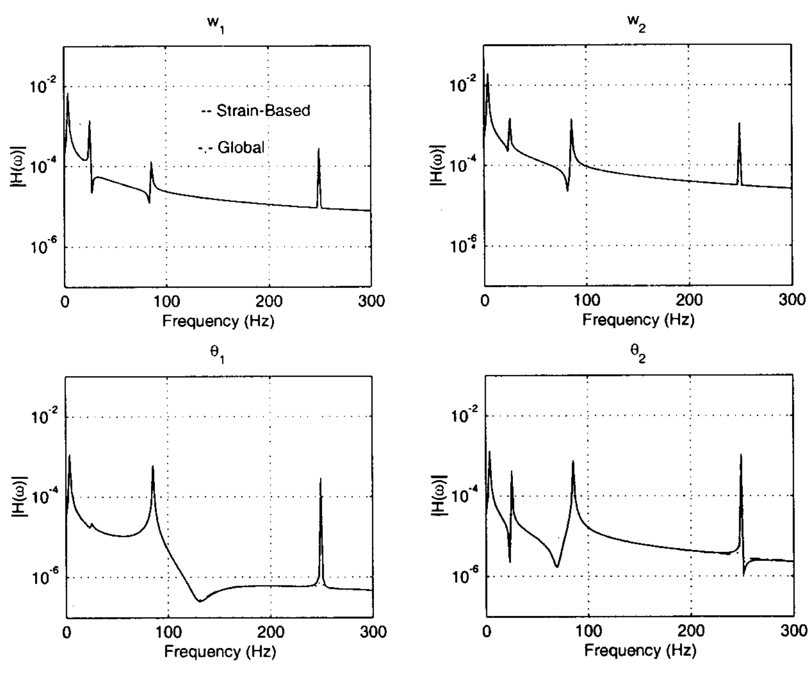

Fig. 3 Comparison of strain-based realization versus global realization

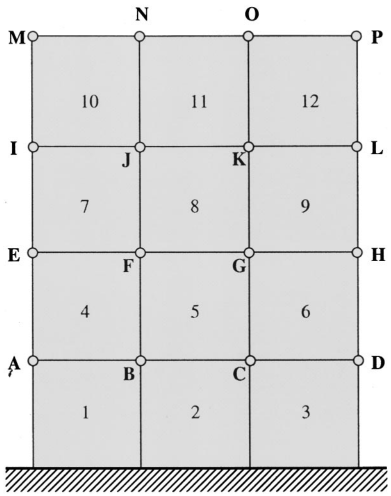

Fig. 4 Cantilevered plate

goal of this exercise is to determine the system parameters of mass and stiffness, or the combination of mass-normalized stiffness as in Eq. (43), based on a reduced set of sensor locations. These may include rotation degrees-of-freedom, which may be difficult or impossible to determine directly. An alternative is to measure strain and then compute rotations in post-processing, for which it is necessary to determine locations at which strain is to be measured. There are a number of equivalent sets of strain measurements possible. The set we choose to measure is pictured in Fig. 5. There are 20 strain gauges on each element used to determine nine bending strains, as we wish to completely describe the dynamics of each element. There are 12 displacements for each free-free plate element, minus three rigid-body modes, leaving nine flexible degrees-of-freedom which must be accounted for. Because we wish to determine not only the strain state, but also the rigid-body dynamics of each element, we also measure the transverse displacement at each node, as in Fig. 5. This allows us to solve for the rigid-body variables as in Eq. (20). Only six strain degrees-of-freedom are required for elements at a natural boundary, equal to the number of degrees-of-freedom of each fixed-free element.

A vibration test for the plate in Fig. 4 was simulated using a burst-random signal at two input locations. The system response, consisting of 16 displacements and 99 strains, was calculated due

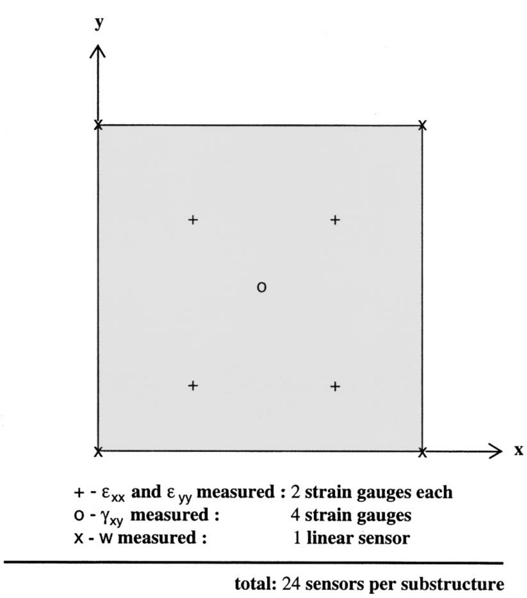

Fig. 5 Elemental strain measurement locations

to the force input at 4 kHz. The input and output were then anti-aliased and resampled at 2 kHz, sufficient to capture the first 15 flexible modes of the system. System identification was done on the resulting 115 degree-of-freedom localized system. For comparison, a separate system identification analysis was done using the 16 translational displacements at the nodes.

A method of comparison of the quality of the identified model is to determine a mass-normalized stiffness

$$\tilde{\mathbf{K}} = \mathbf{M}^{-1/2}\mathbf{K}\mathbf{M}^{-1/2}. \tag{43}$$

Reduced-order mass and stiffness matrices based on the measured system modes corresponding to selected sensor locations can be computed as in the previous example. For instance, if the sensor locations at nodes I, J, K, and N are chosen, then the transverse displacement-only (TDO) mass-normalized stiffness matrix $\tilde{\mathbf{K}}$ from Eq. (43) is determined to be

$$\tilde{\mathbf{K}}_{TDO} = 10^6 \begin{bmatrix} 3.9370 & -3.7017 & -0.1439 & -0.8441 \\ -3.7017 & 4.4683 & 0.0743 & 0.7395 \\ -0.1439 & 0.0743 & 0.3131 & -0.1796 \\ -0.8441 & 0.7395 & -0.1796 & 0.3989 \end{bmatrix} \tag{44}$$

where

$$\tilde{\mathbf{K}}_{exact} = 10^6 \begin{bmatrix} 4.8399 & -4.4907 & 0.2824 & -1.3607 \\ -4.4907 & 5.1490 & -0.3743 & 1.2469 \\ 0.2824 & -0.3743 & 0.3461 & -0.3015 \\ -1.3607 & 1.2469 & -0.3015 & 0.6058 \end{bmatrix} \tag{45}$$

is the analytical Guyan-reduced matrix ([8]) for the selected sensor set (which is determined based on a full set of eigensolutions, rather than the measured set used to determine $\tilde{\mathbf{K}}_{TDO}$). The error norm of the matrices, defined as

$$\frac{\|\tilde{\mathbf{K}}_{TDO} - \tilde{\mathbf{K}}_{exact}\|}{\|\tilde{\mathbf{K}}_{exact}\|} \tag{46}$$

can also be determined to compare the results. $\tilde{\mathbf{K}}_{TDO}$ has about 21 percent error in the matrix norm as compared with $\tilde{\mathbf{K}}_{exact}$.

On the other hand, the strain-based identification procedure, using the same set of measured modes, can be used to determine a 12 degree-of-freedom equivalent model which contains transverse displacements as well as the two rotations at the selected nodes. The resultant model matrices can then be reduced to the four transverse displacements using Guyan reduction. This strain-based (SB) mass-normalized stiffness matrix is found to be

$$\tilde{\mathbf{K}}_{SB} = 10^6 \begin{bmatrix} 5.4342 & -4.6592 & -0.3427 & -0.8092 \\ -4.9235 & 5.1698 & 0.2558 & 0.6672 \\ -0.4680 & 0.3512 & 0.3461 & -0.1516 \\ -0.9527 & 0.7674 & -0.1602 & 0.3705 \end{bmatrix}. \tag{47}$$

This matrix has approximately 15 percent error in matrix norm as compared to the analytical model. Additionally, the transverse displacement model ($\tilde{\mathbf{K}}_{TDO}$) has an average of about 19 percent error in the diagonal value of the matrix, while the strain-based version contains approximately 13 percent error on the diagonal. Finally, Table 1 shows that the reduced-order eigenvalues from the strain-based (SB) model offer definite improvement over the transverse displacement-only model. The eigenvectors, in Table 2, are of comparable quality with respect to the analytical model, as evidenced by similar values in the modal assurance criterion (MAC). This shows that the inclusion of rotation degree-of-freedom may be able to improve the quality of the identified model parameters for reduced sensor set selection, even if rotation sensors are not included in the final sensor set.

Table 1 Eigenvalue comparison for the reduced-order models

	Analytical Model	TDO Model		SB Model	
Mode #	E'Value	E'Value	% Error	E'Value	% Error
1	3.81×10^4	3.80×10^4	-0.17	3.85×10^4	0.98
2	4.76×10^5	4.63×10^5	-2.83	4.94×10^4	3.64
3	5.44×10^5	5.38×10^5	-1.04	5.43×10^5	-0.14
4	9.88×10^6	8.08×10^6	-18.26	1.02×10^7	3.67

6.3 Discussion. One criticism of the present methodology in regards to continuum structures is the large number of sensors required to completely describe the dynamics of a single substructure or element. It is true that there is a considerable increase in the model order, and therefore computational cost of determining such models. However, consider the situation where we wish to determine the local displacements and rotations such that an element is completely characterized. A common setup for this situation is pictured on the left in Fig. 6. While this is an acceptable configuration for measuring response, the eight measured degrees-of-freedom are not sufficient to completely characterize the element. It is important to note that we are not interested in simply measuring response. We are interested in localization, which requires us to measure enough spatial data to resolve the dynamics of each substructure independently.

On the right in Fig. 6 we have a more realistic setup for determining the rotations at each of the four corner nodes of the plate element. Because we cannot mount the rotation sensors on top of the displacement sensor at the node, we must place two sensors on sides opposite the node and then interpolate the value at the node. This must be done for both rotation angles at the node, and therefore requires four sensors to measure the two rotations at each node. In the end, in order to completely determine the displacement field for one free-free element, 20 measurements must be taken, whereas 24 must be taken using a combination of displacements and strains as was suggested in Section 5.

It may seem then that it would be of greater advantage to use these 20 translational sensors to characterize the dynamics on one element. However, there are several issues which force consideration of a strain-based system. The first of these is clutter. The strain-based measurements are spread out over the surface of the structure, which improves the access to each sensor and greatly reduces the amount of sensor clutter occurring around the node locations. The second issue is weight. The weight difference between accelerometers or rotation rate sensors and strain gauges is very large. Strain gauges add essentially no nonstructural mass to the system. The same cannot be said for accelerometers or rotational sensors.

Table 2 Eigenvector comparison for the reduced-order models

	TDO Model	SB Model
Mode #	MAC	MAC
1	1.000	1.000
2	0.999	0.997
3	1.000	0.973
4	0.977	0.962

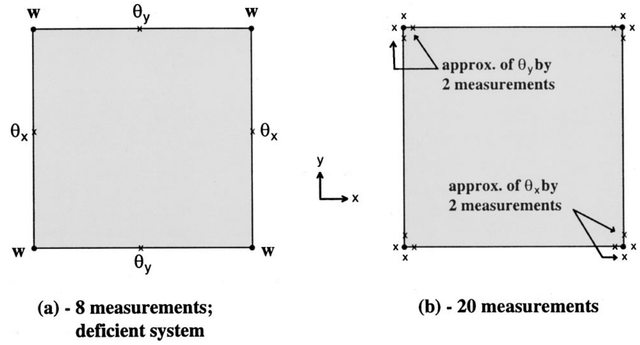

Fig. 6 Two methods for measuring rotation angles

Finally, the issue of cost must be addressed. Rotation sensors are expensive, costing anywhere from \$500–2500 each. Strain gauges, on the other hand, are extremely inexpensive, on the order of \$1–10 each. Even in the ideal case where the number of required rotation angle sensors equals the number of rotation degrees-of-freedom, a large cost disparity still exists between the two methods of measurement. So, in terms of hardware cost and sensor clutter, it appears that a combination of nodal displacements and elemental strains may be a better method of determining the local dynamics of a continuum structure.

7 Conclusions

A theory for strain-based structural identification is developed. The present theory, when used in conjunction with strain and translational displacement sensors, can identify the system characteristics that consist of translational as well as rotational degrees-of-freedom. The state variables consist of the strains and the rigid-body amplitudes of substructures for which the corresponding set of measured strains are utilized.

The present theory becomes attractive in utilizing embedded piezoelectric sensors, embedded fiber optics and other microelectronic high-precision sensors, thus opening possibilities in tune with recent advances in sensor miniaturization technology. To the best of the authors' knowledge, this has not been presented in the literature.

In order to render the present strain output-based identification theory practical to the structural identification community, several implementation and computational procedures need to be developed. These include the development of an instrumentation guide so that measured strain gauge outputs can reflect the theory as closely as possible, and experimental validation for typical structural elements and substructures.

Acknowledgments

It is a pleasure to acknowledge support by the National Science Foundation under a grant entitled High Performance Computer Simulation of Multiphysics Problems (Grant Number ECS-9725504), Sandia National Laboratories (Contract AP-1461), and a donation from Shimizu Corporation. The support of the first author was provided by the U.S. Air Force under the Palace Knight Program. We would like to thank Dr. K. F. Alvin of Sandia and Dr. Haru Namba of Shimizu for their enthusiasm and interest during the course of the research reported herein.

References

[1] Juang, J. N., and Pappa, R. S., 1985, "An Eigensystem Realization Algorithm for Modal Parameter Identification and Model Reduction," J. Guid. Control Dyn., **8**, No. 5, pp. 620–627.
[2] Alvin, K. F., and Park, K. C., 1994, "Second-Order Structural Identification Procedure via State-Space-Based System Identification," AIAA J., **32**, No. 2, pp. 397–406.
[3] Park, K. C., and Felippa, C. A., 1998, "A Variational Framework for Solution Method Developments in Structural Mechanics," ASME J. Appl. Mech., **65**, No. 1, pp. 242–249.
[4] Zienkiewicz, O. C., and Taylor, R. E., 1989, *The Finite Element Method*, Vol. 1, 4th Ed., McGraw-Hill, New York.
[5] Park, K. C., and Reich, G. W., 1999, "A Procedure to Determine Accurate Rotations From Measured Strains and Displacements for System Identification," *Proc. 17th International Modal Analysis Conference*, Kissimmee, FL.
[6] Reich, G. W., and Park, K. C., 2001, "Use of Substructural Transmission Zeros for Structural Health Monitoring," AIAA J., **38**, No. 6, pp. 1040–1046.
[7] Robertson, A. N., Park, K. C., and Alvin, K. F., 1998, "Extraction of Impulse Response Data via Wavelet Transform for Structural System Identification," ASME J. Vibr. Acoust., **120**, No. 1, pp. 252–260.
[8] Guyan, R. J., 1965, "Reduction of Stiffness and Mass Matrices," AIAA J., **3**, No. 2, p. 380.

J. J. Luo
Research Associate,
Mem. ASME

I. M. Daniel
Professor,
Fellow ASME

Robert R. McCormick School of Engineering
and Applied Science,
Northwestern University,
Evanston, IL 60208

Deformation of Inhomogeneous Elastic Solids With Two-Dimensional Damage

A general correlation is derived between macroscopic stresses/strains and microscopic deformation on the damage surfaces for inhomogeneous elastic solids with two-dimensional damage. Assuming linear elastic behavior for the undamaged materials, the macroscopic deformation associated with nonlinear strains, or damage strains, is shown to be the weighted sum of the microscopic deformations on the damage surfaces. For inhomogeneous materials with periodic structures (laminated composites, for example) and various identifiable damage modes, simple relations are derived between the macroscopic deformation and microscopic damage. When the number of identifiable damage modes is less than or equal to the number of relevant measurable macroscopic strains, the correlation can be used to evaluate the damage progression from simple macroscopic stress and strain measurements. The simple case of a unidirectional fiber-reinforced composite under longitudinal load is used to show how the results can help detect and characterize the damage using macroscopic measurements, without resorting to assumptions of detailed microscopic deformation mechanisms. [DOI: 10.1115/1.1380384]

Introduction

It was shown by the authors ([1]) that the macroscopic mechanical behavior of unidirectional fiber-reinforced brittle matrix composites can be correlated explicitly with the microscopic deformation and damage. Although the statement was verified by an ad hoc cylinder theory, in this paper it is shown to be a result of a more general theory based on first principles.

Throughout this study, damage is assumed to occur only on two-dimensional internal surfaces. Linear elasticity is assumed at every point of the material. Results are presented after a general description of the deformation of solids with two-dimensional damage is given. For inhomogeneous materials with periodic structures, such as fiber composites, the results are much simpler and thus special attention is directed to unidirectional composites with brittle matrix damaged by longitudinal loading.

Various approaches have been developed in the past to study damage in elastic solids. In an important branch of micromechanics, the overall moduli of solids with voids and other inhomogeneities were studied by many investigators, see Mura [2] for an extensive list of references in the field. Several analytical and numerical methods ([3–7]) have been developed to determine the microscopic stress and strain distributions, and overall elastic moduli were calculated through clever averaging schemes. While based on first principles of mechanics, the approach usually requires explicit stress and strain distributions or crack-opening displacements in the damaged solids under study. This restricts their application to simple cases, and numerical schemes are often necessary for more complex ones.

For periodic structures like unidirectional fiber composites with identifiable damage modes, one has the luxury of estimating stress distributions in closed form, and a different approach can be adopted. Since the problems of periodic structures with damage usually defy analytical attempts to obtain exact closed form solutions, drastic assumptions (shear lag assumption, for example) are usually required ([8–14]). This approach usually leads to simplified equations and great physical insight to the problems under study. The drawback is that the model has to be developed case by case, for different materials and different loading conditions. Sometimes a mechanical phenomenon may not be covered by a theory, not because it is not mechanically related, but because the assumptions simply exclude any possibility to explain it. For example, transverse strains typically cannot be easily explained by a one-dimensional theory of unidirectional composites under longitudinal loading.

One can also make phenomenological assumptions on the constitutive equations of the materials with damage ([15–17]). Internal variables describing damage are linked to macroscopic deformation either through energy considerations or direct assumption of certain functional forms. Experimental data is required to characterize necessary phenomenological parameters. Solutions for microscopic stresses and strains are not necessary. The selection of internal variables and phenomenological laws are required to be mechanically sound so that useful results can be obtained—a goal not easily achieved. Phenomenological parameters acquired from experimental data are expected to have physical significance, but the lack of their correlation to fundamental properties through first principles leaves something to be desired.

In this paper, the authors try to approach the problems from first principles of solid mechanics, so that the results can be general and elegant. The correlation between macroscopic and microscopic deformation is also presented in a way that physical insight can be easily obtained and all parameters have solid physical significance. While no attempt is made to obtain the microscopic stress or strain distributions, the results are useful for material characterization and damage evaluation, especially for inhomogeneous materials with periodic structures.

Betti's Reciprocal Theorem

A modified version of Betti's reciprocal theorem is derived in this section so that the effect of initial (or residual) stresses is included. Consider a linear elastic body V with surface S and initial stress σ_{ij}^R. From Hooke's law, the strain ϵ_{kl} induced by the additional stress $(\sigma_{ij}-\sigma_{ij}^R)$ is determined by

$$\sigma_{ij}-\sigma_{ij}^R=c_{ijkl}\epsilon_{kl}, \tag{1}$$

Contributed by the Applied Mechanics Division of THE AMERICAN SOCIETY OF MECHANICAL ENGINEERS for publication in the ASME JOURNAL OF APPLIED MECHANICS. Manuscript received by the ASME Applied Mechanics Division, March 20, 2000; final revision, January 1, 2001. Associate Editor: D. Kouris. Discussion on the paper should be addressed to the Editor, Prof. Lewis T. Wheeler, Department of Mechanical Engineering, University of Houston, Houston, TX 77204-4792, and will be accepted until four months after final publication of the paper itself in the ASME JOURNAL OF APPLIED MECHANICS.

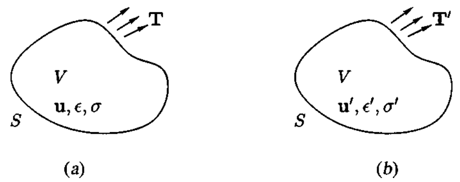

Fig. 1 An elastic body under traction T in (*a*) and T′ in (*b*)

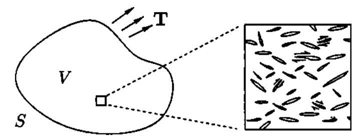

Fig. 2 A representative volume element in a solid with crack-like brittle damage occurring on two-dimensional surfaces. (The damage surfaces can be curved and possibly opened by the load T. Typical sizes of the damage and constituents are assumed to be much smaller than the element size.)

where c_{ijkl} is the stiffness tensor. The italic indices i and j range from 1 to 3 unless specified otherwise, and the Einstein summation convention is adopted. For the same body V, we assume two configurations, one under external loading T_i, and the other under T_i', as shown in Fig. 1.

Integrating the product of traction T_i and displacement u_i' over S, and using the divergence theorem, we have

$$\int_S T_i u_i' dS = \int_S \sigma_{ji} n_j u_i' dS = \int_V \sigma_{ij} \epsilon_{ij}' dV,$$

in which body forces are neglected. Substituting Eq. (1) into the above, we have

$$\int_S T_i u_i' dS = \int_V (\sigma_{ij}^R \epsilon_{ij}' + c_{ijkl} \epsilon_{kl} \epsilon_{ij}') dV.$$

The first term on the right-hand side can be converted to a surface integral

$$\int_V \sigma_{ij}^R \epsilon_{ij}' dV = \int_S \sigma_{ij}^R u_i' n_j dS = \int_S T_i^R u_i' dS,$$

where T_i^R is defined as the initial traction on surface S given by

$$T_i^R = \sigma_{ji}^R n_j . \tag{2}$$

Thus, we have

$$\int_S (T_i - T_i^R) u_i' dS = \int_V c_{ijkl} \epsilon_{kl} \epsilon_{ij}' dV.$$

Similarly, integrating the product of traction T_i' and displacement u_i over S gives

$$\int_S (T_i' - T_i^R) u_i dS = \int_V c_{ijkl} \epsilon_{kl}' \epsilon_{ij} dV.$$

From the above two equations and the symmetry property $c_{ijkl} = c_{klij}$, we obtain Betti's reciprocal theorem in the following form:

$$\int_S (T_i - T_i^R) u_i' dS = \int_S (T_i' - T_i^R) u_i dS. \tag{3}$$

Note that if the surface S is the external surface of the body, the initial traction T_i^R vanishes, and the regular form of Betti's reciprocal theorem is recovered. However, it will be made clear in the next section that the presence of T_i^R in the above equation is important when fictitious damage surfaces are involved.

Macroscopic Strains and Microscopic Damage

Consider a damaged inhomogeneous solid of volume V and surface S. Assume the damage in the solid to be "crack-like," i.e., the damage only occurs on internal surfaces S_k in the solid. The subscript k is used to index all damage surfaces so that S_k refers to the kth damage surface. At any point in any of the constituents Hooke's law is assumed to hold without being affected by the damage. The macroscopic behavior of the damaged composite can be nonlinear due to contact and/or friction of damage surfaces. If representative cells in the body can be chosen to give statistically meaningful averages of field quantities of interest, the macroscopic definition of mechanical properties of the composite in a damaged state can be justified. One way to achieve this is to have representative elements much larger than all physical sizes of damage surfaces and constituents of the structure, while still small enough for macroscopic properties to be meaningful in regions with higher strain gradients, as shown in Fig. 2.

With the above restriction in mind, macroscopic tractions $\overline{T_i}$, stresses $\overline{\sigma_{ij}}$, displacements $\overline{u_i}$, and strains $\overline{\epsilon_{ij}}$ are assumed to be well defined over the volume V. Since the concept of continuum is assumed on the macroscopic scale, the macroscopic traction $\overline{T_i}$ can be related to the macroscopic stress tensor $\overline{\sigma_{ij}}$ and surface normal n_i through

$$\overline{T_i} = \overline{\sigma_{ji}} n_i . \tag{4}$$

The macroscopic strain-displacement relations are given by

$$\overline{\epsilon_{ij}} = \frac{1}{2} (\overline{u_{i,j}} + \overline{u_{j,i}}). \tag{5}$$

For the same solid in the undamaged state, the material is assumed to follow Hooke's law:

$$\overline{\sigma_{ij}^o} = \overline{S_{ijkl}^o} \overline{\epsilon_{kl}^o}, \tag{6}$$

where superscript "o" is used for the field quantities in the undamaged state, $\overline{S_{ijkl}^o}$ is the elastic compliance tensor of the solid in the undamaged state.

Consider the solid in both the damaged and undamaged configurations, as shown in Fig. 3. The undamaged configuration can be considered as a damaged solid with fictitious damage surfaces recovered or closed by tractions on the damage surfaces. Neglecting body forces, we obtain the following from Betti's reciprocal theorem (3)

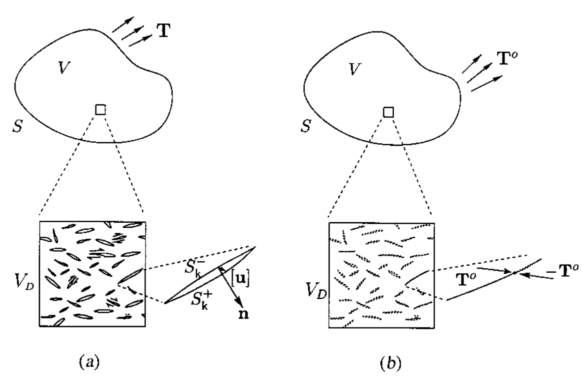

Fig. 3 Solid with crack-like damage in (*a*) damaged configuration with or without friction and sliding, and (*b*) undamaged configuration with fictitious damage surfaces recovered or closed by tractions $\mathbf{T}^o$ on S_k^-, and $-\mathbf{T}^o$ on S_k^+

$$\int_S (T_i - T_i^R) u_i^o dS = \int_S (T_i^o - T_i^R) u_i dS - \sum_{\mathsf{k}} \int_{S_{\mathsf{k}}^-} (T_i^o - T_i^R)[u_i] dS, \tag{7}$$

where T_i and u_i are, respectively, microscopic tractions and displacements of *damaged configuration*; T_i^o and u_i^o are, respectively, microscopic tractions and displacements of *undamaged configuration*. The summation in the second term on the right-hand side is taken over all damage surfaces S_{k}^-, indexed by subscript k. The *displacement jump vector* $[u_i]$ on the damage surface is defined by $[u_i] = u_i^+ - u_i^-$. The tractions T_i^o on the fictitious damage surface are defined on the same surface S_{k}^- on which u_i^- is defined. The selection between S_{k}^- and S_{k}^+ is arbitrary. Notice that *friction* and/or *bonding traction* on the damage surfaces are allowed, but they do not contribute to the above equation due to the absence of displacement jump on the fictitious damage surface in the undamaged configuration.

The left-hand side and the first term on the right-hand side of Eq. (7) are in the form of work done by tractions. Since the concept of continuum is assumed to hold for the damaged configuration, it is obvious that any work term due to loading has to be able to be expressed in terms of macroscopic tractions and displacements, so that the energy pumped into the system can be expressed by macroscopic tractions and displacements. Thus, the following conditions must be met:

$$\int_S T_i u_i^o dS = \int_S \overline{T_i}\,\overline{u_i^o} dS, \quad \int_S T_i^o u_i dS = \int_S \overline{T_i^o}\,\overline{u_i} dS,$$

$$\int_S T_i^R u_i^o dS = \int_S \overline{T_i^R}\,\overline{u_i^o} dS \text{ and } \int_S T_i^R u_i dS = \int_S \overline{T_i^R}\,\overline{u_i} dS.$$

The self-equilibrium condition of the initial stress σ_{ij}^R requires that the macroscopic initial stress $\overline{\sigma_{ij}^R}$ vanishes, so the initial traction $\overline{T_i^R} = \overline{\sigma_{ji}^R} n_j$ vanishes too, or

$$\overline{T_i^R} = 0.$$

Substituting these conditions into Eq. (7), we obtain

$$\int_S \overline{T_i}\,\overline{u_i^o} dS = \int_S \overline{T_i^o}\,\overline{u_i} dS - \sum_{\mathsf{k}} \int_{S_{\mathsf{k}}^-} (T_i^o - T_i^R)[u_i] dS.$$

Replacing $\overline{T_i}$ by $\overline{\sigma_{ji}} n_j$, and $\overline{T_i^o}$ by $\overline{\sigma_{ji}^o} n_j$, with the aid of the divergence theorem, the above equation can be rewritten as

$$\int_V \overline{\sigma_{ji}}\,\overline{u_{i,j}^o} dV = \int_V \overline{\sigma_{ji}^o}\,\overline{u_{i,j}} dV - \sum_{\mathsf{k}} \int_{S_{\mathsf{k}}^-} (T_i^o - T_i^R)[u_i] dS.$$

Noticing that $\overline{\sigma_{ji}}\,\overline{u_{i,j}^o} = \overline{\sigma_{ij}}\,\overline{\epsilon_{ij}^o}$, and $\overline{\sigma_{ji}^o}\,\overline{u_{ij}} = \overline{\sigma_{ij}^o}\,\overline{\epsilon_{ij}}$, we can rewrite the above equation as

$$\int_V \overline{\sigma_{ij}}\,\overline{\epsilon_{ij}^o} dV = \int_V \overline{\sigma_{ij}^o}\,\overline{\epsilon_{ij}} dV - \sum_{\mathsf{k}} \int_{S_{\mathsf{k}}^-} (T_i^o - T_i^R)[u_i] dS.$$

Since the volume V is arbitrary, we have

$$\overline{\sigma_{ij}}\,\overline{\epsilon_{ij}^o} = \overline{\sigma_{ij}^o}\,\overline{\epsilon_{ij}} - \frac{1}{V_D} \sum_{\mathsf{k}} \int_{S_{\mathsf{k}}^-} (T_i^o - T_i^R)[u_i] dS,$$

where volume V_D represents the unit volume that contains a sufficient number of damage cracks to achieve stable averages of field quantities. Substituting Hooke's law (6) into the above equation, and rearranging the indices, we obtain

$$\overline{\sigma_{ij}^o}(\overline{\epsilon_{ij}} - \overline{S_{ijkl}^o}\,\overline{\sigma_{kl}}) = \frac{1}{V_D} \sum_{\mathsf{k}} \int_{S_{\mathsf{k}}^-} (T_i^o - T_i^R)[u_i] dS. \tag{8}$$

The left-hand side of the above equation is determined by the macroscopic stresses $\overline{\sigma_{ij}^o}$, $\overline{\sigma_{kl}}$, macroscopic strains $\overline{\epsilon_{ij}}$, and undamaged macroscopic compliances $\overline{S_{ijkl}^o}$. The right-hand side is determined by the microscopic traction T_i^o of the *undamaged configuration* on the fictitious damage surfaces, and the displacement jump $[u_i]$ on the damage surfaces. Thus, the equation basically relates the macroscopic and microscopic deformations. Define the *damage strain tensor* $\overline{\epsilon_{ij}^D}$ by

$$\overline{\epsilon_{ij}^D} = \overline{\epsilon_{ij}} - \overline{S_{ijkl}^o}\,\overline{\sigma_{kl}}, \tag{9}$$

then Eq. (8) can be rewritten as

$$\overline{\sigma_{ij}^o}\,\overline{\epsilon_{ij}^D} = \frac{1}{V_D} \sum_{\mathsf{k}} \int_{S_{\mathsf{k}}^-} (T_i^o - T_i^R)[u_i] dS. \tag{10}$$

Ruling out any nonlinearity in the undamaged configuration, microscopic stresses σ_{ij}^o of the linear system can be represented by the sum of the initial stresses σ_{ij}^R and linear combinations of the macroscopic stresses $\overline{\sigma_{ij}^o}$, or

$$\sigma_{ij}^o = \sigma_{ij}^R + h_{klij} \overline{\sigma_{kl}^o}, \tag{11}$$

where h_{klij} are nondimensional stress factors. The component h_{klij} is interpreted as the *load-induced microscopic stress* component $(\sigma_{ij}^o - \sigma_{ij}^R)$ caused by a unit macroscopic stress component $\overline{\sigma_{kl}^o}$ in the *undamaged state*. Since $(\sigma_{ij}^o - \sigma_{ij}^R)$ is symmetric and $\overline{\sigma_{kl}^o}$ arbitrary, we have

$$h_{klij} = h_{klji}. \tag{12}$$

Since $\overline{\sigma_{kl}^o}$ is also symmetric, there is no contribution to the right-hand side of Eq. (11) from the antisymmetric part (w.r.t. *k*, *l*) of h_{klij}. Without loss of generality, we can restrict ourselves to the symmetric part of h_{klij} by observing the following condition:

$$h_{klij} = h_{lkij}. \tag{13}$$

Using $T_i^o = \sigma_{ji}^o n_j$, $T_i^R = \sigma_{ji}^R n_j$ and Eq. (11), with indices rearranged, Eq. (10) can be rewritten as

$$\overline{\sigma_{ij}^o}\,\overline{\epsilon_{ij}^D} = \frac{\overline{\sigma_{ij}^o}}{V_D} \sum_{\mathsf{k}} \int_{S_{\mathsf{k}}^-} h_{ijkl}[u_l] n_k dS.$$

Since $\overline{\sigma_{ij}^o}$ is arbitrary and symmetric, we have

$$\overline{\epsilon_{ij}^D} = \frac{1}{V_D} \sum_{\mathsf{k}} \int_{S_{\mathsf{k}}^-} \frac{1}{2}(h_{ijkl}[u_l] n_k + h_{jikl}[u_l] n_k) dS.$$

Considering the symmetry relations (12) and (13), the above equation can be rewritten as

$$\overline{\epsilon_{ij}^D} = \frac{1}{V_D} \sum_{\mathsf{k}} \int_{S_{\mathsf{k}}^-} \frac{h_{ijkl}}{2}([u_k] n_l + [u_l] n_k) dS. \tag{14}$$

The above equation correlates the macroscopic deformation described by the damage deformation tensor $\overline{\epsilon_{ij}^D}$, and microscopic displacement jump $[u_k]$ on the damage surfaces S_k. From the deriviation, it is clear that the above equation is valid regardless of the existence of initial stresses σ_{ij}^R, friction and/or bonding traction on the damage surface.

Special Cases

For inhomogeneous materials with arbitrarily distributed constituents, the determination of h_{ijkl} through Eq. (11) is far from a trivial task even though the calculation is done in the undamaged configuration. For certain cases of engineering importance, h_{ijkl} can be determined fairly easily. In this section we will discuss a few such cases.

Homogeneous Materials With Crack-Like Damage. For homogeneous material, Eq. (14) can be greatly simplified and simple physical interpretation of the damage strain ϵ_{ij}^D can be

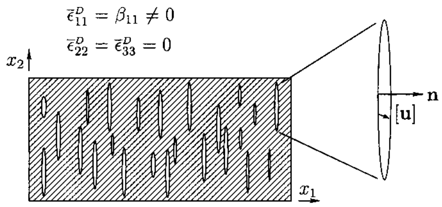

Fig. 4 For homogeneous materials the macroscopic damage strain component $\bar{\epsilon}^D_{11}$ is equivalent to the damage deformation tensor component β_{11} which is the crack-opening volume ratio in the x_1-direction. (Note that $\bar{\epsilon}^D_{22}=\bar{\epsilon}^D_{33}=\beta_{22}=\beta_{33}=0$ when all damage surface normals are in the x_1-direction.)

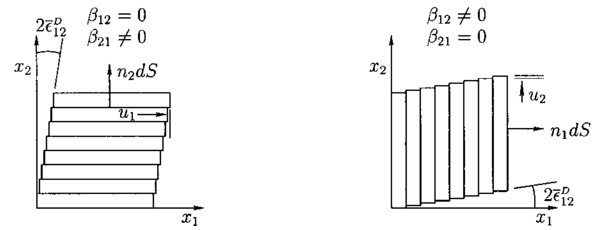

Fig. 5 Two different microscopic deformation mechanisms could produce the same macroscopic damage shear strain component $\bar{\epsilon}^D_{12}$

obtained. Since microscopic stresses are equivalent to macroscopic stresses for undamaged homogeneous materials,

$$\sigma^o_{ij}=\overline{\sigma}^o_{ij}.$$

Considering Eq. (11) and the above, h_{ijkl} can be written as

$$h_{ijkl}=\frac{1}{2}(\delta_{ik}\delta_{jl}+\delta_{jk}\delta_{il}).$$

Substituting the above into Eq. (14), we obtain

$$\overline{\epsilon}^D_{ij}=\frac{1}{V_D}\sum_{\mathrm{k}}\int_{S^-_{\mathrm{k}}}\frac{1}{2}([u_i]n_j+[u_j]n_i)dS.$$

The right-hand side of the above equation is the volume average of the symmetric part of the tensor $[u_i]n_j$. Define the *damage deformation tensor* β_{ij} by

$$\beta_{ij}=\frac{1}{V_D}\sum_{\mathrm{k}}\int_{S^-_{\mathrm{k}}}[u_j]n_i dS, \tag{15}$$

then, we have

$$\overline{\epsilon}^D_{ij}=\frac{1}{2}(\beta_{ij}+\beta_{ji}) \quad \text{for homogeneous materials.} \tag{16}$$

This is a well-known result used for calculating the elastic moduli of materials with damage [4,15]. The physical interpretation of the damage deformation tensor β_{ij} is very simple and described in the following.

First let us consider the summation of diagonal components

$$\beta_{ii}=\beta_{11}+\beta_{22}+\beta_{33}=\frac{1}{V_D}\sum_{\mathrm{k}}\int_{S^-_{\mathrm{k}}}[u_i]n_i dS.$$

Thus, β_{ii} (or $\overline{\epsilon}^D_{ii}$) for homogeneous materials is interpreted as the *crack-opening volume ratio*, or the volume average of all crack openings. The component β_{11} (or $\overline{\epsilon}^D_{11}$) is the *projected crack-opening volume ratio*, given by the volume average of the projected damage area in the x_1-direction ($n_1 dS$), times the crack-opening displacement in the x_1-direction ($[u_1]$). This leads to an interesting result for the special case in which all damage surface normals are parallel, as depicted in Fig. 4. Since the damage surface normals **n** are parallel to the x_1-direction, it follows from Eqs. (15) and (16) that

$$\epsilon^D_{22}=\epsilon^D_{33}=0.$$

This is true regardless of external loads, the distribution of damage locations, size, and existence of friction or contact on damage surfaces. Similar interpretations exist for the other diagonal components of β_{ij}.

The off-diagonal component β_{12} is the *projected sliding volume ratio*, given by the volume average of the projected damage area in the x_1-direction ($n_1 dS$), times the sliding displacement in the x_2-direction ($[u_2]$). It is obvious that $\beta_{ij}\neq\beta_{ji}$ in general, but the damage strain $\overline{\epsilon}^D_{ij}$ is symmetric. This means that different microscopic mechanisms could give the same macroscopic damage strains, as depicted in Fig. 5. Interpretations of other off-diagonal components of β_{ij} are similar.

Inhomogeneous Materials With Periodic Structure and Damage Modes. In inhomogeneous materials with periodic structure, very often damage occurs in such a manner that various *damage modes* associated with a specific location, pattern, and loading can be identified. For example, transverse matrix cracks are observed in cross-ply composites with $[0_m/90_n]_s$ layup under longitudinal tension. Transverse matrix cracks, fiber matrix debonding, and also fiber breaks occur in unidirectional ceramic composites under longitudinal tension.

In many cases, it is possible to have analytical micromechanical stress analyses for the undamaged composites, and then to determine the stress factors h_{klij} from Eq. (11). In general, the factors h_{klij} depend on the distribution, location of potential damage, and elastic properties of the constituents of the inhomogeneous material. For periodic structures, very often the undamaged microscopic stresses σ^o_{ij} depend on the damage modes, but not on the location of the potential damage. For example, with parallel fibers in its matrix, an undamaged unidirectional fiber composite can be assumed to have a periodic structure. The *undamaged* microscopic stresses at the potential damage surfaces (fiber/matrix interface, transverse sections in matrix and fibers) depend, through the stress factor h_{klij}, on the type of potential damage surface or failure mode and not on global location, since there is no damage yet and the material has a periodic structure. This allows us to take h_{klij} out of the integral sign in Eq. (14). Grouping the damage surfaces according to different damage modes, and renumbering the damage surfaces so that the notation $S^-_{k^{\mathrm{m}}}$ refers to the k^{m}th damage surface of the mth damage mode, now we can rewrite Eq. (14) as

$$\overline{\epsilon}^D_{ij}=\sum_{\mathrm{m}} h^{\mathrm{m}}_{ijkl}\left(\frac{1}{2V_D}\sum_{\mathrm{k^m}}\int_{S^-_{\mathrm{k^m}}}([u_k]n_l+[u_l]n_k)dS\right),$$

where the summation over $\mathrm{k^m}$ is taken over all damage surfaces for the mth damage mode, and the summation over m is taken over all damage modes. Note that the Einstein summation convention is applied only to italic indices like *k* and *l*, but not to nonitalics like k or m. The above equation can be rewritten as

$$\overline{\epsilon}^D_{ij}=\sum_{\mathrm{m}} h^{\mathrm{m}}_{ijkl}\frac{1}{2}(\beta^{\mathrm{m}}_{lk}+\beta^{\mathrm{m}}_{kl}) \tag{17}$$

where β^{m}_{ij} is the *damage deformation tensor for damage mode* m, or simply the *damage mode tensor* ([17]), defined by

$$\beta^{\mathrm{m}}_{ij}=\frac{1}{V_D}\sum_{k^{\mathrm{m}}}\int_{S^-_{\mathrm{k^m}}}[u_j]n_i dS. \tag{18}$$

The physical interpretation of damage deformation tensor β^{m}_{ij} for damage mode m is similar to β_{ij} described before, except that only the contribution of the mth damage mode is considered. For example, β^{m}_{ii} is the crack-opening volume ratio of damage mode

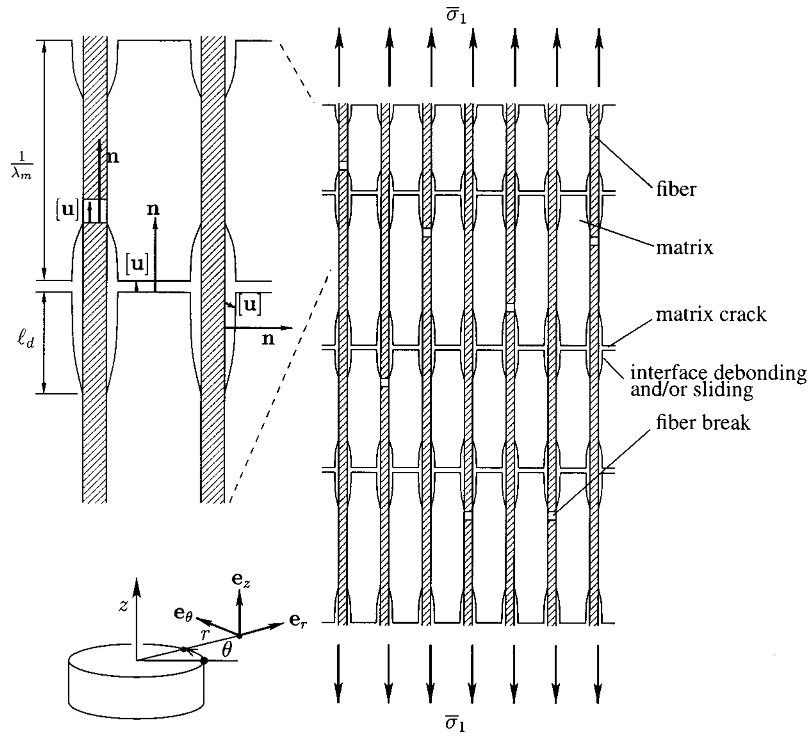

Fig. 6 Common damage modes in unidirectional brittle matrix composites under longitudinal tension: matrix cracking (mode *M*), interface debonding/sliding (mode *I*), and fiber breakage (mode *F*). (The theory does not require the matrix crack spacing, interface debonding length, or fiber break spacing to be uniform or periodic.)

m, the component β_{11}^{m} is the projected crack-opening volume ratio of damage mode m in the x_1-direction, and the off-diagonal component β_{12}^{m} is the projected sliding volume ratio of damage mode m in the x_1-direction for sliding in the x_2-direction.

For homogeneous materials, the damage strain tensor $\overline{\epsilon}_{ij}^{D}$ is the symmetric part of the damage deformation tensor β_{ij}, as shown in Eq. (16). Thus, the interpretation of damage strain tensor $\overline{\epsilon}_{ij}^{D}$ directly follows that of damage deformation tensor β_{ij}. This is not the case for inhomogeneous materials with periodic structures. Considering Eq. (17), the damage strain tensor $\overline{\epsilon}_{ij}^{D}$ is the weighted sum of the symmetric part of damage deformation tensors β_{ij}^{m} for all damage modes. In the next section we will use an example of a unidirectional composite under longitudinal loading to demonstrate the nature of the stress factors h_{ijkl}^{m}, which serve as the weighted parameters in Eq. (17).

Unidirectional Composite Material With Crack-Like Damage

Unidirectional composite materials fall into the category of inhomogeneous materials with periodic structure and damage modes, as described before. The damage of these materials is discussed in detail because of its engineering importance.

General Results. There are three easily identifiable damage modes in unidirectional composites under longitudinal tension: matrix cracking (mode *M*), fiber-matrix interface debonding/sliding (mode *I*), and fiber breakage (mode *F*), as shown in Fig. 6. The sequence of damaged modes is immaterial as far as the theory is concerned. They can occur in any order, or simultaneously. The above damage modes are commonly seen in a typical brittle matrix composite, SiC/CAS (Silicon Carbide/Calcium Aluminosilicate), under unidirectional loading. We will start by determining the damage deformation tensor β_{ij}^{m} for damage mode $\mathsf{m}=M$, I, and F.

Matrix Cracking. For matrix cracking, the displacement jump vector, $[\mathbf{u}]=[u_z]\mathbf{e}_z$, is parallel to the matrix crack surface normal, $\mathbf{n}=\mathbf{e}_z$ (see Fig. 6). From the definition of damage deformation tensor, Eq. (18), the only nonzero component for matrix cracking is β_{zz}^{M}, which is the matrix crack-opening volume ratio. Call the crack density (average number of matrix cracks per unit length) λ_m, average matrix crack-opening displacement COD_m, and fiber volume ratio f, then, β_{zz}^{M} can be written as

$$\beta_{zz}^{M}=(1-f)\lambda_m\mathsf{COD}_m. \tag{19}$$

Interface Debonding/Sliding. For interface debonding/sliding, the displacement jump vector is given by $[\mathbf{u}]=[u_r]\mathbf{e}_r+[u_z]\mathbf{e}_z$, and the debonding crack surface normal $\mathbf{n}=\mathbf{e}_r$ (see Fig. 6). From the definition of damage deformation tensor, Eq. (18), the only nonzero components for interface debonding/sliding are β_{rr}^{I} and β_{rz}^{I}. Call the average debonding length l_d and average interface crack-opening displacement COD_i, then, it can be easily shown that β_{rr}^{I} which describes the interface crack opening is given by

$$\beta_{rr}^{I}=4f\lambda_m l_d\mathsf{COD}_i/R_f, \tag{20}$$

where R_f is the fiber radius. The matrix crack density λ_m enters into the equation simply for the convenience of using $1/\lambda_m$ as the length scale to calculate the percentage of debonded interface.

The other nonzero component β_{fz}^{I} describes the volume average of interface sliding. However, there are only two relevant measurable damage strain components, $\overline{\epsilon}_{rr}^{D}$ and $\overline{\epsilon}_{zz}^{D}$, under unidirectional loading. It is not difficult to see that the stress factors h_{rrrz}^{I} and h_{zzrz}^{I} are zero because of the absence of shear stress (σ_{rz}^{of} or σ_{rz}^{om})

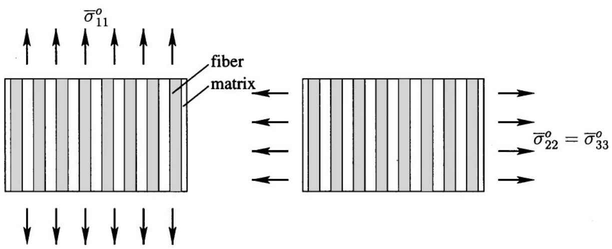

Fig. 7 Arbitrary macroscopic stress components $\overline{\sigma}^o_{11}$ in (*a*) and $\overline{\sigma}^o_{22}=\overline{\sigma}^o_{33}$ in (*b*) applied to the undamaged unidirectional composite

at the interface of the undamaged composite cylinder under longitudinal or two-dimensional hydrostatic pressure. Thus, from Eq. (17), there is no direct contribution to the macroscopic strains ϵ^D_{rr} and ϵ^D_{zz} from the interface sliding component β^I_{rz}. The effect of interface sliding on the macroscopic mechanical behavior is therefore implied in other microscopic deformation.

Fiber Breakage. For fiber breakage, the displacement jump vector, $[\mathbf{u}]=[u_z]\mathbf{e}_z$, is parallel to the fiber crack surface normal, $\mathbf{n}=\mathbf{e}_z$ (see Fig. 6). From the definition of damage deformation tensor, Eq. (18), the only nonzero component is β^F_{zz}, which is the crack-opening volume ratio of fiber breaks. Call the fiber break density λ_f, and average fiber break opening displacement COD_f, then, β^F_{zz} can be written as

$$\beta^F_{zz}=f\lambda_f\mathrm{COD}_f. \tag{21}$$

For the macroscopic deformation, use direction 1 for the fiber direction, 2 for the in-plane transverse direction, and 3 for the out-of-plane transverse direction. Since the selection of stresses $\overline{\sigma}^o_{kl}$ in Eq. (11) is arbitrary, we can limit ourselves to discuss only two independent macroscopic stress components, $\overline{\sigma}^o_{11}$ and $\overline{\sigma}^o_{22}$ $(=\overline{\sigma}^o_{33})$. From Eqs. (11) and (17), we have

$$\overline{\epsilon}^D_{11}=\frac{\sigma^{om}_{zz}}{\overline{\sigma}^o_{11}}\beta^M_{zz}+\frac{\sigma^{of}_{rr}}{\overline{\sigma}^o_{11}}\beta^I_{rr}+\frac{\sigma^{of}_{zz}}{\overline{\sigma}^o_{11}}\beta^F_{zz}, \tag{22}$$

for an arbitrary stress component $\overline{\sigma}^o_{11}$ applied to the undamaged composite, as shown in Fig. 7(*a*).

In the above equation, σ^{om}_{zz}, σ^{of}_{rr}, and σ^{of}_{zz} are the stress components induced by the macroscopic stress component $\overline{\sigma}^o_{11}$ in the undamaged composite on the fictitious damage surfaces of mode *M*, *I*, and *F*, respectively. Since the calculation of these stress components involves only the undamaged configuration, various mechanical models are available. In what follows we use the results from the composite cylinder model by Christensen [18] to determine these components, which can be easily proved to be

$$\frac{\sigma^{om}_{zz}}{\overline{\sigma}^o_{11}}=\frac{b_{22}}{b_{11}b_{22}-b_{12}b_{21}}\equiv a_{11}, \tag{23a}$$

$$\frac{\sigma^{of}_{rr}}{\overline{\sigma}^o_{11}}=\frac{-b_{12}}{2(b_{11}b_{22}-b_{12}b_{21})}\equiv\frac{a_{12}}{2}, \tag{23b}$$

$$\frac{\sigma^{of}_{zz}}{\overline{\sigma}^o_{11}}=\frac{1}{f}[1-(1-f)a_{11}]\equiv a_{13}, \tag{23c}$$

where superscripts *f* and *m* refer to fiber and matrix, respectively, and constants b_{ij} are given by

$$b_{11}=1+\frac{f(\nu_f-\nu_m)}{1-\nu_f\nu_m}+\frac{f(1+\nu_f)(1-\nu_m)}{1-\nu_f\nu_m}\left(\frac{\mu_f}{\mu_m}-1\right), \tag{24a}$$

$$b_{12}=-\frac{(1-f)(\nu_f-\nu_m)}{1-\nu_f\nu_m}, \tag{24b}$$

$$b_{21}=\frac{f(\nu_f-\nu_m)}{1-\nu_f\nu_m}-\frac{f\nu_m(1+\nu_f)}{2(1-\nu_f\nu_m)}\left(\frac{\mu_f}{\mu_m}-1\right), \tag{24c}$$

$$b_{22}=1-\frac{(1-f)(\nu_f-\nu_m)}{1-\nu_f\nu_m}-\frac{(1-f)(1+\nu_m)(1-2\nu_f)}{2(1-\nu_f\nu_m)}\left(1-\frac{\mu_m}{\mu_f}\right). \tag{24d}$$

For an arbitrary two-dimensional hydrostatic pressure $\overline{\sigma}^o_{22}=\overline{\sigma}^o_{33}$ applied to the undamaged composite (see Fig. 7(*b*)), we have

$$\overline{\epsilon}^D_{22}+\overline{\epsilon}^D_{33}=2\overline{\epsilon}^D_{22}=\frac{\sigma^{om}_{zz}}{\overline{\sigma}^o_{22}}\beta^M_{zz}+\frac{\sigma^{of}_{rr}}{\overline{\sigma}^o_{22}}\beta^I_{rr}+\frac{\sigma^{of}_{zz}}{\overline{\sigma}^o_{22}}\beta^F_{zz}. \tag{25}$$

In the above equation, σ^{om}_{zz}, σ^{of}_{rr}, and σ^{of}_{zz} are the stress components induced by the macroscopic hydrostatic pressure $\overline{\sigma}^o_{22}=\overline{\sigma}^o_{33}$ in the undamaged composite on the fictitious damage surfaces of mode *M*, *I*, and *F*, respectively. Note that the axisymmetry of the composite cylinder model dictates that strains $\overline{\epsilon}^D_{22}$ and $\overline{\epsilon}^D_{33}$ occur together as the coupling terms of the applied hydrostatic pressure. It can be easily shown from Lamé's solution [19] that these components are given by

$$\frac{\sigma^{om}_{zz}}{\overline{\sigma}^o_{22}}=\frac{-2b_{21}}{b_{11}b_{22}-b_{12}b_{21}}\equiv 2a_{21}, \tag{26a}$$

$$\frac{\sigma^{of}_{rr}}{\overline{\sigma}^o_{22}}=\frac{b_{11}}{b_{11}b_{22}-b_{12}b_{21}}\equiv a_{22}, \tag{26b}$$

$$\frac{\sigma^{of}_{zz}}{\overline{\sigma}^o_{22}}=-2a_{21}\frac{1-f}{f}\equiv 2a_{23}. \tag{26c}$$

Using the following notation commonly used for unidirectional composites, with overbar denoting macroscopic quantities,

$$\overline{\epsilon}^D_1=\overline{\epsilon}^D_{11},\quad \overline{\epsilon}^D_2=\overline{\epsilon}^D_{22},$$

we can rewrite Eqs. (22) and (25) as

$$\begin{Bmatrix}\overline{\epsilon}^D_1\\ \overline{\epsilon}^D_2\end{Bmatrix}=\begin{bmatrix}a_{11} & a_{12} & a_{13}\\ a_{21} & a_{22} & a_{23}\end{bmatrix}\begin{Bmatrix}(1-f)\lambda_m\mathrm{COD}_m\\ 2f\lambda_m l_d\mathrm{COD}_i/R_f\\ f\lambda_f\mathrm{COD}_f\end{Bmatrix}. \tag{27}$$

The above equations relate the macroscopic damage deformation (described by $\overline{\epsilon}^D_1$ and $\overline{\epsilon}^D_2$) with the microscopic damage deformation of the three damage modes (matrix cracking, interface debonding/sliding and fiber breaking). It is worth mentioning that the stress factors a_{ij} in the above equations are functions of fiber volume ratio and elastic moduli. Models other than the composite cylinder model might generate slightly different values for these constants, but the damage strains $\overline{\epsilon}^D_{ij}$ are always representable as linear combinations of the components of the damage deformation tensor β^m_{ij}, as indicated in Eq. (17). It will be shown in the next section, for several specific applications, that the physical significance of the above relation lies in the linear relationship between the macroscopic damage strains $\overline{\epsilon}^D_{ij}$ and damage deformation tensor β^{m}_{ij}. The estimates of the deformation tensor components from the above equations would be reasonable as long as the stress calculation from the cylinder model is acceptable. The importance of the relationship is not limited by the selection of the stress analysis model. If another model were selected the calculated stress components might be different but the relationship above would still be linear.

Simpler representations of constants a_{ij} and b_{ij} are desirable so that the physical meaning would be clearer. When the difference of Poisson's ratios is ignored, or $\nu_f=\nu_m\equiv\nu$, simpler forms for a_{ij} and b_{ij} can be obtained:

$$b_{11}\approx\frac{fE_f+(1-f)E_m}{E_m}, \tag{28a}$$

$$b_{12}\approx 0, \tag{28b}$$

$$b_{21}\approx -\frac{f\nu(E_f-E_m)}{2(1-\nu)E_m}, \tag{28c}$$

$$b_{22}\approx \frac{E_f+(1-2\nu)[fE_f+(1-f)E_m]}{2(1-\nu)E_f}, \tag{28d}$$

and

$$a_{11}\approx \frac{E_m}{fE_f+(1-f)E_m}, \tag{29a}$$

$$a_{12}\approx 0, \tag{29b}$$

$$a_{13}\approx \frac{E_f}{fE_f+(1-f)E_m}, \tag{29c}$$

$$a_{21}\approx \frac{f\nu E_f(E_f-E_m)}{[fE_f+(1-f)E_m]\{E_f+(1-2\nu)[fE_f+(1-f)E_m]\}}, \tag{29d}$$

$$a_{22}\approx \frac{2(1-\nu)E_f}{E_f+(1-2\nu)[fE_f+(1-f)E_m]}, \tag{29e}$$

$$a_{23}\approx -\frac{(1-f)\nu E_f(E_f-E_m)}{[fE_f+(1-f)E_m]\{E_f+(1-2\nu)[fE_f+(1-f)E_m]\}}. \tag{29f}$$

Special Cases. Equations (27) apply to unidirectional composites with all three damage modes present. There are two independent measurable damage strains ($\bar{\epsilon}_1^{\mathcal{D}}$ and $\bar{\epsilon}_2^{\mathcal{D}}$), but three damage deformation tensor components. The difficulty can be overcome in many engineering applications for which not all three damage modes occur at the same time. Several cases are discussed below.

Matrix Cracking and Interface Debonding/Sliding. If fiber breakage does not occur in the process, or $\mathrm{COD}_f=0$, then the last one ($f\lambda_f\mathrm{COD}_f$) of the microscopic deformation terms on the right-hand side of Eq. (27) can be dropped, and we have

$$\begin{Bmatrix}\bar{\epsilon}_1^{\mathcal{D}}\\ \bar{\epsilon}_2^{\mathcal{D}}\end{Bmatrix}=\begin{bmatrix}a_{11} & a_{12}\\ a_{21} & a_{22}\end{bmatrix}\begin{Bmatrix}(1-f)\lambda_m\mathrm{COD}_m\\ 2f\lambda_m l_d\mathrm{COD}_i/R_f\end{Bmatrix}, \tag{30}$$

or, by left-multiplying the inverse of $[a_{ij}]$, we have

$$\begin{Bmatrix}(1-f)\lambda_m\mathrm{COD}_m\\ 2f\lambda_m l_d\mathrm{COD}_i/R_f\end{Bmatrix}=\begin{bmatrix}b_{11} & b_{12}\\ b_{21} & b_{22}\end{bmatrix}\begin{Bmatrix}\bar{\epsilon}_1^{\mathcal{D}}\\ \bar{\epsilon}_2^{\mathcal{D}}\end{Bmatrix}, \tag{31}$$

which states that the microscopic damage represented by $\lambda_m\mathrm{COD}_m$ and $\lambda_m l_d\mathrm{COD}_i$ can be determined by the readily measurable macroscopic damage strains $\bar{\epsilon}_1^{\mathcal{D}}$ and $\bar{\epsilon}_2^{\mathcal{D}}$. This is the same as the result obtained by the cylinder theory ([1]).

In general, the coupling constants a_{12} and a_{21} in Eqs. (30) are not zero. Therefore, matrix crack-opening (COD_m, in the longitudinal direction) will result in macroscopic nonlinear transverse strain $\bar{\epsilon}_2^{\mathcal{D}}$ unless $a_{21}=0$, which can be achieved by letting fiber and matrix have the same elastic constants ($\nu_f=\nu_m$ and $E_f=E_m$). Interface crack-opening (COD_i, in the radial direction) will result in macroscopic nonlinear longitudinal strain $\bar{\epsilon}_1^{\mathcal{D}}$ unless $a_{12}=0$, or $\nu_f=\nu_m$.

Fiber Breakage and Interface Debonding/Sliding. If matrix cracking does not occur in the process, or $\mathrm{COD}_m=0$, we have to use another length scale instead of $1/\lambda_m$ to characterize the percentage of interface debonding. In this case, the average fiber break spacing $1/\lambda_f$ is more suitable as the length scale. Letting COD_m be zero and replacing λ_m by λ_f in Eq. (27), we obtain

$$\begin{Bmatrix}\bar{\epsilon}_1^{\mathcal{D}}\\ \bar{\epsilon}_2^{\mathcal{D}}\end{Bmatrix}=\begin{bmatrix}a_{12} & a_{13}\\ a_{22} & a_{23}\end{bmatrix}\begin{Bmatrix}2f\lambda_f l_d\mathrm{COD}_i/R_f\\ f\lambda_f\mathrm{COD}_f\end{Bmatrix}. \tag{32}$$

With the constants a_{13} and a_{23} previously defined, this is the same as the result obtained from the cylinder theory ([1]).

In general, the coupling constants a_{12} and a_{23} $(=-(1-f)a_{21}/f)$ in Eqs. (32) are not zero. Therefore, fiber break opening (COD_f, in the longitudinal direction) will result in macroscopic nonlinear transverse strain $\bar{\epsilon}_2^{\mathcal{D}}$, unless $a_{23}=0$, which can be achieved by letting fiber and matrix have the same elastic constants ($\nu_f=\nu_m$ and $E_f=E_m$). Interface crack-opening (COD_i, in the radial direction) will result in macroscopic nonlinear longitudinal strain $\bar{\epsilon}_1^{\mathcal{D}}$ unless $a_{12}=0$, or $\nu_f=\nu_m$.

Matrix Cracking Only. If only matrix cracking occurs in the process, or $\mathrm{COD}_i=0$ and $\mathrm{COD}_f=0$, from Eq. (27), we have

$$\bar{\epsilon}_1^{\mathcal{D}}=a_{11}(1-f)\lambda_m\mathrm{COD}_m, \tag{33a}$$

$$\bar{\epsilon}_2^{\mathcal{D}}=a_{21}(1-f)\lambda_m\mathrm{COD}_m, \tag{33b}$$

from which one quickly recognizes that

$$\frac{\bar{\epsilon}_2^{\mathcal{D}}}{\bar{\epsilon}_1^{\mathcal{D}}}=\frac{a_{21}}{a_{11}}=-\frac{b_{21}}{b_{22}}. \tag{34}$$

This requires the damage strains $\bar{\epsilon}_2^{\mathcal{D}}$ and $\bar{\epsilon}_1^{\mathcal{D}}$ to be proportional, a necessary mechanical result for the unidirectional composite with matrix cracking as the only damage mode present. The ratio a_{21}/a_{11} vanishes only when $a_{21}=0$, which can be achieved by letting fiber and matrix have the same elastic constants ($\nu_f=\nu_m$ and $E_f=E_m$).

Matrix Cracking and Nonopening Debonding/Sliding Interface. If the material has matrix cracking and nonopening interface debonding and/or sliding, we have $\mathrm{COD}_i=0$. Therefore, the effects are similar to the case with matrix cracking only, and the previous result (34) applies. It is interesting that the presence of another nonopening damage mechanism has no effect on the proportional relation.

Fiber Breakage Only. If only fiber breakage occurs in the process, or $\mathrm{COD}_m=0$ and $\mathrm{COD}_i=0$, from Eq. (27), we have

$$\bar{\epsilon}_1^{\mathcal{D}}=a_{13}f\lambda_f\mathrm{COD}_f, \tag{35a}$$

$$\bar{\epsilon}_2^{\mathcal{D}}=a_{23}f\lambda_f\mathrm{COD}_f, \tag{35b}$$

from which one quickly recognizes that

$$\frac{\bar{\epsilon}_2^{\mathcal{D}}}{\bar{\epsilon}_1^{\mathcal{D}}}=\frac{a_{23}}{a_{13}}=-\frac{(1-f)b_{21}}{b_{11}b_{22}-b_{12}b_{21}-(1-f)b_{22}}. \tag{36}$$

Again this requires the damage strains $\bar{\epsilon}_2^{\mathcal{D}}$ and $\bar{\epsilon}_1^{\mathcal{D}}$ to be proportional, a necessary mechanical result for the unidirectional composite with fiber breakage as the only damage mode present. The ratio a_{23}/a_{13} vanishes only when $a_{23}=0$, which can be achieved by letting fiber and matrix have the same elastic constants ($\nu_f=\nu_m$ and $E_f=E_m$).

Fiber Breakage and Nonopening Debonding/Sliding Interface. If the material has fiber breakage and nonopening debonding and/or sliding interface, we have $\mathrm{COD}_i=0$. Therefore, the effects are similar to the case with fiber breakage only, and the previous result (36) applies. Again the presence of the nonopening debonding/sliding interface has no effect on the proportional relation.

Application to a Brittle Matrix Composite

Equation (27), or Eq. (30) without fiber breakage, correlates the macroscopic deformation with the microscopic damage and deformation of unidirectional composites for specific damage modes. Note that the application of the equation does not require the matrix crack spacing, interface debonding length, or fiber break spacing to be uniform or periodic, as long as the crack spacing and crack opening are understood to represent average quantities.

The interface bonding condition (friction type, bonding, stick-slip, or debonding) and residual stress also do not affect the validity of the equation. Therefore, the equation can be very useful in evaluating the damage development and identifying interface bonding (or debonding) conditions. This requires only macroscopic test data (stresses and strains), and constituent properties for the calculation of a_{ij}.

To demonstrate how this can be achieved, we will re-examine the damage development of a unidirectional brittle matrix composite, documented by several investigators ([11,20–28]). The most well-understood part of the damage is matrix cracking, typically starting from microcracking at various weak sites in the brittle matrix. With increasing load, the microcracks develop into longer macrocracks and gradually evolve into a pattern of parallel cracks with more or less uniform crack spacing. Interface damage generally follows the impingement of matrix cracks on the fiber/matrix interface, although the lack of direct observation makes it difficult to identify its initiation and development. Fiber breakage usually occurs at the last loading stage prior to failure and can be reasonably separated from matrix cracking and interface damage.

Stresses and strains from tensile tests of two different batches of a ceramic matrix composite (SiC/CAS) are used to calculate the crack opening volume ratios according to Eq. (30). For convenience, define the crack-opening volume ratios β_m and β_i as

$$\beta_m = (1-f)\lambda_m \mathrm{COD}_m, \tag{37a}$$

$$\beta_i = 2f\lambda_m l_d \mathrm{COD}_i / R_f. \tag{37b}$$

The constituent properties used in the calculation are: $E_f = 188$ GPa (27.2 Msi), $E_m = 97.9$ GPa (14.2 Msi), $\nu_f = 0.3$, and $\nu_m = 0.25$ ([20,22,29,30]). The measured fiber volume ratio is $f = 0.36$. The stresses and strains used in the calculation are taken from results from tensile tests of unidirectional composite coupons. The calculated results of crack-opening volume ratios β_m and β_i are shown in Figs. 8(a) and 8(b).

First, the matrix crack-opening volume ratio β_m curves for both batches have almost the same well-defined starting point, which corresponds to initiation of matrix cracking. In Fig. 8(a), the β_m and β_i curves start at almost the same strain level, and both increase linearly afterwards. This suggests that the initial matrix cracks develop immediately into a pattern of long parallel cracks accompanied by interface debonding. On the other hand, in Fig. 8(b) the delay in initiation of interface debonding volume ratio β_i after matrix crack initiation suggests that smaller matrix cracks initiate without noticeable interface debonding or that the debonded interface is not open.

Note that if there is no debonding at all ($l_d = 0$), the interface crack-opening volume ratio β_i would be zero. The existence of nonzero β_i implies not only the *debonding* of interface, but also the *opening* of such debonded interface during the matrix crack development stage.

The opening of the interface cracks does not exclude the existence of interface sliding stress or compressive normal stress at the interface, because the debonding and sliding of the fiber-matrix interface with rough contact would justify their coexistence ([31]). A small degree of fiber misalignment in composites also allows friction to coexist with interface crack opening. Therefore, the existence of interface crack opening does not automatically preclude interface sliding stress. Since rough debonding surface and fiber misalignment are common in composites, the coexistence of interface crack-opening, compressive interface normal stress, and interface sliding stress is very likely.

Based on the macroscopic stress-strain data, the above observation is reached without assuming a specific failure criterion or interface bonding condition. These results should be taken into account for both the damage observation and mechanical modeling. A mechanical model inaccurately conceived to assume *a priori* the knowledge of interface bonding condition could lead to erroneous interpretation of the interface behavior and especially the transverse strain behavior.

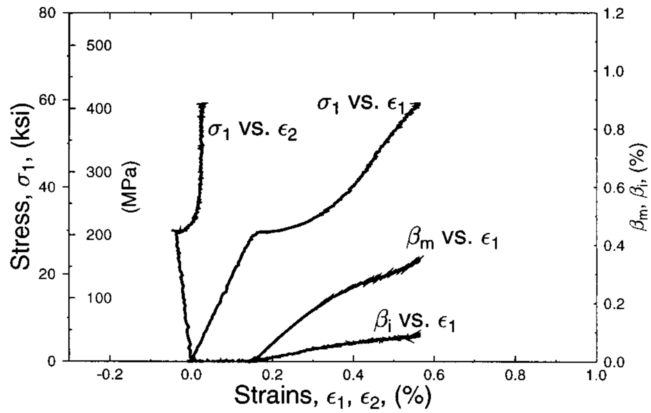

(a)

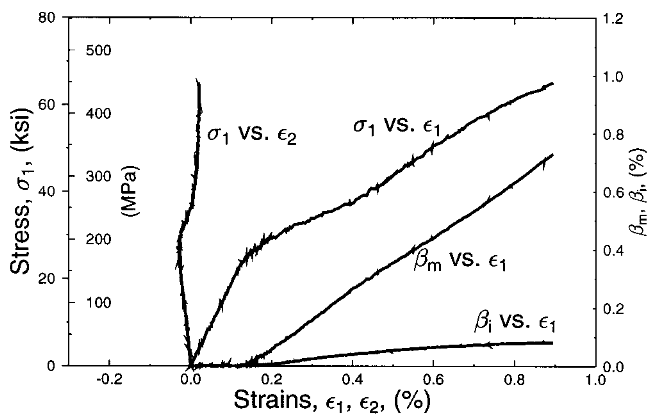

(b)

Fig. 8 Stress-strain curves and calculated crack-opening volume ratios β_m and β_i of two batches of unidirectional composite (SiC/CAS) under longitudinal tension

The transverse strain reversal phenomenon occuring during damage is the direct result of the mechanical interaction between fiber and matrix. Physical mechanisms (for example, interface debonding, interface asperities, surface roughness, or residual stresses) behind the transverse strain reversal contribute as a lumped effect on the macroscopic mechanical behavior, and cannot be separated by the current analysis. However, the lumped effect manifests itself in the transverse strains and allows us to calculate the interface crack-opening volume ratio.

Fiber breakage is ignored in the above calculation, because it occurs at the last loading stage prior to failure. For the current analysis, the debonding length l_d and matrix crack density λ_m cannot be separated from the microscopic deformation COD_m and COD_i. Nonetheless it provides helpful information about the damage development and can be useful for further modeling efforts.

Summary and Discussion

The correlation between macroscopic mechanical behavior and microscopic damage is derived for elastic solids with two-dimensional damage. For homogeneous materials, the damage strains are well known to be the symmetric part of the damage deformation tensor. For inhomogeneous materials, the macroscopic and microscopic deformation can still be correlated in a more complex way. For inhomogeneous materials with periodic structure and identifiable damage modes, the damage strains are the weighted sum of the symmetric parts of the damage deformation tensors for all damage modes. This is demonstrated for unidirectional fiber composites in Eq. (27), which describes a general relationship between measurable macroscopic macroscopic damage deformation, $\overline{\epsilon}_{ij}^{D}$, and the damage deformation tensor β_{ij}^{m} associated with specific damage modes, e.g., transverse matrix cracking, interfacial debonding, and fiber fractures. When the number of identifiable damage modes is smaller than or equal to that of relevant measurable macroscopic strains, the correlation can be used to detect and characterize the damage and its development from simple macroscopic stress and strain measurements.

The proposed approach does not incorporate a specific failure criterion or a damage evolution law, but as a general framework, can accomodate various failure criteria or failure modes. It can, however, track the damage progress in terms of the damage deformation tensors as shown in Fig. 8. The lack of a specific failure criterion or damage evolution law is considered as a strength as well as a weakness of the proposed approach. It is a strength because the observation can be based on purely theoretical grounds and does not rely upon questionable assumptions of failure mechanisms, evolution laws or unreliable strength/toughness parameters. The information obtained from this approach can be of great help before a researcher jumps into a specific mechanical model. The obvious weakness is that it is not able to fully predict the damage progress, and this limits its applicability at this moment. Instead of trying to predict the mechanical behavior for a given undamaged state, this approach is better suited for evaluation, inversely, of damage progress from the macroscopic mechanical behavior. When multiple failure mechanisms are involved, a smaller number of macroscopic measurements might be insufficient to interpret the underlying damage effectively.

Acknowledgments

The work described here was sponsored by the Air Force Office of Scientific Research (AFOSR). We are grateful to Dr. Walter F. Jones and Dr. Ozden O. Ochoa of AFOSR for their encouragement and cooperation.

References

[1] Luo, J. J., and Daniel, I. M., 2000, ''A cylinder Model for Characterization of Deformation and Damage Development in a Unidirectional Composite,'' Compos. Sci. Technol., **60**, No. 15, pp. 2791–2802.
[2] Mura, T., 1987, *Micromechanics of Defects in Solids*, 2nd Ed., Nijhoff, Boston.
[3] Budiansky, B., and O'Connel, R. J., 1976, ''Elastic Moduli of a Cracked Solid,'' Int. J. Solids Struct., **12**, pp. 81–97.
[4] Horii, H., and Nemat-Nasser, S., 1983, ''Overall Moduli of Solids With Microcracks: Load-Induced Anisotropy,'' J. Mech. Phys. Solids, **31**, No. 2, pp. 155–171.
[5] Taya, M., and Nemat-Nasser, S., 1981, ''On Effective Moduli of an Elastic Body Containing Periodically Distributed Voids: Comments and Corrections,'' Q. Appl. Math., **39**, pp. 43–59.
[6] Deng, H., and Nemat-Nasser, S., 1992, ''Microcrack Arrays in Isotropic Solids,'' Mech. Mater., **13**, No. 1, pp. 15–36.
[7] Accorsi, M. L., and Nemat-Nasser, S., 1986, ''Bounds on the Overall Elastic and Instantaneous Elastoplastic Moduli of Periodic Composites,'' Mech. Mater., **5**, pp. 209–220.
[8] Aveston, J., Cooper, G. A., and Kelly, A., 1971, ''The Properties of Fibre Composites,'' *Conference Proceedings, National Physical Laboratory*, IPC Science and Technology Press, Ltd., Guildford, UK, pp. 12–26.
[9] Aveston, J., and Kelly, A., 1973, ''Theory of Multiple Fracture of Fibrous Composites,'' J. Mater. Sci., **8**, pp. 352–362.
[10] Daniel, I. M., Anastassopoulos, G., and Lee, J.-W., 1989, ''Experimental Micromechanics of Brittle-Matrix Composites,'' *Micromechanics: Experimental Techniques*, Vol. 102, ASME, New York, pp. 133–146.
[11] Daniel, I. M., Anastassopoulos, G., and Lee, J.-W., 1993, ''The Behavior of Ceramic Matrix Composites Under Longitudinal Loading,'' Compos. Sci. Technol., **46**, pp. 105–113.
[12] Lee, J.-W., and Daniel, I. M., 1992, ''Deformation and Failure of Longitudinally Loaded Brittle-Matrix Composites,'' ASTM, STP 1120, American Society for Testing and Materials, Philadelphia, PA.
[13] McCartney, L. N., 1989, ''New Theoretical Model of Stress Transfer Between Fibre and Matrix in a Uniaxially Fibre-Reinforced Composite,'' Proc. R. Soc. London, Ser. A, **425**, pp. 215–244.
[14] Weitsman, Y., and Zhu, H., 1993, ''Multi-fracture of Ceramic Composites,'' J. Mech. Phys. Solids, **41**, No. 2, pp. 351–388.
[15] Kachanov, M., 1980, ''Continuum Model of Medium With Cracks,'' J. Eng. Mech., pp. 1089–1051.
[16] Mauge, C., and Kachanov, M., 1994, ''Effective Elastic Properties of an Anisotropic Material With Arbitrarily Oriented Interacting Cracks,'' J. Mech. Phys. Solids, **42**, No. 4, pp. 561–584.
[17] Talreja, R., 1989, ''Damage Development in Composites: Mechanisms and Modelling,'' J. Strain Anal., **24**, No. 4, pp. 215–222.
[18] Christensen, R. M., 1979, *Mechanics of Composite Materials*. John Wiley and Sons, New York.
[19] Timoshenko and Goodier, 1970, *Theory of Elasticity*, 3rd. Ed., McGraw-Hill, New York.
[20] Prewo, K. M., and Brennan, J. J., 1980, ''High-Strength Silicon Carbide Fiber-Reinforced Glass-Matrix Composites,'' J. Mater. Sci., **15**, pp. 463–468.
[21] Prewo, K. M., and Brennan, J. J., 1982, ''Silicon Carbide Yarn Reinforced Glass Matrix Composites,'' J. Mater. Sci., **17**, pp. 1201–1206.
[22] Prewo, K. M., 1986, ''Tension and Flexural Strength of Silicon Carbide Fibre-Reinforced Glass Ceramics,'' J. Mater. Sci., **21**, pp. 3590–3600.
[23] Prewo, K. M., 1987, ''Fatigue and Stress Rupture of Silicon Carbide Fibre-Reinforced Glass-Ceramics,'' J. Mater. Sci., **22**, pp. 2695–2701.
[24] Prewo, K. M., Johnson, B., and Starrett, S., 1989, ''Silicon Carbide Fiber-Reinforced Glass-Ceramic Composite Tensile Behaviour at Elevated Temperature,'' J. Mater. Sci., **24**, pp. 1373–1379.
[25] Marshall, D. B., and Evans, A. G., 1985, ''Failure Mechanisms in Ceramic-Fiber/Ceramic Matrix Composites,'' J. Am. Ceram. Soc., **68**, No. 5, pp. 225–231.
[26] Wooh, S. C., and Daniel, I. M., 1992, ''Real-Time Ultrasonic Investigation of Damage Development in Ceramic-Matrix Composite,'' *Review of Progress in Quantitative Nondestructive Evaluation*, Vol. 11, D. O. Thompson and D. E. Chimenti, eds., Plenum Press, New York, pp. 1523–1530.
[27] Luo, J.-J., Wooh, S.-C., and Daniel, I. M., 1994, ''Acoustic Emission Study of Failure Mechanisms in Ceramic Matrix Composite Under Longitudinal Tensile Loading,'' *Review of Progress in Quantitative Nondestructive Evaluation*, Vol. 13, D. O. Thompson and D. E. Chimenti, eds., Plenum Press, New York, pp. 469–476.
[28] Mall, S., and Kim, R. Y., 1992, ''Failure Mechanisms in Laminates of Silicon Carbide/Calcium-Aluminosilicate Ceramic Composite,'' Composites, **23**, No. 4, pp. 215–222.
[29] Larsen, D. C., 1992, Corning Glass Works, private communication.
[30] Tsai, C.-L., and Daniel, I. M., 1994, ''Method for Thermo-Mechanical Characterization of Single Fibers,'' Compos. Sci. Technol., **50**, pp. 7–12.
[31] Sørensen, B. F., 1993, ''Effect of Fibre Roughness on the Overall Stress-Transverse Strain Response of Ceramic Composites,'' Scr. Metall. Mater., **28**, pp. 435–439.

T. C. T. Ting
Professor,
Department of Civil and Materials Engineering,
University of Illinois at Chicago,
842 West Taylor Street (M/C 246),
Chicago, IL 60607-7023
Fellow ASME

Y. Hu
Associate Professor,
Department of Mechanics,
Huazhong University of Science and Technology,
Wuhan 430074, China

H. O. K. Kirchner
Professor,
Institut de Science des Materiaux, bat. 413
Universite Paris Sud,
F91405 Orsay Cedex, France

Anisotropic Elastic Materials With a Parabolic or Hyperbolic Boundary: A Classical Problem Revisited

When an anisotropic elastic material is under a two-dimensional deformation that has a hole of given geometry Γ subjected to a prescribed boundary condition, the problem can be solved by mapping Γ to a circle of unit radius. It is important that (i) each point on Γ is mapped to the same point for the three Stroh eigenvalues p_1, p_2, p_3 and (ii) the mapping is one-to-one for the region outside Γ. In an earlier paper it was shown that conditions (i) and (ii) are satisfied when Γ is an ellipse. The paper did not address to the case when Γ is an open boundary, such as a parabola or hyperbola that was studied by Lekhnitskii. We examine the mappings employed by Lekhnitskii for a parabola and hyperbola, and show that while the mapping for a parabola satisfies conditions (i) and (ii), the mapping for a hyperbola does not satisfy condition (i). Nevertheless, a valid solution can be obtained for the problem with a hyperbolic boundary, although the prescription of the boundary condition is restricted. We generalize Lekhnitskii's solutions for general anisotropic elastic materials and for more general boundary conditions. Using known identities and new identities presented here, real form expressions are given for the displacement and hoop stress vector at the parabolic and hyperbolic boundary.
[DOI: 10.1115/1.1381393]

1 Introduction

When an isotropic elastic material is under a two-dimensional deformation the solution can be expressed in terms of the complex variable

$$z = x_1 + i x_2, \tag{1}$$

and its complex conjugate $\overline{z}$. If the material has a hole of a given geometry Γ, the curve Γ is mapped to a circle of unit radius by a conformal mapping

$$z = w(\zeta). \tag{2}$$

The mapping must be *one-to-one*. Every point outside Γ in the (x_1, x_2)-plane is mapped to only one point in the ζ-plane, and vice versa. This condition is satisfied if ([1])

$$\frac{d}{d\zeta} w(\zeta) \neq 0 \quad \text{for} |\zeta| > 1. \tag{3}$$

If the material is anisotropic, the solution can be expressed in terms of three complex variables ([2,3])

$$z_k = x_1 + p_k x_2 \quad (k = 1,2,3) \tag{4}$$

and their complex conjugates $\overline{z_k}$. The complex constants p_k ($k = 1,2,3$) depend on elastic constants only. The imaginary part of p_k is positive and nonzero. To map the curve Γ to a unit circle we need three mapping functions

$$z_k = w_k(\zeta_k) \quad (k = 1,2,3). \tag{5}$$

It is important that

(i) each point on Γ in the (x_1, x_2)-plane is mapped to the *same* point on the unit circle in the ζ_k-plane for all three mapping functions $w_k(\zeta_k)$.
(ii) the mapping is one-to-one between the region outside Γ and the region outside the unit circle for each $w_k(\zeta_k)$. This is assured if

$$\frac{d}{d\zeta_k} w_k(\zeta_k) \neq 0 \quad \text{for} \quad |\zeta_k| > 1 \quad (k = 1,2,3). \tag{6}$$

If the condition (i) is violated, the boundary condition on Γ cannot be satisfied for all points on Γ because each point is mapped to three different points on the unit circle in the ζ_k-plane for $k = 1,2,3$. If the condition (ii) is violated, a Riemann surface with a branch cut must be introduced in the (x_1, x_2)-plane so that the mapping is one to one. The region outside Γ is no longer a continuous medium. The stress and the displacement are discontinuous across the branch cut.

When the curve Γ is a *closed* curve, it is shown in ([4]) that conditions (i) and (ii) are satisfied if Γ is an ellipse. If Γ is an *open* curve, Lekhnitskii [5] has employed mapping functions for a parabola and a hyperbola. We will show that condition (i) is sufficient, not necessary, for a valid solution. However, when a solution exists, the boundary conditions cannot be prescribed arbitrarily. The problems considered by Lekhnitskii for a parabolic and a hyperbolic boundary are rather specialized in that he limited the deformation to plane stress or plane strain. Hence the material is restricted to monoclinic materials with the symmetry plane at $x_3 = 0$. Moreover, the applied loads are also limited.

The purpose of this paper is to consider the Lekhnitskii's problems for general anisotropic elastic materials and for more general loading conditions. We present new identities and give real-form expressions for the displacement and hoop stress vector at the parabolic and hyperbolic boundary. We also discuss the mapping of parabola and hyperbola for anisotropic elasticity, which has not been discussed in detail in the literature, and show why a solution for the hyperbolic boundary can be obtained despite the fact that it violates condition (i).

Contributed by the Applied Mechanics Division of THE AMERICAN SOCIETY OF MECHANICAL ENGINEERS for publication in the ASME JOURNAL OF APPLIED MECHANICS. Manuscript received by the ASME Applied Mechanics Division, Aug. 29, 2000; final revision, Jan. 2, 2001. Associate Editor: J. R. Barber. Discussion on the paper should be addressed to the Editor, Prof. Lewis T. Wheeler, Department of Mechanical Engineering, University of Houston, Houston, TX 77204-4792, and will be accepted until four months after final publication of the paper itself in the ASME JOURNAL OF APPLIED MECHANICS.

2 The Stroh Formalism

In a fixed rectangular coordinate system x_i $(i=1,2,3)$ let u_i and σ_{ij} be, respectively, the displacement and stress in an anisotropic elastic material. The equation of equilibrium and the stress-strain law are

$$\sigma_{ij,j}=0, \quad \sigma_{ij}=C_{ijks}u_{k,s} \tag{7}$$

in which the comma denotes differentiation, repeated indices imply summation, and C_{ijks} are the elastic stiffnesses that are assumed to possess the full symmetry. For a two-dimensional deformation for which u_i depends on x_1 and x_2 only, a solution to (7) is ([3,6–8])

$$\mathbf{u}=\mathbf{a}F(z), \quad \phi=\mathbf{b}F(z), \quad z=x_1+px_2, \tag{8}$$

$$\sigma_{i1}=-\phi_{i,2}, \quad \sigma_{i2}=\phi_{i,1}, \tag{9}$$

where F is an arbitrary function of z, and p and $\mathbf{a}$ satisfy the eigenrelation

$$\{\mathbf{Q}+p(\mathbf{R}+\mathbf{R}^T)+p^2\mathbf{T}\}\mathbf{a}=\mathbf{0}. \tag{10}$$

The superscript T stands for the transpose, $\mathbf{I}$ is the unit matrix, and **Q, R, T** are 3×3 matrices whose elements are

$$Q_{ik}=C_{i1k1}, \quad R_{ik}=C_{i1k2}, \quad T_{ik}=C_{i2k2}. \tag{11}$$

The three-vector $\mathbf{b}$ in (8) is related to the three-vector $\mathbf{a}$ by

$$\mathbf{b}=(\mathbf{R}^T+p\mathbf{T})\mathbf{a}=-(p^{-1}\mathbf{Q}+\mathbf{R})\mathbf{a} \tag{12}$$

in which the second equality follows from (10).

There are six eigenvalues p from (10) that consist of three pairs of complex conjugates. If p_1,p_2,p_3 are the eigenvalues with a positive imaginary part, the remaining three eigenvalues are the complex conjugates $\bar{p}_1,\bar{p}_2,\bar{p}_3$. Let $\mathbf{a}_k,\mathbf{b}_k$ $(k=1,2,3)$ be the corresponding eigenvectors computed from (10) and (12). A general solution obtained by superposing three solutions of (8) associated with p_1,p_2,p_3 with three arbitrary constant multipliers q_k $(k=1,2,3)$ is ([8])

$$\mathbf{u}=\mathrm{Im}\{\mathbf{A}\langle F(z_*)\rangle\mathbf{q}\}, \quad \phi=\mathrm{Im}\{\mathbf{B}\langle F(z_*)\rangle\mathbf{q}\}, \tag{13}$$

where Im stands for the imaginary part and

$$\mathbf{A}=[\mathbf{a}_1,\mathbf{a}_2,\mathbf{a}_3], \quad \mathbf{B}=[\mathbf{b}_1,\mathbf{b}_2,\mathbf{b}_3], \tag{14}$$

$$\langle F(z_*)\rangle=\mathrm{diag}[F(z_1),F(z_2),F(z_3)], \quad z_k=x_1+p_kx_2. \tag{15}$$

Let $\mathbf{t}$ be the surface traction on a boundary Γ. If s is the arc-length measured along Γ such that, when facing the direction of increasing s, the material is on the right-hand side, it can be shown that ([3])

$$\mathbf{t}=\frac{d}{ds}\phi. \tag{16}$$

Hence

$$\phi=\text{constant on } \Gamma, \quad \text{if } \Gamma \text{ is traction-free.} \tag{17}$$

If ϕ is not a constant, the total traction $\mathbf{f}$ between two points $s_2>s_1$ on Γ is

$$\mathbf{f}=\int_{s_1}^{s_2}\mathbf{t}ds=\phi(s_2)-\phi(s_1). \tag{18}$$

When there is a concentrated force $\mathbf{f}$ applied at a point, the value of ϕ increases by $\mathbf{f}$ if (18) is integrated counterclockwise around the point one full circle.

3 Parabolic Boundary

Consider an anisotropic elastic material that occupies the region

$$x_2\leqslant ax_1^2, \quad a>0. \tag{19}$$

The boundary Γ is a parabola given by

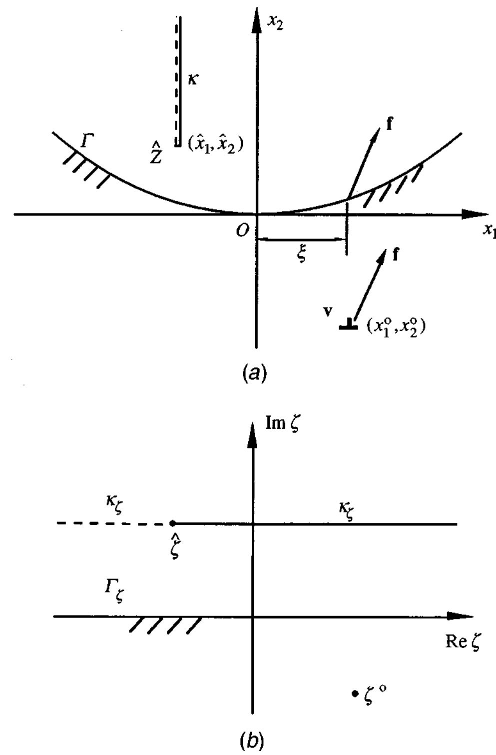

Fig. 1 Mapping of a parabola (drawn for Re $p>0$); (*a*) the (x_1,x_2)-plane, (*b*) the ζ-plane

$$x_2=ax_1^2 \quad \text{on } \Gamma. \tag{20}$$

The parabola degenerates to a crack when $a=\infty$ and to a plane boundary when $a=0$. Following ([5]), let

$$z=\zeta+ap\zeta^2 \quad \text{or} \quad \zeta\frac{\sqrt{1+4apz}-1}{2ap}. \tag{21}$$

For simplicity, we have suppressed the subscript k for p_k,z_k,ζ_k $(k=1,2,3)$ in (21). It is easily seen from (20) and $(21)_1$ that

$$\zeta=x_1 \quad \text{on } \Gamma. \tag{22}$$

Thus the parabola Γ is mapped to the real axis (denoted by Γ_ζ in Fig. 1) in the ζ-plane. The region below the parabola is mapped to the lower half-space in the ζ-plane. Since (22) is independent of p, if p_1,p_2,p_3 are different, each point on Γ is mapped to the same point on Γ_ζ. This satisfies condition (i).

Let $\hat{\zeta}$ be the root of $dz/d\zeta=0$, which is a *branch* point. From $(21)_1$ we have

$$\hat{\zeta}=\frac{-1}{2ap}=\frac{-\bar{p}}{2ap\bar{p}}. \tag{23}$$

The $\hat{z}$ associated with $\hat{\zeta}$ is obtained from $(21)_1$ as

$$\hat{z}=\hat{x}_1+p\hat{x}_2=\frac{-1}{4ap}. \tag{24}$$

It is the vanishing of the quantity inside the square root in $(21)_2$. The second equality in (24) allows us to compute the branch point $(\hat{x}_1,\hat{x}_2)$ in the (x_1,x_2)-plane. It is denoted by $\hat{Z}$ in Fig. 1. The branch cut κ is extended from $\hat{Z}$ to infinity in the positive x_2-direction. It is mapped to a horizontal line κ_ζ that passes through $\hat{\zeta}$ in the ζ-plane. The right (or left) side of the branch cut κ in the (x_1,x_2)-plane is mapped to the right (or left) of $\hat{\zeta}$. They are denoted by a solid and a dashed line, respectively. It can be shown that a horizontal line in the ζ-plane is a parabola in the

(x_1, x_2)-plane whose axis of the symmetry is parallel to the x_2-axis and whose apex is on the line that connects the branch point $\hat{Z}$ and the origin O.

The imaginary part of p is positive and nonzero so that the $\hat{\zeta}$ given by (23) is located outside the half-plane $\mathrm{Im}\,\zeta \leqslant 0$. This implies that the branch point $\hat{Z}$ and the branch cut κ are outside the parabolic boundary occupied by the material. Hence the mapping for the region below the parabola is one to one. This satisfies condition (ii). It is clear that we cannot consider the region above the parabola because there is a branch cut in that region.

Consider the surface Green's function due to a concentrated force $\mathbf{f}$ applied at

$$x_1 = \xi, \quad \mathbf{x}_2 = a\xi^2, \tag{25}$$

on the surface Γ. The parabolic surface is otherwise traction-free. The solution has been obtained by Hu and Zhao [9] as

$$\mathbf{u} = \frac{1}{\pi}\mathrm{Im}\{\mathbf{A}\langle \ln(\zeta_* - \xi)\rangle \mathbf{B}^{-1}\}\mathbf{f},$$

$$\phi = \frac{1}{\pi}\mathrm{Im}\{\mathbf{B}\langle \ln(\zeta_* - \xi)\rangle \mathbf{B}^{-1}\}\mathbf{f}. \tag{26}$$

On the parabolic surface Γ, $\zeta_* = x_1$ so that

$$\ln(\zeta_* - \xi) = \ln(x_1 - \xi) \quad \text{for} \quad x_1 > \xi,$$

$$\ln(\zeta_* - \xi) = \ln|x_1 - \xi| - i\pi \quad \text{for} \quad x_1 < \xi. \tag{27}$$

Using the identity $(A1)$ presented in the Appendix the displacement at the surface Γ can be obtained in a real form as

$$\mathbf{u}(x_1) = \frac{-1}{\pi}(\ln r)\mathbf{L}^{-1}\mathbf{f}, \quad \text{for} \quad x_1 > \xi,$$

$$\mathbf{u}(x_1) = \frac{-1}{\pi}(\ln r)\mathbf{L}^{-1}\mathbf{f} + \mathbf{S}\mathbf{L}^{-1}\mathbf{f}, \quad \text{For} \quad x_1 < \xi. \tag{28}$$

In the above, $r = |x_1 - \xi|$ and $\mathbf{S}$ and $\mathbf{L}$ are two of the three Barnett-Lothe tensors. They are real. It should be pointed out that the displacement is unique up to a constant rigid-body translation and rotation. Hence we could subtract $\frac{1}{2}\mathbf{S}\mathbf{L}^{-1}\mathbf{f}$ from (28) so that it has a symmetric expression

$$\mathbf{u}(x_1) = \frac{-1}{\pi}(\ln r)\mathbf{L}^{-1}\mathbf{f} - \frac{1}{2}\mathbf{S}\mathbf{L}^{-1}\mathbf{f}, \quad \text{for} \quad x_1 > \xi,$$

$$\mathbf{u}(x_1) = \frac{-1}{\pi}(\ln r)\mathbf{L}^{-1}\mathbf{f} + \frac{1}{2}\mathbf{S}\mathbf{L}^{-1}\mathbf{f}, \quad \text{For} \quad x_1 < \xi. \tag{29}$$

Equation (29) is independent of a, indicating that the surface displacement is independent of the shape of the parabola. In particular, the surface displacement is identical to the half-space with a plane boundary.

Let $\mathbf{t}_h(x_1)$ be the *hoop stress vector* on Γ acting on a surface perpendicular to the boundary Γ. If s is the arclength measured along the perpendicular line, we obtain from $(26)_2$ and (16),

$$\mathbf{t}_h(x_1) = \frac{1}{\pi(x_1 - \xi)}\mathrm{Im}\left\{\mathbf{B}\left\langle \frac{d\zeta_*}{ds}\right\rangle \mathbf{B}^{-1}\right\}\mathbf{f}. \tag{30}$$

It can be shown that

$$\frac{d}{ds} = \cos\eta\frac{\partial}{\partial x_1} - \sin\eta\frac{\partial}{\partial x_2} = (\cos\eta - p\sin\eta)\frac{d}{dz} \tag{31}$$

where η is the angle the tangent to Γ makes with the x_1-axis. Inserting $(21)_2$ in (30) using (31), and evaluating the result on Γ leads to

$$\mathbf{t}_h(x_1) = \frac{-\cos\eta}{\pi(x_1 - \xi)}\mathrm{Im}\left\{\mathbf{B}\left\langle \frac{p_* - \tan\eta}{1 + p_*\tan\eta}\right\rangle \mathbf{B}^{-1}\right\}\mathbf{f}, \tag{32}$$

$$\eta = \tan^{-1}(2ax_1). \tag{33}$$

The identity $(A21)$ allows us to write (32) in a real form as

$$\mathbf{t}_h(x_1) = \frac{-\cos^3\eta}{\pi(x_1 - \xi)}\{2ax_1[\mathbf{N}_3(\eta)(\mathbf{N}_1 - 2ax_1\mathbf{I}) + \mathbf{N}_1^T(\eta)\mathbf{N}_3] - \mathbf{N}_3\}\mathbf{L}^{-1}\mathbf{f}, \tag{34}$$

where $\mathbf{N}_k$, $\mathbf{N}_k(\theta)$ $(k = 1,2,3)$ are defined in $(A4)$ and $(A8)$. If $\mathbf{m}(x_1)$ is the normal vector to the parabolic boundary, it can be shown that $\mathbf{t}_h(x_1)$ and $\mathbf{m}(x_1)$ are orthogonal to each other. The hoop stress vector at $x_1 = 0$ is

$$\mathbf{t}_h(0) = \frac{-1}{\pi\xi}\mathbf{N}_3\mathbf{L}^{-1}\mathbf{f}. \tag{35}$$

This is independent of a, the shape of the parabola.

With the surface Green's function given by (26), the solution for the problem for which the surface Γ is subjected to a distributed load can be easily obtained by an integration. This was done in ([5]) for a monoclinic material. Hu and Zhao [9] also presented the Green's function for which the applied force $\mathbf{f}$ is inside the half-space. Their solution can be easily extended to include a line dislocation.

4 Hyperbolic Boundary

Let the material be bounded by a pair of hyperbolas defined by

$$\frac{x_2^2}{a^2} - \frac{x_1^2}{b^2} = 1 \tag{36}$$

where a, b are real and positive (Fig. 2). Consider the mapping ([5])

$$z = \frac{1}{2}\left\{\zeta + \frac{a^2p^2 - b^2}{\zeta}\right\}, \quad \zeta = z + \sqrt{z^2 - a^2p^2 + b^2}. \tag{37}$$

If Γ^+, Γ^- denotes the upper and lower branches of the hyperbola, we have

$$x_1 = b\,sh\,\gamma = \frac{b}{2}(e^{\gamma} - e^{-\gamma}),$$

$$x_2 = \pm a\,ch\,\gamma = \pm\frac{a}{2}(e^{\gamma} + e^{-\gamma}), \quad \text{on} \quad \Gamma^{\pm}, \tag{38}$$

where $-\infty < \gamma < \infty$ is a real parameter. In the ζ-plane they are

$$\zeta = (b \pm ap)e^{\gamma} \quad \text{on} \quad \Gamma_{\zeta}^{\pm}. \tag{39}$$

Let

$$b + ap = \rho^+ e^{i\psi^+}, \quad b - ap = \rho^- e^{-i\psi^-}, \tag{40}$$

in which $\rho^{\pm} > 0$ and $\psi^{\pm}$ are real. The $\Gamma_{\zeta}^{\pm}$ are radial lines making an angle ψ^+ and $-\psi^-$ with the $\mathrm{Re}\,\zeta$-axis (Fig. 2). Thus the region bounded by the hyperbolas $\Gamma^{\pm}$ is mapped to the wedge region bounded by the radial lines $\Gamma_{\zeta}^{\pm}$.

The square root in $(37)_2$ suggests that a branch cut is needed for the mapping to be one to one. The vanishing of the square root gives, using (40),

$$\hat{z} = \hat{x}_1 + p\hat{x}_2 = i\hat{\rho}e^{-i\hat{\psi}}, \tag{41}$$

$$\hat{\rho} = \sqrt{\rho^+\rho^-}, \quad \hat{\psi} = \frac{1}{2}(\psi^- - \psi^+). \tag{42}$$

The branch points $\pm(\hat{x}_1, \hat{x}_2)$ are determined by equating the real and imaginary parts of $(41)_2$. They are denoted by $\hat{Z}$ and $-\hat{Z}$ in Fig. 2. If the line that connects $\hat{Z}$ and $-\hat{Z}$ is called the Y-axis, one branch cut extends from $\hat{Z}$ to $Y = \infty$ (denoted by κ^+) while the other branch cut extends from $-\hat{Z}$ to $Y = -\infty$ (denoted by κ^-). Inserting $\hat{z}$ of (41) into $(37)_2$, or setting $dz/d\zeta = 0$ in $(37)_1$, we obtain

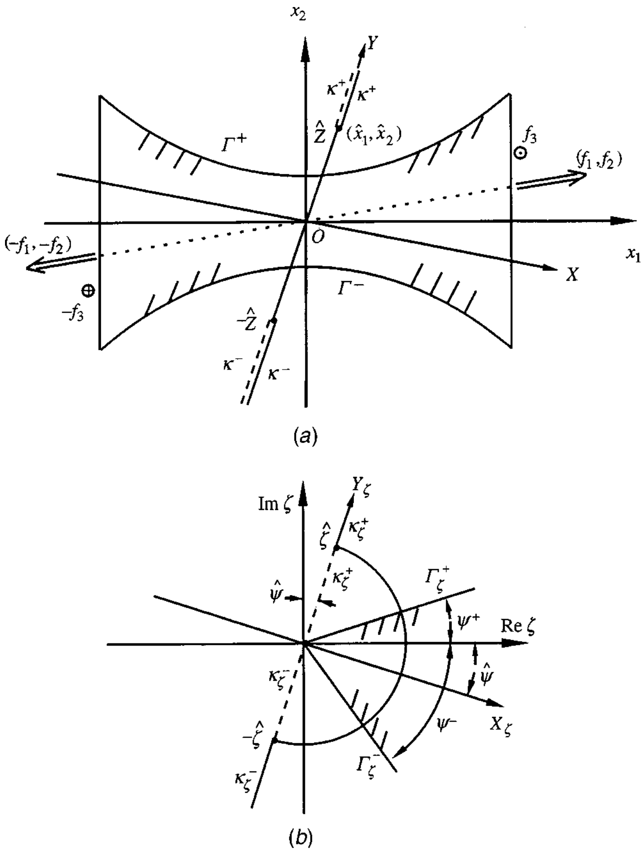

Fig. 2 Mapping of a hyperbola (drawn for Re $p>0$); (*a*) the (x_1,x_2)-plane, (*b*) the ζ-plane

$$\hat{\zeta}=i\hat{\rho}e^{-i\hat{\psi}}. \tag{43}$$

If we denote the line that connects $\hat{\zeta}$ and $-\hat{\zeta}$ as the Y_ζ-axis, the right (or left) side of the branch cut κ^+ in the (x_1,x_2)-plane is mapped to the positive Y_ζ-axis above (or below) $\hat{\zeta}$. Likewise, the right (or left) of κ^- is mapped to the negative Y_ζ-axis below (or above) $-\hat{\zeta}$. They are denoted by a solid and a dashed line, respectively. The points on the *Y*-axis between $\hat{Z}$ and $-\hat{Z}$ are mapped to a half-circle in the ζ-plane that passes through $\hat{\zeta}$ and $-\hat{\zeta}$ with its center at the origin. The half-plane to the right (or left) of the *Y*-axis in the (x_1,x_2)-plane is mapped to the right of the Y_ζ-axis and outside (or inside) the half-circle.

It can be shown that all radial lines and concentric circles with their center at the origin in the ζ-plane are confocal hyperbolas and ellipses in the (x_1,x_2)-plane when referred to an oblique coordinate system (*X, Y*). The corresponding axes X_ζ and Y_ζ in the ζ-plane are orthogonal to each other (pp. 86–89, ([8])).

The branch points $\hat{\zeta}$ and $-\hat{\zeta}$ are outside the wedge region bounded by $\Gamma_\zeta^\pm$. Hence the branch points $\hat{Z}$ and $-\hat{Z}$ and the branch cuts $\kappa^\pm$ in the (x_1,x_2)-plane are outside the region bounded by the hyperbolas $\Gamma^\pm$. Thus the mapping for the region inside the hyperbolas is one to one. It satisfies condition (ii). However, it does not satisfy condition (i) because (39) depends on *p*. If p_1, p_2, p_3 are different, each point on $\Gamma^\pm$ maps to three different points. It would be a problem to satisfy an arbitrarily prescribed boundary condition.

What is remarkable about the hyperbolic boundary is that, although the ζ given in (39) is different for p_1, p_2, p_3,

$$\ln\zeta=\ln(b\pm ap)+\gamma \quad \text{on} \quad \Gamma^\pm \tag{44}$$

so that the *difference* in $(\ln\zeta)$ for p_1, p_2, p_3 is independent of γ. Hence, consider the solution

$$\mathbf{u}=\frac{1}{\pi}\operatorname{Im}\{\mathbf{A}\langle\ln\zeta_*\rangle\mathbf{B}^{-1}\mathbf{q}\},$$

$$\phi=\frac{1}{\pi}\operatorname{Im}\{\mathbf{B}\langle\ln\zeta_*\rangle\mathbf{B}^{-1}\mathbf{q}\}, \tag{45}$$

where $\mathbf{q}$ is a constant vector. Let

$$\mathbf{q}=\mathbf{g}+i\mathbf{h} \tag{46}$$

in which $\mathbf{g}$ and $\mathbf{h}$ are the real and imaginary parts of $\mathbf{q}$. On the boundary $\Gamma^\pm$ we have

$$\phi=\frac{1}{\pi}\operatorname{Im}\{\mathbf{B}\langle\ln(b\pm ap_*)\rangle\mathbf{B}^{-1}\}\mathbf{g}+\frac{1}{\pi}\operatorname{Re}\{\mathbf{B}\langle\ln(b\pm ap_*)\rangle\mathbf{B}^{-1}\}\mathbf{h}$$

$$+\frac{1}{\pi}\gamma\mathbf{h}, \tag{47}$$

where Re stands for the real part. Let *s* be the arclength measured along $\Gamma^\pm$. It can be shown from (38) that

$$ds=\pm\sqrt{(dx_1)^2+(dx_2)^2}=\pm\sqrt{b^2+[1+(a/b)^2]x_1^2}\,d\gamma. \tag{48}$$

Hence, the traction $\mathbf{t}$ applied on the hyperbolic surface $\Gamma^\pm$ is, by (47) and (16),

$$\mathbf{t}=\frac{\pm\mathbf{h}}{\pi\sqrt{b^2+[1+(a/b)^2]x_1^2}} \quad \text{on} \quad \Gamma^\pm. \tag{49}$$

If $\mathbf{f}$ is the total force on a cross section $x_1=$ constant, we have from (18),

$$\mathbf{f}=\phi(\Gamma^-)-\phi(\Gamma^+). \tag{50}$$

Substitution from (47) gives

$$\mathbf{f}=-(\mathbf{Gh}+\mathbf{Kg}), \tag{51}$$

$$\mathbf{G}+i\mathbf{K}=\frac{1}{\pi}\mathbf{B}\left\langle\ln\frac{b+ap_*}{b-ap_*}\right\rangle\mathbf{B}^{-1}. \tag{52}$$

The 3×3 matrices $\mathbf{G}$ and $\mathbf{K}$ are the real and imaginary parts of the right side in (52). In summary, the solution (45) satisfies the following boundary conditions:
(I) On the hyperbolic surface, the traction is specified by (49) and
(II) on any cross section $x_1=$ constant, the total force $\mathbf{f}$ is specified by (51). The vectors $\mathbf{g}$ and $\mathbf{h}$ are assumed prescribed.

We see that the traction $\mathbf{t}$ on $\Gamma^\pm$ cannot be prescribed arbitrarily. Its dependence on x_1 has to be specified according to (49). Also, we can only prescribe the *total* force $\mathbf{f}$ applied on any cross section $x_1=$ constant. The precise distribution of the traction on the cross section cannot be prescribed.

In the rest of the paper we let $\mathbf{h}=\mathbf{0}$ so that (45) is written as

$$\mathbf{u}=\frac{-1}{\pi}\operatorname{Im}\{\mathbf{A}\langle\ln\zeta_*\rangle\mathbf{B}^{-1}\}\mathbf{K}^{-1}\mathbf{f},$$

$$\phi=\frac{-1}{\pi}\operatorname{Im}\{\mathbf{B}\langle\ln\zeta_*\rangle\mathbf{B}^{-1}\}\mathbf{K}^{-1}\mathbf{f}. \tag{53}$$

The body is subjected to a pair of forces $\mathbf{f}$ and $-\mathbf{f}$, and the hyperbolic surface is traction-free (Fig. 2(*a*)). An approximate solution to this problem was given in ([10]) for an isotropic material and in ([11,12]) for an orthotropic material. Lekhnitskii [5] considered the problem for a plane-strain or plane-stress deformation. Hence the material is limited to monoclinic materials with the symmetry plane at $x_3=0$. He also restricted the force $\mathbf{f}$ to be along the x_1-axis. The solution (53) is for a general anisotropic elastic material and for an arbitrary force $\mathbf{f}$. In the following we present a real form expression of $\mathbf{K}$ and the displacement and the hoop stress vector at the hyperbolic boundary for a general anisotropic elastic material.

The matrix $\mathbf{K}$ is, from (52),

$$\mathbf{K}=\frac{1}{\pi}\operatorname{Im}\{\mathbf{B}\langle\ln(b+ap_*)\rangle\mathbf{B}^{-1}\}-\frac{1}{\pi}\operatorname{Im}\{\mathbf{B}\langle\ln(b-ap_*)\rangle\mathbf{B}^{-1}\}. \tag{54}$$

Making use of the identity $(A11)_2$ the real form expression is

$$\mathbf{K}=\mathbf{L}(\alpha,-\alpha)\mathbf{L}^{-1},\quad \alpha=\tan^{-1}(a/b), \tag{55}$$

where, using $(A9)$,

$$\mathbf{L}(\theta,-\theta)=\mathbf{L}(\theta)-\mathbf{L}(-\theta)=\frac{-1}{\pi}\int_{-\theta}^{\theta}\mathbf{N}_3(\omega)d\omega. \tag{56}$$

The explicit expression of $\mathbf{L}(\theta)$ for orthotropic materials can be found in ([13]).

The displacement at the hyperbolic boundary $\Gamma^{\pm}$ is, from $(53)_1$ and (39),

$$\mathbf{u}(x_1)=\frac{-1}{\pi}\operatorname{Im}\{\mathbf{A}\langle\ln(b\pm p_*a)\rangle\mathbf{B}^{-1}+\gamma\mathbf{A}\mathbf{B}^{-1}\}\mathbf{K}^{-1}\mathbf{f} \tag{57}$$

or, using $(A1)$, $(A11)$, and (55),

$$\mathbf{u}(x_1)=\left\{\frac{1}{\pi}(\ln\delta+\gamma)\mathbf{I}+\mathbf{S}(\pm\alpha)\right\}[\mathbf{L}(\alpha,-\alpha)]^{-1}\mathbf{f}. \tag{58}$$

In the above,

$$\delta=\sqrt{a^2+b^2},\quad \alpha=\tan^{-1}(a/b). \tag{59}$$

The γ in (58) can be expressed in terms of x_1 in (38) as

$$\gamma=\ln[(x_1/b)+\sqrt{1+(x_1/b)^2}]. \tag{60}$$

Let $\mathbf{t}_h(x_1)$ be the *hoop stress vector* on Γ acting on a surface perpendicular to the boundary Γ. If s is the arclength measured along the perpendicular line, we obtain from $(53)_2$ and (16),

$$\mathbf{t}_h(x_1)=\frac{-1}{\pi}\operatorname{Im}\left\{\mathbf{B}\left\langle\frac{1}{\zeta_*}\frac{d\zeta_*}{ds}\right\rangle\mathbf{B}^{-1}\right\}\mathbf{K}^{-1}\mathbf{f}. \tag{61}$$

Inserting $(37)_2$ in (61) using (31), and evaluating the result on $\Gamma^{\pm}$ leads to

$$\mathbf{t}_h^{\pm}(x_1)=\frac{\cos\eta}{\pi\sqrt{b^2+x_1^2}}\operatorname{Im}\left\{\mathbf{B}\left\langle\frac{p_*-\tan\eta}{1+p_*\tan\eta}\right\rangle\mathbf{B}^{-1}\right\}\mathbf{K}^{-1}\mathbf{f}, \tag{62}$$

$$\eta=\pm\tan^{-1}\frac{ax_1}{b\sqrt{b^2+x_1^2}}. \tag{63}$$

The identities $(A21)$ and (55) allow us to write (62) in a real form as

$$\mathbf{t}_h^{\pm}(x_1)=\frac{\cos^3\eta}{\pi\sqrt{b^2+x_1^2}}\{\tan\eta[\mathbf{N}_3(\eta)(\mathbf{N}_1-\tan\eta\mathbf{I})+\mathbf{N}_1^T(\eta)\mathbf{N}_3]-\mathbf{N}_3\}[\mathbf{L}(\alpha,-\alpha)]^{-1}\mathbf{f}. \tag{64}$$

It can be shown that $\mathbf{t}_h^{\pm}(x_1)$ is orthogonal to $\Gamma^{\pm}$. At $x_1=0$,

$$\mathbf{t}_h(0)=\frac{-1}{\pi b}\mathbf{N}_3[\mathbf{L}(\alpha,-\alpha)]^{-1}\mathbf{f}. \tag{65}$$

When the material is orthotropic with p_1, p_2 being purely imaginary and the force $\mathbf{f}$ is along the x_1-axis, $\mathbf{t}_h(0)$ has only one nonzero component. For this special case (65) recovers the result obtained in ([5]).

The traction σ_{i1} $(i=1,2,3)$ on any cross section $x_1=x_1^0$ is obtained by inserting $(53)_2$ into $(9)_1$. We have

$$[\sigma_{i1}]=\frac{1}{\pi}\operatorname{Im}\left\{\mathbf{B}\left\langle\frac{p_*}{\zeta_*-z_*}\right\rangle\mathbf{B}^{-1}\right\}\mathbf{K}^{-1}\mathbf{f}. \tag{66}$$

If f_1, f_2, f_3 are the components of the total force $\mathbf{f}$ it can be shown that

$$\int_{\Gamma^-}^{\Gamma^+}\sigma_{11}(x_1^0,x_2)x_2dx_2=f_2x_1^0. \tag{67}$$

The proof requires new identities, and is omitted here. Let (x_1^0,x_2^0) be the point of application for the normal force f_1 at the cross section $x_1=x_1^0$. Since

$$\int_{\Gamma^-}^{\Gamma^+}\sigma_{i1}(x_1^0,x_2)dx_2=f_i, \tag{68}$$

the left side of (67) is $f_1x_2^0$. Hence (67) gives

$$f_2/f_1=x_2^0/x_1^0. \tag{69}$$

The point of application of the shear force f_2 is immaterial. We may assume that f_2 is also applied at (x_1^0,x_2^0). Equation (69) tells us that the vector (f_1,f_2) is along a radial line in the (x_1,x_2)-plane. It is *collinear* with $(-f_1,-f_2)$ as shown in Fig. 2(a). The point of application for the antiplane shear f_3 need not be at (x_1^0,x_2^0). It should be noted from (68) that the vanishing of f_1, f_2 or f_3 does not necessarily imply the vanishing of σ_{11}, σ_{21} or σ_{31}.

5 Concluding Remarks

We have shown that, for an anisotropic elastic material under a two-dimensional deformation that has a parabolic boundary, the mapping employed by Lekhnitskii satisfies conditions (i) and (ii) delineated in the Introduction. If the material has a hyperbolic boundary, the mapping employed by Lekhnitskii satisfies condition (ii) but not condition (i). Nevertheless, a valid solution can be obtained for a special boundary condition. Hence, for an open boundary Γ, condition (i) is sufficient, not necessary, for a valid solution. It should be stressed that a valid solution may not exist. When it exists, the boundary condition may not be prescribed arbitrarily.

Appendix

The following identities are employed in the paper.

$$\mathbf{A}\mathbf{B}^{-1}=-\mathbf{S}\mathbf{L}^{-1}-i\mathbf{L}^{-1}, \tag{A1}$$

$$\mathbf{L}=-2i\mathbf{B}\mathbf{B}^T, \tag{A2}$$

$$\mathbf{B}\langle p_*\rangle\mathbf{B}^{-1}=(\mathbf{N}_1^T-\mathbf{N}_3\mathbf{S}\mathbf{L}^{-1})-i\mathbf{N}_3\mathbf{L}^{-1}, \tag{A3}$$

where

$$\mathbf{N}_1=-\mathbf{T}^{-1}\mathbf{R}^T,\quad \mathbf{N}_2=\mathbf{T}^{-1},\quad \mathbf{N}_3=\mathbf{R}\mathbf{T}^{-1}\mathbf{R}^T-\mathbf{Q}. \tag{A4}$$

In the above $\mathbf{S}$, $\mathbf{L}$, and $\mathbf{H}$ (to appear below) are the three Barnett-Lothe tensors. They are real. Explicit expression of the Barnett-Lothe tensors can be found in ([14]). Let

$$x_1=r\cos\theta,\quad x_2=r\sin\theta, \tag{A5}$$

$$\mathbf{n}=\begin{bmatrix}\cos\theta\\ \sin\theta\\ 0\end{bmatrix},\quad \mathbf{m}=\begin{bmatrix}-\sin\theta\\ \cos\theta\\ 0\end{bmatrix}, \tag{A6}$$

$$Q_{ik}(\theta)=C_{ijks}n_jn_s,\quad R_{ik}(\theta)=C_{ijks}n_jm_s,\quad T_{ik}(\theta)=C_{ijks}m_jm_s, \tag{A7}$$

$$\mathbf{N}_1(\theta)=-\mathbf{T}^{-1}(\theta)\mathbf{R}^T(\theta),\quad \mathbf{N}_2(\theta)=\mathbf{T}^{-1}(\theta),\quad \mathbf{N}_3(\theta)=\mathbf{R}(\theta)\mathbf{T}^{-1}(\theta)\mathbf{R}^T(\theta)-\mathbf{Q}(\theta). \tag{A8}$$

The matrices $\mathbf{N}_k(\theta)$ reduce to $\mathbf{N}_k$ when $\theta=0$. Consider the integrals

$$\mathbf{S}(\theta)=\frac{1}{\pi}\int_0^\theta \mathbf{N}_1(\omega)d\omega, \quad \mathbf{H}(\theta)=\frac{1}{\pi}\int_0^\theta \mathbf{N}_2(\omega)d\omega,$$

$$\mathbf{L}(\theta)=\frac{-1}{\pi}\int_0^\theta \mathbf{N}_3(\omega)d\omega. \tag{A9}$$

The tensors $\mathbf{S}(\theta)$, $\mathbf{H}(\theta)$, $\mathbf{L}(\theta)$ reduce to $\mathbf{S}$, $\mathbf{H}$, $\mathbf{L}$ when $\theta=\pi$ ([16]). It can be shown that (see (7.9–23) in ([8]))

$$2\mathbf{A}\langle \ln z_*\rangle \mathbf{B}^T=[(\ln r)\mathbf{I}+\pi\mathbf{S}(\theta)](\mathbf{I}-i\mathbf{S})+i\pi\mathbf{H}(\theta)\mathbf{L},$$

$$2\mathbf{B}\langle \ln z_*\rangle \mathbf{B}^T=i[(\ln r)+\pi\mathbf{S}^T(\theta)]\mathbf{L}-\pi\mathbf{L}(\theta)(\mathbf{I}-i\mathbf{S}). \tag{A10}$$

Making use of $(A2)$, $(A10)$ can be written as

$$\mathbf{A}\langle \ln z_*\rangle \mathbf{B}^{-1}=-[(\ln r)\mathbf{I}+\pi\mathbf{S}(\theta)](i\mathbf{I}+\mathbf{S})\mathbf{L}^{-1}+\pi\mathbf{H}(\theta),$$

$$\mathbf{B}\langle \ln z_*\rangle \mathbf{B}^{-1}=[(\ln r)\mathbf{I}+\pi\mathbf{S}^T(\theta)]+\pi\mathbf{L}(\theta)(i\mathbf{I}+\mathbf{S})\mathbf{L}^{-1}. \tag{A11}$$

We now derive a new identity that can convert (32) and (62) to a real form. The two equations in (12) can be written in a standard eigenrelation as

$$\mathbf{N}\begin{bmatrix}\mathbf{a}\\ \mathbf{b}\end{bmatrix}=p\begin{bmatrix}\mathbf{a}\\ \mathbf{b}\end{bmatrix}, \tag{A12}$$

where the 6×6 matrix $\mathbf{N}$ is ([15])

$$\mathbf{N}=\begin{bmatrix}\mathbf{N}_1 & \mathbf{N}_2\\ \mathbf{N}_3 & \mathbf{N}_1^T\end{bmatrix}. \tag{A13}$$

Equation $(A12)$ is generalized as

$$\{\mathbf{I}+(\tan\theta)\mathbf{N}\}\begin{bmatrix}\mathbf{a}\\ \mathbf{b}\end{bmatrix}=(1+p\tan\theta)\begin{bmatrix}\mathbf{a}\\ \mathbf{b}\end{bmatrix}. \tag{A14}$$

This can be written as

$$(1+p\tan\theta)^{-1}\begin{bmatrix}\mathbf{a}\\ \mathbf{b}\end{bmatrix}=\{\mathbf{I}+(\tan\theta)\mathbf{N}\}^{-1}\begin{bmatrix}\mathbf{a}\\ \mathbf{b}\end{bmatrix}$$

$$=\cos^2\theta\{\mathbf{I}-(\tan\theta)\mathbf{N}(\theta)\}\begin{bmatrix}\mathbf{a}\\ \mathbf{b}\end{bmatrix} \tag{A15}$$

in which the 6×6 matrix $\mathbf{N}(\theta)$ is

$$\mathbf{N}(\theta)=\begin{bmatrix}\mathbf{N}_1(\theta) & \mathbf{N}_2(\theta)\\ \mathbf{N}_3(\theta) & \mathbf{N}_1^T(\theta)\end{bmatrix}. \tag{A16}$$

The second equality in $(A15)$ follows by employing the identity (7.5–19) in ([8]). For $p=p_1,p_2,p_3$ $(A15)$ takes the form

$$\begin{bmatrix}\mathbf{A}\langle(1+p_*\tan\theta)^{-1}\rangle\\ \mathbf{B}\langle(1+p_*\tan\theta)^{-1}\rangle\end{bmatrix}$$

$$=\cos^2\theta\begin{bmatrix}\mathbf{I}-(\tan\theta)\mathbf{N}_1(\theta) & -(\tan\theta)\mathbf{N}_2(\theta)\\ -(\tan\theta)\mathbf{N}_3(\theta) & \mathbf{I}-(\tan\theta)\mathbf{N}_1^T(\theta)\end{bmatrix}\begin{bmatrix}\mathbf{A}\\ \mathbf{B}\end{bmatrix}. \tag{A17}$$

In particular, using $(A1)$ we obtain

$$\mathbf{B}\langle(1+p_*\tan\theta)^{-1}\rangle\mathbf{B}^{-1}=\cos^2\theta\{\tan\theta[\mathbf{N}_3(\theta)\mathbf{S}-\mathbf{N}_1^T(\theta)\mathbf{L}+i\mathbf{I}]\mathbf{L}^{-1}+\mathbf{I}\}. \tag{A18}$$

Equation $(A3)$ can be modified as

$$\mathbf{B}\langle p_*-\mu\rangle\mathbf{B}^{-1}=(\mathbf{N}_1^T\mathbf{L}-\mathbf{N}_3\mathbf{S}-i\mathbf{N}_3)\mathbf{L}^{-1}-\mu\mathbf{I}, \tag{A19}$$

where μ is an arbitrary parameter. Observing that the matrices

$$\mathbf{N}_3\mathbf{S}-\mathbf{N}_1^T\mathbf{L} \quad\text{and}\quad \mathbf{N}_3(\theta)\mathbf{S}-\mathbf{N}_1^T(\theta)\mathbf{L} \tag{A20}$$

are symmetric ([16]) (see (7.8–10), and (6.8–8) in ([8])) and $\mathbf{SL}^{-1}$ is skew-symmetric, multiplication of $(A19)$ and $(A18)$ and taking the imaginary part leads to

$$\mathrm{Im}\left\{\mathbf{B}\left\langle\frac{p_*-\mu}{1+p_*\tan\theta}\right\rangle\mathbf{B}^{-1}\right\}=\cos^2\theta\{\tan\theta[\mathbf{N}_3(\theta)(\mathbf{N}_1-\mu\mathbf{I})+\mathbf{N}_1^T(\theta)\mathbf{N}_3]-\mathbf{N}_3\}\mathbf{L}^{-1}. \tag{A21}$$

It should be noted that (see (7.8-3) in ([8])) the matrix

$$\mathbf{N}_3(\theta)\mathbf{N}_1+\mathbf{N}_1^T(\theta)\mathbf{N}_3$$

is symmetric.

References

[1] Muskhelishvili, N. I., 1953, *Some Basic Problems of the Mathematical Theory of Elasticity*, transl. by J. R. M. Radok, Noordhoff, Groningen.
[2] Lekhnitskii, S. G., 1950, *Theory of Elasticity of an Anisotropic Body*, Gostekhizdat, Moscow (in Russian); *Theory of Elasticity of an Anisotropic Elastic Body*, Holden-Day, San Francisco (in English, 1963), and Mir Pub. Moscow (in English, 1981).
[3] Stroh, A. N., 1958, ''Dislocations and Cracks in Anisotropic Elasticity,'' Philos. Mag., **3**, pp. 625–646.
[4] Ting, T. C. T., 2000, ''Common Errors on Mapping of Non-Elliptic Curves in Anisotropic Elasticity,'' ASME J. Appl. Mech., **67**, pp. 655–657.
[5] Lekhnitskii, S. G., 1957, *Anisotropic Plates*, 2nd Ed., Gostekhizdat, Moscow (in Russian); transl. by S. W. Tsai and T. Cheron, Gordon and Breach, New York (1968, 1984, 1987).
[6] Barnett, D. M., and Lothe, J., 1973, ''Synthesis of the Sextic and the Integral Formalism for Dislocations, Greens Function and Surface Waves in Anisotropic Elastic Solids,'' Phys. Norv., **7**, pp. 13–19.
[7] Chadwick, P., and Smith, G. D., 1977, ''Foundations of the Theory of Surface Waves in Anisotropic Elastic Materials,'' Adv. Appl. Mech., **17**, pp. 303–376.
[8] Ting, T. C. T., 1996, *Anisotropic Elasticity: Theory and Applications*, Oxford University Press, Oxford, UK.
[9] Hu, Y. T., and Zhao, X. H., 1996, ''Green's Functions of Two-Dimensional Anisotropic Body With a Parabolic Boundary,'' Appl. Math. Mech., **17**, pp. 393–402.
[10] Neuber, H., 1958, *Kerbspannungslehre*, Springer-Verlag, Berlin, Chapter 4.
[11] Smith, C. B., 1949, ''Effect of Hyperbolic Notches on the Stress Distribution in a Wood Plate,'' Q. Appl. Math., **6**, No. 4, pp. 452–456.
[12] Okubo, H., 1949, ''On the Problem of a Notched Plate of an Aeolotropic Material,'' Philos. Mag., **40**, Ser. 7, No. 308.
[13] Dongye, Changsong, and Ting, T. C. T., 1989, ''Explicit Expressions of Barnett-Lothe Tensors and Their Associated Tensors for Orthotropic Materials,'' Q. Appl. Math., **47**, pp. 723–734.
[14] Ting, T. C. T., 1997, ''New Explicit Expression of Barnett-Lothe Tensors for Anisotropic Linear Elastic Materials,'' J. Elast., **47**, pp. 23–50.
[15] Ingebrigtsen, K. A., and Tonning, A., 1969, ''Elastic Surface Waves in Crystal,'' Phys. Rev., **184**, pp. 942–951.
[16] Kirchner, H. O. K., and Lothe, J., 1986, ''On the Redundancy of the $\overline{N}$ Matrix of Anisotropic Elasticity,'' Philos. Mag., **A53**, pp. L7–L10.

Flow Past Rotating Cylinders: Effect of Eccentricity

S. Mittal
Associate Professor,
Department of Aerospace Engineering,
Indian Institute of Technology,
Kanpur, UP 208 016, India
e-mail: smittal@iitk.ac.in

Computational results are presented for flows past a translating and rotating circular cylinder. A stabilized finite element method is utilized to solve the incompressible Navier-Stokes equations in the primitive variables formulation. To validate the formulation and its implementation certain cases, for which the flow visualization and computational results have been reported by other researchers, are computed. Results are presented for Re=5, 200 and 3800 and rotation rate, (ratio of surface speed of cylinder to the freestream speed of flow), of 5. For all these cases the flow reaches a steady state. The values of lift coefficient observed for these flows exceed the limit on the maximum value of lift coefficient suggested by Goldstein based on intuitive arguments by Prandtl. These observations are in line with measurements reported, earlier, by other researchers via laboratory experiments. To investigate the stability of the computed steady-state solution, receptivity studies involving an eccentrically rotating cylinder are carried out. Computations are presented for flow past a rotating cylinder with wobble; the center of rotation of the cylinder does not match its geometric center. These computations are also important from the point of view that in a real situation it is almost certain that the rotating cylinder will be associated with a certain degree of wobble. In such cases the flow is unsteady and reaches a temporally periodic state. However, the mean values of the aerodynamic coefficients and the basic flow structure are still quite comparable to the case without any wobble. In this sense, it is found that the two-dimensional solution is stable to purely two-dimensional disturbances. [DOI: 10.1115/1.1380679]

1 Introduction

Flow past a spinning and translating cylinder has been a subject of numerous computational and experimental studies. Interest in this problem arises not only from the point of view of basic fluid mechanics but also from its applications to flow control. Tokumaru and Dimotakis [1,2] have demonstrated, via laboratory experiments, that a significant control on the structure of the wake can be achieved by subjecting the cylinder to rotary oscillations. Gad-el-Hak and Bushnel [3] review various techniques that are employed for separation control including the moving-surface boundary layer control (MSBC) in which rotating cylinder elements are employed to inject momentum into the already existing boundary layer.

Flow past an isolated rotating cylinder has been studied by various researchers in the past. The results of Prandtl and Reid from laboratory experiments have been reported by Goldstein [4]. These include the effect of the aspect ratio and end plates attached to the end of a cylinder that lead to an increase in the overall lift coefficient. Some of the later work on this flow problem include the development of the near-wake behind an impulsively started cylinder via flow visualization by Coutanceau and Menard [5]. The time evolution of the vortices in the near-wake for short time after the impulsive start comes out very clearly from their study. The highest Reynolds number in their study is less than 1000 and the rotation rate varies between 0 and 3.25. The nondimensional value of the rotation rate corresponds to the ratio of the speed on the surface of the cylinder and the freestream speed of flow. Badr and Dennis [6] gave numerical solutions for the viscous flow equations for small rotation rates 0.5, 1.0, and Re=200 and 500 in which comparisons with experiments of Coutanceau and Menard [5] have been made. Later, Badr et al. [7] presented computational and experimental results for Re=1000 and rotation rates between 0.5 and 3. Excellent match was obtained between the two except at high rotation rates where it is suspected that the experimental results show three-dimensional features. Computational results for the Re=10^4 flow were also presented.

Tokumaru and Dimotakis [2] measured the lift coefficient acting on rotating cylinders from their laboratory experiments. They have reported values of lift coefficient that exceed the limit set by Goldstein [4] based on the intuitive arguments given by Prandtl. According to Prandtl's arguments, the maximum value of the lift coefficient that can be achieved via Magnus effect is 4π (~12.6). For example, for Re=3.8×10^3 and $\alpha=10$ Tokumaru and Dimotakis [2] report an estimated lift coefficient that is more than 20 percent larger than this limit. This was observed for a cylinder with a span to diameter ratio of 18.7. Further, the trend of results that they have reported suggests that the value can be made larger for higher rotation rates and by taking cylinders of larger aspect ratio. They have suggested that perhaps it is the unsteady effects that weaken Prandtl's hypothesis and that the three-dimensional/end effects are responsible for lowering the value of lift coefficient that could be achieved in a purely two-dimensional flow. However, Chew et al. [8] have reported that their two-dimensional

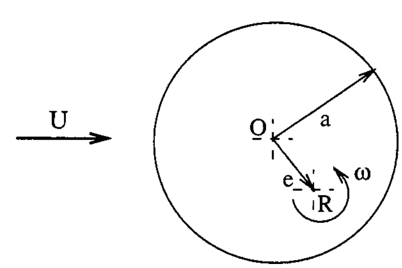

Fig. 1 Description of the eccentricity (*e*) of the rotating cylinder. The geometric center of the cylinder is at *O* while its axis of spin passes through *R*.

Contributed by the Applied Mechanics Division of THE AMERICAN SOCIETY OF MECHANICAL ENGINEERS for publication in the ASME JOURNAL OF APPLIED MECHANICS. Manuscript received by the ASME Applied Mechanics Division, Aug. 7, 2000; final revision, Nov. 29, 2000. Associate Editor: T. E. Tezduyar. Discussion on the paper should be addressed to the Editor, Prof. Lewis T. Wheeler, Department of Mechanical Engineering, University of Houston, Houston, TX 77204-4792, and will be accepted until four months after final publication of the paper itself in the ASME JOURNAL OF APPLIED MECHANICS.

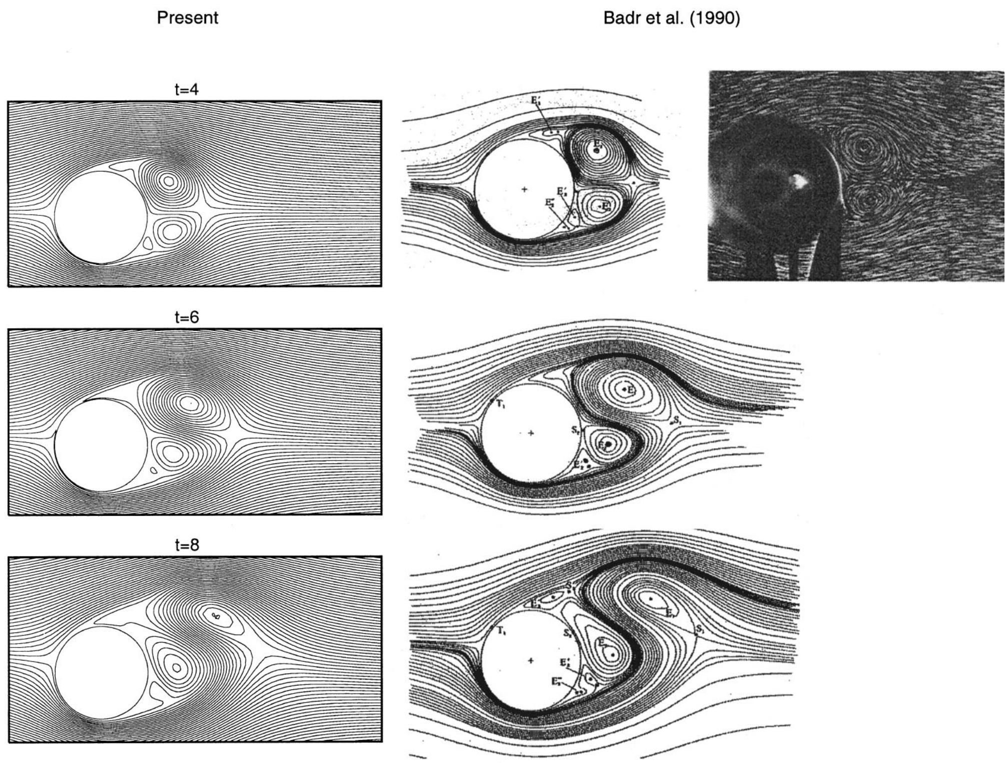

Fig. 2 Re$=10^3$, $\alpha=0.5$ flow past a rotating cylinder: comparison of the instantaneous streamline patterns at various time instants from the present computations and those from Badr et al. [8]

computations are in agreement with Prandtl's postulate. They find that for Re$=1000$, the estimated mean lift coefficient approaches asymptotic values with increase in α. At $\alpha=6$ they predict a mean lift coefficient of 9.1. The magnitude of lift generated by a cylinder for higher rates of rotation is an issue that remains unresolved even to this date. In this sense, the present work assumes significance in contributing to the efforts of resolving the issue regarding the limit on maximum lift that is possible via Magnus effect.

The objective of the present work is to investigate flows past spinning and translating cylinder at high rotation rates and determine the correctness of the limit on maximum lift set due to arguments by Prandtl. Stabilized space-time formulations for incompressible flows that have, earlier, been applied to a variety of flow problems are utilized for computations. First, the formulation and its implementation are validated for flows involving rotating cylinders by carrying out computations for Re$=1000$ and rotation rates of 0.5 and 2.0. The results are in excellent agreement with the flow visualizations and computational studies carried out by other researchers, earlier. For rotation rate of 3.0 the results from present computations match very well with other computed results, reported earlier. However, the experimental results show certain differences as compared to the two-dimensional computations for larger times. This may be attributed to the three-dimensional nature of the flow. At high rotation rates it is seen that the lift for purely two-dimensional setup can be very large. The values of the lift coefficient obtained in the present work exceed the maximum limit based on the arguments of Prandtl. The observations are consistent with the result of Tokumaru and Dimotakis [2]. For the Reynolds number considered in the present study the flow achieves a steady state for a rotation rate of 5. The stability of this steady-state solution, at least to two-dimensional disturbances, is an issue that needs investigation. The result of this study will play a vital role in resolving the validity (or nonvalidity) of the Prandtl's limit on maximum lift coefficient.

Computations are carried out to study the receptivity of the flow for eccentric/wobbly rotation of the cylinder. The center of rotation of the cylinder is slightly displaced with respect to the geometric center. This introduces an unsteadiness in the flow via the motion of the cylinder. The results are compared with those for noneccentrically rotating cylinder. Computations for various values of eccentricities show that the basic flow structure and the mean value of the lift coefficient do not differ much from that for the basic solution. This reflects the stability of the purely two-dimensional flow to two-dimensional disturbances. This study also brings out the effect of the eccentricity of the cylinder on the flow and the time histories of the aerodynamic coefficients.

The outline of the rest of the article is as follows. We begin by reviewing the governing equations for incompressible fluid flow in Section 2. The SUPG (streamline-upward/Petrov-Galerkin) and PSPG (pressure-stabilizing/Petrov-Galerkin) stabilization technique ([9–11]) is employed to stabilize our computations against spurious numerical oscillations and to enable us to use equal-order-interpolation velocity-pressure elements. Computations for the eccentrically rotating cylinders have been carried out with the DSD/SST (deforming-spatial-domain/stabilized-space-time) formulation ([12,13]). Section 3 describes the finite element formulations. In Section 4 computational results for flows involving rotating cylinder are presented and discussed. In Section 5 the results are summarized and a few concluding remarks are made.

2 The Governing Equations

Let $\Omega_t \subset \mathbb{R}^{n_{sd}}$ and $(0,T)$ be the spatial and temporal domains, respectively, where n_{sd} is the number of space dimensions, and let Γ_t denote the boundary of Ω_t. The spatial and temporal coordinates are denoted by $\mathbf{x}$ and t. The Navier-Stokes equations governing incompressible fluid flow are

$$\rho\left(\frac{\partial \mathbf{u}}{\partial t}+\mathbf{u}\cdot\nabla\mathbf{u}-\mathbf{f}\right)-\nabla\cdot\boldsymbol{\sigma}=0 \quad \text{on} \quad \Omega_t \quad \text{for } (0,T), \tag{1}$$

$$\nabla\cdot\mathbf{u}=0 \quad \text{on} \quad \Omega_t \quad \text{for } (0,T). \tag{2}$$

Table 1 Re=5, 200 and 3800, α=5 flow past a rotating cylinder: steady-state values of the lift and drag coefficients

Case	Re	C_L	C_D	C_L/C_D
1	5	19.11	1.054	18.13
2	200	27.28	0.783	34.83
3	3800	25.94	0.709	36.60

Here ρ, $\mathbf{u}$, $\mathbf{f}$, and $\boldsymbol{\sigma}$ are the density, velocity, body force, and the stress tensor, respectively. The stress tensor is written as the sum of its isotropic and deviatoric parts:

$$\boldsymbol{\sigma}=-p\mathbf{I}+\mathbf{T}, \quad \mathbf{T}=2\mu\boldsymbol{\varepsilon}(\mathbf{u}) \quad \boldsymbol{\varepsilon}(\mathbf{u})=\frac{1}{2}((\nabla\mathbf{u})+(\nabla\mathbf{u})^T), \quad (3)$$

where p and μ are the pressure and viscosity and $\mathbf{I}$ is the identity tensor. Both the Dirichlet and Neumann-type boundary conditions are accounted for, represented as

$$\mathbf{u}=\mathbf{g} \quad \text{on} \quad (\Gamma_t)_g, \quad \mathbf{n}\cdot\boldsymbol{\sigma}=\mathbf{h} \quad \text{on} \quad (\Gamma_t)_h, \quad (4)$$

where $(\Gamma_t)_g$ and $(\Gamma_t)_h$ are the complementary subsets of the boundary Γ_t and $\mathbf{n}$ is its unit normal vector. The initial condition on the velocity is specified on Ω_t at $t=0$:

$$\mathbf{u}(\mathbf{x},0)=\mathbf{u}_0 \quad \text{on} \quad \Omega_0, \quad (5)$$

where $\mathbf{u}_0$ is divergence free. The force coefficients are computed by carrying an integration, that involves the pressure and viscous stresses, around the circumference of the cylinder:

$$C_D=\frac{1}{(1/2)\rho_\infty U_\infty^2 2a}\int_{\Gamma_{cyl}}(\boldsymbol{\sigma}\mathbf{n})\cdot\mathbf{n}_x d\Gamma \quad (6)$$

$$C_L=\frac{1}{(1/2)\rho_\infty U_\infty^2 2a}\int_{\Gamma_{cyl}}(\boldsymbol{\sigma}\mathbf{n})\cdot\mathbf{n}_y d\Gamma. \quad (7)$$

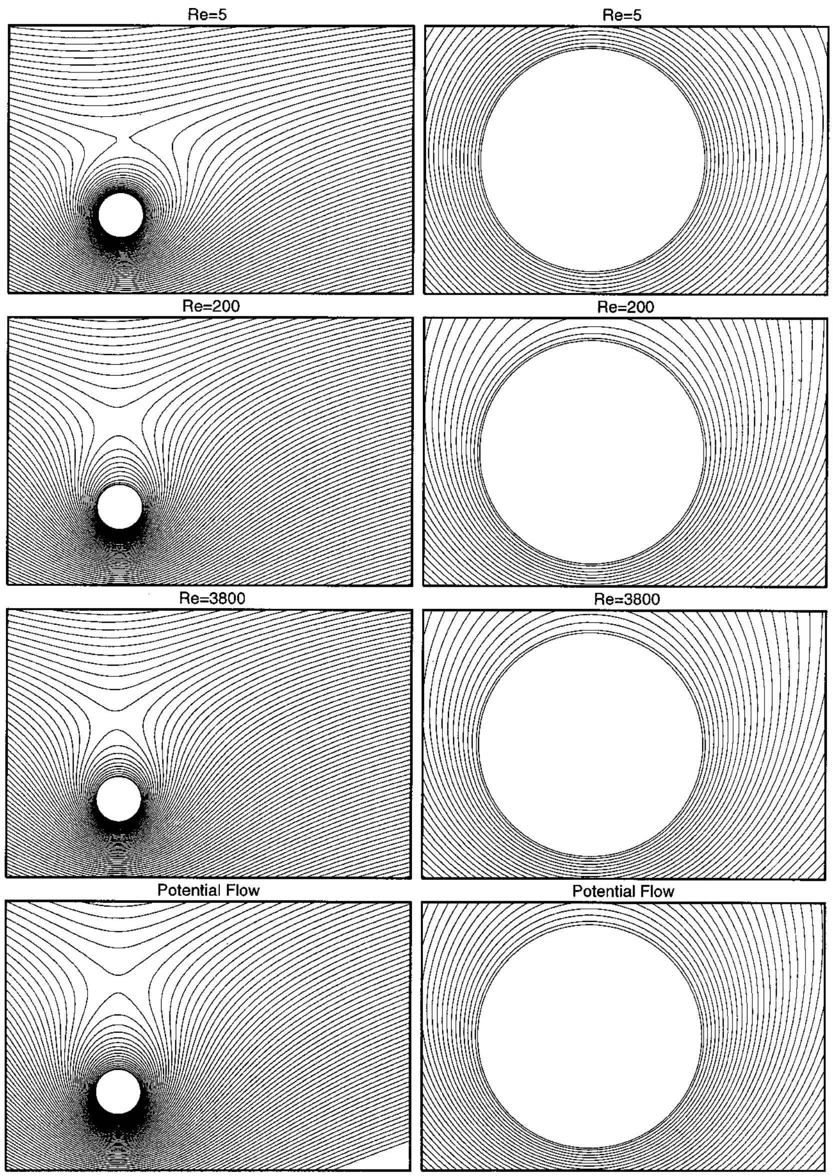

Fig. 3 Re=5,200 and 3800, α=5.0 flow past a rotating cylinder: streamlines for the steady-state solution. The potential flow solution is also shown for comparison.

Here, $\mathbf{n}_x$ and $\mathbf{n}_y$ are the Cartesian components of the unit vector $\mathbf{n}$ that is normal to the cylinder boundary Γ_{cyl} and a is the radius of the cylinder.

3 Finite Element Formulation

To accommodate the motion of the cylinder and the deformation of the mesh, a formulation that can handle moving boundaries and interfaces is employed. In order to construct the finite element function spaces for the space-time method, we partition the time interval $(0,T)$ into subintervals $I_n=(t_n,t_{n+1})$, where t_n and t_{n+1} belong to an ordered series of time levels: $0=t_0<t_1<\cdots<t_N=T$. Let $\Omega_n=\Omega_{t_n}$ and $\Gamma_n=\Gamma_{t_n}$. We define the space-time slab Q_n as the domain enclosed by the surfaces Ω_n, Ω_{n+1}, and P_n, where P_n is the surface described by the boundary Γ_t as t traverses I_n. As is the case with Γ_t, the surface P_n is decomposed into $(P_n)_g$ and $(P_n)_h$ with respect to the type of boundary condition (Dirichlet or Neumann) being imposed. For each space-time slab we define the corresponding finite element function spaces: $(\mathcal{S}^h_{\mathbf{u}})_n$, $(\mathcal{V}^h_{\mathbf{u}})_n$, $(\mathcal{S}^h_p)_n$, and $(\mathcal{V}^h_p)_n$. Over the element domain, this space is formed by using first-order polynomials in space and time. Globally, the interpolation functions are continuous in space but discontinuous in time.

The stabilized space-time formulation for deforming domains is then written as follows: given $(\mathbf{u}^h)_{n^-}$, find $\mathbf{u}^h\in(\mathcal{S}^h_{\mathbf{u}})_n$ and $p^h\in(\mathcal{S}^h_p)_n$ such that $\forall \mathbf{w}^h\in(\mathcal{V}^h_{\mathbf{u}})_n$, $q^h\in(\mathcal{V}^h_p)_n$,

$$\begin{aligned}
&\int_{Q_n}\mathbf{w}^h\cdot\rho\left(\frac{\partial\mathbf{u}^h}{\partial t}+\mathbf{u}^h\cdot\nabla\mathbf{u}^h-\mathbf{f}\right)dQ+\int_{Q_n}\boldsymbol{\varepsilon}(\mathbf{w}^h):\boldsymbol{\sigma}(p^h,\mathbf{u}^h)dQ\\
&\quad+\int_{Q_n}q^h\nabla\cdot\mathbf{u}^h dQ+\sum_{e=1}^{n_{el}}\int_{Q_n^e}\tau\frac{1}{\rho}\left[\rho\left(\frac{\partial\mathbf{w}^h}{\partial t}+\mathbf{u}^h\cdot\nabla\mathbf{w}^h\right)\right.\\
&\quad\left.-\nabla\cdot\boldsymbol{\sigma}(q^h,\mathbf{w}^h)\right]\cdot\left[\rho\left(\frac{\partial\mathbf{u}^h}{\partial t}+\mathbf{u}^h\cdot\nabla\mathbf{u}^h-\mathbf{f}\right)-\nabla\cdot\boldsymbol{\sigma}(p^h,\mathbf{u}^h)\right]dQ\\
&\quad+\sum_{e=1}^{n_{el}}\int_{Q_n^e}\delta\nabla\cdot\mathbf{w}^h\rho\nabla\cdot\mathbf{u}^h dQ+\int_{\Omega_n}(\mathbf{w}^h)_n^+\cdot\rho((\mathbf{u}^h)_n^+\\
&\quad-(\mathbf{u}^h)_n^-)d\Omega=\int_{(P_n)_h}\mathbf{w}^h\cdot\mathbf{h}^h dP. \qquad (8)
\end{aligned}$$

This process is applied sequentially to all the space-time slabs $Q_0,Q_1,\ldots Q_{n-1}$. In the variational formulation given by Eq. (8), the following notation is being used:

$$(\mathbf{u}^h)_n^{\pm}=\lim_{\varepsilon\to 0}\mathbf{u}(t_n\pm\varepsilon), \qquad (9)$$

$$\int_{Q_n}(\ldots)dQ=\int_{I_n}\int_{\Omega_n}(\ldots)d\Omega dt, \qquad (10)$$

$$\int_{P_n}(\ldots)dP=\int_{I_n}\int_{\Gamma_n}(\ldots)d\Gamma dt. \qquad (11)$$

The computations start with

$$(\mathbf{u}^h)_0^-=\mathbf{u}_0, \qquad (12)$$

where $\mathbf{u}_0$ is divergence free.

The variational formulation given by Eq. (8) includes certain stabilization terms added to the basic Galerkin formulation to enhance its numerical stability. Details on the formulation, including the definitions of the coefficients τ and δ, can be found in the references [9,12,13].

4 Numerical Simulations

Flow past a cylinder spinning about its own axis has been studied by various researchers in the past. Most of the computations reported earlier, for this flow problem, have been carried out using the vorticity/stream-function formulations [7,8] or the vorticity/velocity formulations ([14]). However, the present effort employs finite element formulation of the Navier-Stokes equations in the primitive variables. The cylinder resides in a rectangular domain and a flow velocity corresponding to the rotation rate, α is specified on the cylinder surface. Freestream value is assigned for the velocity at the upstream boundary while at the downstream boundary, a Neumann-type boundary condition for the velocity is specified that corresponds to zero viscous stress vector. On the upper and lower boundaries, the component of velocity normal to and the component of stress vector along these boundaries is prescribed zero value. The Reynolds number is defined as $\mathrm{Re}=2Ua/\nu$ where a is the radius of cylinder, U the freestream speed (after an impulsive start) and ν is the coefficient of kinematic viscosity of the fluid. The rotation rate of the cylinder is nondimensionalized with respect to the freestream speed and is given as $\alpha=a\omega/U$ where ω is the angular velocity of the cylinder. the cylinder spins about an axis that is off-centered and is located at a distance e from its geometric center as shown in Fig. 1.

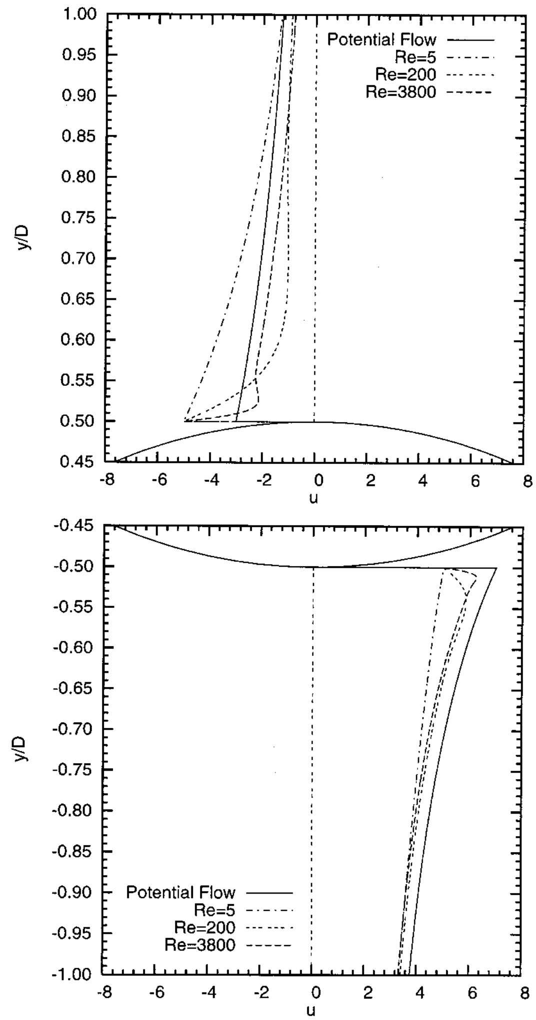

Fig. 4 Re=5, 200 and 3800, α=5.0 flow past a rotating cylinder: variation of the x-component of velocity along normals located at the uppermost and lowest points on the cylinder. The potential flow solution is also shown for comparison.

4.1 Re=1000, e=0, α=0.5, 2.0, 3.0. To establish confidence in the formulation and its implementation, the computed results for various rotation rates are compared with numerical and experimental results, reported earlier. The eccentricity is 0 in these cases; the cylinder spins about its own axis. Figure 2 shows the

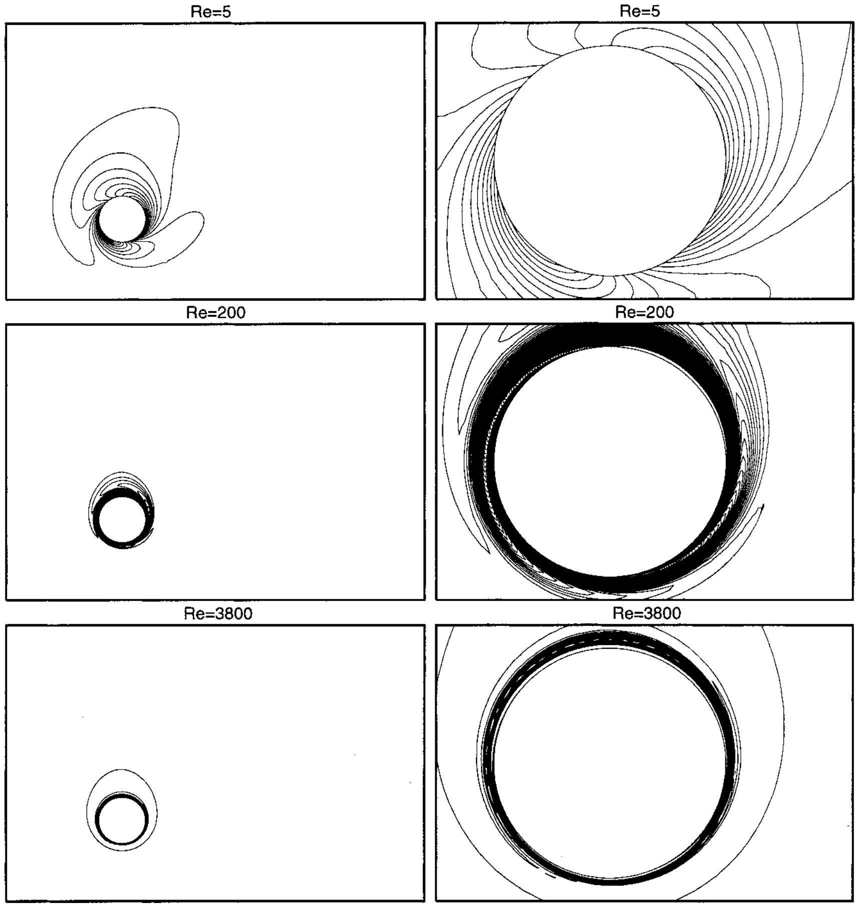

Fig. 5 Re=5, 200 and 3800, α=5.0 flow past a rotating cylinder: vorticity field for the steady-state solution

results for the computation of Re$=10^3$ flow past a cylinder with $\alpha=0.5$ with an impulsive start. Also shown in the figure are the computational and experimental results from Badr et al. [7]. The computations have been carried out with a mesh containing 12,408 nodes and 12,176 quadrilateral elements. All the external boundaries are located at eight cylinder diameters from the cylinder center. The time-step for the computations is 0.01. It can be observed from the figure that the present computations reproduce all the essential features of the flow and their time evolution. The instantaneous streamlines, shown in the figure, have been derived from the computed velocity field via a least squares procedure. The results for Re=1000 and $\alpha=2$, 3 (not shown here) also result in excellent agreement.

4.2 Re=5, 200 and 3800, $e=0$, α=5.0. The next set of results are for long time behavior of the flow for rotation rate $\alpha=5$, and various Reynolds numbers. During the entire simulation for Re=5 only one clockwise vortex (the startup vortex) is shed from the rotating cylinder. A set of closed streamlines form around the rotating cylinder. In this computation, the finite element mesh consists of 12,678 nodes and 12,420 four-noded quadrilateral elements. The mesh is fine enough to resolve the boundary layer and other flow features, adequately, for this low Reynolds number. The external boundaries are located at 25 cylinder diameters from the center of the cylinder. Computations with a domain with the boundaries located at 20 cylinder diameters from the cylinder result in an almost indistinguishable solution. For more details on the effect of placement of lateral boundaries on the computed flow past a cylinder at Re=100 the reader may refer to the article by Behr et al. [15]. The steady-state value of the lift and drag coefficients from the simulations are listed in Table 1. Note that the steady-state lift coefficient obtained from the present simulation is much larger than the limit set by Goldstein [4] based on intuitive arguments by Prandtl.

The streamlines for the steady-state solution for all the three Reynolds numbers are shown in Fig. 3. Also shown in the same figure are the streamlines for the potential flow solution. It is interesting to observe the effect of Reynolds number on the location of the saddle point compared to that for potential flows. While for higher Re the saddle point is located close to the vertical line of symmetry passing through the center of the cylinder, for Re=5, departure of the saddle point from this line is quite significant. Figure 4 shows the variation of the x component of velocity along normals located at the uppermost and lowest points on the cylinder. Also, shown in the same figure are the profiles for the potential flow solution. On the upper surface, the max speed (nondimensionalized with the freestream speed of the flow) for the potential flow is 3. For the viscous flow, the speed on the surface of the cylinder is 5. For Re=5, close to the cylinder, the speed decreases monotonically with height while it shows a nonmonotonic behavior for higher Reynolds numbers. For Re=3800, the speed first decreases, then increases and decreases again. On the lower surface the potential flow solution predicts a speed of 7 on the cylinder and it decreases, monotonically, away from the cylinder. For the viscous flow, this value is 5 and again a nonmonotonic variation of the speed distribution can be noticed. This results in an interesting pattern of the vorticity distribution as will be seen shortly.

The vorticity fields for various Reynolds numbers are shown in Fig. 5. The distribution of the vorticity on the surface of the cylinder for various Reynolds numbers shows very similar trends for

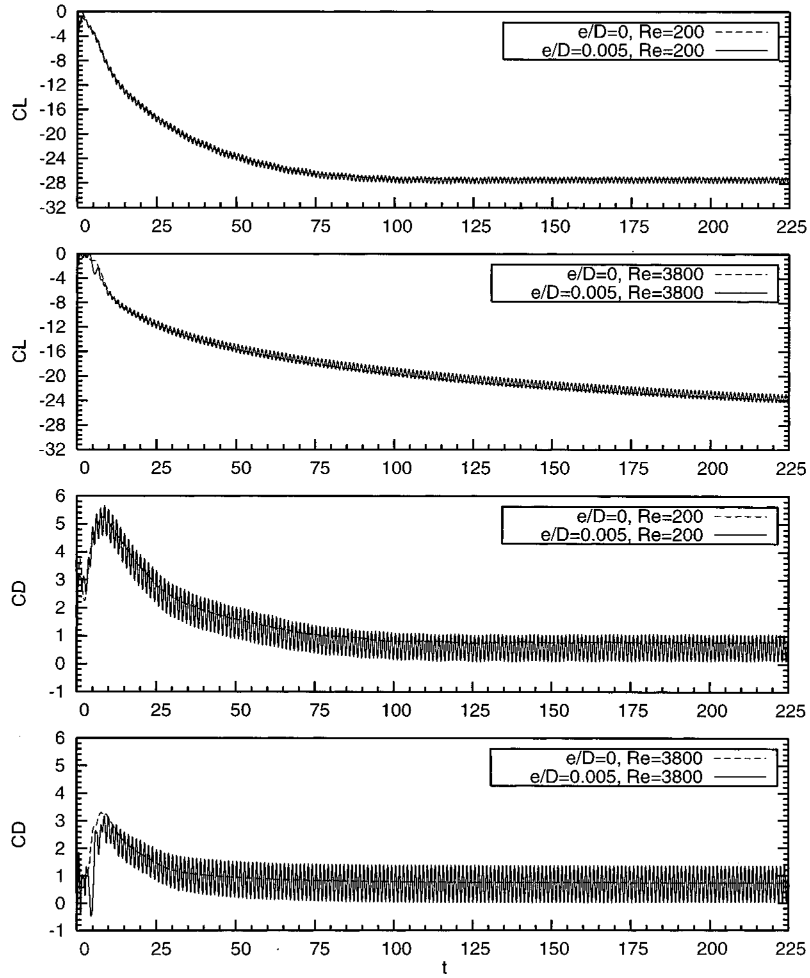

Fig. 6 Re=200, 3800, α=5.0, e=0.005 D flow past an eccentrically rotating cylinder: time-histories of the lift and drag coefficients

all the three cases. However, its magnitude is larger for higher Reynolds numbers. Since the cylinder is assigned a rotation in the counterclockwise direction, one might expect the surface vorticity to have the same sign all along the entire surface of the cylinder for the viscous flow solution. However, it is seen from the results that it changes sign twice. This suggests that the flow separates once and then reattaches on the cylinder surface. Notice, from the plot from stream function, that there is a set of closed streamlines near the cylinder. Also, the *Magnus effect* causes the pressure on the lower side of the cylinder to be substantially lower than that on the upper side. As a result, the fluid particles, close to the cylinder surface, experience a favorable pressure gradient on the windward side and an adverse pressure gradient on the leeward side of the cylinder. These pressure gradients are responsible for the separation and reattachment of the flow close to the cylinder surface. This observation is consistent with that from Fig. 5 which shows that the iso-vorticity contours close to the cylinder appear as spirals. The variation of the vorticity near the lowest and uppermost regions close to the cylinder can also be correlated to the variation of the *x*-component of velocity as shown in Fig. 4. It is expected that for larger Reynolds numbers this effect will be much stronger and may lead to unsteadiness in the flow.

4.3 Re=200, e=0.005 D, 0.025 D, 0.05 D, α=5.0. It has been pointed out in the previous section that for purely two-dimensional flows the high rotation rate of the cylinder ($\alpha=5$) results in a steady-state flow and very large value of the lift coefficient. For such flows to exist in real situations, it is essential that they are stable. It is known from work of certain researchers, for example, Tokumaru and Dimotakis [2] that the three-dimensional effects result in a reduction of the lift values that can be achieved for two-dimensional flows. However, this issue has not been addressed yet in the context of a purely two-dimensional environment. Therefore, it is of interest to study the stability of the two-dimensional flows, to two-dimensional disturbances. One way of investigating the stability of a solution is by introducing a disturbance in the basic flow and then monitoring its time evolution. In the present work, the stability has been investigated via a receptivity study. Computations are carried out for an eccentrically rotating cylinder. It is hoped that the periodic forcing of the flow due to the eccentric/wobbly motion of the cylinder will excite any possible instabilities associated with the flow. As a result of this receptivity study, the final solution is expected to be unsteady. However, for a basic flow that is stable, it is expected that the time-averaged disturbed flow will not be too different from the basic solution. The computations are carried out using a space-time finite element method where the spatial domain is allowed to deform with respect to time. Calculations for $e=0$ with the space-time formulation yields results that are almost indistinguishable from those obtained in the previous section. This further adds to our confidence in the present results.

Various degrees of eccentricity are considered. In all cases, the computations begin with an impulsive start. The initial condition for the flow is the potential flow past a stationary cylinder. The geometric center is located at the rightmost location with respect

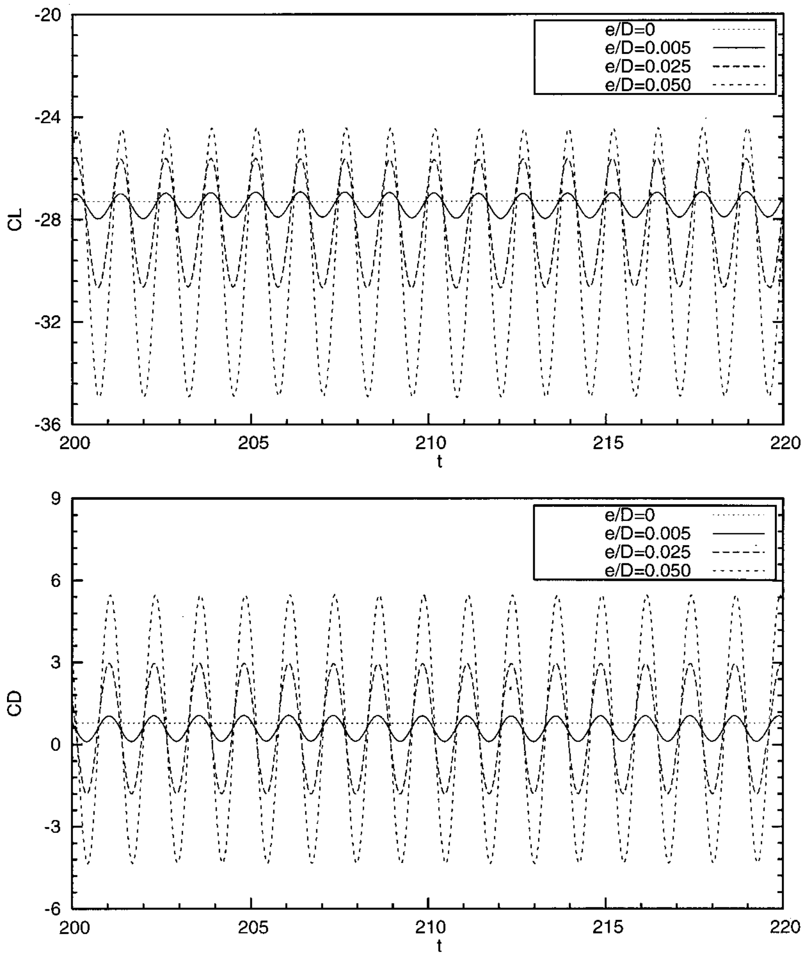

Fig. 7 Re=200, α=5.0 flow past an eccentrically rotating cylinder: close-up of the time histories of the lift and drag coefficients for various values of the eccentricity

to the center of rotation. With respect to Fig. 1 the coordinates of R relative to O are $(-e,0)$, at the start of computations.

Figure 6 shows the time histories of the lift and drag coefficients for the simulation with $e=0.005$ D. The aerodynamic coefficients show an oscillatory behavior. The frequency of oscillations is the same as that of the rotation of cylinder. It is interesting to note that the time histories of the mean values of the aerodynamic coefficients appear quite similar to the ones obtained for a cylinder with $e=0$. Similar observation is also made from the time histories of C_L and C_D for $e=0.025$ D and 0.05 D. A closeup of the time histories for various values of e are presented in Fig. 7. In all the cases, the frequency of the time variation of the aerodynamic coefficients is same and corresponds to the rotation rate of the cylinder. It can be observed that the amplitude of the unsteady force coefficients increase with eccentricity. However, the phase is same for all values of e. For values of e larger than 0.005 D, negative value of drag is observed during a certain part of each cycle of the cylinder motion. However, the mean drag over the entire cycle is always positive. A summary of the variation of the aerodynamic coefficients for various values of e is presented in Fig. 8. The magnitude of the mean lift coefficient increases with e. This could, perhaps, be explained by the increased strength of vortices for larger eccentricities of rotation. The mean drag coefficient shows a significant reduction for the case even with the lowest value of eccentricity ($e=0.005$ D) and then seems to change little with any further increase in eccentricity. However, the unsteady component of the drag coefficient shows a linear increase in amplitude with eccentricity. In all the cases the fully developed solution achieves a limit cycle and the basic flow structure remains the same. This suggests that the basic two-dimensional flow is quite stable, at least, to two-dimensional disturbances.

The vorticity fields at various instants during one cycle of cylinder rotation for the fully developed temporally periodic flows are shown in Fig. 9. From this figure it can be observed that the eccentric motion of the cylinder causes a vortex to be shed during each cycle of rotation of the cylinder. The size and strength of the vortex, that is shed, increase with increase in eccentricity of rotation. the dynamics of the vortex formation, its release and dissipation is quite clear from the figure for $e=0.05$ D. Somewhere between the second and third frames, a counterclockwise rotating vortex is shed from the cylinder. It travels around the periphery of the cylinder in the counterclockwise direction and is dissipated during the next cycle of rotation of the cylinder. These strong vortices also result in certain weaker induced vortices of opposite sign. The vortical activity due to the eccentricity of the rotation takes place very close to the cylinder, and its effect on the outer flow seems to be insignificant. These computations help us in concluding that the two-dimensional flow past the spinning cylinder, presented in the previous section, is stable to two-dimensional disturbances. Therefore, in a purely two-dimensional environment, the solutions presented in the earlier section can exist. This strengthens our point of view that the Prandtl's limit on the maximum lift coefficient generated by a spinning cylinder may not hold.

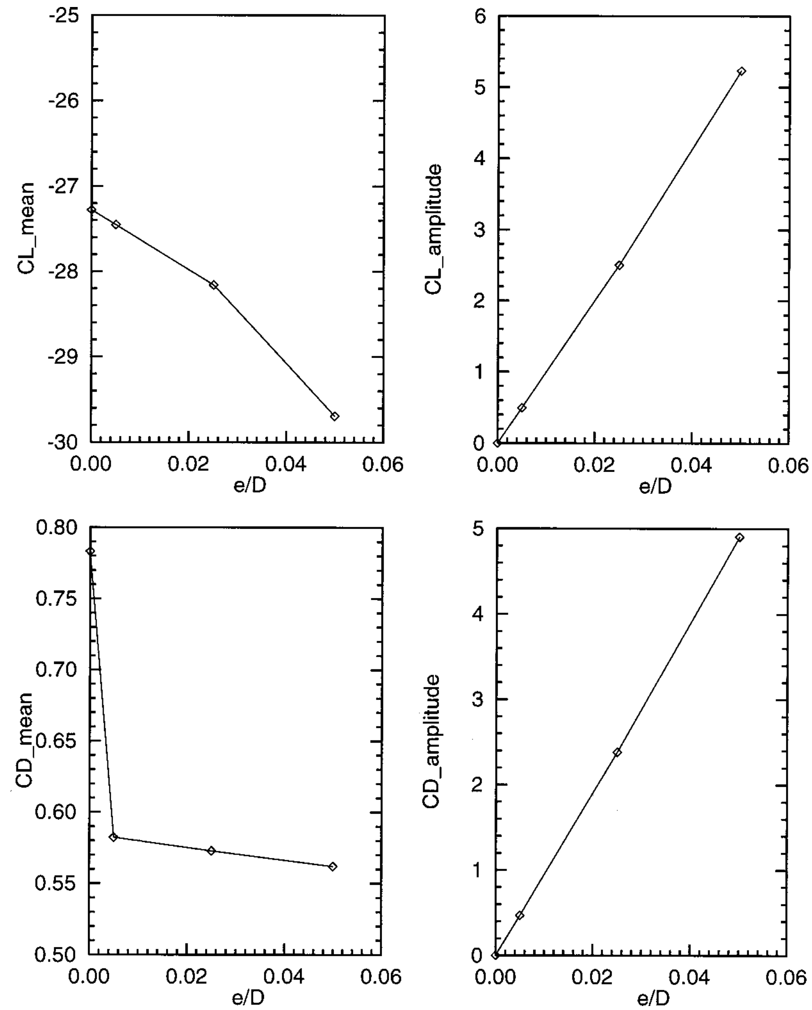

Fig. 8 Re=200, α=5.0 flow past an eccentrically rotating cylinder: summary of the aerodynamic coefficients for different values of the eccentricity

4.4 Re=3800, e=0.005 D, α=5.0. To determine the stability of the Re=3800 flow in a purely two-dimensional setup computations are carried out with $e=0.005$ D. Figure 6 shows the time histories of the aerodynamic coefficients. Also shown in the same figure are the time histories for the computations with $e=0$. As was observed for Re=200, the time evolution of the mean value of the aerodynamic coefficients follow the same trend as that for $e=0$. The eccentricity of rotation causes a sinusoidal variation in the temporal data and its frequency content is same as that of the rotation of cylinder. This shows that the eccentricity of the rotation of cylinder does not cause any significant change to the original steady solution. This reflects the stability of the two-dimensional solution, to purely two-dimensional disturbances. Figure 10 shows the vorticity, pressure and magnitude of velocity, close to the cylinder, at one time instant for the temporally periodic solution. On comparing this figure to Fig. 5 it can be observed that the effect of eccentricity in the rotational motion of the cylinder is restricted to a region very close to it.

To check the dependence of the solution on the spatial and temporal discretization, the solution was projected on a finer mesh with 26,830 nodes and 26,500 elements and the computations continued with a time step of 0.01. The aerodynamic coefficients for the new solution showed less than 0.1 percent difference in the mean values and less than 1.0 percent in the unsteady values.

5 Concluding Remarks

Flow past a rotating circular cylinder placed in a uniform stream has been studied numerically. A stabilized finite element method is utilized to solve the incompressible Navier-Stokes equations in the primitive variables formulation. Good agreement with some of the flow visualization and computational results from other researchers, reported earlier, is observed. Computations have been carried out for Re=5, 200, and 3800 and rotation rate, α, of 5. It is seen that for these parameters the flow achieves a steady-state and that the lift for purely two-dimensional setup can be very large. Both the semidiscrete and the space-time formulations have been utilized to compute the solution for α=5. They result in almost indistinguishable results adding further to the correctness of the present results. The flow close to the cylinder, for various Reynolds numbers, is compared to the potential flow solution. Interesting differences are observed in the various solutions. The vorticity distribution along the cylinder surface points to mild separation and reattachment of the flow. This is attributed to the adverse and favorable pressure gradients of the flow on the windward and leeward sides of the cylinder. It is expected that for even larger Reynolds numbers, the separation would become stronger and result in an unsteady flow. The values of the lift coefficient obtained in the present work exceed the maximum limit set by Goldstein based on the intuitive arguments

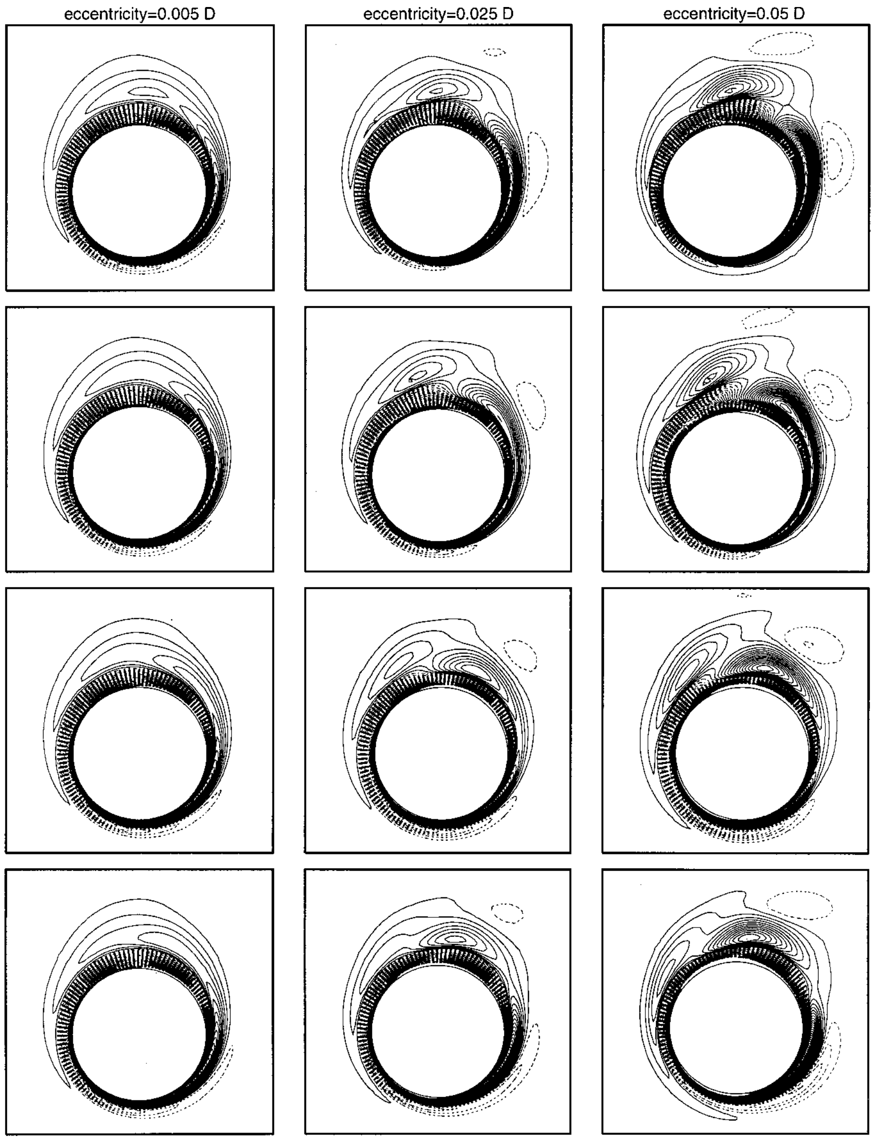

Fig. 9 Re=200, α=5.0 flow past an eccentrically rotating cylinder: vorticity field at four time instants during one period of rotation for the temporally periodic solution. The frames in the various rows from top to bottom correspond to the time instants when the geometric center of the cylinder is at its left-most, bottom-most, right-most, and top-most location, respectively, with respect to the center of rotation. The clockwise vorticity is shown in broken lines while the counterclockwise component is shown in solid lines.

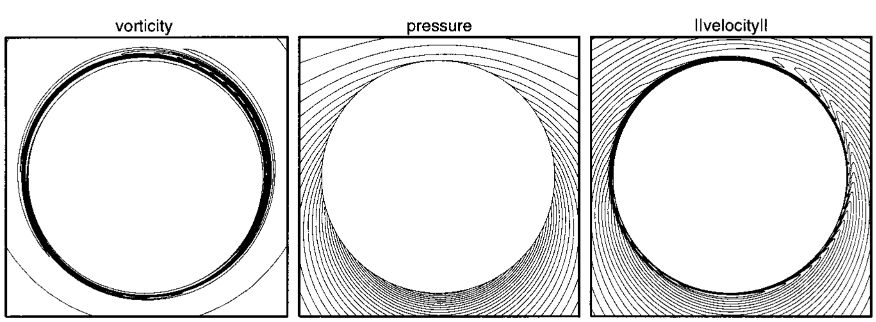

Fig. 10 Re=3800, α=5.0, e=0.005 D flow past an eccentrically rotating cylinder: vorticity, pressure, and magnitude of velocity fields for the temporally periodic solution when the geometric center of the cylinder is at its left-most location with respect to the center of rotation

by Prandtl. To investigate the stability of the steady-state solution, computations are carried out for eccentrically rotating cylinder. In this set-up the center of rotation of the cylinder does not match the geometric center of the cylinder. The unsteady disturbances introduced by the motion of the cylinder results in an overall unsteady flow. However, the mean values of the aerodynamic coefficients are still quite comparable to those from the basic solution. In this sense, the two-dimensional solution is stable to purely two-dimensional disturbances. This implies that, for purely two-dimensional flows, the mean value of the lift coefficient can exceed the maximum limit due to arguments by Prandtl by a very significant amount. Similar observations have also been made by other researchers in the past for three-dimensional flows.

It is being suggested that for three-dimensional flows one should expect lower values for lift coefficient than those predicted by purely two-dimensional simulations. The contributions to this loss of lift come from centrifugal instabilities along the span of the cylinder and end effects. The present study is also useful in establishing the effect of *wobble* in flows past spinning cylinders. These results are particularly useful in the context of flow control devices where a slight degree of wobble would be almost unavoidable in real situations.

References

[1] Tokumaru, P. T., and Dimotakis, P. E., 1991, ''Rotary Oscillation Control of Cylinder Wake,'' J. Fluid Mech., **224**, pp. 77–90.

[2] Tokumaru, P. T., and Dimotakis, P. E., 1993, ''The Lift of a Cylinder Executing Rotary Motions in a Uniform Flow,'' J. Fluid Mech., **255**, pp. 1–10.

[3] Gad-el-Hak, M., and Bushnell, D. M., 1991, ''Separation Control: Review,'' ASME J. Fluids Eng., **113**, pp. 5–29.

[4] Goldstein, S., 1938, *Modern Developments in Fluid Dynamics*, Clarendon Press, Oxford, U.K.

[5] Coutanceau, M. and Menard, C., 1985, ''Influence of Rotation on the Near-Wake Development Behind an Impulsively Started Circular Cylinder,'' J. Fluid Mech., **158**, pp. 399–446.

[6] Badr, H. M., and Dennis, S. C. R., 1985, ''Time-Dependent Viscous Flow Past an Impulsively Started Rotating and Translating Circular Cylinder,'' J. Fluid Mech., **158**, pp. 447–488.

[7] Badr, H. M., Coutanceau, M., Dennis, S. C. R., and Menard, C., 1990, ''Unsteady Flow Past a Rotating Cylinder at Reynolds Numbers 10^3 and 10^4,'' J. Fluid Mech., **220**, pp. 459–484.

[8] Chew, Y. T., Cheng, M., and Luo, S. C., 1995, ''A Numerical Study of Flow Past a Rotating Circular Cylinder Using a Hybrid Vortex Scheme,'' J. Fluid Mech., **299**, pp. 35–71.

[9] Tezduyar, T. E., Mittal, S., Ray, S. E., and Shih, R., 1992, ''Incompressible Flow Computations With Stabilized Bilinear and Linear Equal-Order-Interpolation Velocity-Pressure Elements,'' Comput. Methods Appl. Mech. Eng., **95**, pp. 221–242.

[10] Hughes, T. J. R., and Brooks, A. N., 1979, ''A Multi-Dimensional Upwind Scheme With No Crosswind Diffusion,'' *Finite Element Methods for Convection Dominated Flows,* T. J. R. Hughes, ed., AMD-Vol. 34, ASME, New York, pp. 19–35.

[11] Tezduyar, T. E., and Hughes, T. J. R., 1983, ''Finite Element Formulations for Convective Dominated Flows With Particular Emphasis on the Compressible Euler Equations,'' *Proceedings of AIAA 21st Aerospace Sciences Meeting*, AIAA Paper 83-0125, Reno, NV.

[12] Tezduyar, T. E., Behr, M., and Liou, J., 1992, ''A New Strategy for Finite Element Computations Involving Moving Boundaries and Interfaces—The Deforming-Spatial-Domain/Space-Time Procedure: I. The Concept and the Preliminary Tests,'' Comput. Methods Appl. Mech. Eng., **94**, No. 3, pp. 339–351.

[13] Tezduyar, T. E., Behr, M., Mittal, S., and Liou, J., 1992, ''A New Strategy for Finite Element Computations Involving Moving Boundaries and Interfaces—The Deforming-Spatial-Domain/Space-Time Procedure: II. Computation of Free-Surface Flows, Two-Liquid Flows, and Flows With Drifting Cylinders,'' Comput. Methods Appl. Mech. Eng., **94**, No. 3, pp. 353–371.

[14] Chen, Yen-Ming, Ou, Yu-Roung, and Pearlstein, A. J., 1993, ''Development of the Wake Behind A Circular Cylinder Impulsively Started Into Rotary and Rectilinear Motion,'' J. Fluid Mech., **253**, pp. 449–484.

[15] Behr, M., Hastreiter, D., Mittal, S., and Tezduyar, T. E., 1995, ''Incompressible Flow Past a Circular Cylinder: Dependence of the Computed Flow Field on the Location of the Lateral Boundaries,'' Comput. Methods Appl. Mech. Eng., **123**, pp. 309–316.

Computationally Efficient Micromechanical Models for Woven Fabric Composite Elastic Moduli

R. Tanov
Graduate Research Assistant

A. Tabiei[1]
Assistant Professor and Director

Center for Excellence in DYNA3D Analysis,
Department of Aerospace Engineering
and Engineering Mechanics,
Uiniversity of Cincinnati,
Cincinnati, OH 45221-0070

This paper presents two newly developed micromechanical models for the analysis of plain weave fabric composites. Both models utilize the representative volume cell approach. The representative unit volume of the woven lamina is divided into subcells of homogeneous material. Starting with the average strains in the representative volume cell and based on continuity requirements at the subcell interfaces, the strains and stresses in the composite fiber yarns and matrix are determined as well as the average stresses in the lamina. Equivalent homogenized material properties are also determined. In their formulation the developed micromechanical models take into consideration all components of the three-dimensional strain and stress tensors. The performance of both models is assessed through comparison with available results from other numerical, analytical, and experimental approaches for composite laminae homogenization. The very good accuracy together with the simplicity of formulation makes these models attractive for the finite element analysis of composite laminates. [DOI: 10.1115/1.1357516]

1 Introduction

Composite laminae are being more and more extensively utilized in modern shell structures. High specific stiffness, specific strength, and toughness are among their advantageous properties, which make composite shells the preferred choice in all kinds of aerospace, automotive, and marine vehicles, industrial, civil and other structures. Of the two major types of composite laminae, woven fabric composites have long been recognized as more competitive than unidirectional composites. This is partly due to their ability to provide good reinforcement in all directions within a single layer, to their better impact resistance, better-balanced properties, easier handling and fabrication, and good ability to conform to surfaces with complex curvatures. Along with that, however, their complex architecture makes the analysis of their behavior much more challenging. Therefore, it is not surprising that there are substantialy fewer approaches for determining the properties of woven fabric laminae and predicting their behavior than for unidirectional composites. Most of them utilize the representative unit cell approach—the properties and behavior of the entire lamina are considered to be the same as the properties of a unit cell. The entire complex geometry of the composite layer can usually be reproduced by using this representative volume cell (RVC) as a building block.

Earlier models for the analysis of woven fabric composites include the works of Ishikawa and Chou [1–4], who developed three different models: the mosaic model, the fiber-undulation model, and the bridging model. The mosaic model is based on the classical lamination theory and represents the woven composite as an assemblage of asymmetrical cross-ply laminates. Using the iso-stress (or series model) and iso-strain (or parallel model) assumptions, the upper and lower bounds of the elastic moduli can be derived with this model. The fiber-undulation model takes into account the fiber undulation and continuity. Both the mosaic and the fiber-undulation models are one-dimensional models. The bridging model was developed for the analysis of satin composites. In this model the regions with straight threads are assumed to act as load-carrying bridges between adjacent interlaced regions.

Naik and Shembekar [5] developed two-dimensional micromechanical models using the parallel-series assumptions. These models are based on the classical lamination theory assuming that it is applicable to each infinitesimal piece of the RVC. The models are capable of describing the RVC geometry in detail, including the fiber yarn cross sections and the undulated portions, and can be used to determine the homogenized in-plane stiffness properties of the RVC.

Karayaka and Kurath [6] used the RVC approach to develop a micromechanical model capable of representing both plain weave and satin weave composite layers. The model is based on the assumption that all in-plane strain and out-of-plane stress components are constant throughout the RVC. It was used in ([6]) to investigate the behavior of a five-harness satin weave Graphite/Epoxy laminate.

Tabiei and Jiang [7] developed a micromechanical model, which considers the two-dimensional extent of woven fabric laminae and is based on nonlinear stress-strain relations. Within this model the RVC is divided into many subcells and an averaging is performed to obtain the effective stress-strain relations. This model is suitable for implementation into nonlinear finite element codes to enable structural analyses of woven composites. Recently, Tabiei et al. [8] presented a nonlinear constitutive model for plain weave composites. The incremental constitutive model was developed based on micromechanics. This model considers material nonlinear behavior of both resin and fill/warp yarns.

A global/local approach to woven metal matrix composites analysis was developed by Bednarcyk and Pindera [9,10]. The approach uses a local unidirectional micromechanical model to represent the fibers and matrix, which constitute the fiber yarns, and a three-dimensional global model to simulate the overall behavior of the RVC. This approach is used to predict the response of eight-harness satin weave Carbon/Copper composites and compare the results to experimental data.

[1]To whom author should be addressed.

Contributed by the Applied Mechanics Division of THE AMERICAN SOCIETY OF MECHANICAL ENGINEERS for publication in the ASME JOURNAL OF APPLIED MECHANICS. Manuscript received by the ASME Applied Mechanics Division, April 18, 2000; final revision, October 24, 2000. Associate Editor: M-J. Pindera. Discussion on the paper should be addressed to the Editor, Professor Lewis T. Wheeler, Department of Mechanical Engineering, University of Houston, Houston, TX 77204-4792, and will be accepted until four months after final publication of the paper itself in the ASME JOURNAL OF APPLIED MECHANICS.

Along with the analytical models of woven fabric composites there are also some numerical approaches utilizing the finite element method. Using a three-dimensional model, Whitcomb [11] analyzed a RVC of a plain weave composite. Whitcomb used his finite element model to assess the influence of different parameters on the stiffness properties of the RVC. In their work Chung and Tamma [12] summarize and compare various homogenization methods via finite element analyses.

The aim of the present work is to develop micromechanical models for plain weave composites, which could be incorporated efficiently into explicit and implicit finite element codes to be able to perform structural analysis of composite and sandwich shells with woven fabric layers. This will enable determination of the state of stress and strain in the constituent fiber yarns and matrix within the finite element analysis, which could be used to perform material failure and property degradation checks within the structural analysis process. Many of the presently existing analytical models lack either accuracy or efficiency or both, to be capable of providing the above features to a finite element analysis. The finite element models usually have a good accuracy and are capable of correctly modeling the three-dimensional state of stress and strain in the RVC and its constituents, but involve too many elements in discretizing the RVC to be used for composite structural analysis. The analytical model of Tabiei and Jiang described in ([7]) proved efficient for an implicit finite element analysis, but the nature of the explicit time integration scheme will make it hard to fit into an explicit finite element analysis code. To a certain degree, this also applies to one of the herein presented models, namely the single-cell model. However, the other model described here, the four-cell model, solves only a small system of six linear equations, which would make it much more efficient in an explicit finite element analysis.

In what follows two new micromechanical models are formulated and their performance is checked and compared with results from other numerical, analytical, and experimental approaches employed in the analysis of plain weave fabric composites.

2 Formulation of the Micromechanical Models

Both models developed and described in this work utilize the RVC approach (see Fig. 1). In that the authors have tried to achieve an optimal balance between the two major parts of the formulation: the geometric description of the RVC, and the micromechanical representation of the developed model. This is something that many existing models lack; a tedious formulation is used to describe the RVC geometry with a very high precision, and at the same time the accuracy of that geometric description cannot be taken advantage of due to overly simplified micromechanical descriptions. This makes these approaches hard to implement in a real world analysis and at the same time the accuracy of the acquired results often does not match the solution effort needed. The geometric description of the RVC in the present models is much simpler compared to other approaches (e.g., see Naik and Shembekar [5]), which translates into computational efficiency and easy implementation. Yet, as the herein presented results show, their accuracy is very good for different values of the RVC geometric and material parameters. An important contribution for this accuracy is due to the three-dimensional micromechanical description of the RVC. Previous micromechanical models implement two-dimensional (Naik and Shembekar [5]) and even one-dimensional (Ishikawa and Chou [1–4]) approaches in the RVC description, which can significantly affect the solution accuracy.

In the present approaches the entire woven fabric lamina can be constructed by using the RVC, Fig. 1(*b*), as a building block. Assuming that the fiber yarns in both direction (the fill and warp) have the same structure and properties, the entire RVC, Fig. 1(*b*), can be constructed by using just one quarter of it, Fig. 1(*c*), and this quarter cell is hereafter referred to as the RVC. In their formulation the models described here consider all components of

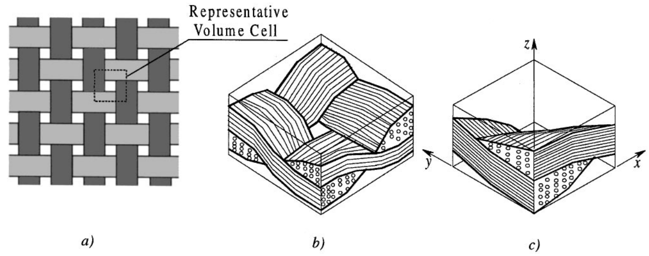

Fig. 1 Plain weave architecture, representative volume cell, and one quarter cell

the strain and stress tensors, and starting with the strains in the RVC are capable of determining the three-dimensional constitutive matrix of the homogenized RVC and all stress and strain components in the composite constituents. Both models assume that the RVC is assembled using certain number of subcells, which are under homogeneous state of stress and strain. The following assumptions are also used in the models: (a) the matrix is isotropic and the yarn fiber bundles are transversely isotropic with principal axis along the yarn axis; (b) the contact between the constituents is perfect, i.e., displacements and traction are continuous across the constituent contact interfaces.

Both formulations are developed with the intention to be used in a finite element composite shell analysis. Therefore, in the formulations, the average strains within the RVC are assumed to be available, which is the case in a standard displacement based finite element analysis. The models are then used to find the strains and stresses in the composite constituents, and the average stresses in the entire RVC or the tangent stiffness matrix.

If $[\mathbf{C}]_m$ and $[\mathbf{C}]_y$ are the constitutive matrices of the matrix and yarn in a material local coordinate system then

$$[\mathbf{C}]_m=\begin{bmatrix} C_{11}^m & C_{12}^m & C_{12}^m & 0 & 0 & 0 \\ C_{12}^m & C_{11}^m & C_{12}^m & 0 & 0 & 0 \\ C_{12}^m & C_{12}^m & C_{11}^m & 0 & 0 & 0 \\ 0 & 0 & 0 & C_{44}^m & 0 & 0 \\ 0 & 0 & 0 & 0 & C_{44}^m & 0 \\ 0 & 0 & 0 & 0 & 0 & C_{44}^m \end{bmatrix}, \tag{1}$$

where

$$C_{11}^m=\frac{E_m(1-\nu_m)}{(1+\nu_m)(1-2\nu_m)}; \quad C_{12}^m=\frac{E_m\nu_m}{(1+\nu_m)(1-2\nu_m)};$$

$$C_{44}^m=G_m=\frac{E_m}{2(1+\nu_m)} \tag{2}$$

and E_m, ν_m, and G_m are the matrix Young's modulus, Poisson's ratio, and shear modulus, respectively. Both fill and warp yarns are assumed to be of the same fiber material, with constitutive matrix of the yarns

$$[\mathbf{C}]_y=\begin{bmatrix} C_{11}^y & C_{12}^y & C_{12}^y & 0 & 0 & 0 \\ C_{12}^y & C_{22}^y & C_{23}^y & 0 & 0 & 0 \\ C_{12}^y & C_{23}^y & C_{22}^y & 0 & 0 & 0 \\ 0 & 0 & 0 & C_{44}^y & 0 & 0 \\ 0 & 0 & 0 & 0 & \dfrac{C_{22}^y-C_{23}^y}{2} & 0 \\ 0 & 0 & 0 & 0 & 0 & C_{44}^y \end{bmatrix}, \tag{3}$$

where

$$C_{11}^{y}=\frac{E_{v,L}(1-\nu_{y,TT}^{2})}{\Delta};\quad C_{12}^{y}=\frac{E_{y,T}\nu_{y,LT}(1+\nu_{y,TT})}{\Delta};$$

$$C_{22}^{y}=\frac{E_{v,T}(1-\nu_{y,LT}\nu_{y,TL})}{\Delta};\tag{4}$$

$$C_{23}^{y}=\frac{E_{y,T}(\nu_{y,TT}+\nu_{y,LT}\nu_{y,TL})}{\Delta};\quad C_{44}^{y}=G_{y,LT};$$

$$\Delta=1-\nu_{y,TT}^{2}-2\nu_{y,LT}\nu_{y,TL}(1+\nu_{y,TT}).$$

Here $\nu_{y,TL}=\nu_{y,LT}(E_{y,T}/E_{y,L})$ and $E_{y,L}, E_{y,T}, \nu_{y,LT}, \nu_{y,TT}, G_{y,LT}$ are the Young's moduli, Poisson's ratios, and the shear modulus of the transversely isotropic yarn; subscripts L and T denote the direction along the yarn axis and the transverse to it direction, respectively. Note that in the above formulas the commas in the subscripts do not represent differentiation. The above constitutive matrices, Eqs. (1) and (3), relate the stress and strain tensor components arranged in vectors as follows:

$$\{\boldsymbol{\sigma}\}=|\sigma_x\ \ \sigma_y\ \ \sigma_z\ \ \sigma_{xy}\ \ \sigma_{yz}\ \ \sigma_{zx}|^T;$$
$$\{\boldsymbol{\varepsilon}\}=|\varepsilon_x\ \ \varepsilon_y\ \ \varepsilon_z\ \ \gamma_{xy}\ \ \gamma_{yz}\ \ \gamma_{zx}|^T,\tag{5}$$

with $\gamma_{ij}=2\varepsilon_{ij}$ being the engineering shear strains.

A description of the geometry and mechanics of the models follows. Since in the first model we divide the quarter cell into four subcells in the lamina plane it will be referenced here as ''*the four-cell model*,'' while the second model, which has only one cell in the lamina plane will be referenced as ''*the single-cell model*.''

2.1 The Four-Cell Model

2.1.1 Geometry of the Model. The geometry of this model is shown in Fig. 2(*a*). To keep the formulation simple, the cross sections of the fill and warp yarns are assumed rectangular and their undulating form is approximated with only horizontal and inclined at angle θ sections, θ being the average undulation angle. This representation makes it possible to divide the RVC into four subcells, denoted by ''ff,'' ''fm,'' ''mm,'' and ''mf'' on Fig. 2(*a*). Subcell ''ff'' is further divided into two sub-subcells, Fig. 2(*b*), which represent the horizontal portions of the two yarns. Subcells ''fm'' and ''mf'' consist of yarn and matrix portions as illustrated on Fig. 2(*c*). Each one of them contains half of the inclined portion of the yarns; by putting two such subcells together we get the entire undulated portion of the yarn. Subcell ''mm'' is entirely of matrix material.

Let us assume that the RVC has height of H units and sides of length one unit each. Then, if both yarns have a rectangular cross section with sides $H/2$ and V_y, V_y being the overall yarn volume fraction, the ratio of the volume of the yarns to the volume of the entire RVC will equal V_y. Furthermore, the undulation angle, θ, can also be expressed through the total RVC height, H, and the yarn volume fraction, V_y from

$$\tan\theta=\frac{H}{4(1-V_y)}.\tag{6}$$

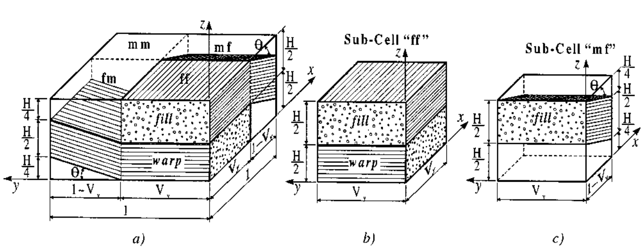

Fig. 2 Geometry of the quarter cell for the four-cell model

Thus, only two parameters, namely H and V_y, or θ and V_y are sufficient to completely define the geometry of the RVC. Furthermore, the dimensions of the sub-subcells are also completely defined with these two parameters. Note that in the present formulation this model does not include a layer of matrix material, which covers the entire RVC. Therefore, the height of the yarns is half the thickness of the entire lamina. If the real lamina to be represented by this model has a matrix layer of significant thickness then the model can be modified to include it, which would not change the basis of the formulation.

2.1.2 Micromechanics of the Model. Within the subcells ''ff,'' ''mf,'' and ''fm'' the constituent yarn and matrix materials are first combined to get an equivalent homogeneous material in each subcell (subcell ''mm'' is entirely matrix so there is no need to homogenize it). The four subcells are then combined to get an equivalent homogeneous RVC. The homogenization is based on the parallel-series assumptions: For some of the strain components the adjacent cells are assumed to work ''in parallel'' and the corresponding strains are equal; for the rest of the strains, the cells are assumed to work ''in series''—the corresponding stress components are equal and the strain components are averaged to get the entire cell resultant strains. Similar assumptions are used as a basis for many micromechanical models for unidirectional and woven composites.

The homogenization of the subcells ''ff'' and ''mf'' is described in the following.

2.1.2.1 Homogenization of subcell ''ff''. The subcell ''ff'' is shown on Fig. 2(*b*). It consists of two homogeneous parts of equal thickness, top fill and bottom warp. Both of them are of the same transversely isotropic material with axis of transverse isotropy along the corresponding yarn axis, which is x for the fill and y for the warp. So, the fill and warp constitutive matrices will be as follows:

$$[\mathbf{C}]_{\text{fill}}=\begin{bmatrix} C_{11}^{y} & C_{12}^{y} & C_{12}^{y} & 0 & 0 & 0\\ C_{12}^{y} & C_{22}^{y} & C_{23}^{y} & 0 & 0 & 0\\ C_{12}^{y} & C_{23}^{y} & C_{22}^{y} & 0 & 0 & 0\\ 0 & 0 & 0 & C_{44}^{y} & 0 & 0\\ 0 & 0 & 0 & 0 & C_{55}^{y} & 0\\ 0 & 0 & 0 & 0 & 0 & C_{44}^{y}\end{bmatrix}\tag{7}$$

and

$$[\mathbf{C}]_{\text{warp}}=\begin{bmatrix} C_{22}^{y} & C_{12}^{y} & C_{23}^{y} & 0 & 0 & 0\\ C_{12}^{y} & C_{11}^{y} & C_{12}^{y} & 0 & 0 & 0\\ C_{23}^{y} & C_{12}^{y} & C_{22}^{y} & 0 & 0 & 0\\ 0 & 0 & 0 & C_{44}^{y} & 0 & 0\\ 0 & 0 & 0 & 0 & C_{44}^{y} & 0\\ 0 & 0 & 0 & 0 & 0 & C_{55}^{y}\end{bmatrix}\tag{8}$$

with $C_{55}^{y}=C_{22}^{y}-C_{23}^{y}/2$.

Assuming we have available the homogeneous strain tensor components, ε_{ij}^{ff}, of the entire subcell ''ff,'' we will express the strains and stresses in the fill and warp portions, and the stresses in the entire subcell. From the perfect contact and the parallel-series assumption we have at the fill-warp interface:

$$\varepsilon_x^{ff}=\varepsilon_x^{f}=\varepsilon_x^{w}\quad \sigma_z^{ff}=\sigma_z^{f}=\sigma_z^{w}$$
$$\varepsilon_y^{ff}=\varepsilon_y^{f}=\varepsilon_y^{w}\quad \sigma_{yz}^{ff}=\sigma_{yz}^{f}=\sigma_{yz}^{w}\tag{9}$$
$$\varepsilon_{xy}^{ff}=\varepsilon_{xy}^{f}=\varepsilon_{xy}^{w}\quad \sigma_{zx}^{ff}=\sigma_{zx}^{f}=\sigma_{zx}^{w}.$$

Here a single superscript f is used to denote that the corresponding quantity refers to the fill yarn, and w refers to the warp yarn.

The rest of the strain and stress tensor components of the subcell are assumed volume averages of the strains and stresses of the constituent fill and warp parts:

$$\begin{aligned}
\varepsilon_z^{ff}&=\tfrac{1}{2}(\varepsilon_z^f+\varepsilon_z^w) \quad \sigma_x^{ff}=\tfrac{1}{2}(\sigma_x^f+\varepsilon_x^w)\\
\varepsilon_{yz}^{ff}&=\tfrac{1}{2}(\varepsilon_{yz}^f+\varepsilon_{yz}^w) \quad \sigma_y^{ff}=\tfrac{1}{2}(\sigma_y^f+\sigma_y^w)\\
\varepsilon_{zx}^{ff}&=\tfrac{1}{2}(\varepsilon_{zx}^f+\varepsilon_{zx}^w) \quad \sigma_{xy}^{ff}=\tfrac{1}{2}(\sigma_{xy}^f+\varepsilon_{xy}^w).
\end{aligned} \tag{10}$$

Note that the above relations combined with the assumption of homogeneous strains and stresses within the subcells will result in violation of the displacement continuity with respect to the surrounding subcells. Therefore, the values of the strains in the subcell should be treated as subcell average values, satisfying the displacement continuity in an average sense. Using the above equations, Eqs. (9) and (10), the unknown strain components in the fill and warp parts can be expressed:

$$\begin{aligned}
&\varepsilon_z^f=\varepsilon_z^{ff}-\frac{C_{12}^y-C_{23}^y}{2C_{22}^y}(\varepsilon_x^{ff}-\varepsilon_y^{ff}) \quad \varepsilon_z^w=\varepsilon_z^{ff}+\frac{C_{12}^y-C_{23}^y}{2C_{22}^y}(\varepsilon_x^{ff}-\varepsilon_y^{ff})\\
&\varepsilon_{yz}^f=\frac{2C_{44}^y}{C_{44}^y+C_{55}^y}\varepsilon_{yz}^{ff} \quad \varepsilon_{yz}^w=\frac{2C_{55}^y}{C_{44}^y+C_{55}^y}\varepsilon_{yz}^{ff}\\
&\varepsilon_{zx}^f=\frac{2C_{55}^y}{C_{44}^y+C_{55}^y}\varepsilon_{zx}^{ff} \quad \varepsilon_{zx}^w=\frac{2C_{44}^y}{C_{44}^y+C_{55}^y}\varepsilon_{zx}^{ff}.
\end{aligned} \tag{11}$$

So, all strains in the constituents are obtained, and knowing the constitutive matrices of the yarns, we can further express the stresses in the constituent. Also, from Eqs. (9) and (10), the average stresses in the entire subcell can be expressed in term of the average strains of the subcell. Thus the elements of the constitutive matrix of the homogenized subcell can be found,

$$\begin{aligned}
C_{11}^{ff}&=C_{22}^{ff}=\frac{1}{2}\left[C_{11}^y+C_{22}^y-\frac{(C_{12}^y-C_{23}^y)^2}{2C_{22}^y}\right]\\
C_{12}^{ff}&=\frac{1}{2}\left[2C_{12}^y+\frac{(C_{12}^y-C_{23}^y)^2}{2C_{22}^y}\right]\\
C_{13}^{ff}&=C_{23}^{ff}=\frac{C_{12}^y+C_{23}^y}{2}\\
C_{33}^{ff}&=C_{22}^y\\
C_{44}^{ff}&=C_{44}^y\\
C_{55}^{ff}&=C_{66}^{ff}=\frac{2C_{44}^yC_{55}^y}{C_{44}^y+C_{55}^y}.
\end{aligned} \tag{12}$$

Finally, the constitutive matrix of subcell ''ff'' is

$$[\mathbf{C}]_{ff}=\begin{bmatrix}
C_{11}^{ff} & C_{12}^{ff} & C_{13}^{ff} & 0 & 0 & 0\\
C_{12}^{ff} & C_{11}^{ff} & C_{13}^{ff} & 0 & 0 & 0\\
C_{13}^{ff} & C_{13}^{ff} & C_{33}^{ff} & 0 & 0 & 0\\
0 & 0 & 0 & C_{44}^{ff} & 0 & 0\\
0 & 0 & 0 & 0 & C_{55}^{ff} & 0\\
0 & 0 & 0 & 0 & 0 & C_{55}^{ff}
\end{bmatrix}. \tag{13}$$

Thus, the homogenization of subcell ''ff'' is complete and provided the average strains, ε_{ij}^{ff}, in the subcell are known, all strains in stresses in the constituents can be determined, as well as the average subcell stresses.

2.1.2.2 Homogenization of subcells ''mf'' and ''fm''. Since subcells ''mf'' and ''fm'' have similar geometry, their constitutive matrices will be also similar and will be related through a simple coordinate rotation. Therefore, only the derivation of the constitutive matrix for subcell ''mf'' will be shown, and the constitutive matrix for subcell ''fm'' will be derived using the appropriate transformation.

Subcell ''mf'' contains matrix and yarn parts of equal volumes. If the undulation angle, θ, is not zero the material local coordinate system of the fill yarn part will not coincide with the *xyz* coordinate system (see Fig. 2(*c*)). However, we can take advantage of the isotropy of the matrix material and homogenize the subcell in the yarn local coordinate system, and then transfer the thus acquired constitutive matrix in the global *xyz* coordinate system. For this purpose we need to transfer the subcell average strains from the RVC global to the yarn local coordinate system

$$\begin{aligned}
(\varepsilon_x^{mf})'&=\varepsilon_x^{mf}\cos^2\theta+\varepsilon_z^{mf}\sin^2\theta-\gamma_{zx}^{mf}\cos\theta\sin\theta\\
(\varepsilon_y^{mf})'&=\varepsilon_y^{mf}\\
(\varepsilon_z^{mf})'&=\varepsilon_x^{mf}\sin^2\theta+\varepsilon_z^{mf}\cos^2\theta+\gamma_{zx}^{mf}\cos\theta\sin\theta\\
(\gamma_{xy}^{mf})'&=\gamma_{xy}^{mf}\cos\theta-\gamma_{yz}^{mf}\sin\theta\\
(\gamma_{xy}^{mf})'&=\gamma_{xy}^{mf}\sin\theta+\gamma_{yz}^{mf}\cos\theta\\
(\gamma_{zx}^{mf})'&=2\varepsilon_x^{mf}\sin\theta\cos\theta-2\varepsilon_z^{mf}\sin\theta\cos\theta\\
&\quad+\gamma_{zx}^{mf}(\cos^2\theta-\sin^2\theta).
\end{aligned} \tag{14}$$

These values of the strains in the yarn local coordinate system will only be needed if the strains and stresses in the matrix and fill parts are needed. If not, the homogenized subcell constitutive matrix constructed below can be directly used to get the subcell average stresses in the RVC global coordinate system.

The yarn local coordinate system, $x'y'z'$, can be obtained by rotating the RVC global coordinate system around the *y*-axis at an angle θ. The variables expressed in that coordinate system will be denoted by a superscript prime. In that coordinate system, similar relations to Eqs. (9) and (10) should hold:

$$\begin{aligned}
(\varepsilon_x^{mf})'&=(\varepsilon_x^f)'=(\varepsilon_x^m)' \quad (\sigma_z^{mf})'=(\sigma_z^f)'=(\sigma_z^m)'\\
(\varepsilon_y^{mf})'&=(\varepsilon_y^f)'=(\varepsilon_y^m)' \quad (\sigma_{yz}^{mf})'=(\sigma_{yz}^f)'=(\sigma_{yz}^m)'\\
(\varepsilon_{xy}^{mf})'&=(\varepsilon_{xy}^f)'=(\varepsilon_{xy}^m)' \quad (\sigma_{zx}^{mf})'=(\sigma_{zx}^f)'=(\sigma_{zx}^m)'
\end{aligned} \tag{15}$$

and

$$\begin{aligned}
(\varepsilon_z^{mf})'&=\tfrac{1}{2}[(\varepsilon_z^f)'+(\varepsilon_z^m)'] \quad (\sigma_x^{mf})'=\tfrac{1}{2}[(\sigma_x^f)'+(\sigma_x^m)']\\
(\varepsilon_{yz}^{mf})'&=\tfrac{1}{2}[(\varepsilon_{yz}^f)'+(\varepsilon_{yz}^m)'] \quad (\sigma_y^{mf})'=\tfrac{1}{2}[(\sigma_y^f)'+(\sigma_m^y)']\\
(\varepsilon_{zx}^{mf})'&=\tfrac{1}{2}[(\varepsilon_{zx}^f)'+(\varepsilon_{zx}^m)'] \quad (\sigma_{xy}^{mf})'=\tfrac{1}{2}[(\sigma_{xy}^f)'+(\sigma_{xy}^m)'].
\end{aligned} \tag{16}$$

From these relations we can determine the unknown strain components in the yarn local coordinate system in the matrix and fill parts, which are

$$\begin{aligned}
(\varepsilon_z^m)'&=\frac{1}{C_{11}^m+C_{22}^y}[2C_{22}^y(\varepsilon_z^{mf})'+(C_{12}^y-C_{12}^m)(\varepsilon_x^{mf})'\\
&\quad+(C_{23}^y-C_{12}^m)(\varepsilon_y^{mf})']\\
(\varepsilon_z^f)'&=\frac{1}{C_{11}^m+C_{22}^y}[2C_{11}^m(\varepsilon_z^{mf})'+(C_{12}^y-C_{12}^m)(\varepsilon_x^{mf})'\\
&\quad-(C_{23}^y-C_{12}^m)(\varepsilon_y^{mf})']\\
(\varepsilon_{yz}^m)'&=\frac{2C_{55}^y}{C_{44}^m+C_{55}^y}(\varepsilon_{yz}^{mf})' \quad (\varepsilon_{yz}^f)'=\frac{2C_{44}^m}{C_{44}^m+C_{55}^y}(\varepsilon_{yz}^{mf})'.\\
(\varepsilon_{zx}^m)'&=\frac{2C_{44}^y}{C_{44}^m+C_{44}^y}(\varepsilon_{zx}^{mf})' \quad (\varepsilon_{zx}^f)'=\frac{2C_{44}^m}{C_{44}^m+C_{44}^y}(\varepsilon_{zx}^{mf})'.
\end{aligned} \tag{17}$$

The constitutive matrix elements of the subcell in the $x'\ y'\ z'$ coordinate system are

$$
\begin{aligned}
(C_{11}^{mf})' &= \frac{1}{2}\left[C_{11}^{m}+C_{11}^{y}-\frac{(C_{12}^{y}-C_{12}^{m})^2}{C_{11}^{m}+C_{22}^{y}}\right]\\
(C_{12}^{mf})' &= \frac{1}{2}\left[C_{12}^{m}+C_{12}^{y}-\frac{(C_{12}^{y}-C_{12}^{m})(C_{23}^{y}-C_{12}^{m})}{C_{11}^{m}+C_{22}^{y}}\right]\\
(C_{13}^{mf})' &= \frac{C_{12}^{y}C_{11}^{m}+C_{12}^{m}C_{22}^{y}}{C_{11}^{m}+C_{22}^{y}}\\
(C_{22}^{mf}) &= \frac{1}{2}\left[C_{11}^{m}+C_{22}^{y}-\frac{(C_{23}^{y})-(C_{12}^{m})^2}{C_{11}^{m}+C_{22}^{y}}\right]\\
(C_{23}^{mf})' &= \frac{C_{23}^{y}C_{11}^{m}+C_{12}^{m}C_{22}^{y}}{C_{11}^{m}+C_{22}^{y}} \quad (C_{33}^{mf})' = \frac{2C_{22}^{y}C_{11}^{m}}{C_{11}^{m}+C_{22}^{y}}\\
(C_{44}^{mf})' &= \frac{1}{2}(C_{44}^{m}+C_{44}^{y})\\
(C_{55}^{mf})' &= \frac{2C_{55}^{y}C_{44}^{m}}{C_{44}^{m}+C_{55}^{y}} \quad (C_{66}^{mf})' = \frac{2C_{44}^{y}C_{44}^{m}}{C_{44}^{m}+C_{44}^{y}}.
\end{aligned}
\tag{18}
$$

Then, the constitutive matrix of subcell ''mf'' in the $x'\ y'\ z'$ coordinate system is

$$
[\mathbf{C}]'_{mf} = \begin{bmatrix}
(C_{11}^{mf})' & (C_{12}^{mf})' & (C_{13}^{mf})' & 0 & 0 & 0\\
(C_{12}^{mf})' & (C_{22}^{mf})' & (C_{23}^{mf})' & 0 & 0 & 0\\
(C_{13}^{mf})' & (C_{23}^{mf})' & (C_{33}^{mf})' & 0 & 0 & 0\\
0 & 0 & 0 & (C_{44}^{mf})' & 0 & 0\\
0 & 0 & 0 & 0 & (C_{55}^{mf})' & 0\\
0 & 0 & 0 & 0 & 0 & (C_{66}^{mf})'
\end{bmatrix}.
\tag{19}
$$

By rotating back the local coordinate system $x'\ y'\ z'$ at angle θ we will get the RVC global coordinate system. Transforming the above constitutive matrix, Eq. (19), accordingly, will give us the subcell ''mf'' constitutive matrix in RVC global coordinate system, which is

$$
[\mathbf{C}]_{mf} = \begin{bmatrix}
C_{11}^{mf} & C_{12}^{mf} & C_{13}^{mf} & 0 & 0 & C_{16}^{mf}\\
C_{12}^{mf} & C_{22}^{mf} & C_{23}^{mf} & 0 & 0 & C_{26}^{mf}\\
C_{13}^{mf} & C_{23}^{mf} & C_{33}^{mf} & 0 & 0 & C_{36}^{mf}\\
0 & 0 & 0 & C_{44}^{mf} & C_{45}^{mf} & 0\\
0 & 0 & 0 & C_{45}^{mf} & C_{55}^{mf} & 0\\
C_{16}^{mf} & C_{26}^{mf} & C_{26}^{mf} & 0 & 0 & C_{66}^{mf}
\end{bmatrix}
\tag{20}
$$

where

$$
\begin{aligned}
C_{11}^{mf} &= (C_{11}^{mf})'\cos^4\theta + (C_{33}^{mf})'\sin^4\theta + 2[(C_{13}^{mf})'\\
&\quad + 2(C_{66}^{mf})']\sin^2\theta\cos^2\theta\\
C_{12}^{mf} &= (C_{12}^{mf})'\cos^2\theta + (C_{23}^{mf})'\sin^2\theta\\
C_{13}^{mf} &= (C_{13}^{mf})'(\cos^4\theta+\sin^4\theta) + [(C_{11}^{mf})'\\
&\quad + (C_{33}^{mf})' - 4(C_{66}^{mf})']\sin^2\theta\cos^2\theta\\
C_{16}^{mf} &= \{[(C_{13}^{mf})' - (C_{11}^{mf})']\cos^2\theta + [(C_{33}^{mf})' - (C_{13}^{mf})']\sin^2\theta\\
&\quad + 2(C_{66}^{mf})'(\cos^2\theta - \sin^2\theta)\}\sin\theta\cos\theta\\
C_{22}^{mf} &= (C_{22}^{mf})'\\
C_{23}^{mf} &= (C_{12}^{mf})'\sin^2\theta + (C_{23}^{mf})'\cos^2\theta\\
C_{26}^{mf} &= [(C_{23}^{mf})' - (C_{12}^{mf})']\sin\theta\cos\theta\\
C_{33}^{mf} &= (C_{11}^{mf})'\sin^4\theta + (C_{33}^{mf})'\cos^4\theta + 2[(C_{13}^{mf})'\\
&\quad + 2(C_{66}^{mf})']\sin^2\theta\cos^2\theta\\
C_{36}^{mf} &= \{[(C_{13}^{mf})' - (C_{11}^{mf})']\sin^2\theta + [(C_{33}^{mf})' - (C_{13}^{mf})']\cos^2\theta\\
&\quad - 2(C_{66}^{mf})'(\cos^2\theta - \sin^2\theta)\}\sin\theta\cos\theta\\
C_{44}^{mf} &= (C_{44}^{mf})'\cos^2\theta + (C_{55}^{mf})'\sin^2\theta\\
C_{45}^{mf} &= [(C_{55}^{mf})' - (C_{44}^{mf})']\sin\theta\cos\theta\\
C_{55}^{mf} &= (C_{44}^{mf})'\sin^2\theta + (C_{55}^{mf})'\cos^2\theta\\
C_{66}^{mf} &= [(C_{11}^{mf})' + (C_{33}^{mf})' - 2(C_{13}^{mf})']\sin^2\theta\cos^2\theta\\
&\quad + (C_{66}^{mf})'(\cos^2\theta - \sin^2\theta)^2.
\end{aligned}
\tag{21}
$$

The constitutive matrix of subcell ''fm'' can be obtained through an appropriate transformation of the above matrix, Eq. (20) and is as follows:

$$
[\mathbf{C}]_{fm} = \begin{bmatrix}
C_{22}^{mf} & C_{12}^{mf} & C_{23}^{mf} & 0 & -C_{26}^{mf} & 0\\
C_{12}^{mf} & C_{11}^{mf} & C_{13}^{mf} & 0 & -C_{16}^{mf} & 0\\
C_{23}^{mf} & C_{13}^{mf} & C_{33}^{mf} & 0 & -C_{36}^{mf} & 0\\
0 & 0 & 0 & C_{44}^{mf} & 0 & -C_{45}^{mf}\\
-C_{26}^{mf} & -C_{16}^{mf} & -C_{36}^{mf} & 0 & C_{66}^{mf} & 0\\
0 & 0 & 0 & -C_{45}^{mf} & 0 & C_{55}^{mf}
\end{bmatrix}.
\tag{22}
$$

Thus, each subcell has been homogenized and its equivalent constitutive properties are available. The strains and stresses in the constituents, and the subcell resultant stresses can be determined, provided that the strains of the subcells are available. We can apply a similar parallel-series approach to the entire RVC and thus determine the strains in the subcells. Let us assume that the average strains in the RVC, $\overline{\varepsilon_{ij}}$, are available. Then, based on the parallel-series assumptions, the following relations will hold:
For strains:

$$
\begin{aligned}
&V_y\varepsilon_x^{ff} + (1-V_y)\varepsilon_x^{mf} = \overline{\varepsilon_x} \quad V_y\varepsilon_x^{fm} + (1-V_y)\varepsilon_x^{mm} = \overline{\varepsilon_x}\\
&V_y\varepsilon_y^{ff} + (1-V_y)\varepsilon_y^{fm} = \overline{\varepsilon_y} \quad V_y\varepsilon_y^{mf} + (1-V_y)\varepsilon_y^{mm} = \overline{\varepsilon_y}\\
&\varepsilon_z^{fm} = \varepsilon_z^{mm} = \varepsilon_z^{ff} = \varepsilon_z^{mf} = \overline{\varepsilon_z}\\
&\varepsilon_{xy}^{fm} = \varepsilon_{xy}^{mm} = \varepsilon_{xy}^{ff} = \varepsilon_{xy}^{mf} = \overline{\varepsilon_{xy}}\\
&V_y(1-V_y)(\varepsilon_{yz}^{fm} + \varepsilon_{yz}^{mf}) + (1-V_y)^2\varepsilon_{yz}^{mm} + V_y^2\varepsilon_{yz}^{ff} = \overline{\varepsilon_{yz}}\\
&V_y(1-V_y)(\varepsilon_{zx}^{fm} + \varepsilon_{zx}^{mf}) + (1-V_y)^2\varepsilon_{zx}^{mm} + V_y^2\varepsilon_{zx}^{ff} = \overline{\varepsilon_{zx}}
\end{aligned}
\tag{23}
$$

For stresses:

$$
\begin{aligned}
&\sigma_x^{fm} = \sigma_x^{mm} \quad \sigma_x^{ff} = \sigma_x^{mf}\\
&V_y\sigma_x^{ff} + (1-V_y)\sigma_x^{fm} = V_y\sigma_x^{mf} + (1-V_y)\sigma_x^{mm} = \overline{\sigma_x}\\
&\sigma_y^{ff} = \sigma_y^{fm} \quad \sigma_y^{mf} = \sigma_y^{mm}\\
&V_y\sigma_y^{ff} + (1-V_y)\sigma_y^{mf} = V_y\sigma_y^{fm} + (1-V_y)\sigma_y^{mm} = \overline{\sigma_y}\\
&V_y(1-V_y)(\sigma_z^{fm} + \sigma_z^{mf}) + (1-V_y)^2\sigma_z^{mm} + V_y^2\sigma_z^{ff} = \overline{\sigma_z}\\
&V_y(1-V_y)(\sigma_{xy}^{fm} + \sigma_{xy}^{mf}) + (1-V_y)^2\sigma_{xy}^{mm} + V_y^2\sigma_{xy}^{ff} = \overline{\sigma_{xy}}\\
&\sigma_{yz}^{fm} = \sigma_{yz}^{mm} = \sigma_{yz}^{ff} = \sigma_{yz}^{mf} = \overline{\sigma_{yz}}\\
&\sigma_{zx}^{fm} = \sigma_{zx}^{mm} = \sigma_{zx}^{ff} = \sigma_{zx}^{mf} = \overline{\sigma_{zx}}
\end{aligned}
\tag{24}
$$

These relations, Eqs. (23) and (24), have been derived based on the assumption that there is a perfect bonding between the subcells, and the assumption of homogeneous strain and stress in each subcell. For example, considering the transverse normal strain component, ε_z, it is obvious that the above assumptions lead to an equality in its value for all subcells, as expressed in Eq. (23). The same applies for the in-plane shear strain ε_{xy}. Using these assumptions in the geometric representation of the RVC, Fig. 2(*a*), all of the above relations, Eqs. (23) and (24), can be easily derived. They contain enough information to be able to express the 24 unknown strain components for all subcells. This will be done by solving a system of 16 linear equations with 16 unknowns. Note that the ε_{xy} and ε_z strain components are readily available. Also, some simple manipulations lead to

$$\varepsilon_{yz}^{mm}=\frac{C_{55}^{mf}\overline{\varepsilon_{yz}}+V_yC_{45}^{mf}\overline{\varepsilon_{xy}}}{C_{55}^{mf}+V_y(C_{44}^{m}-C_{55}^{mf})}\quad \varepsilon_{yz}^{mf}=\frac{C_{44}^{m}\overline{\varepsilon_{yz}}-(1-V_y)C_{45}^{mf}\overline{\varepsilon_{xy}}}{C_{55}^{mf}+V_y(C_{44}^{m}-C_{55}^{mf})}$$

$$\varepsilon_{zx}^{mm}=\frac{C_{55}^{mf}\overline{\varepsilon_{zx}}-V_yC_{45}^{mf}\overline{\varepsilon_{xy}}}{C_{55}^{mf}+V_y(C_{44}^{m}-C_{55}^{mf})}\quad \varepsilon_{zx}^{fm}=\frac{C_{44}^{m}\overline{\varepsilon_{zx}}+(1-V_y)C_{45}^{mf}\overline{\varepsilon_{xy}}}{C_{55}^{mf}+V_y(C_{44}^{m}-C_{55}^{mf})}. \tag{25}$$

This reduces the rank of the system of equations to 12. Furthermore, by using some of the simple relations in the equations the system of linear equations can be reduced to six equations with six unknown—the remaining strain components of the subcells. The coefficient matrix of this system is not fully populated, which makes it possible to explicitly express the six unknowns. After solving this system all strain components in the subcells will be available. Then with the values of these strains all strains and stresses in the fill, warp, and matrix parts of the subcells can be determined, as well as the average stresses in the subcells. These stress values can be finally used in Eq. (24) to calculate the average stresses in the homogenized RVC. Thus, the micromechanical description of the RVC will be complete. As already stated this approach would result in violations of the physical continuity between the adjacent subcells. However, the continuity requirements are satisfied in an average sense.

2.2 The Single-Cell Model

2.2.1 Geometry of the Model. The geometry of the single-cell model is shown on Fig. 3. The entire quarter cell is represented by a single cell, which has four layers: two matrix, one fill, and one warp. The layers will be denoted with m_t, f, w, and m_b for the top matrix, fill, warp, and bottom matrix, respectively. They are separated by inclined planes, defined by appropriate dimensioning and the angles θ_1 and θ_2 (Fig. 3). The undulating form of the yarns is represented by prisms with trapezoidal cross section, inclined at an angle $+\theta_1$ or $-\theta_1, \theta_1$ being the average undulation angle. Only two parameters are needed to describe the geometry of the entire RVC—the yarn volume fraction, V_y, and the lamina thickness, H_t. If we assume the in-plane dimensions of the RVC to be of a unit length, then the volume of the entire RVC will be equal to H_t. The volume of the two yarns will be $H/2+a$ (Fig. 3). Then

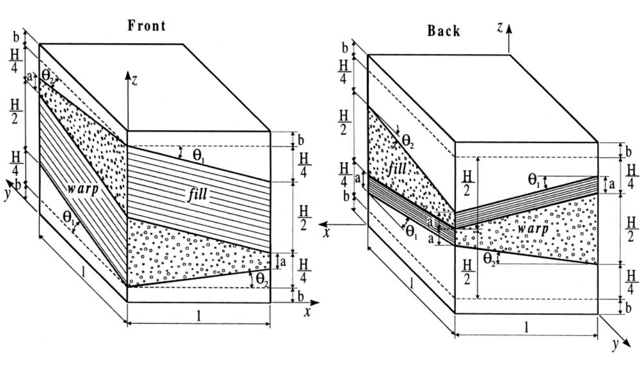

Fig. 3 Geometry of the quarter cell for the single-cell model

$$\frac{H}{2}+a=V_yH_t\quad b=\frac{H_t-H}{2}$$

$$\tan\theta_1=\frac{H}{4}\quad \tan\theta_2=\frac{H}{4}-a. \tag{26}$$

If $V_y\leqslant 0.5$ we assume that $a=0$. Then

$$H=2V_yH_t\quad b=H_t\left(\frac{1}{2}-V_y\right)$$

$$\tan\theta_1=\tan\theta_2=\frac{V_yH_t}{2}. \tag{27}$$

If $V_y>0.5$ we assume that $b=0$. Then

$$H=H_t\quad a=H_t\left(V_y-\frac{1}{2}\right)$$

$$\tan\theta_1=\frac{H_t}{4}\quad \tan\theta_2=H_t\left(\frac{3}{4}-V_y\right). \tag{28}$$

Note that the maximum yarn volume fraction that this model can represent is 0.75. Therefore, if it is higher, 0.75 will be used in the geometry description, Eq. (28), and the actual value is used in the micromechanical calculations. This is not expected to affect significantly the accuracy of the model. Experiments with values higher than 0.75 showed that the homogenized properties from this model compare very well with the values predicted by the four-cell model.

2.2.2 Micromechanics of the Model. The micromechanic description of this model is quite straightforward. In addition to the assumptions listed at the beginning of Section 2 it is also assumed that the strains and stresses of the entire RVC are weighted averages of the strains and stresses of the four layers. Thus, for the average RVC strain components we have

$$\overline{\varepsilon_{ij}}=\frac{1-V_y}{2}(\varepsilon_{ij}^{m_t}+\varepsilon_{ij}^{m_b})+\frac{V_y}{2}(\varepsilon_{ij}^{f}+\varepsilon_{ij}^{w}). \tag{29}$$

Assuming that the RVC average strain components, $\overline{\varepsilon_{ij}}$, are known, the above relation represents six equations for the 24 unknown strain components ε_{ij}^k, where $k=m_t,f,w,m_b$. In addition to these six relations we have six continuity and traction conditions at each interface between the adjacent layers. These are 18 relations, which together with the above, Eq. (29), form a system of 24 equations of 24 unknowns, the strain components in the four layers. The interface relations, however, have to be expressed in a coordinate system defined by the orientation of the interface. Here, we assume that the fibers of the fill and warp yarns lie in the *xz* and *yz*-planes, respectively (see Fig. 3). Therefore, if the interface coordinate system is defined in such a way that one axis lies in one of these planes, it will be a principal material axis for that yarn. Then, the interface coordinate system will be the principal coordinate system in which the transverse isotropy of the yarn is expressed and the constitutive matrix of the yarn in this coordinate system will be that defined in Eqs. (3) and (4) above. Such coordinate systems are defined for the three layer interfaces. For example, at the m_t-f interface, to define the interface local coordinate system we first need to rotate the global coordinate system about the *y*-axis at an angle θ_1 and then rotate it about the *x*-axis at θ_2. Although for the fill-warp interface the local *x* and *y*-axes cannot lie in the global *xz* and *yz*-planes if $\theta_1\neq 0$, we will assume that they are close enough to be able to use the principal constitutive matrices for both layers without having to transfer them in a nonprincipal coordinate system. Simple trigonometric relations would show that the angles between the local x and y-axes and the corresponding principal axes are negligibly small for any realistic value of H_t.

So, at each of the three layer interfaces we have the following relations, which should hold expressed in the local interface coordinate system:

At interface m_t-f:

$$\varepsilon_{x'}^{m_t}=\varepsilon_{x'}^{f}, \quad \varepsilon_{y'}^{m_t}=\varepsilon_{y'}^{f}, \quad \varepsilon_{x'y'}^{m_t}=\varepsilon_{x'y'}^{f},$$

$$\sigma_{z'}^{m_t}=\sigma_{z'}^{f}, \quad \sigma_{y'z'}^{m_t}=\sigma_{y'z'}^{f}, \quad \sigma_{z'x'}^{m_t}=\sigma_{z'x'}^{f} \tag{30}$$

At interface f-w:

$$\varepsilon_{x'}^{f}=\varepsilon_{x'}^{w}, \quad \varepsilon_{y'}^{f}=\varepsilon_{y'}^{w}, \quad \varepsilon_{x'y'}^{f}=\varepsilon_{x'y'}^{w},$$

$$\sigma_{z'}^{f}=\sigma_{z'}^{w}, \quad \sigma_{y'z'}^{f}=\sigma_{y'z'}^{w}, \quad \sigma_{z'x'}^{f}=\sigma_{z'x'}^{w} \tag{31}$$

At interface w-m_b:

$$\varepsilon_{x'}^{w}=\varepsilon_{x'}^{m_b} \quad \varepsilon_{y'}^{w}=\varepsilon_{y'}^{m_b} \quad \varepsilon_{x'y'}^{w}=\varepsilon_{x'y'}^{m_b},$$

$$\sigma_{z'}^{w}=\sigma_{z'}^{m_b} \quad \sigma_{y'z'}^{w}=\sigma_{y'z'}^{m_b}, \quad \sigma_{z'x'}^{w}=\sigma_{z'x'}^{m_b} \tag{32}$$

In the above relations, Eqs. (30)–(32), the local coordinate system is denoted with a superscript prime. Since the strains in the four layers are the primary unknowns, the stress relations have to be expressed through the strains by using the corresponding constitutive relations. Then, these relations have to be transferred into the RVC global coordinate system where the primary unknowns live. The transformation matrices from RVC global to interface local coordinate system can be expressed through the angles θ_1 and θ_2 as indicated above. Equations (29)–(32) form a system of 24 equations with 24 unknowns, the strains in the four layers in global RVC CS. After solving this system, the stresses in the layers have to be calculated. For that purpose, for the fill and warp layers, the constitutive matrices have to be transformed into RVC global coordinates by a simple rotation about the y and x-axis, respectively. Finally, the average stresses in the RVC are calculated by volume averaging the stresses in the four layers:

$$\bar{\sigma}_{ij}=\frac{1-V_f}{2}(\sigma_{ij}^{m_t}+\sigma_{ij}^{m_b})+\frac{V_f}{2}(\sigma_{ij}^{f}+\sigma_{ij}^{w}). \tag{33}$$

Thus, all strain and stress components in the four cell layers and in the RVC are determined, provided that the strains of the RVC are known.

Compared to the four-cell model the single-cell model has both different geometric and mechanical description. The geometry of this model would more accurately represent tightly woven composites where there is no (or almost no) portion of the thickness entirely occupied by the matrix. Its micromechanical representation is relatively straightforward but would be more appropriate for implementation in an implicit finite element analysis scheme due to the fact that a system of 24 equations has to be solved at each time iteration step. The four-cell model representation requires only the solution of a system of six equations, which would make it very efficient for an explicit finite element scheme. It was actually implemented as a separate constitutive model into the nonlinear dynamic explicit finite element code DYNA3D and used there to model the behavior of sandwich shells with woven composite facings. Some results from this study can be found in Chapters 4 and 5 of [13].

3 Results and Discussion

To test the performance of the two models presented here, several RVC's with different constituent materials, yarn volume fractions, and undulation angles are homogenized and the results are compared to other published analytical, numerical, and experimental results.

Example 1

Table 1

	E_x, GPa	E_y, GPa	G_{xy}, GPa	G_{yz}, GPa	ν_{xy}	ν_{yz}
Epoxy	3.5	3.5	1.3	1.3	0.35	0.35
65% E-glass/ 35% Epoxy	47.77	18.02	5.494	3.877	0.314	0.249
Timetalβ21-S	112.0	112.0	41.8	41.8	0.34	0.34
65% SCS-6/ 35% Timetal	293.88	253.84	93.46	83.08	0.278	0.2846

Chung and Tamma [12] used a finite element model to determine the elements of the homogenized constitutive matrix of a plain weave RVC. The RVC consists of epoxy matrix and fiber bundles, which are 65 percent E-glass/epoxy. The values for the material properties of the E-glass/epoxy yarns and the epoxy matrix are presented in Table 1. The overall fiber volume fraction is 0.35, but taking into account the 0.65 fiber volume fraction in the yarns, the yarn volume fraction that has to be used is $V_y=0.35/0.65=0.5385$. The average undulation angle determined approximately from the finite element model shown in [12] is $\tan(\theta)=1/6$. The results for the RVC properties from upper and lower bound estimates from [12] and from the present models are shown in Table 2. The results from [12] were obtained by using prescribed displacement boundary conditions to get the upper bound, and prescribed stress boundary conditions to get the lower bound. As seen from this table, the results of both present models are good, the single-cell model being somewhat closer to the finite results from [12].

Table 3 presents results for the homogenized RVC material constants for the above-described case, and for the same RVC geometry with different materials shown in Table 1—Timetalβ21-S matrix and 65 percent SCS-6/Timetal yarns. The results from [12] were acquired using the described there strain energy balance method, which gives an upper bound to the elastic constants. As seen, all values have very good agreement.

Example 2

Results are compared with the finite element based micromechanical method of Marrey and Sankar [14]. The yarn is of Glass/Epoxy with properties $E_L=58.61$ GPa, $E_T=14.49$ GPa, $G_{LT}=5.38$ GPa, $\nu_{LT}=0.250$, $\nu_{TT}=0.247$; the isotropic matrix is of Epoxy with $E=3.45$ GPa, $\nu=0.37$. The yarn volume fraction $V_y=0.26$, and from the RVC dimensions, the average undulation angle was estimated to be $\theta=4.2$ deg. The results from Reference [14] are compared to the present results in Table 4. Some discrepancies of the values are probably due to the geometry of the

Table 2

	Upper Bound [12]	Lower Bound [12]	Four-Cell Model	Single-Cell Model
C_{11}, GPa	21.2	17.7	20.3	20.8
C_{12}, GPa	5.40	5.40	5.02	5.29
C_{13}, GPa	4.42	4.37	4.60	4.38
C_{22}, GPa	21.2	17.7	20.3	20.8
C_{23}, GPa	4.42	4.37	4.60	4.38
C_{33}, GPa	9.82	9.23	11.5	9.23
C_{44}, GPa	3.20	3.14	3.53	3.41
C_{55}, GPa	2.42	2.23	2.50	2.29
C_{66}, GPa	2.42	2.23	2.50	2.29

Table 3

	E-glass/Epoxy			SCS-6/Timetal		
	Reference [12]	Four-Cell Model	Single-Cell Model	Reference [12]	Four-Cell Model	Single-Cell Model
E_x, GPa	18.634	17.853	18.209	196.05	194.47	196.32
E_y, GPa	18.634	17.853	18.209	196.05	194.47	196.32
E_z, GPa	8.346	9.788	7.798	174.15	180.30	170.60
G_{xy}, GPa	3.190	3.529	3.407	67.23	69.44	68.83
G_{yz}, GPa	2.422	2.497	2.294	60.00	61.00	59.15
G_{zx}, GPa	2.422	2.497	2.294	60.00	61.00	59.15
ν_{xy}	0.1745	0.1724	0.1739	0.2790	0.2810	0.2779
ν_{yz}	0.3720	0.3321	0.3923	0.3180	0.3086	0.3237
ν_{zx}	0.3720	0.3321	0.3923	0.3180	0.3086	0.3237

Table 4

Approach	E_x, E_y GPa	E_z, GPa	G_{zx}, G_{yz} GPa	G_{xy}, GPa	ν_{xz}, ν_{yz}	ν_{xy}
Reference [14]	11.81	6.14	1.84	2.15	0.408	0.181
Four-Cell Model	11.86	6.21	1.70	2.33	0.404	0.166
Single-Cell Model	11.93	5.67	1.59	2.31	0.436	0.159

Table 5

Approach	E_x, E_y GPa	E_z, GPa	G_{zx}, G_{yz} GPa	G_{xy}, GPa	ν_{xz}, ν_{yz}	ν_{xy}
Reference [15]	46.35	–	–	3.83	–	0.0538
Reference [16]	48.3*/49.8**	–	–	5.41*/3.83**	–	0.062*/0.068**
Four-Cell Model	45.08	10.12	2.763	3.815	0.4643	0.0562
Single-Cell Model	45.17	9.782	2.585	3.813	0.4784	0.0542

* Number of plies = 1; ** Number of plies = 4.

RVC—V_y is low and there are entirely matrix layers on both sides of the lamina, as well as between the fill and warp. Both our models do not consider a matrix layer between the fill and warp, and in the present formulation of the four-cell model there are also no matrix layers on the outer sides of the lamina.

Example 3

With this example the performance of the present models is compared to the micromechanical model of Tabiei and Jiang [7], Jiang et al. [15], and the experimental results of Ishikawa et al. [16]. The Graphite/Epoxy RVC is described in ([15]) and ([16]) and consists of yarns with properties $E_L = 137.3$ GPa, $E_T = 10.79$ GPa, $G_{LT} = 5.394$ GPa, $\nu_{LT} = 0.26$, $\nu_{TT} = 0.46$, and isotropic matrix with $E = 4.511$ GPa, $\nu = 0.38$. The RVC parameters of the geometry are $V_y = 0.58$, and $\theta = 1.4$ deg. As seen from Table 5 the values of the moduli from the present approach are close to the analytical results from ([15]) and the experimental results from ([16]).

4 Conclusions

The micromechanical models developed in this study have relatively simple formulations, yet they provide very good accuracy of the results for the elastic properties for all examined cases. The new models are formulated based on three-dimensional representations, and thus consider all components of the strain and stress tensors. They can be used to determine the strains and stresses in the constituent fiber yarns and matrix of a plain weave composite, and to acquire homogenized constitutive properties of the entire composite lamina. The models have been developed to be easy to implement into finite element analysis of laminated shells with composite layers, and will fit well into both explicit and implicit time integration schemes. Their very good accuracy was shown here through several tests, and together with the simplicity of formulation makes these models attractive for the finite element analysis of composite laminates.

Acknowledgments

The research within this study was supported by grant F49620-98-1-0384 from the Airforce Office of Scientific Research. This support is gratefully acknowledged.

References

[1] Ishikawa, T., 1981, "Antisymmetric Elastic Properties of Composite Plates of Satin Weave Cloth," Fibre Sci. Technol., **15**, pp. 127–145.
[2] Ishikawa, T., and Chou, T. W., 1982, "Elastic Behavior of Woven Hybrid Composites," J. Compos. Mater., **16**, pp. 2–19.
[3] Ishikawa, T., and Chou, T. W., 1982, "Stiffness and Strength Behavior of Fabric Composites," J. Mater. Sci., **17**, pp. 3211–3220.
[4] Ishikawa, T., and Chou, T. W., 1983, "One-Dimensional Micromechanical Analysis of Woven Fabric Composites," AIAA J., **21**, No. 12, pp. 1714–1721.
[5] Naik, N. K., and Shembekar, P. S., 1992, "Elastic Behavior of Woven Fabric Composites: I—Lamina Analysis," J. Compos. Mater., **26**, No. 15, pp. 2196–2225.
[6] Karayaka, M., and Kurath, P., 1994, "Deformation and Failure Behavior of Woven Composite Laminates," J. Eng. Mater. Technol., **116**, pp. 222–232.
[7] Tabiei, A., and Jiang, Y., 1999, "Woven Fabric Composite Material Model with Material Nonlinearity for Nonlinear Finite Element Simulation," Int. J. Solids Struct., **36**, No. 18, pp. 2757–2771.
[8] Tabiei, A., Jiang, Y., and Yi, W., 2000, "A Novel Micromechanics-Based Plain Weave Fabric Composite Constitutive Model With Material Nonlinear Behavior," AIAA J., **38**, No. 5.
[9] Bednarcyk, B. A., and Pindera, M.-J., "Micromechanical Modeling of Woven Metal Matrix Composites," NASA-CR-204153, Oct.
[10] Bednarcyk, B. A., and Pindera, M.-J., 2000, "Inelastic Response of a Woven Carbon/Copper Composite—Part II: Micromechanics Model," J. Compos. Mater., **34**, No. 4, pp. 299–331.
[11] Whitcomb, J. D. 1991, "Three-Dimensional Stress Analysis of Plain Weave Composites," *Composite Materials: Fatigue and Fracture*, ASTM STP 1110, T. K. O'Brien, ed., American Society for Testing and Materials, Philadelphia, PA, pp. 417–438.
[12] Chung, P. W., and Tamma, K. K., 1999, "Woven Fabric Composites—Developments in Engineering Bounds, Homogenization and Applications," Int. J. Numer. Methods Eng., **45**, pp. 1757–1790.
[13] Tanov, R., 2000, "A Contribution to the Finite Element Formulation for the Analysis of Composite Sandwich Shells," Ph.D. dissertation, University of Cincinnati.
[14] Marrey, R. V., and Sankar, B. V., 1977, "A Micromechanical Model for Textile Composite Plates," J. Compos. Mater., **31**, No. 12, pp. 1187–1213.
[15] Jiang, Y., Tabiei, A., and Simitses, G. J., 2001, "A Novel Micromechanics-Based Plain Weave Fabric Composite Constitutive Equations for Local/Global Analysis," Compos. Sci. Technol., to appear.
[16] Ishikawa, T., Matsushima, M., and Hayashi, Y., 1985, "Experimental Confirmation of the Theory of Elastic Moduli of Fabric Composites," J. Compos. Mater., **19**, pp. 443–458.

The Elastic Stability of Twisted Plates

E. M. Mockensturm
Assistant Professor,
Department of Mechanical and
Nuclear Engineering,
Pennsylvania State University,
University Park, PA 16802
Mem. ASME

Since Coulomb's and Saint-Venant's fundamental work, many researches have studied the effect of twisting on elastic bodies. The work presented here investigates instabilities that can occur when thin bodies are subject to large twists and extends work by A. E. Green published in 1937. Because large twists are considered, a fully nonlinear plate theory is used. This theory predicts compressive lateral membrane stresses not predicted by Green's weakly nonlinear theory. These stresses can significantly alter the twist angle at which buckling occurs. Two conditions for the opposing twisted end supports are considered. In one case the supports are held a fixed distance apart and in the other case the force applied to the supports is held fixed during twist. The buckling modes and critical twist angles vary significantly depending on the support condition used.
[DOI: 10.1115/1.1357517]

Introduction

Scientists and engineers have studied how elastic bodies respond to twisting moments for centuries. These studies date back to 1784 with Coulomb's fundamental work on the twisting of circular bars ([1]). By assuming a more general form of solution that introduced the warping function, Saint-Venant was able to determine the stresses, induced by twisting, in prisms of many shapes ([2]). Saint-Venant's solution for rectangular prisms was the motivation for work by Green [3,4]. In this work Green used a weakly nonlinear (von Kármán) plate theory and was the first to investigate instabilities caused by twisting.

Green's work showed that if the longitudinal force applied to the twisted ends is held constant during twisting, compressive longitudinal stresses will develop in the strip. The phenomena can be explained by noting that twisting stretches material near the edges of the strip more than it does material near the midwidth. Thus, if the force on the twisted ends is held constant and the stress near the edges increases with twist, the stress near the midwidth must decrease with twist. At some critical twist angle, the midwidth stress will become sufficiently compressive to buckle the strip. The nodal lines of the buckled strip extend from edge to edge, perpendicular to the twist axis.

Crispino and Benson [5] extended the work of Green to orthotropic plates. They found that the critical twist angle is significantly altered by the ratio of the Young's moduli of the plate. The buckled shape, however, was similar to that obtained by Green.

During experimental studies of the effect of twisting on thin, wide elastic sheets, a much different instability was observed. Instead of buckling into a mode with nodal lines perpendicular to the twist axis, the sheets wrinkled into a mode with nodal lines *parallel* to the twist axis. This buckled configuration is consistent with lateral compressive stress. However, all previous work found this stress to be zero throughout the plate for all twists.

Mockensturm and Mote [6] used a fully nonlinear plate theory to study the steady motions of translating, twisted plates. In this analysis, the twisted ends were constrained to be a fixed distance apart, supported by whatever force necessary. In this case, the longitudinal compressive stress found by Green and others does not occur. However, it was found that lateral compressive stress, such as those suggested by experiments, is produced. While small, the magnitude of this compressive stress increases with increasing twist angle and may be sufficient to buckle a thin plate.

In the present study, the elastic stability of twisted plates is reexamined. It is found that, for sufficiently thin plates, the lateral compressive stress is large enough to produce buckling observed in experiments and overlooked by previous authors. The results for the case when the twisted supports are a fixed distance apart are found to be much different from those when the supports are free to move longitudinally and the force applied to them is held constant. In the later case the fully nonlinear plate theory predicts both lateral and longitudinal compressive membrane stress and, depending on the system parameters, buckling may occur in the lateral or longitudinal direction.

Mathematical Model

Mockensturm and Mote [6] used two nonlinear plate models to predict steady motions of a uniformly tensioned, axially moving, twisted plate. One model incorporated transverse straining, and the other assumed it to be zero. The stress fields predicted by the two models differed substantially only in regions near the free edges of the plate. As the relative thickness of the plate decreases, these regions become smaller. Here, as the plates modeled are supposed thin, the model without transverse strain is extended to analyze the stability of an unbuckled configuration.

Three configurations of the plate are considered: the *reference* configuration is flat and uniformly tensioned; the *unbuckled* configuration results from twisting opposite ends of the plate; the *buckled* configuration results from infinitesimal displacements about the unbuckled configuration (see Fig. 1). Bifurcations from the unbuckled configuration are predicted from the equations governing the buckled configuration. In the following $(\hat{\ })$ denotes a normalized vector. Latin indices take the values 1, 2, and 3; Greek indices take the values 1 and 2. Summation over all values occurs when an index is repeated.

Let $\mathbf{R}_0$ specify the positions of particles in the reference configuration. It will prove convenient to associate the particles in the reference configuration with a fixed Cartesian coordinate system. Then

$$\mathbf{R}_0 = \psi^{\alpha}\hat{\mathbf{E}}_{\alpha} + \psi^{3}\hat{\mathbf{E}}_{3} \tag{1}$$

where $\{\hat{\mathbf{E}}_i\} = \{\hat{\mathbf{E}}^i\}$ form a fixed, orthonormal basis and the coordinates ψ^i are convected and material. If $|\psi^1| < L/2$, $|\psi^2| < B/2$, and $|\psi^3| < H/2$ the body has uniform length (L), width (B), and thickness (H) as shown in Fig. 1. The reference configuration is mapped by $\mathbf{X}^*(\psi^i)$ into the unbuckled configuration and by $\mathbf{x}^*(\psi^i)$ into the buckled configuration. Let

Contributed by the Applied Mechanics Division of THE AMERICAN SOCIETY OF MECHANICAL ENGINEERS for publication in the ASME JOURNAL OF APPLIED MECHANICS. Manuscript received by the ASME Applied Mechanics Division, Apr. 12, 2000; final revision, Oct. 18, 2000. Associate Editor: S. Kyriakides. Discussion on the paper should be addressed to the Editor, Professor Lewis T. Wheeler, Department of Mechanical Engineering, University of Houston, Houston, TX 77204-4792, and will be accepted until four months after final publication of the paper itself in the ASME JOURNAL OF APPLIED MECHANICS.

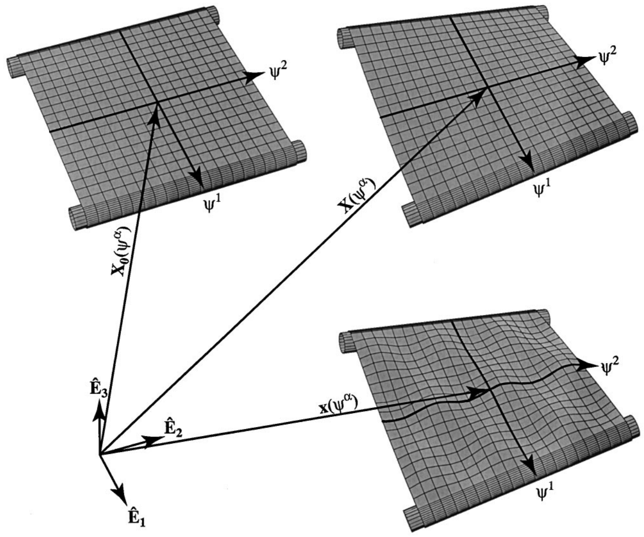

Fig. 1 The initial, $\mathbf{X}_0(\psi^\alpha)$, unbuckled, $\mathbf{X}(\psi^\alpha)$, and buckled, $\mathbf{x}(\psi^\alpha)$, configurations of the plate

$$\mathbf{R}=\mathbf{X}^*(\psi^i)=\mathbf{X}(\psi^\alpha)+\psi^3\hat{\mathbf{A}}^3(\psi^\alpha) \tag{2}$$

specify the position of particles in the unbuckled configuration and

$$\mathbf{r}=\mathbf{x}^*(\psi^i)=\mathbf{x}(\psi^\alpha)+\psi^3\hat{\mathbf{a}}^3(\psi^\alpha) \tag{3}$$

specify the position of particles in the buckled configuration. The vectors, $\hat{\mathbf{A}}^3$ and $\hat{\mathbf{a}}^3$, are the outward unit normals to the surfaces, $\mathscr{S}$ and $\mathscr{s}$, defined by $\mathbf{X}(\psi^\alpha)$ and $\mathbf{x}(\psi^\alpha)$, respectively. This form of the deformation assumes unit normals to the surface $\psi^\alpha\hat{\mathbf{E}}_\alpha$ are mapped into unit normals to the surfaces $\mathscr{S}$ and $\mathscr{s}$. The transverse strains then vanish. The infinitesimal displacement field $\mathbf{u}(\psi^i)=\mathbf{x}(\psi^i)-\mathbf{X}(\psi^i)$ distinguishes the buckled and unbuckled configurations.

The covariant basis on $\mathscr{S}$ is given by $\mathbf{A}_\alpha=\mathbf{X}_{,\alpha}=\partial\mathbf{X}/\partial\psi^\alpha$. A reciprocal, contravariant basis, $\mathbf{A}^\alpha$, to $\mathscr{S}$ can then be constructed such that

$$\hat{\mathbf{A}}_3\cdot\mathbf{A}_\alpha=0,\quad \hat{\mathbf{A}}_3=\hat{\mathbf{A}}^3,\quad A_{\alpha\beta}=\mathbf{A}_\alpha\cdot\mathbf{A}_\beta,\quad \mathbf{A}^i\cdot\mathbf{A}_j=\delta^i_j,$$
$$\Gamma^\lambda_{\alpha\beta}=\mathbf{A}_{\alpha,\beta}\cdot\mathbf{A}^\lambda,\quad \Gamma^3_{\alpha\beta}=B_{\alpha\beta}=\mathbf{A}_{\alpha,\beta}\cdot\hat{\mathbf{A}}_3,$$
$$\Gamma^\beta_{3\alpha}=-B^\beta_\alpha=\hat{\mathbf{A}}_{3,\alpha}\cdot\mathbf{A}^\beta,\quad \Gamma^3_{3i}=\Gamma^i_{33}=0 \tag{4}$$

where δ^i_j is the Kronecker delta, and $A_{\alpha\beta}$, $B_{\alpha\beta}$, and $\Gamma^\lambda_{\alpha\beta}$ are the first and second fundamental forms and Christoffel symbols of $\mathscr{S}$, respectively. Analogous relations, obtained by replacing upper with lower case letters, hold for the buckled configuration.

The covariant derivatives of the components of $\mathbf{V}$, denoted by a vertical bar, with respect to the basis $\mathbf{A}_i$ are then

$$V_{\alpha|\beta}=V_{\alpha,\beta}+\Gamma^i_{\alpha\beta}V_i,\quad V_{3|\beta}=V_{3,\beta}+\Gamma^\alpha_{3\beta}V_\alpha,$$
$$V_{\beta|3}=V_{\beta,3}+B^\alpha_\beta V_\alpha,\quad V_{\alpha|\beta\gamma}=V_{\alpha|\gamma\beta}. \tag{5}$$

Note that this is the covariant derivative with respect to a Euclidean three-space, not a Riemannian surface, resulting in Eq. (5.4).

The membrane stretch and bending strain in the buckled configuration are given by

$$\mathbf{c}=a_{\alpha\beta}(\hat{\mathbf{E}}^\alpha+\otimes\hat{\mathbf{E}}^\beta)+\hat{\mathbf{E}}^3\otimes\hat{\mathbf{E}}^3,\quad \boldsymbol{\lambda}=-(b_{\alpha\beta}+b_{\beta\alpha})(\hat{\mathbf{E}}^\alpha\otimes\hat{\mathbf{E}}^\beta), \tag{6}$$

respectively. Upon linearization about the unbuckled configuration $\mathbf{c}=\mathbf{C}+\tilde{\mathbf{C}}$ and $\boldsymbol{\lambda}=\boldsymbol{\Lambda}+\tilde{\boldsymbol{\Lambda}}$ where

$$\mathbf{C}=A_{\alpha\beta}(\hat{\mathbf{E}}^\alpha\otimes\hat{\mathbf{E}}^\beta)+\hat{\mathbf{E}}^3\otimes\hat{\mathbf{E}}^3,\quad \tilde{\mathbf{C}}=(u_{\alpha|\beta}+u_{\beta|\alpha})(\hat{\mathbf{E}}^\alpha\otimes\hat{\mathbf{E}}^\beta),$$
$$\boldsymbol{\Lambda}=-(B_{\alpha\beta}+B_{\beta\alpha})(\hat{\mathbf{E}}^\alpha\otimes\hat{\mathbf{E}}^\beta),$$
$$\tilde{\boldsymbol{\Lambda}}=[(u_{3|\beta})_{|\alpha}+B^\gamma_\alpha u_{\gamma|\beta}](\hat{\mathbf{E}}^\alpha\otimes\hat{\mathbf{E}}^\beta+\hat{\mathbf{E}}^\beta\otimes\hat{\mathbf{E}}^\alpha). \tag{7}$$

It should be noted that $(u_{3|\alpha})_{|\beta}\neq(u_{i|\alpha\beta})|_{i=3}$. In the present case, the second covariant derivative is of the *vector* components $u_{3|\alpha}$.

The resultant stress tensors $\mathbf{n}(\mathbf{c},\boldsymbol{\lambda})=n^{\alpha\beta}\hat{\mathbf{E}}_\alpha\otimes\hat{\mathbf{E}}_\beta$ and $\mathbf{m}(\mathbf{c},\boldsymbol{\lambda})=m^{\alpha\beta}\hat{\mathbf{E}}_\alpha\otimes\hat{\mathbf{E}}_\beta$ are related to the second Piola-Kirchhoff stress tensor $\mathbf{s}$ and decomposed as

$$\mathbf{n}=\int_{-H/2}^{H/2}\mathbf{s}\,d\psi^3=\mathbf{N}+\tilde{\mathbf{N}},\quad \mathbf{m}=\int_{-H/2}^{H/2}\mathbf{s}\psi^3\,d\psi^3=\mathbf{M}+\tilde{\mathbf{M}} \tag{8}$$

where $\mathbf{N}(\mathbf{C},\boldsymbol{\Lambda})$ and $\mathbf{M}(\mathbf{C},\boldsymbol{\Lambda})$ are the resultant stress tensors in the unbuckled configuration. The deformation taking the unbuckled configuration to the buckled configuration produces the additional resultant stresses $\tilde{\mathbf{N}}(\tilde{\mathbf{C}},\tilde{\boldsymbol{\Lambda}})$ and $\tilde{\mathbf{M}}(\tilde{\mathbf{C}},\tilde{\boldsymbol{\Lambda}})$. The kinematic constraint that unit normals to the reference surface remain unit normals after deformation is enforced by constraint stress

$$\mathbf{q}=q^\alpha(\hat{\mathbf{E}}_\alpha\otimes\hat{\mathbf{E}}_3+\hat{\mathbf{E}}_3\otimes\hat{\mathbf{E}}_\alpha)+q^3\hat{\mathbf{E}}_3\otimes\hat{\mathbf{E}}_3=\mathbf{Q}+\tilde{\mathbf{Q}}.$$

The fully nonlinear equations of equilibrium governing the buckled configuration

$$[n^{\alpha\Gamma}\mathbf{a}_\alpha+q^\Gamma\hat{\mathbf{a}}_3+m^{\alpha\Gamma}\hat{\mathbf{a}}_{3,\alpha}]_{,\Gamma}=\mathbf{0},\quad [m^{\alpha\Gamma}\mathbf{a}_\alpha]_{,\Gamma}-[\mathbf{q}^\alpha\mathbf{a}_\alpha+q^3\hat{\mathbf{a}}_3]=\mathbf{0} \tag{9}$$

provide the equations describing the unbuckled configuration $(\mathbf{u}=\mathbf{0})$

$$[N^{\alpha\Gamma}\mathbf{A}_\alpha+Q^\Gamma\hat{\mathbf{A}}_3+M^{\alpha\Gamma}\hat{\mathbf{A}}_{3,\alpha}]_{,\Gamma}=\mathbf{0},$$
$$[M^{\alpha\Gamma}\mathbf{A}_\alpha]_{,\Gamma}-[Q^\alpha\mathbf{A}_\alpha+Q^3\hat{\mathbf{A}}_3]=\mathbf{0} \tag{10}$$

and, upon linearization about this state, the equations governing the buckled configuration

$$\{\tilde{N}^{\alpha\Gamma}\mathbf{A}_\alpha+N^{\alpha\Gamma}\mathbf{u}_{,\alpha}+\tilde{M}^{\alpha\Gamma}\hat{\mathbf{A}}_{3,\alpha}+[(\tilde{M}^{\alpha\beta}\mathbf{A}_\alpha)_{,\beta}\mathbf{A}^\Gamma]\hat{\mathbf{A}}_3\}_{,\Gamma}=\mathbf{0} \tag{11}$$

where, because the plate is thin, terms involving $M^{\alpha\Gamma}$ and Q^Γ have been neglected. These equations are derived in detail from the referential balance laws of finite elasticity in Mockensturm [7] and are based on the work of Naghdi [8,9].

If there exists a strain energy function, $\varphi(\mathbf{c},\boldsymbol{\lambda})$, the stress resultants are

$$\mathbf{N}=2\frac{\partial\varphi(C,\Lambda)}{\partial\mathbf{C}},\quad \tilde{\mathbf{N}}=\mathbf{K}_1[\tilde{\mathbf{C}}]+\mathbf{K}_2[\tilde{\boldsymbol{\Lambda}}],$$
$$\mathbf{M}=2\frac{\partial\varphi(C,\Lambda)}{\partial\boldsymbol{\Lambda}},\quad \tilde{\mathbf{M}}=\mathbf{K}_2[\tilde{\mathbf{C}}]+\mathbf{K}_3[\tilde{\boldsymbol{\Lambda}}] \tag{12}$$

where

$$\mathbf{K}_1=2\left[\frac{\partial^2\varphi}{\partial c\,\partial c}\right]_E,\quad \mathbf{K}_2=2\left[\frac{\partial^2\varphi}{\partial\mathbf{c}\partial\boldsymbol{\lambda}}\right]_E,\quad \mathbf{K}_3=2\left[\frac{\partial^2\varphi}{\partial\boldsymbol{\lambda}\partial\boldsymbol{\lambda}}\right]_E \tag{13}$$

are fourth-order tensors, and $[\cdot]_E$ denotes quantities evaluated in the unbuckled configuration.

Although solutions can be obtained for any, nonlinear, isotropic material ([7]), here attention is focused on the Saint-Venant-Kirchhoff material,

$$\varphi(\mathbf{c},\boldsymbol{\lambda})=\frac{kH^2}{24}\left\{\nu\frac{(\boldsymbol{\lambda}\cdot\mathbf{I})^2}{4}+(1-\nu)\frac{\boldsymbol{\lambda}\cdot\boldsymbol{\lambda}}{4}\right\}$$
$$+\frac{K}{2}\left\{\nu\frac{(\mathbf{c}\cdot\mathbf{I}-3)^2}{4}+(1-\nu)\frac{(\mathbf{c}-\mathbf{I})\cdot(\mathbf{c}-\mathbf{I})}{4}\right\} \tag{14}$$

where $K=EH/(1-\nu^2)$, E, and ν are material constants.

After deformation the twisted ends of the plate ($\psi^1 = \pm L/2$) must pass through the lines

$$\left(\pm\frac{\lambda_1 L}{2}\right)\hat{\mathbf{E}}_1 + \zeta\cos\left(\pm\frac{\tau}{2}\right)\hat{\mathbf{E}}_2 + \zeta\sin\left(\pm\frac{\tau}{2}\right)\hat{\mathbf{E}}_3 \tag{15}$$

where $\zeta \in \{-\infty,\infty\}, \lambda_1$ is the nominal (untwisted) stretch in the plate, and $\tau/2$ is the angle between each support and the horizontal. The total twist in the plate is then τ. Additionally, it is assumed the plate is free to slide laterally along the supports and they provide no bending moment,

$$N^{21} + 2\Gamma^2_{3\beta}M^{\beta 1} = 0, \quad M^{11} = 0. \tag{16}$$

Correspondingly, for the buckled configuration

$$\tilde{N}^{21} + 2\Gamma^2_{3\beta}\tilde{M}^{\beta 1} = 0, \quad \tilde{M}^{11} = 0, \quad \overline{u_1} = 0, \quad \overline{u_3} = 0. \tag{17}$$

The boundary conditions on the traction-free lateral edges ($\psi^2 = \pm B/2$) are

$$N^{\alpha 2} + 2\Gamma^\alpha_{3\beta}M^{\beta 2} = 0, \quad (M^{\alpha\beta}\mathbf{A}_\alpha)_{,\beta}\cdot\mathbf{A}^2 + M^{12}_{,1} = 0, \quad M^{22} = 0, \text{ and}$$

$$\tilde{N}^{\alpha 2} + 2\Gamma^\alpha_{3\beta}\tilde{M}^{\beta 2} = 0, \quad (\tilde{M}^{\alpha\beta}\mathbf{A}_\alpha)_{,\beta}\cdot\mathbf{A}^2 + \tilde{M}^{12}_{,1} = 0, \quad \tilde{M}^{22} = 0 \tag{18}$$

for the unbuckled and buckled configurations, respectively.

Unbuckled Solutions. The fully nonlinear equations of equilibrium are solved by assuming a solution of the plate midsurface,

$$\frac{\overline{\mathbf{X}}(x,y)}{B} = \lambda_1 x\hat{\mathbf{E}}_1 + f(y)\cos(ax)\hat{\mathbf{E}}_2 + f(y)\sin(ax)\hat{\mathbf{E}}_3 \tag{19}$$

where $\{x,y\} = \{\psi^1,\psi^2\}/B$, $a = \tau B/L$, and $f(y)$ governs the lateral stretch in the twisted plate. Under this assumption

$$[A_{\alpha\beta}] = \begin{bmatrix} \lambda_1^2 + a^2 f^2 & 0 \\ 0 & (f')^2 \end{bmatrix}, \quad B[B_{\alpha\beta}] = \frac{\lambda_1 a f'}{\sqrt{\lambda_1^2 + a^2 f^2}}\begin{bmatrix} 0 & 1 \\ 1 & 0 \end{bmatrix},$$

$$B[\Gamma^1_{\alpha\beta}] = \frac{a^2 f f'}{\lambda_1^2 + a^2 f^2}\begin{bmatrix} 0 & 1 \\ 1 & 0 \end{bmatrix}, \quad B[\Gamma^2_{\alpha\beta}] = \frac{1}{f'}\begin{bmatrix} -a^2 f & 0 \\ 0 & f'' \end{bmatrix} \tag{20}$$

where a prime denotes differentiation with respect to y. Resolved onto the bases $\mathbf{A}^i$, the three, nonlinear, partial differential equations of equilibrium (10) reduce to a single, nonlinear, ordinary differential equation

$$N^{22}_{,2} + N^{11}\Gamma^2_{11} + N^{22}\Gamma^2_{22} - 2(M^{12}_{,2} + M^{12}\Gamma^1_{12})B^2_1 - M^{12}(B^2_{1,2} + \Gamma^2_{22}B^2_1 + \Gamma^1_{11}B^1_2) = 0 \tag{21}$$

where with Eq. (14), $e = (\lambda_1^2 - 1)/2$, and $\varepsilon = H/B$

$$\frac{N^{11}}{K} = \frac{2e + a^2 f^2 + \nu(f'^2 - 1)}{2}, \quad \frac{N^{22}}{K} = \frac{f'^2 - 1 + \nu(2e + a^2 f^2)}{2},$$

$$\frac{M^{12}}{KB^2} = \frac{\varepsilon^2(\nu - 1)\lambda_1 a f'}{12\sqrt{\lambda_1^2 + a^2 f^2}} \tag{22}$$

and all other components of the resultant stress tensors are 0. All boundary conditions are identically satisfied except for Eq. (18.1) with index $\alpha = 2$. The dimensionless, longitudinal support force

$$T = \int_{-1/2}^{1/2} \frac{K}{2EH}\left[\frac{\varepsilon^2\lambda_1^2(1-\nu)a^2 f'^2}{3(\lambda_1^2 + a^2 f^2)^2} + 2e - \nu + a^2 f^2 + \nu f'^2\right]dy. \tag{23}$$

Equation (21) is solved using a perturbation method. The dimensionless twist, a, is assumed small, ε and e are assumed of order a^2, and $f(y) = y + \Sigma_{I=1}^{\infty} a^{2I} f_{(2I)}(y)$.

Fixed Support Separation. If the supports are a fixed distance apart, the strain, e, is prescribed. In this case (illustrated in Fig. 2), T which equals e in the reference configuration, increases with increasing twist (see Figs. 3 and 4).

In the present analysis, it is assumed that the plate is first elongated by an amount e, and then twisted. One could also assume that the plate was first twisted and then strained. For an infinitesimal, linear theory these two assumptions give identical results. For the nonlinear analysis done here, the twist then stretch case can be obtained from the results presented by replacing "a" with $\lambda_1 a$.

To zeroth order in "a" the equations of equilibrium (21) are identically satisfied. Higher order equations, for $f_{(2)}$ and $f_{(4)}$,

$$f_{(2)}'' + \nu y = 0, \quad f'_{(2)}(\pm 1/2) + \nu(e + 1/8) = 0$$

$$f_{(4)}'' + \frac{y^3}{6}(2\nu^2 - 3) - ey = 0,$$

$$f_{(4)}'\left(\pm\frac{1}{2}\right) + \frac{\nu^2}{24}\left(12e^2 - 3e - \frac{1}{16}\right) = 0 \tag{24}$$

are readily solved. While even higher order solutions are easily obtained, results to fourth order in "a" agree well with numerical results at least to $a = 0.5$ ([6]).

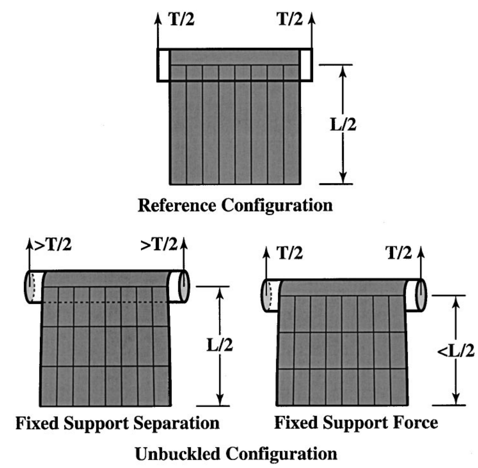

Fig. 2 Illustration of the difference between the case with fixed support separation and the case with fixed support force

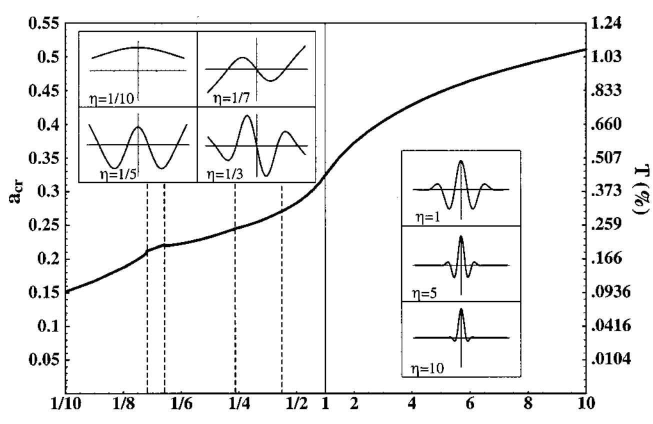

Fig. 3 Dependence of critical twist on longitudinal mode number and aspect ratio for an initially untensioned plate and fixed support separation. Insets show lateral mode shapes for various aspect ratios.

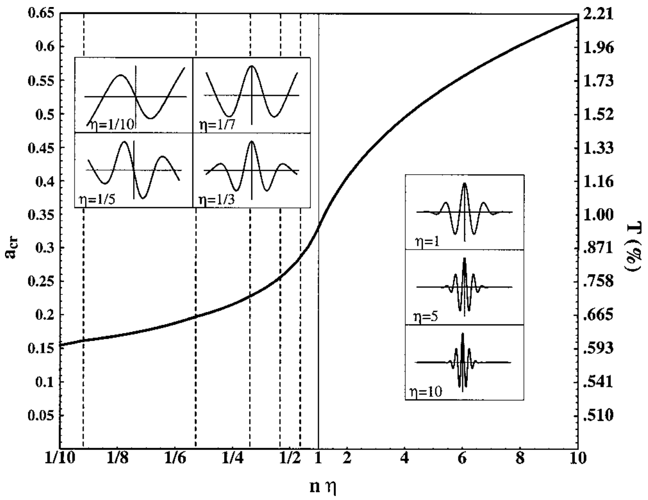

Fig. 4 Dependence of critical twist on longitudinal mode number and aspect ratio for a plate initially strained 0.5 percent and fixed support separation. Insets show lateral mode shapes for various aspect ratios.

Fixed Support Force. Alternatively, one may consider the case in which the supports are free to slide longitudinally (in the $\hat{\mathbf{E}}_1$-direction) and the longitudinal force applied to the supports is held constant during twist. This situation is illustrated in Fig. 2 and is the case considered by previous authors ([3–5]). Substituting the expansion for $f(y)$ into Eq. (23), expanding in series about $a=0$, and solving for e gives

$$e=T-a^2\left\{\frac{1}{24}+2\nu\left[f_{(2)}\left(\frac{1}{2}\right)+a^2 f_{(4)}\left(\frac{1}{2}\right)\right]\right.$$
$$\left.+2a^2\int_0^{1/2} y f_{(2)}+\frac{\nu}{2}(f'_{(2)})^2 dy\right\} \tag{25}$$

where the fact that $f(y)$ is an odd function has been used.

Again, to zeroth order in "a" the equations of equilibrium (21) are identically satisfied and higher order equations, governing $f_{(2)}$ and $f_{(4)}$,

$$f_{(2)}''+\nu y=0,$$
$$f_{(2)}'\left(\pm\frac{1}{2}\right)+\nu\left\{T(1-\nu^2)+\frac{1}{12}-\nu\left[f_{(2)}\left(-\frac{1}{2}\right)-f_{(2)}\left(\frac{1}{2}\right)\right]\right\}=0$$
$$f_{(4)}''+\frac{y}{2}\left[\frac{1}{12}-2T+y^2\left(\frac{2}{3}\nu^2-1\right)\right]=0,$$
$$f_{(4)}'\left(\pm\frac{1}{2}\right)+\nu^2\left[\frac{1}{480}-\frac{\nu^2}{1440}-\frac{T}{12}+\frac{T^2}{2}(1-\nu^2)\right.$$
$$\left.+f_{(4)}\left(-\frac{1}{2}\right)-f_{(4)}\left(\frac{1}{2}\right)\right]=0 \tag{26}$$

are readily solved.

Bifurcations. Once the unbuckled configuration has been found, bifurcations from this state can be sought. The three, coupled, linear partial differential equations governing small perturbation from the unbuckled configuration are obtained from Eq. (11) by substituting the series approximation $f(y)=y+a^2 f_{(2)}(y)+a^4 f_{(4)}(y)$ determined above and taking the dot product with $\mathbf{A}^i$. The resulting equations are expanding in series—to fourth order—about $a=0$. As these equations are homogeneous, a trivial solution ($\mathbf{u}=\mathbf{0}$) always exists. However for certain combinations of parameters, nontrivial solutions exist. To find these nontrivial solutions, all parameters but the dimensionless twist, a, are assumed fixed. The smallest "a" at which a nontrivial solution exists is called the critical twist, a_{cr}.

The equations governing the buckled configuration can be reduced further, and the boundary condition along the supported edges satisfied, by assuming a separable solution of the form

$$\overline{u_1}(x,y)=\sqrt{A_{11}}U_1(y)\sin[\alpha\pi(x-\phi/2)]$$
$$\overline{u_2}(x,y)=\sqrt{A_{22}}U_2(y)\cos[\alpha\pi(x-\phi/2)]$$
$$\overline{u_3}(x,y)=U_3(y)\sin[\alpha\pi(x-\phi/2)] \tag{27}$$

where $\phi=1/\eta=L/B$, $\alpha=n\eta$, and n is an integer.

Inserting Eq. (27) into Eq. (11) and Eq. (18) removes the dependence on x from the equations and yields three, coupled, linear ordinary differential equations for U_i. These equations are fourth order in U_3 and second order in U_1 and U_2. When written in first-order form they become

$$\left(\sum_{I=0}^{2} y^I[P_I]\right)[S]'(y)=\left(\sum_{I=0}^{4} y^I[Q_I]\right)[S](y) \tag{28}$$

where the 8×8 matrices, $[P_I]$ and $[Q_I]$, are independent of y (but functions of "a" and the other system parameters) and

$$[S]=[U_1\ U_2\ U_3\ U_1'\ U_2'\ U_3'\ U_3''\ U_3''']^T. \tag{29}$$

Solutions even in U_2 and U_3 and odd in U_1 are independent of those odd in U_2 and U_3 and even in U_1. Thus, solutions can be found in the range $y\in(0,1/2)$ instead of $y\in(-1/2,1/2)$. As a trial solution for Eq. (28) assume

$$[S](y)=\left\{[I]+\sum_{I=1}^{\infty} y^I[A_I]\right\}[S](0) \tag{30}$$

where

$$[S](0)=[B_1\ 0\ B_2\ 0\ B_3\ 0\ B_4\ 0] \quad \text{or}$$
$$[S](0)=[0\ B_1\ 0\ B_2\ 0\ B_3\ 0\ B_4]. \tag{31}$$

Substituting Eq. (30) into Eq. (28) and equating like power of y yields the following recursive relations for $[A_I]$,

$$[A_I]=\frac{1}{I}[P_0]^{-1}\left\{\sum_{N=0}^{I-1}([Q_{I-N-1}]-N[P_{I-N}])[A_N]\right\}. \tag{32}$$

Substituting Eq. (32) into Eq. (30) and using the boundary conditions at the free edge, Eq. (18), yields an eigenvalue problem for "a."

Results

The twisted support conditions significantly alter the stress state in the unbuckled configuration and, thus, change the state where bifurcations occur. For both support conditions, twisting generates compressive stress in the plate. When the supports have a fixed separation, the longitudinal membrane stress is always positive as twisting only stretches the plate in this direction. However, the lateral membrane stress, which is zero in the untwisted state, become increasingly compressive with increasing twist ([6]). For the fixed support case, the lateral membrane stress causes the plate to buckle.

When the supports are free to move in the longitudinal direction and the longitudinal force applied to them remains constant during twisting, both longitudinal and lateral membrane stresses may be compressive. In this case, increasing twist again causes increasing longitudinal membrane stress near the free edges of the plate. However, because the total longitudinal traction acting on the supported edges remains constant, the longitudinal stress near the midwidth must decrease with increasing twist. Thus, depending on the initial tension in the plate (i.e., force on the supports), the longitudinal membrane stress may be compressive near the plate midwidth.

In the following results, unless otherwise stated, $\nu=0.3$, $\varepsilon=10^{-3}$, $\eta=1$, and T or $e=0$.

Fixed Support Separation. When the supports have a fixed separation, the lateral membrane stress, N^{22}, is the cause of buckling in a twisted plate. As this membrane stress decreases with increasing twist, there will be some critical value of twist that causes the plate to buckle. This critical twist is dependent on the material properties, geometry, and initial stress of the plate. Previous analyses using weakly nonlinear plate theories ([3–5]) predict the lateral membrane stress is zero for all twists and, thus, do not predict this instability.

If the thickness, initial tension and material properties of the plate are held fixed at the values assumed previously, the dimensionless critical twist a_{cr} increases monotonically with increasing $\alpha=n\eta$ (see Fig. 3). The longitudinal mode number, n, is thus always one as this will produce the lowest a_{cr}. While a_{cr} increases with η, the twist *angle*, $\tau=a/\eta$, that causes buckling *decreases* with η.

Since $n=1$ the longitudinal dependence of the buckling mode is always a half sine. However, the lateral dependence varies significantly with aspect ratio as shown inset in Fig. 3. For some aspect ratios, the buckling mode is an even function of y. For other aspect ratios, it is odd in y. These regions are divided in Fig. 3 by dashed lines. As η increases, the lateral profile becomes increasingly oscillatory. As η increases, the buckled region also becomes more localized near the midwidth.

If an initial stretch (tension) is applied to the plate and then it is twisted, the critical twist angles do not increase for all plate geometries as one might expect. This can be established by comparing Figs. 3 and 4. In the first case (Fig. 3), as noted above, there is no initial strain in the plate before it is twisted. In the second case (Fig. 4), the plate is initially strained 0.5 percent and then twisted. Again, $a_{cr}(\tau_{cr})$ increases (decreases) monotonically with α, and buckling always occurs with $n=1$. While the longitudinal mode profile does not change with initial strain, the lateral profiles do, as shown inset in Fig. 4. Also illustrated by the insets in Figs. 3 and 4, increasing the initial strain in the plate causes the lateral buckling profile to become more spatially oscillatory for a given η.

The dimensionless plate thickness alters the critical twist angle significantly. As shown in the right (e=one percent) and left ($e=0$) panels of Fig. 5, with $\nu=1/3$, a_{cr} decreases from 0.825 when $\varepsilon=10^{-2}$ to 0.129 when $\varepsilon=10^{-4}$ and from 0.807 when $\varepsilon=10^{-2}$ to 0.121 when $\varepsilon=10^{-4}$, respectively. For the square plate illustrated in this figure, the initial strain has little effect on the critical twist angle. For a plate with $\varepsilon=10^{-4}$, the critical twist angle initially increases from 0.129 at $e=0$ to 0.148 at $e=0.1$ percent and then decreases with further increases of initial strain. For a plate with $\varepsilon=10^{-2}$, the critical twist angle decreases continuously with increasing initial strain.

The aspect ratio also influences how a_{cr} depends on the initial plate strain. As seen in Figs. 5 and 6, for a square plate with $\varepsilon=10^{-3}$, a_{cr} initially increases from 0.324 at $e=0$ to 0.332 at $e=0.3$ percent and then decreases to 0.323 at e=one percent. However, when the width is greater than three times the length, the critical twist increases monotonically as the initial strain increase from 0 to one percent. For a plate with $\eta=1/2$, a_{cr} decreases monotonically as e increase from 0 to one percent. However, this monotonic behavior does not remain for all narrower plates. The nonmonotonic behavior reappears for a plate with $\eta=1/9$ as the wrinkling mode changes from even to odd and back to even as the tension increases.

Fixed Support Force. When the supports are allowed to move longitudinally to keep the force applied to them constant during twisting, behavior much different from the fixed support separation case is observed. Here, both lateral and longitudinal compressive stress can develop and the plate may buckle in either a lateral ($n=1$) or longitudinal ($n>1$) mode. In this case, direct comparisons can be made to the weakly nonlinear results of Green [4]. In the following discussion the applied, nondimensional support force is given as a percentage. This is done for easier comparison with the case when the rollers are a fixed distance apart. Noting Eq. (25), one can think of T as the strain induced by the applied force before twisting.

The possibility that the fundamental buckling mode occurs with the longitudinal mode number greater than one is illustrated by the nonmonotonic behavior of the curves in Fig. 7. For the case when the supports are free of any applied force ($T=0$), the critical twist increases monotonically with α. Thus, in this case the plate always buckles in the first longitudinal mode; a result also obtained by Green [3]. However, as noted in Green [4], when a force is applied to the supports and held fixed during twist, the critical twist does not necessarily increase monotonically with α. Thus, for a given η, the minimum a_{cr} may occur with $n>1$. For example, for a plate with $\eta=1/10$ and $T=0.01$ percent, a_{cr} $(=0.05874)$ occurs with $n=39$. For a square plate with $T=0.01$ percent, the fundamental buckling mode occurs with $n=4$ and $a_{cr}=0.05875$. When $T=0.1$ percent the possibility of a buckling mode with $n>1$ remains. When $\eta=1/10$, the plate buckles in the first longitudinal mode ($n=1$) and $a_{cr}=0.1533$; however, when $\eta=1/8$, $n=53$ and $a_{cr}=0.1641$, and when $\eta=1$, $n=7$ and $a_{cr}=0.167$. As the initial stretch in the plate increases, a_{cr} again becomes a monotonically increasing function of α and the plate buckles in the first longitudinal mode. There is also a decrease in critical twist with an increase in applied tension from

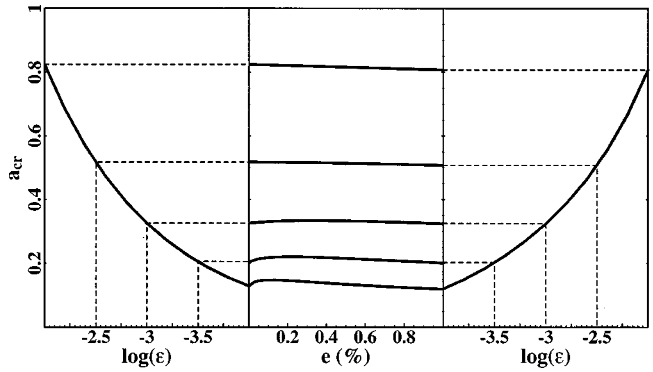

Fig. 5 Critical twist as a function of initial strain and thickness for a square plate and fixed support separation

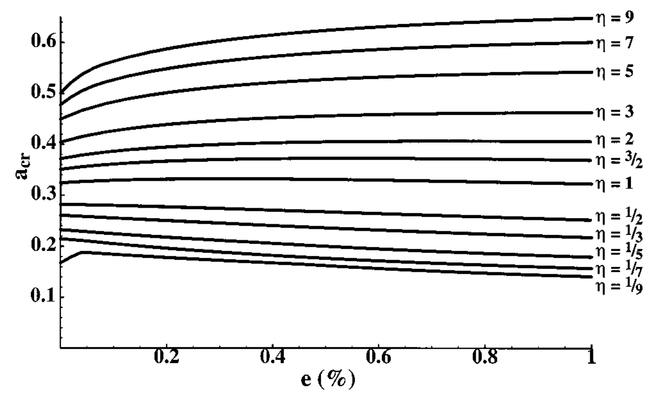

Fig. 6 Critical twist as a function of initial strain for various aspect ratios and fixed support separation

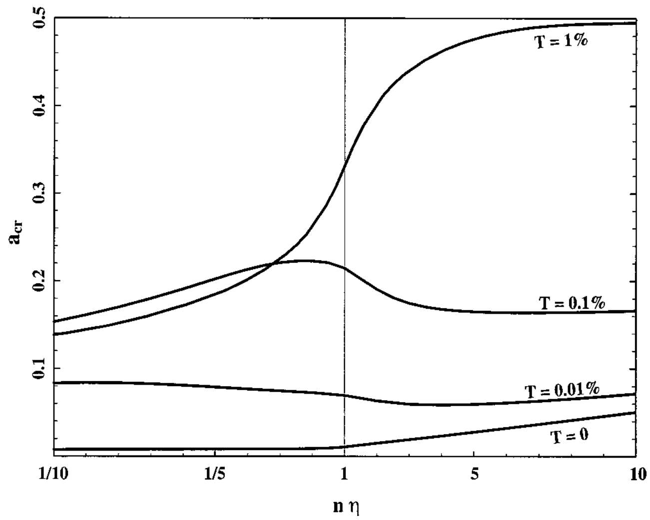

Fig. 7 Dependence of critical twist on longitudinal mode number and aspect ratio for a plates with various fixed support forces

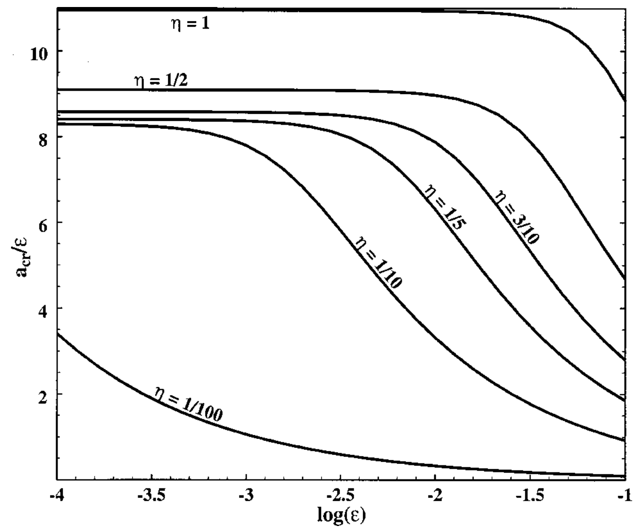

Fig. 9 Critical twist normalized by plate thickness as a function of plate thickness for various aspect ratios and no support force

0.1 percent to 1 percent for plates with $\eta<1/3.25$, a phenomena also seen in the case when the rollers have a fixed separation.

As the tension increases, a transition occurs from longitudinal buckling ($n>1$) to lateral buckling ($n=1$) as seen in the fixed support separation case. Previous analyses ([4,5]) predict that the critical twist angle increases monotonically with increasing tension. The weakly nonlinear theory used in these studies only predicted the possibility of longitudinal compressive stress. By increasing the support force, it was predicted that ever greater twists would be necessary to produce an instability. Here, the fully nonlinear theory also predicts compressive lateral stress. Figure 8 illustrates how, for large support forces, it is the lateral membrane stress that causes the instability. Shown for three values of $\alpha = n\eta$ is the critical twist as a function of T. For T below 0.2 percent the critical twist increases with tension as predicted previously. The dotted line represents the twist at which, for a given T, the minimum longitudinal membrane stress (at the midwidth) is zero. To the right of this curve, the longitudinal membrane stress is positive everywhere in the plate. Previous analyses predict the critical twist to always be above this curve, in the region where compressive longitudinal stress exists. Here, the critical twist curves cross this line, illustrating that a different instability mechanism (lateral compressive stress) is at work.

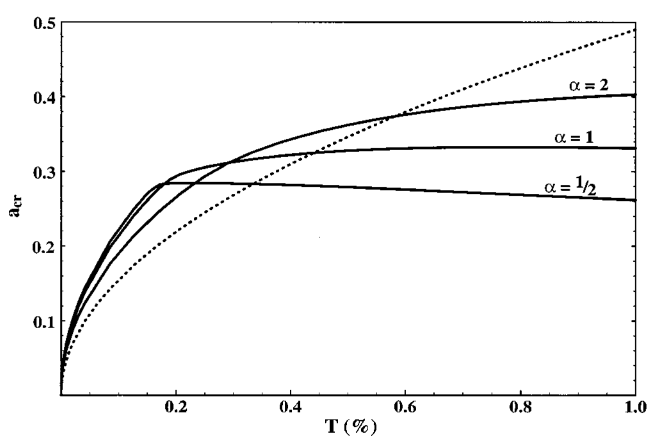

Fig. 8 Dependence of critical twist on fixed support force for α=1/2,1,2

When the force applied to the supports remains zero as the plate is twisted, $n=1$ and the dimensionless parameter a_{cr}/ε becomes nearly independent of plate thickness as the thickness decreases. As shown in Fig. 9, as the plate gets narrower the value of ε at which a_{cr}/ε becomes independent of ε decreases. For $\eta>1/2$, a_{cr}/ε is constant for $\varepsilon<1/100$. For a plate with $\eta=1/10$, a_{cr}/ε is nearly independent of ε for $\varepsilon<1/10{,}000$. As the plate thickness increases, a_{cr}/ε decreases (but a_{cr} increases) for all aspect ratios.

Summary

Using a fully nonlinear plate theory, the elastic stability of a plate twisted out-of-plane by opposing end supports is studied. Two support configurations are investigated and compared. In the first case the end supports are held a fixed distance apart as the plate is twisted. Because the plate is stretched during twist, the force applied to the supports and the longitudinal membrane stress increase with twist. If the plate is not initially in compression, the longitudinal membrane stress will always be positive. However, the fully nonlinear plate theory predicts a compressive lateral membrane stress that increases (in magnitude) with twist. Thus, buckling can occur for this support configuration. In this case, buckling always occurs in the first longitudinal mode. In the second support configuration, studied by previous authors, the force applied to the supports is held constant during twist. The end supports move closer together in this case. Here, both compressive lateral and longitudinal membrane stresses can develop and the plate may buckle in fundamentally different modes. In some cases the mode is spatially oscillatory in the longitudinal direction and in other cases the mode is spatially oscillatory in the lateral direction. Previous investigations, using weakly nonlinear plate theories, do not predict the occurrence of the second type of mode and can significantly overpredict the critical twist angle.

References

[1] Thomson, W. (Lord Kelvin) and Tait, P. G., 1883, *Treatise on Natural Philosophy*, Cambridge University Press, London.
[2] de Saint-Venant, A., 1855, "De la Torsion des Prismes, avec des considérations sur leur Flexion," *Mémoires des Savants Étrangers*.
[3] Green, A. E., 1936, "The Equilibrium and Elastic Stability of a Thin Twisted Strip," Proc. R. Soc. London, **A125**, pp. 430–455.
[4] Green, A. E., 1937, "The Elastic Stability of a Thin Twisted Strip—II," Proc. R. Soc. London, **A161**, pp. 197–220.

[5] Crispino, D. J., and Benson, R. C., 1986, ''Stability of Twisted Orthotropic Plates,'' Int. J. Solids Struct., **28**, No. 6, pp. 371–379.
[6] Mockensturm, E. M., and Mote, C. D., 1999, ''Steady Motions of Translating, Twisted Webs,'' Int. J. Non-Linear Mech., **34**, No. 2, pp. 247–257.
[7] Mockensturm, E. M., 1998, ''On the Finite Twisting of Translating Plates,'' Ph.D. thesis, University of California, Berkeley, CA.
[8] Naghdi, P. M., 1972, ''The Theory of Shells and Plates,'' *S. Flügge's Handbuch der Physik*, Vol. VIa/2, C. Truesdell, ed., Springer-Verlag, Berlin, pp. 425–633.
[9] Naghdi, P. M., 1980, ''Finite Deformation of Elastic Rods and Shells,'' *Proceedings of the IUTAM Symposium on Finite Elasticity*, D. E. Carlson and R. T. Shield, eds., Martinus Nijhoff, Dordrecht, The Netherlands, pp. 47–103.

R. Miroshnik
Expert Researcher,
The Israel Electric Corporation, Ltd.
R&D Division,
Amir Bldg.
Haifa 31000, Israel
e-mail: mir@iec.co.il

The Phenomenon of Steady-State String Motion

The paper examines the phenomenon of steady-state motion for a string traveling with constant velocity along an invariant curve under gravity in a viscous medium. This technically important phenomenon has been known in the literature for about 120 years and may be applied in high-speed turbines, the textile industry, etc. The conditions for the phenomenon's existence are found. Concepts of two critical string velocities as well as sub, super, and hypercritical domains are introduced. The analytical solutions for the nonlinear differential equations and arbitrary constants for the general boundary conditions are found. The theoretical results are very close to the experimental ones.
[DOI: 10.1115/1.1380677]

1 Introduction

The paper examines the technically important phenomenon of a steady-state string traveling with constant velocity along an invariant curve (mode) under gravity in a viscous medium. The phenomenon is illustrated schematically in Fig. 1. The string comes out from outlet device 2 (outlet), moves along invariant mode 1 or 4, and enters into inlet device 3 (inlet). One sees the string frozen in space, because the motion along the mode is invisible. The string in fact moves only along itself and its velocity at every point is constant and directed to the mode tangent. This phenomenon may be applied in high-speed turbines cooling, thread coiling in the textile industry, design of easily unrolled mobile radio antennas, etc.

This problem has a long research history and still no complete solution. In the last century Aitkin [1] and Radinger [2] wrote about the string ''rigidity'' that in their opinion is produced by the centrifugal forces. Smith and Weathezchon [3] and Burge [4] examined the phenomenon's heat exchange for practical use in high-speed turbine cooling. Voevodin [5] had carried out numerous experiments with different textile cords elevation up to the height of 30 m.

Kurkin and Lebedev [6] showed experimentally in a vacuum chamber that the phenomenon ceases to exist when the air is removed. A heavy metallic cord was also elevated due to its specially heightened aerodynamic resistance. These experiments showed that a dominant reason for the phenomenon's existence is the friction of string-on-air.

Svetlicky and Gabruk [7], Cohen and Epstein [8], and Nordenholz and O'Reilly [9] examined the kinematical conditions of steady-state string motion. Svetlicky and Miroshnik [10], Kurkin and Miroshnik [11], Healey and Papadopoulos [12], and Schagerl et al. [13] analyzed different particular cases of string traveling. Perkins and Mote [14,15] analyzed the vibration and stability conditions of traveling cables while neglecting the resistance of the medium.

The purposes of this paper are to present analytical solutions of the above boundary value problem for different domains of string traveling when considering the resistance of the medium and compare these solutions with the experiment results. The analyses below and given discussion of the results provide the explanation for the phenomenon's existence.

Contributed by the Applied Mechanics Division of THE AMERICAN SOCIETY OF MECHANICAL ENGINEERS for publication in the ASME JOURNAL OF APPLIED MECHANICS. Manuscript received by the ASME Applied Mechanics Division, May 23, 2000; final revision, November 18, 2000. Editor: N. C. Perkins. Discussion on the paper should be addressed to the Editor, Prof. Lewis T. Wheeler, Department of Mechanical Engineering, University of Houston, Houston, TX 77204-4792, and will be accepted until four months after final publication of the paper itself in the ASME JOURNAL OF APPLIED MECHANICS.

2 The Differential Equations

We assume that a homogeneous, inextensible, ideally flexible string without bending and torsional stiffness travels with a constant velocity along an invariant mode having length L. Gravity and resistance of the medium (drag force) load the string. The drag force is assumed as constant, always directed along the mode tangently opposite to the traveling velocity. The differential equations of the steady-state plane motion may be derived ([7]) from ''equilibrium'' of string element shown in Fig. 2. The equations' derivation in general form is given in the Appendix. These equations in projections onto Cartesian coordinates X, Y in nondimensional form are

$$\frac{d}{ds}\left(p^*\frac{dx}{ds}\right)-\frac{dx}{ds}=0;$$
$$\frac{d}{ds}\left(p^*\frac{dy}{ds}\right)-\frac{dy}{ds}-n=0;$$
$$\left(\frac{dx}{ds}\right)^2+\left(\frac{dy}{ds}\right)^2=1, \tag{1}$$

where the nondimensional variables x, y, s, p^*, n are equal to

$$x=\frac{X}{L};\ \ y=\frac{Y}{L};\ \ s=\frac{S}{L};\ \ p^*=\frac{P^*}{m\mu L};\ \ n=\frac{g}{\mu};$$

$P^*=P-mV^2$ is the fictitious string tension; P is the real tension; V is the traveling velocity; and μ is the drag force of the string unit mass (acceleration). The drag force that depends on the string geometry and material, medium viscosity, etc., ([6]) increases monotonically with the traveling velocity; g is the gravity acceleration; m is the string linear mass; and S is the arc (Euler) coordinate along the mode.

The fictitious tension P^* may have any sign, however, the real tension P is assumed to be positive.

3 Equations' Analytical Solution

Integrating the first of Eq. (1) gives

$$p^*\frac{dx}{ds}-x=C_1. \tag{2}$$

Substitution of p^* from Eq. (2) into the second Eq. (1) in terms of

$$\frac{d}{ds}=\frac{dx}{ds}\,\frac{d}{dx};\ \ ds=\pm dx\sqrt{1+\left(\frac{dy}{dx}\right)^2} \tag{3}$$

yields (while considering the sign plus of ds)

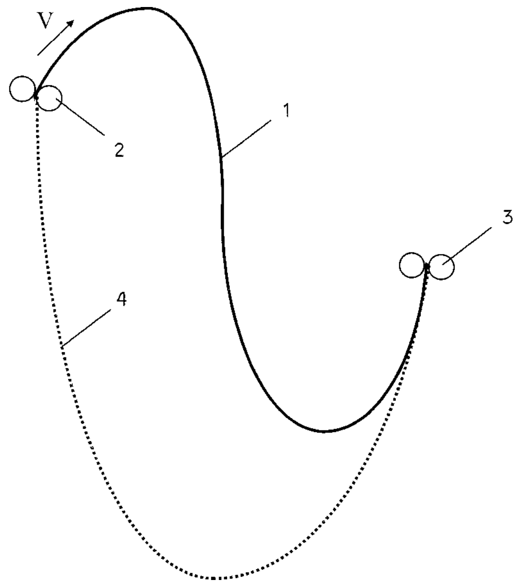

Fig. 1 Schematic illustration of the phenomenon

$$\frac{d}{dx}\left[(C_1+x)\frac{dy}{dx}\right]-\frac{dy}{dx}-n\sqrt{1+\left(\frac{dy}{dx}\right)^2}=0. \tag{4}$$

Separating variables and integration of Eq. (4) leads to

$$\frac{dy}{dx}=-\frac{1}{2}\left[\frac{|C_1+x|^n}{C_2}-\frac{C_2}{|C_1+x|^n}\right]. \tag{5}$$

Additional integration gives

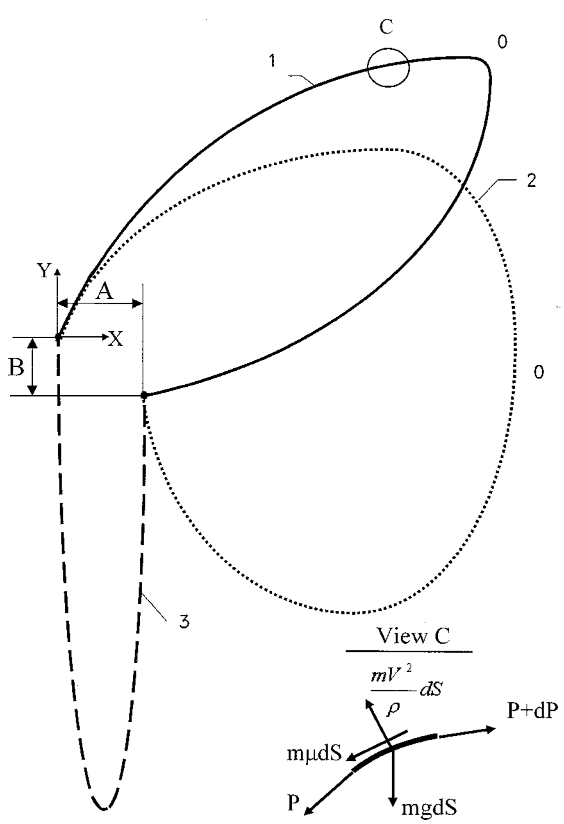

Fig. 2 Three kinds of steady-state string motion

$$y=\frac{1}{2}\left[\frac{|C_1+x|^{1+n}}{C_2(1+n)}-\frac{C_2|C_1+x|^{1-n}}{1-n}\right]+C_3. \tag{6}$$

The values p^* and s are found from Eqs. (3)–(6) after manipulations:

$$p^*=-\frac{1}{2}\left[\frac{|C_1+x|^{1+n}}{C_2}+C_2|C_1+x|^{1-n}\right], \tag{7}$$

$$s=\frac{1}{2}\left[\frac{|C_1+x|^{1+n}}{C_2(1+n)}+\frac{C_2|C_1+x|^{1-n}}{1-n}\right]+C_4, \tag{8}$$

where C_1, C_2, C_3, C_4 are arbitrary constants.

Equation (7) has a singular point at $x=-C_1$, where the "tension" p^* either vanishes or is infinite regardless of the boundary conditions. At this point the tangent to the string mode is always perpendicular to the X-axis ($dy/dx=\infty$). Evidently, the solutions (6)–(8) exist at the singularity only for the case $n<1$.

We name the minimum velocity for which the solution exists at the singularity as the first critical velocity. This velocity V_{1cr} is found from

$$\mu(V_{1cr})=g \quad (n=1). \tag{9}$$

Substituting Eq. (5) into

$$\rho=\frac{\left[1+\left(\frac{dy}{dx}\right)^2\right]^{3/2}}{\frac{d^2y}{dx^2}} \tag{10}$$

allows one to find the radius of curvature ρ

$$\rho=\pm\frac{|C_1+x|^{1+2n}+C_2^4|C_1+x|^{1-2n}+2C_2^2|C_1+x|}{4nC_2^2}. \tag{11}$$

Investigation of Eq. (11) shows that the curvature radius can either vanish or become infinite at the singularity. We name the minimum velocity for which the curvature radius vanishes at the singularity as the second critical velocity. This velocity V_{2cr} is found from

$$\mu(V_{2cr})=2g \quad (n=0.5). \tag{12}$$

Thus, there are three domains of the string motion:

- subcritical, when $0<V<V_{1cr}$, $0<\nu<1$, $n>1$, $\mu<g$,
- supercritical, when $V_{1cr}<V<V_{2cr}$, $1<\nu<2$, $0.5<n<1$, $g<\mu<2g$, and
- hypercritical, when $V>V_{2cr}$, $\nu>2$, $n<0.5$, $\mu>2g$,

where the parameter $\nu=1/n$.

4 Subcritical String Motion

First we examine the string having a traveling velocity smaller than the first critical one (in subcritical domain). In this case as it follows from the abovementioned domain the string mode cannot contain the singularity.

When the origin of Cartesian coordinates is located at the outlet, the boundary conditions are

$$y(0)=0;\ y(a)=b;\ s(0)=0;\ s(a)=1, \tag{13}$$

where $a=A/L$, $b=B/L$, A, B are the horizontal and vertical distances between the outlet and the inlet.

Substitution of Eqs. (6) and (8) into Eq. (13) and manipulation give the equation of the constant C_1

$$[|C_1+a|^{1+n}-|C_1|^{1+n}][|C_1+a|^{1-n}-|C_1|^{1-n}]=$$
$$=(1-b^2)(1-n^2). \tag{14}$$

After numerical finding of C_1 from (14), the constants C_2, C_3, and C_4 are calculated as follows:

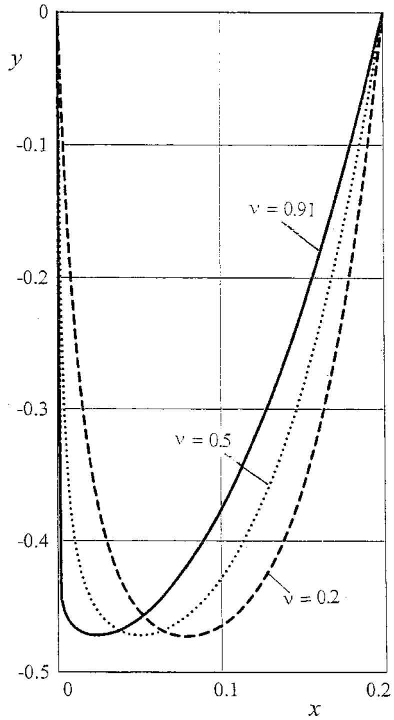

Fig. 3 The theoretical string modes for subcritical velocities

$$C_2 = \frac{(1-b)(1-n)}{|C_1+a|^{1-n} - |C_1|^{1-n}}; \tag{15}$$

$$C_3 = -\frac{1}{2}\left[\frac{|C_1|^{1+n}}{C_2(1+n)} - \frac{C_2|C_1|^{1-n}}{1-n}\right]; \tag{16}$$

$$C_4 = -\frac{1}{2}\left[\frac{|C_1|^{1+n}}{C_2(1+n)} + \frac{C_2|C_1|^{1-n}}{1-n}\right]. \tag{17}$$

The influence of traveling velocities' on string modes in the subcritical domain is presented in Fig. 3. The modes are shown for $a=0.2, b=0$. The analysis shows that the modes do not practically differ from the catenary (motionless equilibrium mode) starting from $\nu<0.2$.

The plots of the nondimensional tension p^* versus nondimensional arc coordinate s for the modes of Fig. 3 are presented in Fig. 4. The analysis shows that the "tension" tends to the one of the catenary, when the traveling velocity vanishes (i.e., the parameter υ approaches 0).

5 Super and Hypercritical String Motions

Now we examine the string having the traveling velocity greater than the first critical one (i.e. super and hypercritical domains). In this case the mode with the singularity, for which the "tension" vanishes, may exist. The continuous "tension" which is positive at the inlet becomes negative at the outlet.

The singular point divides the mode into two parts. In a general case the arbitrary constants C_1, C_2, C_3, C_4 in Eq. (5)–(8) may be different for each part. The arbitrary constants of the first mode part, which is located between the outlet and singularity, are lettered by subscripts "$'$" and the ones of the second part—by subscripts "$''$." Using the continuity conditions at the singularity, one can obtain

$$C_1' = C_1'' = C_1;\;\; C_3' = C_3'' = C_3;\;\; C_4' = C_4'' = C_4;\;\; C_2' \neq C_2''. \tag{18}$$

The derivative dx/dy is always infinite at the singularity regardless of the boundary conditions, therefore, the differing constants C_1', C_2'' satisfy the derivative continuous condition. Thus, there are four boundary conditions (13) for determining of five constants C_1, C_2', C_2'', C_3, C_4. The deficient boundary condition can be found when considering the string equilibrium in the outlet vicinity (on its both sides). One can prove that due to the negative "tension" the outlet cannot "break" the string direction. Consequently, the deficient conditions is

$$\frac{dy}{dx}(0) = \tan\alpha \tag{19}$$

where α is the known starting angle between the axis X and string outlet tangent. This angle is determined by the given direction of the outlet. Experiments also confirm the strong influence of the starting angle on the string mode.

Substitution of Eq. (5), (6), and (8) into the boundary conditions (13) and (19) permits to find five arbitrary constants C_1, C_2', C_2'', C_3, C_4

$$C_1 = \frac{(1-b^2)(1-n^2)-a^2}{2a-(1+b)(1+n)\tan\left(\frac{\pi}{4}-\frac{\alpha}{2}\right)-(1-b)(1-n)\cot\left(\frac{\pi}{4}-\frac{\alpha}{2}\right)}; \tag{20}$$

$$C_2' = -|C_1|^n \tan\left(\frac{\pi}{4}-\frac{\alpha}{2}\right); \tag{21}$$

$$C_2'' = \frac{C_2'|C_1|^{1-n}+(1-b)(1-n)}{|C_1+a|^{1-n}}; \tag{22}$$

$$C_3 = -\frac{1}{2}\left[\frac{|C_1|^{1+n}}{C_2'(1+n)} - \frac{C_2'|C_1|^{1-n}}{1-n}\right]; \tag{23}$$

$$C_4 = -\frac{1}{2}\left[\frac{|C_1|^{1+n}}{C_2'(1+n)} + \frac{C_2'|C_1|^{1-n}}{1-n}\right]. \tag{24}$$

There are four solutions for the examined problem satisfying the given boundary conditions due to signs "$\pm$" in Eq. (3) and two possible values (roots) of C_2' (in the process of Eq. (21) derivation). These solutions are shown schematically in Fig. 5. Modes 1, 2 correspond to the plus sign in Eq. (3) while modes 3, 4 correspond to the minus sign. Modes 2, 4 have mutually intersecting parts and are not of practical interest. Mode 3 can be built by setting the starting angle 180 deg greater than in mode 1.

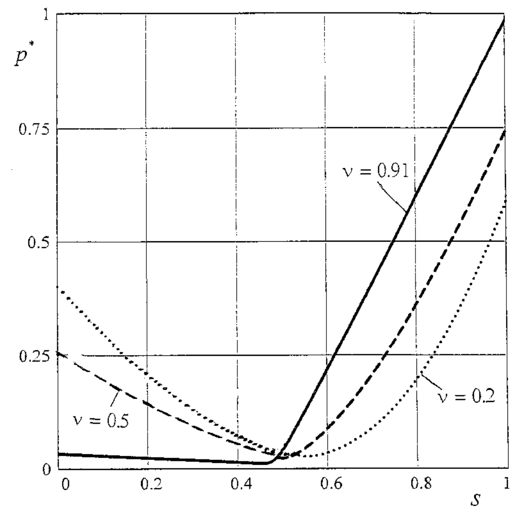

Fig. 4 The theoretical string tension for subcritical velocities

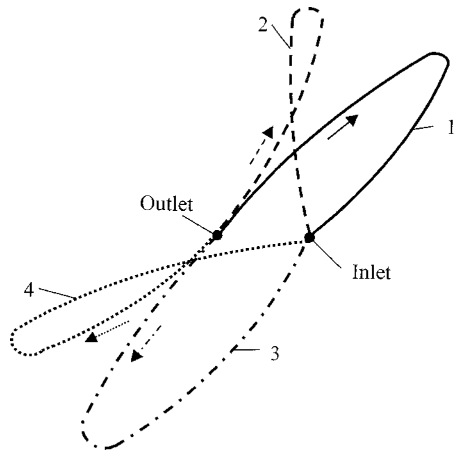

Fig. 5 The four possible solutions satisfying the given boundary conditions

Thus, only the plus sign in Eq. (3) and defined value C_2' (Eq. (21)) are considered in the paper. Corresponding string mode 1 is similar to the experimentally observed one. This mode having the singularity at positive x, may exist, if the constant C_1 is negative, thereby leading to the inequality

$$\frac{(1-b^2)(1-n^2)-a^2}{2a-(1+b)(1+n)\tan\left(\frac{\pi}{4}-\frac{\alpha}{2}\right)-(1-b)(1-n)\cot\left(\frac{\pi}{4}-\frac{\alpha}{2}\right)}<0. \tag{25}$$

Thus, the motion with the velocity greater than the first critical one exists if its parameters n, a, b, and α satisfy the inequality (25).

The string modes in Fig. 6 correspond to velocities, which are slightly greater than the first critical one. The modes with velocities which are considerably greater than the first critical velocity are presented in Fig. 7. All the modes in Figs. 6 and 7 have the starting angle $\alpha=45$ deg and parameters $a=0.2$, $b=0$.

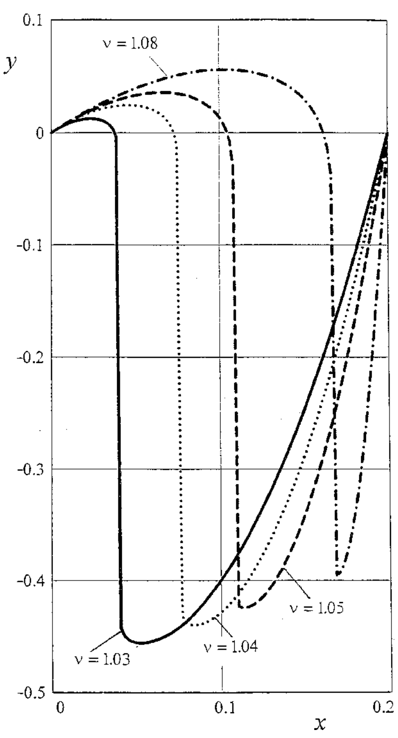

Fig. 6 The theoretical string modes ($\alpha=45$ deg) for small super critical velocities

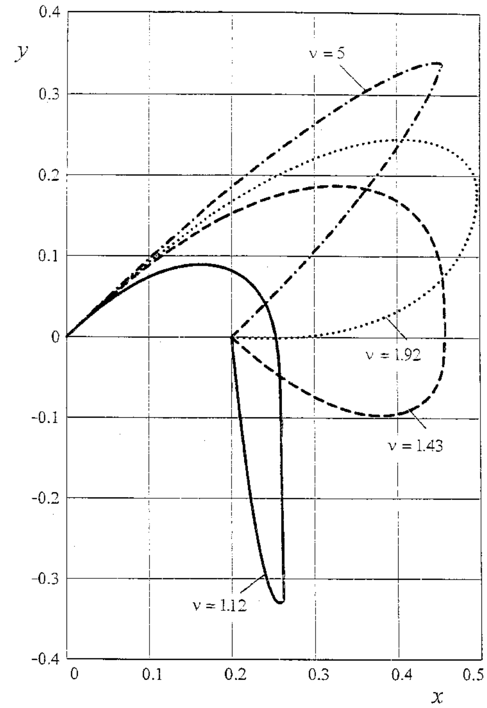

Fig. 7 The theoretical string modes ($\alpha=45$ deg) for large super and hyper critical velocities

Outlet and inlet can be assumed coinciding $(a=b=0)$, when the distance between them is considerably greater than the length L. The influence of the starting angle on the modes having constant velocity ($\mu=21\,\mathrm{m/sec^2}$) is shown in Fig. 8 for this case.

The string modes are experimentally determined using the experimental apparatus illustrated in Fig. 9. The closed cylindrical woven textile cord 1 which has weight/length 4.5 g/m, length 7 *m*, and diameter 4 mm wraps around flanged pulley 2 with the diameter 0.2 m. A surgical groove in the pulley perimeter increases the pulley-cord friction. The cord is pressed to the pulley by pinch rollers 3 and 4. The location of rollers 3 and 4 can be changed and then fixed along the pulley's circumference. The pulley attached to a DC motor moves the cord. The experiments were carried out with velocities up to 30 m/sec, which were measured with a stroboscope. A simple camera photographed the cord modes.

The comparison between theoretical and experimental modes (the theoretical ones are dotted) is presented in Figs. 10 and 11. The modes with constant velocity $V=19.6\,\mathrm{m/sec}$ ($\mu=28.2\,\mathrm{m/sec^2}$) and different starting angles are presented in Fig. 10. The modes with constant starting angle $\alpha=45$ deg and different velocities are shown in Fig. 11. The theoretical plots of "tension" p^* versus coordinate s, corresponding to the modes of Figs. 10, and 11, are shown in Figs. 12 and 13 accordingly.

The "equilibrium" of free string part is considered in Fig. 14 for which the weight mgL and drag force mμ of unit mass and end (outlet, inlet) "tension" forces P_1^*, P_2^* load the string. The equilibrium of moments with respect to the intersection point O of the end forces' directions gives

$$gLD=\mu\Omega, \tag{26}$$

where Ω is the corresponding area of the mode; d is the distance between the center of gravity of the mode's area and point of end forces' intersection.

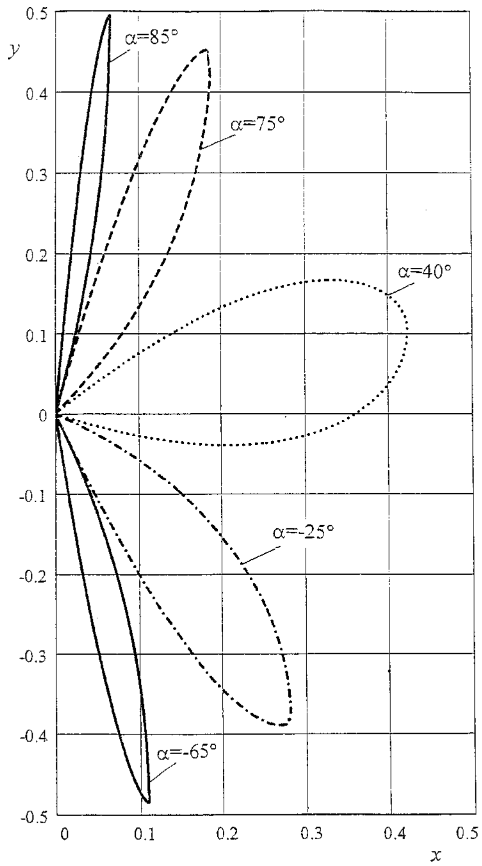

Fig. 8 The theoretical string modes ($\mu=21$ m/sec^2) for different starting angles

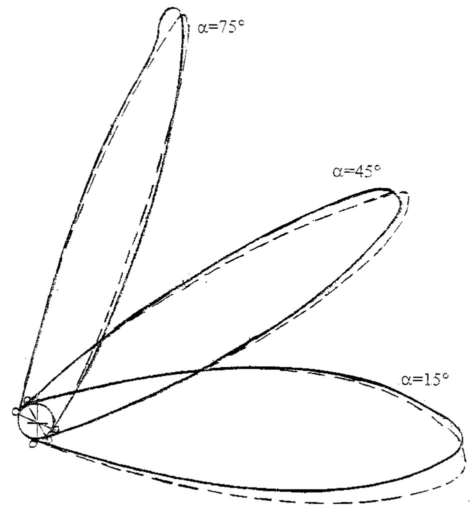

Fig. 10 The theoretical and experimental modes ($\mu=28.3$ m/sec^2) for different start angles

Equation (26) enables to find the drag force acceleration μ from Eq. (26) when the experimental string mode is known.

6 Discussion of Results

As shown above there are three kinds of string modes (Fig. 2):

- falling mode 3 without the singularity (in the subcritical domain);
- roundish mode 2 with the singularity when the radius of curvature at the singularity is infinite (in the supercritical domain); and
- extended, sharp at the top mode 1 with the singularity when the radius of curvature at the singularity vanishes (in the hypercritical domain).

The boundary conditions for the subcritical motion are the same as for the motionless string equilibrium because there is no singularity. The singularity leads to an additional boundary condition at the outlet. The modes strongly depend on the solution behavior at the singularity. The supercritical motion may occur only if the solution exists at the singularity. The conditions for existence of the solution are derived for unlimited string length. However, string stability and strength, motor power, etc, limit the length. This issue is a separate subject for investigation that is not considered in the paper.

The analogy between the steady-state motion and equilibrium is also interesting. The equilibrium equations of any mode part may be written (as though the string does not travel) when changing the real tension P to the fictitious one $P^*=P-mV^2$.

The phenomenon's existence may be explained while considering the momentum "equilibrium" of the string part which is shown in Fig. 14. The string does not "fall" under the weight influence because the moment of the drag force balances the moment of the weight. One should pay attention to the paradox of negative value of the "tension" p_1^* in the equilibrium, despite the fact that the real tension P_1 is always positive.

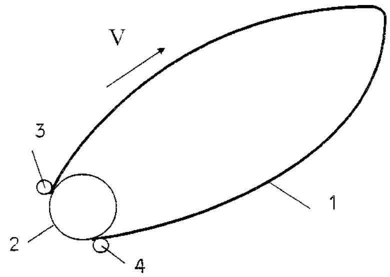

Fig. 9 The schematic diagram of experimental apparatus

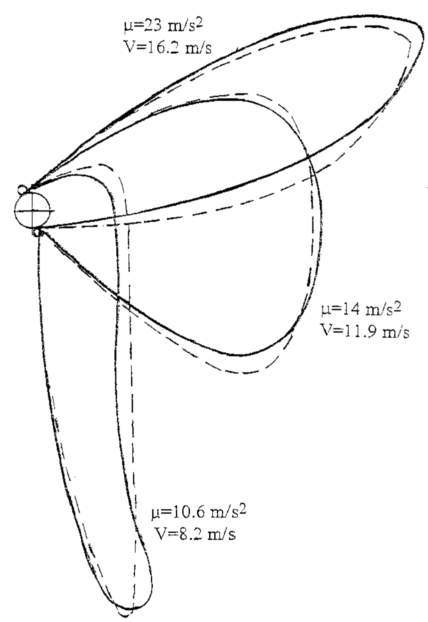

Fig. 11 The theoretical and experimental modes ($\alpha=45$ deg) for different velocities

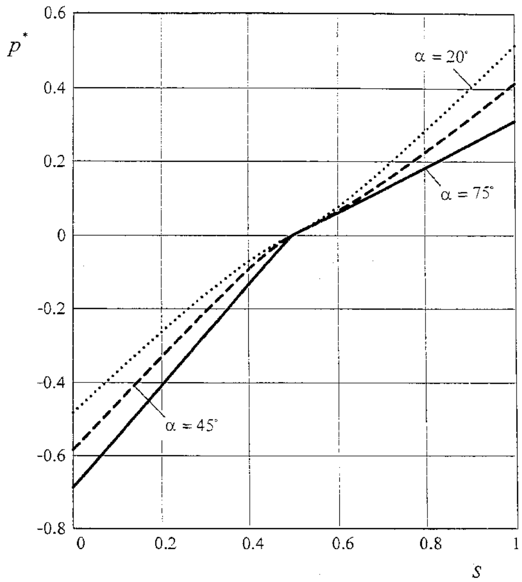

Fig. 12 The theoretical string tension for the modes of Fig. 9

Figures 3, 6, and 7 show the string elevation starting from the catenary, as the longitudinal velocity increases. The tension changes along with velocity as shown in Fig. 5. The modes and tension that correspond to small traveling velocity are close to the ones of the catenary. Figure 8 shows strong dependence of modes on the starting angle.

Theoretical modes agree well with experimental ones. This agreement may be explained by minimum of assumptions that are made at the transition from the real string to its mathematical model. The experiments also show that the string ''falls'' when the condition (25) is not satisfied. This may occur, for example, if the starting angle or the distance between the outlet and inlet is changed.

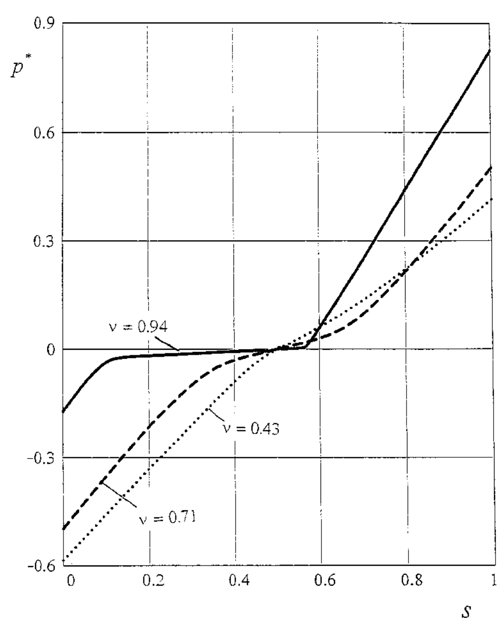

Fig. 13 The theoretical string tension for the modes of Fig. 10

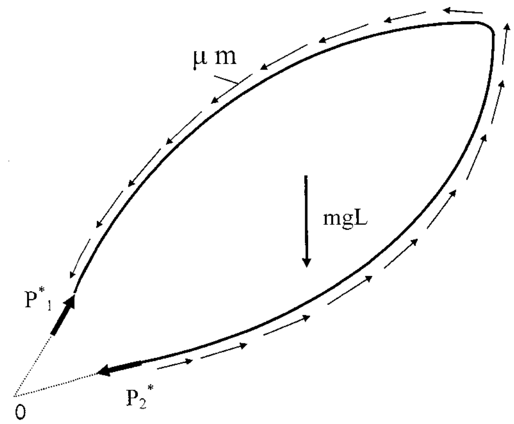

Fig. 14 The explanation of the phenomenon's existence

Acknowledgment

The author acknowledges his daughter Elena for her aid in editing of this paper.

Appendix

Derivation of Differential Equations of Steady-State String Motion. We write planar dynamic equations for an element of homogeneous, ideally flexible string without bending and torsional stiffness. The string travels with a constant velocity along an invariant mode

$$m\,\frac{\partial \overline{V}}{\partial t}=\frac{\partial \overline{Q}}{\partial S}-\overline{q} \tag{27}$$

where $\overline{V}=V\overline{e_1}$ is the string velocity vector having the module V and directed along the tangent to the mode unit vector $\overline{e_1}$; $\overline{Q}=T\overline{e_1}$ is the cross-section string force vector which is directed along the unit vector $\overline{e_1}$; T is the string tension; $\overline{q}$ is the vector of distributed linear external force acting on string; m is the string linear mass; t is the time; and S is the arc coordinate along the string mode.

Performing differentiation with respect to coordinate S when taking into consideration that $\partial S/\partial t=V=\text{const}$ gives

$$\frac{\partial \overline{V}}{\partial t}=\frac{\partial \overline{V}}{\partial S}\,\frac{\partial S}{\partial t}=V^2\frac{\partial \overline{e_1}}{\partial S}. \tag{28}$$

Substitution of Eq. (28) into Eq. (27) in terms of

$$\frac{\partial \overline{Q}}{\partial S}=\frac{\partial (T\overline{e_1})}{\partial S}=\frac{\partial T}{\partial S}\overline{e_1}+T\,\frac{\partial \overline{e_1}}{\partial S}, \tag{29}$$

while using total derivatives instead of partial ones (the string mode does not depend on time) and manipulations lead to

$$(T-mV^2)\,\frac{d\overline{e_1}}{dS}+\frac{d(T-mV^2)}{dS}\overline{e_1}+\overline{q}=0. \tag{30}$$

Applying of variable $T^*=T-mV^2$ gives

$$\frac{\partial \overline{T^*}}{\partial S}+\overline{q}=0 \tag{31}$$

where $\overline{T^*}=T^*\overline{e_1}$.

Equation (31) is almost identical to the equation of the string equilibrium with difference in use of fictitious tension T^* instead of the real one T. This allows one to apply Eq. (31) as equilibrium equation for an arbitrary string part.

We obtain the equations in projections onto Cartesian coordinates X, Y using Eq. (31) and relations for "tension" projections T_X^* and T_Y^*

$$T_X^* = T^* \frac{dX}{dS}; \quad T_Y^* = T^* \frac{dY}{dS}. \tag{32}$$

The third equation necessary for solution is the relation between the cosines

$$\frac{d}{dS}\left(T^* \frac{dX}{dS}\right) + q_X = 0;$$

$$\frac{d}{dS}\left(T^* \frac{dY}{dS}\right) + q_Y = 0; \tag{33}$$

$$\left(\frac{dX}{dS}\right)^2 + \left(\frac{dY}{dS}\right)^2 = 1$$

where q_X and q_Y are the projections of the distributed external force.

References

[1] Aitkin, J., 1878, "An Account of Some Experiments on Rigidity Produced by Centrifugal Forces," Philos. Mag., **5**.

[2] Radinger, G., 1878, Dampfmachinen, **5**.

[3] Smith, W. E., and Weathezchon, R. C., 1961, "A New Type of Thermal Radiator of Space Vehicle," ARS, **20**, No. 1, pp. 32–36.

[4] Burge, H., 1962, "Revolving Bolt Space Radiator," ARS, **32**, No. 8, pp. 17–25.

[5] Voevodin, A. A., 1965, "Dynamic Equilibrium of Closed String in Earth Conditions," *Proceedings of USSR Connection department*, Vol. 2, pp. 89–108.

[6] Kurkin, V. I., and Lebedev, I. P., 1965, "Calculation of String Air Resistance," Izvestia Vuzov, Tehnologia Tekstilnoi Prom., **1**, M., pp. 166–169.

[7] Svetlicky, V. A., and Gabruk, V. I., 1966, "Critical Velocities of the Steady State Motion," Soviet Applied Mechanics, **6**, pp. 13–17.

[8] Cohen, H., and Epstein, M., 1994, "On a Class of Planar Motions of Flexible Rods," ASME J. Appl. Mech., **61**, pp. 206–208.

[9] Nordenholz, T. R., and O'Reilly, O. M., 1995, "On Kinematical Conditions for Steady Motion of Strings and Rods," ASME J. Appl. Mech., **62**, pp. 820–822.

[10] Svetlicky, V. A., and Miroshnik, R. A., 1972, "Critical Velocities of the Steady State Motion of an Elastic Fiber in a Planar Homogeneous Flow," Soviet Applied Mechanics, **6**, pp. 52–57.

[11] Kurkin, V. A., and Miroshnik, R. A., 1988, "The Spatial Stationary Movement of the Heavy Perfectly Flexible Bar," Soviet Applied Mechanics, **24**, pp. 113–116.

[12] Healey, T. J., and Papadopoulos, J. N., 1990, "Steady Axial Motion of Strings," ASME J. Appl. Mech., **57**, pp. 785–787.

[13] Schagerl, M., Steiner, W., and Troger, H., 1997, "On the Paradox of the Free Falling Folded Chair," Acta Mech., **125**, pp. 155–168.

[14] Perkins, N. C., and Mote, C. D., Jr., 1987, "Three-Dimensional Vibration of Travelling Elastic Cables," J. Sound Vib., **114**, No.2, pp. 305–340.

[15] Perkins, N. C., and Mote, C. D., Jr., 1989, "Theoretical and Experimental Stability of Two Translating Cable Equilibria," J. Sound Vib., **128**, No. 3, pp 397–410.

A New Look at an Old Problem: Newton's Cradle

V. Ceanga
Y. Hurmuzlu
Mechanical Engineering Department,
Southern Methodist University,
Dallas, TX 75275

In this paper we consider the most basic multi-impact system, the so-called "Newton's Cradle." The task of developing an analytical method to predict the post impact velocities of the balls in the cradle has baffled investigators in the field of impact research for many years. The impulse-based rigid-body body as well as the alternative compliance-based time-base approaches have failed to produce valid solutions to this problem. Here, we present a new method that produces energetically consistent solutions to the problem. Our method is based on the traditional impulse-momentum-based rigid-body approach. We do, however, resolve the nonuniqueness difficulty in the rigid-body approach by introducing a new constant called the Impulse Transmission Ratio. Finally, we verify our method by conducting a set of experiments and comparing the theoretical predictions with the experimental outcomes. [DOI: 10.1115/1.1344902]

1 Introduction

Multi-impact problems pose many difficulties and unanswered questions ([1]). The simplest of these problems, the linear chain or the "Newton's Cradle," represents the most basic problem of this type. This classical problem involves a collision problem where one ball strikes one end of a linear chain of stationary balls in contact with each other. The system represents the simplest of the multibody impact problems that one may consider. Yet, it encapsulates the difficulties that are present in more complex systems. Many investigators attempted to develop analytical solutions that produce post-impact velocities in this class of problems. The fact remains, however, that the methods that have been proposed possess deficiencies and inconsistencies that are yet to be resolved.

One approach to the solution of the problem has been the consideration of sequential impacts and use of impulse-momentum rules and coefficients of restitution. Johnson [2] introduced the notion of sequential impacts. The method was based on a succession of simple impacts that occur one at a time. Han and Gilmore [3] proposed a solution algorithm that accommodated multiple impacts, but their methods resulted in multiple sets of feasible post-impact velocities that were valid for the same initial conditions. Brogliato [4] also considered the three-ball impact problem. The conclusion drawn by this author was that the rigid-body rules did not possess sufficient information to yield a unique post-impact solution. He proceeded by stating that the only way to solve the rigid-body indeterminacy was to add compliance to the bodies in contact.

The second approach is the compliance-based method that introduce linear springs between consecutive balls in the chain. The approach results in a set of second-order linear differential equations that can be cast as functions of the ratios of the spring constants. One of the earliest studies of this type was presented in Smith [5]. Walkiewicz and Newby [6] considered the possible solutions of the three-ball chain that simultaneously satisfied momentum and energy equations. They showed that there were infinitely many solutions that fit this description. Newby [7] studied the three-ball impacts by placing linear springs to model the contacts. He used the spring stiffness ratio as a parameter, and analyzed its effect on the velocity outcomes. He demonstrated that it was not always possible to determine the values of the necessary stiffness ratio that yielded a specific velocity outcome. Hinch and Saint-Jean [8] studied the case of a very long rectilinear array of balls. The compliance-based methods are significantly more difficult to apply than the impulse-momentum-based ones. To the best of our knowledge, the investigators that applied these methods, never included damping in their analysis, and have always assumed perfectly elastic collisions. In addition, complexity of such methods makes it very difficult to experimentally estimate the model parameters, specifically for chains with large number of balls.

Cholet [9] uses the methods of convex analysis that is inspired by an adaptation of Moreau's sweeping process ([10,11]) to analyze the multiple impacts in a three-ball cradle. This work represents the most advanced up to date and produces unique and energetically consistent results. The only drawback of the approach is that the solution is formulated in terms of three parameters that do not have obvious physical meanings. For example, with this method, it becomes very difficult to identify the parameter values that lead to purely elastic impacts. In addition, the post-impact velocities are nonlinear functions of the parameters. Thus, one may encounter difficulties in estimating the parameter values from experiments. Often, there is not a one to one correspondence between a particular post-impact velocity set and parameter set. One may obtain the same outcome for different set of parameters. We believe that, a solution method that is based on physically meaningful parameters such as the coefficient of restitution will be more effective in dealing with the multiple impact problem at hand.

The objective of the present article is to develop an impulse-momentum-based method to determine the post impact velocities of the general N-Ball chain. The method should produce unique and energetically consistent solutions. The predicted outcomes should be physically consistent and experimentally verifiable (experimental verification of the previous methods is almost nonexistent). For this purpose we present a new methodology that uses the energetic coefficient of restitution ([12]). We propose a new constant, that we call the "Impulse Correlation Ratio." We test our method by conducting a set of experiments, and comparing the theoretical outcomes with the experimental ones.

Contributed by the Applied Mechanics Division of THE AMERICAN SOCIETY OF MECHANICAL ENGINEERS for publication in the ASME JOURNAL OF APPLIED MECHANICS. Manuscript received by the ASME Applied Mechanics Division, Sept. 15, 1999; final revision, Apr. 16, 2000. Associate Editor: N. C. Perkins. Discussion on the paper should be addressed to the Editor, Professor Lewis T. Wheeler, Department of Mechanical Engineering, University of Houston, Houston, TX 77204-4792, and will be accepted until four months after final publication of the paper itself in the ASME JOURNAL OF APPLIED MECHANICS.

2 Three-Ball Chain

2.1 Problem Description. Consider the three balls that are depicted in Fig. 1. Ball B_1 strikes the other two balls (with initial velocities of v_2^- and v_3^-) that are in contact at time $t=t^-$ with a

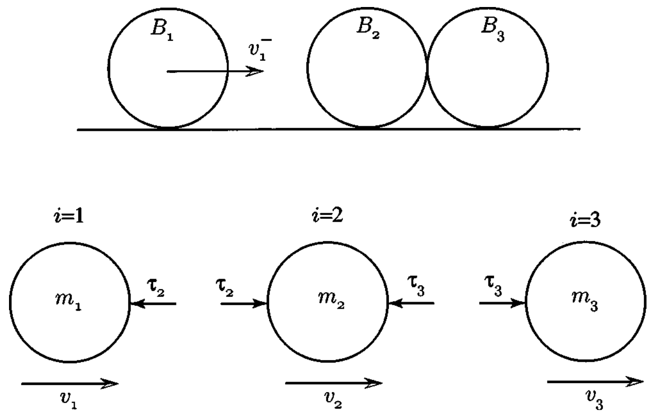

Fig. 1 Impulses

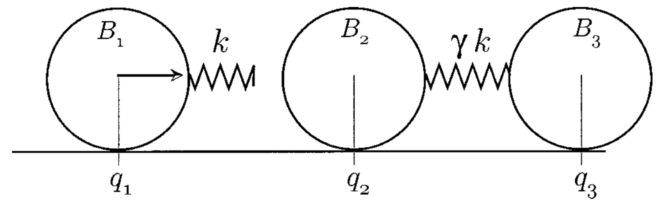

Fig. 2 The compliant, three-ball chain

velocity of v_1^- subject to $v_1^- \geqslant v_2^- \geqslant v_3^-$. The collision causes the two normal impulses τ_2 and τ_3 as shown in the figure. The problem at hand is to determine the post impact velocities v_1^+, v_2^+, and v_3^+. For this purpose one can write the conservation of linear momentum equations for the three balls, this yields

$$m_1 \Delta v_1 = -\Delta \tau_2 \tag{1}$$

$$m_2 \Delta v_2 = \Delta \tau_2 - \Delta \tau_3 \tag{2}$$

$$m_3 \Delta v_3 = \Delta \tau_3 \tag{3}$$

where Δv_i and $\Delta \tau_i$ are the changes in velocities and impulses as a result of the collision. Here, we have three equations in terms of the three post-impact velocities and the two changes that occur in normal impulses. Additional assumptions are needed to obtain the two additional equations that are necessary to solve the problem. One can use coefficients of restitution between pairs of balls to resolve this problem. Since the balls can be treated as particles, the kinematic coefficient of restitution e_2^k between B_1 and B_2 can be used to obtain one additional velocity relationship:

$$v_1^+ - v_2^+ = -e_2^k (v_1^- - v_2^-) \tag{4}$$

where the superscript ''+'' denotes the quantity at the end of the collision. One encounters problems in applying the restitution law between B_2 and B_3 because two assumptions regarding their contact situation at the instant of collision yield different solutions. Accordingly, Han and Gilmore [3] report the following solutions for three equal mass balls and $e=1$, $v_1^-=1$, $v_2^-=0$, and $v_3^-=0$:

$$v_1^+ = -\tfrac{1}{3} v_2^+ = v_3^+ = \tfrac{2}{3} \tag{5}$$

$$v_1^+ = v_2^+ = 0 \quad v_3^+ = 1. \tag{6}$$

The former solution is obtained by assuming that B_2 and B_3 are in contact when B_1 strikes and they can be treated as a single mass $(v_2^+ = v_3^+)$. The second solution, on the other hand, is obtained by assuming that B_2 and B_3 are not in contact when B_1 strikes, which leads to the impulse condition $\tau_3 = 0$. Having two equally possible solutions poses a serious difficulty in accepting this approach as a valid way of solving this problem.

2.2 Impulse Correlation Ratio. We now consider the compliant model that is presented in Fig. 2, which is the example considered in Brogliato [4]. For simplicity, we will choose $m_1 = m_2 = m_3 = v_1^- = 1$ and $v_2^- = v_3^- = 0$. When all the balls are in contact, their displacements can be obtained as follows:

$$q_1 = \frac{t}{3} - \frac{k(2\gamma - \gamma_1)\sin(\sqrt{k\gamma_1}t)}{(k\gamma_1)^{3/2}(\gamma_1 - \gamma_2)} + \frac{k(2\gamma - \gamma_2)\sin(\sqrt{k\gamma_2}t)}{(k\gamma_2)^{3/2}(\gamma_1 - \gamma_2)} \tag{7}$$

$$q_2 = \frac{t}{3} + \frac{k(\gamma - \gamma_1)\sin(\sqrt{k\gamma_1}t)}{(k\gamma_1)^{3/2}(\gamma_1 - \gamma_2)} - \frac{k(\gamma - \gamma_2)\sin(\sqrt{k\gamma_2}t)}{(k\gamma_2)^{3/2}(\gamma_1 - \gamma_2)} \tag{8}$$

$$q_3 = \frac{t}{3} + \frac{k\gamma \sin(\sqrt{k\gamma_1}t)}{(k\gamma_1)^{3/2}(\gamma_1 - \gamma_2)} - \frac{k\gamma \sin(\sqrt{k\gamma_2}t)}{(k\gamma_2)^{3/2}(\gamma_1 - \gamma_2)} \tag{9}$$

where $\gamma_1 = 1 + \gamma + \sqrt{1 - \gamma + \gamma^2}$ and $\gamma_2 = 1 + \gamma - \sqrt{1 - \gamma + \gamma^2}$. The left and right impulses acting on B_2 can be written as follows:

$$\Delta \tau_2 = \int_0^t k(q_2 - q_1)dt = \frac{(3\gamma - 2\gamma_1)\gamma_2^2 \sin^2(\frac{1}{2}\sqrt{k\gamma_1}t) - (3\gamma - 2\gamma_2)\gamma_1^2 \sin^2(\frac{1}{2}\sqrt{k\gamma_2}t)}{\frac{1}{2}\gamma_1^2\gamma_2^2(\gamma_1 - \gamma_2)} \tag{10}$$

$$\Delta \tau_3 = \int_0^t k\gamma(q_3 - q_2)dt = \frac{[1 - \cos(\sqrt{k\gamma_1}t)]\gamma\gamma_2 - [1 - \cos(\sqrt{k\gamma_2}t)]\gamma\gamma_1}{\gamma_1\gamma_2(\gamma_1 - \gamma_2)}. \tag{11}$$

Now, we investigate the relationship between $\Delta \tau_2$ and $\Delta \tau_3$. First we form the following linear relationship between the impulses:

$$\delta = \alpha_2 \Delta \tau_2 + \Delta \tau_3. \tag{12}$$

Substituting Eqs. (10) and (11) into (12) and simplifying we obtain

$$\delta = \frac{2[3\alpha_2\gamma + (\gamma - 2\alpha_2)\gamma_1]}{\gamma_1^2(\gamma_1 - \gamma_2)} \sin^2\left(\frac{1}{2}\sqrt{k\gamma_1}t\right) - \frac{2[3\alpha_2\gamma + (\gamma - 2\alpha_2)\gamma_2]}{\gamma_2^2(\gamma_1 - \gamma_2)} \sin^2\left(\frac{1}{2}\sqrt{k\gamma_2}t\right). \tag{13}$$

Considering the first extreme case when the first spring is much stiffer than the second ($\gamma \ll 1$) in Eq. (13) yields

$$\delta_1 \approx -\frac{(\alpha_2 + \gamma)[1 - \cos(\sqrt{\alpha k}t)]}{2\gamma} = 0 \quad \text{for } \alpha_2 = -\gamma. \tag{14}$$

Thus, the impulses can be related as $\Delta \tau_3 = \gamma \Delta \tau_2$ when the first spring is much stiffer than the second. Next, we consider the other extreme, $\gamma \gg 1$ in Eq. (13) yields

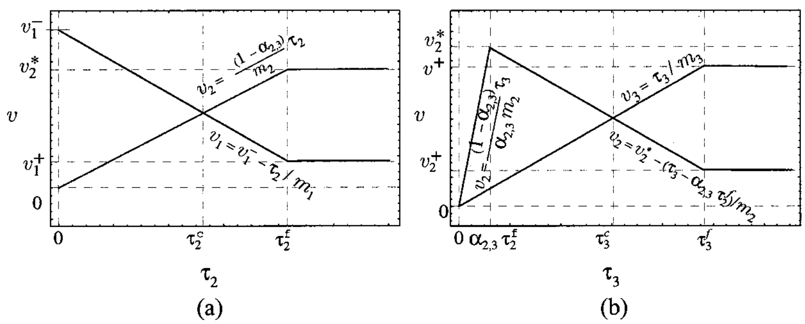

Fig. 3 Velocity-impulse graphs

$$\delta_2 \approx -\frac{2\gamma(1+2\alpha_2)\sin^2(\sqrt{3k/8}t)}{3\gamma}=0 \quad \text{for } \alpha_2=-1/2. \tag{15}$$

Once again we have a proportional relationship in the form of $\Delta\tau_3 = 1/2\Delta\tau_2$.

Based on the two extreme trends that we have shown, we form the following hypothesis that we assume is valid for triplets of balls:

Consider a linear sequence of three balls: B_{i-1}, B_i, and B_{i+1}, where B_{i-1} impacts B_i while it is in contact with B_{i+1}. Then, the impulses that develop subsequent to the impact between the pair B_{i-1}-B_i and the pair B_i-B_{i+1} are proportional, and related through a constant $\alpha_i \geqslant 0$. This constant, we term as the Impulse Correlation Ratio, depends on the specific sequence, mass, and material properties of the three adjacent balls.

We can apply this hypothesis to establish a relationship between the normal impulses when B_i establishes contact and initiates a collision with B_{i+1} during the impact of B_{i-1} and B_i. This relationship is given by

$$\Delta\tau_{i+1} = \alpha_{i,i+1}\Delta\tau_i. \tag{16}$$

This relationship should be understood in the context of the impact direction, as in this chapter we assume that the impact propagates in the increasing direction of ball indices. Adaptation of these definitions to cases with reverse impact direction is a matter of reversing the indexing.

In the next subsection we use the momentum-based approach and the Impulse Correlation Ratio, to formulate an energetically consistent solution to obtain the post-impact velocities.

2.3 The Solution Method. Solving Eqs. (1), (2), (3), and (16) for the velocity changes Δv_1, Δv_2, in terms of $\Delta\tau_2$ and Δv_2, Δv_3 in terms of $\Delta\tau_3$ yields

$$\Delta v_1 = -\frac{1}{m_1}\Delta\tau_2 \tag{17}$$

$$\Delta v_2 = \frac{1-\alpha_{2,3}}{m_2}\Delta\tau_2 = \frac{1-\alpha_{2,3}}{\alpha_{2,3}m_2}\Delta\tau_3 \tag{18}$$

$$\Delta v_3 = \frac{1}{m_3}\Delta\tau_3. \tag{19}$$

Figures 3(a) and 3(b) depict the velocity-impulse diagrams for the collisions between the balls B_1, B_2 and B_2, B_3, respectively. In this study we use the energetic coefficient of restitution ([12]) to determine the terminal impulse for each collision. Accordingly, for the first diagram we have (see Fig. 3(a))

$$v_1 = v_1^- - \frac{1}{m_1}\tau_2 \tag{20}$$

$$v_2 = v_1^- + \frac{1-\alpha_{2,3}}{m_2}\tau_2. \tag{21}$$

Now, setting $v_2 = v_1$ and solving for the maximum compression impulse τ_2^c, results in the following expression:

$$\tau_2^c = \frac{m_1 m_2(v_1^- - v_2^-)}{(1-\alpha_{2,3})m_1 + m_2}. \tag{22}$$

Next, we compute the work done during the compression and restitution phases and use the definition of the energetic coefficient of restitution to get the following equation:

$$e_2^2\int_0^{\tau_2^c}(v_1-v_2)\,d\tau_2 + \int_{\tau_2^c}^{\tau_2^f}(v_1-v_2)\,d\tau_2 = 0 \tag{23}$$

where e_2 is the coefficient of restitution between B_1 and B_2. Solving Eq. (23) for τ_2^f yields

$$\tau_2^f = \frac{(1+e_2)m_1 m_2(v_1^- - v_2^-)}{(1-\alpha_{2,3})m_1 + m_2}. \tag{24}$$

Moving on to the second diagram (see Fig. 3(b)) where we have

$$v_2 = \begin{cases} v_2^- + \dfrac{1-\alpha_{2,3}}{\alpha_{2,3}m_2}\tau_3 & \text{if } 0 \leqslant \tau_3 \leqslant \alpha_{2,3}\tau_2^f \\[2ex] v_2^* - \dfrac{\tau_3 - \alpha_{2,3}\tau_2^f}{m_2} & \text{if } \tau_3 \geqslant \alpha_{2,3}\tau_2^f \end{cases} \tag{25}$$

where

$$v_2^* = v_2^- + \frac{(1-\alpha_{2,3})(1+e_2)m_1(v_1^- - v_2^-)}{(1-\alpha_{2,3})m_1 + m_2}. \tag{26}$$

Note that, when $\tau_3 \geqslant \alpha_{2,3}\tau_2^f$, the impact between B_1 and B_2 is over. Thus, only the right impulse τ_3 acts on the ball B_2 $(-m_2(v_2 - v_2^*) = \tau_3 - \alpha_{2,3}\tau_2^f)$. This leads to the second part of the expression given for v_2 in Eq. (25). Finally the expression for v_3 can be written as follows:

$$v_3 = v_3^- + \frac{1}{m_3}\tau_3. \tag{27}$$

Once again, we compute the maximum compression impulse between B_2 and B_3 by setting $v_3 = v_2$, which yields

$$\tau_3^c = \frac{\{(v_1^- - v_2^-)(1+e_2)m_1 + (v_2^- - v_3^-)[m_1(1-\alpha_{2,3}) + m_2]\} m_2 m_3}{[(1-\alpha_{2,3})m_1 + m_2](m_2+m_3)}. \tag{28}$$

Now, set up the energy equation as

$$e_3^2 \int_0^{\tau_3^c} (v_2 - v_3)\, d\tau_3 + \int_{\tau_3^c}^{\tau_3^f} (v_2 - v_3)\, d\tau_3 = 0 \tag{29}$$

where e_3 is the coefficient of restitution between B_2 and B_3. It is important to note that using different definitions of the coefficient of restitution would lead to different outcomes. Although we are dealing with particle collisions, simultaneous impacts lead to the two segment configuration of v_2 in the velocity impulse diagram (see Fig. 3(*b*)). Thus, one has to use the energetic definition of the coefficient of restitution to get energetically consistent results. Now, solving Eq. (29) for τ_3^f yields

$$\tau_3^f = \{(v_1^- - v_2^-)(1+e_2)m_1 + (v_2^- - v_3^-)[m_1(1-\alpha_{2,3}) + m_2]\} m_2 m_3 \times \frac{1 + e_3\sqrt{1 - \alpha_{2,3}\left(\frac{m_2}{m_3}+1\right)\left[1 + \frac{(v_2^- - v_3^-)}{(v_1^- - v_2^-)}\frac{(1-\alpha_{2,3})m_1 + m_2}{(1+e_2)m_1}\right]^{-2}}}{[(1-\alpha_{2,3})m_1 + m_2](m_2+m_3)}. \tag{30}$$

The post-impact velocities can now be computed as follows:

$$v_1^+ = v_1^- - \frac{1}{m_1}\tau_2^f \tag{31}$$

$$v_2^+ = v_2^* - \frac{\tau_3^f - \alpha_{2,3}\tau_2^f}{m_2} \tag{32}$$

$$v_3^+ = v_3^- + \frac{1}{m_3}\tau_3^f. \tag{33}$$

We note that the positiveness of the inside of the radical in Eq. (30) can be used to establish an upper bound on the correlation ratio $\alpha_{2,3}$. If we consider $\alpha_{2,3} \leqslant 1$, and impose the two underlying conditions $v_1^- - v_2^- \geqslant 0$ and $v_2^- - v_3^- \geqslant 0$, we can write the upper limit of the correlation ratio as follows:

$$0 \leqslant \alpha_{2,3} \leqslant \frac{m_3}{m_2 + m_3}. \tag{34}$$

Figure 4 depicts the three post-impact velocities for $m_1 = m_2 = m_3 = e_2 = e_3 = v_1^- = 1$ as $\alpha_{2,3}$ is varied in its limiting interval $0 \leqslant \alpha_{2,3} \leqslant 0.5$. We note that the two outcomes that are produced by the solution method of Han and Gilmore [3] corresponds to the two limiting values of the Impulse Correlation Ratio. Our method exposes a spectrum of solutions that bridge the gap between the two limiting outcomes. The lower bound corresponds to sequential impacts while the upper limit represents simultaneous time of compression at two contacts. By specifying the value of the Impulse Correlation Ratio, one can obtain a unique solution for the problem. The question of the validity of the ratio as a material constant remains to be answered. In the latter part of this section we will present the results of an experimental study that addresses this issue.

2.4 Multiple Impacts. To explain the multiple impacts that may arise during the present problem, we consider a specific example that leads to the velocity impulse diagrams that are depicted in Fig. 5. The example corresponds to a three-ball case with initial velocities of $v_1^- = 1$ m/s, $v_2^- = 0.8$ m/s, and $v_3^- = 0$ m/s. At the onset of the collision, we have the ball B_2 having simultaneous impacts with B_1 and B_3. The first B_1-B_2 collision takes place during the impulse intervals $0 \leqslant \tau_2 \leqslant \tau_{2,1}^f$ $(0 \leqslant \tau_3 \leqslant \tau_{3,1}^* = \alpha_{2,3}\tau_{2,1}^f)$. Meanwhile, the first B_2-B_3 collision takes place during the impulse intervals $0 \leqslant \tau_2 \leqslant \tau_{2,1}^*$ $(0 \leqslant \tau_3 \leqslant \tau_{3,1}^f)$. When the B_1-B_2 impact ends, the velocity of B_2 continues to decrease as result of the continuing collision between B_2 and B_3 during the

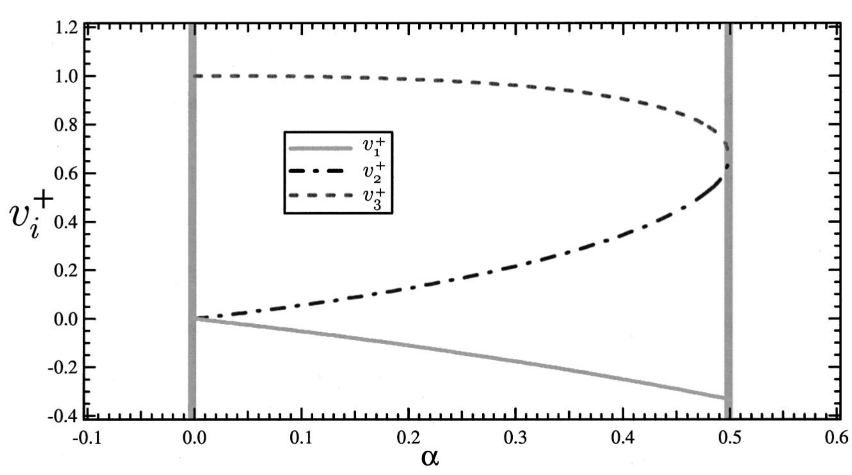

Fig. 4 Effect of α on the post impact velocities

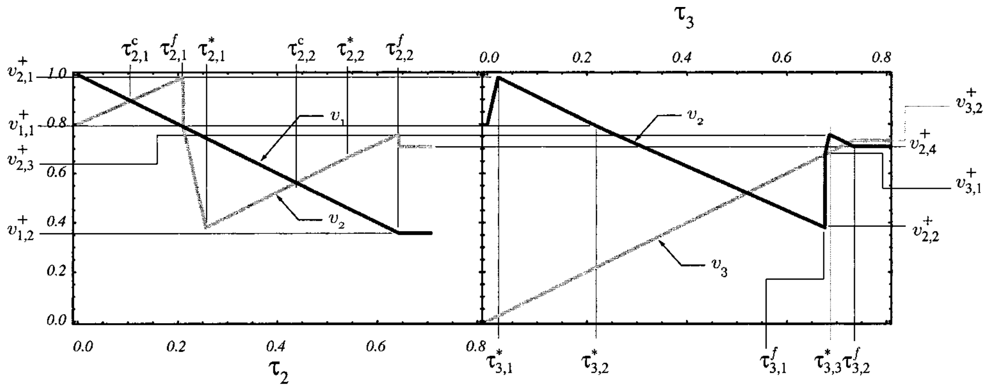

Fig. 5 Multiple impacts on the velocity-impulse diagram

interval $\tau^*_{3,1} \leqslant \tau_3 \leqslant \tau^*_{3,2}$. The decrease in v_2 during this interval can be observed as the sudden change in the velocity on the diagram that corresponds to τ_2. This is true because during this interval B_1 and B_2 do not interact, and thus the impulse τ_2 between these balls remains constant. Subsequently, the slowdown in the velocity v_2 initiates a backward impact between B_1 and B_2 when $v_2 = v_1 = v^+_{1,1}$ at $\tau_3 = \tau^*_{3,2}$. During the next interval $\tau^f_{2,1} \leqslant \tau_2 \leqslant \tau^*_{2,1}$ ($\tau^*_{3,2} \leqslant \tau_3 \leqslant \tau^f_{3,1}$) we have simultaneous collisions between B_1-B_2 and B_2-B_3. Next, the first B_2-B_3 collision ends at $\tau_2 = \tau^*_{2,1}$ ($\tau_3 = \tau^f_{3,1}$). But, when this collision ends the velocity of B_2 continues to increase as a result of the collisions between B_1 and B_2. Once again, the increase in this velocity can be observed as the vertical jump at $\tau_3 = \tau^f_{3,1}$ on the τ_3 diagram. Subsequently, the increase in v_2 leads to a forward collision between B_2 and B_3 at $v_2 = v_3 = v^+_{3,1}$ and $\tau_2 = \tau^*_{2,2}$. Then, we have simultaneous B_1-B_2,B_2-B_3 impacts during the impulse interval $\tau^*_{2,2} \leqslant \tau_2 \leqslant \tau^f_{2,2}$ ($\tau^f_{3,1} \leqslant \tau_3 \leqslant \tau^*_{3,3}$). Finally, the B_2-B_3 collision continues during the interval $\tau^*_{3,3} \leqslant \tau_3 \leqslant \tau^f_{3,2}$, which is also reflected as the sudden jump in v_2 on the τ_2 diagram. The overall process ends at $\tau_2 = \tau^f_{2,2}$ ($\tau_3 = \tau^f_{3,2}$) since $v^+_{2,4} < v^+_{1,2}$.

Now, using the Impulse Correlation Ratio according to the rules that were enumerated in Section 2.2 along with Eqs. (1), (2), and (3) we may express the velocities as follows:

$$v_1 = \begin{cases} v_1^- - \tau_2/m_1 & \text{if } 0 \geqslant \tau_2 < \tau^f_{2,2} \\ v^+_{1,2} & \text{if } \tau_2 \geqslant \tau^f_{2,2} \end{cases} \tag{35}$$

$$v_2 = \begin{cases} v_2^- + (1-\alpha_{2,3})\dfrac{\tau_2}{m_2} & \text{if } 0 \leqslant \tau_2 < \tau^f_{2,1} \\ v^+_{1,1} + \left(1 - \dfrac{1}{\alpha_{3,2}}\right)\dfrac{\tau_2 - \tau^f_{2,1}}{m_2} & \text{if } \tau^f_{2,1} \leqslant \tau_2 \leqslant \tau^*_{2,1} \\ v^+_{2,2} + \dfrac{\tau_2 - \tau^*_{2,1}}{m_2} & \text{if } \tau^*_{2,1} \leqslant \tau_2 \leqslant \tau^*_{2,2} \\ v^+_{3,1} + \dfrac{\tau_2 - \tau^*_{2,2}}{m_2} & \text{if } \tau^*_{2,2} \leqslant \tau_2 < \tau^f_{2,2} \\ v^+_{2,4} & \text{if } \tau_2 \geqslant \tau^f_{2,2} \end{cases} \tag{36}$$

$$v_2 = \begin{cases} v_2^- + \left(\dfrac{1}{\alpha_{2,3}} - 1\right)\dfrac{\tau_3}{m_2} & \text{if } 0 \leqslant \tau_3 \leqslant \tau^*_{3,1} \\ v^+_{2,1} - \dfrac{\tau_3 - \tau^*_{3,1}}{m_2} & \text{if } \tau^*_{3,1} \leqslant \tau_3 \leqslant \tau^*_{3,2} \\ v^+_{1,1} + (\alpha_{3,2} - 1)\dfrac{\tau_3 - \tau^*_{3,2}}{m_2} & \text{if } \tau^*_{3,2} \leqslant \tau_3 < \tau^f_{3,1} \\ v^+_{3,1} + \left(\dfrac{1}{\alpha_{2,3}} - 1\right)\dfrac{\tau_3 - \tau^f_{3,1}}{m_2} & \text{if } \tau^f_{3,1} \leqslant \tau_3 < \tau^*_{3,3} \\ v^+_{2,3} - \dfrac{\tau_3 - \tau^*_{3,3}}{m_2} & \text{if } \tau^*_{3,3} \leqslant \tau_3 < \tau^f_{3,2} \\ v^+_{2,4} & \text{if } \tau_3 \geqslant \tau^f_{3,2} \end{cases} \tag{37}$$

$$v_3 = \begin{cases} v_3^- + \tau_3/m_3 & \text{if } 0 \leqslant \tau_3 < \tau^f_{3,2} \\ v^+_{3,2} & \text{if } \tau_3 \geqslant \tau^f_{3,2} \end{cases}. \tag{38}$$

The specific computation of final impulses is carried out using the energetic definition of the coefficient of restitution. The respective final impulses and velocities can be found by sequentially solving the following equations for $\tau^f_{2,1}, \tau^f_{3,1}, \tau^f_{2,2}, \tau^f_{3,2}$:

$$e_2^2 \int_0^{\tau^c_{2,1}} (v_1 - v_2)\, d\tau_2 + \int_{\tau^c_{2,1}}^{\tau^f_{2,1}} (v_1 - v_2)\, d\tau_2 = 0 \tag{39}$$

$$e_3^2 \int_0^{\tau^c_{3,1}} (v_2 - v_3)\, d\tau_3 + \int_{\tau^c_{3,1}}^{\tau^f_{3,1}} (v_2 - v_3)\, d\tau_3 = 0 \tag{40}$$

$$e_2^2 \int_{\tau^f_{2,1}}^{\tau^c_{2,2}} (v_1 - v_2)\, d\tau_2 + \int_{\tau^c_{2,2}}^{\tau^f_{2,2}} (v_1 - v_2)\, d\tau_2 = 0 \tag{41}$$

$$e_3^2 \int_{\tau^f_{3,1}}^{\tau^c_{3,2}} (v_2 - v_3)\, d\tau_3 + \int_{\tau^c_{3,2}}^{\tau^f_{3,2}} (v_2 - v_3)\, d\tau_3 = 0 \tag{42}$$

where $\tau^c_{2,1}$, $\tau^c_{2,2}$, $\tau^c_{3,1}$, and $\tau^c_{3,2}$ are the maximum compression impulses as shown in Fig. 5. It should be obvious from this example that one may have to go through a complex set of computations in order to solve even this simple example. For this purpose, we have written a computer program using the software package Mathematica that automatically performs the computations required to compute the final impulses, the maximum compression impulses, etc.

2.5. Post-Impact Bouncing Patterns of a Three-Ball Cradle Having developed our solution method, now we study the effect of various parameters on the possible bouncing patterns that can

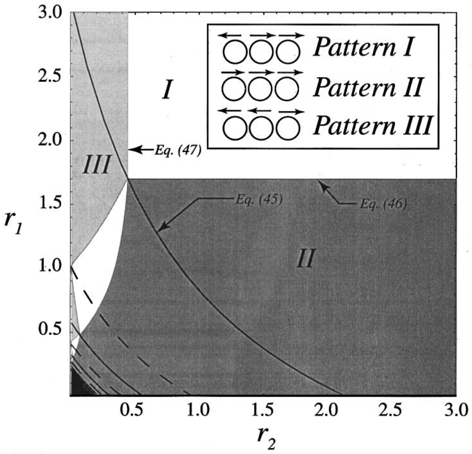

Fig. 6 Bouncing pattern regions on the $r_1 - r_2$ plane

be exhibited by the three-ball case. Here, we let $v_2^- = v_3^- = 0$, and used $\alpha_{2,3} = \alpha_{3,2} = \alpha_2 = 0.15$, $e_2 = e_3 = 0.5$ in order to obtain the regions in Fig. 6. Yet, we should point out that the regions would be qualitatively preserved if one chooses to use different values of impulse correlation ratio and coefficients of restitution.

Now, we divide the post-impact patterns according to occurrence of multiple collisions. Multiple collisions exist if we have at least one back impact between B_2 and B_1. This occurs if $v_1^+ = v_2$ during the B_2-B_3 impact. The impulse condition that would lead to this situation can be obtained by setting $v_1^+ = v_2$ and solving for τ_3, which yields

$$\tau_{3,1}^* = \frac{m_2(\alpha_2 m_1 + e_2(m_1 + m_2))v_1^-}{(1-\alpha_2)m_1 + m_2}. \tag{43}$$

Multiple impacts take place only when $\alpha_2 \tau_{2,1}^f \leqslant \tau_{3,1}^* \leqslant \tau_{3,1}^f$, which leads to the following condition:

$$r_1 \leqslant \frac{(1+e_2)(1+e_3\sqrt{1-\alpha_2(1+r_2)})}{e_2(1+r_2)} - \left(1 + \frac{\alpha_2}{e_2}\right) \tag{44}$$

where $r_1 = m_2/m_1$ and $r_2 = m_2/m_3$. Thus, we may divide the $r_1 - r_2$ plane into two regions that are below and above the uppermost curve shown in Fig. 6. The region above this curve is the distinct collision area, while in the lower region we have at least one back impact. We may continue in the same fashion to obtain the boundary for the region where we have at least one forward impact between B_2 and B_3 as a result of the back impact between B_2 and B_1. We obtain a condition for the forward impact in a similar manner to the one we obtained Eq. (44). This results in the dashed curve that is situated below the topmost curve. Then, we can continue in the same manner to obtain further alternating boundaries that lead to more pairs of back and forward impacts.

We may also partition the $r_1 - r_2$ plane into three regions that correspond to post-impact velocity directions. Each of these regions corresponds to a unique post-impact bouncing pattern (see Fig. 6). The expression for the line that separates regions *I* and *II* in the distinct-collision region can be obtained by setting v_1^+ in Eq. (31) equal to zero and solving for r_1 as

$$r_1 = \frac{1-\alpha_2}{e_2}. \tag{45}$$

The line that separates regions *I* and *III* in the distinct-collision region can be obtained by setting v_2^+ in Eq. (32) equal to zero and solving for r_2 as

$$r_2 = e_3\sqrt{1-\alpha_2 + (\tfrac{1}{2}\alpha_2 e_3)^2} - \tfrac{1}{2}\alpha_2 e_3^2. \tag{46}$$

We may obtain similar partitioning in the multiple collisions zones by setting respective velocity pairs equal to one another and obtaining conditions.

Figure 6 depicts all possible solutions and demonstrates the consistency and uniqueness of the solutions that are obtained by the method proposed in this chapter. One particularly interesting region of the parameter plane is the lower left corner where we have a dense set of multiple collisions. This region corresponds to configurations where the middle ball (B_2) is significantly lighter than the other two balls. Figure 7 depicts the impulse velocity diagrams of a three-ball cradle with $v_1^- = 1$ m/s, $e_2 = e_3 = 1$, $\alpha_2 = 0.15$, and $r_1 = r_2 = 0.01$. The post-impact velocities computed for this case are $v_1^+ = -0.003$ m/s, $v_2^+ = 0.348$ m/s, and $v_3^+ = 0.999$ m/s. In this example, we have a very small central ball and two very large peripheral balls. If we have neglected the central ball then the resulting post-impact velocities of the large balls would have been 0 and 1 m/s, respectively. The presence of the central ball does not effect this outcome, yet it introduces several microcollisions that transmit the momentum from the incident large ball to the other. As the central ball becomes smaller we may expect more multiple collisions to arise, which is why we see a dense region of separator curves in the lower left of Fig. 6.

3 A General Solution Method for the *N*-Ball Case

The system under consideration consists of *N* balls of given masses m_i. The last *N*-1 balls are arranged in a chain such that all consecutive pairs of balls are in contact. One ball strikes one end of the chain with a nonzero pre-impact velocity of v_1^-, while the other balls are in contact with ($v_i^- \geqslant v_{i+1}^-$ for $i = 2,N$). As in the previous section, our objective is to determine the post-impact velocities v_i^+ of the balls.

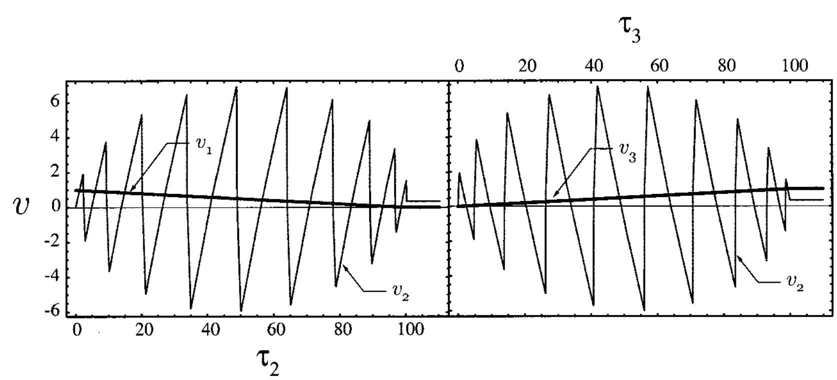

Fig. 7 Velocity-impulse diagram of a small center-ball example

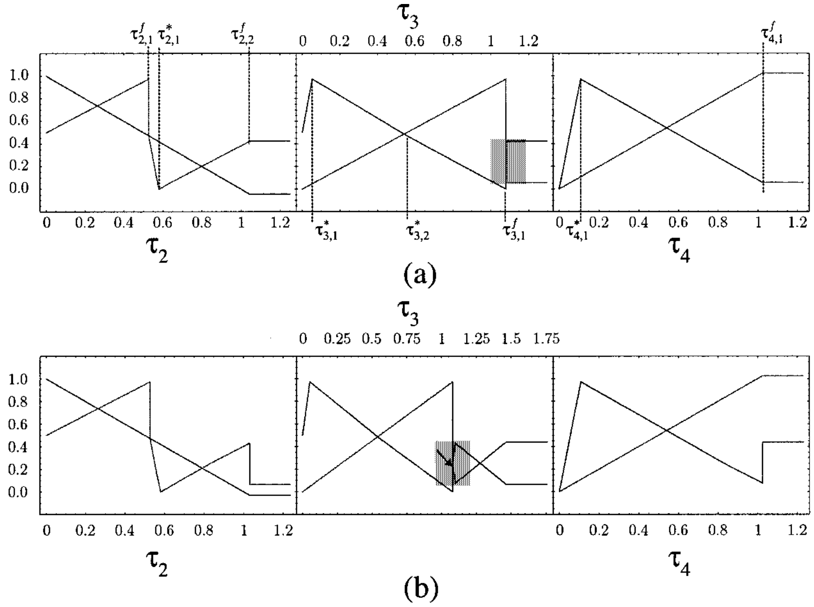

Fig. 8 Intermittent collisions

3.1 Generalization of the Three-Ball Approach to *N*-Balls We start by writing the conservation of momentum equations for a ball B_i, which yields the following N equations:

$$m_i \Delta v_i = \Delta \tau_i - \Delta \tau_{i+1} \quad \text{for} \quad i = 1,N \tag{47}$$

with

$$\Delta \tau_1 = \Delta \tau_{N+1} = 0 \tag{48}$$

where, Δv_i and $\Delta \tau_i$ are the changes in velocities and impulses as a result of the collision. The Impulse Correlation Ratios for each ball B_i can be used to obtain additional $N-2$ equations in the following form:

$$\Delta \tau_i = \begin{cases} \alpha_{i-1,i} \Delta \tau_{i-1} & \text{for} \quad i \in \mathcal{I}_f \subseteq \{1,\ldots,m_f\} \\ \alpha_{i+1,i} \Delta_{i+1} & \text{for} \quad i \in \mathcal{I}_b \subseteq \{1,\ldots,m_b\} \end{cases} \tag{49}$$

where $\mathcal{I}_f$ and $\mathcal{I}_b$ are index sets that represent the triplets of balls undergoing simultaneous collisions in the direction of increasing and decreasing ball indices, respectively. Solving for Δv_i yields solutions of the form

$$\Delta v_1 = -\frac{1}{m_1} \Delta \tau_2 \tag{50}$$

$$\Delta v_i = \begin{cases} \dfrac{1-\alpha_{i-1,i}}{m_i} \Delta \tau_i = \dfrac{1-\alpha_{i-1,i}}{\alpha_{i-1,i} m_i} \Delta \tau_{i+1} & \text{for} \quad i \in \mathcal{I}_f \subseteq \{1,\ldots,m_f\} \\ \dfrac{\alpha_{i+1,i}-1}{\alpha_{i+1,i} m_i} \Delta \tau_i = \dfrac{\alpha_{i+1,i}-1}{m_i} \Delta \tau_{i+1} & \text{for} \quad i \in \mathcal{I}_b \subseteq \{1,\ldots,m_b\} \end{cases} \tag{51}$$

$$\Delta v_N = \frac{1}{m_N} \Delta \tau_N. \tag{52}$$

The next step in solving the impact problem is to proceed as we have done for the three-ball case. That is, the velocities should be tracked on the impulse diagrams. The points where the balls lose and reestablish contact should be calculated and the related impulse expressions should be adjusted properly. As we have mentioned in the three-ball case, this is a very complex procedure and we have developed a Mathematica package that will automatically set up the calculations for N number of balls.

Finally, a symbolic analysis of the velocity outcomes similar to the three-ball case yields the following bounds on the Impulse Correlation Ratios for the N-ball case:

$$0 \leqslant \alpha_{i-1,i} \leqslant \frac{m_{i+1}}{m_{i+1} + m_i(1-\alpha_{i,i+1})}$$
$$\text{for} \quad i = 2,N-1 \quad \text{with} \quad \alpha_{N-1,N} = 0. \tag{53}$$

3.2 Intermittent Collisions. There is a special situation that may arise during collisions for chains with $N \geqslant 4$. Figure 8 depicts a 4-ball collision with $m_1 = m_2 = m_3 = m_4 = e_2 = e_3 = e_4 = 1$, $\alpha_2 = \alpha_3 = 0.1$, and initial velocities of $v_1 = 1$, $v_2 = 0.5$, $v_3 = v_4 = 0$ m/s. At the onset of the impact we have simultaneous collisions at all three contact points. The first B_1-B_2 collision takes place during the impulse intervals $0 \leqslant \tau_2 \leqslant \tau^f_{2,1} (0 \leqslant \tau_3 \leqslant \tau^*_{3,1})$. Meanwhile, the first B_2-B_3 and B_3-B_4 collisions occur during $0 \leqslant \tau_3 \leqslant \tau^f_{3,1}$ $(0 \leqslant \tau_4 \leqslant \tau^*_{4,1})$ and $0 \leqslant \tau_4 \leqslant \tau^f_{4,1}$, respectively. Yet, the continuing B_2-B_3 impact leads to a second B_1-B_2 collision that causes the slope change at $\tau^*_{3,2}$ on the τ_3 diagram. The special case arises when the B_2-B_3 impact ends at $\tau^f_{3,1}$. At this point, we encounter an unusual case on the τ_3 diagram (see Fig. 8(*a*)). We observe an upward vertical jump in v_2 due to the continuing second B_1-B_2 collision and downward jump in v_3 caused by the ongoing B_3-B_4 impact. The problem that is encountered here is to determine the point where we have the onset of the second B_2-B_3 impact. If we continue the B_1-B_2 and B_3-B_4 collisions by ignoring the possible contact between B_2-B_3 we obtain the shaded region that is shown in Fig. 8(*a*). The onset of the second B_2-B_3 collision will be somewhere in the shaded region where the two velocities overlap. When this situation arises, we assume that the two balls meet in the midpoint of the overlap region. This assumption leads to the final diagrams that are depicted in Fig. 8(*b*).

4 Experiments

4.1 The Experimental Setup. The objective of the present study was to analyze multiple impacts in a multibody system for the nonfrictional case. For this purpose the classical collision experiment known as Newton's Cradle was set up (see Fig. 9). Various chains with three to six balls of different masses and materials were arranged by suspending each ball from a frame using two

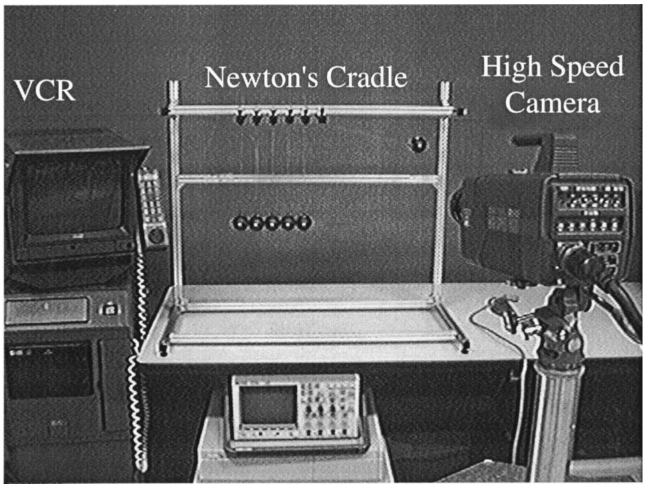

Fig. 9 The experimental set-up

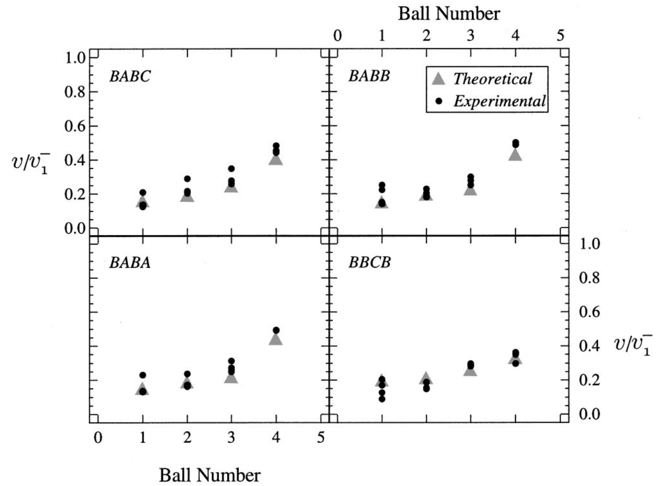

Fig. 10 Velocity predictions in four ball experiments

threads. The strings are attached to the frame through sliding guides to ensure properly aligned balls before impact. Proper alignment of the mass centers ensured the elimination of the rotation of the balls and tangential forces at the points of impact. A chain of central impacts was generated by releasing the first ball in the chain from a predetermined elevation.

The experimental data was captured by using a high-speed video system capable of 1000 frames per second. Retro-reflective markers were used to mark the mass center of each ball. The relative positions of the balls before and after the impact were determined with respect to a fixed marker, used as reference. The acquired video images were transferred to a personal computer, where a specialized program was used to digitize the markers positions. The digitized positions were used to compute the dropping height of the first ball and the maximum post impact heights attained by each ball. Finally, the pre-impact velocity of the first ball and post-impact velocities of all balls were computed from the calculated heights. The experiments were conducted using three types of balls, designated as A, B, C, and D. The masses of the A, B, and C balls were 45, 53, 53, and 166 grams, respectively. An initial set of experiments with pairs of balls were conducted to determine the coefficients of restitution that are presented in Table 1.

Table 1 Coefficients of restitution

Ball Type	A	B	C	D
A	0.97	0.53	0.31	0.94
B	0.53	0.36	0.28	0.38
C	0.31	0.28	0.27	0.3
D	0.94	0.38	0.3	0.85

4.2 Experimental Verification of the Impulse Correlation Ratio. The hypothesis of the Impulse Correlation Ratio is based on the fact that it is a constant which depends on the material and geometric properties of triplet of balls in contact. To check this hypothesis, we first determined the Impulse Correlation Ratios for all possible combinations of the three balls arranged in triplets. For this purpose, 27 experiments were conducted. Each experiment involved a chain of three balls. The analytical algorithm and the coefficients of restitution in Table 1 were used to compute the impulse correlation ratios that produced the best fit to the experimentally acquired post-impact velocities. The resulting impulse correlation ratios are listed in Table 2.

Now, to test the hypothesis, we conducted ten sets of experiments: five with four-ball, three with five-ball, and two with six-ball sequences. Each set of experiments included four individual experiments with four incident velocities of the first ball. The drop height of the first ball was adjusted such that we would have approximately 0.5, 1.0, 1.5, and 2.0 m/s pre-impact velocities v_1^-. Next, we used the proposed analytical procedure and the experimental values listed in Tables 1 and 2 to compute the post impact velocities.

Figures 10, 11, and 12 depict the experimental results. The figures depict the results of eight sets of experiments conducted

Table 2 Experimental impulse correlation ratios

Sequence	ICR	Sequence	ICR	Sequence	ICR	Sequence	ICR
AAA	0.167	AAB	0.232	AAC	0.218	AAD	0.131
BAA	0.374	BAB	0.296	BAC	0.088	BAD	0.050
CAA	0.495	CAB	0.499	CAC	0.400	CAD	0.129
DAA	0.215	DAB	0.090	DAC	0.101	DAD	0.782
ABA	0.127	ABB	0.104	ABC	0.111	ABD	0.600
BBA	0.340	BBB	0.310	BBC	0.216	BBD	0.390
CBA	0.435	CBB	0.455	CBC	0.342	CBD	0.390
DBA	0.416	DBB	0.710	DBC	0.755	DBD	0.730
ACA	0.262	ACB	0.268	ACC	0.216	ACD	0.664
BCA	0.389	BCB	0.408	BCC	0.319	BCD	0.731
CCA	0.462	CCB	0.414	CCC	0.338	CCD	0.744
DCA	0.430	DCB	0.449	DCC	0.441	DCD	0.744
ADA	0.101	ADB	0.055	ADC	0.001	ADD	0.329
BDA	0.041	BDB	0.046	BDC	0.001	BDD	0.446
CDA	0.196	CDB	0.171	CDC	0.122	CDD	0.495
DDA	0.056	DDB	0.058	DDC	0.001	DDD	0.080

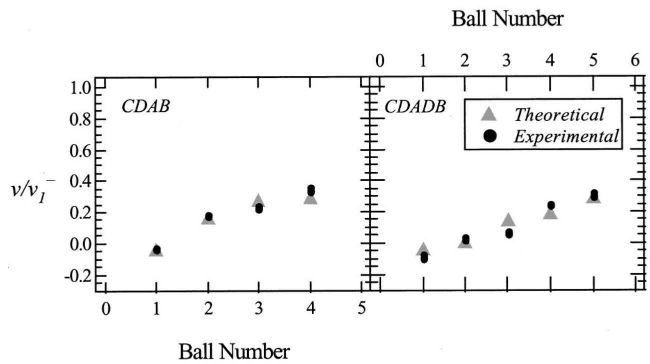

Fig. 11 Velocity predictions in sequences with the heavy balls

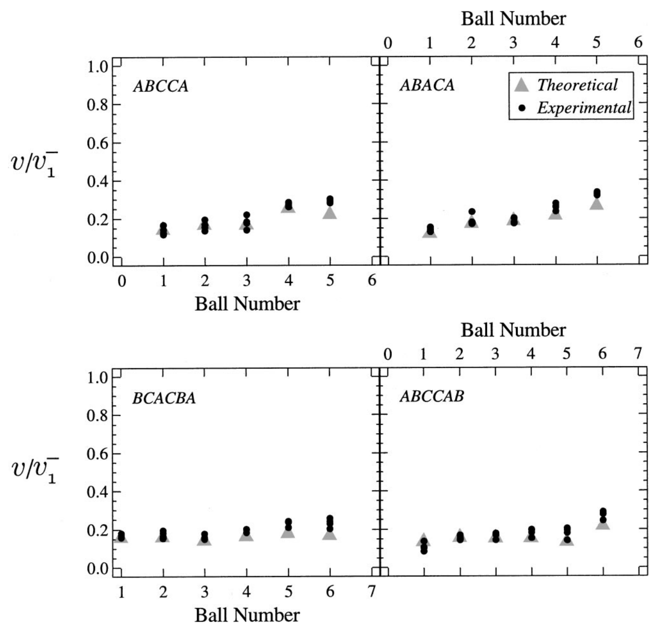

Fig. 12 Velocity predictions in five and six ball experiments

with a specific sequence of balls as shown on individual graphs. The results clearly demonstrate that the theoretical outcomes are in agreement with the experimental results.

5 Discussion and Conclusion

In this paper we develop a new method that produces a unique and energetically consistent solution to the *N*-Ball linear chain problem. The method is based on the impulse-momentum methods, the energetic coefficient of restitution, and the Impulse Correlation Ratio that is introduced the first time in this paper.

Multi-impact problems pose many difficulties and unanswered questions. The simplest of these problems, the linear chain or the Newton's Cradle, represents the simplest and the most basic problem of this type. The dynamic problem is simple because one only has to deal with motion of particles, yet it includes the difficulties that are encountered in more complex systems. The solution of the multi-impact problem has been confounded by the lack of sufficient means in the rigid-body impact theory to resolve the collisions of stationary bodies that are in contact. This shortcoming manifested itself as the nonuniqueness of solutions obtained using the theory.

Here, we amended the rigid-body theory by introducing the Impulse Correlation Ratio. This constant serves as a mechanism to coordinate the force transmission through the chain. Effective use of the energetic coefficient of restitution leads to energetically consistent results. Moreover, the method is the only one we know of that captures the commonly observed grouping of balls through the proposed back-propagation process.

Finally, we conducted a set of experiments to verify the proposed theoretical methods and procedures. We have shown that the Impulse Transmission Ratio can be measured with relative ease. We have also demonstrated that the predictions of our method produces excellent agreement with the experimentally measured outcomes.

Acknowledgment

The authors express their appreciation to Dr. Bernard Brogliato (Laboratoire d'Automatique de Grenoble) for his valuable discussions and suggestions that contributed to the completeness of the paper.

References

[1] Marghitu, D. B., and Hurmuzlu, Y., 1995, ''Three-Dimensional Rigid-Body Collisions With Multiple Contact Points,'' ASME J. Appl. Mech., **62**, pp. 725–732.
[2] Johnson, W., 1976, ''Simple Linear Impact,'' ImechE. IJMEE, **4**, No. 2, pp. 167–181.
[3] Han, I., and Gilmore, B. J., 1993, ''Multi-Body Impact Motion With Friction—Analysis, Simulation, and Experimental Validation,'' ASME J. Mech. Des., **115**, pp. 412–422.
[4] Brogliato, B., 1996, *Nonsmooth Impact Mechanics: Models, Dynamics and Control*, Springer-Verlag, New York, LNCIS 220.
[5] Smith, E. A. L., 1955, ''Impact and Longitudinal Wave Transmission,'' Trans. ASME, **77**, pp. 963–973.
[6] Walkiewicz, T. A., and Newby, N. D., Jr., 1972, ''Linear Collisions,'' Am. J. Phys., **40**, pp. 133–137.
[7] Newby, N. D., Jr., 1979, ''Linear Collisions With Harmonic Oscillator Forces: The Inverse Scattering Problem,'' Am. J. Phys., **47**, No. 2, pp. 161–165.
[8] Hinch, E. J., and Saint-Jean, S., 1999, ''The Fragmentation of a Line of Balls by an Impact,'' Proc. R. Soc. London, Ser. A, **455**, pp. 3201–3220.
[9] Cholet, C., 1998, ''Chocs de Solids Rigid,'' Ph.D. thesis, University of Paris 6 and LCPC-CNRS.
[10] Moreau, J. J., 1994, ''Some Numerical Methods in Multibody Dynamics: Application to Granular Materials,'' Eur. J. Mech. A/Solids, **13**, No. 4, pp. 93–114.
[11] Fremond, M., 1995, ''Rigid Bodies Collisions,'' Phys. Lett. A, **204**, pp. 33–41.
[12] Stronge, W. J., 1990, ''Rigid Body Collisions with Friction,'' Proc. R. Soc. London, Ser. A, **431**, pp. 169–181.

Dynamic Crack Analysis Under Coupled Thermoelastic Assumption

P. Hosseini-Tehrani

M. R. Eslami
Fellow ASME

H. R. Daghyani

Mechanics Department,
Amirkabir University of Technology,
Hafez Avenue No. 424,
Tehran, Iran

A boundary element method using Laplace transform in time domain is developed for the analysis of fracture mechanic under coupled thermoelastic assumption. The transient coupled thermoelastic field is solved without need for domain discretization. The singular behavior of the temperature and displacement fields in the vicinity of the crack tip is modeled by quarter-point elements. Thermal dynamic stress intensity factors for mode I are evaluated from computed nodal values, using the well-known displacement and traction formulas. The accuracy of the method is investigated through comparison of the results with the available data in literature. The conditions where the inertia term plays an important role is discussed and variations of the dynamic stress intensity factor is investigated. [DOI: 10.1115/1.1364490]

1 Introduction

In many practical engineering applications, severe thermal shock is the dominating load on the structure. When this type of load is applied into a structure in the presence of a crack, the results may be catastrophic. In these cases, where the order of magnitude of the thermomechanical coupling parameter is significant, the coupling with energy equation must be taken into account. The initiation of rapid crack growth, the path and speed of the propagation, crack branching, and arrest are of particular interest in dynamic fracture mechanics. They are controlled by the dynamic stress intensity factors.

Just now there is no report on the evaluation of the dynamic stress intensity factor for thermal shock problems with the coupled thermoelastic assumption with the inertia term. The previous works are limited to evaluation of the stress intensity factor and/or the thermal shock stress intensity factor for transient or coupled thermoelasticity problems where the inertia term is ignored.

In the classical study of thermoelastic crack problems, the theoretical solutions are available only for very few problems in which cracks are contained in infinite media under special thermal loading conditions, such as in the work of Sih [1] and Kassir and Bergman [2]. For cracked bodies of finite dimensions, exact solutions are impossible to obtain. Wilson and Yu [3] employed the finite element method to deal with these problems. The method is combined with the modified *J*-integral theory proposed by Wilson and Yu [3]. The other prevailing methods employed by Nied [4] and Chen and Weng [5] is based on the concept of principle superposition. That is, in the absence of a crack, the thermal loading is replaced by a traction force, which is equivalent to the internal force at the prospective crack face. Lee and Sim [6] solved the problem of a surface cracked infinite strip under sudden conductive cooling and evaluated the mode I thermal shock stress intensity factor using Bueckner's weight function method. Rizk [7] analyzed the same problem with heating instead of cooling, under which crack closure occurs. Raveenda et al. [8] used a sub region technique to solve thermally loaded crack problems using a boundary only formulation. Portela et al. [9] presented a formulation called the dual boundary element method which facilitates the analysis of arbitrary crack problems in a single region. This method was later extended to steady-state and uncoupled transient thermoelasticity problems by Pasad et al.[10,11] Chen and Weng [5] developed a general finite element model dealing with the coupled transient thermoelastic problems of fracture in an edge-cracked plate, without considering the inertia term. Katsareas et al. [12] used a boundary-only element method to compute shock stress intensity factors for a surface cracked infinite strip and a finite edge cracked plate. They considered uncoupled quasi-static thermoelasticity.

This paper presents a boundary element formulation for the crack analysis under the coupled thermoelastic assumption. An isotropic and homogeneous material in two-dimensional plain-strain geometry with an initial edge crack on its boundary is considered. The body is exposed to a thermal shock on its boundary and the resulting thermal stress waves are investigated through the coupled thermoelastic equations. Due to the short time interval of the imposed thermal shock, the Laplace transforms method is employed to model the time variable in the boundary element formulation. The discretized forms of the equations are obtained by the approximation of boundary variations by quadratic elements, and the quarter-point singular element is used at the crack tip. The present approach is used to evaluate the thermal dynamic stress intensity factor at the first opening crack mode. An infinite strip with a crack on its surface under sudden cooling is considered. The thermal dynamic stress intensity factor is computed from crack-opening displacement of a quarter-point element, considering the one-point and two-point displacement formulas. For thermal shock loading the time-dependent thermal dynamic stress intensity factor is obtained using the Durbin method. The results are compared with the available quasi-static results.

Governing Equations

A homogeneous isotropic thermoelastic solid is considered. In the absence of body forces and heat generation, the governing equations for the dynamic coupled thermoelasticity in dimensionless form may be written as

$$\frac{\mu}{\lambda+2\mu}u_{i,jj}+\frac{\lambda+\mu}{\lambda+2\mu}u_{j,ij}-T_i-\ddot{u}_i=0 \tag{1}$$

Contributed by the Applied Mechanics Division of THE AMERICAN SOCIETY OF MECHANICAL ENGINEERS for publication in the ASME JOURNAL OF APPLIED MECHANICS. Manuscript received by the ASME Applied Mechanics Division, Oct. 7, 1999; final revision, Sept. 19, 2000. Associate Editor: A. K. Mal. Discussion on the paper should be addressed to the Editor, Professor Lewis T. Wheeler, Department of Mechanical Engineering, University of Houston, Houston, TX 77204-4792, and will be accepted until four months after final publication of the paper itself in the ASME JOURNAL OF APPLIED MECHANICS.

$$T_{,ii}-\dot{T}-\frac{T_0\gamma^2}{\rho c_\epsilon(\lambda+2\mu)}\dot{u}_{j,j}=0 \tag{2}$$

where a dot indicates time differentiation and the subscript i after a comma refers to partial differentiation with respect to $x_i(i=1,2)$, and λ, μ, u_i, ρ, T, T_0, k, γ, and c_ϵ are Lame's constant, the components of displacement vector, mass density, absolute temperature, reference temperature, thermal conductivity, stress-temperature modulus, and specific heat at constant strain, respectively. The dimensionless variables are defined as

$$\begin{aligned}\hat{x}&=\frac{x}{\alpha}; \quad \hat{t}=\frac{tC_1}{\alpha}\;\hat{\sigma}_{ij}=\frac{\sigma_{ij}}{\gamma T_0}\\ \hat{u}_i&=\frac{(\lambda+2\mu)u_i}{\alpha\cdot\gamma\cdot T_0}; \quad T=\frac{T-T_0}{T_0}.\end{aligned} \tag{3}$$

Here, $\alpha=k/\rho c_\epsilon C_1$ is the dimensionless unit length and $C_1=\sqrt{(\lambda+2\mu)/\rho}$ is the velocity of the longitudinal wave stress propagation. The *hat* is dropped from the terms of Eqs. (1) and (2) for convenience. Transfering Eqs. (1) and (2) into the Laplace domain with respect to time yields

$$\frac{\mu}{\lambda+2\mu}u_{i,jj}+\frac{\lambda+\mu}{\lambda+2\mu}u_{j,ij}-T_{,i}-s^2u_i=0 \tag{4}$$

$$T_{,ii}-sT-\frac{T_0\gamma^2}{\rho c_\epsilon(\lambda+2\mu)}su_{j,j}=0. \tag{5}$$

Equations (4) and (5) are rewritten in matrix form as

$$L_{ij}U_j=0. \tag{6}$$

The boundary conditions are assumed to be as follows:

$$\begin{aligned}u_i&=\overline{u_i} \quad \text{on} \quad \Gamma_u\\ \tau_i&=\overline{\tau_i}=\sigma_{ij}n_j \quad \text{on} \quad \Gamma_\tau\\ T&=\overline{T} \quad \text{on} \quad \Gamma_T\\ q&=\overline{q_n}=q_in_i \quad \text{on} \quad \Gamma_q\end{aligned} \tag{7}$$

where $\overline{u}$, $\overline{\tau_i}$, $\overline{T}$, and $\overline{q}$ are the specified displacement, traction, temperature, and heat flux vector on the boundary, respectively.

In order to drive the boundary integral problem, the following weak formulation of the differential equation set (6) for the fundamental solution tensor V^*_{ik} is considered,

$$\int_\Omega (L_{ij}U_j)V^*_{ik}d\Omega=0. \tag{8}$$

After integrating the byparts over the domain and taking a limiting procedure approaching the internal source point to the boundary point, the following boundary integral equation is obtained:

$$\begin{aligned}C_{kj}U_k(y,s)=&\int_\Gamma \tau_\alpha(x,s)V^*_{\alpha j}(x,y,s)-U_\alpha(x,s)\Sigma^*_{\alpha j}(x,y,s)d\Gamma(x)\\ &+\int_\Gamma T_{,n}(x,s)V^*_{3j,n}(x,y,s)\\ &-T(x,s)V^*_{3j,n}(x,y,s)d\Gamma(x)\end{aligned} \tag{9}$$

where $U_\alpha=u_\alpha(\alpha=1,2)$ and $U_3=T$ and C_{kj} denote the shape coefficient tensor. The kernel $\Sigma^*_{\alpha j}$ in (9) is defined by

$$\begin{aligned}\Sigma^*_{\alpha j}=&\left[\left(\frac{\lambda}{\lambda+2\mu}V^*_{kj,k}+\frac{T_0\gamma^2}{\rho c_\epsilon(\lambda+2\mu)}sV^*_{3j}\right)\delta_{\alpha\beta}\right.\\ &\left.+\frac{\mu}{\lambda+2\mu}(V^*_{\alpha j,\beta}+V^*_{\beta j,\alpha})\right]n_\beta.\end{aligned} \tag{10}$$

The detailed mathematical formulations may be found in Hosseini-Tehrani and Eslami [13]. In order to solve numerically the boundary element integral Eq. (9), the standard boundary element procedure may be applied. When transformed numerical solutions are specified, transient solutions may be obtained using an appropriate numerical inversion technique. In this paper, a method presented by Durbin [14] is adopted for the numerical inversion in the time domain.

Evaluation of the Thermal Dynamic Stress Intensity Factor

The stress intensity factor may be determined either from nodal traction or from the crack-opening displacement defined by Kanninen and Popelar [15]:

$$\begin{aligned}K_I&=t_A^2\sqrt{2\pi l}\\ K_{II}&=t_A^1\sqrt{2\pi l}\end{aligned} \tag{11}$$

where K_I and K_{II} are mode I and mode II stress intensity factors, respectively; t_A refers to traction at node A in Fig. 1 (the crack tip), while superscripts 2 and 1 indicate the opening and shearing mode, respectively. The length of the singular element at the crack tip is represented by l.

From the crack-opening displacement shown in Fig. 1, considering two-point displacement on each edge of the crack, the stress intensity factors are given by Blandford et al. [16] as follows:

$$\begin{aligned}K_I&=\frac{\mu}{\alpha+1}\sqrt{\frac{2\pi}{l}}[4(v_B-v_D)+v_E-v_C]\\ K_{II}&=\frac{\mu}{\alpha+1}\sqrt{\frac{2\pi}{l}}[4(u_B-u_D)+u_E-u_C]\end{aligned} \tag{12}$$

where $\alpha=3-4\nu$ for the plane-strain and $(3-\nu)/(1+\nu)$ for the plane stress condition. The points B, C, D, and E are shown in Fig. 1, where $AC=l$ and $AB=l/4$.

For symmetric crack $v_B=-v_D$ and $v_C=-v_E$, and the expression for K_I is simplified to

$$K_I=\frac{2\mu}{\alpha+1}\sqrt{\frac{2\pi}{l}}(4v_B-v_C) \tag{13}$$

$$K_{II}=0. \tag{14}$$

A different formula is obtained if v_B at $r=l/4$ is considered. This formula is [17]

$$K_I=\frac{\mu}{\alpha+1}\sqrt{\frac{2\pi}{l}}v_B \tag{15}$$

$$K_{II}=0. \tag{16}$$

To evaluate K_I, the quarter-point singular element at the crack tip is used.

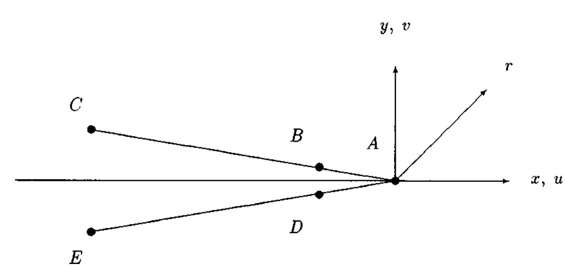

Fig. 1 Element geometries for stress intensity factor computations

Results and Discussion

Structures covered with coatings and lining may be subjected to the severe loading conditions. The load might be applied in the form of mechanical and/or thermal shocks. If the period of shock duration is small enough compared to the first natural frequency, then the solution is found through the coupled field. Consider an infinite strip shown in Fig. 2, initially subjected to a uniform temperature θ_0 with an edge crack perpendicular to its top surface. The strip is rapidly cooled by conduction at its upper surface $x_2 = 0$, whereas the bottom surface $x_2 = W$ is insulated. This is a mode I crack-opening problem. The crack edges are assumed to be thermally insulated. Due to the symmetry about the x_2-axis, only half of the strip is discretized.

To solve the problem by the boundary element method, a proper length-to-width ratio must be defined. Different length-to-width ratios have different effects on the maximum stress intensity factor. Katsareas and Anifantis [12] showed that the ratios of $L/W \geqslant 1$ have a minor effect on the maximum stress intensity factor around the crack tip. Therefore, to select a minimum and reliable solution domain and consequently a minimum number of boundary elements, $L/W = 1$ is selected. The boundary element model is presented in Fig. 2(b), for a crack depth of $\alpha^* = .05$ and $L/W = 1$, where $\alpha^* = \alpha/W$. K_I^* is defined as the dimensionless thermal dynamic stress intensity factor, which for a plain-strain condition is $K_I^* = K_I(1-\upsilon)/[E\sqrt{W}(\theta_0 - \theta_e)]$. Where E is the modulus of elasticity and $t^* = Kt/\rho c W^2$ is the dimensionless time known as the Fourier number.

In all preceding computations the thermal dynamic stress intensity factors are obtained using the one-point displacement formula, and the crack-element length to crack-depth ratio l/α is considered 0.3. The justification for this choice is illustrated in Fig. 3. Many investigators such as Boley and Winer [18] and Jadeja and Loo [19] indicated that the effect of the inertia term becomes more significant only when parameter B_1, the ratio of the characteristic thermal time ($L^2 \rho c_\epsilon / k$) to the characteristic mechanical time (proportional to the natural period of vibration of the structure), becomes small. This is the condition corresponding to the very thin structures. For comparison purposes, B_1 is considered in the order of 10^7, therefore the effect of inertia term is negligible. Figure 4 shows the variation of the stress intensity K_I^* versus t^*. The calculations are carried out for a quarter-point crack-tip element using the uncoupled theory of thermoelasticity. In Fig. 4 the variation of K_I^* versus time derived by the analytical method obtained by Lee and Sim [6] the boundary element method ([2]), and the method described in the present work are compared. The analytical solution of Lee and Sim [6] and the boundary element method solution used by Katsareas and Anifantis [12] are obtained ignoring the inertia term. The analysis of the present work with the assumed B_1 has good agreement with the analytical and boundary element method results. To study the effect of thermomechanical coupling, the variation of K_I^* versus the dimensionless time for different coupling parameters are shown in Fig. 5. As the coupling parameter is increased, the peak value of K_I^* increases. As it is shown in Fig. 6 when the coupling parameter is increased the temperature gradient rises, consequently the crack opening that is a result of the temperature gradient increases. The increase of the coupling parameter, however, causes the peak value of K_I^* to occur at larger time. This is the same result obtained by Chen and Weng [5]. They considered coupled thermoelastic equations without consideration of the inertia term.

Figures 4 and 5 are the plots of K_I^* versus time, but the time scale is selected large enough to compare the results with the known data ($t^* = 1$ is of the order of 10 sec). To see the effect of the inertia term, however, the time scale must be selected small. To observed the effect of the inertia term, $t^* = 1$ must be in the order of 10^{-11} sec, which is equivalent to 400 times $\hat{t} = 1$.

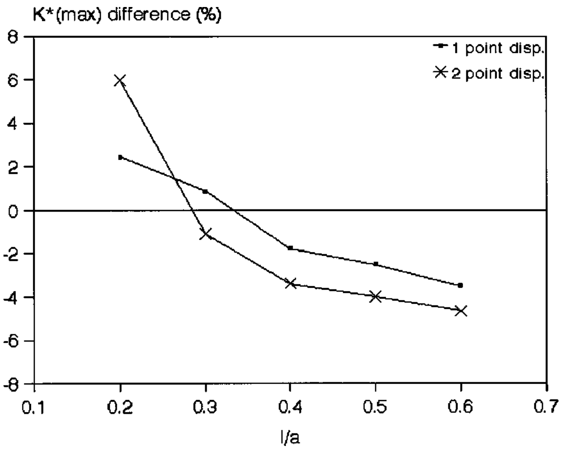

Fig. 3 Effect of crack-element length to crack-depth ratio l/α on accuracy of computed K_I^* peak value

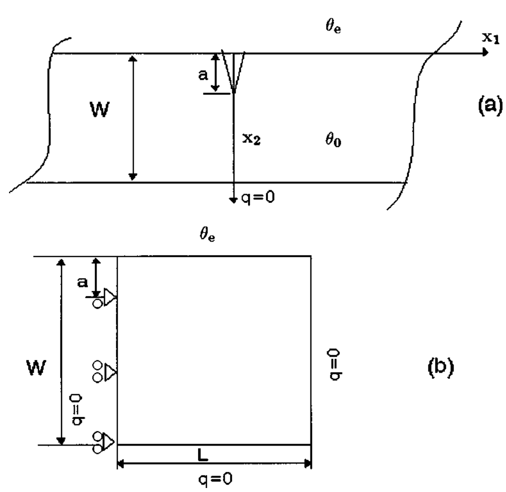

Fig. 2 (a) Cracked strip initially at θ_0, under sudden cooling θ_e, (b) boundary conditions

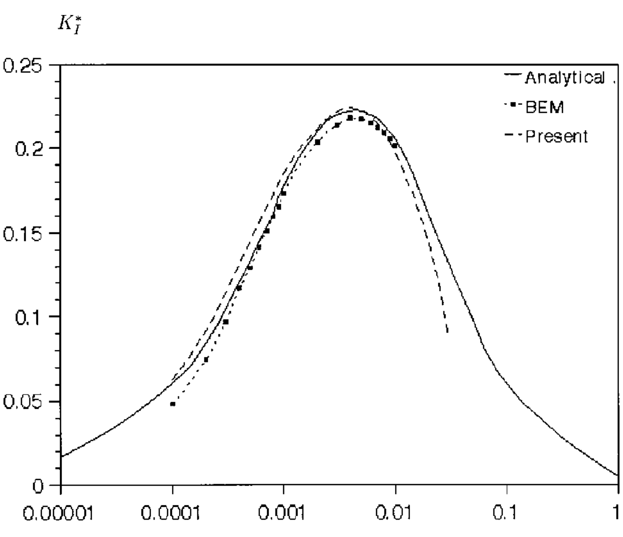

Fig. 4 Comparison of the dimensionless thermal dynamic stress intensity factor K_I^* versus dimensionless time t^*, with analytical and numerical quasi-static results

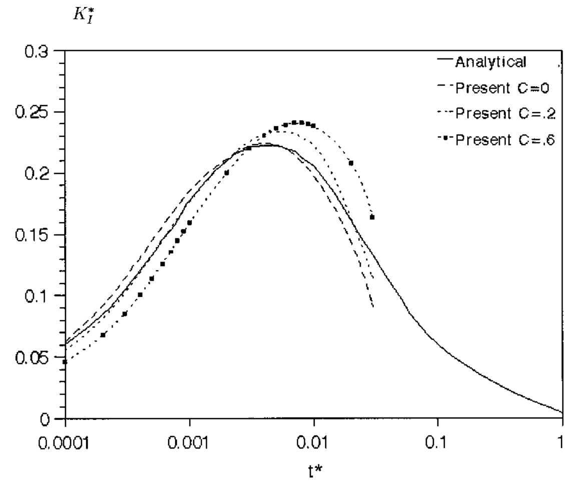

Fig. 5 Comparison of the dimensionless thermal dynamic stress intensity factor K_I^* versus dimensionless time t^*, with analytical and numerical quasi-static results for different coupling parameters

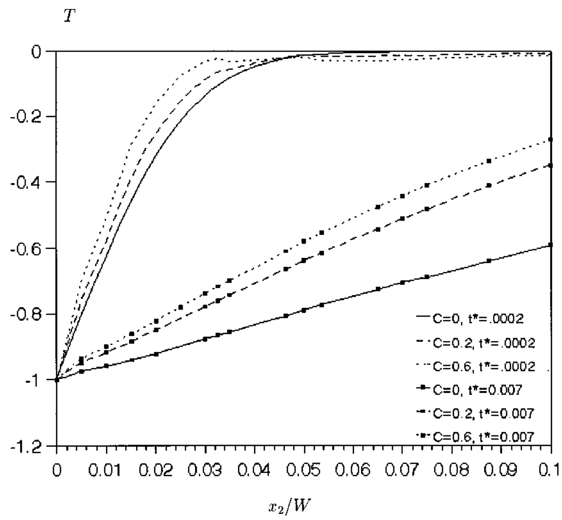

Fig. 6 Temperature distribution for different coupling parameters at different dimensionless times

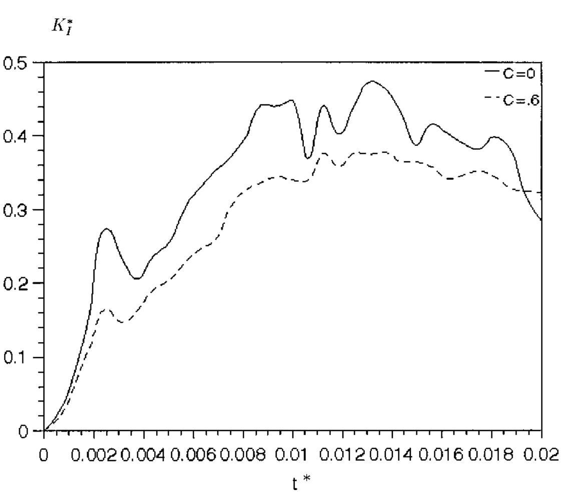

Fig. 7 Variation of the dimensionless thermal dynamic stress intensity factor K_I^* versus dimensionless time t^*, for coupled and uncoupled models

In Fig. 7 K_I^* is increased instantaneously after the application of sudden cooling. At time $t^*=0.0025$, the thermoelastic wavefront reaches the tip of the crack. This cold shock produces tensile stress in the x_2-direction and due to the effect of the Poisson's ratio, compressive stress is produced in the x_1-direction. This phenomena results in the crack opening and thus K_I^* increases by time, as shown in Fig. 7.

When the thermoelastic wavefront passes through the crack tip, a compressive stress is produced in the x_2-direction and the tensile stress in the x_1-direction. This phenomenon results in the crack closure and thus K_I^* decreases by time. This decrease is shown in Fig. 7 following $t^*=0.0025$ to about $t^*=0.0035$. From $t^*=0.0035$ the K_I^* value is increased with a slower rate compared to the initial increase. As time is advanced, the thermoelastic waves are reflected from the boundaries and cause fluctuations in the K_I^* value versus time.

The K_I^*-curve for the coupled case of $C=0.6$ is shown in Fig. 7. This curve is below the K_I^*-curve for the uncoupled case. This result is justified with Fig. 5 for the small values of time.

Conclusions

A boundary element method and Laplace transform in the time domain are developed for the analysis of fractured planar bodies subjected to thermal shock-type loads. The transient coupled thermoelasticity are solved without domain discretization. The singular behavior of the temperature and displacement fields, in the vicinity of the crack tip, is modeled by quarter-point elements. Thermal dynamic stress intensity factors for mode I are evaluated from computed nodal values, using the well-known displacement and traction formulas. The accuracy of the method is investigated through comparison of present results with other analytical and computational works. The important features of this study are as follows:

1 The fracture analysis due to thermal shock with the consideration of the thermomechanical coupling term through the coupled thermoelasticity equations shows that as the coupling parameter is increased the peak value of K_I^* increases and occurs at larger time.

2 Treatment of the time domain in this paper is through the Laplace transform method. This is an essential concept to realistically evaluate the field variables under the coupled thermoelastic filed assumptions.

3 The appropriate time scale in which the effect of the inertia term is observed is considered and the importance of the inertia term is shown. When the inertia term is considered, higher values for K_I^* is achieved. The maximum value of K_I^* is about double compared to the case where the inertia term is ignored.

References

[1] Sih, G. C., 1962, ''On the Singular Character of Thermal Stress Near a Crack Tip,'' ASME J. Appl. Mech., **29**, pp. 587–589.
[2] Kassir, M. K., and Bergman, A. M., 1971, ''Thermal Stress in a Solid Containing Parallel Circular Crack,'' Appl. Sci. Res., **25**, pp. 262–280.
[3] Wilson, W. K., and Yu, I. W., 1979, ''The Use of the *J*-Integral in Thermal Stress Crack Problems,'' Int. J. Fract., **15**, pp. 377–387.
[4] Nied, H. F., 1983, ''Thermal Shock Fracture in an Edge-Cracked Plate,'' J. Therm. Stresses, **6**, pp. 217–229.
[5] Chen, T. C., and Weng, C. I., 1991, ''Coupled Transient Thermoelastic Response in an Edge-Cracked Plate,'' Eng. Fract. Mech., **39**, pp. 915–925.
[6] Lee, K. Y., and Sim, K., 1990, ''Thermal Shock Stress Intensity Factor by Bueckner's Weight Function Method,'' Eng. Fract. Mech., **37**, pp. 799–804.
[7] Rizk, A. E. A., 1993, ''A Cracked Plate Under Transient Thermal Stresses Due to Surface Heating,'' Eng. Fract. Mech., **45**, pp. 687–696.
[8] Raveendra, S. T., and Banerjee, P. K., 1992, ''Boundary Element Analysis of Cracks in Thermally Stressed Planar Structures,'' Int. J. Solids Struct., **29**, No. 18, pp. 2301–2317.
[9] Portela, A., and Aliabadi, M. H., 1992, ''The Dual BEM Effective Implementation for Crack Problems,'' Int. J. Numer. Methods Eng., **33**, pp. 1269–1287.
[10] Prasad, N. N. V., and Aliabadi, M. A., 1994, ''The Dual BEM for Thermoelastic Crack Problems,'' Int. J. Numer. Methods Eng., **35**, pp. 169–187.
[11] Prasad, N. N. V., and Aliabadi, M. A., 1996, ''The Dual BEM for Transient

Thermoelastic Crack Problems,'' Int. J. Numer. Methods Eng., **35**, pp. 169–187.
[12] Katsareas, D. E., and Anifantis, N. K., 1995, ''On the Computation of Mode I and II Thermal Shock Stress Intensity Factors Using a Boundary-Only Element Method,'' Int. J. Numer. Methods Eng., **38**, pp. 4157–4169.
[13] Hosseini-Tehrani, P., and Eslami, M. R., 2000, ''Boundary Element Analysis of Coupled Thermoelasticity With Relaxation Times in Finite Domain,'' AIAA J., **38**, No. 3, pp. 534–541.
[14] Durbin, F., 1974, ''Numerical Inversion of Laplace Transforms: An Efficient Improvement to Dubner and Abate's method,'' Comput. J., **17**, pp. 371–378.
[15] Kanninen, M. F., and Popelar, C. H., 1985, *Advanced Fracture Mechanics, Oxford University Press, New York*.
[16] Blanford, G. E., 1981, ''T-D Stress Intensity Factor Computations Using the BEM,'' Int. J. Numer. Methods Eng., **17**, pp. 387–404.
[17] Martinez, J., and Dominguez, J., 1984, ''On the Use of Quarter-Point Boundary Elements for Stress Intensity Factor Computations,'' Int. J. Numer. Methods Eng., **20**, pp. 1941–1950.
[18] Boley, B. A., and Winer, J. H., 1960, *Theory of Thermal Stresses*, John Wiley and Sons, New York.
[19] Jadeja, N. D., and Loo, T. C., 1974, ''Heat Induced Vibration of a Rectangular Plate,'' J. Eng. Ind., **96**, pp. 1015–1021.
[20] Tosaka, N., 1986, ''Boundary Integral Equation *Formulations* for Linear Coupled Thermoelasticity,'' *Proc. 3rd Japan Symp. on BEM, Jascome, Tokyo*, pp. 207–212.

D. L. Chertok
Springfield Financial Services LLC,
8700 W. Bryn Mawr Avenue, 12th Floor,
Chicago, IL 60631
e-mail: dchertok@siichi.com

J. M. Golden
School of Mathematics, Statistics
and Computer Science,
Dublin Institute of Technology,
Dublin 8, Ireland
e-mail: jmgolden@maths.kst.dit.ie

G. A. C. Graham
Applied and Computational
Mathematics Program,
Simon Fraser University,
Burnaby, BC V5A 1S6, Canada
e-mail: gac@cs.sfu.ca

Hysteretic Friction for the Transient Rolling Contact Problem of Linear Viscoelasticity

The problem of a smooth rigid indentor under variable loading moving across a viscoelastic half-space in one direction with variable speed is considered. The motion is assumed to be frictionless and the standard linear model is adopted to describe the viscoelastic material response. An integral equation is derived and a numerical algorithm for its solution subject to appropriate subsidiary conditions is constructed. The contact interval length, pressure, and coefficient of hysteretic friction are presented and the results discussed. [DOI: 10.1115/1.1354622]

1 Introduction

The problem of a rigid regular-shaped indentor moving across a viscoelastic half-space has been addressed by a number of authors over the last four decades. The pioneering experimental work of Tabor [1] on the phenomenon of rolling friction within the elastic range (i.e., no plastic flow) lead to the conclusion that resistance to rolling is a bulk effect due primarily to elastic hysteresis; and to the work of Hunter [2] and Morland [3], modeling the effect in the linear viscoelastic context. Golden [4,5] and Golden and Graham [6,7], developed a general methodology for problems of this kind based on a decomposition of hereditary integrals. The transient case is discussed in Golden and Graham [8], while Fan et al. [9] solve the two-indentor steady-state problem. Inertial effects are included in Golden and Graham [10] for the one-indentor case.

In this paper we consider a uniformly infinite cylindrical indentor of large radius rolling in one direction across the surface of a viscoelastic half-space, the response of which is modeled as that of a standard linear solid. In the contact region, the indentor shape can be approximated as parabolic for small indentation as required by the linear theory. Thus, we are also modeling a parabolic or cylindrical indentor moving on a frictionless viscoelastic half-space. This is a plane-strain configuration. There is no dependence on the z-coordinate, taken to be along the axis of the cylinder.

We adopt the noninertial approximation. This configuration provides a framework for theoretical analysis of the phenomenon of hysteretic friction allowing at the same time for substantial mathematical simplifications. An integral equation is derived together with subsidiary conditions and an algorithm for their numerical solution is developed. Alternately accelerating and decelerating periodic and aperiodic motions are considered and the results compared with those for the steady-state solution known from Golden and Graham [6]. The model developed and the results obtained are of potential significance in assessing the effect of material hysteresis on the startup and slowdown of moving machinery; and also in evaluating the effect of vibrations on hysteretic friction losses.

Contributed by the Applied Mechanics Division of THE AMERICAN SOCIETY OF MECHANICAL ENGINEERS for publication in the ASME JOURNAL OF APPLIED MECHANICS. Manuscript received by the ASME Applied Mechanics Division, October 3, 1997; final revision, September 27, 2000. Associate Editor: J. T. Jenkins. Discussion on the paper should be addressed to the Editor, Professor Lewis T. Wheeler, Department of Mechanical Engineering, University of Houston, Houston, TX 77204-4792, and will be accepted until four months after final publication of the paper itself in the ASME JOURNAL OF APPLIED MECHANICS.

2 Formulation of the Problem

Consider a smooth rigid indentor on a viscoelastic half-space as shown in Fig. 1 under total load $W(t)$.

The indentor, initially at rest, starts moving across the half-space in the negative direction of the x-axis at time t_0, taken to be zero for convenience, with speed $V(t)$. The region of contact between the indentor and the surface underneath is $C(t) =[a(t),b(t)]$. The indentor is of circular cross section and its radius R is large compared with the length of the contact interval $C(t)$. The boundary conditions for the vertical displacement $u(x,t)$ and pressure $p(x,t)$ are

$$u(x,t)=\begin{cases} d(t)-\dfrac{(x-x_0(t))^2}{2R}, & x\in C(t), \\ \text{unknown}, & x\notin C(t), \end{cases} \tag{1}$$

$$p(x,t)=\begin{cases} \text{unknown}, & x\in C(t), \\ 0, & x\notin C(t), \end{cases} \tag{2}$$

where $x_0(t)$ is the coordinate of the point of deepest indentation, $d(t)$ the vertical displacement at $x_0(t)$, while x and t are current space and time coordinates, respectively.

Starting from the viscoelastic Kolosov-Muskhelishvili equations as described by Muskhelishvili [11] and Golden and Graham [6], these boundary conditions can be reduced to the following relations obeyed by the complex potential $\phi(z,t)$, where $z=x+iy$ is a complex variable:

$$\begin{cases} \phi^+(x,t)-\phi^-(x,t)=0, & x\notin C(t), \\ \phi^+(x,t)-\phi^-(x,t)=iv(x,t), & x\in C(t). \end{cases} \tag{3}$$

Here the limits taken from above and below the x-axis are

$$\phi^+(x,t)=\lim_{\Im z\to 0+}\phi(z,t);\phi^-(x,t)=\lim_{\Im z\to 0+}\phi(\overline{z},t), \tag{4}$$

and the overbar denotes complex conjugate. The function $v(x,t)$ is given by

$$v(x,t)=\int_{-\infty}^{t}dt'l(t-t')u'(x,t'), \tag{5}$$

where $u'(x,t)=\partial u(x,t)/\partial x$, $l(t)$ is a causal function determined from

$$\hat{l}(\omega)=\frac{\hat{\mu}(\omega)}{1-\nu}, \tag{6}$$

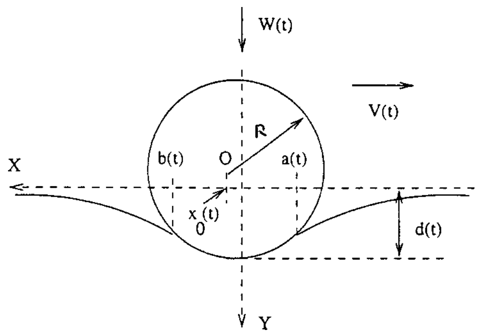

Fig. 1 Schematic representation of the problem: $C(t) = [a(t), b(t)]$—contact interval, O—center of the cylinder, R—radius of the cylinder, $x_0(t)$—point of deepest indentation of the half-space, x—current point coordinate, $u(x,t)$—vertical displacement at x, $d(t)$—maximum displacement, $V(t)$—indentor speed, $W(t)$—total load

for a material with unique Poisson's ratio ν, where ''$\hat{}$'' denotes Fourier transform and $\hat{\mu}$ is the complex modulus of the material. This latter quantity is the Fourier transform of the singular viscoelastic shear modulus $\mu(t)$. For a standard linear solid

$$l(t) = l_0\delta(t) + l_1 e^{-\alpha t}H(t), \tag{7}$$

where l_0, l_1 are experimentally determined constants, $\delta(t)$ the Dirac delta function, α the inverse relaxation decay time, and $H(t)$ the Heaviside step function. The nonvanishing resultant of external forces acting on the half-space implies that absolute (as opposed to relative) displacements cannot be calculated. In particular, $d(t)$ in (1) is indeterminate.

The quantity $v(x,t)$ is not known. If, however, we proceed as if it were known, then Eqs. (3) constitute a Hilbert problem for $\phi(z,t)$, and the solution without singularities at the ends of the contact interval is found by Muskhelishvili [11] and Golden and Graham [6] to be

$$\phi(z,t) = \frac{X(z,t)}{2\pi}\int_{C(t)} dx' \frac{v(x',t)}{(x'-z)X^+(x',t)}, \tag{8}$$

where

$$X(z,t) = [z-a(t)]^{1/2}[z-b(t)]^{1/2}; X^+(z,t) = \lim_{\Im z \to 0+} X(z,t). \tag{9}$$

From the second of (3) it follows that for any $x \notin C(t)$

$$v(x,t) = \pm\frac{n(x,t)}{\pi}\int_{a(t)}^{b(t)} dx' \frac{v(x',t)}{(x'-x)m(x',t)}. \tag{10}$$

Here

$$\begin{aligned} m(x,t) &= [b(t)-x]^{1/2}[x-a(t)]^{1/2}, \\ n(x,t) &= |x-a(t)|^{1/2}|x-b(t)|^{1/2}, \end{aligned} \tag{11}$$

and ''$-$'' corresponds to $x > b(t)$ and ''$+$'' to $x < a(t)$.

Equation (10) allows one to express $v(x,t)$ outside $C(t)$ in terms of its values inside $C(t)$. This fact plays an important role in the derivation of the integral Eq. (17) below.

3 The Fundamental Integral Equation and Subsidiary Conditions

Let $t_1(x)$ be the time when the point x first enters the contact interval $C(t) = [a(t), b(t)]$. in other words, $x = a(t_1(x))$. Then, from Eq. (5) for any $x \in C(t)$:

$$v(x,t) = \int_{-\infty}^{t_1(x)} dt' l(t-t')u'(x,t') + \int_{t_1(x)}^{t} dt' l(t-t')u'(x,t'). \tag{12}$$

Inverting the convolution in Eq. (5), we obtain

$$u'(x,t) = \int_{-\infty}^{t} dt' k(t-t')v(x,t'), \tag{13}$$

where $k(t)$ satisfies

$$\int_{-\infty}^{t} dt' l(t-t')k(t') = \int_{-\infty}^{t} dt' k(t-t')l(t') = \delta(t). \tag{14}$$

Substituting from Eq. (13) into the first term of Eq. (12) and interchanging the order of integration over an infinite triangular region allows us to rewrite the above-mentioned equation as

$$v(x,t) = \int_{t_1(x)}^{t} dt' l(t-t')u'(x,t') + \int_{-\infty}^{t_1(x)} dt' T_1(t,t';x)v(x,t'), \tag{15}$$

where

$$T_1(t,t';x) = \int_{t'}^{t_1(x)} dt'' l(t-t'')k(t''-t'). \tag{16}$$

The first integral in Eq. (15) is evaluated over the period of time when $u'(x,t)$ is known, because for each t' between $t_1(x)$ and t the point x lies inside $C(t)$. The second integral contains the values of $v(x,t')$ for $x \notin C(t')$. Substituting for these from Eq. (10), we obtain the main integral equation

$$v(x,t) = \int_{-\infty}^{t_1(x)} dt' \int_{a(t')}^{b(t')} dx' K(x,x';t,t')v(x',t') + I(x,t), \quad x \in C(t) \tag{17}$$

where

$$K(x,x';t,t') = \frac{n(x,t')T_1(t,t';x)}{\pi m(x',t')(x'-x)}, \tag{18}$$

$$I(x,t) = \int_{t_1(x)}^{t} dt' l(t-t')u'(x,t'). \tag{19}$$

The two subsidiary conditions have the form given by Golden and Graham [6]

$$\int_{a(t)}^{b(t)} dx' \frac{v(x',t)}{m(x',t)} = 0 \tag{20}$$

$$\int_{a(t)}^{b(t)} dx' \frac{x'v(x',t)}{m(x',t)} = -W(t), \tag{21}$$

where Eq. (20) is a condition necessary for a suitably smooth solution to exist and $W(t)$ in Eq. (21) is the normal load acting upon the indentor.

4 Standard Linear Solid

For the case of a standard linear solid $k(t)$ in Eq. (13) has the form

$$k(t) = k_0\delta(t) + k_1 e^{-\beta t}H(t). \tag{22}$$

Here k_0, k_1 and β are related to l_0, l_1 and α as follows:

$$k_0 = \frac{1}{l_0}, \quad k_1 = -\frac{l_1}{l_0^2}, \quad \beta = \alpha - \frac{k_1}{k_0}. \tag{23}$$

It is assumed that the system is in equilibrium up to time $t = 0$. Equation (17) can be given for a standard linear solid by employing Eqs. (7), (22), and (23). The result, after carrying out all relevant integration, yields for $a(t) \leqslant x \leqslant b(t)$

$$v(x,t)=l_1 e^{-\alpha t+(\alpha-\beta)t_1(x)}\Bigg\{-\frac{1}{\alpha R}(x+\sqrt{x^2-a_0^2})$$

$$+\frac{k_0}{\pi}\int_0^{t_1(x)} dt' n(x,t')e^{\beta t'}$$

$$\times\int_{a(t')}^{b(t')} dx' \frac{v(x',t')}{m(x',t')(x'-x)}\Bigg\}+I(x,t), \qquad (24)$$

where

$$I(x,t)=-\frac{1}{R}\Bigg\{\left(l_0+\frac{l_1}{\alpha}\right)(x-x_0(t))$$

$$-\frac{l_1}{\alpha}e^{-\alpha(t-t_1(x))}(x-x_0(t_1(x)))$$

$$+e^{-\alpha t_1(x)}\int_{t_1(x)}^{t} dt' e^{\alpha t'}V(t')\Bigg\}. \qquad (25)$$

and where a_0 is the semi-contact length for an indentor at rest. It is easy to observe that for the limiting case of an indentor at rest ($x_0(t)\equiv 0$, $t_1(x)=-\infty$) Eq. (24) reduces to

$$v(x,0)=I(x,0)=-\frac{1}{R}\left(l_0+\frac{l_1}{\alpha}\right)x_0 \qquad (26)$$

Therefore, Eqs. (17) and (20) are satisfied identically, while Eq. (21) gives the elastic solution for the constant (initial) load (cf. Golden and Graham [6]):

$$W(0)=\frac{\pi a_0^2}{2R}\left(l_0+\frac{l_1}{\alpha}\right). \qquad (27)$$

Following the procedure outlined by Muskhelishvili [11], we obtain an expression for the pressure inside the contact interval $C(t)$,

$$p(x,t)=-\frac{m(x,t)}{\pi}\int_{a(t)}^{b(t)}\frac{dx' v(x',t)}{(x'-x)m(x',t)}. \qquad (28)$$

Hysteretic frictional effects (see, e.g., Golden and Graham [6], Rabotnov [12]; also Moore [13] for a phenomenological discussion) result in a force resisting the motion of the indentor in the horizontal direction. The coefficient of hysteretic friction is given by

$$f_h=\frac{1}{W}\int_{a(t)}^{b(t)} dx\, p(x,t)u'(x,t). \qquad (29)$$

5 Numerical Algorithm

5.1 General Algorithm. The general Eq. (17) and the subsidiary conditions (20), (21) present a system of three equations in three unknowns: $a(t)$, $b(t)$, and $v(x,t)$. Traditional methods of solving such systems, e.g., [14,15], cannot handle the unknown contact interval boundaries at an arbitrary time t. Moreover, the dependency of the upper limit of time integration on the space variable x provides yet another obstacle, which renders any alternative method known to the authors, e.g., the finite element method, the Nyström method or collocation methods inapplicable. A comprehensive survey of numerical techniques applicable to problems similar to the one under consideration, together with a justification for the suggested algorithm can be found in Chertok [16].

We begin with the initial solution given by Eq. (27), which yields

$$a_0=\sqrt{\frac{2RW(0)}{\pi\left(l_0+\frac{l_1}{\alpha}\right)}}. \qquad (30)$$

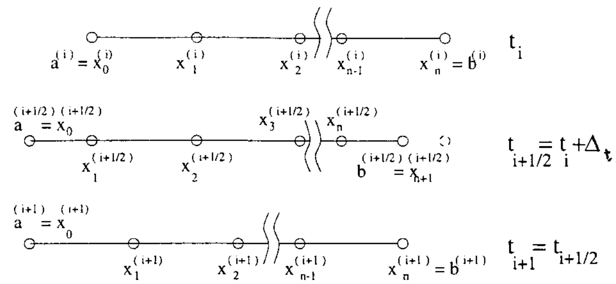

Fig. 2 Schematic representation of the discretization procedure for the spatial domain

Using Eq. (26) and noticing the symmetry of the initial contact interval, we obtain the starting point for the iterative procedure: $v^{(0)}=v(x,0)$.

To construct an algorithm allowing us to evaluate $v^{(k)}(x,t)$, we must discretize both the spatial and the temporal domain. At $t=t_0=0$, when the motion has started, we use a uniform spatial grid. During each iteration we use an unequally spaced mesh as explained below, but then revert to equal spacing. The temporal grid is naturally chosen to be adaptive to accommodate the change in the indentor velocity.

The discretization procedure for the spatial domain is illustrated in Fig. 2. Suppose that we have computed $v^{(i)}=v(x_j,t_i)$, where $(x_j^{(i)},t_i)$ are the mesh points such that $a(t_i)=x_0^{(i)}<x_1^{(i)},\ldots,x_{n-1}^{(i)}<x_n^{(i)}=b(t_i)$ and $[a(t_i),b(t_i)]=C(t_i)$ is the contact interval at t_i. In determining a new temporal mesh point $t_{i+1}=t_i+\Delta t_i$, we require that the size of the time step Δt_i be small in the following sense. We wish to retain all the ''old'' mesh points $x_j^{(i)}$ that are in the interior of the ''new'' contact interval $C(t_{i+1})$, specifically, we require that $a(t_{i+1})<a(t_i)=x_0^{(i)}$; $x_{n-1}^{(i)}<b(t_{i+1})<b(t_i)$. This allows us to compute $v^{(i+1)}$ at the points $x_j^{(i)}$, $j=0,1,2,\ldots,n-1$, since for such points the iteration scheme is explicit in the sense that the expression for $v^{(i+1)}$ at these interior points depends only on previously computed quantities. This point is discussed further in Section 5.2. We choose Δt_i so as to satisfy

$$\Delta t_i<D\frac{2\min_{j=\overline{0,n-1}}|x_{j+1}-x_j|}{V(t_{i-1})+V(t_{i-1}+\Delta t_{i-1})}, \qquad (31)$$

where D is a constant determined by trial and error and Δt_{i-1} is the previous time step.

We take Δt_0 to be 0.01 and $D=0.3$. These values delivered a reasonable balance between accuracy and computation time. We now compute $v(x_j^{(i+1)},t_{i+1})$ at all $x_j^{(i+1)}\in C(t_i)$, i.e., at the ''old'' mesh points that coincide with the ''new'' ones using Eq. (24) and (25) (or (26), which is applicable to the initial step). We evaluate the spatial integrals using interpolated values for $v(x,t)$ in the combination of modified Clenshaw-Curtis and Gauss-Kronrod formulas used in an IMSL routine DQDAWS. For the temporal integral in Eq. (24), which involves multiple evaluation of spatial integrals, we employ the trapezoid formula modified as described in Section 5.2.

Next we compute $v(a^{(0)}(t_{i+1}),t_{i+1})$ and $v(b^{(0)}(t_{i+1}),t_{i+1})$ by extrapolation, respectively carried out over the known values of $v(x_j,t_{i+1})$, $j=0,1,2,\ldots,n-1$ for some initial approximation $a^{(0)}(t_{i+1}),b^{(0)}(t_{i+1})$ to $a(t_{i+1}),b(t_{i+1})$. These estimates are obtained by adding $-V(t_i)\Delta t_i$ to $a(t_i)$ and $b(t_i)$. Now construct a cost function

$$f(a,b)=\left\{\int_a^b dx'\frac{v(x',t)}{m(x',t)}\right\}^2+\left\{\int_a^b dx'\frac{x'v(x',t)}{m(x',t)}+W(t)\right\}^2. \qquad (32)$$

Clearly, a, and b satisfying the subsidiary conditions (20), (21) will deliver a minimum to $f(a,b)$. This is an iterative procedure. At each iteration k, $v(a^{(k)}(t_{i+1}),t_{i+1})$ and $v(b^{(k)}(t_{i+1}),t_{i+1})$ are re-evaluated using cubic spline extrapolation, respectively. Denote the minimizing values of a and b as $a^{(i+1)}$ and $b^{(i+1)}$ and compute $v(a^{(i+1)},t_{i+1}), v(b^{(i+1)},t_{i+1})$ using the integral Eq. (24). These two new values together with $v(x_j^{(i+1)},t_{i+1})$, $j=0,1,2,\ldots,n-1$, form the numerical solution of Eq. (17) with subsidiary conditions (20), (21). Note here, that $[a^{(i+1)},x_0^{(i+1)}]$ and $[x_{n-1}^{(i+1)},b^{(i+1)}]$ differ in length from $[x_l^{(i+1)},x_{l+1}^{(i+1)}]$ for $l=0,1,2,\ldots,n-2$. These $(n+2)$ points are now replaced by $(n+1)$ equally spaced points as indicated in Fig. 2.

Since $v(x,t)$ is infinitely smooth inside $C(t)$, the error arising from approximating $v(x,t_{i+1})$ by a cubic spline is $O(h^4)$ for all interior points (de Boor [17]). Thus, for a sufficiently large number of spatial mesh points inside the contact interval, we can expect the error in estimating $v(a^{(i+1)},t_{i+1})$ and $v(b^{(i+1)},t_{i+1})$ to be negligible.

Further description of the algorithm can be found in Chertok [16].

5.2 Treatment of Integral Singularities. The integrand in Eq. (17) possesses integrable singularities at $x'=a(t')$, $x'=b(t')$ that can be handled, e.g., by employing Gaussian-type quadrature formulas. Another singularity occurs when t' in the time integral becomes equal to $t_1(x)$. In this case $a(t')=a(t_1(x))=x$ and the inner integrand becomes undefined at $x'=a(t')$. Nevertheless,

$$\lim_{t'\to t_1(x)} n(x,t')\int_{a(t')}^{b(t')} dx' \frac{v(x',t')}{m(x',t')(x'-x)} = E, \tag{33}$$

where E is finite and so no non-integrable singularity arises. However, in choosing an appropriate quadrature formula to evaluate the temporal integral in Eq. (24), it is desirable to avoid handling the values of $v(x,t)$ at $t=t_1(x)$. To this end, we apply the trapezoid formula for $t\in[0,t_i]$ and the rectangle formula for $t\in[t_i,t_1(x)]$ as follows:

$$\int_0^{t_1(x)} dt' f(x,t') \approx \sum_{k=1}^{i} \frac{f(x,t_k)+f(x,t_{k-1})}{2}(t_k-t_{k-1}) + f(x,t_i)(t_1(x)-t_i), \tag{34}$$

where

$$f(x,t) = n(x,t)e^{\beta t}\int_{a(t)}^{b(t)} dx' \frac{v(x',t)}{m(x',t)(x'-x)}. \tag{35}$$

A consequence of this is that the iterative expression for $v(a_{i+1},t_{i+1})$ does not contain $v(a_{i+1},t_{i+1})$, but only previously computed values. This is true in any case for a point in the interior of the contact interval. Thus, as noted earlier, the iteration scheme is entirely explicit, in contrast with one which would emerge from a standard Fredholm-type equation, e.g., Atkinson [14] and Davis and Rabinowitz [18]. For a fine temporal mesh a reduction in accuracy in the quadrature formula due to the correction given by Eq. (34) is outweighed by a substantial gain in the computational speed.

To evaluate $p(x_j^{(i)},t_i)$ using Eq. (28) and the known values of $v(x_j^{(i)},t_i)$ we have to eliminate a first-order singularity in the integrand. Utilizing the Kantorovich method (Davis and Rabinowitz [18]) and bearing in mind the differentiability of $v(x,t)$, we obtain

$$p(x,t) = -\frac{m(x,t)}{\pi}\left\{\int_{a(t)}^{b(t)} \frac{dx'[v(x',t)-v(x,t)]}{m(x',t)(x'-x)} + v(x,t)\int_{a(t)}^{b(t)} \frac{dx'}{m(x',t)(x'-x)}\right\}. \tag{36}$$

However, the second term in Eq. (36) is equal to zero, whereas

$$\lim_{x'\to x} \frac{v(x',t)-v(x,t)}{x'-x} = v'(x,t) \tag{37}$$

and $p(x_j^{(i)},t_i)$ can thus be numerically evaluated for any $(x_j^{(i)},t_i)$ without difficulty. Thereupon the hysteretic friction can be computed from Eq. (29).

6 Results and Discussion

The computational realization of the algorithm described in Section 5 was carried out on a networked SUN SPARC 20 workstation with available 163 Mb RAM and two 150 MHz CPU. The program required 18–20 Mb of operating memory and a single computational run at the given level of discretization extended from 25 to 72 hours of CPU time, depending on the chosen pattern of speed/loading variation. Such a substantial difference in CPU time can be explained bearing in mind that for high speed/loading amplitude, smaller time steps are required, which leads to substantial increase in the computation time.

For the discretization of the spatial domain we chose $NX=51$ mesh points, whereas the time domain had up to $NT=3000$ mesh points. The results presented below pertain to a viscoelastic material with $G_1/G_0=1/4$. Computational experiments with higher viscoelasticities ($G_1/G_0=1/2$ and $G_1/G_0=1$) did not reveal any qualitative difference from the case under consideration. We also chose the dimensionless combination $R\alpha/V_0=12.5\alpha=1.25$ and $R=10$, where V_0 is a characteristic speed for each case.

On the graphs below the subindex T corresponds to the transient solution and S corresponds to the steady-state solution. What this means, is the following: A steady-state solution assumes a velocity constant over all time. The current velocity $V(t)$ is assigned as this constant velocity. The quantities C_T and C_S are the normalized lengths of the transient and steady-state contact intervals, respectively, computed as $C_S(t)=(b_S(t)-a_S(t))/(2R)$, $C_T(t)=(b_T(t)-a_T(t))/(2R)$, h_S and h_T are the indentor tip shifts: $h_T(t)=-(a_T(t)+b_T(t)-2x_0(t))/(b_T(t)-a_T(t))$, $h_S(t)=-(a_S(t)+b_S(t))/(b_S(t)-a_S(t))$, where $x_0(t)$ is the current position of the indentor tip. Transient and steady-state coefficients of hysteretic friction f_{H_T} and f_{H_S} are computed with the help of Eq. (29). The normalized speed is $V_N(t)=V(t)/(K\alpha R)$, where $K=10$ for the graphs containing C_S and C_T, h_S and h_T, while $K=100$ for the graphs containing f_{H_S} and f_{H_T}. The different scaling of V for the different graphs is done in order to conveniently fit the plot of velocity on the graph. The load $W(t)$ is taken to be unity when constant, while the pressure coefficient $p(x,t)$ lies between 0 and 1. In our subsequent discussion we shall assume that all quantities have been normalized as described above.

6.1 Constant Acceleration. As our first example we choose $V=t$ for $t\geqslant 0$ and $V=0$ for $t<0$. The length of the contact interval and the shift of the indentor tip are each plotted against time in Fig. 3. The hysteretic friction and the speed of the indentor are shown in Fig. 4.

The contact interval width eventually tends to a stable value which corresponds to the "high speed" elastic limit as described in Golden and Graham [6]. The hysteretic friction, however, increases to its maximum value and then deceases steadily tending to zero. Observing the curve in Fig. 4, we can see a time delay between the steady-state peak of the hysteretic friction and its transient counterpart. Initially, the transient hysteretic friction is less than the steady-state value, but becomes larger soon after the time corresponding to the peak in the steady-state value. Follow-

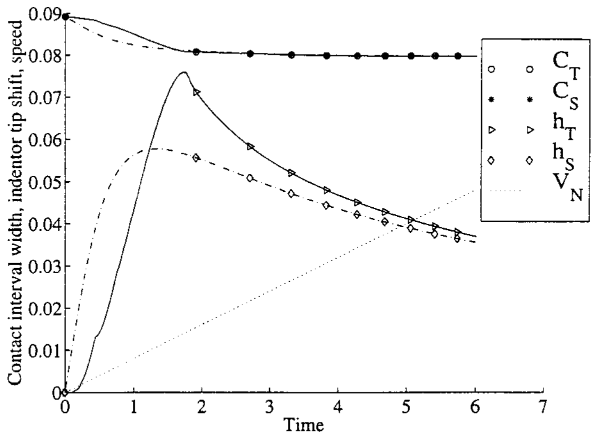

Fig. 3 Constantly accelerating indentor: $V=t$. History of contact interval width C, indentor tip shift h and speed V.

ing the peak in the transient value of the hysteretic friction, the difference between it and its steady-state counterpart steadily declines to zero, as do both quantities at large speeds. Observe that the history of the indentor tip shift mimics the history of the hysteretic friction here and in all cases described below. This is an expression of the fact that hysteretic friction is related to the uneven pressure distribution inside $C(t)$ and the indentor tip shift is a measure of such asymmetry.

6.2 Acceleration Followed by Deceleration. We now consider the case of an indentor accelerating smoothly from rest to a prescribed speed V_1 and then, after a period of constant velocity motion, decelerating to the speed V_2 (which is substantially less than V_1). As an example we consider

$$V(t)=\begin{cases} \sin t, & 0\leqslant t<\frac{\pi}{2} \\ 1, & \frac{\pi}{2}\leqslant t<7 \\ 1+0.9\sin(t+\pi-7), & 7\leqslant t<7+\frac{\pi}{2} \\ 0.1, & t>7+\frac{\pi}{2}. \end{cases} \tag{38}$$

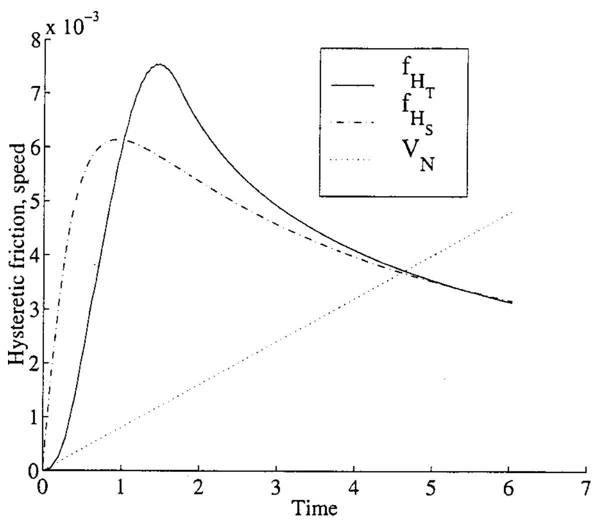

Fig. 4 Constantly accelerating indentor: $V=t$. History of hysteretic friction f_H and speed V. The solid lines indicate the transient solution and the broken lines indicate the steady-state solution. The dotted line indicates the speed.

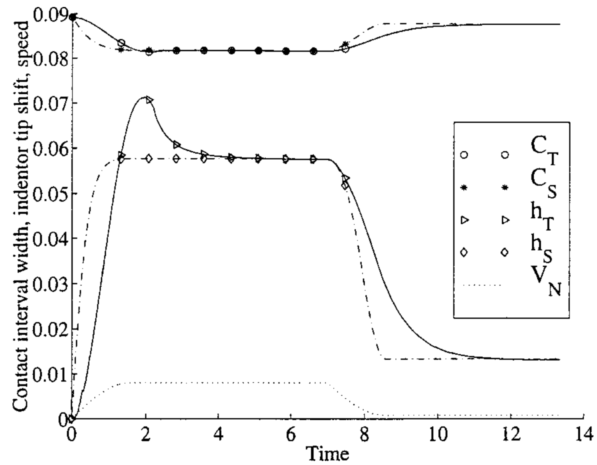

Fig. 5 Alternately accelerating and decelerating indentor with $V(t)$ varying as described by (38). History of contact interval width C, indentor tip shift h and speed V. The solid lines indicate the transient solution and the broken lines indicate the steady-state solution. The dotted line indicates the speed.

The results are presented in Figs. 5 and 6. We can observe the characteristic trough in the length of the contact interval after the initial period of acceleration. Thereupon, for the constant speed motion the lengths of the contact interval for the transient and the steady-state case merge and for the deceleration phase the transient contact interval width lags behind the steady-state case catching up to the latter shortly after the speed has become constant. The behavior of the hysteretic friction is a mirror image of that of the contact interval width in that for those periods of time when the transient contact interval width exceeds its steady-state counterpart, the transient hysteretic friction is smaller than the steady-state one. It is also interesting to notice that, even though at the beginning of the deceleration period the transient hysteretic friction is slightly smaller than the steady-state one, by the end of this period it is larger. We also observe (Fig. 7) that the pressure distribution at the end of the simulation period is very close to the initial pressure distribution.

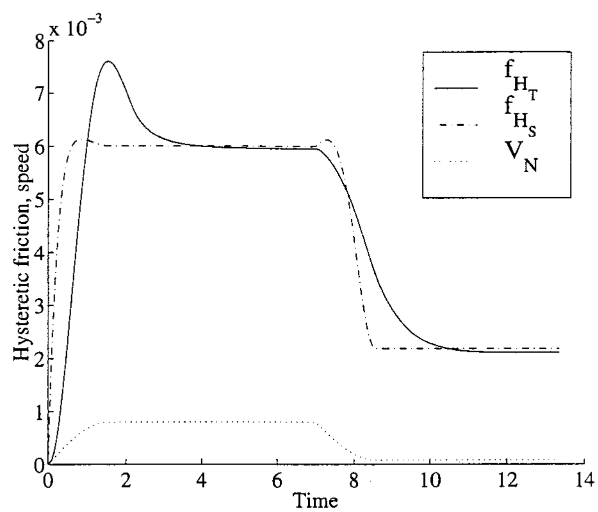

Fig. 6 Alternately accelerating and decelerating indentor with $V(t)$ varying as described by (38). History of hysteretic friction f_H and speed V. The solid lines indicate the transient solution and the broken lines indicate the steady-state solution. The dotted line indicates the speed.

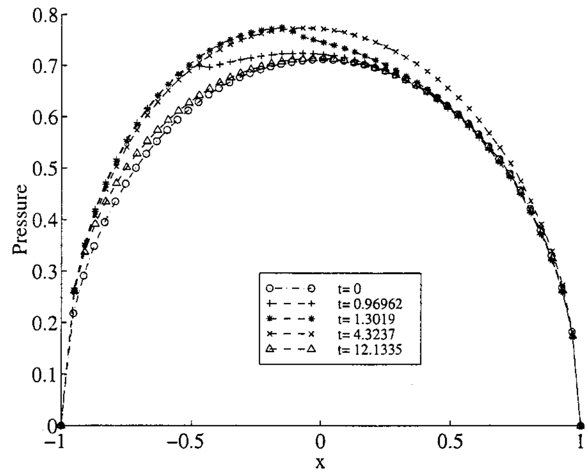

Fig. 7 History of pressure distribution for an alternately accelerating and decelerating indentor

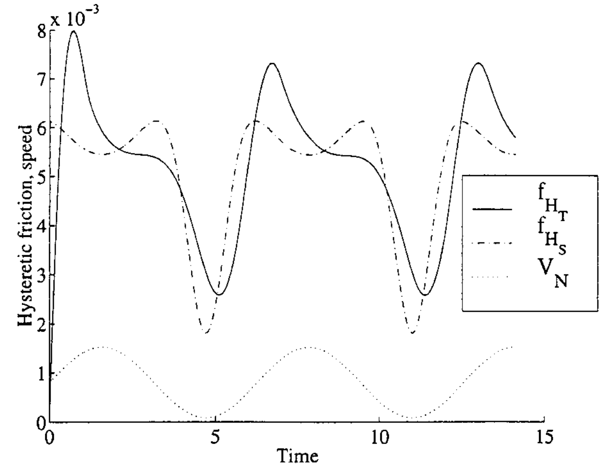

Fig. 9 Periodically accelerating indentor: $V(t)=1+0.9\sin(t)$. History of hysteretic friction f_H and speed V.

6.3 Periodically Varying Speed and Load. For the case of a periodically varying speed, we consider

$$V(t)=A+B\sin t, \tag{39}$$

where $A>B>0$. Three combinations of A and B were considered: $A=1.0$, $B=0.9$, $A=1.0$, $B=0.25$ and $A=0.5$, $B=0.25$. The graphs for the first set of values are presented. These are the most interesting results that were obtained.

Consider the case of a relatively high average speed with periodic variations of large amplitude about this value: $A=1$, $B=0.9$ (see Figs. 8 and 9).

The width of the transient contact interval follows its steady-state counterpart, but with a delay. The steady-state hysteretic friction qualitatively follows the velocity, but the neighborhood of the peak is ''inverted,'' i.e., the friction decreases as the normalized speed $V/100\alpha R$ increases to values above 0.01. This is in line with the fact that for the steady-state problem the hysteretic friction reaches its peak at medium velocities and decreases as speed deviates to either side of these values Hunter [2], Golden and Graham [6], Fan et al. [9], and Golden and Graham [8].

The transient hysteretic friction, however, presents a totally different picture. After a sharp increase corresponding to the accelerating indentor, it starts to decrease after the normalized speed $V/100\alpha R$ becomes greater than 0.01. The rate of decrease slows down shortly after the speed reaches its maximum. The hysteretic friction attempts to stabilize at a certain level. As the speed further continues to decline, the hysteretic friction drops rapidly and then starts to increase with the beginning of a new acceleration period. Maximum and minimum values of hysteretic friction and the indentor tip shift are larger in the transient analysis than in the steady-state analysis. The shapes of the resulting graphs somewhat resemble those of the ones in Figs. 5 and 6.

For the case of a medium mean value of speed and a medium amplitude ($A=0.5$, $B=0.25$) the transient and the steady-state contact interval width are very close. The transient indentor tip shift and hysteretic friction follow their steady-state counterparts with a time delay as in the case discussed above. The instance of relatively high mean speed varying with small amplitude ($A=1$, $B=0.25$) qualitatively lies between the first and the second of the previously considered cases Chertok [16].

For a periodically varying load moving with constant speed (Figs. 10 and 11), we notice that the transient and the steady-state contact interval widths become equal after a short period of initial stabilization. The transient indentor tip shift and hysteretic friction follow the variations in the contact interval width with a time delay. The transient hysteretic friction mimics its steady-state counterpart with a time delay as well. However, the steady-state indentor tip shift varies very slightly, in contrast with the transient indentor tip shift, which varies significantly.

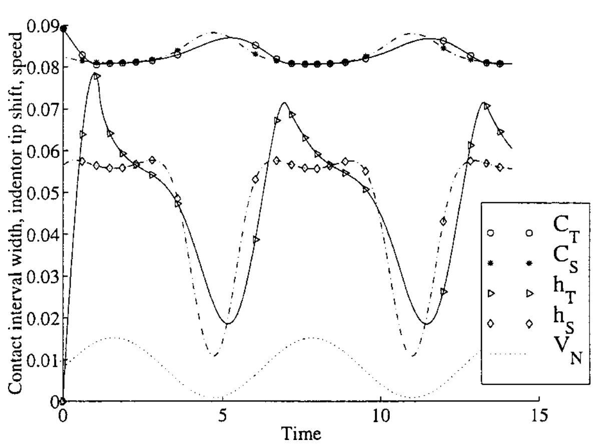

Fig. 8 Periodically accelerating indentor: $V(t)=1+0.9\sin(t)$. History of contact interval width C, indentor tip shift h and speed V.

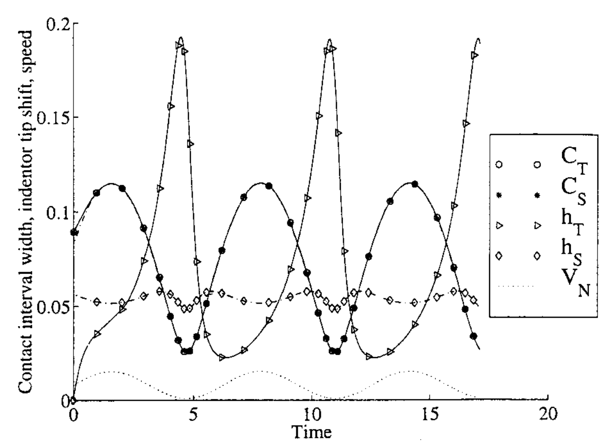

Fig. 10 Periodically varying load: $W(t)=1+0.9\sin(t)$. History of contact interval width C, indentor tip shift h and speed V. W is scaled by a factor of 10 to fit on the graph.

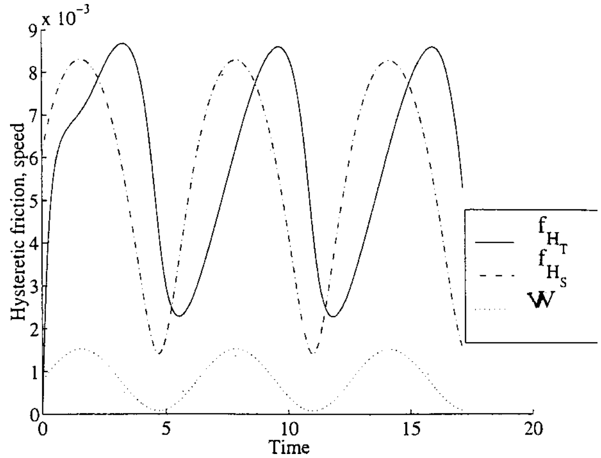

Fig. 11 Periodically varying load: $W(t)=1+0.9\sin(t)$. History of hysteretic friction f_H and speed V. W is scaled by a factor of 100 to fit on the graph.

7 Conclusion

The integral Eq. (17) subject to subsidiary conditions (20), (21) has been solved for the first time in the transient case. Several patterns of speed variation/loading conditions have been analyzed and histories of transient contact interval width, hysteretic friction and indentor tip shift compared with their steady-state counterparts. For *all types* of speed/load variation the transient and steady-state contact interval widths are quite close. For variable *speed*, however, the graph shapes of transient and steady-state hysteretic friction are substantially different; the indentor tip shift generally mimics the behavior of the hysteretic friction. After a period of acceleration, the transient value of the hysteretic friction exceeds the steady-state value. Finally, for a variable *load* the transient hysteretic friction follows the steady-state hysteretic friction with a time delay.

To the authors' knowledge, the current work is the first example of a numerical technique for solving transient viscoelastic mixed boundary value problems that involve moving boundary regions. Further research may include the rolling in one direction of a train of indentors and the to-and-fro motion of a single indentor. However, those two cases require substantial modification of the current algorithm and its software implementation.

Acknowledgment

Improvements were incorporated into the paper following the comments of the reviewers. This work was partially supported by funds provided by the Natural Sciences and Engineering Research Council of Canada.

References

[1] Tabor, D., 1952, "The Mechanism of Rolling Friction," Philos. Mag., **43**, pp. 1055–1059.
[2] Hunter, S. C., 1961, "The Rolling Contact of a Rigid Cylinder With a Viscoelastic Half-Space," ASME J. Appl. Mech., **28**, pp. 611–617.
[3] Morland, L. W., 1962, "A Plane Problem of Rolling Contact in Linear Viscoelasticity Theory," ASME J. Appl. Mech., **29**, pp. 345–352.
[4] Golden, J. M., 1977, "Hysteretic Friction of a Plane Punch on a Half-Plane With Arbitrary Viscoelastic Behavior," Q. J. Mech. Appl. Math., **30**, pp. 23–49.
[5] Golden, J. M., 1979, "The Problem of a Moving Rigid Punch on an Unlubricated Viscoelastic Half-Plane," Q. J. Mech. Appl. Math., **32**, pp. 25–52.
[6] Golden, J. M., and Graham, G. A. C., 1988, *Boundary Value Problems in Linear Viscoelasticity*, Springer-Verlag, Berlin.
[7] Golden, J. M., and Graham, G. A. C., 1995, "General Methods in Non-Inertial Viscoelastic Boundary Value Problems," *Crack and Contact Problems for Viscoelastic Bodies*, G. A. C. Graham and J. R. Walton, ed., Springer-Verlag, Vienna, pp. 103–225.
[8] Golden, J. M., and Graham, G. A. C., 1987, "The Transient Quasi-Static Plane Viscoelastic Moving Load Problem," Int. J. Eng. Sci., **25**, pp. 65–84.
[9] Fan, H. Z., Golden, J. M., and Graham, G. A. C., 1995, "The Problem of Several Indentors Moving on a Viscoelastic Half-Plane," ASME J. Appl. Mech., **62**, pp. 380–389.
[10] Golden, J. M., and Graham, G. A. C., 1996, "The Viscoelastic Moving Contact Problem With Inertial Effects Included," Q. J. Mech. Appl. Math., **49**, pp. 107–135.
[11] Muskhelishvili, N. I., 1963, *Some Basic Problems of the Mathematical Theory of Elasticity*, Noordhoff, Groningen (translated from the Russian by J. R. M. Radok).
[12] Rabotnov, Yu. N., 1977, *Elements of Hereditary Mechanics of Solid Bodies* Nauka, Moscow (in Russian).
[13] Moore, D. F., 1993, *Viscoelastic Machine Elements: Elastomers and Lubricants in Machine Systems*, Butterworth-Heinemann, Oxford, UK.
[14] Atkinson, K. E., 1976, *A Survey of Numerical Methods for the Solution of Fredholm Integral Equations of the Second Kind*, SIAM, Philadelphia, PA.
[15] Squire, W., 1970, *Integration for Engineers and Scientists*, American Elsevier, New York.
[16] Chertok, D. L., 1998, "Hysteretic Friction in the Transient Rolling Contact Problem of Linear Viscoelasticity," Ph.D. thesis, Simon Fraser University, Burnaby, BC, Canada.
[17] de Boor, C., 1978, *A Practical Guide to Splines*, Springer-Verlag, New York.
[18] Davis, P. J., and Rabinowitz P., 1984, *Methods of Numerical Integration* 2nd ed., Academic Press, San Diego, CA.

Vibrations of Tapered Timoshenko Beams in Terms of Static Timoshenko Beam Functions

D. Zhou
School of Mechanical Engineering,
Nanjing University of Science and Technology,
Nanjing 210014, P. R. China

Y. K. Cheung[1]
Department of Civil Engineering,
The University of Hong Kong,
Hong Kong

In this paper, the free vibrations of a wide range of tapered Timoshenko beams are investigated. The cross section of the beam varies continuously and the variation is described by a power function of the coordinate along the neutral axis of the beam. The static Timoshenko beam functions, which are the complete solutions of a tapered Timoshenko beam under a Taylor series of static load, are developed, respectively, as the basis functions of the flexural displacement and the angle of rotation due to bending. The Rayleigh-Ritz method is applied to derive the eigenfrequency equation of the tapered Timoshenko beam. Unlike conventional basis functions which are independent of the cross-sectional variation of the beam, these static Timoshenko beam functions vary in accordance with the cross-sectional variation of the beam so that higher accuracy and more rapid convergence have been obtained. Some numerical results are presented for both truncated and sharp-ended Timoshenko beams. On the basis of convergence study and comparison with available results in the literature it is shown that the first few eigenfrequencies can be given with quite good accuracy by using a small number of terms of the static Timoshenko beam functions. Finally, some valuable results are presented systematically. [DOI: 10.1115/1.1357164]

1 Introduction

Beams with varying cross section are widely used as structural elements in aeronautical, civil, naval, and mechanical engineering. Therefore, it is necessary for designers to understand their dynamic characteristics. It is well known that the Bernoulli-Euler beam theory has been successfully applied to the slender beam analysis. This classical beam theory, however, overpredicts all the eigenfrequencies for thick beams and the higher eigenfrequencies for slender beams, as it neglects the effects of transverse shear deformation and rotary inertia. This shortcoming of classical beam theory results in the presentation of the Timoshenko beam theory ([1]). Unlike the single deflection variable in Bernoulli-Euler beam theory, the governing characteristic equations of Timoshenko beam are two coupled differential equations expressed in terms of two independent variables: the flexural displacement and the angle of rotation due to bending. Therefore, the analysis of Timoshenko beams is more difficult than that of Bernoulli-Euler beams. Consequently, no exact solutions in the closed form for vibrations of tapered Timoshenko beams have been obtained. In most cases approximate numerical methods have to be used, such as the finite element method ([2–4]), the spline function method ([5]), the optimized Rayleigh-Ritz method ([6]), the Galerkin method ([7,8]), the transfer matrix method ([9]), the step-reduction method ([10]), and series solutions based on the method of Frobenius ([11]). A survey on the study of Timoshenko beams ([12]) can be found in the literature.

In the present analysis, the static Timoshenko beam functions are developed as the basis functions to analyze the free vibrations of tapered Timoshenko beams. The Rayleigh-Ritz method is used to derive the eigenfrequency equation of the beam. Both convergence and comparison studies show that the present method has quite high accuracy and the first few eigenfrequencies can be obtained by using a small number of the static Timoshenko beam functions.

2 The Eigenfrequency Equation of a Tapered Beam

The tapered Timoshenko beam considered here and its coordinate system are shown in Fig. 1. The cross section of the beam varies continuously and is described by a power function of the coordinate along the neutral axis of the beam. The origin of the coordinate system is fixed at such a position that the power function describing the cross section of the beam takes up zero value or infinity. Both truncated beams and sharp-ended beams are studied in the present analysis. The length of the sharp-ended beam is L. A truncated beam is considered as part of a sharp-ended beam and has the length $l=(1-\alpha)L$ where α is referred to as truncation factor. Assuming that the cross-sectional area $A(x)$ and the cross-sectional moment of inertia $I(x)$ can be, respectively, written in the form of

$$A(x)=A_1(x/L)^r, \quad I(x)=I_1(x/L)^s \tag{1}$$

where A_1 and I_1 are, respectively, the values of $A(x)$ and $I(x)$ at $x=L$. Indices r and s are referred to as taper factors. Equation (1) expresses a wide range of tapered beams at different values of r and s. Some common linearly tapered beams are shown in Table 1. According to the Timoshenko beam theory, the strain energy U and the kinetic energy T of a nonuniform Timoshenko beam can be given as follows:

$$U=\frac{1}{2}\int_{\alpha L}^{L}\left\{EI_1(x/L)^s\left[\frac{\partial\varphi(x,t)}{\partial x}\right]^2+\kappa GA_1(x/L)^r \times\left[\varphi(x,t)+\frac{\partial y(x,t)}{\partial x}\right]^2\right\}dx, \tag{2}$$

$$T=\frac{1}{2}\int_{\alpha L}^{L}\left\{\rho A_1(x/L)^r\left[\frac{\partial y(x,t)}{\partial t}\right]^2+\rho I_1(x/L)^s\left[\frac{\partial\varphi(x,t)}{\partial t}\right]^2\right\}dx$$

[1]To whom correspondence should be sent.

Contributed by the Applied Mechanics Division of THE AMERICAN SOCIETY OF MECHANICAL ENGINEERS for publication in the ASME JOURNAL OF APPLIED MECHANICS. Manuscript received by the ASME Applied Mechanics Division, Nov. 30, 1999; final revision, Aug. 15, 2000. Associate Editor: A. K. Mal. Discussion on the paper should be addressed to the Editor, Professor Lewis T. Wheeler, Department of Mechanical Engineering, University of Houston, Houston, TX 77204-4792, and will be accepted until four months after final publication of the paper itself in the ASME JOURNAL OF APPLIED MECHANICS.

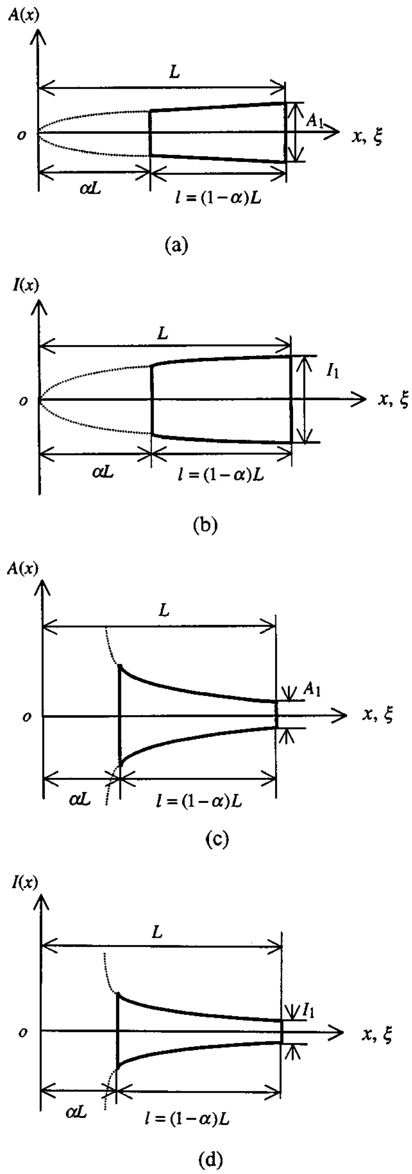

Fig. 1 The sketch of beams with continuously varying cross section; (*a*) the variation of cross-sectional area when $r>0$; (*b*) the variation of cross-sectional moment of inertia when $s>0$; (*c*) the variation of cross-sectional area when $r<0$; (*d*) the variation of cross-sectional moment inertia when $s<0$

where $y(x,t)$ is the flexural displacement, $\varphi(x,t)$ is the angle of rotation due to bending and t is the time. E is the Young's modulus and G is the shear modulus. ρ is the mass per unit volume of the beam and κ is the shear correction factor.

For the free vibration of a beam, the flexural displacement and the angle of rotation due to bending may be written as

$$y(x,t)=Y(x)e^{-i\omega t},\quad \varphi(x,t)=\psi(x)e^{-i\omega t}/L \tag{3}$$

where ω is the eigenfrequency of the beam and $i=\sqrt{-1}$.

Table 1 Some common linearly tapered beams

Type of tapered beams	Taper factors
A uniform beam	$r=0$, $s=0$
A rectangular beam with linearly varying width	$r=1$, $s=1$
A rectangular beam with linearly varying thickness	$r=1$, $s=3$
A rectangular beam with linearly varying both width and thickness	$r=2$, $s=4$
A circular beam with linearly varying radius	$r=2$, $s=4$

Introducing the following nondimensional coordinate and parameters

$$\xi=x/L,\quad \Omega^2=\rho A_1\omega^2 l^4/EI_1,\quad \delta=EI_1/(\kappa GA_1L^2),$$
$$\eta=I_1/(A_1L^2) \tag{4}$$

and substituting Eq. (3) into Eq. (2), the Lagrangian function Λ can be given as follows:

$$\Lambda=\frac{1}{2}\int_\alpha^1\left\{\xi^s\left[\frac{d\psi(\xi)}{d\xi}\right]^2+\frac{1}{\delta}\xi^r\left[\psi(\xi)+\frac{dY(\xi)}{d\xi}\right]^2\right\}d\xi$$
$$-\frac{\Omega^2}{2(1-\alpha)^4}\int_\alpha^1[\xi^rY(\xi)^2+\eta\xi^s\psi(\xi)^2]d\xi. \tag{5}$$

Assuming that the displacement function $Y(\xi)$ and the rotational angle function $\psi(\xi)$ can be written as

$$Y(\xi)=\sum_{j=j_0}^{\infty}a_jY_j(\xi),\quad \psi(\xi)=\sum_{n=j_0}^{\infty}b_n\psi_n(\xi) \tag{6}$$

where both a_j and b_n are unknown coefficients and j_0 is the lowest order of the basis functions. For truncated beams, $j_0=0$, however, for sharp-ended beams, j_0 is determined by the taper factor s of cross-sectional moment of inertia, which will be discussed later. $Y_j(\xi)$ and $\psi_n(\xi)$ are the basis functions, which satisfy at least the geometric boundary conditions of the beam and if possible, all the boundary conditions.

Truncating j and n, respectively, after j_0+J, then substituting Eq. (6) into Eq. (5) and applying the Rayleigh-Ritz method

$$\frac{\partial\Lambda}{\partial a_j}=0,\quad j=j_0,j_0+1,j_0+2,\ldots,j_0+J,$$
$$\frac{\partial\Lambda}{\partial b_n}=0,\quad n=j_0,j_0+1,j_0+2,\ldots,j_0+J, \tag{7}$$

one obtains the eigenfrequency equation as follows:

$$\begin{bmatrix}K_{j\bar{j}} & K_{j\bar{n}}\\ K_{n\bar{j}} & K_{n\bar{n}}\end{bmatrix}\begin{bmatrix}\{A\}\\ \{B\}\end{bmatrix}-\frac{\Omega^2}{(1-\alpha)^4}\begin{bmatrix}M_{j\bar{j}} & M_{j\bar{n}}\\ M_{n\bar{j}} & M_{n\bar{n}}\end{bmatrix}\begin{bmatrix}\{A\}\\ \{B\}\end{bmatrix}=\begin{Bmatrix}0\\ 0\end{Bmatrix} \tag{8}$$

where

$$K_{j\bar{j}}=\frac{1}{\delta}\int_\alpha^1\xi^r\frac{dY_j(\xi)}{d\xi}\frac{dY_{\bar{j}}(\xi)}{d\xi}d\xi,$$

$$K_{j\bar{n}}=\frac{1}{\delta}\int_\alpha^1\xi^r\frac{dY_j(\xi)}{d\xi}\psi_{\bar{n}}(\xi)d\xi,$$

$$K_{n\bar{j}}=\frac{1}{\delta}\int_\alpha^1\xi^r\psi_n(\xi)\frac{dY_{\bar{j}}(\xi)}{d\xi}d\xi,$$

$$K_{n\bar{n}}=\int_\alpha^1\left[\xi^s\frac{d\psi_n(\xi)}{d\xi}\frac{d\psi_{\bar{n}}(\xi)}{d\xi}+\frac{1}{\delta}\xi^r\psi_n(\xi)\psi_{\bar{n}}(\xi)\right]d\xi,$$

$$M_{j\bar{j}}=\int_\alpha^1\xi^rY_j(\xi)Y_{\bar{j}}(\xi)d\xi,\quad M_{j\bar{n}}=M_{n\bar{j}}=0,$$

$$M_{n\bar{n}}=\eta\int_\alpha^1\xi^s\psi_n(\xi)\psi_{\bar{n}}(\xi)d\xi,$$

$$\{A\}=[a_{j_0}\ a_{j_0+1}\ldots a_{j_0+j}]^T,\quad \{B\}=[b_{j_0}\ b_{j_0+1}\ldots b_{j_0+J}]^T. \tag{9}$$

Using the standard eigenvalue program to solve Eq. (8), $2(J+1)$ eigenfrequencies and the unknown coefficients a_j ($j=j_0,j_0+1,\ldots,j_0+J$) and b_n ($n=j_0,j_0+1,\ldots,j_0+J$) corresponding to every eigenfrequency can be easily obtained.

3 The Static Timoshenko Beam Functions (STBF)

Once again consider the tapered beam analyzed in the last section. The differential characteristic equation of the tapered beam under a transverse nondimensional static load $Q(\xi)$ can be given as follows:

$$\delta \frac{d}{d\xi}\left\{\xi^r\left[\frac{dY(\xi)}{d\xi}-\psi(\xi)\right]\right\}=Q(\xi) \tag{10a}$$

$$\frac{d}{d\xi}\left[\xi^s\frac{d\psi(\xi)}{d\xi}\right]+\delta\xi^r\left[\frac{dY(\xi)}{d\xi}-\psi(\xi)\right]=0. \tag{10b}$$

The bending moment $M(\xi)$ and the transverse shear force $V(\xi)$ of the beam are, respectively, given as

$$M(\xi)=-\frac{EI_1}{L^2}\xi^s\frac{d\psi(\xi)}{d\xi},\quad V(\xi)=\frac{\kappa GA_1}{L}\xi^r\left[\frac{dY(\xi)}{d\xi}-\psi(\xi)\right]. \tag{11}$$

At each end of the beam, two boundary equations can be prescribed. For example, at the end $\xi=\alpha$, one has

$$Y(\alpha)=0,\quad \psi(\alpha)=0 \quad \text{for the clamped end} \tag{12a}$$

$$Y(\alpha)=0,\quad M(\alpha)=0 \quad \text{for the simply-supported end} \tag{12b}$$

$$M(\alpha)=0,\quad V(\alpha)=0 \quad \text{for the free end.} \tag{12c}$$

Similarly, the boundary equations at the end $\xi=1$ can also be written.

From equations (10*a*) and (10*b*), an uncoupled differential equation about $\psi(\xi)$ can be derived as follows:

$$\frac{d^2}{d\xi^2}\left[\xi^s\frac{d\psi(\xi)}{d\xi}\right]=Q(\xi). \tag{13}$$

An arbitrary load $Q(\xi)$ can be expanded into a Taylor series

$$Q(\xi)=\sum_{j=0}^{\infty}Q_j(\xi-\xi_c)^j=\sum_{j=0}^{\infty}Q_j\sum_{k=0}^{j}(-1)^{j-k}D_k^j\xi_c^{j-k}\xi^k \tag{14}$$

where ξ_c is the center of the Taylor series expansion and $D_k^j=j!/[k!(j-k)!]$.

Substituting Eq. (14) into Eq. (13), the general solution of the angle of rotation due to bending can be easily given as follows:

$$\psi(\xi)=\sum_{j=0}^{\infty}Q_j\psi_j(\xi) \tag{15}$$

where

$$\psi_j(\xi)=\sum_{k=0}^{j}(-1)^{j-k}D_k^j\xi_c^{j-k}f^k(\xi)+f_0(\xi)C_0^j+f_1(\xi)C_1^j+C_2^j \tag{16}$$

and

$$f^k(\xi)=\frac{1}{(k+1)(k+2)}\begin{cases}\ln(\xi), & k=s-3\\ \xi^{k+3-s}/(k+3-s), & k\neq s-3,\end{cases}$$
$$f_0(\xi)=\begin{cases}\ln(\xi), & s=2\\ \xi^{2-s}/(2-s), & s\neq 2,\end{cases} \tag{17}$$
$$f_1(\xi)=\begin{cases}\ln(\xi), & s=1\\ \xi^{1-s}/(1-s), & s\neq 1.\end{cases}$$

Substituting Eq. (14)–(17) into Eq. (10*a*) or (10b), the general solutions of the transverse displacement can be solved and written in the form of

$$Y(\xi)=\sum_{j=0}^{\infty}Q_jY_j(\xi), \tag{18}$$

where

$$Y_j(\xi)=\sum_{k=0}^{j}(-1)^{j-k}D_k^j\xi_c^{j-k}[F^{1k}(\xi)-\delta F^{2k}(\xi)]+[F_{01}(\xi)-\delta F_{02}(\xi)]C_0^j+F_1(\xi)C_1^j+\xi C_2^j+C_3^j, \tag{19}$$

and

$$F^{1k}(\xi)=\frac{1}{(k+1)(k+2)}\begin{cases}\xi[\ln(\xi)-1], & k=s-3\\ \ln(\xi), & k=s-4\\ \xi^{k+4-r}/[(k+3-s)(k+4-s)], & k\neq s-3;\ k\neq s-4,\end{cases}$$
$$F^{2k}(\xi)=\frac{1}{k+1}\begin{cases}\ln(\xi), & k=r-2\\ \xi^{k+2-r}/(k+2-r), & k\neq r-2,\end{cases}$$
$$F_{01}(\xi)=\begin{cases}\xi[\ln(\xi)-1], & s=2\\ \ln(\xi), & s=3\\ \xi^{3-s}/[(2-s)(3-s)], & s\neq 2;\ s\neq 3,\end{cases}$$
$$F_{02}(\xi)=\begin{cases}\ln(\xi), & r=1\\ \xi^{1-r}/(1-r), & r\neq 1,\end{cases}$$
$$F_1(\xi)=\begin{cases}\xi[\ln(\xi)-1], & s=1\\ \ln(\xi), & s=2\\ \xi^{2-s}/[(1-s)(2-s)], & s\neq 1;\ s\neq 2.\end{cases} \tag{20}$$

In Eq. (16) and (19), C_k^j $(k=0,1,2,3)$ are the unknown constants.

3.1 Truncated Beam. For the truncated beams without rigid-body movements, the unknown coefficients C_k^j $(k=0,1,2,3)$ in Eq. (16) and (19) can be uniquely determined from the four boundary equations of the beam for every j. However, for a beam with rigid-body movements, these unknown coefficients cannot be determined directly from the boundary equations of the beam. In such a case, one can divide the basis functions into two parts: the rigid-body modes and a set of basic solutions which are

Table 2 The static beam functions (SBF) $y_i(\xi)$ ($i=1,2,3,\ldots$) for truncated tapered Timoshenko beams with rigid-body movements

B. C.	The first STBF	The second STBF	The third and higher STBF
F-F	$Y_1(\xi)=1$; $\psi_1(\xi)=0$	$Y_2(\xi)=\xi-(1-\alpha)/2$; $\psi_2(\xi)=1$	The first and higher STBF for the S-S beam
S-F	$Y_1(\xi)=\xi-\alpha$; $\psi_1(\xi)=1$	The first STBF for the S-S beam	The second and higher STBF for the S-S beam
F-S	$Y_1(\xi)=\xi-1$; $\psi_1(\xi)=1$	The first STBF for the S-S beam	The second and higher STBF for the S-S beam

Table 3 The static beam functions (SBF) $y_i(\xi)$ ($i=1,2,3,\ldots$) for sharp-ended Timoshenko beams with rigid-body movements

B. C.	The first STBF	The second STBF	The third and higher STBF
F-F	$Y_1(\xi)=1$; $\psi_1(\xi)=0$	$Y_2(\xi)=\xi-1$; $\psi_2(\xi)=1$	The first and higher STBF for the F-C beam
F-S	$Y_1(\xi)=\xi-1$; $\psi_1(\xi)=1$	The first STBF for the F-C beam	The second and higher STBF for the F-C beam

Table 4 The convergence study on eigenfrequencies of a cantilevered beam clamped at the wider end and with linearly varying width, $h_1/l=0.3$

J	Ω_1	Ω_2	Ω_3	Ω_4
		$\alpha=0$		
0	6.4302	82.426		
1	6.4264	21.548	84.686	103.79
2	6.4102	21.546	43.220	84.675
3	6.4099	21.151	43.218	67.344
4	6.4098	21.147	40.977	67.314
5	6.4098	21.145	40.973	61.631
6	6.4098	21.145	40.929	61.631
7	6.4098	21.145	40.929	61.389
8	6.4098	21.145	40.929	61.389
9	6.4098	21.145	40.929	61.385
		$\alpha=0.5$		
0	4.0250	79.766		
1	4.0020	17.391	81.982	100.17
2	4.0020	16.734	38.350	82.148
3	4.0020	16.732	35.702	61.416
4	4.0020	16.732	35.638	55.671
5	4.0020	16.731	35.626	55.432
6	4.0020	16.730	35.613	55.353
7	4.0020	16.730	35.608	55.292
8	4.0020	16.730	35.605	55.266
9	4.0020	16.730	35.604	55.258
		$\alpha=0.75$		
0	3.6037	79.271		
1	3.5781	16.848	81.714	100.05
2	3.5780	16.092	38.218	81.928
3	3.5780	16.092	35.143	61.603
4	3.5780	16.092	35.125	55.025
5	3.5780	16.091	35.114	54.927
6	3.5780	16.090	35.103	54.850
7	3.5780	16.090	35.097	54.799
8	3.5780	16.090	35.094	54.769
9	3.5780	16.090	35.092	54.760

the basis functions of the beam with additional restraints eliminating the rigid-body movements ([13]). The authors used this simple method time and again to analyze the vibrations of beams and plates ([14–16]). Up to now, no failure case has been found. In the present analysis, the static Timoshenko beam functions for the beam with simply supported two ends are selected as the basic solutions, which are supplemented by the modes of rigid-body movements as given in Table 2.

3.2 Sharp-Ended Beam. For the sharp-ended beams, the sharp end cannot sustain a bending or a shear force, hence one has

$$C_0^j=0, \quad C_1^j=0. \tag{21}$$

Moreover, the displacement and rotational angle of the beam should be finite at the sharp end, so that there is a limit to the lowest order of the Taylor series load as follows:

$$j>s-2. \tag{22}$$

Therefore, the lowest order of the Taylor series should be taken as

$$j_0=\mathrm{Max}\{\mathrm{Int}(s-1),0\} \tag{23}$$

and Eq. (13) should be replaced by

$$Q(\xi)=\sum_{j=j_0}^{\infty} Q_j(\xi-\xi_c)^j=\sum_{j=j_0}^{\infty} Q_j\sum_{k=j_0}^{j}(-1)^{j-k}D_k^j\xi_c^{j-k}\xi^k \tag{24}$$

For the cantilevered sharp-ended beams (F-C beams), the unknown coefficients C_2^j and C_3^j in Eq. (16) and (19) can be uniquely determined from the boundary equations of the beam at $\xi=1$ for each j. While for a beam with rigid-body movements, the static Timoshenko beam functions for the cantilevered sharp-ended beam are taken as the basic solutions, which are supplemented by the modes of rigid-body movements as given in Table 3.

4 Convergence and Comparison Study

Using the static Timoshenko beam functions derived in the last section as the basis functions of the tapered Timoshenko beams, the convergence and comparison study is carried out in this section. It should be pointed out that the convergence is concerned with the center ξ_c of the Taylor series expansion ([13]). The best convergence can be obtained when the midpoint of the beam is taken as the center of the Taylor series expansion, i.e., $\xi c=(1+\alpha)/2$. This phenomenon can be easily explained: $\xi_c=(1+\alpha)/2$ can provide the optimal convergence for the Taylor series expansion in the interval $[\alpha,1]$. Without lose of generality, in all the following computations, only the tapered beams with rectangular cross section are analyzed and parameters $\xi_c=(1+\alpha)/2$, $\kappa=5/6$, Poisson's ratio $\nu=0.3$ are used unless otherwise stated. In such a case, $\delta=0.26(1-\alpha)^2(h_1/l)^2$ and $\eta=(1-\alpha)^2(h_1/l)^2/12$ where h_1 is the thickness of the tapered beam at $\xi=1$ and h_1/l is the thickness-length ratio of the beam.

The convergence study on eigenfrequencies of a cantilevered beam with linearly varying width, which is clamped at the wider end, is first considered. The first four eigenfrequencies versus the number of terms of the static Timoshenko beam functions from 1 to 10 are given in Table 4 for the beam with a thickness-length ratio $h_1/l=0.3$. It can be seen that in general, four to eight terms of the static Timoshenko beam functions are sufficient to give the first four eigenfrequencies with quite satisfactory accuracy. It should be reminded that when the value of the truncation factor α is close to 1, the tapered beams approximate to the uniform beams. However, it is obvious that Eqs. (16) and (19) are singular at $\alpha=1$. Therefore, the larger is α (especially when $\alpha>0.8$), the smaller number of terms of the static beam functions can be used in the computation. For example, when $\alpha=0.9$ only no more than three terms of the static Timoshenko beam functions can provide stable numerical computations under double precision. In order to prevent the occurrence of ill-conditioning and increase the number of significant figures, quadruple precision is used in the following computations by taking $J=7$ for $\alpha<0.7$; $J=6$ for $0.7\leqslant\alpha<0.8$; $J=5$ for $0.8\leqslant\alpha<0.9$, and $J=4$ for $\alpha=0.9$.

The comparison study on the first four eigenfrequencies is given in Table 5 for both thick beams (Timoshenko beams) with linearly varying thickness and slender beams (Bernoulli-Euler beams) with linearly varying thickness. The reference data come from finite element method ([4]), step-reduction method ([10]), Frobenius' method ([17]), and series solution ([11]), respectively.

Table 5 The comparison study on the first four eigenfrequencies of tapered beams with linearly varying thickness

α, h_1/l	B.C.	Sources	Ω_1	Ω_2	Ω_3	Ω_4
0, 0.001	F-C	Present	5.3151	15.207	30.020	49.765
		Naguleswaran (1994)+	5.3151	15.207	30.020	49.763
0.2, 0.001	F-C	Present	4.2925	15.743	36.884	68.158
		Naguleswaran (1994)+	4.2925	15.743	36.885	—
0.5, 0.001	F-C	Present	3.8233	18.313	47.345	90.476
		Naguleswaran (1994)+	3.8238	18.317	47.265	—
0.0, 0.001	F-S	Present	10.902	24.631	43.205	66.688
		Naguleswaran (1994)+	10.902	24.631	43.205	66.683
0.2, 0.001	F-S	Present	10.739	29.407	58.115	97.105
		Naguleswaran (1994)+	10.739	29.407	58.115	—
0.0, 0.001	F-F	Present	12.757	27.755	47.577	72.571
		Naguleswaran (1994)+	12.758	27.755	47.576	72.295
0.2, 0.001	F-F	Present	13.384	34.488	65.753	107.36
		Naguleswaran (1994)+	13.384	34.488	65.737	—
0.6, $0.04\sqrt{3}$	F-C	Present	3.7250	18.783	48.385	90.442
		Rossi et al. (1990)	3.72	18.77	48.36	90.46
0.6, $0.08\sqrt{3}$	F-C	Present	3.6894	17.890	43.735	77.155
		Rossi et al. (1990)	3.69	17.88	43.74	77.32
0.6, $0.12\sqrt{3}$	F-C	Present	3.6326	16.659	38.450	64.527
		Rossi et al. (1990)	3.62	16.65	38.48	64.77
0.6, $0.16\sqrt{3}$	F-C	Present	3.5579	15.309	33.646	54.482
		Rossi et al. (1990)	3.55	15.30	33.69	54.75
0.6, $0.2\sqrt{3}$	F-C	Present	3.4688	13.984	29.618	46.704
		Rossi et al. (1990)	3.47	13.98	29.68	46.97
0.5, 0.09928	C-C	Present++	15.638	40.923	75.554	117.24
		Tong et al. (1995)++	15.639	40.923	75.543	116.96
0.8, $0.04\sqrt{3}$	S-C	Present*	14.034	43.411	86.952	142.75
		Lee and Lin (1995)*	14.035	43.400	87.008	142.372
0.8, $0.04\sqrt{3}$	C-C	Present**	19.563	52.223	98.419	156.11
		Lee and Lin (1995)**	19.561	52.208	98.365	155.358

+ Bernoulli-Euler beam theory is used; ++ $\kappa=0.667$ and $\nu=0.3125$ are used; * $\nu=29/96$ is used;
** $\nu=7/24$ is used.

Table 6 The accuracy comparison of the first two eigenfrequencies for a simply-simply supported Timoshenko beam with linearly varying thickness, respectively, using the static Timoshenko beam functions (STBF) on the tapered beam and vibrating Timoshenko beam functions (VTBF) of uniform beam

α	h_1/l	Methods	J	Ω_1	Ω_2
0.1	0.1	STBF	3	3.8731	17.866
			7	3.8712	17.863
		VTBF	3	4.1072	19.707
			7	3.9164	18.162
	0.3	STBF	3	3.7353	16.184
			7	3.7332	16.179
		VTBF	3	3.9792	17.517
			7	3.8019	16.401
0.2	0.1	STBF	3	4.8911	20.984
			7	4.8911	20.930
		VTBF	3	4.9607	21.687
			7	4.9003	20.987
	0.3	STBF	3	4.6793	18.465
			7	4.6792	18.412
		VTBF	3	4.7683	18.919
			7	4.7137	18.451
0.3	0.1	STBF	3	5.7055	23.621
			7	5.7055	23.508
		VTBF	3	5.7290	23.820
			7	5.7097	23.522
	0.3	STBF	3	5.4164	20.242
			7	5.4164	20.140
		VTBF	3	5.4604	20.336
			7	5.4433	20.150
uniform beam	0.3	STBF	3	8.6839	27.319
			7	8.6839	27.315
		Exact solution		8.6839	27.315

Three kinds of support conditions are considered: beams with the clamped thicker end and the free thinner end (F-C); beams with two clamped ends (C-C); and beams clamped at the thicker end; and simply supported at the thinner end (S-C). Good agreement has been observed for all cases.

The comparison study on the first two eigenfrequencies of a simply-simply supported Timoshenko beam with linearly varying thickness based on three values of truncation factors ($\alpha=0.1,0.2,0.3$), respectively, by using the static Timoshenko beam functions developed from the tapered beam and the conventional vibrating Timoshenko beam functions developed from the uniform beam are given in Table 6. It is seen that accuracy and convergence of the vibrating Timoshenko beam functions are worse than those of the static Timoshenko beam functions. This is always true for fundamental eigenfrequencies of tapered beams with any truncation factor although the vibrating Timoshenko beam functions are the exact solutions for uniform Timoshenko beams. It is shown that using the vibrating Timoshenko beam functions as basis functions in the Rayleigh-Ritz method, the accuracy and convergence of eigenfrequencies of a tapered beam will decrease with the decrease of the truncation factor α. The above analysis demonstrates that when developing the basis functions for tapered beams, especially for the beams with a small truncation factor, the effect of both the variation of cross section and the shear correction factor should be considered.

5 Numerical Results

A survey on the literature reveals that the available results for vibrations of Timoshenko beams with varying cross section are very limited and only results about beams with larger truncation factor ($\alpha\geqslant 0.6$) can be found. Therefore, it is meaningful to systematically provide some data what can serve as a benchmark of further reference for researchers and present useful information for designers. In this section, three types of tapered beams are first analyzed in detail: beams with linearly varying thickness; beams with linearly varying width; and beams with linearly varying both width and thickness. In the analysis, three kinds of support conditions are considered: clamped-clamped beams (C-C); simply-simply supported beams (S-S); cantilevered beams with the clamped larger end (F-C). The first three eigenfrequencies of the tapered Timoshenko beams with three types of varying cross sections are given, respectively, in Table 7, Table 8, and Table 9 for truncation factor α varying from 0 to 0.9 with an increment 0.1. In every case, two kinds of thickness-length ratios: $h_1/l=0.1$; $h_1/l=0.2$ are considered. From these tables, one can see that in most cases, the eigenfrequencies of the beams increase with the increase of the truncation factor α. However, for the F-C beams with linearly varying thickness and the F-C beams with both linearly varying thickness and linearly varying width, the fundamental eigenfrequencies decrease with the increase of the truncation factor. And for the F-C beams with linearly varying width, the first

Table 7 The first three eigenfrequencies of Timoshenko beams with linearly varying thickness, Case A: F-C beams; Case B: C-C beams; Case C: S-S beams

α	Case A			Case B			Case C		
	Ω_1	Ω_2	Ω_3	Ω_1	Ω_2	Ω_3	Ω_1	Ω_2	Ω_3
					$h_1/l=0.1$				
0.1	4.6047	14.685	31.739	9.7429	26.136	49.829	3.8712	17.863	38.796
0.2	4.2680	15.426	35.319	11.609	31.052	58.868	4.8911	20.930	45.528
0.3	4.0576	16.230	38.513	13.148	35.024	65.995	5.7055	23.508	51.069
0.4	3.9100	17.008	41.403	14.512	38.470	72.038	6.4142	25.822	55.937
0.5	3.7992	17.746	44.056	15.759	41.558	77.337	7.0552	27.960	60.343
0.6	3.7120	18.444	46.795	16.920	44.373	82.071	7.6475	29.967	64.395
0.7	3.6411	19.106	48.825	18.011	46.970	86.520	8.2026	31.869	68.181
0.8	3.5821	19.736	51.012	19.045	49.391	90.583	8.7279	33.685	71.740
0.9	3.5317	20.335	—	20.031	52.420	—	9.2282	35.793	—
					$h_1/l=0.2$				
0.1	4.5294	14.016	29.057	9.3525	23.969	43.530	3.8178	17.159	35.827
0.2	4.1971	14.586	31.677	10.987	27.730	49.597	4.8082	19.845	41.045
0.3	3.9880	15.204	33.912	12.280	30.550	53.933	5.5912	22.019	45.070
0.4	3.8401	15.786	35.841	13.382	32.835	57.309	6.2655	23.905	48.407
0.5	3.7284	16.321	37.533	14.351	34.754	60.049	6.8685	25.689	51.272
0.6	3.6401	16.808	39.036	15.220	36.400	62.330	7.4193	27.120	53.781
0.7	3.5677	17.253	40.384	16.007	37.831	64.310	7.9290	28.525	56.022
0.8	3.5070	17.658	41.613	16.725	39.091	66.132	8.4048	29.828	58.082
0.9	3.4550	18.028	—	17.387	40.554	—	8.8520	31.500	—

Table 8 The first three eigenfrequencies of Timoshenko beams with linearly varying width, Case A: F-C beams; Case B: C-C beams; Case C: S-S beams

α	Case A			Case B			Case C		
	Ω_1	Ω_2	Ω_3	Ω_1	Ω_2	Ω_3	Ω_1	Ω_2	Ω_3
				$h_1/l=0.1$					
0.1	5.9984	25.804	60.448	19.434	51.368	94.370	9.3397	36.988	78.048
0.2	5.3395	24.302	58.483	20.103	52.484	95.746	9.4891	37.113	78.208
0.3	4.8822	23.406	57.452	20.452	53.017	96.357	9.5734	37.132	78.217
0.4	4.5418	22.786	56.789	20.659	53.317	96.689	9.6256	37.127	78.202
0.5	4.2760	22.315	56.312	20.789	53.498	96.885	9.6591	37.118	78.186
0.6	4.0611	21.937	55.943	20.871	53.611	97.005	9.6807	37.109	78.173
0.7	3.8829	21.622	55.646	20.922	53.681	97.077	9.6942	37.103	78.164
0.8	3.7318	21.353	55.397	20.953	53.721	97.120	9.7023	37.099	78.159
0.9	3.6018	21.118	—	20.964	53.778	—	9.7063	37.099	—
				$h_1/l=0.2$					
0.1	5.7994	22.532	47.837	16.599	39.188	66.621	8.8012	31.751	60.904
0.2	5.1777	21.303	46.413	17.214	40.133	67.627	9.0027	32.033	61.294
0.3	4.7438	20.553	45.643	17.529	40.580	68.073	9.1098	32.118	61.399
0.4	4.4195	20.022	45.137	17.715	40.832	68.315	9.1746	32.149	61.436
0.5	4.1656	19.615	44.767	17.831	40.984	68.458	9.2155	32.160	61.450
0.6	3.9600	19.284	44.478	17.904	41.078	68.545	9.2417	32.165	61.455
0.7	3.7890	19.005	44.244	17.950	41.136	68.598	9.2581	32.166	61.457
0.8	3.6440	18.765	44.051	17.977	41.170	68.629	9.2678	32.166	61.458
0.9	3.5190	18.554	—	17.992	41.215	—	9.2726	32.170	—

three eigenfrequencies all decrease with the increase of the truncation factor. Furthermore, it is seen that the effect of the truncation factor on the eigenfrequencies of C-C and S-S beams with linearly varying width is substantially lower than that on the eigenfrequencies of other cases.

In Fig. 2, the first three eigenfrequencies of the sharp-ended Timoshenko beams clamped at the larger end are also given with respect to different thickness-length ratio h_1/l. Three types of varying cross sections are considered. Moreover, the first three eigenfrequencies of the truncated tapered beams with the clamped larger end and the free smaller end for thickness-length ratio h_1/l from 0.001 to 0.5 are given, respectively, in Fig. 3, Fig. 4, and Fig. 5. Three types of varying cross sections are also considered, respectively. From the results, one can find that the thickness-length ratio h_1/l has an important effect on the eigenfrequencies of Timoshenko beams, which increases with both the increase of h_1/l and the order of the eigenfrequencies. It is seen that increasing the thickness-length ratio trends to lower the eigenfrequencies.

When the truncation factor α=0.5, the fundamental eigenfrequencies of cantilevered truncated Timoshenko beams with the same thickness and width variations are given in Fig. 6 with respect to the thickness-length ratio h_1/l for 0.001 to 0.5. Six groups of taper factors: $r=4$ and $s=8$; $r=3$ and $s=6$; $r=2$ and $s=4$; $r=1$ and $s=2$; $r=-1$ and $s=-2$; $r=-2$ and $s=-4$ are considered. In Fig. 7, the first two eigenfrequencies of cantilevered sharp-ended Timoshenko beams are given with respect to

Table 9 The first three eigenfrequencies of Timoshenko beams with linearly varying both width and thickness, Case A: F-C beams; Case B: C-C beams; Case C: S-S beams

α	Case A			Case B			Case C		
	Ω_1	Ω_2	Ω_3	Ω_1	Ω_2	Ω_3	Ω_1	Ω_2	Ω_3
				$h_1/l=0.1$					
0.1	7.1452	18.327	35.809	10.597	27.299	51.109	3.0302	18.794	40.176
0.2	6.1488	17.987	38.088	12.128	31.743	59.608	4.3201	21.490	46.364
0.3	5.4681	18.178	40.582	13.483	35.462	66.451	5.3150	23.866	51.602
0.4	4.9720	18.528	42.985	14.727	38.750	72.321	6.1527	26.051	56.276
0.5	4.5909	18.929	45.262	15.893	41.730	77.507	6.8874	28.102	60.551
0.6	4.2865	19.343	47.416	16.998	44.474	82.166	7.5474	30.049	64.516
0.7	4.0351	19.757	49.486	18.052	46.925	86.615	8.1498	31.912	68.244
0.8	3.8282	20.175	51.340	19.060	49.433	90.586	8.7055	33.703	71.759
0.9	3.6453	20.538	—	20.035	52.428	—	9.2230	35.800	—
				$h_1/l=0.2$					
0.1	6.9749	17.382	32.626	10.142	24.983	44.562	2.9692	17.988	36.975
0.2	6.0125	16.940	34.061	11.456	28.311	50.156	4.2261	20.322	41.701
0.3	5.3505	16.985	35.666	12.575	30.907	54.258	5.1894	22.312	45.467
0.4	4.8661	17.170	37.168	13.567	33.055	57.499	5.9941	24.084	48.648
0.5	4.4932	17.394	38.534	14.464	34.886	60.157	6.6930	25.696	51.413
0.6	4.1948	17.622	39.773	15.284	36.474	62.388	7.3137	27.179	53.859
0.7	3.9491	17.838	40.898	16.039	37.867	64.358	7.8727	28.555	56.062
0.8	3.7399	18.025	41.987	16.738	39.105	66.133	8.3811	29.840	58.067
0.9	3.5644	18.211	—	17.390	40.557	—	8.8463	31.519	—

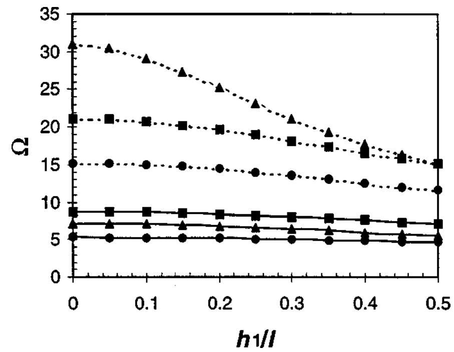

Fig. 2 The first two eigenfrequencies of cantilevered sharp-ended Timoshenko beams with linearly varying thickness and/or width via the thickness-length ratio h_1/l: –●– Ω_1 and - -●- - Ω_2 for the beams with linear varying thickness; –▲– Ω_1 and - -▲- - Ω_2 for the beams with linear varying width; –■– Ω_1 and - -■- - Ω_2 for the beams with linear varying both thickness and width

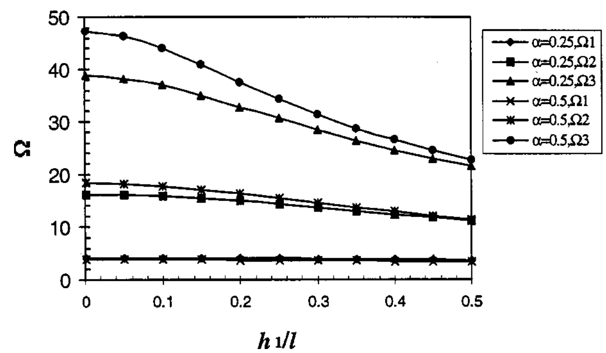

Fig. 3 The first three eigenfrequencies of cantilevered Timoshenko beams with linearly varying thickness via the thickness-length ratio h_1/l for two values of truncation factors α=0.25 and α=0.5

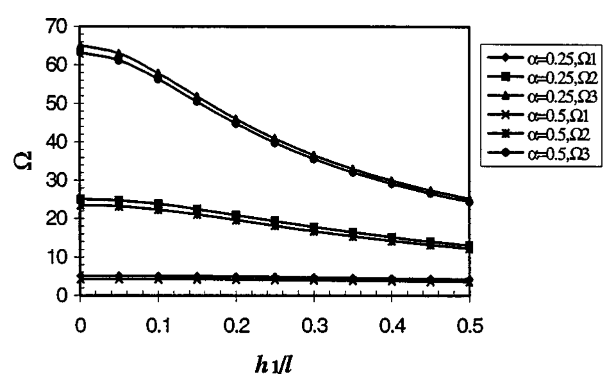

Fig. 4 The first three eigenfrequencies of cantilevered Timoshenko beams with linearly varying width via the thickness-length ratio h_1/l for two values of truncation factors α=0.25 and α=0.5

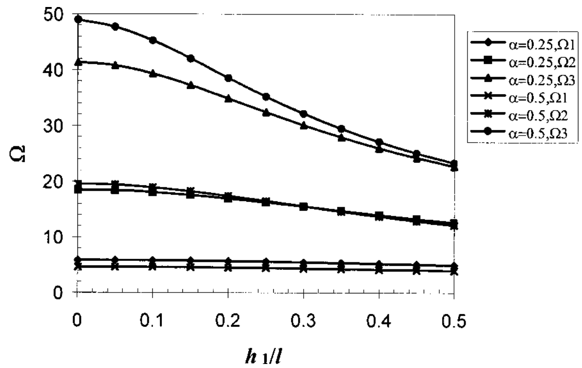

Fig. 5 The first three eigenfrequencies of cantilevered Timoshenko beams with linearly varying both thickness and width via the thickness-length ratio h_1/l for two values of truncation factors $\alpha=0.25$ and $\alpha=0.5$

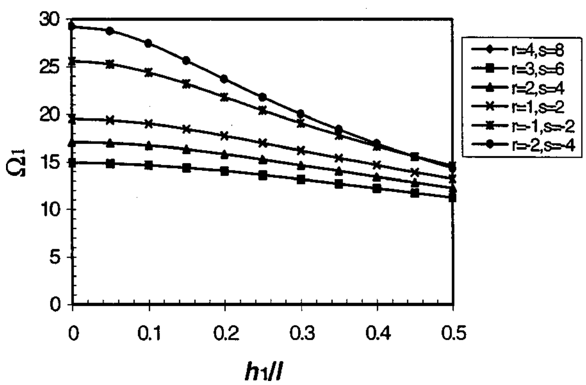

Fig. 6 The fundamental eigenfrequencies of cantilevered Timoshenko beams with the same thickness and width variation via the thickness-length ratio h_1/l for the truncation factor $\alpha=0.5$

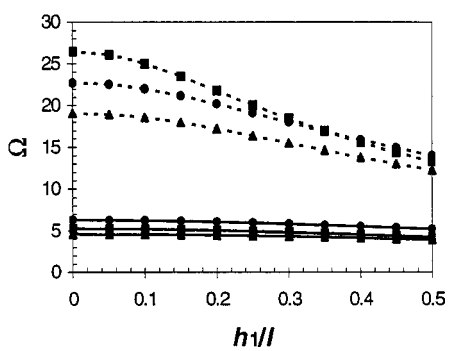

Fig. 7 The first two eigenfrequencies of cantilevered sharp-ended Timoshenko beams via the thickness-length ratio h_1/l: –●– Ω_1 and - -●- - Ω_2 for taper factors $r=1$, $s=2$; –▲– Ω_1 and - -▲- - Ω_2 for taper factors $r=1/2$, $s=3/2$; –■– Ω_1 and - -■- - Ω_2 for taper factors $r=1/2$, $s=1/2$

the thickness-length ratio h_1/l from 0.001 to 0.5. Three groups of taper factors: $r=1$ and $s=2$; $r=1/2$ and $s=3/2$; $r=1/2$ and $s=1/2$ are considered. It is seen that the present method can be applied to analyze the vibratory characteristics of a wide range of tapered Timoshenko beams.

6 Conclusions

The static Timoshenko beam functions which are the complete solutions of the tapered Timoshenko beams under a Taylor series of static loads, are developed as the basis functions of the flexural displacement and the angle of rotation due to bending to analyze the vibrations of Timoshenko beams with varying cross section in the Rayleigh-Ritz method. Unlike conventional basis functions such as vibrating Timoshenko beam functions for uniform Timoshenko beams which are independent of the cross-sectional variation of the beam, the static Timoshenko beam functions developed in this paper closely tie with the cross-sectional variation of the beam. Therefore, they are, in a sense, a set of optimal basis functions for vibration analysis of tapered Timoshenko beams. A wide range of tapered Timoshenko beams with the cross section of power variation is studied for both truncated beams and sharp-ended beams. The convergence and comparison studies show that the first few eigenfrequencies can be given with sufficiently satisfactory accuracy by using only a small number of terms of the static Timoshenko beam functions. Finally, some valuable results are presented systematically.

Acknowledgment

This research was supported by a CRCG grant from The University of Hong Kong.

References

[1] Timoshenko, S. P., 1922, ''On the Transverse Vibrations of Bars of Uniform Cross Section,'' Philos. Mag., **43**, (Series 6), pp. 379–384.
[2] To, C. W. S., 1981, ''A Linearly Tapered Beam Finite Element Incorporating Shear Deformation and Rotary Inertia for Vibration Analysis,'' J. Sound Vib., **78**, pp. 475–484.
[3] Cleghorn, W. L., and Tabarrok, B., 1992, ''Finite Element Formulation of a Tapered Timoshenko Beam of Non-uniform Thickness,'' J. Sound Vib., **152**, pp. 461–470.
[4] Rossi, R. E., Laura, P. A. A., and Gutierrez, R. H., 1990, ''A Note on Transverse Vibrations of a Timoshenko Beam of Non-uniform Thickness Clamped at One End and Carrying a Concentrated Mass at the Other,'' J. Sound Vib., **143**, pp. 491–502.
[5] Irie, T., Yamada, G., and Takahashi, I., 1979, ''Determination of the Steady State Response of a Timoshenko Beam of Varying Cross-Section by Use of the Spline Interpolation Technique,'' J. Sound Vib., **63**, pp. 287–295.
[6] Gutierrez, R. H., Laura, P. A. A., and Rossi, R. E., 1991, ''Fundamental Frequency of Vibration of a Timoshenko Beam of Non-uniform Thickness,'' J. Sound Vib., **145**, pp. 341–344.
[7] Chehil, D. S., and Jategaonkar, R., 1987, ''Determination of Natural Frequencies of a Beam With Varying Cross Section Properties,'' J. Sound Vib., **115**, pp. 423–436.
[8] Jategaonkar, R., and Chehil, D. S., 1989, ''Natural Frequencies of a Beam With Varying Section Properties,'' J. Sound Vib., **133**, pp. 303–322.
[9] Irie, T., Yamada, G., and Takahashi, I., 1980, ''Vibration and Stability of a Non-uniform Timoshenko Beam Subjected to a Follower Force,'' J. Sound Vib., **70**, pp. 503–512.
[10] Tong, X., Tabarrok, B., and Yeh, K. Y, 1995, ''Vibration Analysis of Timoshenko Beams With Non-homogeneity and Varying Cross-section,'' J. Sound Vib., **186**, pp. 821–835.
[11] Lee, S. Y., and Lin, S. M., 1992, ''Exact Vibration Solutions for Nonuniform Timoshenko Beams With Attachments,'' AIAA J., **30**, pp. 2930–2934.
[12] Laura, P. A. A., Maurizi, M. J., and Rossi, R. E., 1990, ''A Survey of Studies Dealing With Timoshenko Beams,'' Shock Vib. Dig., **22**, No. 11, pp. 3–10.
[13] Zhou, D., and Cheung, Y. K., 2000, ''The Free Vibration of a Type of Tapered Beams,'' Comput. Methods Appl. Mech. Eng., **188**, pp. 203–216.
[14] Cheung, Y. K., and Zhou, D., 1999, ''Eigenfrequencies of Tapered Rectangular Plates With Intermediate Line Supports,'' Int. J. Solids Struct., **36**, pp. 143–166.
[15] Cheung, Y. K., and Zhou, D., 1999, ''The Free Vibrations of Tapered Rectangular Plates Using a New Set of Beam Functions with the Rayleigh-Ritz Method,'' J. Sound Vib., **223**, pp. 703–722.
[16] Zhou, D., 1996, ''Natural Frequencies of Rectangular Plates Using a Set of Static Beam Functions in Rayleigh-Ritz Method,'' J. Sound Vib., **189**, pp. 81–97.
[17] Naguleswaran, S., 1994, ''A Direct Solution for the Transverse Vibration of Euler-Bernoulli Wedge and Cone Beams,'' J. Sound Vib., **172**, pp. 289–304.

T. L. Yip

T. Sahoo

A. T. Chwang
Fellow ASME

Department of Mechanical Engineering,
The University of Hong Kong,
Pokfulam Road,
Hong Kong

Wave Oscillation in a Circular Harbor With Porous Wall

The wave resonance in a circular harbor surrounded by a porous seawall is analyzed. Matching the velocity and pressure along the porous seawall and the harbor entrance, the full solution is obtained. The resonance condition is found to depend on the wave frequency, the complex porous-effect parameter and the internal dimension of the porous seawall. The oscillation characteristics are analyzed in different cases. The condition for natural oscillation is derived by studying the wave resonance in a closed circular harbor surrounded by a porous seawall. [DOI: 10.1115/1.1379955]

1 Introduction

In the last decade, there has been a significant change in the nature of harbor traffic in Hong Kong, which results in the deterioration of wave conditions in Victoria Harbor. As a result, the dynamic and mooring forces acting on ships and docks are seriously affected by the high wave oscillation and in turn create serious problems to different marine structures, affecting loading and unloading of cargoes. As a means to dissipate wave energy, a porous seawall is introduced inside an existing harbor, which will reduce the wave oscillation and improve the general wave climate.

The vertical-wall harbors are widely used for their simple design and construction. In the presence of waves, a vertical harbor wall reflects most of the wave energy incident on it. With strong harbor oscillations, vertical walls are subjected to large wave forces. Recently, permeable breakwaters, detached breakwaters, and submerged breakwaters have received much attention and their capability to dissipate wave energy is widely studied. Some of the energy-dissipating breakwaters are being tested in harbors ([1,2]).

On the other hand, wave agitation in harbor due to an incoming wave of a particular frequency may last for a long time. This agitation leads to a resonant state and is the cause of extremely high wave oscillations inside the harbor. The dynamic and mooring forces acting on marine structures are increased during this high oscillation which usually create serious problems to loading and unloading of cargoes. Thus, during the harbor planning, measures should be taken to avoid such harbor resonance. There are two kinds of oscillations existing in a harbor, one is the free oscillation and the other forced oscillation. Lamb [3] analyzed the effect of free oscillation in closed rectangular, circular, and elliptical basins. McNown [4] investigated the forced oscillation in a circular harbor having a narrow opening. In a rectangular harbor, the effect of forced oscillation was analyzed by Kravtchnenko and McNown [5]. Further study on harbor resonance was done by Miles and Munk [6], LeMehaute [7] and Ippen and Goda [8]. Miles and Munk [6] found that the wider the harbor mouth, the smaller the amplitude of the resonant oscillation which is contradictory to the fact that less wave energy will be transmitted to the harbor through a smaller opening. This phenomenon was known as the harbor paradox. Lee [9] considered rectangular and circular harbors with their openings located on a straight coastline while Mei and Petroni [10] dealt with a circular harbor protruding halfway into the open sea. To deal with arbitrary harbor configuration, Hwang and Tuck [11] and Lee [9] developed integral equation methods while Mei and Chen [12] provided a hybrid element method. Numerical studies for harbors of arbitrary geometry have also been verified by field and experimental data (e.g. [9,11]). Recently, certain amount of numerical work is available to include the reflectivity of the harbor wall ([13,14]). However, because of the deficiency of numerical methods, the results can only represent special conditions, not the general relationship between the reflectivity and the harbor oscillation.

In recent times, porous breakwaters are being constructed for dissipating wave energy in order to reduce the hydrodynamic forces on breakwaters. With the assumption of Darcy's law, Sollitt and Cross [15] and Chwang [16] separately developed models to study the flow past porous structures. These methods were unified and combined by Yu and Chwang [17] to become the most acceptable one in the recent literature of flow past porous structures. Yu and Chwang [17] studied the problem of wave resonance in a harbor with a porous breakwater. It is observed that a porous breakwater can reduce the amplitude of resonant frequency significantly. A small but finite permeability of the breakwater is found to be optimal to diminish the resonant oscillation.

In the present paper, we investigate the problem of wave resonance in a circular basin surrounded by a porous breakwater. The basin has an entrance located on a straight coastline. As a particular case, the wave resonance in a closed circular basin surrounded by a permeable breakwater is analyzed. Matching the velocity as well as the pressure along the porous seawall and the harbor entrance, the full solution is obtained and the resonance condition is derived. The effect of the porous-effect parameter and the position of the breakwater on wave oscillation are analyzed. The present work should be useful in future harbor design and modifications.

2 Formulation of the Problem

The problem under consideration is three dimensional in nature and is studied in a cylindrical coordinate system with uniform depth h. The opening of the harbor is along the coastline at a distance $b\cos\varepsilon$ from the center of the harbor with 2ε being the opening angle of the harbor (see Fig. 1). The circular harbor is of radius b with an inner permeable circular wall of radius a. Assuming that the fluid is inviscid and incompressible and its motion irrotational, we can define a velocity potential $\Phi(r,\theta,z,t)$ which satisfies the Laplace equation. Assuming the motion is simple harmonic in time, we can express Φ as $\Phi(r,\theta,z,t) = \mathrm{Re}[\phi(r,\theta,z)e^{-i\omega t}]$ with ω being the angular frequency. The fluid domain is divided into three regions: (i) the open sea region, (ii) the region between the porous wall and the solid harbor wall and (iii) the inner harbor region surrounded by the porous wall. ϕ_j $(j=1,2,3)$ denotes the velocity potential in region j. The spatial velocity potential ϕ satisfies the Laplace equation

Contributed by the Applied Mechanics Division of THE AMERICAN SOCIETY OF MECHANICAL ENGINEERS for publication in the ASME JOURNAL OF APPLIED MECHANICS. Manuscript received by the ASME Applied Mechanics Division, June 24, 2000; final revision, Sept. 26, 2000. Associate Editor: D. A. Siginer. Discussion on the paper should be addressed to the Editor, Prof. Lewis T. Wheeler, Department of Mechanical Engineering, University of Houston, Houston, TX 77204-4792, and will be accepted until four months after final publication of the paper itself in the ASME JOURNAL OF APPLIED MECHANICS.

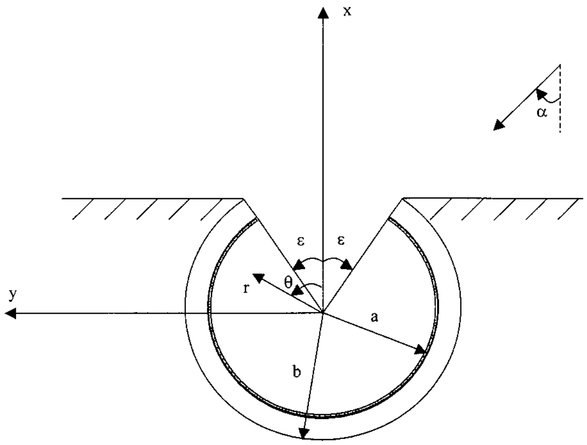

Fig. 1 Schematic diagram of a circular harbor

$$\frac{1}{r}\frac{\partial}{\partial r}\left(r\frac{\partial\phi}{\partial r}\right)+\frac{1}{r^2}\frac{\partial^2\phi}{\partial\theta^2}+\frac{\partial^2\phi}{\partial z^2}=0. \tag{1}$$

The free surface boundary condition is given by

$$\frac{\partial\phi}{\partial z}-\frac{\omega^2}{g}\phi=0 \quad \text{at } z=0, \tag{2}$$

where g is the gravitational constant. The bottom boundary condition is given by

$$\frac{\partial\phi}{\partial z}=0 \quad \text{at } z=-h. \tag{3}$$

As r tends to infinity, the scattered wave potential ϕ_s satisfies the radiation condition

$$\sqrt{r}\left(\frac{\partial\phi_s}{\partial r}-ik_0\phi_s\right)\to 0, \quad \text{as } r\to\infty, \tag{4}$$

where k_0 is the wave number of the incoming progressive wave. Along the straight coastline, the velocity potential satisfies the condition

$$\frac{\partial\phi}{\partial x}=0 \quad \text{at } x=b\cos\varepsilon. \tag{5}$$

The continuity of pressure along the harbor opening requires

$$\phi_1=\phi_2 \quad \text{on} \quad r=b, \quad -\varepsilon<\theta<\varepsilon. \tag{6}$$

The vanishing of velocity along the impermeable harbor wall and the continuity of velocity along the opening is given by

$$\phi_{2r}=\begin{cases}0, & \text{at } r=b, \quad \varepsilon<\theta<2\pi-\varepsilon,\\ \phi_{1r} & \text{at } r=b, \quad -\varepsilon<\theta<\varepsilon.\end{cases} \tag{7}$$

The condition along the porous wall and the opening of the porous wall is given by

$$ik_0G(\phi_3-\phi_2)=\begin{cases}0, & \text{at } r=a, \quad -\varepsilon<\theta<\varepsilon,\\ \phi_{3r}, & \text{at } r=a, \quad \varepsilon<\theta<2\pi-\varepsilon,\end{cases} \tag{8}$$

where G is the porous-effect parameter or the Chwang parameter ([18]), which is different from the Chwang's wave-effect parameter ([19]). The porous-effect parameter G is a complex number with non-negative real and imaginary parts. The real part of G represents the resistance effect of a porous medium against the flow. The imaginary part of G denotes the inertia effect of fluids in the porous medium.

Finally, the continuity of velocity along the opening of the porous wall is given by

$$\frac{\partial\phi_2}{\partial r}=\frac{\partial\phi_3}{\partial r} \quad \text{on} \quad r=a, \quad -\varepsilon<\theta<\varepsilon. \tag{9}$$

3 The Method of Solution

The velocity potential for the open sea region is the superposition of plane waves with the coastline reflection in the absence of the harbor, ϕ_I, and the scattered wave ϕ_s due to the presence of the harbor,

$$\begin{aligned}\phi_I&=A_I\{e^{-ik_0[-(x-b\cos\varepsilon)\cos\alpha+y\sin\alpha]}\\&\quad+e^{ik_0[(x-b\cos\varepsilon)\cos\alpha+y\sin\alpha]}\}f_0(z)\\&=A_If_0(z)\sum_{m=0}^{\infty}\beta_m\{\Omega_m^c\psi_m^c+\Omega_m^s\psi_m^s\}J_m(k_0r),\end{aligned} \tag{10}$$

$$\begin{aligned}\phi_S=\sum_{m=0}^{\infty}\Bigg[&(A_{m0}^c\psi_m^c+A_{m0}^s\psi_m^s)\frac{H_m(k_0r)}{H_m'(k_0b)}f_0(z)\\&+\sum_{n=1}^{\infty}(A_{mn}^c\psi_m^c+A_{mn}^s\psi_m^s)\frac{K_m(k_nr)}{K_m'(k_nb)}f_n(z)\Bigg],\end{aligned} \tag{11}$$

where $f_0(z)=\cosh k_0(h+z)/\cosh k_0h$, $f_n(z)=\cos k_n(h+z)$, $A_I=gH/2\omega$, α is the incident wave angle, H is the incident wave height, $\beta_0=1$, $\beta_n=2$, $(n=1,2,3\ldots)$, $J_m(\cdot)$ is the Bessel function of the first kind, $H_m(\cdot)$ is the Hankel function of the first kind, $K_m(\cdot)$ is the modified Bessel function of the second kind, A_{mn}^c, A_{mn}^s are unknown constants to be determined,

$$\psi_m^c=\cos m\theta, \quad \psi_m^s=\sin m\theta,$$

$$\Omega_m^c=[(-i)^me^{ik_0b\cos\varepsilon\cos\alpha}+(i)^me^{-ik_0b\cos\varepsilon\cos\alpha}]\cos m\alpha,$$

$$\Omega_m^s=[-(-i)^me^{ik_0b\cos\varepsilon\cos\alpha}+(i)^me^{-ik_0b\cos\varepsilon\cos\alpha}]\sin m\alpha.$$

Superscripts c and s represent the terms associated with ψ_m^c and ψ_m^s, respectively. In (4) and (11), wave numbers $k_n(n=0,1,2,\ldots)$ satisfy the dispersion relations

$$\omega^2=gk_0\tanh k_0h=-gk_n\tan k_nh. \tag{12}$$

Hence, in region 1,

$$\phi_1=\phi_I+\phi_S. \tag{13}$$

The velocity potentials $\phi_j(j=2,3)$ are of the form

$$\begin{aligned}\phi_2=\sum_{m=0}^{\infty}\Bigg\{\Bigg[&(B_{m0}^c\psi_m^c+B_{m0}^s\psi_m^s)\frac{J_m(k_0r)}{J_m'(k_0b)}+(C_{m0}^c\psi_m^c\\&+C_{m0}^s\psi_m^s)\frac{Y_m(k_0r)}{Y_m'(k_0b)}\Bigg]f_0(z)+\sum_{n=1}^{\infty}\Bigg[(B_{mn}^c\psi_m^c+B_{mn}^s\psi_m^s)\\&\times\frac{I_m(k_nr)}{I_m'(k_nb)}+(C_{mn}^c\psi_m^c+C_{mn}^s\psi_m^s)\frac{K_m(k_nr)}{K_m'(k_nb)}\Bigg]f_n(z)\Bigg\},\end{aligned} \tag{14}$$

$$\begin{aligned}\phi_3=\sum_{m=0}^{\infty}\Bigg\{&(D_{m0}^c\psi_m^c+D_{m0}^s\psi_m^s)\frac{J_m(k_0r)}{J_m'(k_0a)}f_0(z)\\&+\sum_{n=1}^{\infty}(D_{mn}^c\psi_m^c+D_{mn}^s\psi_m^s)\frac{I_m(k_nr)}{I_m'(k_na)}f_n(z)\Bigg\},\end{aligned} \tag{15}$$

where B_{mn}^p, C_{mn}^p, D_{mn}^p $(p=c,s;m,n=0,1,2,\ldots)$ are unknown constants to be determined, $I_m(\cdot)$ is the modified Bessel function of the first kind, and $Y_m(\cdot)$ is the Bessel function of the second kind.

From (6), (7), (13), (14) and the orthogonality of f_n and ψ_m^p $(p=c,s)$, we have

$$\sum_{j=0}^{\infty}\left\{B_{j0}^{p}\frac{J_j(k_0b)}{J_j'(k_0b)}+C_{j0}^{p}\frac{Y_j(k_0b)}{Y_j'(k_0b)}-A_{j0}^{p}\frac{H_j(k_0b)}{H_j'(k_0b)}-A_I\beta_j\Omega_j^p\psi_j^pJ_j(k_0b)\right\}e_{jm}^{p}=0,\quad (p=c,s;m=0,1,2,\ldots), \tag{16}$$

$$\sum_{j=0}^{\infty}\left\{B_{jn}^{p}\frac{I_j(k_nb)}{I_j'(k_nb)}+C_{jn}^{p}\frac{K_j(k_nb)}{K_j'(k_nb)}-A_{jn}^{p}\frac{K_j(k_nb)}{K_j'(k_nb)}\right\}e_{jm}^{p}=0,\quad (p=c,s;n=1,2,\ldots;m=0,1,2,\ldots), \tag{17}$$

$$(B_{m0}^p+C_{m0}^p)d_m^p=\sum_{j=0}^{\infty}[A_I\beta_j\Omega_j^pJ_m'(k_0b)+A_{m0}^p]e_{jm}^p\quad (m=0,1,2,\ldots), \tag{18}$$

$$(B_{mn}^p+C_{mn}^p)d_m^p=\sum_{j=0}^{\infty}e_{mj}^pA_{jn}\quad (n=1,2,3,\ldots;m=0,1,2,\ldots), \tag{19}$$

where

$$d_m^p=\int_0^{2\pi}[\psi_m^p]^2d\theta,\ \ e_{jm}^p=\int_{-\varepsilon}^{\varepsilon}\psi_j^p\psi_m^pd\theta.$$

From (8), (9), (14), (15) and the orthogonality of f_n and $\psi_m^p(p=c,s)$, we obtain

$$ik_0G\left[\frac{J_m(k_0a)}{J_m'(k_0a)}D_{m0}^p-\left(\frac{J_m(k_0a)}{J_m'(k_0b)}B_{m0}^p+\frac{Y_m(k_0a)}{Y_m'(k_0b)}C_{m0}^p\right)\right]d_m^p=\sum_{j=0}^{\infty}k_0D_{j0}^pf_{mj}^p\quad (m=0,1,2,\ldots), \tag{20}$$

$$ik_0G\left[\frac{I_m(k_na)}{I_m'(k_na)}D_{mn}^p-\left(\frac{K_m(k_na)}{K_m'(k_nb)}B_{mn}^p+\frac{I_m(k_na)}{I_m'(k_nb)}C_{mn}^p\right)\right]d_m^p=\sum_{j=0}^{\infty}k_nD_{jn}^pf_{mj}^p\quad (n=1,2,3,\ldots;m=0,1,2,\ldots), \tag{21}$$

where

$$f_{mj}^p=\int_{\varepsilon}^{2\pi-\varepsilon}\psi_m^p\psi_j^pd\theta. \tag{22}$$

$$\frac{J_m'(k_0a)}{J_m'(k_0b)}B_{m0}^p+\frac{Y_m'(k_0a)}{Y_m'(k_0b)}C_{m0}^p=D_{m0}^p\quad (p=c,s;m=0,1,2,\ldots),$$

$$\frac{I_m'(k_na)}{I_m'(k_nb)}B_{mn}^p+\frac{K_m'(k_na)}{K_m'(k_nb)}C_{mn}^p=D_{mn}^p\quad (p=c,s;m=0,1,2,\ldots;n=1,2,3,\ldots). \tag{23}$$

The system of equations (16)–(23) can be solved to obtain the complete solution.

4 Oscillation in a Closed Basin

In such a case, we have $\varepsilon=0$. The velocity potential ϕ_1 will not be taken into account. Without loss of generality, the velocity potentials are

$$\phi_2=\sum_{m=0}^{\infty}\left\{\left[B_{m0}\frac{J_m(k_0r)}{J_m'(k_0b)}+C_{m0}\frac{Y_m(k_0r)}{Y_m'(k_0b)}\right]f_0(z)+\sum_{n=1}^{\infty}\left[B_{mn}\frac{I_m(k_nr)}{I_m'(k_nb)}+C_{mn}\frac{K_m(k_nr)}{K_m'(k_nb)}\right]f_n(z)\right\}\cos m\theta, \tag{24}$$

$$\phi_3=\sum_{m=0}^{\infty}\left\{D_{m0}\frac{J_m(k_0r)}{J_m'(k_0a)}f_0(z)+\sum_{n=1}^{\infty}D_{mn}\frac{I_m(k_nr)}{I_m'(k_na)}f_n(z)\right\}\cos m\theta. \tag{25}$$

It may be noted that $k_n\,(n=0,1,2,\ldots)$ are related to the angular frequency of the free oscillation of the harbor. In this case, we have $\phi_{2r}=0$ on $r=b$ which gives

$$B_{mn}=-C_{mn}\quad (m,n=0,1,2,\ldots). \tag{26}$$

Condition (8) along the permeable wall becomes

$$\frac{\partial\phi_2}{\partial r}=\frac{\partial\phi_3}{\partial r}=ik_0G(\phi_3-\phi_2)\quad \text{at } r=a(j=2,3). \tag{27}$$

The orthogonality of $f_n\,(n=0,1,2,\ldots)$ and $\cos m\theta$ leads to

$$\left[\frac{J_m'(k_0a)}{J_m'(k_0b)}-\frac{Y_m'(k_0a)}{Y_m'(k_0b)}\right]B_{m0}=D_{m0}\quad (m=0,1,2,\ldots), \tag{28}$$

$$\left[\frac{I_m'(k_na)}{I_m'(k_nb)}-\frac{K_m'(k_na)}{K_m'(k_nb)}\right]B_{mn}=D_{mn}\quad (n=1,2,3,\ldots;m=0,1,2,\ldots), \tag{29}$$

$$ik_0G\left[\frac{J_m(k_0a)}{J_m'(k_0a)}D_{m0}-\left(\frac{J_m(k_0a)}{J_m'(k_0b)}-\frac{Y_m(k_0a)}{Y_m'(k_0b)}\right)B_{m0}\right]=k_0D_{m0}\quad (m=0,1,2,\ldots), \tag{30}$$

$$ik_0G\left[\frac{I_m(k_na)}{I_m'(k_na)}D_{mn}-\left(\frac{I_m(k_na)}{I_m'(k_nb)}-\frac{K_m(k_na)}{K_m'(k_nb)}\right)B_{mn}\right]=k_nD_{mn}\quad (n=1,2,3,\ldots;m=0,1,2,\ldots). \tag{31}$$

From Eq. (28)–(31), we derive the resonance conditions relating the porous-effect parameter, the radius of the circular basin, the permeable wall and the wave number of the progressive wave mode as

$$iG\left[\frac{J_m(k_0a)}{J_m'(k_0a)}\left(\frac{J_m'(k_0a)}{J_m'(k_0b)}-\frac{Y_m'(k_0a)}{Y_m'(k_0b)}\right)-\left(\frac{J_m(k_0a)}{J_m'(k_0b)}-\frac{Y_m(k_0a)}{Y_m'(k_0b)}\right)\right]=\left(\frac{J_m'(k_0a)}{J_m'(k_0b)}-\frac{Y_m'(k_0a)}{Y_m'(k_0b)}\right)\quad (m=0,1,2,\ldots), \tag{32}$$

$$ik_0G\left[\frac{I_m(k_na)}{I_m'(k_na)}\left(\frac{I_m'(k_na)}{I_m'(k_nb)}-\frac{K_m'(k_na)}{K_m'(k_nb)}\right)-\left(\frac{I_m(k_na)}{I_m'(k_nb)}-\frac{K_m(k_na)}{K_m'(k_nb)}\right)\right]=k_n\left(\frac{I_m'(k_na)}{I_m'(k_nb)}-\frac{K_m'(k_na)}{K_m'(k_nb)}\right)\quad (n=1,2,3,\ldots;m=0,1,2,\ldots). \tag{33}$$

From (32) and (33), it is obvious that there is no real root for real G. Hence, there is no steady oscillation in a circular harbor with a permeable wall, which is similar to the observation of Yu and Chwang [17].

From (32) after rearrangement, we have

$$\frac{J_m'(k_0a)}{J_m'(k_0b)Y_m'(k_0a)}-\frac{iGJ_m(k_0a)-J_m'(k_0a)}{iGY_m(k_0a)J_m'(k_0b)-Y_m'(k_0b)J_m'(k_0a)}=0. \tag{34}$$

When $G=0$, the inner permeable wall behaves like a solid wall and we have a closed circular region and another annular region. From (34),

$$J_m'(k_0 a)=0 \quad (m=0,1,2,\ldots) \tag{35a}$$

or

$$J_m'(k_0 a)Y_m'(k_0 b)-J_m'(k_0 b)Y_m'(k_0 a)=0 \quad (m=0,1,2,\ldots). \tag{35b}$$

The solution of (35a) represents the wave modes due to a closed circular basin of radius a, while the solution of (35b) represents the wave modes inside the closed annular basin with inner and outer radii a and b, respectively. On the other hand, as $G \to \infty$, the permeable wall becomes transparent to the fluid and the resonance is due to the free oscillation of a closed circular basin of radius b. In such a case, from (34), we derive

$$J_m'(k_0 b)=0 \quad (m=0,1,2,\ldots). \tag{36}$$

5 Discussion

The amplification factor R which is a measure of wave oscillation inside the harbor is defined as

$$R=\left|\frac{\phi_3(r,\theta,0)}{A_I}\right|. \tag{37}$$

In the two-dimensional analysis of Chwang and Dong [20], when the porous-effect parameter $G=1$ and gap length $(b-a)=(2n+1)\lambda/4$, the reflection coefficient vanishes and the phenomenon of wave trapping takes place. From Yip and Chwang [21] it was noted that the curves for complex values of G are of similar shape as those for real values. To avoid repetition of similar results which have been investigated before, the curves for complex values of G are not presented in the present paper.

Figure 2 shows the variation of amplification factor R at the center versus wave number $k_0 b$ for different values of the porous-effect parameter G. As $0<a<b$, we must have $0<2\pi(b-a)/\lambda<k_0 b$. The amplification factor R increases generally as G increases. As G increases, the porous wall becomes transparent to the fluid and most of the wave energy is reflected back by the vertical harbor wall with an increase in the wave oscillation and thus an increase in the amplification factor. However, it should be noted that when $G=1$, the wave dissipation is maximum (see [17,20]) and in the process the wave resonance is minimum. The amplification factor R attains maxima for certain values of the wave number irrespective of the porous-effect parameter. The real porous-effect parameter only reduces the amplification factor without affecting the wave number.

In Fig. 3, the amplification factor R is plotted versus wave number $k_0 b$ at different locations in the inner region of the harbor.

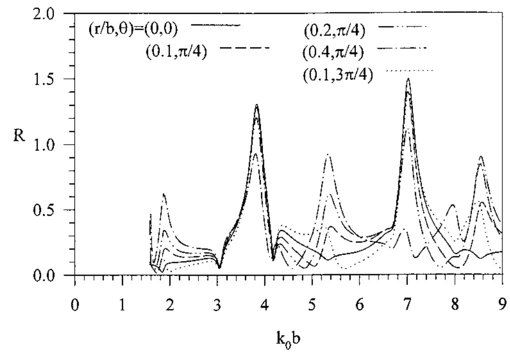

Fig. 3 Variation of amplification factor R versus wave number $k_0 b$ at different locations with $\alpha=0$ deg, $b/h=0.75$, $2\varepsilon=10$ deg, $G=1$, and $(b-a)/\lambda=0.25$

The amplification factor R attains its maximum value at different locations for different wave number $k_0 b$. Generally speaking, the wave amplification is large near the center compared to a point towards the harbor wall. It should be noted that, for normal incidence $\alpha=0$ deg, the wave condition inside the harbor is symmetric with respect to $\theta=0$ deg.

Figure 4 shows the variation of amplification factor R at the harbor center versus the gap length $(b-a)/\lambda$ for different values of the porous-effect parameter G. The two-dimensional result of Chwang and Dong [20] showed that the wave dissipation is maximum at $(b-a)/\lambda=0.25$, and the amount of dissipated energy depends on the porous-effect parameter G. The same phenomenon was observed later by Fugazza and Natale [22] and Suh and Park [23] although their analyses were different. Similar phenomemon is observed in the case of a circular harbor. However, the wave dissipation is more sensitive in the two-dimensional case ([20]) near $(b-a)/\lambda=0.25$, while in the present case of a circular harbor, large dissipation occurs at a wider range of $(b-a)/\lambda$ near 0.25. It should be noted that the wave incidence at the porous wall is not always normal but varying along the porous wall. In general, the incidence angle along the porous wall is very difficult to predict for three-dimensional cases. As shown in Fig. 4, the wave is dissipated most for a moderate value of G. Larger G represents a more porous wall and less wave energy is dissipated. As $G \to \infty$, the porous wall becomes transparent to the fluid and no dissipation occurs.

Figure 5 shows the variation of amplification factor R at the harbor center versus harbor opening 2ε for different values of the porous-effect parameter G. When the opening of the harbor vanishes, the amplification factor R becomes zero, as no wave is allowed to enter the harbor. A large amplification factor R is observed at moderate values of opening 2ε, similar to "the harbor

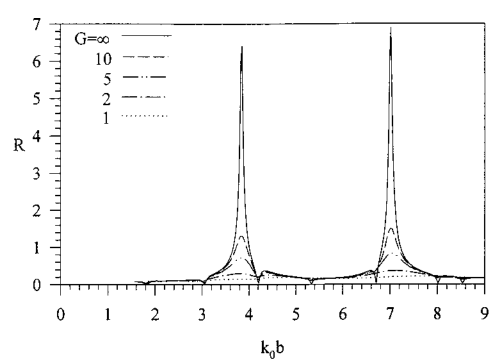

Fig. 2 Variation of amplification factor R at the center versus wave number $k_0 b$ for different values of G with $\alpha=0$ deg, $b/h=0.75$, $2\varepsilon=10$ deg, and $(b-a)/\lambda=0.25$

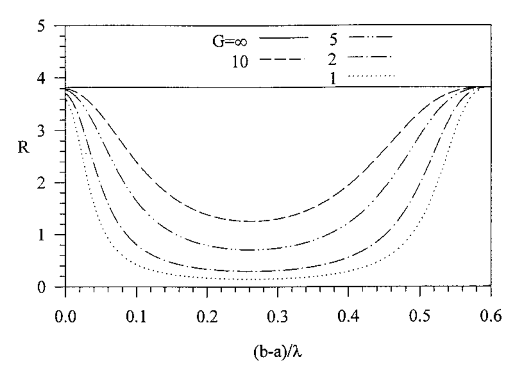

Fig. 4 Variation of amplification factor R at the center versus $(b-a)/\lambda$ for different values of G with $\alpha=0$ deg , $b/h=0.75$, $2\varepsilon=10$ deg, and $k_0 b=3.8$

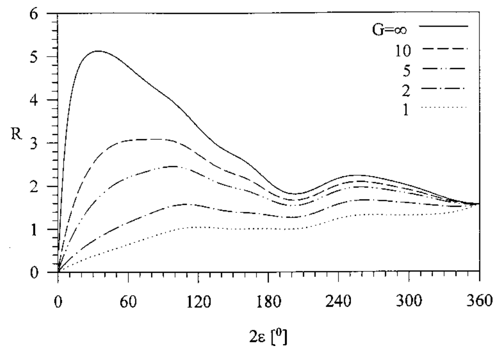

Fig. 5 Variation of amplification factor *R* at the center versus harbor opening 2ε for different values of *G* with α=0 deg, *b/h* =0.75, $k_0 b$=3.8, and (*b*−*a*)/λ=0.25

paradox,'' and the harbor oscillation decreases generally as the opening 2ε further increases. There is a sharp decrease in the amplification factor R with a decrease of the porous-effect parameter G. There is a shift in the maximum of the amplification factor as G decreases and the opening angle of the harbor increases. When the harbor becomes a point and only the straight coast remains, all curves come to the same limiting value.

Figure 6 illustrates the variation of amplification factor R at the center versus incidence angle α of incident waves. Because of the symmetry of the problem, the curves are symmetric with respect to $\alpha=0$ deg. The increase of incidence angle α allows less wave energy to transmit through the opening to the harbor. Thus, the normal incidence allows the most wave energy into the harbor. The amplification factor R tends to fixed values as incidence angle α approaches ± 90 deg.

Just as a remark to the current practice in numerical computation, the partially reflective boundary condition

$$\frac{\partial \phi}{\partial n} = k_0 \frac{1-K_r}{1+K_r}\phi,$$

where K_r is the normal reflection coefficient at the boundary, is widely used by prescribing K_r as a constant. However, K_r depends on the wave number and incidence direction and no analytical solution can be obtained if the partially reflective boundary condition is applied in this problem. To sum up, the above analyses are for a harbor of circular geometry. As previous analyses have demonstrated, the harbor geometry is a critical factor to harbor oscillations.

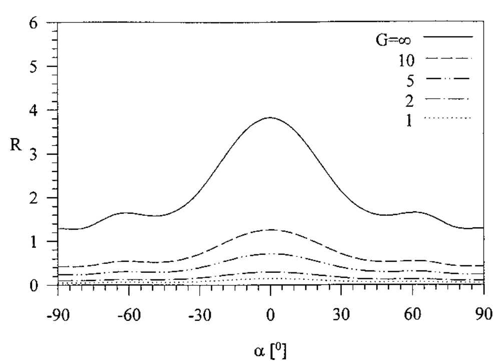

Fig. 6 Variation of amplification factor *R* at the center versus incidence angle α for different values of *G* with *b/h*=0.75, 2ε=10 deg, $k_0 b$=3.8 and (*b*−*a*)/λ=0.25

6 Conclusions

The problem of wave oscillation in a circular harbor is analyzed in the presence of a porous wall. For maximum wave dissipation the gap between the porous wall and the harbor wall should be approximately a quarter of the wavelength of the incident waves. A moderate value of the porous-effect parameter G dissipates the maximum wave energy. For a large angle of incidence, wave amplification inside the harbor reduces. The amplification factor depends on the wave number of the incident waves and the location inside the harbor. The amplification factor in the harbor can be adjusted with a proper opening angle and using a porous wall with moderate porosity.

Acknowledgments

This research was sponsored by the Hong Kong Research Grants Council under Grants HKU 568/96E and NSFC/HKU8. The first author was supported financially by a Post-Doctoral Fellowship for the Area of Excellence in Harbor and Coastal Environment Studies.

References

[1] Chwang, A. T., 1998, ''Study of Ship Waves in Victoria Harbour,'' *Proc. 3rd Intl. Conf. Fluid Mech.*, Beijing, China, Beijing Institute of Technology Press, pp. 9–16.
[2] McConnell, K. J., Ethelston, D. M., and Allsop, N. W. H., 1999, ''Low Reflection Walls for Harbours: Development of New Structures and Applications in Hong Kong,'' *Coastlines, Structures and Breakwaters*, N. W. H. Allsop ed., Proc. ICE Breakwaters Conference, London, UK, Mar. 19–20, Thomas Telford, pp. 58–69.
[3] Lamb, H., 1932, *Hydrodynamics*, Dover, New York.
[4] McNown, J. S., 1952, ''Waves and Seiches in Idealised Ports,'' Gravity Waves Symp., National Bureau of Standards, Cir. 521, pp. 153–164.
[5] Kravtchnenko, J., and McNown, J. S., 1955, ''Seiche in Rectangular Ports,'' Q. Appl. Math., **13**, pp. 19–26.
[6] Miles, J., and Munk, W., 1961, ''Harbour Paradox,'' J. Waterways Harbours Div., **87**, No. 3, pp. 111–130.
[7] LeMehaute, B., 1961, ''Theory of Wave Agitation in Harbour,'' J. Hydraul. Div., Am. Soc. Civ. Eng., **87**, No. 2, pp. 31–50.
[8] Ippen, A. T., and Goda, Y., 1963, ''Wave Induced Oscillation in Harbours: The Solution for a Rectangular Harbour Connected to the Open Sea,'' Report No. 59, Hydrodynamics Lab, M.I.T., Cambridge, MA.
[9] Lee, J. J., 1971, ''Wave Induced Oscillation in Harbours of Arbitrary Geometry,'' J. Fluid Mech., **45**, pp. 375–394.
[10] Mei, C. C., and Petroni, R. V., 1973, ''Waves in a Harbour With Protruding Breakwaters,'' J. Waterways, Harbours, Coastal Engrg. Div., **99**, No. 2, pp. 209–229.
[11] Hwang, L. S., and Tuck, E. O., 1970, ''On the Oscillations of Harbours of Arbitrary Shape,'' J. Fluid Mech., **42**, pp. 447–464.
[12] Mei, C. C., and Chen, H. S., 1975, ''Hybrid Element Methods for Water Waves,'' *2nd Annual Symp. of Waterways, Harbour, and Coastal Engrg.*, Vol. 1, ASCE, New York, pp. 63–81.
[13] Chen, H. S., 1986, ''Effects of Bottom Friction and Boundary Absorption on Water Wave Scattering,'' Appl. Ocean. Res., **8**, No. 2, pp. 99–104.
[14] Tsay, T. K., Zhu, W., and Liu, P. L. F., 1989, ''A Finite Element Model for Wave Refraction, Diffraction, Reflection and Dissipation,'' Appl. Ocean. Res., **11**, No. 1, pp. 33–38.
[15] Sollitt, C. K., and Cross, R. H., 1972, ''Wave Transmission Through Permeable Breakwaters,'' *Proc. 13th Conf. on Coastal Engrg.*, Vol. 3, ASCE, Reston, VA, pp. 1827–1846.
[16] Chwang, A. T., 1983, ''A Porous Wavemaker Theory,'' J. Fluid Mech., **132**, pp. 395–405.
[17] Yu, X., and Chwang, A. T., 1994, ''Wave-Induced Oscillation in Harbour With Porous Breakwater,'' J. Waterways, Ports, Coastal Ocean Eng., **120**, No. 2, pp. 125–144.
[18] Lee, M. M., and Chwang, A. T., 2000, ''Scattering and Radiation of Water Waves by Permeable Barriers,'' Phys. Fluids, **12**, No. 1, pp. 54–65.
[19] Williams, A. N., and Li, W., 1998, ''Wave Interaction With a Semi-Porous Cylindrical Breakwater Mounted on a Storage Tank,'' Ocean Eng., **25**, No. 2–3, pp. 195–219.
[20] Chwang, A. T., and Dong, Z., 1984, ''Wave Trapping due to a Porous Plate,'' *Proc. 15th ONR Symp. Naval Hydrodyn.*, National Academy Press, Washington, DC, pp. 407–417.
[21] Yip, T. L., and Chwang, A. T., 2000, ''Perforated Wall Breakwater With an Internal Horizontal Plate,'' J. Eng. Mech., **126**, No. 5, pp. 533–538.
[22] Fugazza, M., and Natale, L., 1992, ''Hydraulic Design of Perforated Breakwaters,'' J. Waterway, Port, Coastal, Ocean Eng., **118**, No. 1, pp. 1–14.
[23] Suh, K. D., and Park, W. S., 1995, ''Wave Reflection From Perforated-Wall Caisson Breakwaters,'' Coastal Eng., **26**, pp. 177–193.

Exact Solution for Simply Supported and Multilayered Magneto-Electro-Elastic Plates

E. Pan
Structures Technology, Inc.
543 Keisler Drive, Suite 204,
Cary, NC 27511
e-mail: pan@ipass.net

Exact solutions are derived for three-dimensional, anisotropic, linearly magneto-electro-elastic, simply-supported, and multilayered rectangular plates under static loadings. While the homogeneous solutions are obtained in terms of a new and simple formalism that resemble the Stroh formalism, solutions for multilayered plates are expressed in terms of the propagator matrix. The present solutions include all the previous solutions, such as piezoelectric, piezomagnetic, purely elastic solutions, as special cases, and can therefore serve as benchmarks to check various thick plate theories and numerical methods used for the modeling of layered composite structures. Typical numerical examples are presented and discussed for layered piezoelectric/piezomagnetic plates under surface and internal loads. [DOI: 10.1115/1.1380385]

Introduction

Because of their analytical nature, exact solutions for simply-supported (layered) plates under static loadings are still of particular values. These solutions can predict exactly the behaviors of elastic deformations and stresses near or across the interface of material layers, and can thus be used to check the accuracy of various numerical methods for more complicated applications ([1]). For anisotropic elastic composites, Pagano [2,3], Srinivas et al. [4], and Srinivas and Rao [5] derived the classic solutions for both the cylindrical and rectangular plates. While the author ([6]) introduced the propagator matrix method ([7]) to handle the corresponding multilayered case, Noor and Burton [8] derived analytical solutions for laminated anisotropic plates.

Recent development of piezoelectric ceramics has stimulated considerable studies on the electric and mechanical behaviors of piezoelectric structures. Again, analytical solutions, even though under certain assumptions, are still desirable. Extensions of the elastostatic solutions for simply-supported plates to the corresponding piezoelectric cases were carried out by Ray and co-workers [9,10], Heyliger and co-workers [11,12], Bisegna and Maceri [13], and Lee and Jiang [14]. Very recently, Vel and Batra [15] presented an analytical solution for multilayered piezoelectric plates in terms of the double Fourier series to handle more general boundary conditions at the edges.

More recent advances are the smart or intelligent materials where piezoelectric and piezomagnetic materials are involved. These materials have the ability of converting energy from one form (among magnetic, electric, and mechanical energies) to the other ([16–18]). Furthermore, composites made of piezoelectric/piezomagnetic materials exhibit magnetoelectric effect that is not present in single-phase piezoelectric or piezomagnetic materials ([19–21]). Although various inclusion-related problems in these materials have been investigated in recent years ([20–24]), no three-dimensional solution is available for the simply supported plate made of piezoelectric/piezomagnetic materials.

In this paper, we derive the exact solutions for three-dimensional, anisotropic magneto-electro-elastic, simply-supported, and multilayered rectangular plates under both surface and internal loads. The general solution in a homogeneous plate is obtained in terms of a new and simple formalism that resembles the Stroh formalism ([25–27]). In order to treat a multilayered plate, the propagator matrix method is introduced with which the corresponding multilayered solution has an elegant and simple expression. To the best of the author's knowledge, it is the first time that a piezoelectric and magnetostrictive multilayered plate under simple supporting conditions is analytically studied. It is also the first time that an internal loading case is investigated and compared to the surface loading case. The present solutions include all the previous solutions, such as the piezoelectric, piezomagnetic, purely elastic solutions, as special cases. Since the present solutions are exact, they can serve as benchmarks to test various thick plate theories and various numerical methods, such as the finite and boundary element methods, used for the modeling of layered composite structures.

As a numerical illustration, a piezoelectric and homogeneous plate under surface and internal loads and a sandwich plate made of piezoelectric $BaTiO_3$ and magnetostrictive $CoFe_2O_4$ under a surface mechanical load are analyzed. It is very interesting that even for a relatively thin plate, responses from an internal load are quite different to those from a surface load. For the sandwich plate made of piezoelectric $BaTiO_3$ and magnetostrictive $CoFe_2O_4$, it is observed that responses from different stacking sequences are completely different, especially for the electric and magnetic quantities. These new numerical results should be of special interest to the design of magneto-electro-elastic composite laminates.

Problem Description and Basic Equations

Let us consider an anisotropic, magneto-electro-elastic, and N-layered rectangular plate with horizontal dimensions L_x and L_y and total thickness H (in the vertical direction) with its four sides being simply supported. A Cartesian coordinate system $(x,y,z)=(x_1,x_2,x_3)$ is attached to the plate in such a way that its origin is at one of the four corners on the bottom surface and the plate is in the positive z region. Let layer j be bonded by the lower interface z_j and the upper interface z_{j+1} with thickness $h_j=z_{j+1}-z_j$. It is obvious that $z_1=0$ and $z_{N+1}=H$. Material properties in each layer can be different, and internal and/or surface loads (mechanical, electric or magnetic) can be applied. Along the interface, the extended displacement and traction vectors (to be defined later) are assumed to be continuous, with the exception of the internal loading level, which will be discussed later. Without loss of generality, we also assume that the surface load is applied on the top surface of the layered plate.

Contributed by the Applied Mechanics Division of THE AMERICAN SOCIETY OF MECHANICAL ENGINEERS for publication in the ASME JOURNAL OF APPLIED MECHANICS. Manuscript received by the ASME Applied Mechanics Division, April 2, 2000; final revision, January 30, 2001. Associate Editor: W. J. Drugan. Discussion on the paper should be addressed to the Editor, Prof. Lewis T. Wheeler, Department of Mechanical Engineering, University of Houston, Houston, TX 77204-4792, and will be accepted until four months after final publication of the paper itself in the ASME JOURNAL OF APPLIED MECHANICS.

For an anisotropic and linearly magneto-electro-elastic solid, the coupled constitutive relation can be written as ([16])

$$\begin{aligned}\sigma_i&=C_{ik}\gamma_k-e_{ki}E_k-q_{ki}H_k\\ D_i&=e_{ik}\gamma_k+\varepsilon_{ik}E_k+d_{ik}H_k\\ B_i&=q_{ik}\gamma_k+d_{ik}E_k+\mu_{ik}H_k\end{aligned} \tag{1}$$

where σ_i, D_i, and B_i are the stress, electric displacement, and magnetic induction (i.e., magnetic flux), respectively; γ_i, E_i, and H_i are the strain, electric field, and magnetic field, respectively; C_{ij}, ε_{ij}, and μ_{ij} are the elastic, dielectric, and magnetic permeability coefficients, respectively; e_{ij}, q_{ij}, and d_{ij} are the piezoelectric, piezomagnetic, and magnetoelectric coefficients, respectively. It is obvious that various uncoupled cases can be reduced from Eq. (1) by setting the appropriate coefficients to zero.

For an orthotropic solid, with transverse isotropy being a special case, the material constant matrices of Eq. (1) are expressed by

$$[C]=\begin{bmatrix}C_{11}&C_{12}&C_{13}&0&0&0\\ &C_{22}&C_{23}&0&0&0\\ &&C_{33}&0&0&0\\ &&&C_{44}&0&0\\ &\text{Sym}&&&C_{55}&0\\ &&&&&C_{66}\end{bmatrix},$$

$$[e]=\begin{bmatrix}0&0&e_{31}\\0&0&e_{32}\\0&0&e_{33}\\0&e_{24}&0\\e_{15}&0&0\\0&0&0\end{bmatrix},\quad [q]=\begin{bmatrix}0&0&q_{31}\\0&0&q_{32}\\0&0&q_{33}\\0&q_{24}&0\\q_{15}&0&0\\0&0&0\end{bmatrix} \tag{2}$$

$$[\varepsilon]=\begin{bmatrix}\varepsilon_{11}&0&0\\0&\varepsilon_{22}&0\\0&0&\varepsilon_{33}\end{bmatrix},\quad [d]=\begin{bmatrix}d_{11}&0&0\\0&d_{22}&0\\0&0&d_{33}\end{bmatrix},$$

$$[\mu]=\begin{bmatrix}\mu_{11}&0&0\\0&\mu_{22}&0\\0&0&\mu_{33}\end{bmatrix}. \tag{3}$$

The extended strain (using tensor symbol for the elastic strain γ_{ik})-displacement relation is

$$\begin{aligned}\gamma_{ij}&=0.5(u_{i,j}+u_{j,i})\\ E_i&=-\phi_{,i},\quad H_i=-\psi_{,i}\end{aligned} \tag{4}$$

where u_i, ϕ, and ψ are the elastic displacement, electric potential, and magnetic potential, respectively.

The equations of equilibrium, including the balance of the body force and electric charge and current, can be written as

$$\begin{aligned}\sigma_{ij,j}+f_i&=0\\ D_{j,j}-f_e&=0\\ B_{j,j}-f_m&=0\end{aligned} \tag{5}$$

where f_i, f_e, and f_m are the body force, electric charge density, and electric current density, respectively. The electric current density is also called magnetic charge density as compared to the electric charge density.

General Solutions

For a simply-supported and homogeneous plate, we seek the solution of the extended displacement vector in the form of

$$\mathbf{u}\equiv\begin{bmatrix}u_1\\u_2\\u_3\\\phi\\\psi\end{bmatrix}=e^{sz}\begin{bmatrix}a_1\cos px\sin qy\\a_2\sin px\cos qy\\a_3\sin px\sin qy\\a_4\sin px\sin qy\\a_5\sin px\sin qy\end{bmatrix} \tag{6}$$

where

$$p=n\pi/L_x,\quad q=m\pi/L_y \tag{7}$$

and n and m are two positive integers.

It is noted that solution (6) represents only one of the terms in a double Fourier series expansion when solving a general boundary value problem. Therefore, in general, summations for n and m over suitable ranges are implied whenever the sinusoidal term appears.

Substitution of Eq. (6) into the strain-displacement relation (4) and subsequently into the constitutive relation (1) yields the extended traction vector

$$\mathbf{t}\equiv\begin{bmatrix}\sigma_{13}\\\sigma_{23}\\\sigma_{33}\\D_3\\B_3\end{bmatrix}=e^{sz}\begin{bmatrix}b_1\cos px\sin qy\\b_2\sin px\cos qy\\b_3\sin px\sin qy\\b_4\sin px\sin qy\\b_5\sin px\sin qy\end{bmatrix}. \tag{8}$$

Introducing two vectors

$$\mathbf{a}=[a_1,a_2,a_3,a_4,a_5]^t,\quad \mathbf{b}=[b_1,b_2,b_3,b_4,b_5]^t \tag{9}$$

we then find that the vector $\mathbf{b}$ is related to $\mathbf{a}$ by

$$\mathbf{b}=(-\mathbf{R}^t+s\mathbf{T})\mathbf{a}=-\frac{1}{s}(\mathbf{Q}+s\mathbf{R})\mathbf{a} \tag{10}$$

where the superscript t denotes matrix transpose, and

$$\mathbf{R}=\begin{bmatrix}0&0&pC_{13}&pe_{31}&pq_{31}\\0&0&qC_{23}&qe_{32}&pq_{32}\\-pC_{55}&-qC_{44}&0&0&0\\-pe_{15}&-qe_{24}&0&0&0\\-pq_{15}&-qq_{24}&0&0&0\end{bmatrix},$$

$$\mathbf{T}=\begin{bmatrix}C_{55}&0&0&0&0\\&C_{44}&0&0&0\\&&C_{33}&e_{33}&q_{33}\\&&&-\varepsilon_{33}&-d_{33}\\&&&&-\mu_{33}\end{bmatrix} \tag{11}$$

$$\mathbf{Q}=\begin{bmatrix} -(C_{11}p^2+C_{66}q^2) & -pq(C_{12}+C_{66}) & 0 & 0 & 0 \\ & -(C_{66}p^2+C_{22}q^2) & 0 & 0 & 0 \\ & & -(C_{55}p^2+C_{44}q^2) & -(e_{15}p^2+e_{24}q^2) & -(q_{15}p^2+q_{24}q^2) \\ & & & \varepsilon_{11}p^2+\varepsilon_{22}q^2 & d_{11}p^2+d_{22}q^2 \\ & & & & \mu_{11}p^2+\mu_{22}q^2 \end{bmatrix}. \tag{12}$$

We mention that matrices **Q** and **T** are symmetric.

The in-plane stresses and electric and magnetic displacements are obtained as

$$\begin{bmatrix} \sigma_{11} \\ \sigma_{12} \\ \sigma_{22} \\ D_1 \\ D_2 \\ B_1 \\ B_2 \end{bmatrix} = e^{sz} \begin{bmatrix} c_1 \sin px \sin qy \\ c_2 \cos px \cos qy \\ c_3 \sin px \cos qy \\ c_4 \cos px \sin qy \\ c_5 \sin px \cos qy \\ c_6 \cos px \sin qy \\ c_7 \sin px \cos qy \end{bmatrix} \tag{13}$$

where

$$\begin{bmatrix} c_1 \\ c_2 \\ c_3 \\ c_4 \\ c_5 \\ c_6 \\ c_7 \end{bmatrix} = \begin{bmatrix} -C_{11}p & -C_{12}q & C_{13}s & e_{31}s & q_{31}s \\ C_{66}q & C_{66}p & 0 & 0 & 0 \\ -C_{12}p & -C_{22}q & C_{23}s & e_{32}s & q_{32}s \\ e_{15}s & 0 & e_{15}p & -\varepsilon_{11}p & -d_{11}p \\ 0 & e_{24}s & e_{24}q & -\varepsilon_{22}q & -d_{22}q \\ q_{15}s & 0 & q_{15}p & -d_{11}p & -\mu_{11}p \\ 0 & q_{24}s & q_{24}q & -d_{22}q & -\mu_{22}q \end{bmatrix} \begin{bmatrix} a_1 \\ a_2 \\ a_3 \\ a_4 \\ a_5 \end{bmatrix}. \tag{14}$$

These extended stresses (Eqs. (8) and (13)) should satisfy the equations of equilibrium (assuming zero body force and zero electric and magnetic charge densities), which in terms of the vector **a**, yields the following eigenequation:

$$[\mathbf{Q}+s(\mathbf{R}+\mathbf{R}')+s^2\mathbf{T}]\mathbf{a}=0 \tag{15}$$

where $\mathbf{R}'=-\mathbf{R}^t$.

It is noted that Eq. (15), derived for a simply supported plate, resembles the Stroh formalism ([25,26]). However, their solution structures are different because of the slightly different features of the **R** matrix (in the Stroh formalism, $\mathbf{R}'=\mathbf{R}^t$). It is known that in the Stroh formalism, positive internal energy requirement guarantees that the characteristic roots of Eq. (15) should be complex numbers with nonvanishing imaginary parts; they cannot be real ([26]). In the present formalism, however, such a feature does not exist. Instead, since a matrix and its transpose have the same determinant value, we conclude that if s is an eigenvalue of Eq. (15), so is $-s$. Furthermore, if s is a complex (or purely imaginary) eigenvalue, then its complex conjugate is also an eigenvalue since all the coefficient matrices in Eq. (15) are real. We name Eq. (15) as the pseudo-Stroh formalism because of its similarity to the Stroh formalism.

With aid of Eq. (10), Eq. (15) can now be recast into a 10×10 linear eigensystem

$$\mathbf{N}\begin{bmatrix} \mathbf{a} \\ \mathbf{b} \end{bmatrix} = s\begin{bmatrix} \mathbf{a} \\ \mathbf{b} \end{bmatrix} \tag{16}$$

where

$$\mathbf{N}=\begin{bmatrix} -\mathbf{T}^{-1}\mathbf{R}' & \mathbf{T}^{-1} \\ -\mathbf{Q}+\mathbf{R}\mathbf{T}^{-1}\mathbf{R}' & -\mathbf{R}\mathbf{T}^{-1} \end{bmatrix}. \tag{17}$$

Depending upon the given material property, the ten eigenvalues of Eq. (16) may not be distinct. Should repeated roots occur, a slight change in the material constants would result in distinct roots with negligible error ([28]) so that the following simple solution structure can still be applied.

Therefore, let us assume that the first five eigenvalues have positive real parts (if the root is purely imaginary, we then pick up the one with positive imaginary part) and the remainder have opposite signs to the first five. We distinguish the corresponding ten eigenvectors by attaching a subscript to **a** and **b**. Then the general solution for the extended displacement and traction vectors (of the z-dependent factor) are derived as

$$\begin{bmatrix} \mathbf{u} \\ \mathbf{t} \end{bmatrix} = \begin{bmatrix} \mathbf{A}_1 & \mathbf{A}_2 \\ \mathbf{B}_1 & \mathbf{B}_2 \end{bmatrix} \langle e^{s^*z} \rangle \begin{bmatrix} \mathbf{K}_1 \\ \mathbf{K}_2 \end{bmatrix} \tag{18}$$

where

$$\mathbf{A}_1=[\mathbf{a}_1,\mathbf{a}_2,\mathbf{a}_3,\mathbf{a}_4,\mathbf{a}_5], \quad \mathbf{A}_2=[\mathbf{a}_6,\mathbf{a}_7,\mathbf{a}_8,\mathbf{a}_9,\mathbf{a}_{10}]$$

$$\mathbf{B}_1=[\mathbf{b}_1,\mathbf{b}_2,\mathbf{b}_3,\mathbf{b}_4,\mathbf{b}_5], \quad \mathbf{B}_2=[\mathbf{b}_6,\mathbf{b}_7,\mathbf{b}_8,\mathbf{b}_9,\mathbf{b}_{10}]$$

$$\langle e^{s^*z} \rangle = \mathrm{diag}[e^{s_1z},e^{s_2z},e^{s_3z},e^{s_4z},e^{s_5z},e^{-s_1z},e^{-s_2z},e^{-s_3z},e^{-s_4z},e^{-s_5z}]$$

and $\mathbf{K}_1$ and $\mathbf{K}_2$ are two 5×1 constant column matrices to be determined.

Equation (18) is a general solution for a homogeneous, magneto-electro-elastic, and simply-supported plate, and contains previous piezoelectric and purely elastic solutions as its special cases. Clearly, in spite of the complicated nature of the problem, the general solution is remarkably simple. Furthermore, certain thin plate results can also be reduced from this solution by expanding the exponential term in terms of a Taylor series ([29,30]). This is particularly easy since one needs only to replace the diagonal exponential matrix with its Taylor series expansion ([6,13]). We mention that although other methods, such as the state space approach ([14]), may also be employed to derive a general solution for such a plate, more algebraic manipulations are needed. Furthermore, reduction to the thin plate result is complicated if a state space approach is followed.

With Eq. (18) being served as a general solution for a homogeneous and magneto-electro-elastic plate, solutions for the corresponding multilayered plate can be obtained using the continuity conditions along the interface and the boundary conditions on the top and bottom surfaces of the plate. In doing so, a system of linear equations for the unknowns can be formed and solved ([3,12]). However, for structures with relatively large numbers of layers (say, up to a hundred layers), the system of linear equations then becomes very large, and the propagator matrix method developed exclusively for layered structures can be conveniently and efficiently applied (for a brief review, see [31]). We discuss this matter in the next section.

Propagator Matrix and Solution of Layered System

Since the matrix **N**, defined in Eq. (17), is not symmetric, the eigenvectors of Eq. (16) are actually the right ones. The left eigenvectors are found by solving the following eigenvalue system:

$$\mathbf{N}^t\boldsymbol{\eta}=\lambda\boldsymbol{\eta}. \tag{19}$$

It is a matter of simple fact that if s and $[\mathbf{a},\mathbf{b}]^t$ are the eigenvalue and eigenvector of Eq. (16), then $\lambda=-s$ and $\eta=[-\mathbf{b},\mathbf{a}]^t$ are the corresponding solutions of Eq. (19). Since the left and right eigenvectors are orthogonal to each other, we then come to the following important relation:

$$\begin{bmatrix} -\mathbf{B}_2^t & \mathbf{A}_2^t \\ \mathbf{B}_1^t & -\mathbf{A}_1^t \end{bmatrix}\begin{bmatrix} \mathbf{A}_1 & \mathbf{A}_2 \\ \mathbf{B}_1 & \mathbf{B}_2 \end{bmatrix}=\begin{bmatrix} \mathbf{I} & \mathbf{0} \\ \mathbf{0} & \mathbf{I} \end{bmatrix} \tag{20}$$

where $\mathbf{I}$ is a 5×5 unit matrix, and the eigenvectors have been normalized according to

$$-\mathbf{B}_2^t\mathbf{A}_1+\mathbf{A}_2^t\mathbf{B}_1=\mathbf{I} \tag{21}$$

Equation (20) resembles the orthogonal relation in the Stroh formalism ([26]) and provides us with a simple way of inverting the eigenvector matrix, which is required in forming the propagator matrix.

Let us assume that Eq. (18) is a general solution in the homogeneous layer j, with the top and bottom boundaries locally at h and 0, respectively. Let $z=0$ in Eq. (18) and solve for the unknown constant column matrix, we find that

$$\begin{bmatrix} \mathbf{K}_1 \\ \mathbf{K}_2 \end{bmatrix}=\begin{bmatrix} \mathbf{A}_1 & \mathbf{A}_2 \\ \mathbf{B}_1 & \mathbf{B}_2 \end{bmatrix}^{-1}\begin{bmatrix} \mathbf{u} \\ \mathbf{t} \end{bmatrix}_0=\begin{bmatrix} -\mathbf{B}_2^t & \mathbf{A}_2^t \\ \mathbf{B}_1^t & -\mathbf{A}_1^t \end{bmatrix}\begin{bmatrix} \mathbf{u} \\ \mathbf{t} \end{bmatrix}_0. \tag{22}$$

The second equation follows from Eq. (20). Therefore, the solution in the homogeneous layer j at any level z can be expressed by that at $z=0$ as

$$\begin{bmatrix} \mathbf{u} \\ \mathbf{t} \end{bmatrix}_z=\mathbf{P}(z)\begin{bmatrix} \mathbf{u} \\ \mathbf{t} \end{bmatrix}_0 \tag{23}$$

where

$$\mathbf{P}(z)=\begin{bmatrix} \mathbf{A}_1 & \mathbf{A}_2 \\ \mathbf{B}_1 & \mathbf{B}_2 \end{bmatrix}\langle e^{s^*z}\rangle\begin{bmatrix} -\mathbf{B}_2^t & \mathbf{A}_2^t \\ \mathbf{B}_1^t & -\mathbf{A}_1^t \end{bmatrix} \tag{24}$$

is called the propagator matrix ([7,31]). Listed below are three important features of the propagator matrix, which can be proved easily.

$$\mathbf{P}(0)=\begin{bmatrix} \mathbf{I} & \mathbf{0} \\ \mathbf{0} & \mathbf{I} \end{bmatrix} \tag{25}$$

$$\mathbf{P}(z_3-z_1)=\mathbf{P}(z_3-z_2)\mathbf{P}(z_2-z_1) \tag{26}$$

$$\mathbf{P}(z_3-z_1)=\mathbf{P}^{-1}(z_1-z_3) \tag{27}$$

The propagating relation (23) can be used repeatedly so that one can propagate the physical quantities from the bottom surface $z=0$ to the top surface $z=H$ of the layered plate. Consequently, we have

$$\begin{bmatrix} \mathbf{u} \\ \mathbf{t} \end{bmatrix}_H=\mathbf{P}_N(h_N)\mathbf{P}_{N-1}(h_{N-1})\ \ldots\ \ldots\mathbf{P}_2(h_2)\mathbf{P}_1(h_1)\begin{bmatrix} \mathbf{u} \\ \mathbf{t} \end{bmatrix}_0 \tag{28}$$

where $h_j=z_{j+1}-z_j$ is the thickness of layer j and $\mathbf{P}_j$ the propagator matrix of the same layer.

Equation (28) is a surprisingly simple relation and, for given boundary conditions, can be solved for the unknowns involved. As an example, we assume that, on the top surface ($z=H$) the z-direction traction component is applied, i.e.,

$$\sigma_{zz}=\sigma_0 \sin px \sin qy \tag{29}$$

which may represent one of the terms in the double Fourier series solution for a general loading case (uniform or point loading), and all other traction components on both surfaces are zero (i.e., the second-type boundary value problem). Equation (28) is then reduced to

$$\begin{bmatrix} \mathbf{u}(H) \\ \mathbf{t}(H) \end{bmatrix}=\begin{bmatrix} \mathbf{C}_1 & \mathbf{C}_2 \\ \mathbf{C}_3 & \mathbf{C}_4 \end{bmatrix}\begin{bmatrix} \mathbf{u}(0) \\ \mathbf{0} \end{bmatrix} \tag{30}$$

where the four submatrices $\mathbf{C}_j$ are the multiplications of the propagator matrices in Eq. (28), and $\mathbf{t}(H)$ is the given boundary condition on the top surface, i.e.,

$$t(H)=[0,0,\sigma_0 \sin px \sin qy,0,0]^t. \tag{31}$$

Solving the unknown extended displacements on both surfaces of the layered plate, we find

$$\mathbf{u}(0)=\mathbf{C}_3^{-1}\mathbf{t}(H)$$
$$\mathbf{u}(H)=\mathbf{C}_1\mathbf{C}_3^{-1}\mathbf{t}(H). \tag{32}$$

In order to obtain the extended displacement and traction vectors at any depth, say $z_k\leqslant z\leqslant z_{k+1}$ in layer k, we propagate the solution from the bottom of the surface to the z-level ([31]), i.e.,

$$\begin{bmatrix} \mathbf{u} \\ \mathbf{t} \end{bmatrix}_z=\mathbf{P}_k(z-z_{k-1})\mathbf{P}_{k-1}(h_{k-1})\ \ldots\ \ldots\mathbf{P}_2(h_2)\mathbf{P}_1(h_1)\begin{bmatrix} \mathbf{u} \\ \mathbf{t} \end{bmatrix}_0. \tag{33}$$

With the extended displacement and traction vectors at a given depth being solved, the corresponding in-plane quantities can be evaluated using Eqs. (13) and (14).

Similar solutions can also be obtained for the first-type boundary value problem (i.e., for given extended displacement vectors on both surfaces) and for the third-type, i.e., the mixed boundary value problem as well. Therefore, for an anisotropic, magneto-electro-elastic, and simply-supported multilayered rectangular plate, we have derived the exact solution based on the pseudo-Stroh formalism and the propagator matrix method.

The present methodology can also be equally and easily extended to the corresponding internal loading case, which is of significance to the Green's function study. We now seek such a solution.

If there is an internal source (force, charge, dislocation, etc.) located at $z=d_0$ level within layer $j(z_{j+1},z_j)$, we artificially divide this layer into two sublayers $j1(d_0,z_j)$ (with $h_{j1}=d_0-z_j$) and $j2(z_{j+1},d_0)$ (with $h_{j2}=z_{j+1}-d_0$), and define the discontinuities across the source level as

$$\begin{bmatrix} \Delta\mathbf{u} \\ \Delta\mathbf{t} \end{bmatrix}\equiv\begin{bmatrix} \mathbf{u}(d_0+0) \\ \mathbf{t}(d_0+0) \end{bmatrix}-\begin{bmatrix} \mathbf{u}(d_0-0) \\ \mathbf{t}(d_0-0) \end{bmatrix}. \tag{34}$$

Again, propagating the propagator matrices from the bottom to the top of the surfaces and making use of the discontinuity relation (34) ([31,32]), we arrive at the following important equation:

$$\begin{aligned}\begin{bmatrix} \mathbf{u} \\ \mathbf{t} \end{bmatrix}_H&-\mathbf{P}_N(h_N)\mathbf{P}_{N-1}(h_{N-1})\ \ldots\ \ldots\mathbf{P}_2(h_2)\mathbf{P}_1(h_1)\begin{bmatrix} \mathbf{u} \\ \mathbf{t} \end{bmatrix}_0\\ &=\mathbf{P}_N(h_N)\mathbf{P}_{N-1}(h_{N-1})\ \ldots\ \ldots\mathbf{P}_{j+1}(h_{j+1})\mathbf{P}_{j2}(h_{j2})\begin{bmatrix} \Delta\mathbf{u} \\ \Delta\mathbf{t} \end{bmatrix}.\end{aligned} \tag{35}$$

Clearly, this equation is more general and includes Eq. (28) as a special case (when there is no discontinuity). Similar to the surface loading case, this equation can be solved for the unknown quantities involved ([31]).

Before carrying out numerical studies using the present formulation, we remark that the present solution is valid for any integers n and m as defined by Eq. (7). In other words, the solution we have derived can be regarded as for one of the terms in a Fourier series expansion. Because of the linearity, the solution corresponding to a general loading (uniform or point loading) can be obtained by expanding the loading as a finite double Fourier series ([13,33]) and adding the responses together term by term.

Numerical Examples

Having derived the exact and simple solutions, we now present some numerical results. Before using our formalism, we first checked our solutions with some previously published results for

Table 1 Material coefficients of the piezoelectric $BaTiO_3$ (C_{ij} in $10^9\,N/m^2$, e_{ij} in C/m^2, ε_{ij} in $10^{-9}C^2/(Nm^2)$, and μ_{ij} in $10^{-6}Ns^2/C^2$)

$C_{11}=C_{22}$ 166	C_{12} 77	$C_{13}=C_{23}$ 78	C_{33} 162	$C_{44}=C_{55}$ 43	$C_{66}=0.5(C_{11}-C_{12})$ 44.5
$e_{31}=e_{32}$	e_{33}	$e_{24}=e_{15}$			
−4.4	18.6	11.6			
$\varepsilon_{11}=\varepsilon_{22}$	ε_{33}		$\mu_{11}=\mu_{22}$	μ_{33}	
11.2	12.6		5	10	

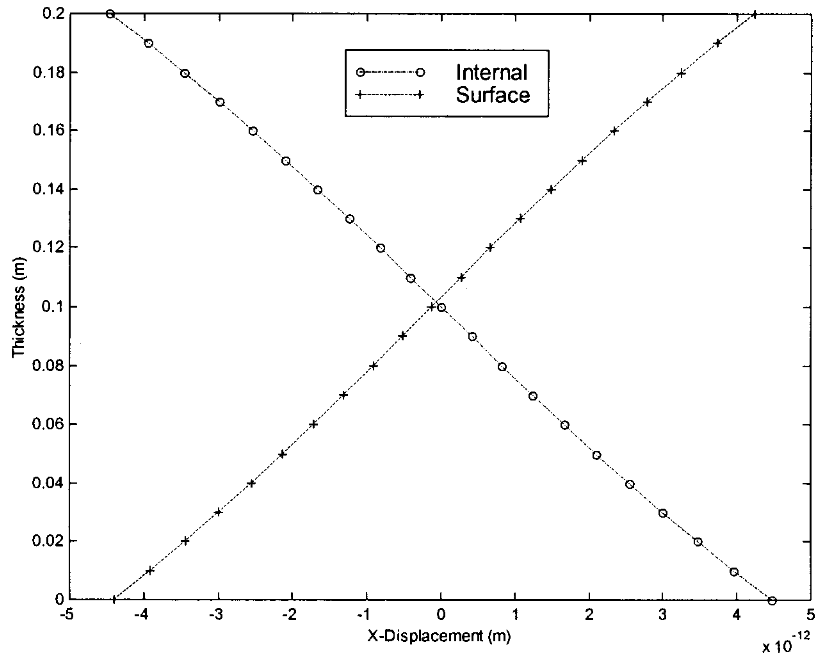

Fig. 1 Variation of the elastic displacement $u_x(=u_y)$ along the thickness direction in a homogeneous and piezoelectric plate caused by an internal load on the middle plane and a surface load on the top surface

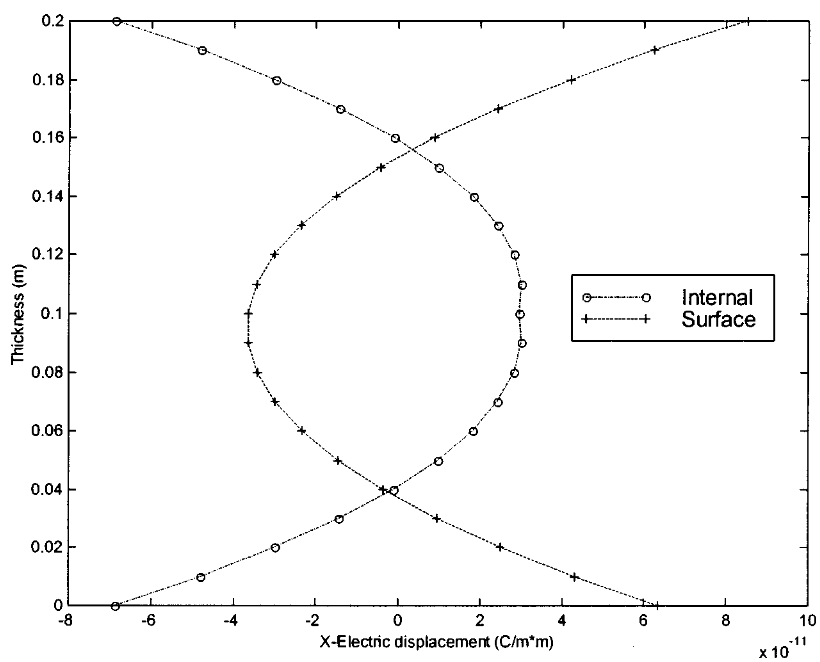

Fig. 2 Variation of the electric displacement $D_x(=D_y)$ along the thickness direction in a homogeneous and piezoelectric plate caused by an internal load on the middle plane and a surface load on the top surface

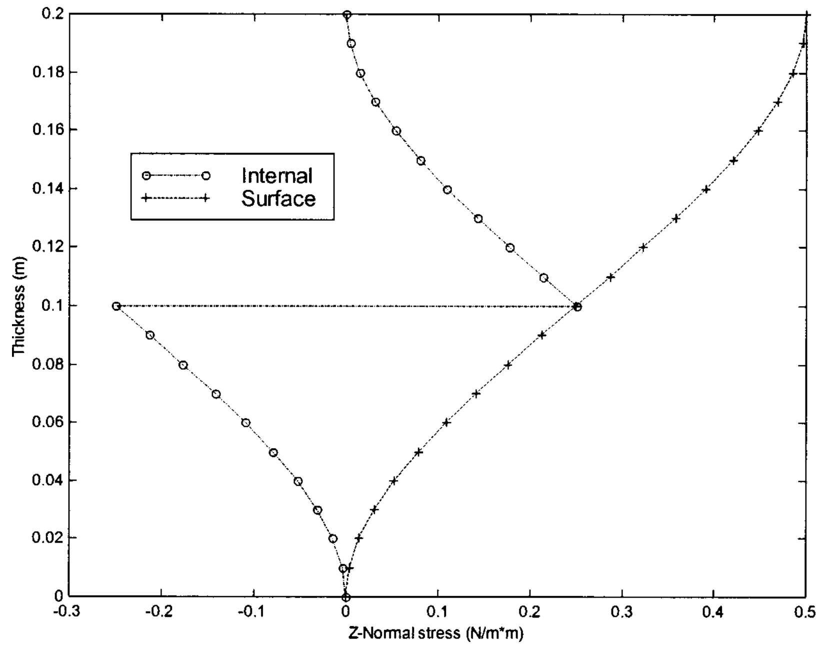

Fig. 3 Variation of the stress component σ_{zz} along the thickness direction in a homogeneous and piezoelectric plate caused by an internal load on the middle plane and a surface load on the top surface

Table 2 Material coefficients of the magnetostrictive $CoFe_2O_4$ (C_{ij} in $10^9 N/m^2$, q_{ij} in N/(Am), ε_{ij} in $10^{-9} C^2/(Nm^2)$, and μ_{ij} in $10^{-6} Ns^2/C^2$)

$C_{11}=C_{22}$	C_{12}	$C_{13}=C_{23}$	C_{33}	$C_{44}=C_{55}$	$C_{66}=0.5(C_{11}-C_{12})$
286	173	170.5	269.5	45.3	56.5
$q_{31}=q_{32}$	q_{33}	$q_{24}=q_{15}$			
580.3	699.7	550			
$\varepsilon_{11}=\varepsilon_{22}$	ε_{33}		$\mu_{11}=\mu_{22}$	μ_{33}	
0.08	0.093		−590	157	

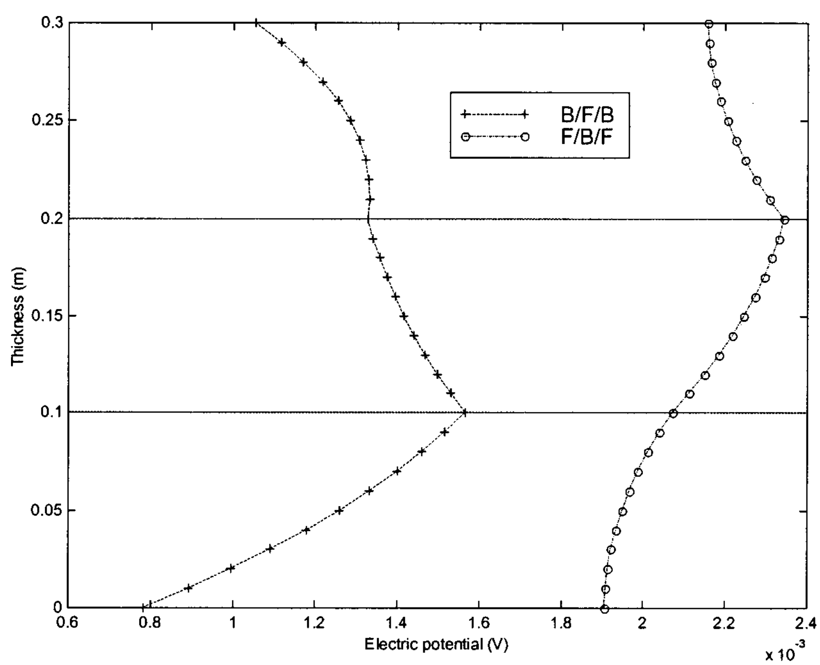

Fig. 4 Variation of the electric potential ϕ along the thickness direction in the sandwich piezoelectric/piezomagnetic plate caused by a surface load on the top surface

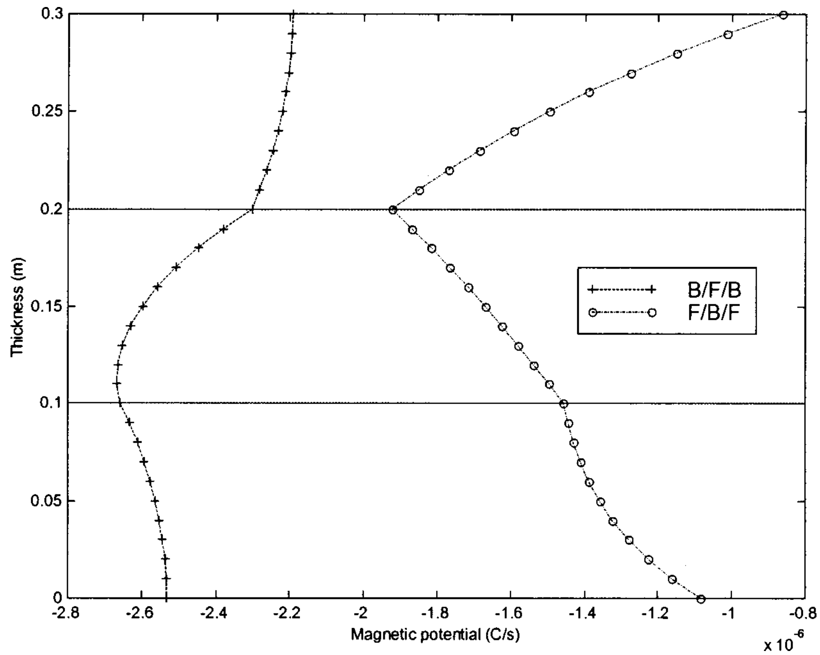

Fig. 5 Variation of the magnetic potential ψ along the thickness direction in the sandwich piezoelectric/piezomagnetic plate caused by a surface load on the top surface

both purely elastic and piezoelectric plates ([3,12,14,34]), and found that the present formulation agrees with these solutions.

The first example is for a homogeneous and transversely isotropic piezoelectric plate. The symmetry axis of the material is along the z-direction with material properties being listed in Table 1 ([14]). The dimension of the plate is $L_x \times L_y \times H = 1 \times 1 \times 0.2$ m. Two cases are studied: (1) A z-direction surface load is applied on the top surface of the plate $z = H$. That is, the extended traction is given by Eq. (31) with $m = n = 1$ (i.e., $p = \pi/L_x$, $q = \pi/L_y$) and amplitude $\sigma_0 = 1$ N/m^2. The bottom surface is assumed to be traction-free. (2) An internal load is applied on the middle plane of the plate ($z = 0.1$ m). The extended traction discontinuity $\Delta\mathbf{t}$ has a similar expression as Eq. (31) with amplitude $\Delta\sigma_{zz}$ equal to 1 N/m^2. Both the top and bottom surfaces are assumed to be traction-free. For both cases, responses are calculated for fixed horizontal coordinates $(x,y) = (0.75L_x, 0.25L_y)$.

Figures 1, 2, and 3 show the variations of the elastic displacement u_x, electric displacement D_x, and normal stress σ_{zz} along

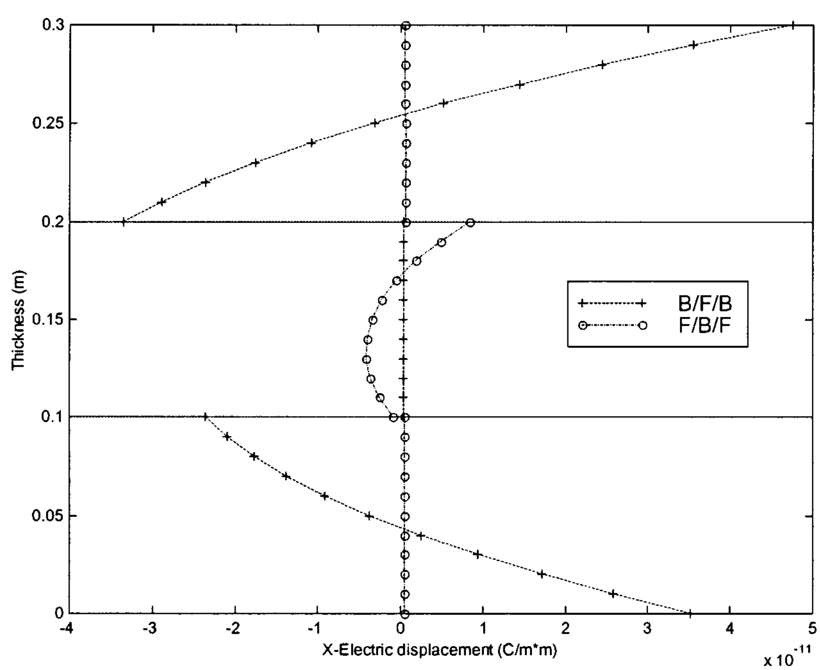

Fig. 6 Variation of the electric displacement $D_x(=D_y)$ along the thickness direction in the sandwich piezoelectric/piezomagnetic plate caused by a surface load on the top surface

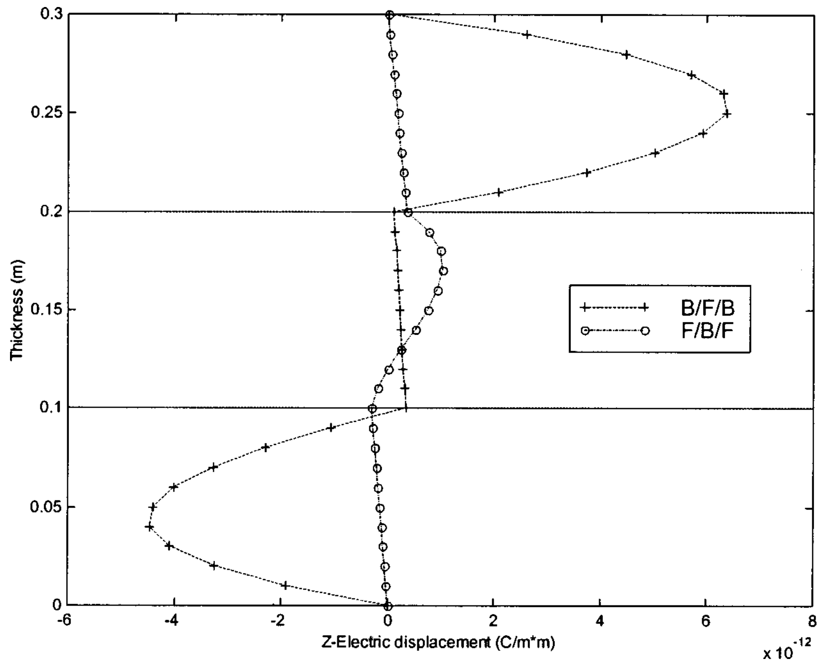

Fig. 7 Variation of the electric displacement D_z along the thickness direction in the sandwich piezoelectric/piezomagnetic plate caused by a surface load on the top surface

the thickness direction of the plate. It is clear that these two loading cases produce quite different responses in the plate, even though the plate is relative thin (with a ratio of thickness to horizontal dimension equal to 0.2). For instance, while the internal loading solution is strictly symmetric or antisymmetric with respect to the middle plane (i.e., the loading plane), the surface loading solution does not possess such features. The latter (for the elastic displacement u_x and electric displacement D_x) is only approximately symmetric or antisymmetric about the middle plane. While the normal stress σ_{zz} due to the surface load is continuous and increases monotonically from zero on the bottom surface to the applied value on the top surface, that due to the internal load is discontinuous across the loading plane $z=0.1$ m and it has opposite sign on both sides of the middle plane. The internal loading case has never been studied and compared to the surface loading case in the literature.

The second example is for sandwich plates made of piezoelectric $BaTiO_3$ and magnetostrictive $CoFe_2O_4$. The three layers have

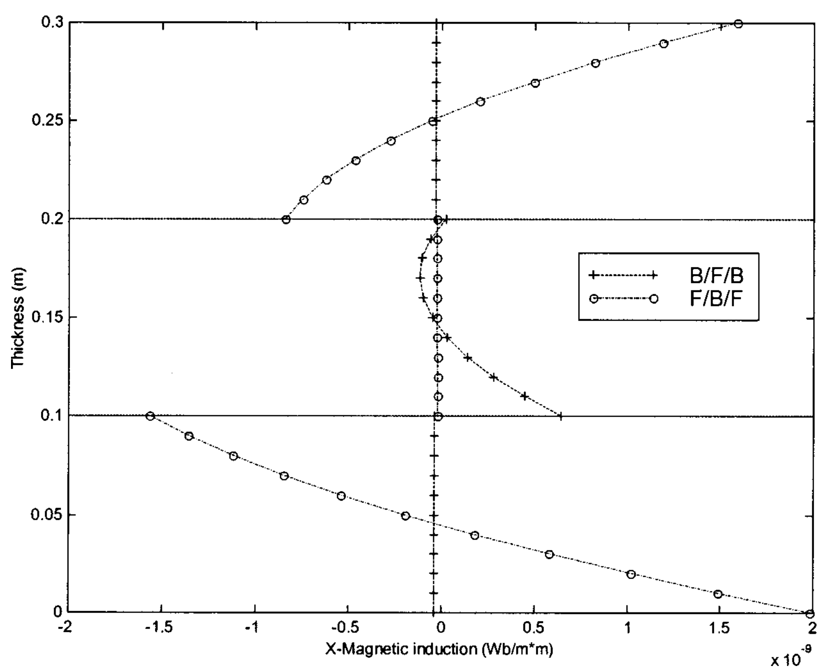

Fig. 8 Variation of the magnetic induction $B_x(=B_y)$ along the thickness direction in the sandwich piezoelectric/piezomagnetic plate caused by a surface load on the top surface

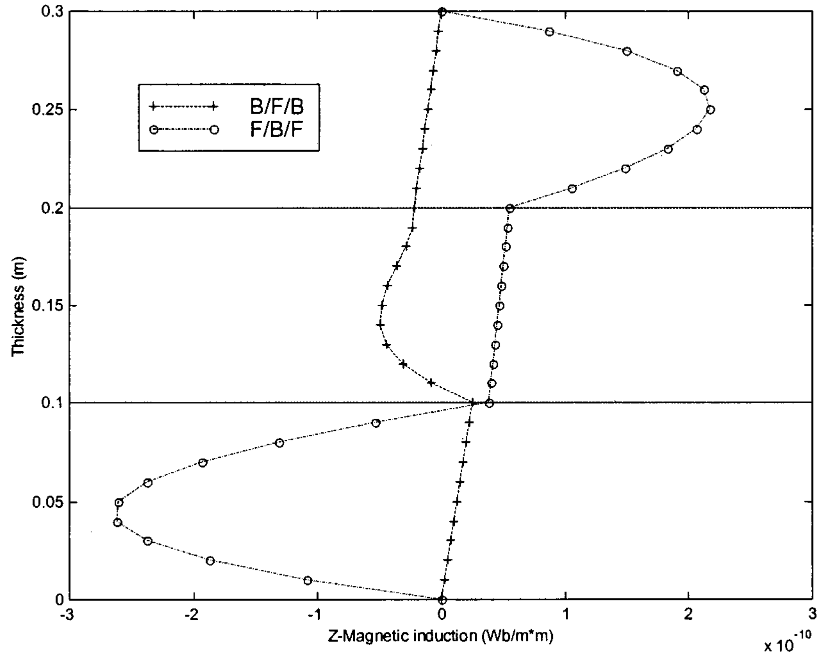

Fig. 9 Variation of the magnetic induction B_z along the thickness direction in the sandwich piezoelectric/piezomagnetic plate caused by a surface load on the top surface

equal thickness of 0.1 m (with a total thickness $H=0.3$ m). While the material properties for the piezoelectric $BaTiO_3$ are those listed in Table 1, the properties for the magnetostrictive $CoFe_2O_4$ are given in Table 2 ([35]). Similar to the piezoelectric $BaTiO_3$, the magnetostrictive $CoFe_2O_4$ is also a transversely isotropic solid with its symmetry axis along the z-axis.

Two sandwich plates with stacking sequences $BaTiO_3/CoFe_2O_4/BaTiO_3$ (called B/F/B) and $CoFe_2O_4/BaTiO_3/CoFe_2O_4$ (called F/B/F) are investigated. The surface loading as for the first example is assumed here (that is, a z-direction traction with amplitude $\sigma_0=1$ N/m^2 is applied on the top surface $z=0.3$ m while all other components on both surfaces are zero). Again, responses are calculated for fixed horizontal coordinates $(x,y)=(0.75L_x,0.25L_y)$.

Figures 4 and 5 show, respectively, the variations of the electric and magnetic potentials along the thickness direction in the sandwich plate. It is obvious that the potential variations for the B/F/B

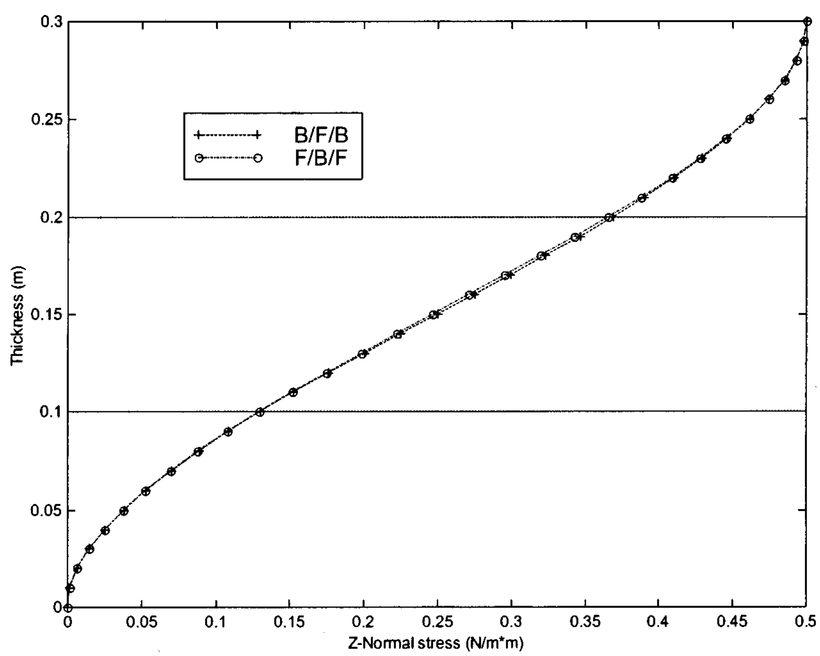

Fig. 10 Variation of the normal stress σ_{zz} along the thickness direction in the sandwich piezoelectric/piezomagnetic plate caused by a surface load on the top surface.

and F/B/F cases are completely different, demonstrating clearly the role played by the material stacking sequences. Furthermore, the slopes of these quantities can be discontinuous across the interface, even though the potentials themselves are continuous.

While Figs. 6 and 7 show the electric displacements D_x $(=D_y)$ and D_z, the magnetic displacements (magnetic induction) $B_x(=B_y)$ and B_z are plotted in Figs. 8 and 9. The following general features are observed from these figures:

1 The horizontal electric and magnetic displacements are discontinuous across the interfaces (Figs. 6 and 8).

2 The magnitude of horizontal electric (magnetic) displacement is very small in magnetostrictive $CoFe_2O_4$ (piezoelectric $BaTiO_3$) layer (Figs. 6 and 8). This is due to the fact that for the magnetostrictive $CoFe_2O_4$ (piezoelectric $BaTiO_3$) material, the piezoelectric e_{ij} (piezomagnetic q_{ij}) coefficients are zero.

3 Within the outer layers, the horizontal and vertical electric displacements (magnetic inductions) change dramatically for the B/F/B (F/B/F) case (Figs. 6–9).

4 For these dramatically changed physical quantities, the vertical components reach their maximum magnitudes in the middle of the outer layers (Figs. 7 and 9), while for the horizontal components, the maximums are on the top and bottom surfaces and the minima at the interfaces.

While the electric and magnetic quantities have been greatly influenced by the stacking sequences, relatively small differences have been observed for the corresponding elastic displacements and stresses for these two sandwich cases. For instance, Fig. 10 shows the variation of the normal stress σ_{zz} along the thickness direction in the sandwich piezoelectric/piezomagnetic plates. It is apparent that both stacking sequences produce nearly the same stress distribution, even though the elastic constants for the two materials are considerably different (Tables 1 and 2). This is obviously a coupling phenomenon and can only be explained by resorting to the coupled constitutive relation (1). For the stress field, it is seen from Eq. (1) that it consists of three parts: the elastic constant and strain, the piezoelectric coefficient and electric field, and the piezomagnetic coefficient and magnetic field. Even though the first part may produce quite different stresses in both sandwich plates, the effect of the second and third parts (i.e., the piezoelectric and piezomagnetic terms) is to wipe out, in the present case, the difference of the stress field produced by the first part.

The model results may have potential applications in the field of smart/intelligent structures. For example, to design a sandwich plate made of the magnetostrictive $CoFe_2O_4$ and piezoelectric $BaTiO_3$ materials that requires a given stress level (or distribution) within the plate under a normal surface loading on the top, then in order to produce a large horizontal electric displacement (D_x or D_y) on both the top and bottom surfaces (Fig. 6), the B/F/B stacking sequence should be selected. On the other hand, if a large horizontal magnetic induction (B_x or B_y) on both the top and bottom surfaces (Fig. 8) is expected, then the F/B/F stacking sequence is the choice.

Conclusions

In this paper, we have derived exact solutions for three-dimensional, anisotropic magneto-electro-elastic, simply-supported, and multilayered rectangular plates under both surface and internal loads. We have developed a new and simple formalism that resembles the Stroh formalism so that the homogeneous solution can be obtained in a simple and elegant form. We have also introduced the propagator matrix method in order to treat efficiently and accurately the multilayered case. Our solutions include all the previous solutions, such as the piezoelectric, piezomagnetic, purely elastic solutions, as special cases, and can provide benchmarks for various thick plate theories and numerical methods, such as the finite and boundary element methods.

Two typical numerical examples presented have also shown some significant and interesting features. For instance, responses to an internal load are quite different from those to a surface load, even for a relatively thin plate. The solution to the internal load and its comparison to the corresponding surface loading solution have never been reported in the literature. For sandwich plates made of the piezoelectric $BaTiO_3$ and magnetostrictive $CoFe_2O_4$, we have observed that the stacking sequences (B/F/B and F/B/F) have a clear influence on most physical quantities, in particular, on the electric and magnetic quantities. These features should be of special interest to the design of magneto-electro-elastic composite laminates.

Acknowledgments

The author would like to thank Prof. Paul Heyliger of Colorado State University for his valuable discussions and to the reviewers for their constructive suggestions.

References

[1] Ochoa, O. O., and Reddy, J. N., 1992, *Finite Element Analysis of Composite Laminates*, Kluwer, Boston, MA.
[2] Pagano, N. J., 1969, ''Exact Solutions for Composites in Cylindrical Bending,'' J. Compos. Mater., **3**, pp. 398–411.
[3] Pagano, N. J., 1970, ''Exact Solutions for Rectangular Bidirectional Composites and Sandwich Plates,'' J. Compos. Mater., **4**, pp. 20–34.
[4] Srinivas, S., Rao, C. V. J., and Rao, A. K., 1969, ''Flexure of Simply Supported Thick Homogeneous and Laminated Rectangular Plates,'' Z. Angew. Math. Mech., **49**, pp. 449–458.
[5] Srinivas, S., and Rao, A. K., 1970, ''Bending, Vibration and Buckling of Simply Supported Thick Orthotropic Rectangular Plates and Laminates,'' Int. J. Solids Struct., **6**, pp. 1463–1481.
[6] Pan, E., 1991, ''An Exact Solution for Transversely Isotropic, Simply Supported and Layered Rectangular Plates,'' J. Elast., **25**, pp. 101–116.
[7] Gilbert, F., and Backus, G., 1966, ''Propagator Matrices in Elastic Wave and Vibration Problems,'' Geophysics, **31**, pp. 326–332.
[8] Noor, A. K., and Burton, W. S., 1990, ''Three-Dimensional Solutions for Antisymmetrically Laminated Anisotropic Plates,'' ASME J. Appl. Mech., **57**, pp. 182–188.
[9] Ray, M. C., Rao, K. M., and Samanta, B., 1992, ''Exact Analysis of Coupled Electroelastic Behavior of a Piezoelectric Plate under Cylindrical Bending,'' Comput. Struct., **45**, pp. 667–677.
[10] Ray, M. C., Bhattacharya, R., and Samanta, B., 1993, ''Exact Solutions for Static Analysis of Intelligent Structures,'' AIAA J., **31**, pp. 1684–1691.
[11] Heyliger, P., and Brooks, S., 1996, ''Exact Solutions for Laminated Piezoelectric Plates in Cylindrical Bending,'' ASME J. Appl. Mech., **63**, pp. 903–910.
[12] Heyliger, P., 1997, ''Exact Solutions for Simply Supported Laminated Piezoelectric Plates,'' ASME J. Appl. Mech., **64**, pp. 299–306.
[13] Bisegna, P., and Maceri, F., 1996, ''An Exact Three-Dimensional Solution for Simply Supported Rectangular Piezoelectric Plates,'' ASME J. Appl. Mech., **63**, pp. 628–638.
[14] Lee, J. S., and Jiang, L. Z., 1996, ''Exact Electroelastic Analysis of Piezoelectric Laminae via State Space Approach,'' Int. J. Solids Struct., **33**, pp. 977–990.
[15] Vel, S. S., and Batra, R. C., 2000, ''Three-Dimensional Analytical Solution for Hybrid Multilayered Piezoelectric Plates,'' ASME J. Appl. Mech., **67**, pp. 558–567.
[16] Berlincourt, D. A., Curran, D. R., and Jaffe, H., 1964, ''Piezoelectric and Piezomagnetic Materials and Their Function in Transducers,'' Phys. Acoust., **1**, pp. 169–270.
[17] Landau, L. D., and Lifshitz, E. M., 1984, *Electrodynamics of Continuous Media*, 2nd Ed., Rev. and Enlarged by E. M. Lifshitz and L. P. Pitaevskii, Pergamon Press, New York.
[18] Avellaneda, M., and Harshe, G., 1994, ''Magnetoelectric Effect in Piezoelectric/Magnetostrictive Multiplayer (2-2) Composites,'' J. Intell. Mater. Syst. Struct., **5**, pp. 501–513.
[19] Harshe, G., Dougherty, J. P., and Newnham, R. E., 1993, ''Theoretical Modeling of Multilayer Magnetoelectric Composites,'' Int. J. Appl. Electromagn. Mater., **4**, pp. 145–159.
[20] Nan, C. W., 1994, ''Magnetoelectric Effect in Composites of Piezoelectric and Piezomagnetic Phases,'' Phys. Rev. B, **B50**, pp. 6082–6088.
[21] Benveniste, Y., 1995, ''Magnetoelectric Effect in Fibrous Composites With Piezoelectric and Piezomagnetic Phases,'' Phys. Rev. B, **B51**, pp. 16424–16427.
[22] Huang, J. H., 1998, ''Analytical Predictions for the Magneto-Electric Coupling in Piezomagnetic Materials Reinforced by Piezoelectric Ellipsoidal Inclusions,'' Phys. Rev. B, **B58**, pp. 12–15.
[23] Li, J., and Dunn, M. L., 1998, ''Anisotropic Coupled-Field Inclusion and Inhomogeneity Problems,'' Philos. Mag. A, **A77**, pp. 1341–1350.
[24] Li, J., and Dunn, M. L., 1998, ''Micromachanics of Magnetoelectroelastic Composite Materials: Average Fields and Effective Behavior,'' J. Intell. Mater. Syst. Struct., **9**, pp. 404–416.

[25] Stroh, A. N., 1958, ''Dislocations and Cracks in Anisotropic Elasticity,'' Philos. Mag., **3**, pp. 625–646.
[26] Ting, T. C. T., 1996, *Anisotropic Elasticity*, Oxford University Press, Oxford, UK.
[27] Ting, T. C. T., 2000, ''Recent Developments in Anisotropic Elasticity,'' Int. J. Solids Struct., **37**, pp. 401–409.
[28] Pan, E., 1997, ''A General Boundary Element Analysis of 2-D Linear Elastic Fracture Mechanics,'' Int. J. Fract., **88**, pp. 41–59.
[29] Kausel, E., and Roesset, J. M., 1981, ''Stiffness Matrices for Layered Soils,'' Bull. Seismol. Soc. Am., **71**, pp. 1743–1761.
[30] Datta, S. K., 2000, ''Wave Propagation in Composite Plates and Shells,'' *Comprehensive Composite Materials*, Vol. 1, A. Kelly and C. Zweben, eds., Elsevier, New York, pp. 511–558.
[31] Pan, E., 1997, ''Static Green's Functions in Multilayered Half Spaces,'' Appl. Math. Modelling, **21**, pp. 509–521.
[32] Pan, E., and Datta, S. K., 1999, ''Ultrasonic Waves in Multilayered Superconducting Plates,'' J. Appl. Phys., **86**, pp. 543–551.
[33] Timoshenko, S., and Woinowsky-Krieger, S., 1987, *Theory of Plates and Shells*, McGraw-Hill, New York.
[34] Smittakorn, W., and Heyliger, P. R., 2000, ''A Discrete-Layer Model of Laminated Hygrothermopiezoelectric Plates,'' Mechanics of Composite Materials and Structures, **7**, pp. 79–104.
[35] Huang, J. H., and Kuo, W. S., 1997, ''The Analysis of Piezoelectric/Piezomagnetic Composite Materials Containing Ellipsoidal Inclusions,'' J. Appl. Phys., **81**, pp. 1378–1386.

H. Bai
A. H. Shah
N. Popplewell
Faculty of Engineering,
University of Manitoba,
Winnipeg, Manitoba R3T 2N2
Canada

S. K. Datta
Department of Mechanical Engineering,
University of Colorado,
Boulder, CO 80309-0427

Scattering of Guided Waves by Circumferential Cracks in Steel Pipes

A novel numerical procedure is presented in this paper to study wave scattering problem by circumferential cracks in steel pipes. The study is motivated by the need to develop a quantitative ultrasonic technique to characterize properties of cracks in pipes. By employing wave function expansion in axial direction and decomposing the problem into a symmetry problem and an antisymmetry problem, a three-dimensional wave scattering problem is then reduced into two quasi-one-dimensional problems. This simplification greatly reduces the computational time. Numerical results for reflection and transmission coefficients of different incident wave modes are presented here for a steel pipe with cracks (may have arbitrary circumferential crack length and radial crack depth) and they are shown to agree quite closely with available but limited experimental data.
[DOI: 10.1115/1.1364493]

Introduction

Circular tubes and pipelines are used extensively in energy and transportation industries. These structural components are normally fabricated from metallic and composite materials. Damage to these components occur with handling, service load, natural disturbances, and environmental causes. Of particular interest in this study is the stress corrosion cracking that occurs in steel pipelines used in oil, gas, and petrochemical industries. Ultrasonic nondestructive techniques are being developed for the inspection of such industrial pipelines. Ultrasonic waves in steel pipes can be generated quite efficiently by ring transducers (see, Alleyne et al. [1] and Lowe et al. [2]) for launching waves that propagate along the pipe axis. Electromagnetic acoustic transducers (EMATs) are also used to generate waves guided along the circumference of the pipe wall ([2]). A major problem that is faced in the ultrasonic evaluation of pipes is the presence of protective coating or insulation on the outside of the pipe wall. The coating or insulation material is much softer than steel and usually has high attenuation. This makes access to the pipe from outside difficult and various devices for access from inside the pipe have been under development. Also, the ultrasonic waves propagating in the pipe wall can be modified by the coating or insulation layer. In a recent paper, Pan et al. [3] examined the effect of a soft viscoelastic layer on guided ultrasonic waves in a bilayered plate. It was found that certain (Lamb wave) modes in a single-layer steel plate are preferable for inspection of damage because they do not suffer significant modification by the soft layer. Thus, mode selection plays a very important role in the success of ultrasonic nondestructive evaluation (NDE) techniques.

Guided waves in cylindrical tubes are similar in nature as the ones in plates. However, many more modes are excited in tubes than in plates (Alleyne et al. [1]). This makes appropriate mode selection very critical for the success of an ultrasonic technique for pipeline inspection. The problem is further complicated if there are large cracks in the pipe wall. Thus, it is important to have accurate theoretical model studies of ultrasonic wave propagation and scattering in cylindrical tubes.

Dispersion of elastic waves in circular cylinders has been studied by many authors. Soldatos [4] reviews the literature on dynamics of cylinders and cylindrical shells. Datta [5] has reviewed the theoretical work on waves in composite cylinders and shells. A semianalytic finite element (SAFE) technique for the analysis of dispersive guided waves in anisotropic homogeneous and composite shells has been discussed in the latter publication.

Studies of wave propagation and reflection in a semi-infinite cylinder and wave propagation in a cylinder with a region of material inhomogeneity have also been reported. Kohl et al. [6], Rattanawangcharoen [7], and Rattanawangcharoen et al. [8] studied the wave propagation in a semi-infinite tube by a superposition of all possible traveling waves and end modes to satisfy the end condition. Recently, hybrid methods have been used to study wave scattering in a tube containing a finite axisymmetric region of inhomogeneity and crack. Rattanawangcharoen et al. [9] and Zhuang et al. [10] used a hybrid technique to investigate reflection and transmission of waves in jointed and welded cylinders and in a welded cylinder containing a circumferential crack. All these studies dealt with the axisymmetric problem.

Recently, Alleyne et al. [1] have reported an experimental and modeling study of wave scattering in a steel pipe containing a circumferential crack. They used a finite element model to study the scattering of the $L(0,2)$ mode (see, the Nomenclature of the modes used in that paper) by a part-circumferential planar notch. In this case, even though the incident mode was axisymmetric, because of the nonaxisymmetric notch scattering occurred in both axisymmetric and nonaxisymmetric modes ($L(m,n)$ and $F(m,n)$). They reported reflection coefficients for only the $L(0,2)$ mode as functions of the circumferential extent and the radial depth of the notch.

As shown in previous studies, the hybrid method is effective for axisymmetric scattering problems. However, for the three-dimensional scattering problem considered by Alleyne et al. [1], the hybrid or the full finite element method entails considerable amount of computational costs. The objective of the present study is to develop a more efficient combined analytical/numerical tool for the investigation of three-dimensional scattering in a cylindrical tube. The cylinder is assumed to be isotropic and homogeneous, although the method is easily extended to the case of anisotropic composite cylinders. In order to model scattering by a partly or fully circumferential crack, the problem is subdivided into a symmetric and an antisymmetric problem about the plane of the crack. This approach has been used by Zhuang et al. [11] to solve for the Green's function for cylindrical shell. In the study

Contributed by the Applied Mechanics Division of THE AMERICAN SOCIETY OF MECHANICAL ENGINEERS for publication in the ASME JOURNAL OF APPLIED MECHANICS. Manuscript received by the ASME Applied Mechanics Division, Apr. 2, 2000; final revision, Sept. 15, 2000. Associate Editor: A. K. Mal. Discussion on the paper should be addressed to the Editor, Professor Lewis T. Wheeler, Department of Mechanical Engineering, University of Houston, Houston, TX 77204-4792, and will be accepted until four months after final publication of the paper itself in the ASME JOURNAL OF APPLIED MECHANICS.

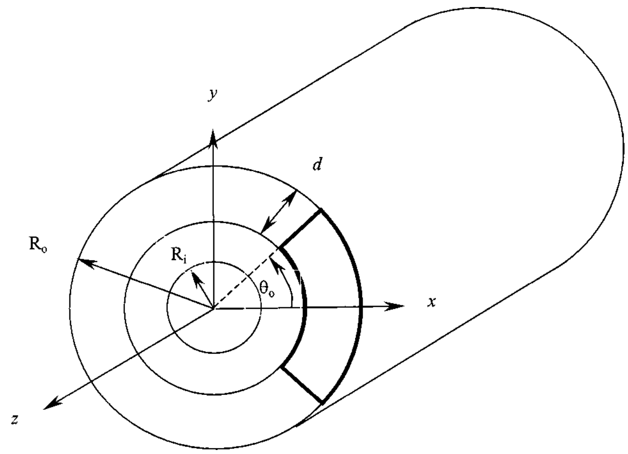

Fig. 1 Geometry of a steel pipe. R_i, inner radius; R_o, outer radius; d, crack depth; θ_o, half circumferential crack angle.

presented here, the crack can be of an arbitrary depth in the radial direction. In this method, the scattered wave fields are expressed as sums of admissible wave functions in the axial direction. The cross section of the tube, in which the crack is located, is divided into a system of six-node planar elements, and the boundary conditions appropriate for the symmetric and antisymmetric problems are imposed on these elements. Using a transfer matrix approach, the problem can then be simplified to a quasi-one-dimensional problem.

The crack considered is an ideal mathematical crack occupying an area located in the plane $z=0$ and can have arbitrary length in circumferential direction and depth in radial direction. The geometry of the pipe and crack is shown in Fig. 1. The objective of this study is to investigate how the length and depth circumferential cracks affect the scattering characteristics in pipes. Reflection and transmission coefficients are presented for a steel pipe for various incident fields. The principle of energy conservation is used to ensure the accuracy of numerical computation. The reflection coefficients of $L(0,2)$ mode are compared with the experiment data in Alleyne et al. [1].

Formulation

The problem of an infinitely long steel pipe is considered here. The circumferential crack is assumed to be located at $z=0$ and it can have arbitrary length and depth in both radial and circumferential directions. To calculate the wave functions, the pipe is first discretized through the thickness into n_{sl} sublayers to determine wave functions travelling in an axial z-direction. During the calculation of the reflection and transmission coefficients, the pipe is then discretized in both circumferential, θ, and radial, r, directions over the cross section $z=0$. A time-harmonic incident wave with angular frequency ω and wave number ξ_{kl} generated at $z=+\infty$ travels in the negative z-direction. Here k denotes the circumferential wave number and l is the axial wave mode. Because of linearity of the governing equations and boundary conditions at $z=0$ the superposition principle can be used in this problem. Also, the displacement and traction components at the plane $z=0$ can be arranged into two groups: one in which the displacement components in the radial and circumferential directions and the traction component in the axial direction are prescribed, and the other contains the axial displacement component and the traction components in the radial and circumferential directions. It can be shown that the quantities in the first group are known when the external forces are symmetric about the plane $z=0$. On the other hand, quantities in the second group are known if the external forces are antisymmetric about $z=0$. In either case, only half of the cylinder $(z\geqslant 0)$ needs to be modeled. Using superposition of the solutions to the two problems, a solution to the general three-dimensional case can be constructed.

In the numerical procedure, a wave function expansion method is used to represent the three-dimensional incident and scattered wave fields travelling in the axial direction. There are two major steps in this method: (1) Use the propagator matrix in the radial direction to form the displacement and stress components in a cross section of the cylinder, and (2) discretize the cross section in radial and circumferential directions and satisfy the displacement and traction boundary conditions according to symmetry and antisymmetry conditions. The details of propagator matrix method and corresponding formulation can be found in Rattanawangcharoen and Shah [12] and the decomposition into symmetric and antisymmetric problems was used by Zhuang et al. [11].

Wave Modes

Time-harmonic wave propagation is considered. The cylinder is divided into coaxial cylinders (layers), say n_{sl} in number. The displacement components, u_r, u_θ, and u_z, in the cylindrical coordinates, r, θ, and z, respectively, of the kth layer which is bounded by $r=r_k$ and $r=r_{k+1}$, are given by (see Gazis [13], Rattanawangcharoen and Shah [12]),

$$\begin{aligned} u_r &= \left[f' - \xi h_1 - \frac{m}{r} h_2 \right] e^{im\theta} e^{i(\xi z-\omega t)} \\ u_\theta &= i\left[\frac{m}{r} f + \xi h_1 - h_2' \right] e^{im\theta} e^{i(\xi z-\omega t)}, \\ u_z &= i\left[\xi f - \frac{m+1}{r} h_1 - h_1' \right] e^{im\theta} e^{i(\xi z-\omega t)} \end{aligned} \tag{1}$$

where

$$\begin{aligned} f(r) &= A_1 Z_m(\alpha r) + B_1 W_m(\alpha r) \\ h_1(r) &= A_2 Z_{m+1}(\beta r) + B_2 W_{m+1}(\beta r), \\ h_2(r) &= A_3 Z_m(\beta r) + B_3 W_m(\beta r) \end{aligned} \tag{2}$$

and

$$\alpha^2 = \omega^2/c_1^2 - \xi^2, \quad \beta^2 = \omega^2/c_2^2 - \xi^2. \tag{3}$$

A prime denotes differentiation with respect to r, m denotes the circumferential wave number, ω the circular frequency, t the time, ξ the wave number in the z-direction, and $i=\sqrt{-1}$. Z_m and W_m in Eq. (2) are Hankel functions $H_m^{(1)}$ and $H_m^{(2)}$, respectively, and A_1, A_2, A_3, B_1, B_2, and B_3 are constants for the layer. The velocity of dilatational and torsional (shear) waves, c_1 and c_2, are defined as

$$c_1^2 = \frac{\lambda+2\mu}{\rho}, \quad c_2^2 = \frac{\mu}{\rho}, \tag{4}$$

where λ and μ are Lamé's constants and ρ the mass density.

By using Eq. (1) together with the stress-strain and strain-displacement relations, the stress components σ_{rr}, $\sigma_{r\theta}$, and σ_{rz} at the interface $r=r_k$ can be expressed as

$$\begin{Bmatrix} U_k \\ S_k \end{Bmatrix} = Q_k \begin{Bmatrix} A \\ B \end{Bmatrix} \tag{5}$$

with

$$U_k = (u_{r,k}\ u_{\theta,k}\ u_{z,k})^T, \quad S_k = (\sigma_{rr,k}\ \sigma_{r\theta,k}\ \sigma_{rz,k})^T \tag{6a}$$

$$A = (A_1\ A_2\ A_3)^T, \quad B = (B_1\ B_2\ B_3)^T. \tag{6b}$$

Superscript T represents the transpose, subscript k means the nodal values at the kth interface. By repeating the above procedure at the surface $r=r_{k+1}$ and considering Eq. (5), the following relation is then achieved:

$$\begin{Bmatrix} U_{k+1} \\ S_{k+1} \end{Bmatrix} = P_k \begin{Bmatrix} U_k \\ S_k \end{Bmatrix} \tag{7}$$

with

$$P_k = Q_{k+1} Q_k^{-1}. \tag{8}$$

The six by six matrix P_k is called the propagator matrix for the kth layer. Once the wave number, ξ, is known for the given frequency, ω, Eq. (7) can be used to evaluate the displacements and stresses at each sublayer.

For a solid cylinder, there is a special consideration at the core cylinder. In order to have a bounded solution in the region of $0 \leqslant r \leqslant r_o$, the function Z_m is taken as J_m, the Bessel function of the first kind, and $B_i = 0$ in Eq. (2). The displacement and stress components at the interface $r = r_1$ satisfy the relation

$$S_1 = K U_1. \tag{9}$$

When the wave number ξ and the displacement components U_1 are known, Eqs. (9) and (7) can then be used to calculate the displacement and stress components at each interface. The matrices K, P_k, and Q_k can be found in Rattanawangcharoen and Shah [12].

Modal Expansion

Assume that the incident wave field is generated at $z = +\infty$ and travels in the negative z-direction. Scattering (reflection and transmission) occurs when the incident wave strikes the crack located at $z = 0$. The scattering wave fields consist of a finite number of propagating modes and an infinite number of nonpropagating modes. Due to the symmetry and antisymmetry consideration, only the reflected wave field needs to be evaluated in the positive z-direction. The displacements and stresses of the wave field can be expanded as follows:

$$\begin{aligned} u_r(r,\theta,z,t) &= \sum_{m=-M}^{M} \sum_{n=1}^{N_m} u_{r,mn}(r) a_{kl,mn} e^{i\xi_{mn}z} e^{im\theta} e^{-i\omega t} \\ &= \sum_{m=-M}^{M} U_{r,m}(r) E_m(z) a_{kl,m} e^{im\theta} e^{-i\omega t} \\ u_\theta(r,\theta,z,t) &= \sum_{m=-M}^{M} \sum_{n=1}^{N_m} u_{\theta,mn}(r) a_{kl,mn} e^{i\xi_{mn}z} e^{im\theta} e^{-i\omega t} \\ &= \sum_{m=-M}^{M} U_{\theta,m}(r) E_m(z) a_{kl,m} e^{im\theta} e^{-i\omega t}, \qquad (10) \\ u_z(r,\theta,z,t) &= \sum_{m=-M}^{M} \sum_{n=1}^{N_m} u_{z,mn}(r) a_{kl,mn} e^{i\xi_{mn}z} e^{im\theta} e^{-i\omega t} \\ &= \sum_{m=-M}^{M} U_{z,m}(r) E_m(z) a_{kl,m} e^{im\theta} e^{-i\omega t} \end{aligned}$$

and

$$\begin{aligned} \sigma_{zr}(r,\theta,z,t) &= \sum_{m=-M}^{M} \sum_{n=1}^{N_m} \sigma_{zr,mn}(r) a_{kl,mn} e^{i\xi_{mn}z} e^{im\theta} e^{-i\omega t} \\ &= \sum_{m=-M}^{M} S_{zr,m}(r) E_m(z) a_{kl,m} e^{im\theta} e^{-i\omega t} \\ \sigma_{z\theta}(r,\theta,z,t) &= \sum_{m=-M}^{M} \sum_{n=1}^{N_m} \sigma_{z\theta,mn}(r) a_{kl,mn} e^{i\xi_{mn}z} e^{im\theta} e^{-i\omega t} \\ &= \sum_{m=-M}^{M} S_{z\theta,m}(r) E_m(z) a_{kl,m} e^{im\theta} e^{-i\omega t}, \qquad (11) \end{aligned}$$

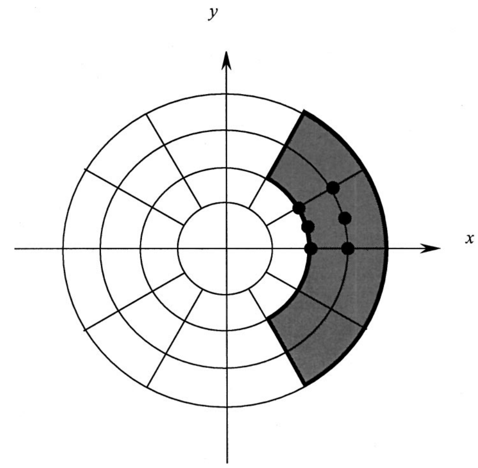

Fig. 2 A typical mesh in the cross section. The shadow region represents the crack.

$$\begin{aligned} \sigma_{zz}(r,\theta,z,t) &= \sum_{m=-M}^{M} \sum_{n=1}^{N_m} \sigma_{zz,mn}(r) a_{kl,mn} e^{i\xi_{mn}z} e^{im\theta} e^{-i\omega t} \\ &= \sum_{m=-M}^{M} S_{zz,m}(r) E_m(z) a_{kl,m} e^{im\theta} e^{-i\omega t} \end{aligned}$$

with

$$\begin{aligned} U_{r,m}(r) &= [u_{r,m1}(r) \ u_{r,m2}(r) \ \cdots \ u_{r,mN_m}(r)] \in \mathbf{C}^{1\times N_m} \\ U_{\theta,m}(r) &= [u_{\theta,m1}(r) \ u_{\theta,m2}(r) \ \cdots \ u_{\theta,mN_m}(r)] \in \mathbf{C}^{1\times N_m} \qquad (12) \\ U_{z,m}(r) &= [u_{z,m1}(r) \ u_{z,m2}(r) \ \cdots \ u_{z,mN_m}(r)] \in \mathbf{C}^{1\times N_m} \\ S_{zr,m}(r) &= [\sigma_{zr,m1}(r) \ \sigma_{zr,m2}(r) \ \cdots \ \sigma_{zr,mN_m}(r)] \in \mathbf{C}^{1\times N_m} \\ S_{z\theta,m}(r) &= [\sigma_{z\theta,m1}(r) \sigma_{z\theta,m2}(r) \ \cdots \ \sigma_{z\theta,mN_m}(r)] \in \mathbf{C}^{1\times N_m}, \qquad (13) \\ S_{zz,m}(r) &= [\sigma_{zz,m1}(r) \sigma_{zz,m2}(r) \ \cdots \ \sigma_{zz,mN_m}(r)] \in \mathbf{C}^{1\times N_m} \\ a_{kl,m} &= \{a_{kl,m1} a_{kl,m2} \ \cdots \ a_{kl,mN_m}\}^T \in \mathbf{C}^{N_m\times 1} \qquad (14) \end{aligned}$$

and

$$E_m(z) = \mathrm{diag}[e^{i\xi_{m1}z} \ e^{i\xi_{m2}z} \ \cdots \ e^{i\xi_{mN_m}z}] \in \mathbf{C}^{N_m\times N_m}$$

where $a_{kl,mn}$s are unknown complex coefficients to be determined. The first two subscripts, k and l, indicate the wave numbers in circumferential and axial directions of the incident wave, and the last two means the coefficients of the scattered wave fields corresponding to the wave numbers, m and n, in the circumferential and axial directions, respectively. The symbol $\mathbf{x} \in \mathbf{C}^{m\times n}$ means that $\mathbf{x}$ is a complex matrix with order m by n. It may be pointed out that the number of axial modes, N_m, need not be the same for different circumferential wave number m. The factor $e^{-i\omega t}$ will be suppressed in the sequel.

For the computational purpose, the continuous functions in the expansions (10) and (11) are evaluated at discrete points on the cross section. The cross section is divided into six-node elements with uniform distribution both in circumferential and radial directions, as shown in Fig. 2. The number of divisions in radial and circumferential directions are p and q, respectively. In order to represent the circular curve in the circumferential direction, three nodes are used in this direction. Two nodes are used in the radial direction in each element. With the geometry of the mesh shown in Fig. 2, the consistent forces can be obtained from the stresses associated with the wave modes using standard procedures (see Bathe [14]).

The expansions (10) and (11) satisfy the traction free conditions on the inner and outer surfaces of the cylinder. Hence, only boundary conditions at the end $z=0$ have to be satisfied. Because of the existence of the crack in the cross section, care must be taken on this part of the cross section when dealing with the boundary conditions. Traction-free boundary conditions for both symmetric and antisymmetric cases are imposed on the crack face. Therefore, for the symmetric case, the boundary conditions are given by

$$S=S^I+S^R=\begin{Bmatrix} S_C^I \\ S_N^I \end{Bmatrix}+\begin{Bmatrix} S_C^R \\ S_N^R \end{Bmatrix}=0, \quad \text{at } z=0 \tag{15}$$

with

$$S_C^I=\begin{Bmatrix} f_r^I \\ f_\theta^I \\ f_z^I \end{Bmatrix}, \quad S_N^I=\begin{Bmatrix} f_r^I \\ f_\theta^I \\ u_z^I \end{Bmatrix}, \quad S_C^R=\begin{Bmatrix} f_r^R \\ f_\theta^R \\ f_z^R \end{Bmatrix}, \quad S_N^R=\begin{Bmatrix} f_r^R \\ f_\theta^R \\ u_z^R \end{Bmatrix} \tag{16}$$

and for antisymmetry, they are,

$$A=A^I+A^R=\begin{Bmatrix} A_C^I \\ A_N^I \end{Bmatrix}+\begin{Bmatrix} A_C^R \\ A_N^R \end{Bmatrix}=0, \quad \text{at } z=0 \tag{17}$$

with

$$A_C^I=\begin{Bmatrix} f_r^I \\ f_\theta^I \\ f_z^I \end{Bmatrix}, \quad A_N^I=\begin{Bmatrix} u_r^I \\ u_\theta^I \\ f_z^I \end{Bmatrix}, \quad A_C^R=\begin{Bmatrix} f_r^R \\ f_\theta^R \\ f_z^R \end{Bmatrix}, \quad A_N^R=\begin{Bmatrix} u_r^R \\ u_\theta^R \\ f_z^R \end{Bmatrix} \tag{18}$$

where f_r, f_θ, and f_z are the consistent force components in r, θ, and z-directions at the boundary $z=0$, respectively. The superscripts I and R represent the quantities associated with the incident and scattered wave fields, respectively. The subscript C and N represent whether the point considered is located in the cracked or the uncracked region, respectively.

Without loss of generality, we assume that the nodal sequence is arranged such that the first P_C points are located in the cracked region and all the rest $P_N=P-P_C$ points are located in the uncracked region.

We now first consider the symmetric case. It should be pointed out that when the mixed displacement and force components f_r, f_θ, and u_z are known, the dual components u_r, u_θ, and f_z are unknown for the point located in the uncracked region and vice versa. For the cracked region, all the force components are known and the corresponding dual displacement components are unknown.

Evaluating the sums in (10) and (11) pointwise at the cross section $z=0$, it is seen that

$$\mathbf{E}_m(0)=\text{diag}[1 \;\; 1 \;\; \cdots \;\; 1]\in\mathbf{R}^{N_m\times N_m}.$$

The vectors S_C^R and S_N^R in the boundary conditions (15) may be written as

$$S_C^R=G_C^R a, \quad S_N^R=G_N^R a \tag{19}$$

where

$$\begin{aligned} G_C^R&=[G_{C,-M}^R \cdots G_{C,m}^R \cdots G_{C,M}^R]\in\mathbf{C}^{3P_C\times N}, \\ G_N^R&=[G_{N,-M}^R \cdots G_{N,m}^R \cdots G_{N,M}^R]\in\mathbf{C}^{3P_N\times N}, \end{aligned} \tag{20}$$

$$a=\{a_{kl,-M} \cdots a_{kl,m} \cdots a_{kl,M}\}^T\in\mathbf{C}^{N\times 1} \tag{21}$$

$$G_{C,m}^R=\begin{bmatrix} F_{C,r,m}^R \\ F_{C,\theta,m}^R \\ F_{C,z,m}^R \end{bmatrix}\in\mathbf{C}^{3P_C\times N_m}, \quad G_{N,m}^R=\begin{bmatrix} F_{N,r,m}^R \\ F_{N,\theta,m}^R \\ U_{N,z,m}^R \end{bmatrix}\in\mathbf{C}^{3P_N\times N_m}. \tag{22}$$

The total number of wave modes, N_T, considered in the wave function expansion is given by

$$N_T=\sum_{m=-M}^{M} N_m$$

where N_m is the axial modes corresponding to the circumferential number m. P is the total number of nodes in the cross section $z=0$, P_C the number of nodes in the cracked region, and $P_N=P-P_C$ the number of nodes in the uncracked region. $a_{kl,m}$ is given by Eq. (14). The specific forms of matrices $F_{C,r,m}^R$, $F_{C,\theta,m}^R$, $F_{C,z,m}^R$, $F_{N,r,m}^R$, $F_{N,\theta,m}^R$, and $U_{N,z,m}^R$ are given in Appendix A.

In a similar manner, the incident wave field S^I can be constructed as

$$S_C^I=a_{kl}^I g_{C,kl}^I, \quad S_N^I=a_{kl}^I g_{N,kl}^I. \tag{23}$$

Here, the vector $g_{C,kl}^I$ is obtained from the lth column of the matrix $G_{C,k}^R$ after replacing each r and θ-directions force component by the negative value of it. The vector $g_{N,kl}^I$ is obtained from lth column of the matrix $G_{N,k}^R$ after replacing each z-direction force component by the negative value of it. a_{kl}^I is the amplitude of the incident wave.

Equation (15) (see also Eq. (19)) is solved using the principle of virtual work. To accomplish this, vectors, T_C^R and T_N^R, which are the dual components of the vectors S_C^R and S_N^R, are formed,

$$T^R=\begin{Bmatrix} T_C^R \\ T_N^R \end{Bmatrix}=\begin{bmatrix} H_C^R \\ H_N^R \end{bmatrix}a \tag{24}$$

with

$$T_C^R=\begin{Bmatrix} u_r^R \\ u_\theta^R \\ u_z^R \end{Bmatrix}, \quad T_N^R=\begin{Bmatrix} u_r^R \\ u_\theta^R \\ f_z^R \end{Bmatrix} \tag{25}$$

$$\begin{aligned} H_C^R&=[H_{C,-M}^R \cdots H_{C,m}^R \cdots H_{C,M}^R]\in\mathbf{C}^{3P_C\times N}, \\ H_N^R&=[H_{N,-M}^R \cdots H_{N,m}^R \cdots H_{N,M}^R]\in\mathbf{C}^{3P_N\times N}, \end{aligned} \tag{26}$$

$$H_{C,m}^R=\begin{bmatrix} U_{C,r,m}^R \\ U_{C,\theta,m}^R \\ U_{C,z,m}^R \end{bmatrix}\in\mathbf{C}^{3P_C\times N_m}, \quad H_{N,m}^R=\begin{bmatrix} U_{N,r,m}^R \\ U_{N,\theta,m}^R \\ F_{N,z,m}^R \end{bmatrix}\in\mathbf{C}^{3P_N\times N_m}. \tag{27}$$

The specific form of block matrices appearing in Eq. (28) can be found in Appendix B.

Now applying the principle of virtual work to boundary conditions (15) by multiplying the dual components, T_C^R and T_N^R, on the both sides of Eq. (15) yields

$$\begin{bmatrix} H_C^R \\ H_N^R \end{bmatrix}^*\begin{bmatrix} G_C^R \\ G_N^R \end{bmatrix}a=-a_{kl}^I\begin{bmatrix} H_C^R \\ H_N^R \end{bmatrix}^*\begin{Bmatrix} g_{C,kl}^I \\ g_{N,kl}^I \end{Bmatrix}. \tag{28}$$

The superscript * denotes the complex conjugate plus matrix transpose.

The solutions of Eq. (28) are the reflection coefficients associated with the wave modes. Having known these coefficients, values of the displacement and stress components at different locations in the cylinder are readily obtained by substituting them into expansions (10) and (11).

Reduction to Quasi-One-Dimensional Problem. It is noted that Eq. (28) is derived by using pointwise conditions. Due to the large number of nodes in the two-dimensional mesh in plane $z=0$, as shown in Fig. 2, it is a computationally demanding procedure. If we consider the idea of a transfer matrix from radius to radius, instead of point to point, calculations can be performed more efficiently. This idea is based upon the circular symmetry of the geometry and the physical characteristics of the problem (see the expansions (10) and (11)).

Take two vectors $f_{C,r,mn}\in\mathbf{C}^{P_C\times 1}$ and $f_{N,r,mn}\in\mathbf{C}^{P_N\times 1}$, which are in the nth column of the matrices $F_{C,r,m}^R$ and $F_{N,r,m}^R$ in (A1)

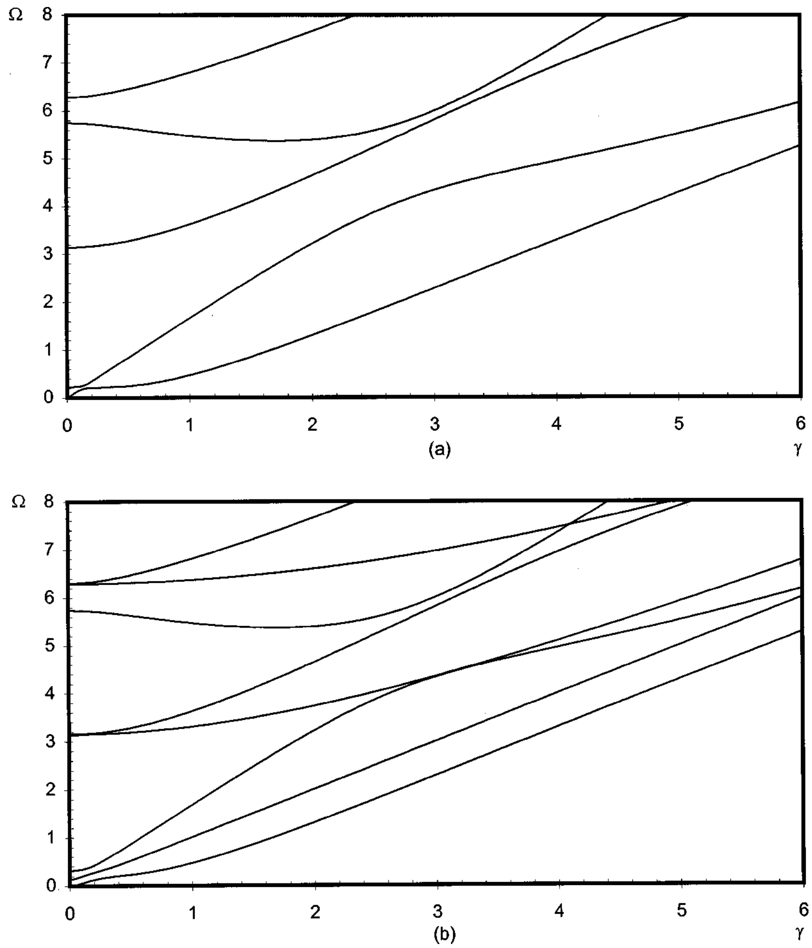

Fig. 3 Frequency spectrum of a steel pipe. $H/R=0.135$, $\nu=0.287$. (*a*) Longitudinal wave $(m=0)$; (*b*) Flexural wave $(m=1)$.

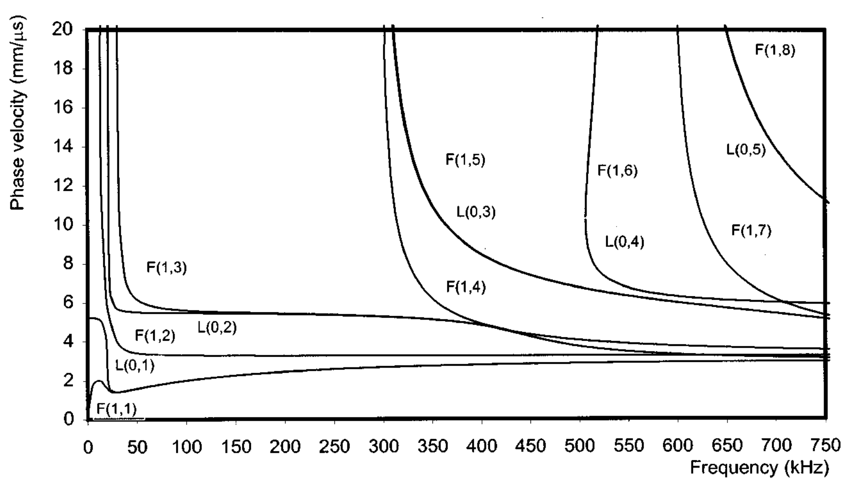

Fig. 4 Phase velocity versus frequency for a steel pipe. $H/R=0.135$, $\nu=0.287$.

and ($A4$), as an example. It is noted that these two vectors are evaluated at all the nodes of the cracked and uncracked regions, respectively. We first construct two vectors $f^{(1)}_{C,r,mn}$ and $f^{(1)}_{N,r,mn}$ corresponding to these two vectors but evaluated at the two adjacent radii $\theta=0$ and $\theta=\pi/q$, where q is the number of subdivisions in the circumferential direction. Also, we denote two radii, $\theta=2j\pi/q$ and $\theta=(2j+1)\pi/q$, for $j=0,1,\ldots,q-1$, the jth radius pair in the following. Without loss of generality, we assume that q_C number of radii pairs are located in the cracked region and q_N in the uncracked region.

By considering the wave functions in Eqs. (10) and (11), it can be shown that the values of the two vectors, $f_{C,r,mn}$ and $f_{N,r,mn}$, on the jth radius pair are obtained only by a rotation, $e^{2imk\pi/q}$, of that of the first radius pair $f^{(1)}_{C,r,mn}$ and $f^{(1)}_{N,r,mn}$. Therefore we have

$$f_{C,r,mn}^{(j)}=\lambda_m^{j-1}f_{C,r,mn}^{(1)}, \quad 1\leqslant j\leqslant q_C \tag{29a}$$

$$f_{N,r,mn}^{(j)}=\lambda_m^{j-1}f_{N,r,mn}^{(1)}, \quad q_C+1\leqslant j\leqslant q=q_C+q_N \tag{29b}$$

where

$$\lambda_m=e^{2im\pi/q}. \tag{29c}$$

Thus, the vectors $f_{C,r,mn}$ and $f_{N,r,mn}$ can be written in a more compact form as

$$f_{C,r,mn}=\Lambda_{C,m}f_{C,r,mn}^{(1)}, \quad f_{N,r,mn}=\Lambda_{N,m}f_{N,r,mn}^{(1)} \tag{30}$$

with transfer matrices $\Lambda_{C,m}$ and $\Lambda_{N,m}$, given by

$$\begin{aligned}\Lambda_{C,m}&=[\hat{I}\ \lambda_m\hat{I}\ \cdots\ \lambda_m^{q_C-1}\hat{I}]^T\in\mathbf{C}^{2pq_C\times 2p}\\ \Lambda_{N,m}&=\lambda_m^{q_C}[\hat{I}\ \lambda_m\hat{I}\ \cdots\ \lambda_m^{q_N-1}\hat{I}]^T\in\mathbf{C}^{2pq_N\times 2p}.\end{aligned} \tag{31}$$

Here, $\hat{I}$ is the unit matrix with order $2p$ by $2p$, $2p$ being the total number of nodes in a radius pair. With the help of Eq. (30), the matrices $F_{C,r,m}^R$ and $F_{N,r,m}^R$ can then be expressed as

$$F_{C,r,m}^R=\Lambda_{C,m}F_{C,r,m}^{(1)R}, \quad F_{N,r,m}^R=\Lambda_{N,m}F_{N,r,m}^{(1)R}. \tag{32}$$

The matrices $F_{C,r,m}^{(1)R}$ and $F_{N,r,m}^{(1)R}$ have similar forms as the original matrices $F_{C,r,m}^R$ and $F_{N,r,m}^R$ after changing each column with $f_{C,r,mn}^{(1)}$ and $f_{N,r,mn}^{(1)}$, respectively. All the other matrices in Appendices A and B have similar expressions, as shown in Eq. (32). Using these expressions, the matrices G_C^R and G_N^R have the following forms:

$$G_C^R=[\tilde{\Lambda}_{C,-M}G_{C,-M}^{(1)R}\ \cdots\ \tilde{\Lambda}_{C,m}G_{C,m}^{(1)R}\ \cdots\ \tilde{\Lambda}_{C,M}G_{C,M}^{(1)R}], \tag{33}$$

$$G_N^R=[\tilde{\Lambda}_{N,-M}G_{N,-M}^{(1)R}\ \cdots\ \tilde{\Lambda}_{N,m}G_{N,m}^{(1)R}\ \cdots\ \tilde{\Lambda}_{N,M}G_{N,M}^{(1)R}], \tag{34}$$

where

$$\begin{aligned}\tilde{\Lambda}_{C,m}&=\begin{bmatrix}\Lambda_{C,m} & & \\ & \Lambda_{C,m} & \\ & & \Lambda_{C,m}\end{bmatrix}\in\mathbf{C}^{6pq_C\times 6p}\\ \tilde{\Lambda}_{N,m}&=\begin{bmatrix}\Lambda_{N,m} & & \\ & \Lambda_{N,m} & \\ & & \Lambda_{N,m}\end{bmatrix}\in\mathbf{C}^{6pq_N\times 6p}.\end{aligned} \tag{35}$$

The block matrices $G_{C,m}^{(1)R}$ and $G_{N,m}^{(1)R}$ are obtained from the matrices $G_{C,m}^R$ and $G_{N,m}^R$ after replacing the corresponding force and displacement components by their reference vectors, which are only evaluated at the first radius pair. Similar relations hold also for the matrices H_C^R, H_N^R and vectors S_C^I, S_N^I.

Table 1 Amplitude of reflection coefficients as a function of total wave modes for Ω=0.74 with circumferential length 50 percent and crack depth 0.5*H*

M	N	$\lvert R_{02,01}\rvert$	$\lvert R_{02,02}\rvert$	$\lvert R_{02,11}\rvert$	$\lvert R_{02,12}\rvert$	$\lvert R_{02,13}\rvert$
0	51	0.242	0.195	⋯	⋯	⋯
1	131	0.241	0.154	0.161	0.041	0.118
2	211	0.254	0.169	0.155	0.034	0.100
3	291	0.237	0.153	0.151	0.033	0.099
4	371	0.252	0.168	0.152	0.032	0.096
5	451	0.233	0.147	0.149	0.032	0.096
6	531	0.240	0.157	0.150	0.032	0.096
7	611	0.236	0.152	0.149	0.032	0.096
8	691	0.237	0.153	0.149	0.032	0.096
9	771	0.235	0.152	0.149	0.032	0.096
10	851	0.235	0.152	0.149	0.032	0.096
11	931	0.235	0.152	0.149	0.032	0.096

With the above simplification, we have the following results:

$$(H_C^R)^*G_C^R=\begin{bmatrix}\cdots & \cdots & \cdots\\ \cdots & \mu_{C,m_1m_2}(H_{C,m_1}^{(1)R})^*G_{C,m_2}^{(1)R} & \cdots\\ \cdots & \cdots & \cdots\end{bmatrix}\in\mathbf{C}^{N\times N} \tag{36}$$

$$(H_N^R)^*G_N^R=\begin{bmatrix}\cdots & \cdots & \cdots\\ \cdots & \mu_{N,m_1m_2}(H_{N,m_1}^{(1)R})^*G_{N,m_2}^{(1)R} & \cdots\\ \cdots & \cdots & \cdots\end{bmatrix}\in\mathbf{C}^{N\times N} \tag{37}$$

$$(H_C^R)^*S_C^I=\begin{Bmatrix}\vdots\\ \mu_{C,mk}(H_{C,m}^{(1)R})^*g_{C,kl}^{(1)R}\\ \vdots\end{Bmatrix}\in\mathbf{C}^{N\times 1} \tag{38}$$

$$(H_N^R)^*S_N^I=\begin{Bmatrix}\vdots\\ \mu_{N,mk}(H_{N,m}^{(1)R})^*g_{N,kl}^{(1)R}\\ \vdots\end{Bmatrix}\in\mathbf{C}^{N\times 1} \tag{39}$$

and

$$\mu_{C,m_1m_2}=\begin{cases} q_C, & \text{for } m_1=m_2\\ \dfrac{1-\lambda_{m_1,m_2}^{q_C}}{1-\lambda_{m_1m_2}}, & \text{for } m_1\neq m_2\end{cases}, \tag{40}$$

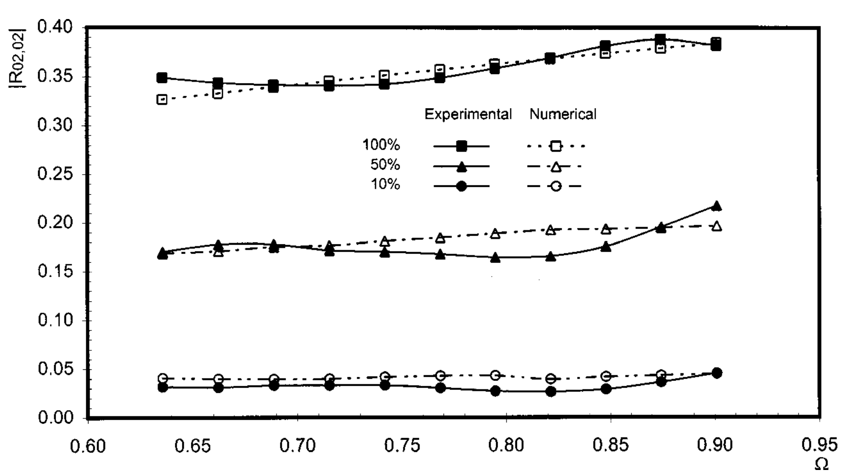

Fig. 5 Reflection coefficients for three different crack extensions. ——, crack depth=0.5*H*; — — —, crack depth=0.55*H*.

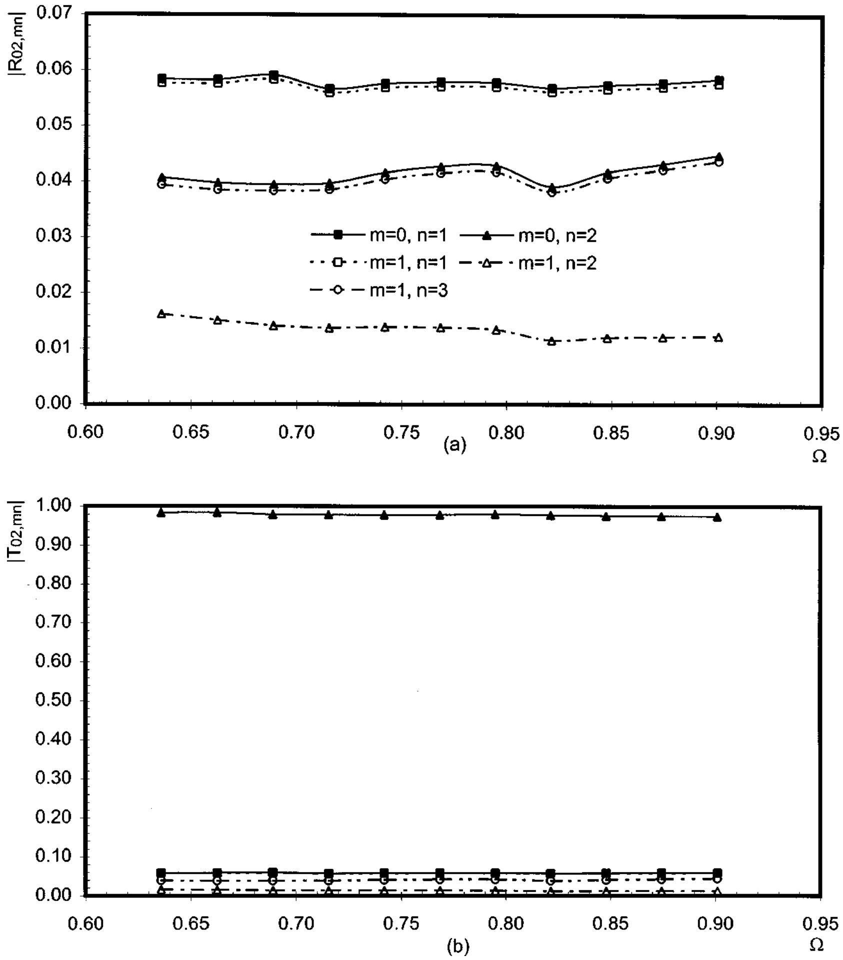

Fig. 6 Normalized reflection and transmission coefficients in a steel pipe. *H/R* =0.135, ν=0.287, crack length is ten percent of the circumference and crack depth=0.55*H*. (*a*) Reflection coefficient; (*b*) transmission coefficient.

$$\mu_{N,m_1m_2}=\begin{cases} q_N, & \text{for } m_1=m_2 \\ -\dfrac{1-\lambda_{m_1,m_2}^{q_C}}{1-\lambda_{m_1m_2}}, & \text{for } m_1\neq m_2 \end{cases}, \tag{41}$$

$$\lambda_{m_1,m_2}=\overline{\lambda}_{m_1}\lambda_{m_2}=e^{2i(m_2-m_1)\pi/q}. \tag{42}$$

Equations (41) and (42) may also be written as

$$\mu_{C,m_1m_2}+\mu_{N,m_1m_2}=q\,\delta_{m_1m_2} \tag{43}$$

$$\delta_{m_1m_2}=\begin{cases} 1, & \text{for } m_1=m_2 \\ 0, & \text{for } m_1\neq m_2 \end{cases}. \tag{44}$$

Substituting Eqs. (36), (37), (38), and (39) into Eq. (28) results in the final equation,

$$[(H_C^R)^*G_C^R+(H_N^R)^*G_N^R]a=-a_{kl}^I[(H_C^R)^*S_C^I+(H_N^R)^*S_N^I]. \tag{45}$$

It can be seen from Eqs. (36) to (41) that, in the computational procedure, all the matrices are evaluated only for the first radius pair. In other words, the circumferential discretization will not affect the size of the matrices nor the computational time. Hence, the problem is now reduced to be quasi-one-dimensional.

When $q_C=q$, then $q_N=0$. This corresponds to the axisymmetric crack. It is then obvious that $\mu_{C,m_1m_2}=0$, when $m_1\neq m_2$, and $\mu_{N,m_1m_2}=0$ for all m_1 and m_2, and $\mu_{C,mm}=q$. Therefore, matrices $(H_C^R)^*G_C^R$ and $(H_N^R)^*G_N^R$ are reduced to diagonal block matrices. Furthermore, vectors in Eqs. (38) and (39), $(H_C^R)^*S_C^I$ and $(H_N^R)^*S_N^I$, are reduced to zero. But the *k*th block vector remains unchanged. So the problem becomes one of smaller dimension and one needs to consider the wave modes only related to the circumferential wave number, *k*, the incident wave number in circumferential direction. In this situation, it is easy to show that the subdivision in circumferential direction will not contribute to the complexity of the numerical procedure, because the parameter *q* will be eliminated from the final linear equation.

Once the linear Eq. (28) is established, the reflection coefficients for the symmetric case are obtained. For the antisymmetric case, it can be solved by a similar procedure, and it will not be repeated for brevity. If knowing the solutions of these two cases, the reflection and transmission coefficients, $R_{kl,mn}$ and $T_{kl,mn}$, for the problem considered here are easily derived respectively as shown below,

$$R_{kl,mn}=\frac{a_{kl,mn}^S+a_{kl,mn}^A}{2a_{kl}^I}, \quad T_{kl,mn}=\frac{a_{kl,mn}^S-a_{kl,mn}^A}{2a_{kl}^I}, \tag{46}$$

where $a_{kl,mn}^S$ and $a_{kl,mn}^A$ represent the solutions for the symmetric and antisymmetric problems, respectively. The numerical accuracy of the coefficients is checked by the principle of energy conservation. The energy flux of each propagating mode has been discussed in Rattanawangcharoen et al. [8].

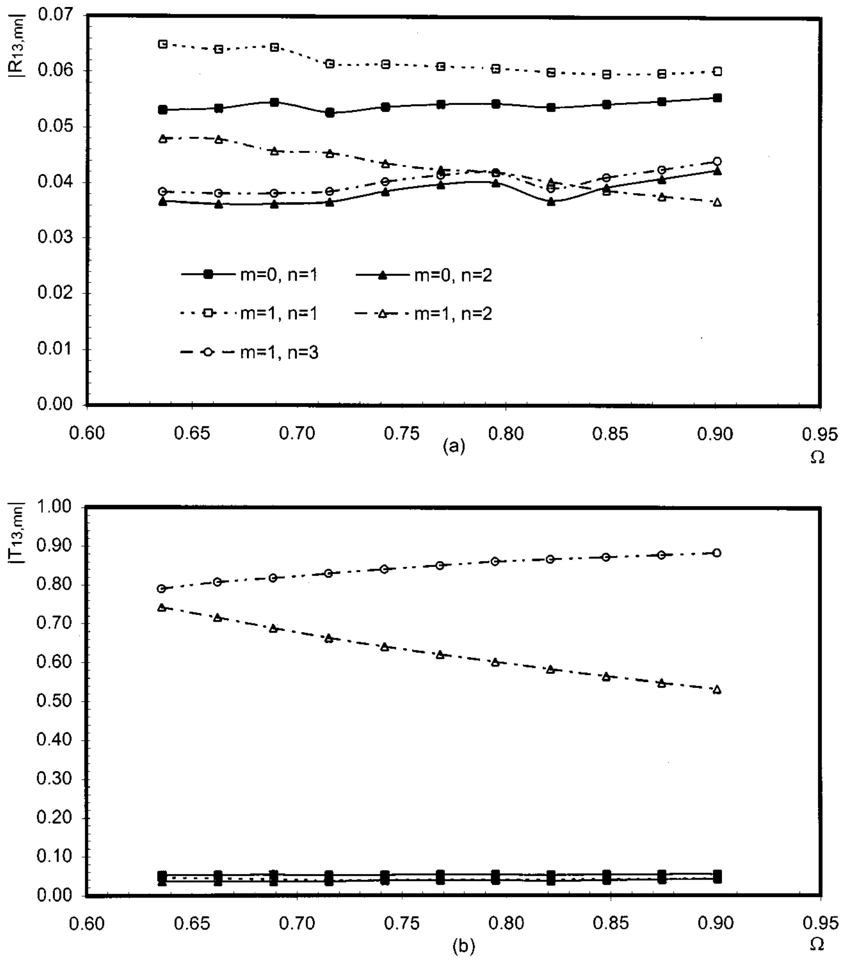

Fig. 7 Normalized reflection and transmission coefficients in a steel pipe. $H/R=0.135$, $\nu=0.287$, crack length is ten percent of the circumference and crack depth$=0.55H$. (*a*) Reflection coefficient; (*b*) transmission coefficient.

Numerical Results and Discussion

The method described in the previous section can be used to analyze the effect of planar cracks located in a cross section of the pipe wall. As shown above, the crack can have arbitrary length, L, in the circumferential direction and depth, d, in the radial direction (Figs. 1 and 2). Note that it is not necessary that the crack breaks the outer surface of the pipe. The problem considered was investigated experimentally and numerically by Alleyne et al. [1] and Lowe et al. [2]. They used the finite element method for analyzing the problem. Here, we will consider the same geometric and material properties of the pipe as used by them so that we can present some results comparing the predictions of the present method with their experimental observations.

The material constants for the all examples presented below are for steel with longitudinal wave and torsional wave velocities given, respectively, by

$$c_1=5.96\times10^3 \text{ m/s}, \quad c_2=3.26\times10^3 \text{ m/s}. \tag{47}$$

The Young's modulus is 216.9 GPa. They considered two different pipes having diameters 76 mm and 152 mm with thicknesses 5.5 mm and 7 mm. Results for both cases were found to be quite similar. For the present study, we have chosen the inner radius, R_i, and thickness, H, of the pipe to be,

$$R_i=38 \text{ mm}, \quad H=5.5 \text{ mm}. \tag{48}$$

Then, the Poisson's ratio, ν, and the thickness over mean radius, H/R, are, respectively,

$$\nu=0.287, \quad H/R=0.135. \tag{49}$$

The frequency spectrum for the longitudinal wave $(m=0)$ and first flexural wave $(m=1)$ are shown in Fig. 3. In the following discussion, we will use the nondimensional frequency, Ω, and the nondimensional wave number, γ, as

$$\Omega=\frac{\omega H}{c_2}, \quad \gamma=\xi H. \tag{50}$$

Thus, for frequency of 100 kHz, $\Omega=1.06$. As Figs. 3 and 4 show, there are two longitudinal modes ($L(0,1)$ and $L(0,2)$) and three flexural modes ($F(1,1)$, $F(1,2)$, and $F(1,3)$) propagating at this frequency. There are other propagating modes $F(n,m)$, $n>1$, at this frequency. These are not shown (see Alleyne et al. [1]).

Alleyene et al. [1] presented results for the reflection of the incident mode $L(0,2)$ from circumferential cracks of different lengths and depths in the frequency range 60–85 kHz ($\Omega=0.64$–0.90). As seen from Fig. 4, the velocity of the $L(0,2)$ mode is nearly independent of frequency in the range $\Omega=0.6$–3. The velocity in this range is 5.29 mm/μs, which is somewhat higher than the velocity ($c=5.22$ mm/μs) of the $L(0,1)$ mode at very low frequencies. Note that the phase velocity of the $F(1,3)$ mode approaches that of the $L(0,2)$ mode at frequencies higher than about 75 kHz and that of $F(1,2)$ approaches the shear wave velocity c_2. In the following, numerical results are presented for the reflection coefficients for mode-converted waves when two different modes

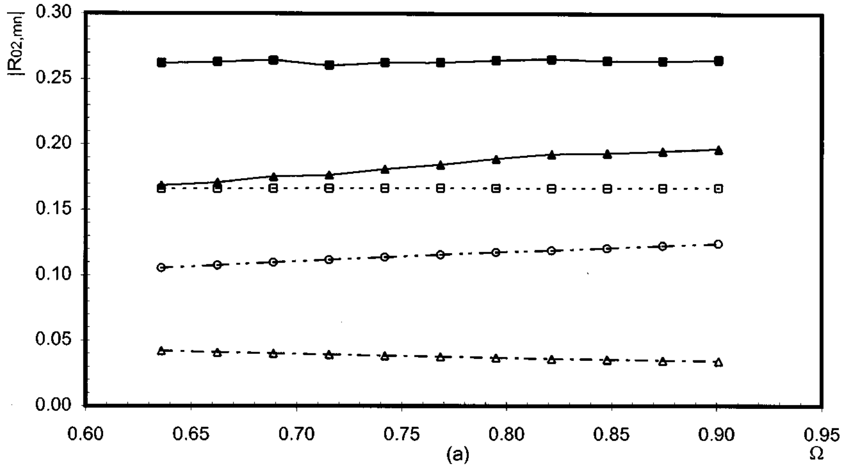

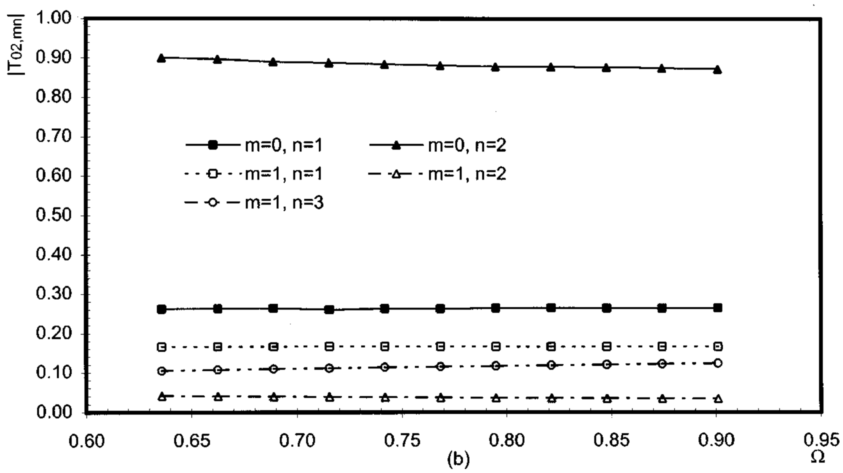

Fig. 8 Normalized reflection and transmission coefficients in a steel pipe. $H/R=0.135$, $\nu=0.287$, crack length is 50 percent of the circumference and crack depth$=0.55H$. (*a*) Reflection coefficient; (*b*) transmission coefficient.

($L(0,2)$, and $F(1,3)$) are incident on circumferential cracks. Comparison with the experimental results, when appropriate, are also discussed.

First, convergence of the numerical procedure was tested with different mesh sizes and results were compared for several scattering problems. For each case, a different number of circumferential and axial modes was chosen in the modal expansion to ensure convergence of the series. The incident wave were chosen to be the second wave mode $L(0,2)$. It was found that the results converged (comparing successive sums with increasing number of terms in the modal expansion) with the choice of mesh having node numbers $p=100$ and $q=10{,}000$, and with the number of modes being $M=11$, $N_m=51$ for $m=0$ and $N_m=40$ for $m=\pm1,\pm2,\ldots,\pm M$. Table 1 shows the rate of convergence of the series for the reflection coefficient from a crack of circumferential length 50 percent of the circumference and depth $0.5H$. As noted in the previous section, the convergence was tested by using the energy conservation. Since attention has been focused here on reflection and transmission coefficients, singularities at the crack corners were not taken into account in the numerical procedure because they would not affect the far field. This has been verified also by comparison with the results reported in [1].

After establishing the convergence, the mesh size and the number of modes were fixed for the rest of the calculations. Reflection coefficients were calculated for two different crack depths, namely $0.5H$ and $0.55H$. It was found that the results for $0.55H$ crack depth agreed better with that of the experiment and the relative error was less than 6 percent for the 100 percent circumferential crack. Using the same mesh and crack depth, the relative error for the reflection coefficient for a 50 percent circumferential crack length was around 10 percent, which was higher than that for the axisymmetric case.

There may be various reasons for this discrepancy. One major reason could be that the notch used in the experiment had a finite width. Also, there could be inaccuracy in the measured notch depth. Furthermore, the notch may not be planar. For all the results presented here we kept the crack depth to be $0.55H$.

The comparison between the experimental data and the model results is shown in Fig. 5. The results for three different cracks with circumferential lengths 10 percent, 50 percent, and 100 percent of the total pipe circumference are given in Fig. 5. In this figure, the reflection coefficients for the $L(0,2)$ mode are shown as functions of frequency ranging from 60 kHz to 85 kHz, or in nondimensional frequency, Ω from 0.64 to 0.90.

The reflection and transmission coefficients, $|R_{02,mn}|$, $|T_{02,mn}|$, and $|R_{13,mn}|$, $|T_{13,mn}|$ are shown in Figs. 6 and 7 for the circumferential crack length $L=$ten percent. All the reflection coefficients are very small, less then 0.07. It is interesting to note that for the incident mode $L(0,2)$ the presence of the crack has little influence on this mode, because this mode is transmitted with most of the energy in it. For the incident $F(1,3)$ mode, most of the transmitted energy is shared between the modes $F(1,2)$ and $F(1,3)$, with the energy going into the former increasing with frequency and the latter losing energy with increasing frequency.

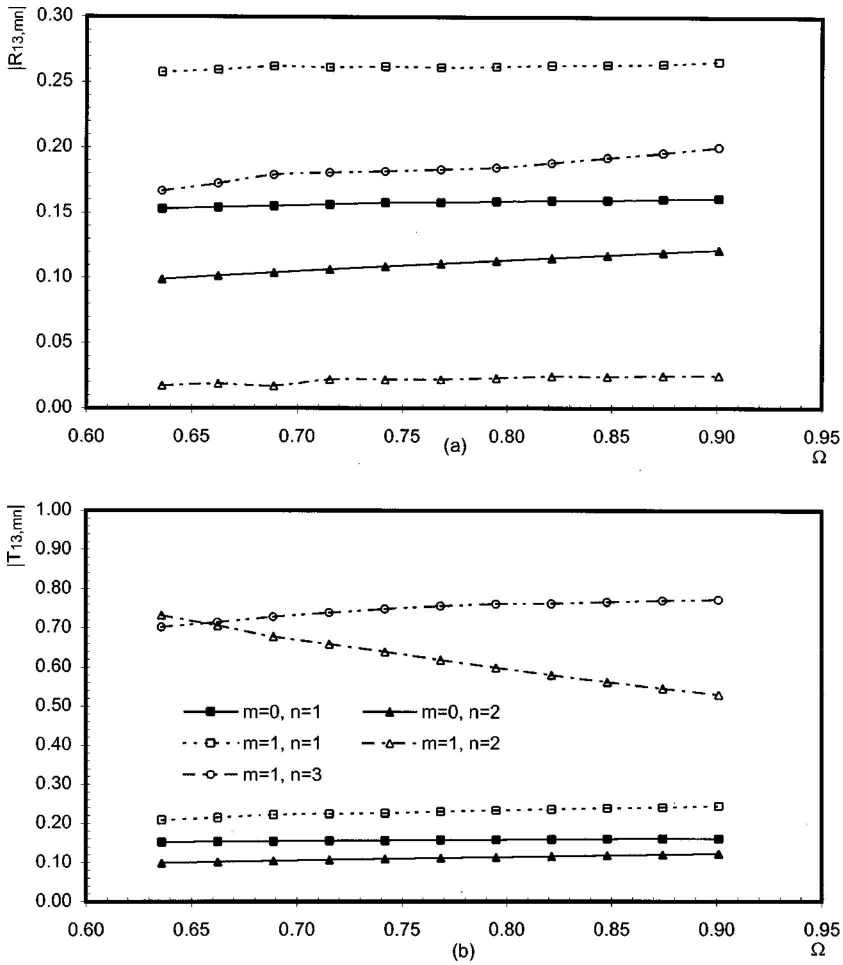

Fig. 9 Normalized reflection and transmission coefficients in a steel pipe. $H/R=0.135$, $\nu=0.287$, crack length is 50 percent of the circumference and crack depth$=0.55H$. (*a*) Reflection coefficient; (*b*) transmission coefficient.

In Figs. 8 and 9, we present similar results for the circumferential crack length $L=50$ percent. Again, the transmitted wave field has very similar characteristics as in the case $L=10$ percent. However, in the reflected field $|R_{02,01}|$ has the largest value, followed by $|R_{02,02}|$ and $|R_{02,11}|$. It is seen that the reflection and transmission coefficients have very weak dependence on frequency. This would be desirable for ultrasonic measurements over long pipes. For the incident mode $F(1,3)$, Fig. 9 shows that the reflected amplitude $|R_{13,11}|$ is the largest, followed by $|R_{13,13}|$ and $|R_{13,01}|$. Thus, the asymmetry of the crack causes more energy going into the bending modes, as expected.

Results of the reflection and transmission coefficients, $|R_{02,mn}|$, $|T_{02,mn}|$, and $|R_{13,mn}|$ and $|T_{13,mn}|$, as functions of the circumferential crack length at frequency $f=70$ kHz are shown in Figs. 10 and 11. The experimental results are also shown in Fig. 10. As noted by Alleyne et al. [1], it is interesting that the reflection coefficient, $|R_{kl,kl}|$, for $k=0$, $l=2$ is nearly a linear function of the circumferential crack length. We also find that the same holds true for $|R_{02,01}|$, $|R_{13,13}|$, and $|R_{13,11}|$. It is to be noted that $|R_{02,01}|$ is larger than $|R_{02,02}|$. For the transmission coefficients, the model results shown in Fig. 10 have the interesting feature that $|T_{02,02}|$ and $|T_{02,01}|$ are also nearly linear functions of L, the former decreasing with increasing L and the latter increasing with L.

Conclusions

Scattering of guided waves in a steel pipe by a planar circumferential crack of arbitrary circumferential length and radial depth was studied by a novel solution technique. In this technique, only the plane of the crack needs to be discretized into surface elements. This is much more computationally cost effective than a fully two or three-dimensional finite element analysis. It was found that the results agreed well with available experimental results. The effects of the crack on the incident wave modes, $L(0,2)$ and $F(1,3)$, are presented in this paper. It is found that the change in the reflection coefficients $|R_{kl,kl}|$, $k=0(1)$, and $l=2(3)$, with circumferential crack length L is linear in L. This was found to be the case by Alleyne et al. [1], who studied only the incident $L(0,2)$ mode. Also, as observed by these authors, the reflection coefficients are found to be nearly independent of frequency in the range of frequency considered. This study should aid in further investigations of scattering of guided waves by cracks in pipes. The method presented can be easily extended to layered or composite anisotropic cylinders.

In this paper, planar cracks in a cross section of a circular pipe has been considered. Other types of cracks that appear in pipelines are axial. The method presented here would have to be modified to analyze scattering by those cracks. This will be explored in the future.

Acknowledgments

The first author would like to acknowledge the financial support from the University of Manitoba through the graduate fellowship award. AHS and NP would like to acknowledge the financial support of the Natural Science of Engineering Research Council of

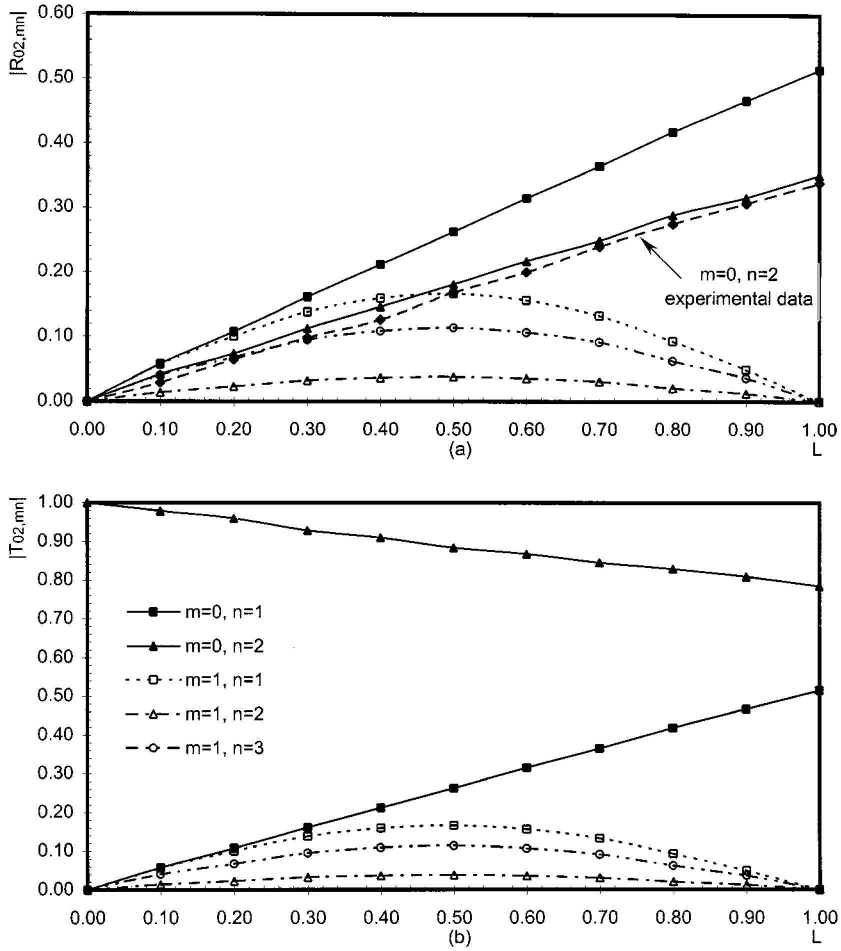

Fig. 10 Normalized reflection and transmission coefficients in a steel pipe as functions of the crack length at $f=70$ kHz. $H/R=0.135$, $\nu=0.287$, crack depth$=0.55H$. (*a*) Reflection coefficient; (*b*) transmission coefficient.

Canada. SKD would like to acknowledge the support provided by the Engineering Research Program, Office of Basic Energy Sciences, U.S. Department of Energy (DE-FG03-97ER14738) and by the University of Colorado in the form of a Faculty fellowship award.

Appendix A

The Specific Form of Matrices in Eq. (22).

$$F^R_{C,r,m}=\begin{bmatrix} f_{r1,m1} & f_{r1,m2} & \cdots & f_{r1,mN_m} \\ f_{r2,m1} & f_{r2,m2} & \cdots & f_{r2,mN_m} \\ \vdots & \vdots & \ddots & \vdots \\ f_{rP_C,m1} & f_{rP_C,m2} & \cdots & f_{rP_C,mN_m} \end{bmatrix} \in \mathbf{C}^{P_C\times N_m}, \tag{A1}$$

$$F^R_{C,\theta,m}=\begin{bmatrix} f_{\theta1,m1} & f_{\theta1,m2} & \cdots & f_{\theta1,mN_m} \\ f_{\theta2,m1} & f_{\theta2,m2} & \cdots & f_{\theta2,mN_m} \\ \vdots & \vdots & \ddots & \vdots \\ f_{\theta P_C,m1} & f_{\theta P_C,m2} & \cdots & f_{\theta P_C,mN_m} \end{bmatrix} \in \mathbf{C}^{P_C\times N_m}, \tag{A2}$$

$$F^R_{C,z,m}=\begin{bmatrix} f_{z1,m1} & f_{z1,m2} & \cdots & f_{z1,mN_m} \\ f_{z2,m1} & f_{z2,m2} & \cdots & f_{z2,mN_m} \\ \vdots & \vdots & \ddots & \vdots \\ f_{zP_C,m1} & f_{zP_C,m2} & \cdots & f_{zP_C,mN_m} \end{bmatrix} \in \mathbf{C}^{P_C\times N_m}, \tag{A3}$$

$$F^R_{N,r,m}=\begin{bmatrix} f_{rP_c+1,m1} & f_{rP_c+1,m2} & \cdots & f_{rP_c+1,mN_m} \\ f_{rP_c+2,m1} & f_{rP_c+2,m2} & \cdots & f_{rP_c+2,mN_m} \\ \vdots & \vdots & \ddots & \vdots \\ f_{rP_c+P_N,m1} & f_{rP_c+P_N,m2} & \cdots & f_{rP_c+P_N,mN_m} \end{bmatrix} \in \mathbf{C}^{P_N\times N_m}, \tag{A4}$$

$$F^R_{N,\theta,m}=\begin{bmatrix} f_{\theta P_c+1,m1} & f_{\theta P_c+1,m2} & \cdots & f_{\theta P_c+1,mN_m} \\ f_{\theta P_c+2,m1} & f_{\theta P_c+2,m2} & \cdots & f_{\theta P_c+2,mN_m} \\ \vdots & \vdots & \ddots & \vdots \\ f_{\theta P_c+P_N,m1} & f_{\theta P_c+P_N,m2} & \cdots & f_{\theta P_c+P_N,mN_m} \end{bmatrix} \in \mathbf{C}^{P_N\times N_m}, \tag{A5}$$

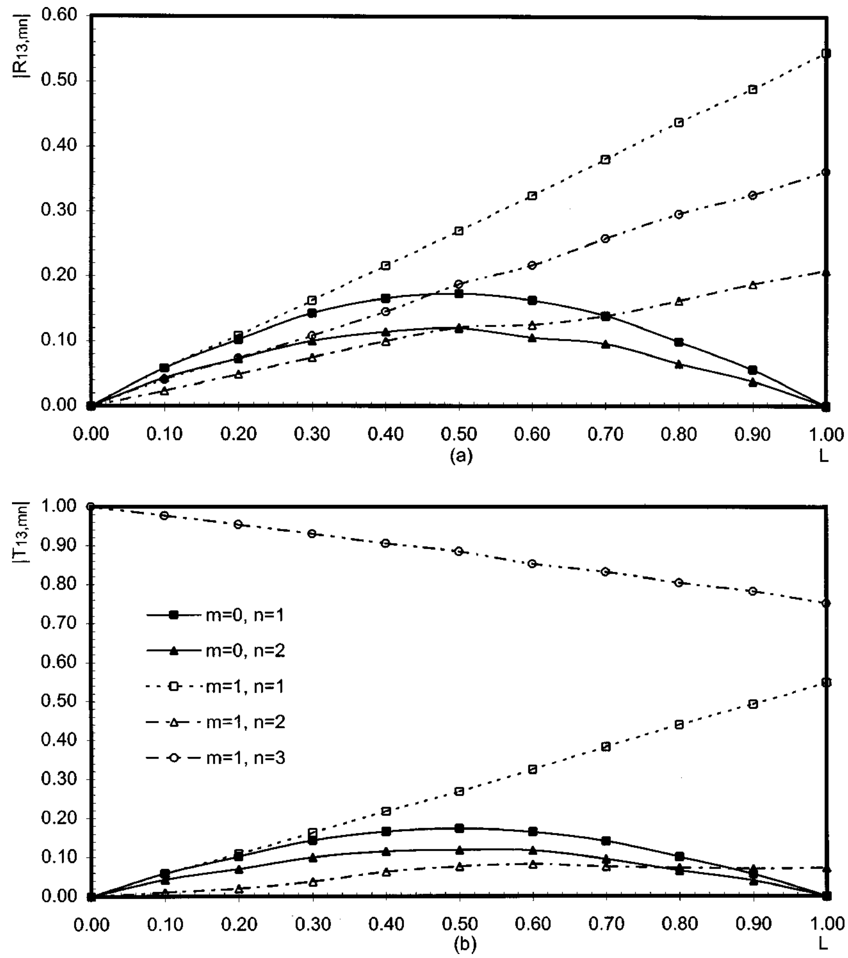

Fig. 11 Normalized reflection and transmission coefficients in a steel pipe as functions of the crack length at $f=70$ kHz. $H/R=0.135$, $\nu=0.287$, crack depth$=0.55H$. (*a*) Reflection coefficient; (*b*) transmission coefficient.

$$U^R_{N,z,m}=\begin{bmatrix} u_{zP_c+1,m1} & u_{zP_c+1,m2} & \cdots & u_{zP_c+1,mN_m} \\ u_{zP_c+2,m1} & u_{zP_c+2,m2} & \cdots & u_{zP_c+2,mN_m} \\ \vdots & \vdots & \ddots & \vdots \\ u_{zP_c+P_N,m1} & u_{zP_c+P_N,m2} & \cdots & u_{zP_c+P_N,mN_m} \end{bmatrix} \in \mathbf{C}^{P_N\times N_m}, \tag{A6}$$

Appendix B

The Specific Form of Matrices in Eq. (27).

$$U^R_{C,r,m}=\begin{bmatrix} u_{r1,m1} & u_{r1,m2} & \cdots & u_{r1,mN_m} \\ u_{r2,m1} & u_{r2,m2} & \cdots & u_{r2,mN_m} \\ \vdots & \vdots & \ddots & \vdots \\ u_{rP_C,m1} & u_{rP_C,m2} & \cdots & u_{rP_C,mN_m} \end{bmatrix} \in \mathbf{C}^{P_C\times N_m}, \tag{B1}$$

$$U^R_{C,\theta,m}=\begin{bmatrix} u_{\theta1,m1} & u_{\theta1,m2} & \cdots & u_{\theta1,mN_m} \\ u_{\theta2,m1} & u_{\theta2,m2} & \cdots & u_{\theta2,mN_m} \\ \vdots & \vdots & \ddots & \vdots \\ u_{\theta P_C,m1} & u_{\theta P_C,m2} & \cdots & u_{\theta P_C,mN_m} \end{bmatrix} \in \mathbf{C}^{P_C\times N_m}, \tag{B2}$$

$$U^R_{C,z,m}=\begin{bmatrix} u_{z1,m1} & u_{z1,m2} & \cdots & u_{z1,mN_m} \\ u_{z2,m1} & u_{z2,m2} & \cdots & u_{z2,mN_m} \\ \vdots & \vdots & \ddots & \vdots \\ u_{zP_C,m1} & u_{zP_C,m2} & \cdots & u_{zP_C,mN_m} \end{bmatrix} \in \mathbf{C}^{P_C\times N_m}, \tag{B3}$$

$$U^R_{N,r,m}=\begin{bmatrix} u_{rP_c+1,m1} & u_{rP_c+1,m2} & \cdots & u_{rP_c+1,mN_m} \\ u_{rP_c+2,m1} & u_{rP_c+2,m2} & \cdots & u_{rP_c+2,mN_m} \\ \vdots & \vdots & \ddots & \vdots \\ u_{rP_c+P_N,m1} & u_{rP_c+P_N,m2} & \cdots & u_{rP_c+P_N,mN_m} \end{bmatrix} \in \mathbf{C}^{P_N\times N_m}, \tag{B4}$$

$$U^R_{N,\theta,m}=\begin{bmatrix} u_{\theta P_c+1,m1} & u_{\theta P_c+1,m2} & \cdots & u_{\theta P_c+1,mN_m} \\ u_{\theta P_c+2,m1} & u_{\theta P_c+2,m2} & \cdots & u_{\theta P_c+2,mN_m} \\ \vdots & \vdots & \ddots & \vdots \\ u_{\theta P_c+P_N,m1} & u_{\theta P_c+P_N,m2} & \cdots & u_{\theta P_c+P_N,mN_m} \end{bmatrix} \in \mathbf{C}^{P_N\times N_m}, \tag{B5}$$

$$F^R_{N,z,m}=\begin{bmatrix} f_{zP_c+1,m1} & f_{zP_c+1,m2} & \cdots & f_{zP_c+1,mN_m} \\ f_{zP_c+2,m1} & f_{zP_c+2,m2} & \cdots & f_{zP_c+2,mN_m} \\ \vdots & \vdots & \ddots & \vdots \\ f_{zP_c+P_N,m1} & f_{zP_c+P_N,m2} & \cdots & f_{zP_c+P_N,mN_m} \end{bmatrix} \in \mathbf{C}^{P_N\times N_m}, \qquad (B6)$$

References

[1] Alleyne, D. N., Lowe, M. J. S., and Cawley, P., 1998, ''The Reflection of Guided Waves from Circumferential Notches in Pipes,'' ASME J. Appl. Mech., **65**, pp. 635–641.

[2] Lowe, M. J. S., Alleyne, D. N., and Cawley, P., 1998, ''The Mode Conversion of a Guided Wave by a Part-Circumferential Notch in a Pipe,'' ASME J. Appl. Mech., **65**, pp. 649–656.

[3] Pan, E., Rogers, J., Datta, S. K., and Shah, A. H., 1999, ''Mode Selection of Guided Waves for Ultrasonic Inspection of Gas Pipelines with Thick Coating,'' Mech. Mater., **31**, pp. 165–174.

[4] Soldatos, K. P., 1994, ''Review of Three-Dimensional Dynamic Analyses of Circular Cylinders and Cylindrical Shells,'' Appl. Mech. Rev., **47**, pp. 501–516.

[5] Datta, S. K., 2000, ''Wave Propagation in Composite Plates and Shells,'' Vol. 1, T.-W. Chou, ed., *Comprehensive Composite Materials*, Elsevier Science Publishers, Oxford, pp. 511–557.

[6] Kohl, T., Datta, S. K., and Shah, A. H., 1992, ''Axially Symmetric Pules Propagation in Semi-Infinite Hollow Cylinders,'' AIAA J., **30**, pp. 1617–1624.

[7] Rattanawangcharoen, N., 1993, ''Propagation and Scattering of Elastic Waves in Laminated Circular Cylinders,'' Ph. D. thesis, University of Manitoba, Winnipeg, MB.

[8] Rattanawangcharoen, N., Shah, A. H., and Datta, S. K., 1994, ''Reflection of Waves at the Free Edge of a Laminated Circular Cylinder,'' ASME J. Appl. Mech., **61**, pp. 323–329.

[9] Rattanawangcharoen, N., Zhuang, W., Shah, A. H., and Datta, S. K., 1997, ''Axisymmetric Guided Waves in Jointed Laminated Cylinders,'' ASME J. Eng. Mechn. **123**, pp. 1020–1026.

[10] Zhuang, W., Shah, A. H., and Datta, S. K., 1997, ''Axisymmetric Guided Wave Scattering by Cracks in Welded Steel Pipes,'' ASME J. Pressure Vessel Technol., **119**, pp. 401–406.

[11] Zhuang, W., Shah, A. H., and Dong, S. B., 1999, ''Elastodynamic Green's Function for Laminated Anisotropic Circular Cylinders,'' ASME J. Appl. Mech., **66**, pp. 665–674.

[12] Rattanawangcharoen, N., and Shah, A. H., 1992, ''Guided Waves in Laminated Isotropic Circular Cylinder,'' Computational Mechanics, **10**, pp. 97–105.

[13] Gazis, D. C., 1959, ''Three-Dimensional Investigation of the Propagation of Waves in Hollow Circular Cylinders. I. Analytical Foundation,'' J. Acoust. Soc. Am., **31**, pp. 568–578.

[14] Bathe, K. J., 1982, *Finite Element Procedures in Engineering Analysis*, Prentice-Hall, Englewood Cliffs, NJ.

A. R. de Faria
J. S. Hansen
Institute for Aerospace Studies,
UTIAS,
4925 Dufferin Street,
Toronto, Ontario M3H 5T6,
Canada

Buckling Optimization of Composite Axisymmetric Cylindrical Shells Under Uncertain Loading Combinations

Optimal elastic buckling loads of composite axisymmetric circular cylinders under uncertain loading conditions are investigated. The mechanical loads applied to the cylinder are a combination of axial compression, lateral pressure, and torsion. Additionally, these loads are allowed to vary within a certain class of admissible loads during the optimization search, as opposed to the restriction of fixed loads in the traditional optimization. The consideration of a degree of uncertainty in the mechanical loads leads to optimal designs which are inherently insensitive to perturbations and/or randomness in the applied loads.
[DOI: 10.1115/1.1311962]

1 Introduction

Composite materials have been gaining increasing importance over the years in the aerospace industry as an alternative to commonly used isotropic materials. The major advantages of composite materials are increased stiffness and strength to weight ratios and the possibility of tailoring composite structural components for very specific applications. For example, composite laminates can be optimized through a proper choice of fibre orientations in order to maximize structural characteristics such as stiffness, strength, natural frequencies, and buckling loads.

The basis for the numerical analysis of shells of revolution was established in the 1960s ([1,2]). The displacement solution for such shells is decomposed into a Fourier series in the circumferential direction and interpolated by polynomials in the meridional direction. Accounting for the uncoupling of the harmonics, the solution process is carried out for each harmonic individually.

In the 1970s analytical methods to study cylindrical shells in the buckling and post-buckling regimes were sharpened ([3–5]). These works are mainly based on the formulations derived from theoretical investigations of Koiter [6] and Budiansky and Hutchinson [7]. The remarkable effect of initial imperfections on the buckling behavior of anisotropic cylindrical shells was modeled and experimentally verified. Also, Thompson and Hunt [8] provided a thorough analysis methodology which may in some sense be understood as a discrete counterpart of Koiter's method.

Optimization of composite cylinders was not systematically addressed until the 1980s when innovative works set the guidelines on the subject ([9–12]). Later in the decade Sun and Hansen [13] presented results for optimized circular cylindrical shells under axial compression, lateral pressure, and torsion having the fiber angles as design variables and considering a general axisymmetric nonlinear prebuckling state.

All the previously mentioned works on buckling optimization share one characteristic in common; the loading configuration is fixed during the optimization procedure. As a result, the obtained optimal design is able to satisfactorily withstand only that particular loading configuration. That is, the load ratios relating axial compression, lateral pressure, and torque are maintained fixed and the buckling load magnitude is maximized for those values of load ratios. However, if the load ratios are changed the design will no longer be optimal and may be unstable to changes in the load ratios. This constitutes a potentially hazardous situation since structural systems are always subjected to loads which are unpredictable, random, or varying in time.

Cherkaev and Cherkaeva [14] were concerned with the sensitivity of optimal designs to perturbations of the applied loads about the design loads. Their proposal was a minimax formulation to minimize the design compliance under the most unfavorable loading situation of a defined set of applied loads. In some sense their formulation and this work may be considered as a battle between an attacker and a defender. The attacker represents that load combination from an admissible set which will cause the most damage; the defender is the optimal design of the structure which responds to the applied loads. Clearly the ''worst'' loads and the ''best'' designs are dependent on one another.

In this work, the composite cylinders to be optimized are subjected to mechanical loads which are assumed to have a degree of uncertainty; the uncertainty is associated with the idea that the applied load may be any member of a prescribed load set. A parameterization is then adopted to represent the loads and which incorporates their variable nature within the load set. Thus the optimization involves a minimax formulation where the objective is to maximize the buckling load with respect to fiber angles and minimize it with respect to load parameters. The developed formulation guarantees that the obtained optimal designs correspond to the most unfavorable loading configuration within the load set and in turn these designs are conservative for any other member of admissible load set. Furthermore, it is guaranteed that the optimal designs are insensitive to changes in load relative to the design load for all members of the set of admissible loads.

2 Formulation of the Problem

The objective function of the problem is the critical load of composite cylinders whose design variables are fiber angles and mechanical loads. The calculation of the objective function is carried out in two steps: the prebuckling problem and the buckling problem. Figure 1 presents the cylinder with applied loads and boundary conditions.

The elastic stability analysis approach as developed by Koiter [6] is used in the present work for the derivation of the equilibrium equations and the stability condition. As such, an equilibrium state $\mathbf{u}_0$ and a perturbed state $\mathbf{v}$ close to $\mathbf{u}_0$ are considered.

Contributed by the Applied Mechanics Division of THE AMERICAN SOCIETY OF MECHANICAL ENGINEERS for publication in the ASME JOURNAL OF APPLIED MECHANICS. Manuscript received by the ASME Applied Mechanics Division, Sept. 29, 1999; final revision, Feb. 7, 2000. Associate Editor: S. Kyriakides. Discussion on the paper should be addressed to the Editor, Professor Lewis T. Wheeler, Department of Mechanical Engineering, University of Houston, Houston, TX 77204-4792, and will be accepted until four months after final publication of the paper itself in the ASME JOURNAL OF APPLIED MECHANICS.

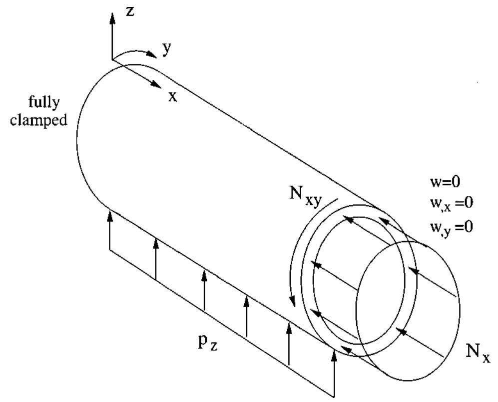

Fig. 1 Cylinder subjected to mechanical loads and boundary conditions

The perturbed state is written as $\mathbf{v}=\mathbf{u}_0+\mathbf{u}$ where $\mathbf{u}$ must be geometrically admissible but are otherwise completely arbitrary perturbations. Expansion of the total potential energy $P(\mathbf{v})$ in Taylor series about $\mathbf{u}_0$ yields the required equilibrium equation and stability condition. Details of the derivation may be found in Koiter [6] or in Sun and Hansen [13], for example.

The shell is modelled using classical thin-shell theory and von Kármán nonlinear strain-displacement relations. Accordingly, the in-plane displacements $\tilde{u}(x,y,z)$ and $\tilde{v}(x,y,z)$ are assumed to vary linearly through the thickness with respect to z and the transverse displacement $\tilde{w}(x,y,z)$ is assumed independent of z. Thus the displacements are taken in the form

$$\tilde{u}(x,y,z)=u(x,y)-zw_{,x}(x,y) \quad \tilde{v}(x,y,z)=v(x,y)-zw_{,y}(x,y)$$
$$\tilde{w}(x,y,z)=w(x,y) \tag{1}$$

where the field variables are u, v, w representing the midsurface displacements. Based on these expressions, the strain vectors are represented as

$$\{\epsilon^L(\mathbf{v})\}=\{\epsilon^0\}+z\{\kappa\}=\begin{Bmatrix} u_{,x} \\ v_{,y}+\dfrac{w}{R} \\ u_{,y}+v_{,x}\end{Bmatrix}+z\begin{Bmatrix} -w_{,xx} \\ -w_{,yy} \\ -2w_{,xy}\end{Bmatrix}$$
$$\{\epsilon^N(\mathbf{v})\}=\frac{1}{2}\begin{Bmatrix} w_{,x}^2 \\ w_{,y}^2 \\ 2w_{,x}w_{,y}\end{Bmatrix} \tag{2}$$

where R is the cylinder radius and $\mathbf{v}=(u,v,w)$. Using the above, the expression for the total potential energy can be written as

$$P(\mathbf{v})=\frac{1}{2}\int_\Omega \begin{Bmatrix}\epsilon^0+\epsilon^N \\ \kappa\end{Bmatrix}^T \begin{bmatrix}[A] & [B] \\ [B] & [D]\end{bmatrix}\begin{Bmatrix}\epsilon^0+\epsilon^N \\ \kappa\end{Bmatrix} d\Omega-\int_\Omega p_z w\, d\Omega$$
$$-\int_\Gamma N_x u\, d\Gamma-\int_\Gamma N_{xy} v\, d\Gamma \tag{3}$$

where Ω is the reference surface domain, Γ the domain where axial compression and torque are applied, and $[A]$, $[B]$, $[D]$ are the laminate stiffness matrices given by

$$([A],[B],[D])=\int_{-h/2}^{h/2}(1,z,z^2)[\overline{Q}]dz \tag{4}$$

where h is the shell total thickness and $[\overline{Q}]$ is the material stiffnesses in structural coordinates.

The mechanical loads applied to the structure are represented by a proportionality parameter λ and a reference state $\overline{\mathbf{f}}$ such that $\mathbf{f}=-\lambda\overline{\mathbf{f}}$. Considerable simplifications can be introduced if the axisymmetry of the prebuckling and initial imperfection displacements are observed because in this case derivatives with respect to the circumferential coordinate y are identically zero and the prebuckling displacements are functions of the axial coordinate x only. A finite element discretization is carried out only in the axial direction using a two-node element with linear interpolation functions for u and v, and cubic Hermite polynomials for w. Assuming a linear prebuckling state, assembly of the global matrices for the finite element method yields

$$\mathbf{K}\mathbf{q}_P=-\lambda\overline{\mathbf{f}} \tag{5}$$

where $\mathbf{K}$ is the stiffness matrix and $\mathbf{q}_P$ are the prebuckling displacements. Unfortunately the axisymmetric property used in the prebuckling problem is not valid for the buckling problem. Thus, for the solution of the buckling problem, the field variables are assumed in the form

$$a_n(x,y)=a_I(x)\cos\left(\frac{ny}{R}\right)+a_{II}(x)\sin\left(\frac{ny}{R}\right) \tag{6}$$

where n is the harmonic number and a stands for u, v, or w. In this manner, the buckling problem dependence on y can be analytically treated while the dependence on x is treated numerically via finite elements. Thus, discretization of a_I and a_{II} is carried out in the axial direction using the finite element technique.

Even assuming a linear prebuckling state, quadratic terms in λ would be present in the stability equation such that the critical load would result from the solution of a quadratic eigenproblem. However, omission of the higher order terms from prebuckling/buckling coupling has been evaluated and, for the problems considered here, the contribution to the optimal design and the bucking load is negligibly small. Therefore, for the sake of considerably speeding up the optimization procedure the coupling term has been neglected resulting in a classical linear eigenvalue problem. The linear eigenproblem assumes the form of Eq. (7)

$$(\mathbf{K}-\lambda\mathbf{K}_G)\mathbf{q}=\mathbf{0} \tag{7}$$

where $\mathbf{K}$ is the stiffness matrix, $\mathbf{K}_G$ the geometric stiffness matrix, and $\mathbf{q}$ an arbitrary geometrically admissible displacement vector. Notice that both $\mathbf{K}$ and $\mathbf{K}_G$ are functions of the harmonic number n; therefore, the eigenproblem must be solved for a number of harmonics from which the least eigenvalue is selected as the critical load.

3 Optimization Procedure

The present work addresses composite laminates and buckling load optimization when a structure is subjected to uncertain combined loads. Let $\mathbf{p}$ be the vector of fiber angle design variables and $\mathbf{r}$ the vector of uncertain design variables (the load ratios). The minimax problem is therefore expressed as

$$\max_{\mathbf{p}}\min_{\mathbf{r}}\lambda(\mathbf{p},\mathbf{r})=\max_{\mathbf{p}}\phi(\mathbf{p}) \quad , \quad \phi(\mathbf{p})=\min_{\mathbf{r}}\lambda(\mathbf{p},\mathbf{r}). \tag{8}$$

The solution of this problem yields the result that the buckling load obtained will be the maximum buckling load for the worst combination of uncertain variables $\mathbf{r}$. Furthermore, Eq. (8) guarantees that if the vector $\mathbf{r}$ differs from that of the optimal design, then the buckling load is always greater than the optimal buckling load in the sense that $\lambda>\lambda_{\mathrm{opt}}$. Therefore, the optimal design is insensitive and stable with respect to variations in load ratios. Thus, the present approach has a major advantage of being capable of treating uncertainties in the loads using a deterministic method which eliminates the necessity of a probabilistic formulation.

The significance of vector $\mathbf{p}$ is relatively well known from the literature. However, $\mathbf{r}$ requires clarification. Consider a composite shell loaded as in Fig. 1. The uniformly distributed applied loads N_x, N_{xy} and lateral pressure p_z are represented in the form

$$N_x=\lambda f_x R_x=\lambda f_x(R_{x0}+\Delta R_x)$$
$$p_z=\lambda f_z R_z=\lambda f_z(R_{z0}+\Delta R_z) \tag{9}$$
$$N_{xy}=\lambda f_{xy} R_{xy}=\lambda f_{xy}(R_{xy0}+\Delta R_{xy})$$

where λ is a nondimensional load parameter and R_x, R_z, R_{xy} are load ratios composed of fixed (specified) components R_{x0}, R_{z0}, R_{xy0} and variable (unspecified) components ΔR_x, ΔR_z, ΔR_{xy}. The fixed components R_{x0}, R_{z0}, R_{xy0} are assigned by the designer and reflect knowledge of the loading state. Also, f_x, f_z, f_{xy} are constant dimensional scaling factors which must be specified; these will be discussed in the following. The vector of uncertain design variables is therefore given by $\mathbf{r}=\{R_x R_z R_{xy}\}$. The load ratios R_x, R_z, R_{xy} are assumed to form a convex set defined by the relationship

$$R_x+R_z+R_{xy}=1 \tag{10}$$

subject to the condition $0\leqslant R_x,\ R_z,\ R_{xy}\leqslant 1$. Furthermore, the fixed and variable load ratios are required to satisfy $0\leqslant R_{x0},\ R_{z0},\ R_{xy0}\leqslant 1$ and $0\leqslant \Delta R_x,\ \Delta R_z,\ \Delta R_{xy}\leqslant 1$. R_{x0}, R_{z0}, R_{xy0} are included to account for specified (deterministic) information available prior to the optimization procedure; they are related to certainty of the applied loads. If $R_{x0}+R_{z0}+R_{xy0}=1$ the loads are specified precisely. If, however, the loads are not know precisely but there is some degree of confidence in their specification, this fact is again reflected in the choice of R_{x0}, R_{z0}, R_{xy0}. For example, if it is known that the load sets are such that 70 percent of the applied load is always axial compression, then $R_{x0}=0.7$, $R_{z0}=R_{xy0}=0$. In such a case ΔR_x, ΔR_z, ΔR_{xy} account for only 30 percent of the applied load. Finally, if no information concerning the load sets is available then $R_{x0}=R_{z0}=R_{xy0}=0$.

The scaling factors, f_x, f_z, f_{xy}, may be chosen arbitrarily but should be chosen to provide a rational reference surface for the optimization process; this will become clear in the following. In the present work f_x, f_z, f_{xy} are equated to the optimal buckling loads obtained by assuming that completely specified unidirectional loads are applied to the structure. Thus, f_x is the maximum buckling load that the structure can sustain under the loading conditions $N_x=P_x$, $p_z=0$, $N_{xy}=0$. Similarly, f_z results from the optimization problem $N_x=0$, $p_z=P_z$, $N_{xy}=0$ and f_{xy} from $N_x=0$, $p_z=0$, $N_{xy}=P_{xy}$.

It is to be noted that the optimal designs corresponding to f_x, f_z, f_{xy} are different; thus, these factors provide a normalization of the final results that relates to the maximum capability of the structure when subjected to independent loads. Therefore, the scaling factors f_x, f_z, f_{xy} provide the capability of accounting for factors such as structural geometry, boundary conditions, and material anisotropy which may result in significant disparities in the relative buckling load magnitudes of the individual load components.

4 Geometric Interpretation

Equation (10) describes a plane in load space (the reference plane). Any load in the space is represented by a point on the reference plane multiplied by the load parameter λ and the constant load factors; these factors are illustrated in Fig. 2 where the loads have been nondimensionalized according to the scaling factors: $n_x=N_x/f_x$, $n_z=p_z/f_z$, $n_{xy}=N_{xy}/f_{xy}$. As λ varies a family of planes parallel to the reference plane is generated. Notice that relation (10) and the assumption $0\leqslant R_x,\ R_z,\ R_{xy}\leqslant 1$ define a tetrahedron in the load space which is a convex set. Thus, properties of convex modelling associated with mechanics of uncertainties are applicable to the present study ([15]).

At this stage a geometric interpretation of the minimax formulation can be given. Consider Fig. 2 which shows a sketch of a representative concave stability boundary. The shape of the stability boundary depends on the design variables $\mathbf{p}$ which are the composite lamina ply angles. The following interpretation can be given: *the minimax optimization procedure selects a design with the stability boundary such that planes parallel to the reference plane can be extended as far as possible from the origin without crossing the stability boundary*. The first point of intersection of the stability boundary and a member of the family of planes as λ increases from zero defines the optimal design and provides the optimal value of λ.

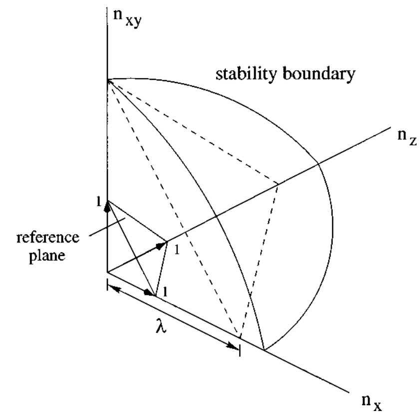

Fig. 2 Geometric interpretation

The stability boundary defined in load space can be quite complex in shape, but for special cases of either convex or concave surfaces (with respect to the origin) relatively simple conclusions can be drawn. For the case when the critical loads are obtained as the solution of a linear eigenvalue problem a tremendous simplification occurs since it can be shown that the stability boundary is concave ([16]). In this case, under ideal conditions with sufficient design flexibility, the optimal design is obtained when the three vertices of the load plane intersect the stability boundary.

It is to be noted that the shape of the stability boundary is controlled by the composite lamina fiber angles; therefore the degree of design flexibility or the ability to control the stability surface may be limited. This means that the optimal design may correspond to the intersection of three, two or one of the vertices of the projection of reference plane with the stability boundary; one of these possibilities will always yield the solution.

If the stability surface is convex the situation is much more straightforward. The optimal design will be found at a single point which has the characteristics of a global minimum. This minimum must be interpreted in the sense that it is the point on the stability surface that yields a minimum distance from the surface to the reference plane. The optimal value of λ corresponds therefore to the plane parallel to the reference plane which passes through this ''minimum.''

From the discussion concerning the concavity of the stability boundary practical conclusions can be drawn regarding the strategy to minimize λ with respect to the load ratios. In the case of linear eigenproblems it was shown that the optimal design geometrically corresponds to a situation where one or more vertices of the reference load plane triangle are on the stability boundary. It can be then concluded that the minimum load ratios are necessarily associated with one of the vertices. Therefore, the minimization of λ with respect to $\mathbf{r}$ is easily performed since it is sufficient to check which of the three vertices yields the least λ. The maximization of function ϕ in Eq. (8) is achieved in a two-step process. First a genetic algorithm (GA) is used to obtain an optimal design in the neighborhood of the global optimum; secondly, Powell's method is used to refine the solution obtained bringing it to the actual optimum. The stopping criterion adopted for Powell's method is based on changes of the new objective function ϕ, which is the minimum critical load among the three vertices. The optimization search stops when the relative difference between the previous and the present values of ϕ does not exceed 0.001.

The incorporation of the constant load ratios R_{x0}, R_{z0}, R_{xy0}

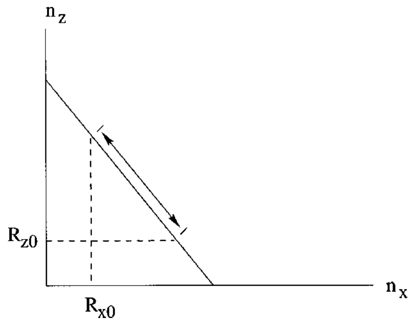

Fig. 3 Constant load ratios

means that the reference plane is bounded; that is, the values of R_x, R_z, R_{xy} are constrained to lie in a smaller triangular subdomain of the reference plane. This subdomain is defined by the constant load ratios via the inequalities

$$R_x \geqslant R_{x0}; \quad R_z \geqslant R_{z0}; \quad R_{xy} \geqslant R_{xy0}. \tag{11}$$

Based on Eq. (11) these inequalities yield the admissible set for ΔR_x, ΔR_z, ΔR_{xy} as

$$\begin{gathered} \Delta R_x + \Delta R_z + \Delta R_{xy} = 1 - R_{x0} - R_{z0} - R_{xy0} \\ \Delta R_x \geqslant 0; \quad \Delta R_z \geqslant 0; \quad \Delta R_{xy} \geqslant 0 \end{gathered} \tag{12}$$

The minimax criterion still applies but now over the appropriate subdomain; the optimal stability boundary ideally contains the three vertices of the load plane subtriangle. As an illustrative example, a two-dimensional situation is shown in Fig. 3 where the torsion load is taken to be zero ($R_{xy}=0$) and positive constant load ratios exist for the axial and pressure loads ($R_{x0}, R_{z0} > 0$).

5 Numerical Simulations and Discussion

The cylindrical shells considered have radius $R = 83.3$ mm and length $L = 152.4$ mm with four composite plies 0.123-mm thick each. The material chosen for simulation is Hercules AS4/3501-6 graphite/epoxy; its properties are given in Table 1.

In the optimal design process, it is assumed the cylinder is initially free of geometric imperfections. This may sound overly simplistic; however, it is based on the assumption that there are no statistical data available for the imperfection pattern resulting from the manufacture process. In this situation, once the specimen is manufactured, the imperfection shape can be measured but then it is too late to perform the optimization. Thus, the point of view has been adopted, that if no data on the imperfections is available during the design process, the best procedure is to consider a perfect structure for the optimization. On the other hand, if such information is available it can easily be incorporated into what follows.

As noted earlier, the optimization involves a two step process combining a genetic algorithm and Powell's method. The parameters associated with the GA are: population size of 200 individuals, probability of crossover of 97 percent and probability of mutation of 50 percent. Each design is encoded as a string (chromosome) of genes, each of them representing the fiber orientations and whose alleles range from -90 deg to $+90$ deg. The crossover process is implemented by randomly selecting a break point in two parents' chromosomes and exchanging substrings in order to generate the offspring. Then, mutation may occur with a probability of 50 percent per chromosome. One gene is randomly chosen in the child's chromosome and it is assigned an angle within the range of alleles. An elitist strategy is adopted such that the best fitted individual of a generation is cloned to the next generation. This strategy provides a useful stopping criterion: The search is assumed to have converged if the best design remains unchanged for three generations. In this work, harmonic numbers from 1 to 20 are evaluated; advantage is taken of the symmetry/antisymmetry about the cylinder mid length in order to model only a half cylinder with 20 elements ([5,13]). The result of the converged GA is then used as a starting point for Powell's method.

Table 1 Material properties of Hercules AS4/3501-6 graphite/epoxy

property	value
Principal modulus of elasticity, E_{11}	146.0 GPa
Principal modulus of elasticity, E_{22}	10.8 GPa
In-plane Poisson's ratio, ν_{12}	0.290
In-plane shear modulus, G_{12}	5.8 GPa
Transverse shear modulus, G_{13}	5.8 GPa
Transverse shear modulus, G_{23}	3.4 GPa

Table 2 Load cases

load	constant load ratios		
case	R_{x0}	R_{z0}	R_{xy0}
1a	1.00	0.00	0.00
1b	0.75	0.00	0.00
1c	0.50	0.00	0.00
1d	0.25	0.00	0.00
2a	0.00	1.00	0.00
2b	0.00	0.75	0.00
2c	0.00	0.50	0.00
2d	0.00	0.25	0.00
3a	0.00	0.00	1.00
3b	0.00	0.00	0.75
3c	0.00	0.00	0.50
3d	0.00	0.00	0.25
4	0.00	0.00	0.00

A four-ply laminate $[\theta_1/\theta_2/\theta_3/\theta_4]$ is considered where θ_1 corresponds to the innermost ply. Thirteen load cases are considered which involve completely specified loads, partially specified loads and completely unspecified loads as described in Table 2. Cases 1a, 2a, and 3a refer to the traditional optimization under prescribed loads. Cases 1b, 1c, 1d correspond to axial compression load cases of increasing degree of uncertainty. Similarly, cases 2b, 2c, 2d, and 3b, 3c, 3d correspond, respectively, to an increasing degree of uncertainty in lateral pressure and torsion. Finally, case 4 represents the situation of completely uncertain loads.

Tables 3(*a–c*) and 4 present the results obtained by the optimization procedures. Columns four, five, and six correspond, in each case, to the vertices of the subtriangle defined by the constant load ratios R_{x0}, R_{z0}, and R_{xy0}. Since cases 1a, 2a, and 3a possess $R_{x0}+R_{z0}+R_{xy0}=1$, the three vertices coalesce to a single point and, therefore, only one column is needed. The critical loads obtained in the final stage by Powell's method are accompanied by superscripts ''a'' or ''n'' meaning, respectively, active or nonactive vertices, and the wave number in parenthesis. An active vertex strikes the stability boundary of the optimal design while a nonactive one lies below the stability boundary.

The buckling load magnitudes achieved when the shell is subjected to certain uniaxial loads are given by $N_x = 8.7770\,10^4$ N/m (case 1a), $p_z = 1.7402\,10^5$ Pa (case 2a), $N_{xy} = 4.6088\,10^4$ N/m (case 3a); these values are used to define the scaling factors f_x, f_z, f_{xy}, respectively, for the optimization with uncertain loads. This means that, in terms of the nondimensional load parameter λ, these values of critical loads correspond to 1.0.

Table 3 (*a*) Optimization under uncertain load ratios—axial compression; (*b*) optimization under uncertain load ratios—lateral pressure; (*c*) optimization under uncertain load ratios—torsion

load case	method	θ_1	θ_2	R_x	R_z	R_{xy}	R_x	R_z	R_{xy}	R_x	R_z	R_{xy}
		θ_3	θ_4	λ (n)			λ (n)			λ (n)		
1a	GA	26.7	-36.8	1.00	0.00	0.00	-			-		
		69.1	-10.6	0.99708 (11)								
	Powell	27.6	-36.9	1.00	0.00	0.00	-			-		
		70.2	-11.8	1.00000 (11)								
	Sun*	26	-42	1.00	0.00	0.00	-			-		
		76	-3	0.97033 (n/a)								
1b	GA	34.5	-33.8	0.75	0.25	0.00	1.00	0.00	0.00	0.75	0.00	0.25
		73.3	-1.2	0.79510 (10)			0.89998 (13)			0.90410 (11)		
	Powell	42.8	-34.8	1.00	0.00	0.00	0.75	0.25	0.00	0.75	0.00	0.25
		73.4	-9.2	0.84413^{a} (1)			0.84422^{a} (9)			0.99221^{n} (11)		
1c	GA	73.5	-74.5	1.00	0.00	0.00	0.50	0.50	0.00	0.50	0.00	0.50
		66.0	-18.1	0.74377 (7)			0.86103 (8)			0.79710 (10)		
	Powell	67.0	-80.1	1.00	0.00	0.00	0.50	0.50	0.00	0.50	0.00	0.50
		66.0	-33.3	0.79887^{a} (4)			0.81853^{n} (8)			0.80426^{a} (9)		
1d	GA	-89.8	-37.7	1.00	0.00	0.00	0.25	0.75	0.00	0.25	0.00	0.75
		-57.1	35.8	0.72863 (11)			0.80557 (8)			0.81769 (10)		
	Powell	-85.2	-34.6	1.00	0.00	0.00	0.25	0.75	0.00	0.25	0.00	0.75
		-59.3	38.4	0.75269^{a} (13)			0.82764^{n} (8)			0.75289^{a} (10)		

* Sun and Hansen (1988)

load case	method	θ_1	θ_2	R_x	R_z	R_{xy}	R_x	R_z	R_{xy}	R_x	R_z	R_{xy}
		θ_3	θ_4	λ (n)			λ (n)			λ (n)		
2a	GA	-87.1	36.9	0.00	1.00	0.00	-			-		
		-18.4	88.2	0.99934 (7)								
	Powell	-86.7	35.4	0.00	1.00	0.00	-			-		
		-20.4	88.8	1.00000 (7)								
	Sun*	-84	40	0.00	1.00	0.00	-			-		
		-17	90	0.99780 (n/a)								
2b	GA	-86.9	41.5	0.00	1.00	0.00	0.25	0.75	0.00	0.00	0.75	0.25
		-24.4	81.7	0.98234 (7)			1.1560 (7)			1.1035 (8)		
	Powell	-86.9	34.2	0.00	1.00	0.00	0.25	0.75	0.00	0.00	0.75	0.25
		-22.0	88.4	0.99991^{a} (7)			1.1769^{n} (7)			1.0127^{a} (8)		
2c	GA	83.1	-40.0	0.00	1.00	0.00	0.50	0.50	0.00	0.00	0.50	0.50
		2.4	-85.1	0.95447 (7)			1.1014 (9)			1.1457 (9)		
	Powell	-89.8	-34.6	0.00	1.00	0.00	0.50	0.50	0.00	0.00	0.50	0.50
		22.9	-88.0	0.99670^{a} (7)			1.0995^{n} (11)			1.0054^{a} (8)		
2d	GA	74.6	-61.6	0.75	0.25	0.00	0.00	1.00	0.00	0.00	0.25	0.75
		5.2	73.6	0.83446 (1)			0.91634 (8)			0.88739 (8)		
	Powell	77.3	-61.8	0.00	0.25	0.75	0.75	0.25	0.00	0.00	1.00	0.00
		-1.2	68.0	0.86577^{a} (8)			0.86587^{a} (1)			0.86596^{a} (8)		

* Sun and Hansen (1988)

Table 3 (Continued).

load case	method	θ_1	θ_2	R_x	R_z	R_{xy}	R_x	R_z	R_{xy}	R_x	R_z	R_{xy}
		θ_3	θ_4	λ (n)			λ (n)			λ (n)		
3a	GA	74.6	-23.5	0.00	0.00	1.00	-			-		
		-25.8	66.8	0.89867 (9)								
	Powell	67.9	-30.0	0.00	0.00	1.00	-			-		
		-26.7	69.8	1.00000 (9)								
	Sun*	67	-30	0.00	0.00	1.00	-			-		
		-26	70	0.99899 (n/a)								
3b	GA	64.7	-31.0	0.00	0.00	1.00	0.25	0.00	0.75	0.00	0.25	0.75
		-36.5	61.9	0.97759 (9)			1.1453 (9)			1.1029 (9)		
	Powell	70.3	-28.1	0.00	0.00	1.00	0.25	0.00	0.75	0.00	0.25	0.75
		-30.5	71.8	0.99901^{a} (9)			1.1266^{n} (9)			1.1443^{n} (9)		
3c	GA	67.5	-10.5	0.00	0.00	1.00	0.50	0.00	0.50	0.00	0.50	0.50
		-27.6	74.4	0.93765 (9)			1.0449 (8)			1.2238 (8)		
	Powell	64.3	-23.3	0.00	0.00	1.00	0.50	0.00	0.50	0.00	0.50	0.50
		-30.2	68.5	0.98972^{a} (9)			0.99600^{a} (6)			1.2356^{n} (8)		
3c	GA	66.0	-31.7	0.75	0.00	0.25	0.00	0.75	0.25	0.00	0.00	1.00
		-54.2	59.7	0.89349 (4)			1.0127 (8)			0.92374 (9)		
	Powell	65.3	-20.1	0.75	0.00	0.25	0.00	0.75	0.25	0.00	0.00	1.00
		-49.3	62.5	0.95393^{a} (5)			1.0472^{n} (8)			0.95375^{a} (9)		

* Sun and Hansen (1988)

Small discrepancies occur between the present results and those due to Sun and Hansen [13]; this results because Sun and Hansen considered a nonlinear prebuckling state.

For brevity, introduce the notation λ_i for the optimal critical load obtained for load case *i*. Notice that for all the cases presented in Tables 3(*a–c*) and 4 the load parameter is always less than 1.0. Furthermore, $\lambda_4<\lambda_{1d}<\lambda_{1c}<\lambda_{1b}<\lambda_{1a}=1.0$, $\lambda_4<\lambda_{2d}<\lambda_{2c}<\lambda_{2b}<\lambda_{2a}=1.0$, and $\lambda_4<\lambda_{3d}<\lambda_{3c}<\lambda_{3b}<\lambda_{3a}=1.0$. An expected result is observed: the more information available regarding the load ratios or stated otherwise, the greater the certainty associated with the applied load the greater the optimal load will be. This is related to the ability of the optimal designs to sustain different loading combinations. The more weapons the ''destructor'' (the loads) has at its disposal (the larger the set of possible loading combinations), the harder it is for the defender (the fibre angles) to do a good job in terms of increasing the critical load.

Investigation of Tables 3(*a–c*) and 4 shows that the majority of optimal designs possess two active vertices. This is true except for cases 2d and 3b. In the former three vertices are active while in the later only one vertex is active. Ideally, the three vertices of the subtriangle should be active in the optimal design but, because of the relatively small number of design variables (composite lamina ply angles), the degree of flexibility of the stability boundary is restrained. Moreover, although one can never be completely sure that the search has not converged to a local optimum, in the present study a sufficient number of GA runs was done in order to provide confidence that the global optimum was reached.

An interesting characteristic of the optimal design obtained in case 4 is worth discussing. If the optimal designs 1a, 2a, 3a obtained under completely specified load ratios are considered, it is found that there is a substantial variation between the critical buckling load and the higher buckling loads associated with other wave numbers. Thus the critical load is a single, well-separated eigenvalue associated with a single wave number. On the other hand, if the optimal design of case 4 is considered, a very small variation is found in terms of buckling loads related to different wave numbers. It is observed that, for the optimal design of case 4, $R_x=1$, all wave numbers between 9 and 14 produce similar buckling loads within the interval $0.7278\leqslant\lambda\leqslant0.7399$. This type of coalescence of eigenvalues is not unexpected since the design process has the tendency of flattening the optimal critical surface

Table 4 Optimization under completely uncertain load ratios

load case	method	θ_1	θ_2	R_x	R_z	R_{xy}	R_x	R_z	R_{xy}	R_x	R_z	R_{xy}
		θ_3	θ_4	λ (n)			λ (n)			λ (n)		
4	GA	90.0	-28.8	1.00	0.00	0.00	0.00	1.00	0.00	0.00	0.00	1.00
		-52.6	46.9	0.70189 (11)			0.73593 (8)			0.74019 (10)		
	Powell	-87.4	-36.2	1.00	0.00	0.00	0.00	1.00	0.00	0.00	0.00	1.00
		-52.6	49.9	0.72787^{a} (13)			0.75056^{n} (8)			0.72790^{a} (10)		

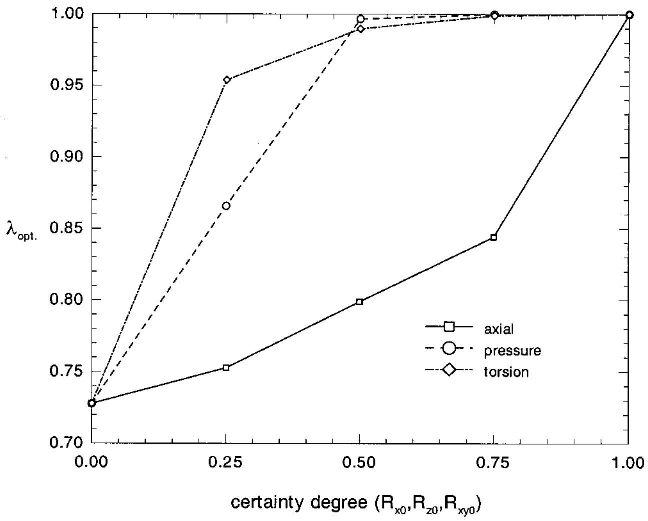

Fig. 4 Effect of uncertainty degree on the optimal critical load

and that different buckling loads and modes (eigenvalues and eigenvectors) are associated with the various locations on the critical load surface.

The effect of the uncertainty degree on the optimal critical loads can be visualized in Fig. 4 where the results obtained in Tables 3(a–c) and 4 are grouped in a single plot. Noticeable is the fact that the axial compression loading case is the most affected by the uncertainties in the load ratios while the optimal λ for lateral pressure and torsion are relatively insensitive for degrees of certainty higher than 50 percent.

Figure 4 gives a good insight into how the degree of uncertainty affects the optimal buckling loads. However, this figure provides neither an insight into design performance over a range of loading combinations nor a comparison between optimal designs. In order to do so, it is helpful to define a parameterization of the load ratios in the form

$$R_x=\alpha \quad R_z=\beta \quad R_{xy}=1-\alpha-\beta \tag{13}$$

where α, β are parameters such that $0\leqslant\alpha\leqslant1$, $0\leqslant\alpha+\beta\leqslant1$. Notice that Eq. (13) identically satisfies the constraint imposed by Eq. (10) and that the vertices of the triangle in (α, β) space correspond to the uniaxial load ratio cases. Based on Eq. (13), Figs. 5(a), 5(b), 5(c), and 5(d) are drawn which show values of λ for all admissible loading combinations for the optimal designs 1a, 2b, 3c, and 4, respectively.

The conclusion readily drawn from Figs. 5(a–b) is that the optimal design for case 4 (Fig. 5(d)) presents a better overall performance; it possesses $\lambda>1$ for more loading combinations than the other three cases (broader lighter region). The enhancement of the buckling loads with respect to a specified set of loads is of course not without penalty and the penalty is paid by the load sets not in the admissible set; this is in fact the reason for adopting

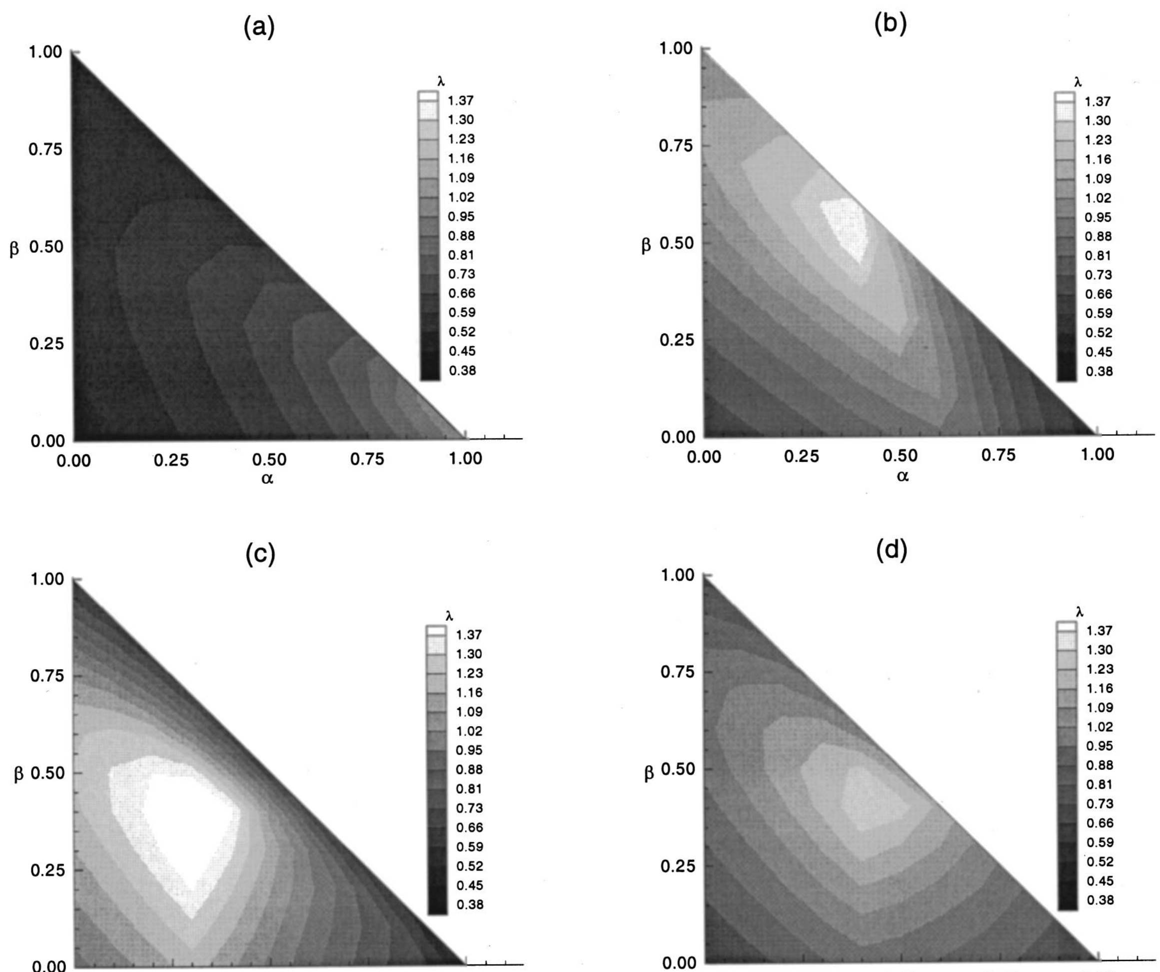

Fig. 5 (*a*) Load space—case 1a; (*b*) load space—case 2b; (*c*) load space—case 3c (*d*) load space—case 4

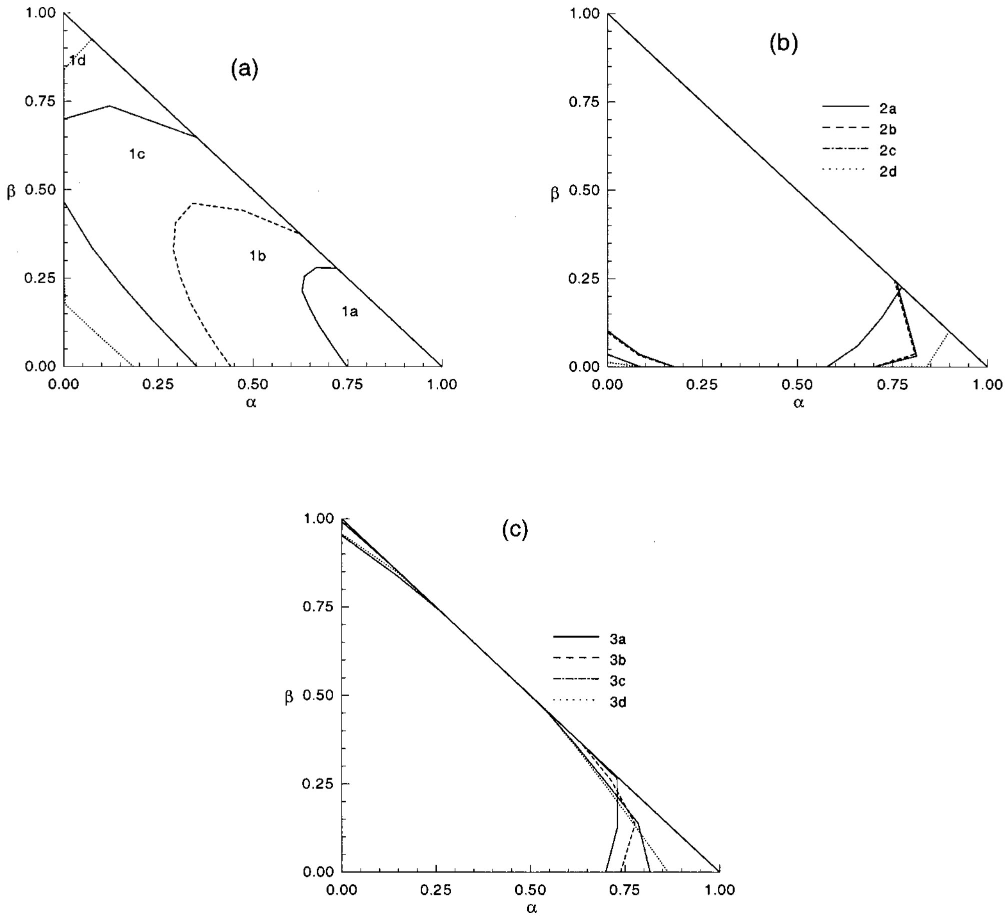

Fig. 6 (*a*) Comparative performance—axial compression; (*b*) comparative performance—lateral pressure; (*c*) comparative performance—torsion

the present approach. This result is clearly illustrated in Fig. 5(*a*) where the region about $\alpha=1$ ($R_x=1$) yields the largest buckling loads. However, the buckling loads decrease quickly as this region of influence is abandoned. The same behavior may be seen in Fig. 5(*b*) about $R_z=1$ ($\beta=1$) and, less pronouncedly, in Fig. 5(*c*) about $R_{xy}=1$ ($\alpha=\beta=0$).

A comparative performance with respect to the optimal buckling load obtained for case 4 ($\lambda=0.72787$) can also be carried out with the aid of Eq. (13). Take, for example, the axial compression case 1a and define, for its optimal design, the set of pairs (α,β) which yield $\lambda=0.72787$. This set corresponds to a line in the $\alpha\beta$-plane that separates the region where $\lambda>0.72787$ from that where $\lambda<0.72787$. Clearly, such a line cannot be drawn for case 4 since $\lambda\geqslant 0.72787$ over the domain of the entire triangle $0\leqslant\alpha\leqslant 1$, $0\leqslant\beta$, $0\leqslant\alpha+\beta\leqslant 1$.

Figure 6(*a*) illustrates the separation lines associated with the axial compression cases 1a, 1b, 1c, 1d. The regions defined by lines 1a, 1b, 1c, 1d that contain the point $\alpha=1$, $\beta=0$ ($R_x=1$) correspond to $\lambda>0.72787$. It can be observed that the region where $\alpha\geqslant 0.75$ is within region 1b, region $\alpha\geqslant 0.50$ is within region 1c and region $\alpha\geqslant 0.25$ is within region 1d. Noticeable is the fact that region 1d contains approximately the entire load space triangle. This can be explained if the results of Table 3(*a*) are compared to those of Table 4 and it is noted that the optimal designs for cases 1d and 4 have fiber orientations close to each other.

The behavior observed in Fig. 6(*b*) is somewhat different than that in Fig. 6(*a*); the separation lines are much closer. This can be rationalized if Fig. 4 is observed because it then becomes clear that the effects of uncertainty degree in lateral pressure are not as pronounced as those for the axial compression case. Notice again that, similarly to line 1d, the region defined by line 2d contains approximately all the load space triangle.

As expected from Fig. 4, Fig. 6(*c*) exhibits a behavior similar to Fig. 6(*b*). The remarkable fact here is that lines 3a, 3b, 3c, 3d intercept each other at various points. In geometric terms (Fig. 2), this means that the stability boundaries of the optimal designs obtained under uncertain torsion load ratios intersect in the load space. This is a perfectly reasonable result in the region outside the admissible set of load ratios since the stability boundaries are always concave but they may possess a curvature distribution which leads to the behavior presented in Fig. 6(*c*).

The results obtained confirm that a degree of uncertainty in the load ratios does have a significant effect on the optimal designs and critical loads of composite cylindrical shells. The sensitivity to applied loads of traditionally optimized cylinders can be compensated for by the use of a minimax formulation which takes into account the variable nature of the loads. It is concluded that an increase in the degree of certainty regarding the applied loads leads to higher optimal critical loads. On the other hand, optimal designs able to withstand a broad range of loading sets yield lower buckling loads. This reduction in the optimal buckling load has, however, a much lower sensitivity to variability of the applied loads and that is the advantage to the present approach. It should also be noted that the sensitivity of the optimal loads to changes in load ratio is most pronounced for the case of axial compression. A relative insensitivity to the load ratio change is found for the lateral pressure and the torsional load situations.

Acknowledgments

This work was supported by the Brazilian agency CAPES, a University of Toronto fellowship and funding from NSERC operating grant No. 3663.

References

[1] Sobel, L. H., 1964, ''Effects of Boundary Conditions on the Stability of Cylinders Subjected to Lateral and Axial Pressures,'' AIAA J., **2**, No. 8, pp. 1437–1440.

[2] Stricklin, J. A., and Haisler, W. E., 1968, ''Nonlinear Analysis of Shells of Revolution by the Matrix Decomposition Method,'' AIAA J., **6**, No. 12, pp. 2306–2311.

[3] Tennyson, R. C., Chan, K. H., and Muggeridge, D. B., 1971, ''The Effect of Axisymmetric Shape Imperfections on the Buckling of Laminated Anisotropic Circular Cylinders,'' CASI Trans., **4**, No. 2, pp. 131–139.

[4] Hansen, J. S., and Roorda, J., 1974, ''On a Probabilistic Stability Theory for Imperfection Sensitive Structures,'' Int. J. Solids Struct., **10**, pp. 341–359.

[5] Booton, M., 1976, ''Buckling of Imperfect Anisotropic Cylinders under Combined Loadings'', UTIAS Report No. 203, University of Toronto, Institute for Aerospace Studies, Downsview, Ontario, Canada.

[6] Koiter, W. T., 1945, ''On the Stability of Elastic Equilibrium (in Dutch with English summary),'' thesis, Delft, H. J. Paris, Amsterdam (English translation, *Air Force Flight Dyn. Lab. Tech.*, report AFFDL-TR-70-25, Feb. 1970).

[7] Budiansky, B., and Hutchinson, J. W., 1966, ''A Survey of Some Buckling Problems,'' AIAA J., **4**, No. 9, pp. 1505–1510.

[8] Thompson, J. M. T., and Hunt, G. W., 1973, *A General Theory of Elastic Stability*, John Wiley and Sons, London.

[9] Nshanian, Y. S., and Papas, M., 1983, ''Optimal Laminated Composite Shells for Buckling and Vibration,'' AIAA J., **21**, No. 3, pp. 430–437.

[10] Tennyson, R. C. and Hansen, J. S., 1983, ''Optimum Design for Buckling of Laminated Cylinders,'' *Proceedings IUTAM Symposium, Collapse: The Buckling of Structures in Theory and Practice*, J. M. T. Thompson and G. W. Hunt eds., Cambridge University Press, Cambridge, UK.

[11] Sun, G., 1989, ''Optimization of Laminated Cylinders for Buckling,'' Doctoral dissertation, Institute for Aerospace Studies, University of Toronto, Toronto, Ontario, Canada.

[12] Zimmerman, R., 1986, ''Optimization of Axially Compressed CFRP Cylinders,'' *Proceedings of the Spacecraft Structures Int. Conference*, CNES, Toulouse, Dec, 3–6, ESA SP-238, pp. 407–412.

[13] Sun, G., and Hansen, J. S., 1988, ''Optimal Design of Laminated-Composite Circular-Cylindrical Shells Subjected to Combined Loads,'' ASME J. Appl. Mech., **55**, pp. 136–142.

[14] Cherkaev, A., and Cherkaeva, E., 1998, ''Stable Optimal Design for Uncertain Loading Conditions,'' *Homogenization*, V. Berdichevsky, ed., World Scientific, Singapore.

[15] Ben-Haim, Y., and Elishakoff, I., 1991, *Convex Models of Uncertainty in Applied Mechanics*, Elsevier, New York.

[16] Huseyin, K., 1975, *Nonlinear Theory of Elastic Stability*, Noordhoff International Publishing, The Netherlands.

One-to-One Internal Resonance of Symmetric Crossply Laminated Shallow Shells

A. Abe[1]
Department of Mechanical Engineering,
Fukui University,
Fukui 910-8507, Japan

Y. Kobayashi

G. Yamada

Division of Mechanical Science,
Hokkaido University,
Sapporo 060-8628, Japan

This paper presents the response of symmetric crossply laminated shallow shells with an internal resonance $\omega_2 \approx \omega_3$, where ω_2 and ω_3 are the linear natural frequencies of the asymmetric vibration modes (2,1) and (1,2), respectively. Galerkin's procedure is applied to the nonlinear governing equations for the shells based on the von Kármán-type geometric nonlinear theory and the first-order shear deformation theory, and the shooting method is used to obtain the steady-state response when a driving frequency Ω is near ω_2. In order to take into account the influence of quadratic nonlinearities, the displacement functions of the shells are approximated by the eigenfunctions for the linear vibration mode (1,1) in addition to the ones for the modes (2,1) and (1,2). This approximation overcomes the shortcomings in Galerkin's procedure. In the numerical examples, the effect of the (1,1) mode on the primary resonance of the (2,1) mode is examined in detail, which allows us to conclude that the consideration of the (1,1) mode is indispensable for analyzing nonlinear vibrations of asymmetric vibration modes of shells.
[DOI: 10.1115/1.1356416]

1 Introduction

With the increasing use of fiber-reinforced plastics in industrial applications, many papers have been published in the area of nonlinear vibrations of laminated plates and shells. Chia [1,2] and Sathyamoorthy [3] have conducted a comprehensive review of the literature dealing with nonlinear problems in plates. The effects of transverse shear deformation, rotatory inertia, and initial geometrical imperfections on the nonlinear vibration and post-buckling of antisymmetric angle-ply cylindrical thick panels and generally laminated circular cylindrical thick shells with nonuniform boundary conditions were discussed by Fu and Chia [4,5]. Raouf and Palazotto [6] performed a single-mode analysis of the nonlinear free vibration of a curved, simply supported orthotropic panel, based on the Donnell-Mushtari-Vlasov shell theory. Xu et al. [7] derived nonlinear equations of transverse motion for a generally laminated, truncated conical shell and solved the nonlinear vibration problem by the method of harmonic balance. Cheung and Fu [8] studied nonlinear static and dynamic responses and dynamic buckling of symmetric crossply shallow spherical shells by using the orthogonal collocation method and the Newmark scheme.

In this paper, we study a one-to-one internal resonance of crossply laminated shallow shells subject to a harmonic transverse load, where the linear natural frequencies ω_2 and ω_3 of the asymmetric vibration modes (2,1) and (1,2) have the relationship $\omega_2 \approx \omega_3$. As for internal resonances of laminated plates, Hadian et al. [9] analyzed two-to-one internal resonances of antisymmetric crossply laminated rectangular plates by using the averaged Lagrangian. The present authors investigated two-mode [10,11] and three-mode [12] responses of laminated plates, in which the combination of Galerkin's procedure and the method of multiple scales was used. However, no papers have been presented for internal resonances of laminated shells treated here, and studies on the topic have been confined to isotropic materials [13–16].

For the purpose of this study, taking into account the von Kármán-type geometric nonlinear theory and the first-order shear deformation theory, the nonlinear governing equations for symmetric crossply laminated shallow shells are derived by means of Hamilton's principle. Chin and Nayfeh [16] investigated the response of an externally excited infinitely long circular cylindrical shell with a one-to-one internal resonance to a primary excitation of one of two orthogonal flexural modes. They compared the results derived by applying the method of multiple scales directly to the nonlinear governing partial differential equations with those derived from a two-mode Galerkin discretization approach, and pointed out that the latter led to incorrect results (i.e., the influence of the quadratic nonlinear terms was neglected). However, because displacements for the shells treated here are governed by the two spatial variables, it is very difficult to solve the present problem with the direct method. Accordingly, we discretize the governing equations by using Galerkin's procedure. In the present analysis, the displacement functions of the shells are approximated by the eigenfunctions for the linear vibration mode (1,1) in addition to the ones for the modes (2,1) and (1,2). This approximation yields ordinary differential equations with not only cubic but also quadratic nonlinear terms and overcomes the shortcomings in Galerkin's procedure using only the modes (2,1) and (1,2).

Finally, we apply the shooting method to the ordinary differential equations, and obtain the frequency-response curves of the shells when a driving frequency Ω is near ω_2. The numerical examples prove that taking the (1,1) mode into consideration is indispensable for analyzing nonlinear vibrations of the asymmetric vibration modes of shells. Furthermore, not only periodic but also quasi-periodic and chaotic responses of the shells are presented in the form of diagrams.

2 Basic Equations

Figure 1 shows a laminated shallow shell of rectangular planform, which consists of N layers of an orthotropic sheet, with lengths a and b, thickness h and radii of curvature R_x and R_y. The coordinates (x, y, z) are assigned as in the figure. The components of the displacement at an arbitrary point of the shell in the x, y and z directions are u, v and w, respectively.

---

[1]To whom correspondence should be addressed. Present address: Department of Information System Engineering, Asahikawa National College of Technology, 2-2-1-6 Syunkodai, Asahikawa, Hokkaido 071-8142, Japan.

Contributed by the Applied Mechanics Division of THE AMERICAN SOCIETY OF MECHANICAL ENGINEERS for publication in the ASME JOURNAL OF APPLIED MECHANICS. Manuscript received by the ASME Applied Mechanics Division, Dec. 22, 1999; final revision, Aug. 22, 2000. Associate Editor: M.-J. Pindera. Discussion on the paper should be addressed to the Editor, Professor Lewis T. Wheeler, Department of Mechanical Engineering, University of Houston, Houston, TX 77204-4792, and will be accepted until four months after final publication of the paper itself in the ASME JOURNAL OF APPLIED MECHANICS.

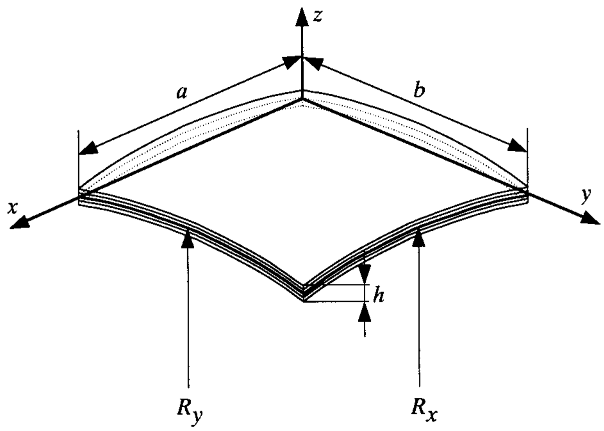

Fig. 1 Geometry of a laminated shallow shell and coordinate systems

According to the first-order shear deformation theory, the in-plane displacements u and v are linear functions of the coordinate z, and the transverse displacement w is constant throughout the thickness of the shell. Under this assumption the displacement field may be given in the following form:

$$u=u_0+z\psi_x,\quad v=v_0+z\psi_y,\quad w=w_0, \tag{1}$$

where u_0, v_0, and w_0 are the displacements at the midsurface, ψ_x and ψ_y are the rotations of the midsurface about the y and x axes, respectively. The nonlinear strain-displacement relations of the shallow shell can be written as

$$\left.\begin{array}{r}\epsilon_x=\epsilon_x^0+z\kappa_x,\quad \epsilon_y=\epsilon_y^0+z\kappa_y,\quad \epsilon_z=0,\\ \epsilon_{xy}=\epsilon_{xy}^0+z\kappa_{xy},\quad \epsilon_{xz}=\psi_x+w_0,_x,\quad \epsilon_{yz}=\psi_y+w_0,_y\end{array}\right\}, \tag{2}$$

in which

$$\epsilon_x^0=u_0,_x+\frac{w_0}{R_x}+\frac{1}{2}w_0,_x^2,\quad \epsilon_y^0=v_0,_y+\frac{w_0}{R_y}+\frac{1}{2}w_0,_y^2,$$

$$\epsilon_{xy}^0=u_0,_x+v_0,_x+w_0,_xw_0,_y, \tag{3}$$

$$\kappa_x=\psi_x,_x,\quad \kappa_y=\psi_y,_y,\quad \kappa_{xy}=\psi_x,_y+\psi_y,_x, \tag{4}$$

and the subscripts following a comma stand for partial differentiation.

The constitutive relations of the shell can be expressed as follows:

$$\begin{Bmatrix}\epsilon_x^0\\ \epsilon_y^0\\ \epsilon_{xy}^0\\ M_x\\ M_y\\ M_{xy}\end{Bmatrix}=\begin{bmatrix}A_{11}^* & A_{12}^* & A_{16}^* & B_{11}^* & B_{12}^* & B_{16}^*\\ A_{12}^* & A_{22}^* & A_{26}^* & B_{21}^* & B_{22}^* & B_{26}^*\\ A_{16}^* & A_{26}^* & A_{66}^* & B_{61}^* & B_{62}^* & B_{66}^*\\ -B_{11}^* & -B_{21}^* & -B_{61}^* & D_{11}^* & D_{12}^* & D_{16}^*\\ -B_{12}^* & -B_{22}^* & -B_{62}^* & D_{12}^* & D_{22}^* & D_{26}^*\\ -B_{16}^* & -B_{26}^* & -B_{66}^* & D_{16}^* & D_{26}^* & D_{66}^*\end{bmatrix}$$

$$\times\begin{Bmatrix}N_x\\ N_y\\ N_{xy}\\ \kappa_x\\ \kappa_y\\ \kappa_{xy}\end{Bmatrix}, \tag{5}$$

$$\begin{Bmatrix}Q_y\\ Q_x\end{Bmatrix}=\begin{bmatrix}S_{44} & S_{45}\\ S_{45} & S_{55}\end{bmatrix}\begin{Bmatrix}\epsilon_{yz}\\ \epsilon_{xz}\end{Bmatrix}, \tag{6}$$

where N, M, and Q are the stress, moment, and shear stress resultants, respectively. The constants A_{ij}^*, B_{ij}^*, D_{ij}^*, and S_{ij} are derived from

$$\begin{Bmatrix}\sigma_x\\ \sigma_y\\ \sigma_{yz}\\ \sigma_{xz}\\ \sigma_{xy}\end{Bmatrix}^{(k)}=\begin{bmatrix}C_{11} & C_{12} & 0 & 0 & C_{16}\\ C_{12} & C_{22} & 0 & 0 & C_{26}\\ 0 & 0 & C_{44} & C_{45} & 0\\ 0 & 0 & C_{45} & C_{55} & 0\\ C_{16} & C_{26} & 0 & 0 & C_{66}\end{bmatrix}^{(k)}\begin{Bmatrix}\epsilon_x\\ \epsilon_y\\ \epsilon_{yz}\\ \epsilon_{xy}\\ \epsilon_{xy}\end{Bmatrix}, \tag{7}$$

$$(A_{ij},B_{ij},D_{ij})=\sum_{k=1}^{N}\int_{h_{k-1}}^{h_k}C_{ij}^{(k)}(1,z,z^2)dz,\quad i,j=1,2,6, \tag{8}$$

$$S_{ij}=K^2A_{ij}=K^2\sum_{k=1}^{N}\int_{h_{k-1}}^{h_k}C_{ij}^{(k)}dz,\quad i,j=4,5, \tag{9}$$

$$\mathbf{A}^*=\mathbf{A}^{-1},\quad \mathbf{B}^*=-\mathbf{A}^{-1}\mathbf{B},\quad \mathbf{D}^*=\mathbf{D}-\mathbf{B}\mathbf{A}^{-1}\mathbf{B}, \tag{10}$$

in which the stiffness matrix elements $C_{ij}^{(k)}$ express the stress-strain relation in the kth layer, K^2 is the shear correction factor, and h_k is the distance from the midsurface to the upper surface of the kth layer.

In this paper, it is assumed that both rotatory and in-plane inertias are negligible [17]. Therefore, the kinetic energy of the shell can be written as

$$T=\frac{\rho}{2}\int_0^b\int_0^a w_0,_t^2dxdy, \tag{11}$$

where ρ is the mass per unit area of the shell. The strain energy of the shell is given by

$$U=\frac{1}{2}\int_0^b\int_0^a(N_x\epsilon_x^0+N_y\epsilon_y^0+N_{xy}\epsilon_{xy}^0+Q_x\epsilon_{xz}+Q_y\epsilon_{yz}+M_x\kappa_x$$

$$+M_y\kappa_y+M_{xy}\kappa_{xy})dxdy. \tag{12}$$

The work done by an external pressure $q(x,y,t)$ acting in the z direction is

$$W=\int_0^b\int_0^a q(x,y,t)w_0dxdy. \tag{13}$$

By substituting Eqs. (11)–(13) into Hamilton's principle

$$\int_{t_0}^{t_1}\delta(T-U+W)dt=0, \tag{14}$$

and taking the variation, in consideration of Eqs. (2)–(4), the governing equations are derived as follows:

$$N_x,_x+N_{xy},_y=0,\quad N_{xy},_x+N_y,_y=0, \tag{15}$$

$$\rho w_0,_{tt}=-\frac{N_x}{R_x}-\frac{N_y}{R_y}+Q_x,_x+Q_y,_y+(N_xw_0,_x+N_{xy}w_0,_y),_x$$

$$+(N_yw_0,_y+N_{xy}w_0,_x),_y+q, \tag{16}$$

$$M_x,_x+M_{xy},_y-Q_x=0,\quad M_{xy},_x+M_y,_y-Q_y=0. \tag{17}$$

A stress function ϕ satisfying Eq. (15) automatically is defined as

$$N_x=\phi,_{yy},\quad N_y=\phi,_{xx},\quad N_{xy}=-\phi,_{xy}. \tag{18}$$

In the following analysis, we consider symmetric crossply laminated shells. In this case, the following elastic coefficients vanish:

$$A_{16}^*=A_{26}^*=B_{ij}^*=D_{16}^*=D_{26}^*=S_{45}=0\quad (i,j=1,2,6). \tag{19}$$

By using relations of Eqs. (5), (6), (10), (15), (18), and (19), Eqs. (16) and (17) can be rewritten as

$$\rho w_{0,tt} - q - \phi_{,yy} w_{0,xx} + 2\phi_{,xy} w_{0,xy} - \phi_{,xx} w_{0,yy} + \frac{1}{R_x}\phi_{,yy} + \frac{1}{R_y}\phi_{,xx} - S_{44}(w_{0,yy} + \psi_{y,y}) - S_{55}(w_{0,xx} + \psi_{x,x}) = 0, \tag{20}$$

$$D_{11}\psi_{x,xx} + D_{66}\psi_{x,yy} + (D_{12}+D_{66})\psi_{y,xy} - S_{55}(w_{0,x} + \psi_x) = 0, \tag{21}$$

$$(D_{12}+D_{66})\psi_{x,xy} + D_{66}\psi_{y,xx} + D_{22}\psi_{y,yy} - S_{44}(w_{0,y} + \psi_y) = 0. \tag{22}$$

The compatibility equation is obtained by eliminating u_0 and v_0 in Eq. (3) and using Eqs. (5) and (18):

$$A_{22}^*\phi_{,xxxx} + (2A_{12}^* + A_{66}^*)\phi_{,xxyy} + A_{11}^*\phi_{,yyyy} = w_{0,xy}^2 - w_{0,xx} w_{0,yy} + \frac{1}{R_x} w_{0,yy} + \frac{1}{R_y} w_{0,xx}. \tag{23}$$

Equations (20)–(23) expressed in terms of w_0, ψ_x, ψ_y, and ϕ are the nonlinear governing equations for symmetric crossply laminated shallow shells based on the first-order shear deformation theory.

We assume that the shell is simply supported and free from in-plane stresses along its four edges. However, it is very difficult to solve the stress function satisfying exactly both the compatibility Eq. (23) and the in-plane boundary conditions (e.g., $N_x = N_{xy} = 0$ at $x = 0,a$) in the analysis. As a convenient approach, it is assumed that the average of the normal and tangential stresses is zero at the boundaries in References [1] and [18]. We adopt this assumption in the present paper, and the boundary conditions can be written

$$\left.\begin{aligned} w_0 = \psi_y = M_x = \int_0^b \phi_{,xy}\,dy = \int_0^b \phi_{,yy}\,dy = 0 \quad \text{at } x = 0,a \\ w_0 = \psi_x = M_y = \int_0^a \phi_{,xy}\,dx = \int_0^a \phi_{,xx}\,dx = 0 \quad \text{at } y = 0,b \end{aligned}\right\}. \tag{24}$$

The displacement functions, which satisfy the out-of-plane boundary conditions (e.g., $w_0 = \psi_y = M_x = 0$ at $x = 0,a$), of the shell can be expressed by using the eigenfunctions of the linear vibration as

$$\left.\begin{aligned} w_0 &= h\sum_{m=1}^{M}\sum_{n=1}^{N} W_{mn}(t)\sin\frac{m\pi x}{a}\sin\frac{n\pi y}{b} \\ \psi_x &= \sum_{m=1}^{M}\sum_{n=1}^{N} X_{mn}(t)\cos\frac{m\pi x}{a}\sin\frac{n\pi y}{b} \\ \psi_y &= \sum_{m=1}^{M}\sum_{n=1}^{N} Y_{mn}(t)\sin\frac{m\pi x}{a}\cos\frac{n\pi y}{b} \end{aligned}\right\}, \tag{25}$$

in which W_{mn} are nondimensional displacements, X_{mn} and Y_{mn} are nondimensional rotation angles, and m and n are the numbers of half wave in the x and y directions, respectively. In the present paper, we consider an internal resonance when the linear natural frequencies ω_2 and ω_3 of the vibration modes (2,1) and (1,2) have the relationship $\omega_2 \approx \omega_3$. It is assumed that only the vibration mode (2,1) is directly excited by the transverse force. Therefore $q(x,y,t)$ is defined as

$$q(x,y,t) = q_0 \sin\frac{2\pi x}{a}\sin\frac{\pi y}{b}\cos\Omega' t, \tag{26}$$

where q_0 and Ω' are the amplitude and angular frequency of the force, respectively.

The stress function satisfying the in-plane boundary conditions (the integrals in Eq. (24)) is assumed to be of the form

$$\phi = \sum_{p=0}^{\infty}\sum_{q=0}^{\infty} B_{pq}\cos\frac{p\pi x}{a}\cos\frac{q\pi y}{b} + \sum_{r=1}^{\infty}\sum_{s=1}^{\infty} C_{rs}\sin\frac{r\pi x}{a}\sin\frac{s\pi y}{b}, \tag{27}$$

in which B_{pq} and C_{rs} are unknown coefficients. If Eqs. (25) and (27) are substituted into the compatibility condition (23), then B_{pq} and C_{rs} can be determined by comparing the coefficients of trigonometric functions in both sides of Eq. (23). Although details of B_{pq} and C_{rs} are omitted due to space restriction, B_{pq} and C_{rs} become the quadratic and first-order forms of W_{mn}, respectively.

Substituting Eqs. (25)–(27) into Eqs. (20)–(22) and applying Galerkin's procedure (i.e., multiplying Eqs. (20), (21), and (22) by $\sin(m\pi x/a)\sin(n\pi y/b)$, $\cos(m\pi x/a)\sin(n\pi y/b)$ and $\sin(m\pi x/a)\cos(n\pi y/b)$, respectively, and then integrating over the area of the shell), nonlinear ordinary differential equations are obtained for the time-dependent variables W_{mn}, X_{mn} and Y_{mn}. By eliminating X_{mn} and Y_{mn} from the equations and adding on the effect of viscous damping, we obtain the following simultaneous nonlinear ordinary differential equations in terms of the vibration modes (1,1), (2,1), and (1,2):

$$\left.\begin{aligned} \ddot{W}_1 + \mu\omega_1\dot{W}_1 + \omega_1^2 W_1 + G_{a1}W_1^2 + G_{a2}W_2^2 + G_{a3}W_3^2 + G_{a4}W_1^3 + G_{a5}W_1W_2^2 + G_{a6}W_1W_3^2 = 0 \\ \ddot{W}_2 + \mu\omega_2\dot{W}_2 + \omega_2^2 W_2 + G_{b1}W_1W_2 + G_{b2}W_1^2W_2 + G_{b3}W_2^3 + G_{b4}W_2W_3^2 = F\cos\Omega\tau \\ \ddot{W}_3 + \mu\omega_3\dot{W}_3 + \omega_3^2 W_3 + G_{c1}W_1W_3 + G_{c2}W_1^2W_3 + G_{c3}W_2^2W_3 + G_{c4}W_3^3 = 0 \end{aligned}\right\}, \tag{28}$$

where μ, ω, G, F, and Ω are the nondimensional damping coefficient, the nondimensional linear natural frequencies, the nondimensional coefficients of the nonlinear terms, the nondimensional amplitude and frequency of the load, respectively. It is to be noted that the terms $\mu\omega_i\dot{W}_i$ mean the modal damping (e.g., [19], [20]). Details of ω, F and Ω are written in the Appendix. However, details of G are omitted due to space restriction. Subscript i of the nondimensional displacements is redefined as $\{W_1, W_2, W_3\} = \{W_{11}, W_{21}, W_{12}\}$. A dot expresses differentiation with respect to the nondimensional time

$$\tau = \sqrt{\frac{E_T h^3}{\rho a^4}}\,t, \tag{29}$$

in which E_T is the minor Young's modulus. It is important to note that the first, second, and third equations in (28) express the motion of the vibration modes (1,1), (2,1) and (1,2), respectively. As can be seen from Eq. (28), when W_2 is excited, W_1 will always be activated by the nonlinear term $G_{a2}W_2^2$ even if there are no internal resonances between the vibration modes (1,1) and (2,1). The amplitude of the (1,1) mode affects the response of the (2,1) mode through the nonlinear terms $G_{b1}W_1W_2$ and $G_{b2}W_1^2W_2$. However, the effect of the quadratic nonlinear terms like $G_{b1}W_1W_2$ on the response of the (2,1) mode is not considered when W_1 is neglected. In view of Eq. (28), it can therefore be said that the addition of the fundamental vibration mode to the displacement functions overcomes the shortcomings of the Galerkin discretization for asymmetric vibration modes of continuous systems with quadratic and cubic nonlinearities.

3 Shooting Method

In the following analysis, we investigate the steady-state response of the shells by using the shooting method when Ω is near ω_2. Although the perturbation method is widely used to solve nonlinear ordinary differential equations, the following problem seems to arise when the method is applied to nonlinear modal equations of shallow shells. A single-mode equation of a shallow shell can be written as follows:

$$\ddot{W}+\omega^2W+\epsilon G_1W^2+\epsilon^2G_2W^3=0, \tag{30}$$

where ϵ is a small dimensionless parameter to express the order of smallness of nonlinear terms, and the coefficient G_1 of the quadratic nonlinear term is generated by the curvature of the shallow shell. The coefficient G_1 of the quadratic nonlinear term may be greater than the coefficient G_2 of the cubic nonlinear term because the radii of curvature of the shallow shell are very large. In this case, it is possible that an assumption ($\epsilon G_1W^2>\epsilon^2G_2W^3$) for the perturbation is not established. In the shooting method, such an assumption is not necessary. Therefore, we adopt the shooting method in the present analysis. In order to apply the shooting method to Eq. (28), we introduce the following vector

$$\mathbf{x}=\{x_1,x_2,x_3,x_4,x_5,x_6\}^T=\{W_1,\dot{W}_1,W_2,\dot{W}_2,W_3,\dot{W}_3\}^T, \tag{31}$$

and convert Eq. (28) into a set of first-order differential equations

$$\frac{d\mathbf{x}}{d\hat{t}}=\mathbf{X}, \tag{32}$$

where

$$\left.\begin{aligned}
&\mathbf{X}=\{X_1,X_2,X_3,X_4,X_5,X_6\}^T,\\
&X_1=x_2,\\
&X_2=-\{\mu\omega_1\omega_2x_2+\omega_1^2x_1+(G_{a1}+G_{a4}x_1)x_1^2+(G_{a2}+G_{a5}x_1)x_3^2+(G_{a3}+G_{a6}x_1)x_5^2\}/\omega_2^2,\\
&X_3=x_4,\\
&X_4=-\mu x_4-x_3-\{(G_{b1}+G_{b2}x_1)x_1x_3+G_{b3}x_3^3+G_{b4}x_3x_5^2-F\cos(\Omega/\omega_2)\hat{t}\}/\omega_2^2,\\
&X_5=x_6,\\
&X_6=-\{\mu\omega_2\omega_3x_6+\omega_3^2x_5+(G_{c1}+G_{c2}x_1)x_1x_5+G_{c3}x_3^2x_5+G_{c4}x_5^3\}/\omega_2^2,
\end{aligned}\right\}, \tag{33}$$

and $\hat{t}$ is a new time variable defined as $\hat{t}=\omega_2\tau$.

Since details of the shooting method were already given by Nayfeh and Balachandran [21] and Tamura and Matsuzaki [22], only the algorithm used in this paper is presented here. According to the shooting method, it is necessary to treat the following equation in addition to Eq. (32):

$$\frac{d\mathbf{\Phi}(\hat{t})}{d\hat{t}}=\mathbf{Y}\mathbf{\Phi}(\hat{t}),\quad \mathbf{\Phi}(0)=\mathbf{E}, \tag{34}$$

in which $\mathbf{\Phi}$ is a 6×6 matrix which is called the transition matrix, $\mathbf{E}$ is the unit matrix, and $\mathbf{Y}$ is the matrix of first partial derivatives of $\mathbf{X}$:

$$\mathbf{Y}=\frac{\partial\mathbf{X}}{\partial\mathbf{x}}=\begin{bmatrix}0&1&0&0&0&0\\Y_{21}&Y_{22}&Y_{23}&0&Y_{25}&0\\0&0&0&1&0&0\\Y_{41}&0&Y_{43}&Y_{44}&Y_{45}&0\\0&0&0&0&0&1\\Y_{61}&0&Y_{63}&0&Y_{65}&Y_{66}\end{bmatrix}, \tag{35}$$

$$\left.\begin{aligned}
&Y_{21}=-\{\omega_1^2+(2G_{a1}+3G_{a4}x_1)x_1+G_{a5}x_3^2+G_{a6}x_5^2\}/\omega_2^2,\\
&Y_{22}=-\mu\omega_1/\omega_2,Y_{23}=-2(G_{a2}+G_{a5}x_1)x_3/\omega_2^2,Y_{25}=-2(G_{a3}+G_{a6}x_1)x_5/\omega_2^2,\\
&Y_{41}=-(G_{b1}+2G_{b2}x_1)x_3/\omega_2^2,Y_{44}=-\mu,Y_{45}=-2G_{b4}x_3x_5/\omega_2^2\\
&Y_{43}=-1-\{(G_{b1}+G_{b2}x_1)x_1+3G_{b3}x_3^2+G_{b4}x_5^2\}/\omega_2^2,\\
&Y_{61}=-(G_{c1}+2G_{c2}x_1)x_5/\omega_2^2,Y_{63}=-2G_{c3}x_3x_5/\omega_2^2\\
&Y_{65}=-\{\omega_3^2+(G_{c1}+G_{c2}x_1)x_1+G_{c3}x_3^2+3G_{c4}x_5^2\}/\omega_2^2,Y_{66}=-\mu\omega_3/\omega_2,
\end{aligned}\right\}. \tag{36}$$

In order to solve Eqs. (32) and (34) simultaneously, we combine the two equations as

$$\frac{d}{d\hat{t}}\left\{\begin{matrix}\mathbf{x}\\ \boldsymbol{\phi}_1\\ \vdots\\ \boldsymbol{\phi}_6\end{matrix}\right\}=\left\{\begin{matrix}\mathbf{X}\\ \mathbf{Y}\cdot\boldsymbol{\phi}_1\\ \vdots\\ \mathbf{Y}\cdot\boldsymbol{\phi}_6\end{matrix}\right\}, \tag{37}$$

where $\boldsymbol{\phi}_i$ is the ith column vector of

$$\boldsymbol{\Phi}=[\boldsymbol{\phi}_1,\boldsymbol{\phi}_2,\cdots,\boldsymbol{\phi}_6]. \tag{38}$$

(Step 1) By applying the fourth-order Runge-Kutta method to Eq. (37), $\mathbf{x}(T)$ and $\boldsymbol{\Phi}(T)$ are obtained under the initial guess $\mathbf{x}(0)=\mathbf{x}^0$, assuming that the period T of the solution is $2\pi/(\Omega/\omega_2)$ because Eq. (32) is a nonautonomous system.

(Step 2) By substituting $\mathbf{x}(T)$, $\boldsymbol{\Phi}(T)$, and $\mathbf{x}^0$ into a successive approximation equation for a nonautonomous system

$$[\boldsymbol{\Phi}(T)-\mathbf{E}]\delta\mathbf{x}=\mathbf{x}^0-\mathbf{x}(T), \tag{39}$$

and by solving the above equation, the correction $\delta\mathbf{x}$ for $\mathbf{x}$ can be determined.

(Step 3) We check whether a certain convergence criterion ([22]) is satisfied or not. In this paper, the convergence criterion is defined as

$$\sqrt{\frac{\sum_{i=1}^{6}\{\mathbf{x}_i(0)-\mathbf{x}_i(T)\}^2}{\sum_{i=1}^{6}\{\mathbf{x}_i(0)^2+\mathbf{x}_i(T)^2\}}}<10^{-10}. \tag{40}$$

If Eq. (40), which measures the relative error between $\mathbf{x}(0)$ and $\mathbf{x}(T)$, is not satisfied, the initial guess $\mathbf{x}^0$ is updated to $\mathbf{x}^0+\delta\mathbf{x}$, and then we return to Step 1.

(Step 4) If Eq. (40) is satisfied, we examine the stability of the obtained periodic solution by calculating the eigenvalues of $\boldsymbol{\Phi}(T)$. If the maximum eigenvalue lies inside (or outside) the unit circle in the complex plane, the periodic solution is considered to be stable (or unstable).

4 Numerical Results and Discussion

In the following numerical examples, we treat symmetric cross-ply laminated shells ($\theta=90$ deg/0 deg/90 deg) of layers with equal thickness. Each layer is assumed to be made of graphite-epoxy with the following material properties ([23]):

$$E_L=138\ \text{GPa},\quad E_T=8.96\ \text{GPa},\quad G_{LT}=7.1\ \text{GPa},\quad \nu_{LT}=0.3,$$

and G_{TZ} is used as $G_{TZ}=E_T/2$. The shear correction factor K^2 and the damping ratio μ are taken to be $K^2=5/6$ and $\mu=0.01$, respectively. The nondimensional linear natural frequencies of the shells and the amplitude F of the excitation are shown in each figure except Figs. 1, 6, and 7.

In Section 2, it was shown that the vibration coupled with the (1,1) mode was generated when the system vibrated in the (2,1) mode. This means coupled vibration between an asymmetric vibration mode and symmetric vibration modes. We hence examine first of all the effects of not only the (1,1) mode but also of the (3,1) mode which is the second symmetric vibration mode in the primary resonance of the second vibration mode. Figure 2 shows the frequency-response curves for a shell with square planform ($a/b=1$, $R_x/a=R_y/a=10$ and $h/a=0.01$). Since the shell does not have the one-to-one internal resonance ($\omega_2\approx\omega_3$), the (1,2) mode can be neglected in this case. Note that the natural frequency ω_4 of the (3,1) mode equals 43.95 and there are no internal resonances among the (1,1), (2,1), (1,2), and (3,1) modes. In Fig. 2, W_4 indicates the amplitude of the (3,1) mode. The dotted, solid, and broken lines denote the results obtained by considering only the (2,1) mode (single-mode analysis), the (1,1) and (2,1) modes (two-mode analysis), and the (1,1), (2,1), and (3,1) modes (three-mode analysis), respectively. It is found from Fig. 2(*b*) that the result of the two-mode analysis is in good agreement with that of the three-mode analysis, whereas that of the single-mode analysis is different from both of them.

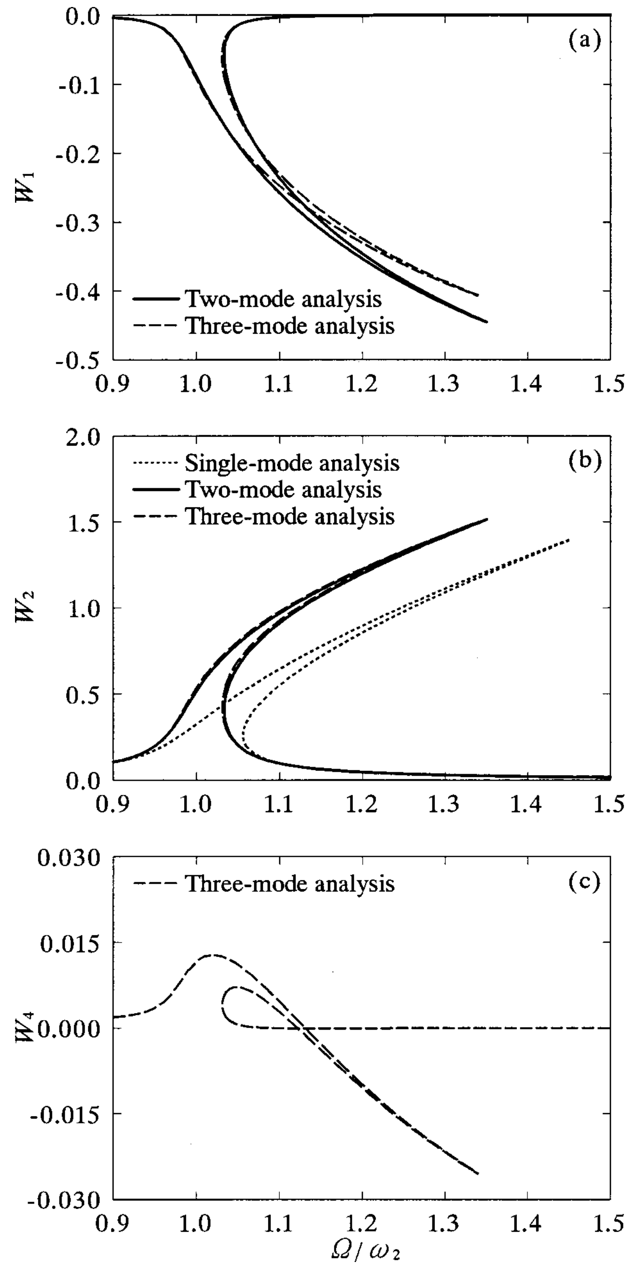

Fig. 2 Frequency-response curves for the shell with $a/b=1$, $R_x/a=R_y/a=10$ and $h/a=0.01$, ($\omega_1=20.68$, $\omega_2=28.59$, $\omega_3=48.77$, $\omega_4=43.95$ and $F/\omega_2^2=0.015$). (*a*) (1,1) mode, (*b*) (2,1) mode and (*c*) (3,1) mode.

Time histories at $\Omega/\omega_2=1.3$ (upper branch) are shown in Fig. 3, where W and T indicate the amplitude of the shell at $(x,y)=(a/4,b/2)$ and the period of the excitation, respectively. It can be seen in Fig. 3(*b*) that the periods of W_1 and W_4 which are activated through nonlinear terms are half of that of W_2 which is excited directly by the load. Moreover, W_1 and W_4 are always negative in a vibratory cycle. Chin and Nayfeh [16] through the direct approach indicated that responses of shells contained terms expressing a drift and a period of half of the period of a harmonic load (see Eqs. (4) and (5) in [16]). This agrees with our results.

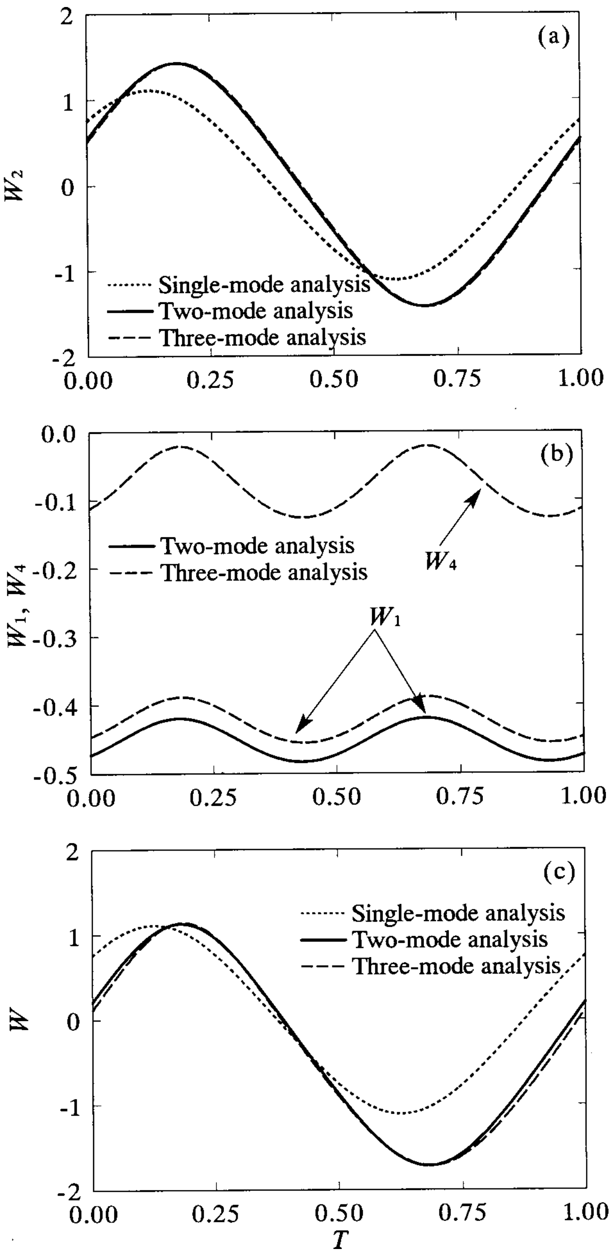

Fig. 3 Time histories at $\Omega/\omega_2=1.3$ (upper branch) in Fig. 2. (*a*) (2,1) mode, (*b*) (1,1) and (3,1) modes, and (*c*) the amplitude of the shell at $(x,y)=(a/4, b/2)$.

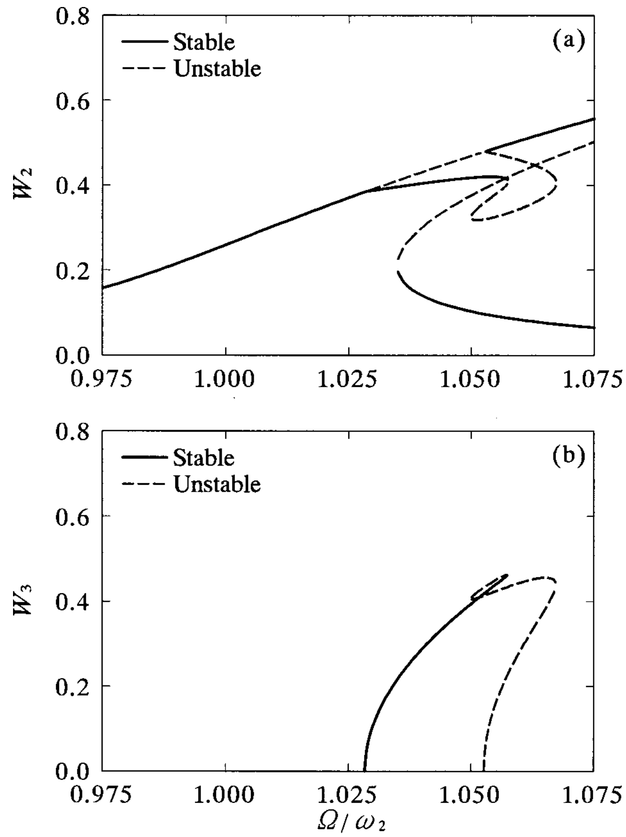

Fig. 4 Frequency-response curves for the shell with $a/b=0.704$, $R_x/a=R_y/a=10$ and $h/a=0.01$ obtained by the two-mode analysis, ($\omega_1=18.79$, $\omega_2=28.15$, $\omega_3=28.68$, and $F/\omega_2^2=0.01$). (*a*) (2,1) mode and (*b*) (1,2) mode.

The present second author and Leissa [24] investigated nonlinear free vibrations of thick isotropic shells and reported that the inward displacement ($W_{\min}$) exceeded in magnitude the outward displacement ($W_{\max}$) in a vibratory cycle. As can be seen from Fig. 3(*c*), the asymmetry of the displacement (i.e., $|W_{\min}|\neq W_{\max}$) appears in the two-mode and in the three-mode analyses. However, the asymmetry does not appear in the single-mode analysis. It can therefore be concluded from Figs. 2 and 3 that the first vibration mode is indispensable for analyzing the asymmetric modes of shells. Furthermore, because the results obtained by the two-mode analysis are in good agreement with those obtained by the three-mode analysis and the effect of the (3,1) mode is very small, the symmetric modes other than the (1,1) mode can be neglected in the analysis.

Next, the effect of the first vibration mode on the internal resonance $\omega_2\approx\omega_3$ is examined. Figure 4 depicts the frequency-response curves for a shell ($a/b=0.704$, $R_x/a=R_y/a=10$ and $h/a=0.01$) obtained by considering only the (2,1) and (1,2) modes (two-mode analysis). The solid and broken lines denote stable and unstable responses, respectively. Stable two-mode responses occur at $\Omega/\omega_2\approx1.028$ via a pitchfork bifurcation and vanish at $\Omega/\omega_2\approx1.057$ via a saddle-node bifurcation. The single-mode response, which loses its stability via the pitchfork bifurcation, becomes stable at $\Omega/\omega_2\approx1.053$ via another pitchfork bifurcation.

Frequency-response curves for the same shell as in Fig. 4 obtained by considering the (1,1) mode in addition to the (2,1) and (1,2) modes (three-mode analysis) are presented in Fig. 5. In this case, a stable W_3, which is activated by the internal resonance, occurs at $\Omega/\omega_2\approx1.000$ via a saddle-node bifurcation and loses its stability at $\Omega/\omega_2\approx1.011$ via a Hopf bifurcation, and the bifurcations are different from those in Fig. 4. It is therefore found from Figs. 4 and 5 as well that the (1,1) mode cannot be neglected in the analysis.

The coupled response between the (1,1) and (2,1) modes loses and recovers its stability at $\Omega/\omega_2\approx1.003$ and 1.018, respectively, via pitchfork bifurcations; hence there do not exist stable periodic responses in the frequency region approximately given by $1.011\leqslant\Omega/\omega_2\leqslant1.018$ in spite of the shell being subjected to the periodic load. Such a phenomenon was also observed in an isotropic circular shell [16]. In order to examine the vibration characteristics in this region, the variation of the largest and the second largest Lyapunov exponents [25] with Ω/ω_2 and Poincaré sections on the W_2-W_3 plane at some points are presented in Figs. 6 and 7, respectively. The Poincaré sections are constructed by sampling the motion at the period of the excitation, and these figures show the results calculated for 30,000 periods after the transient response decayed. The stable response which loses its stability

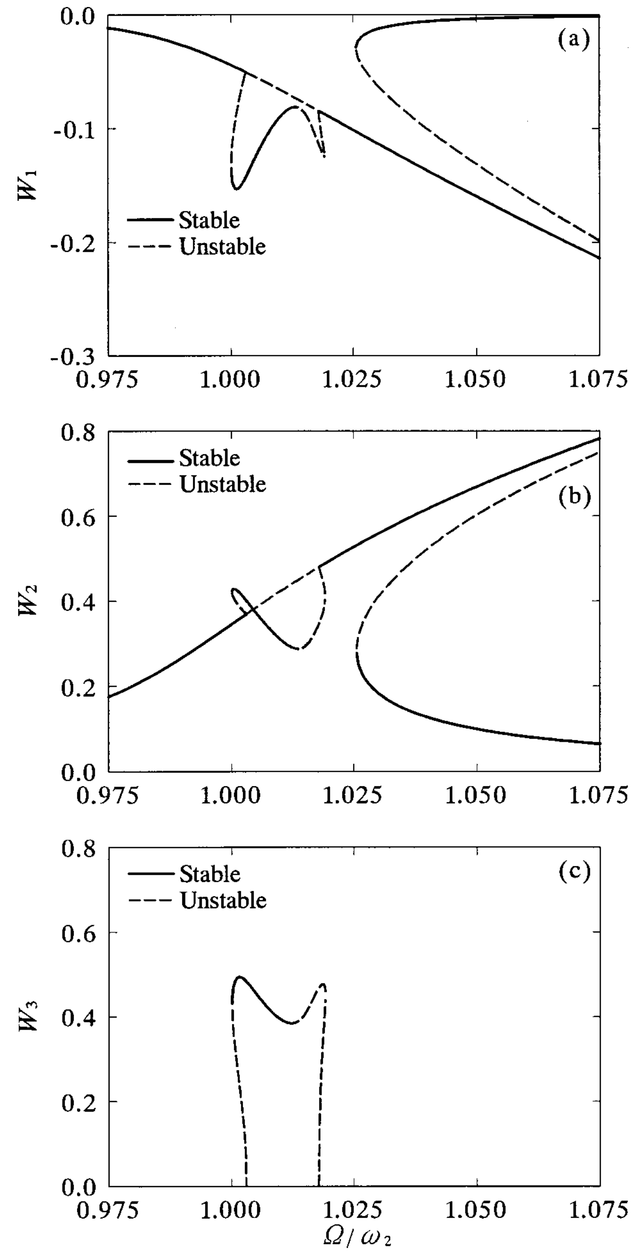

Fig. 5 Frequency-response curves for the same shell as in Fig. 4 obtained by the three-mode analysis. (*a*) (1,1) mode, (*b*) (2,1) mode, and (*c*) (1,2) mode.

through the Hopf bifurcation point becomes a quasi-periodic vibration, as shown in Fig. 7(*a*). It can be seen in Figs. 6, 7(*b*), and 7(*c*) that as the frequency is increased further, the quasi-periodic vibration undergoes a sequence of period-doubling bifurcations, eventually giving rise to chaotic vibration. It is to be noted that the second largest Lyapunov exponent is not positive, and hence this is not hyper chaos. Since the largest Lyapunov exponent at the point D in Fig. 6 is a very small positive value and can be taken to be zero, its motion is quasi-periodic (see also Fig. 7(*d*)). In comparing Figs. 7(*a*) and (*b*) with (*d*), it is observed that the type of the quasi-periodic motion at the point D is different from that at the points A and B.

Figure 8 presents frequency-response curves for a shell ($a/b = 0.581$, $R_x/a = R_y/a = 50$ and $h/a = 0.01$) whose radii of curvature are five times larger than those of the shell used in Fig. 5. As may be expected, the (1,1), (2,1), and (1,2) modes are considered in the analysis. The magnitude of W_1 is smaller than that in Fig. 5,

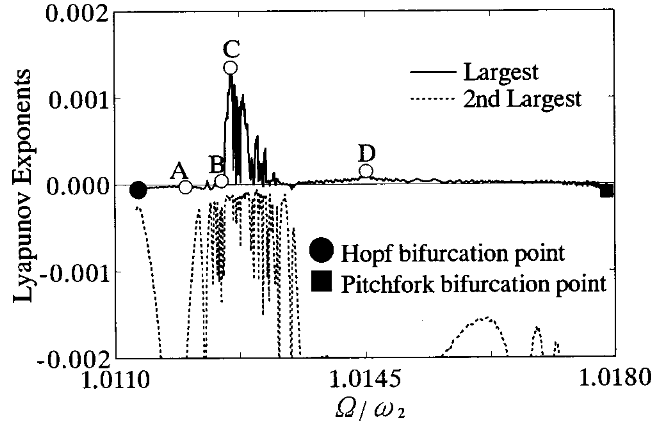

Fig. 6 Lyapunov exponents in the region where stable periodic responses do not exist

and the frequency region of W_3 is narrower than that in Fig. 5. The stable W_3-response occurs and vanishes via the same bifurcations as in Fig. 4 where the (1,1) mode is neglected. We have also confirmed that the same tendency is obtained with an increase of the thickness ratio. It can therefore be said that increases in the radius of curvature and the thickness ratio reduce the influence of the (1,1) mode on the primary resonance of the second vibration mode.

In Fig. 9, the effect of damping ratio on the frequency-response curves is shown for the same shell as Fig. 4. Only stable responses are plotted in the figure. The symbols ○, △, and □ denote Hopf, saddle-node, and pitchfork bifurcation points, respectively. The amplitude of the coupled responses between the (1,1) and (2,1) modes does not change greatly with the value of the damping ratio, whereas that of the (1,2) mode does greatly with it. Especially, in the case of $\mu = 0.005$, there exist two coupled responses among the (1,1), (2,1), and (1,2) modes in the frequency region $1.003 \leqslant \Omega/\omega_2 \leqslant 1.011$.

5 Summary

In the present study, we investigated the response of symmetric crossply laminated shallow shells with a one-to-one internal reso-

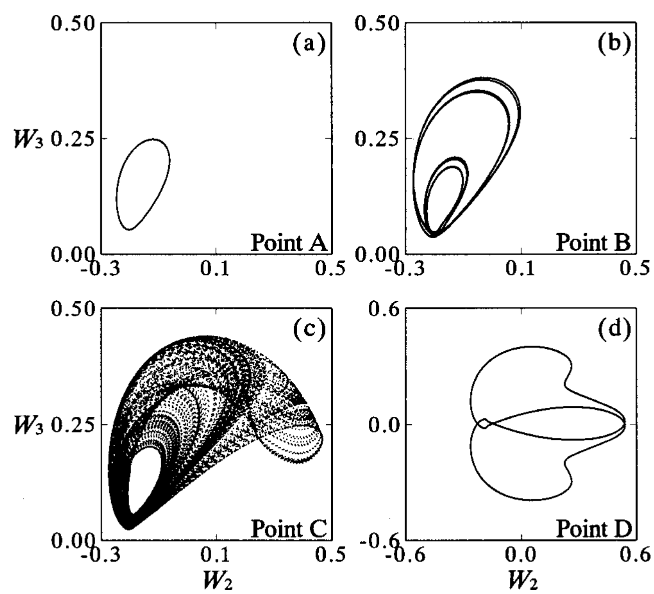

Fig. 7 Poincaré sections. (*a*) $\Omega/\omega_2 = 1.01200$, (*b*) $\Omega/\omega_2 = 1.01250$, (*c*) $\Omega/\omega_2 = 1.01263$, and (*d*) $\Omega/\omega_2 = 1.01451$.

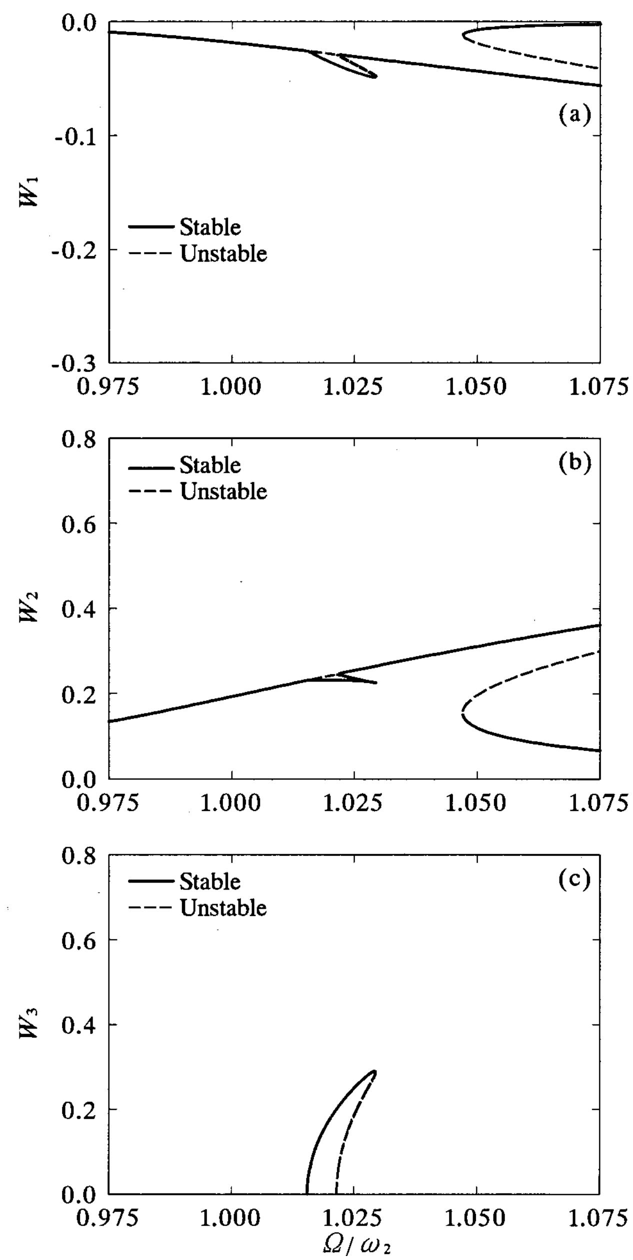

Fig. 8 Frequency-response curves for the shell with $a/b = 0.581$, $R_x/a = R_y/a = 50$, and $h/a = 0.01$ obtained by the three-mode analysis, ($\omega_1 = 7.075$, $\omega_2 = 16.69$, $\omega_3 = 16.90$, and $F/\omega_2^2 = 0.01$). (*a*) (1,1) mode, (*b*) (2,1) mode, and (*c*) (1,2) mode.

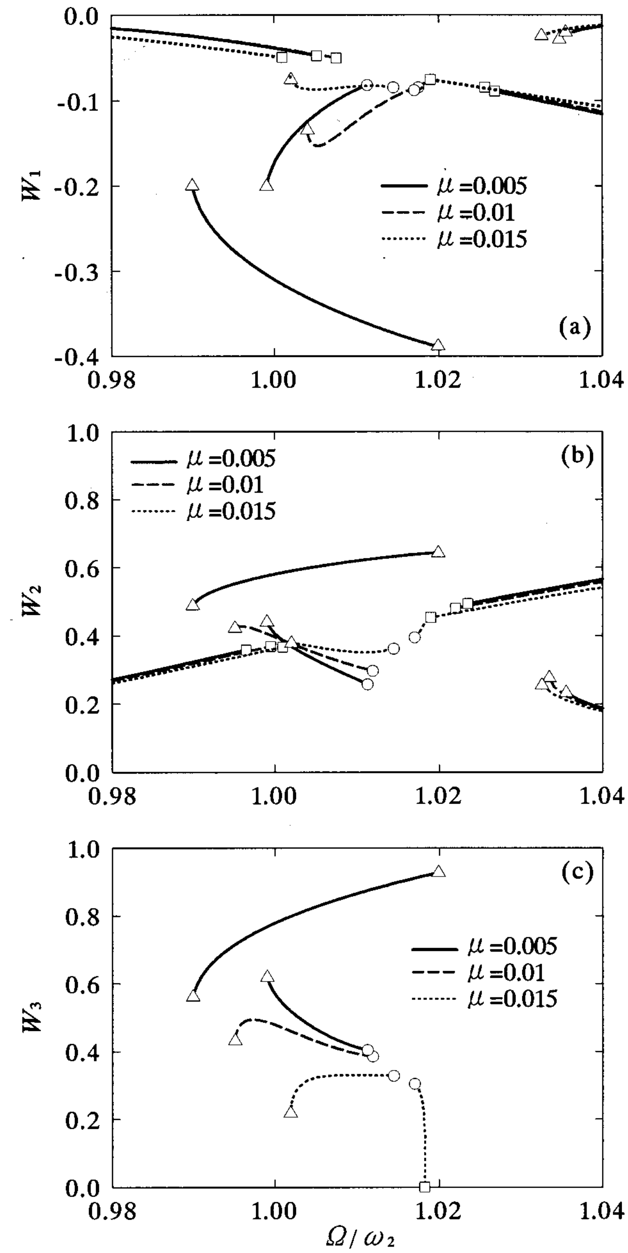

Fig. 9 Effect of damping ratio on frequency-response curves for the same shell as in Fig. 4 obtained by the three-mode analysis, ($F/\omega_2^2 = 0.01$, ○: Hopf bifurcation point, △: saddle-node bifurcation point and □: pitchfork bifurcation point). (*a*) (1,1) mode, (*b*) (2,1) mode, and (*c*) (1,2) mode.

nance $\omega_2 \approx \omega_3$, where ω_2 and ω_3 were linear natural frequencies of asymmetric vibration modes (2,1) and (1,2), respectively. We attempted to approximate the displacements of the shell by the eigenfunctions for the linear vibration mode (1,1) in addition to the ones for the modes (2,1) and (1,2), and then applied Galerkin's procedure to the nonlinear governing equations for the shell yielding ordinary differential equations with both quadratic and cubic nonlinear terms. These equations indicated that when the (2,1) mode was excited, the (1,1) mode was always activated even if there were no internal resonances between the (1,1) and (2,1) modes. Frequency-response curves when a driving frequency Ω is near ω_2 were obtained by the shooting method.

In the numerical examples, we investigated in detail the nonlinear vibration characteristics of laminated shells having a ply layup of ($\theta = 90$ deg/0 deg/90 deg). First, we treated a shell with no internal resonances, and studied the effect of not only the (1,1) mode but also of the (3,1) mode which is the second symmetric vibration mode on the primary resonance. The analysis considering the (1,1) mode led to an asymmetry of the displacement (i.e., the absolute values of the outward and inward displacements did not agree with each other), whereas the analysis neglecting the (1,1) mode did not show this asymmetry. We concluded therefore that the (1,1) mode is indispensable to the analysis of the nonlinear vibrations of the shells. On the other hand, the higher symmetric modes could be negligible because the effect of the (3,1) mode on the response was very small. Next, we investigated the effect of the (1,1) mode on the frequency-response curves for the shell with one-to-one internal resonance, and showed that neglect of the (1,1) mode led to incorrect results. Furthermore, it was proven through both the Lyapunov exponents and the Poincaré sections that chaotic vibrations may occur over a certain range of the driving frequency. Finally, the effects of radii of curvature and damping ratio on the one-to-one internal resonance were illustrated. We showed that the effect of the (1,1) mode became smaller with an increase of the radius of curvature, and that the responses activated by the internal resonance were changed greatly with the value of the damping ratio.

Appendix

Details of ω, F, and Ω are as follows:

$$\omega_i^2 = L_{WiWi} + \frac{L_{XiWi}(L_{YiYi}L_{WiXi} - L_{YiXi}L_{WiYi}) + L_{YiWi}(L_{XiXi}L_{WiYi} - L_{XiYi}L_{WiXi})}{L_{XiYi}L_{YiXi} - L_{XiXi}L_{YiYi}} \quad (i=1,2,3),$$

$$F = \frac{q_0}{E_T H^4}, \quad \Omega = \Omega' \sqrt{\frac{\rho a^4}{E_T h^3}},$$

where

$$L_{X1X1} = -\pi^2(d_{11} + \alpha^2 d_{66}) - s_{55}, \quad L_{X2X2} = -\pi^2(d_{11} + 4\alpha^2 d_{66}) - s_{55},$$

$$L_{X3Y3} = -\pi^2(4d_{11} + \alpha^2 d_{66}) - s_{55}, \quad L_{X1X1} = L_{Y1X1} = -\pi^2 \alpha(d_{12} + d_{66}),$$

$$L_{X2Y2} = L_{Y2X2} = L_{X3Y3} = L_{Y3X3} = -2\pi^2\alpha(d_{12} + d_{66}), \quad L_{Y1Y1} = -\pi^2(\alpha^2 d_{22} + d_{66}) - s_{44},$$

$$L_{Y2Y2} = -\pi^2(\alpha^2 d_{22} + 4d_{66}) - s_{44}, \quad L_{Y3Y3} = -\pi^2(4\alpha^2 d_{22} + d_{66}) - s_{44},$$

$$L_{X1W1} = \frac{L_{X2W2}}{2} = L_{X3W3} = -\pi^2 H s_{55}, \quad L_{Y1W1} = L_{Y2W2} = \frac{L_{Y3W3}}{2} = -\pi^2 \alpha H s_{44},$$

$$L_{W1X1} = \frac{L_{W2X2}}{2} = L_{W3X3} = -\frac{\pi s_{55}}{H}, \quad L_{W1Y1} = L_{W2Y2} = \frac{L_{W3Y3}}{2} = -\frac{\pi \alpha S_{44}}{H},$$

$$L_{W1W1} = \pi^2(\alpha^2 s_{44} + s_{55}) + \frac{a_{11}a_{12}a_{22}a_{66}(r_x + \alpha^2 r_y)^2}{H^2 r_x^2 r_y^2 \{a_{11}a_{12}a_{66} + \alpha^2 a_{11}a_{22}(a_{12} + 2a_{66}) + \alpha^4 a_{12}a_{22}a_{66}\}},$$

$$L_{W2W2} = \pi^2(\alpha^2 s_{44} + 4s_{55}) + \frac{a_{11}a_{12}a_{22}a_{66}(r_x + \alpha^2 r_y)^2}{H^2 r_x^2 r_y^2 \{16a_{11}a_{12}a_{66} + 4\alpha^2 a_{11}a_{22}(a_{12} + 2a_{66}) + \alpha^4 a_{12}a_{22}a_{66}\}},$$

$$L_{W3W3} = \pi^2(4\alpha^2 s_{44} + s_{55}) + \frac{a_{11}a_{12}a_{22}a_{66}(r_x + \alpha^2 r_y)^2}{H^2 r_x^2 r_y^2 \{a_{11}a_{12}a_{66} + 4\alpha^2 a_{11}a_{22}(a_{12} + 2a_{66}) + 16\alpha^4 a_{12}a_{22}a_{66}\}},$$

$$(A_{11}^*, A_{12}^*, A_{22}^*, A_{66}^*) = \frac{1}{E_T h}\left(\frac{1}{a_{11}}, \frac{1}{a_{12}}, \frac{1}{a_{22}}, \frac{1}{a_{66}}\right),$$

$$(D_{11}, D_{12}, D_{22}, D_{66}) = E_T h^3 (d_{11}, d_{12}, d_{22}, d_{66}), \quad (S_{44}, S_{55}) = \frac{E_T h^3}{a^2}(s_{44}, s_{55}),$$

$$\alpha = \frac{a}{b}, \quad H = \frac{h}{a}, \quad r_x = \frac{R_x}{a}, \quad r_y = \frac{R_y}{a}.$$

It is to be noted that the nondimensional linear natural frequency ω_i is related to the linear natural frequency $\overline{\omega_i}$ by $\omega_i = \overline{\omega_i}(\rho a^4/E_T h^3)^{1/2}$.

References

[1] Chia, C. Y., 1980, *Nonlinear Analysis of Plates*, McGraw-Hill, New York.

[2] Chia, C. Y., 1988, ''Geometrically Nonlinear Behavior of Composite Plates: A Review,'' ASME Appl. Mech. Rev., **41**, pp. 439–451.

[3] Sathyamoorthy, M., 1987, ''Nonlinear Vibration Analysis of Plates: A Review and Survey of Current Developments,'' ASME Appl. Mech. Rev., **40**, pp. 1553–1561.

[4] Fu, Y. M., and Chia, C. Y., 1989, ''Multi-Mode Non-Linear Vibration and Post-buckling of Anti-Symmetric Imperfect Angle-Ply Cylindrical Thick Panels,'' Int. J. Non-Linear Mech., **24**, pp. 365–381.

[5] Fu, Y. M., and Chia, C. Y., 1993, ''Non-Linear Vibration and Postbuckling of Generally Laminated Circular Cylindrical Thick Shells With Non-Uniform Boundary Conditions,'' Int. J. Non-Linear Mech., **28**, pp. 313–327.

[6] Raouf, R. A., and Palazotto, A. N., 1994, ''On the Non-Linear Free Vibrations of Curved Orthotropic Panels,'' Int. J. Non-Linear Mech., **29**, pp. 507–514.

[7] Xu, C. S., Xia, Z. Q., and Chia, C. Y., 1996, ''Non-Linear Theory and Vibration Analysis of Laminated Truncated, Thick, Conical Shells,'' Int. J. Non-Linear Mech., **31**, pp. 139–154.

[8] Cheung, Y. K., and Fu, Y. M., 1995, ''Nonlinear Static and Dynamic Analysis for Laminated, Annular, Spherical Caps of Moderate Thickness,'' Nonlinear Dyn., **8**, pp. 251–268.

[9] Hadian, J., Nayfeh, A. H., and Nayfeh, J. F., 1995, ''Modal Interaction in the Response of Antisymmetric Cross-ply Laminated Rectangular Plates,'' J. Vib. Control, **1**, pp. 159–182.

[10] Abe, A., Kobayashi, Y., and Yamada, G., 1998, ''Two-Mode Response of Simply Supported, Rectangular Laminated Plates,'' Int. J. Non-Linear Mech., **33**, pp. 675–690.

[11] Abe, A., Kobayashi, Y., and Yamada, G., 1998, ''Internal Resonance of Rectangular Laminated Plates With Degenerate Modes,'' JSME Int. J., Ser. C, **41**, pp. 718–726.

[12] Abe, A., Kobayashi, Y., and Yamada, G., 1998, ''Three-Mode Response of Simply Supported, Rectangular Laminated Plates,'' JSME Int. J., Ser. C, **41**, pp. 51–59.

[13] Yasuda, K., and Kushida, G., 1984, ''Nonlinear Forced Oscillations of a Shallow Spherical Shell,'' Bull. JSME, **27**, pp. 2233–2240.

[14] Nayfeh, A. H., and Raouf, R. A., 1987, ''Nonlinear Forced Response of Infinitely Long Circular Cylindrical Shells,'' ASME J. Appl. Mech., **54**, pp. 571–577.

[15] Nayfeh, A. H., Raouf, R. A., and Nayfeh, J. F., 1991, ''Nonlinear Response of Infinitely Long Circular Cylindrical Shells to Subharmonic Radial Loads,'' ASME J. Appl. Mech., **58**, pp. 1033–1041.

[16] Chin, C., and Nayfeh, A. H., 1996, ''Bifurcation and Chaos in Externally Excited Circular Cylindrical Shells,'' ASME J. Appl. Mech., **63**, pp. 565–574.

[17] Chia, C. Y., 1987, ''Nonlinear Vibration and Postbuckling of Unsymmetrically Laminated Imperfect Shallow Cylindrical Panels with Mixed Boundary Conditions Resting on Elastic Foundation,'' Int. J. Eng. Sci., **25**, pp. 427–441.

[18] Yamaguchi, T., and Nagai, K., 1997, ''Chaotic Vibrations of Cylindrical Shell-Panel With an In-Plane Elastic-Support at Boundary,'' Nonlinear Dyn., **13**, pp. 259–277.

[19] Eslami, H., and Kandil, O. H., 1989, ''Nonlinear Forced Vibration of Ortho-

tropic Rectangular Plates using Method of Multiple Scales,'' AIAA J., **27**, pp. 961–967.
[20] Sassi, S., Thomas, M., and Laville, F., 1996, ''Dynamic Response Obtained by Direct Numerical Integration for Pre-Deformed Rectangular Plates Subjected to In-Plane Loading,'' J. Sound Vib., **191**, pp. 67–83.
[21] Nayfeh, A. H., and Balachandran, B., 1995, *Applied Nonlinear Dynamics*, John Wiley and Sons, New York.
[22] Tamura, H., and Matsuzaki, K., 1996, ''Numerical Scheme and Program for the Solution and Stability Analysis of a Steady Periodic Vibration Problem,'' JSME Int. J., Ser. C, **39**, pp. 456–463.
[23] Vinson, J. R., and Seerakowski, R. L., 1986, *The Behavior of Structures Composed of Composite Materials*, Martinus Nijhoff Publishers, Dordrecht.
[24] Kobayashi, Y., and Leissa, A. W., 1995, ''Large Amplitude Free Vibration of Thick Shallow Shells Supported by Shear Diaphragms,'' Int. J. Non-Linear Mech., **30**, pp. 57–66.
[25] Wolf, A., Swift, J. B., Swinney, H. L., and Vastano, J. A., 1985, ''Determining Lyapunov Exponents From a Time Series,'' Physica D, **16**, pp. 285–317.

Effect of Curved Bar Properties on Bending of Curved Pipes

V. P. Cherniy
Department of Strength and Stability of Pipelines,
Scientific Research Institute of Natural Gases and Gas Technologies,
VNIIGAZ,
Russian Joint-Stock Company "GAZPROM,"
Moscow, Russia

A general solution is presented for in-plane bending of a thin-walled short-radius curved pipe. The problem is solved considering the properties of a curved bar—an actual radius of curvature of longitudinal fibers and the neutral line displacement. The theory is developed using minimization of the total energy. The relationships of the theory of elastic thin shells are used. The obtained results for the strains and stresses in curved short-radius pipe bends are compared with published theoretical and experimental data. The properties of a curved bar being taken into account enable to correct seriously the distribution and peak values of the strains which take place in curved pipes of large curvature subjected to bending. [DOI: 10.1115/1.1357518]

Introduction

Bending of a curved pipe is accompanied by the flattening forces. They transform initial circular cross sections of a pipe into oval cross sections. As a result, longitudinal stresses in the curved pipe increase and their distribution changes. The rigidity of a curved pipe subjected to bending decreases as compared to that of a straight pipe with the same cross section. It causes significant meridional bending stresses. The classical theory for bending of curved pipes was developed by Karman [1]. He was the first who analyzed the reasons for significant decrease of their bending rigidity. His work and the majority of other studies assumed that actual curvature of longitudinal fibers of a curved pipe should not be taken into account. This curvature was considered to be equal to the center line curvature. This assumption leads to an error in results if applied to pipes with a small radius of curvature. The study by Clark and Reissner [2] presents an example in which an actual curvature of longitudinal fibers is given in problem formulation but ignored in problem solution. A few works tried to take actual curvature of longitudinal fibers into account. The most complete solution for this problem was developed by Cheng and Thailer [3,4].

It is known that the approximate theory of bending of a curved rigid bar deals with the two factors:

(1) actual curvature of longitudinal fibers;
(2) displacement of the neutral line from the center line of a bar cross section.

The second factor was ignored in the theory of bending of a curved pipe. The appropriate question seems to be first raised in the study by Stasenko and Rakhmanova [5]. However, their paper contains a mistaken hypothesis applied to the statics condition. As a result, the neutral line displacement in a curved pipe was supposed to be equal to that in a rigid curved tubular bar with the same cross section. It will be shown in the present paper that this way of solving the problem is incorrect.

The problem of in-plane bending of a curved short-radius pipe bend solved in the present paper allows for both the actual radius of curvature of longitudinal fibers and the neutral line displacement. The latter factor's consideration provides the conditions of pure bending of a curved pipe since it meets the requirement that the longitudinal force equals zero. The neutral line displacement is assumed to be unknown and is determined through the statics condition. The relationships of the theory of elastic thin shells are used for the displacements, strains, and stresses. The solution uses the minimization of the total energy in the manner of Rayleigh-Ritz. The strain energy and neutral line displacement are determined through integration in the closed form. The analysis applied to pipes of uniform thickness with a constant mean radius of the cross section and constant curvature of the center line, and made of an isotropic material. Our solution is compared to the ordinary theory of curved pipes, the results of studies by Cheng and Thailer [3], and the published experimental data by Vissat and Del Buono [6]. As a whole, consideration of the new parameters has resulted in essential correction of the diagrams and peak values of the strains in short-radius curved pipes.

Contributed by the Applied Mechanics Division of THE AMERICAN SOCIETY OF MECHANICAL ENGINEERS for publication in the ASME JOURNAL OF APPLIED MECHANICS. Manuscript received by the ASME Applied Mechanics Division, May 23, 2000; final revision, Oct. 19, 2000. Associate Editor: S. Kyriakides. Discussion on the paper should be addressed to the Editor, Professor Lewis T. Wheeler, Department of Mechanical Engineering, University of Houston, Houston, TX 77204-4792, and will be accepted until four months after final publication of the paper itself in the ASME JOURNAL OF APPLIED MECHANICS.

Formulation of Problem

Figure 1 shows a curved, circular thin-walled pipe with the center line curvature radius R, mean radius of cross section r and wall thickness t. It is assumed that the curved pipe has no restrictions on size of the radius ratio $\lambda = r/R$. The only condition is $\lambda < 1$. This condition is both a natural limit for a curved pipe design and a sine qua non for existence of the certain integrals used further in the paper. Thus, the presented theory is applicable to pipes of any large curvature.

It is supposed that the theory of thin shells may be applied to the pipes in question. Under pure in-plane bending of the pipe by the moments M, the central angle ψ has a change $\Delta\psi$. It is also implied that the neutral line is displaced from the central line at a distance of s_n. The points on the middle line of the pipe cross section are determined through the radius r and angular coordinate β. The vertical coordinate (in the direction of the OY-axis) is

$$y = r\cos\beta. \tag{1}$$

Flattening of the cross section is accompanied by the radial displacement w and tangential displacements v of the points on the cross section middle line (Fig. 1), and also by vertical displacements (parallel to the axis OY) of the same points w_y. The following geometrical formula describes their interrelations:

$$w_y = w\cos\beta - v\sin\beta. \tag{2}$$

Let the approximate theory of curved bars be applied to the "bar" components of longitudinal strains in a curved pipe. It assumes that the hypothesis of flat cross sections is true. A longitudinal filament *a-a* is located at a distance of $s_n + y$ from the neutral line. The "bar" component of the longitudinal strain for *a-a* filament with a curvature radius $R_y = R + y$ is equal to

$$(\varepsilon_1^0)_{a-a} = \frac{(s_n + y)\Delta\psi}{R_y\psi} = \frac{r}{R} * \frac{s + \cos\beta}{1 + \lambda\cos\beta} * \frac{\Delta\psi}{\psi}, \tag{3}$$

where $s = s_n/r$.

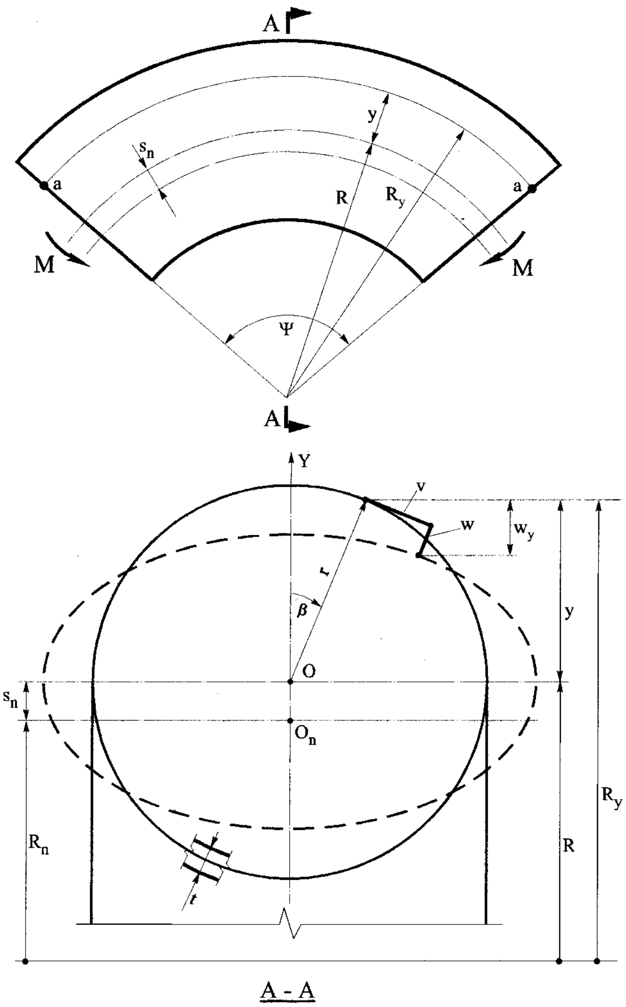

Fig. 1 Bending of a curved circular pipe

A relative change of the central angle of the curved pipe $\Delta\psi/\psi$ is expressed further through a curvature change κ_0 of the appropriate straight pipe with the same length L and the same cross section. For this purpose we use the definition of rigidity factor K for a curved pipe. Under influence of the identical bending moments M on curved and straight pipes the rigidity factor is equal to

$$K=\frac{(\Delta\psi)_0}{\Delta\psi}, \tag{4}$$

where $(\Delta\psi)_0$ is the angle change in a straight pipe under bending.

According to the beam theory there are relationships which connect the curvature change of a straight pipe with the angle change and the bending moment:

$$(\Delta\psi)_0=\kappa_0 L; \quad \kappa_0=M/EI, \tag{5}$$

where EI is the straight pipe rigidity under bending.

It also necessary to mention that the central angle of a curved pipe is equal to

$$\psi=L/R. \tag{6}$$

Putting the relations (4)–(6) together we have

$$\frac{\Delta\psi}{\psi}=\frac{R}{r}\frac{1}{K}(\kappa_0 r). \tag{7}$$

Substituting (7) into (3) we obtain the formula for longitudinal "bar" strains:

$$\varepsilon_1^0=\frac{1}{K}\frac{s+\cos\beta}{1+\lambda\cos\beta}(\kappa_0 r). \tag{8}$$

It should be noticed that the product $\kappa_0 r$ is a value convenient for comparison because it means the maximal longitudinal strain in a straight pipe subjected to bending by the moment M.

Longitudinal Strains

The total longitudinal strains consist of the bar strains (8) and the strains caused by flattening the cross section contours in a curved pipe:

$$\varepsilon_1=\frac{1}{K}\frac{s+\cos\beta}{1+\lambda\cos\beta}(\kappa_0 r)+\frac{w_y}{R+y}. \tag{9}$$

Radial components of the displacements may be presented as a series:

$$w=(\kappa_0 r^2)\sum_{n=2}^{\infty} X_n\cos n\beta, \tag{10}$$

where X_n are unknown coefficients of the series.

The expression for tangential displacements may be obtained based on the thin shells theory hypothesis of inextensibility of the middle surface in the meridional direction:

$$\frac{\partial v}{\partial\beta}+w\approx 0: \tag{11}$$

$$v=-(\kappa_0 r^2)\sum_{n=2}^{\infty} n^{-1}X_n\sin n\beta. \tag{12}$$

It is important to pay attention to the "inextensibility" concept which means no as absence of lengthening of a mean line of cross section as a result of displacements in a curved pipe as a thin shell only. However, there are meridional membrane stresses in curved pipes, and this fact was mentioned, for example, by Cheng and Thailer [3,4].

According to (2), (10) and (12) the expression (9) takes the following form:

$$\varepsilon_1=\left(\frac{1}{K}\frac{s+\cos\beta}{1+\lambda\cos\beta}+\frac{1}{2}\frac{r}{R}\sum_{n=2}^{\infty} X_n w_n^*\right)(\kappa_0 r) \tag{13}$$

where

$$w_n^*=\frac{1}{1+\lambda\cos\beta}\left[\frac{n+1}{n}\cos(n-1)\beta+\frac{n-1}{n}\cos(n+1)\beta\right]. \tag{14}$$

It should be emphasized that the radius ratio λ is applied only to those terms which refer to the actual curvature of longitudinal fibers. At the same time, the ratio r/R is used in the same way as in the ordinary theory of curved pipe bending.

A relative displacement of the neutral line s and rigidity factor K can be found from the statics conditions:

$$N=0: \quad Ert\int_0^{2\pi}\varepsilon_1 d\beta=0. \tag{15}$$

$$M=Ert\int_0^{2\pi}\varepsilon_1 y\, d\beta. \tag{16}$$

The former condition (15) provides pure bending of a curved pipe (N is the longitudinal force).

Hereinafter (in the definition of potential strain energy) the integration is carried out in the closed form. All certain integrals may be presented as a sum of integrals described by the following general formula:

$$\int_0^{2\pi}\frac{\cos n\beta}{1+\lambda\cos\beta}d\beta=(-1)^n\frac{2e^n}{a}\pi\quad n=0,1,2,3,\ldots;\quad \lambda<1, \tag{17}$$

where

$$e=\frac{1}{\lambda}(1-\sqrt{1-\lambda^2});\quad (\lambda<1), \tag{18}$$

$$a=1-\lambda e. \tag{19}$$

From (15) and (16) it follows that

$$s=K\frac{a}{1-e^2}e, \tag{20}$$

$$K=\left(\frac{a}{1-e^2}-\frac{1}{2}\frac{r}{R}\sum_{n=2}^{\infty}C_nX_n\right)^{-1}, \tag{21}$$

$$C_n=(-1)^n\frac{1}{n}e^{n-2}[(n+1)+(n-1)e^2]. \tag{22}$$

The e value (see (18)) has a quite certain physical interpretation. This is the neutral line displacement divided by radius r for a conditionally rigid curved pipe subjected to bending. This is equal to the displacement in a curved bar with a tubular cross section. In such rigid bar there is conditionally no flattening of cross sections. The expression (18) for e is received by consideration of the statics conditions (15) and (16) for this curved bar.

Formulating the problem, Stasenko and Rakhmanova [5] assume the parameter s in the formula (9) for longitudinal strains in a curved pipe to be equal to the parameter e for a rigid curved bar with a tubular cross section. As the ratio of the parameters s and e is equal approximately to the rigidity factor K according to the expression (20), the results of Stasenko and Rakhmanova [5] are rather far from reality.

Finally, with (20) and (21), the formula for longitudinal strains (13) may be rewritten as

$$\varepsilon_1=\left[\frac{a}{1-e^2}\frac{e+\cos\beta}{1+\lambda\cos\beta}+\frac{1}{2}\frac{r}{R}\sum_{n=2}^{\infty}X_n\left(w_n^*-C_n\frac{\cos\beta}{1+\lambda\cos}\right)\right]\times(\kappa_0 r). \tag{23}$$

The ratio $a/(1-e^2)$ in the formula (23) is the rigidity factor of a curved bar with a tubular cross section.

Determination of Unknown Coefficients

Coefficients X_n of the series (10) are determined through minimization of the total energy V

$$V=U-W, \tag{24}$$

where

U is strain energy;
W is potential energy of end moments.

Strain energy is determined according to the expression:

$$U=\frac{1}{2}r(R\psi)\int_0^{2\pi}(1+\lambda\cos\beta)(Et\varepsilon_1^2+D\kappa_2^2)d\beta, \tag{25}$$

where ε_1 is the longitudinal strain, κ_2 is the curvature change of the middle line of a pipe cross section, E is the modulus of elasticity, $D=Et^3/12(1-\nu^2)$, ν is Poisson's ratio.

Potential energy of end moments,

$$W=-M*\Delta\psi=-\kappa_0^2EI(R\psi)\left(\frac{1}{1-e^2}-\frac{1}{2}\frac{r}{R}\sum_{n=2}^{\infty}C_nX_n\right). \tag{26}$$

In (26) the expressions (5), (7), (21) are used.

The curvature change of the middle line κ_2 is determined according to the theory of shells,

$$\kappa_2=-\frac{1}{r^2}\left(\frac{d^2}{d\beta^2}+1\right)w. \tag{27}$$

If (10) is taken into account, then

$$\kappa_2=\kappa_0\sum_{n=2}^{\infty}(n^2-1)X_n\cos n\beta. \tag{28}$$

The minimum of total energy may be obtained in the Rayleigh-Ritz manner if

$$\frac{\partial V}{\partial X_n}=0. \tag{29}$$

Substituting (25) and (26) into (24), integrating it and meeting the requirements (29) we have an infinite system of linear equations describing unknown coefficients:

$$a_{n,n}X_n+\sum_{\substack{i=2\\ i\neq n}}^{\infty}a_{n,i}X_i=b_n,\quad n=2,3,4,\ldots. \tag{30}$$

The coefficients $a_{n,n}$, $a_{n,i}$ and free terms b_n in the set of Eqs. (30) are determined by the following expressions:

$$a_{n,n}=4\left[U_{n,n}^*+\frac{(n^2-1)^2}{3(1-\nu^2)}h^2\right]$$

$$a_{n,i}=4U_{n,i}^*+\delta_{i(n\pm1)}\left[\lambda\frac{2}{3(1-\nu^2)}(n^2-1)(i^2-1)h^2\right]$$

$$b_n=-8\frac{R}{r}\frac{1-e^2}{a}C_n, \tag{31}$$

where h is the curved pipe parameter: $h=Rt/r^2$,

$$U_{n,n}^*=(a^{-1})\left[(1+e^{2n-2})\left(1+2\frac{n-1}{n+1}e^2\right)\left(\frac{n+1}{n}\right)^2+(1+e^{2n+2})\times\left(\frac{n-1}{n}\right)^2\right]-\frac{1+e^2}{a}C_n^2;$$

$$U_{n,i}^*=\frac{(-1)^{n-i}}{ani}[(n+1)u_1+(n-1)u_2]-\frac{1+e^2}{a}C_nC_i;$$

$$u_k=(i+1)\lfloor e^{n+i+2(k-2)}+e^{|n-i+2(k-1)|}\rfloor+(i-1)\lfloor e^{n+i+2(k-1)}+e^{|n-i+2(k-2)|}\rfloor;\quad (k=1,2)$$

$$\delta_{i(n\pm1)}=\begin{cases}1 & (i=n\pm1)\\ 0 & (i\neq n\pm1).\end{cases} \tag{32}$$

The C_i values are calculated under the formula (22) in which n is replaced with i.

Strains and Stresses

The longitudinal strains are determined under (23). The expression for meridional bending strains follows from (28) (the top mark refers to the outer surface of a pipe):

$$\varepsilon_2=\pm\frac{1}{2}h\frac{r}{R}\kappa_0 r\sum_{n=2}^{\infty}(n^2-1)X_n\cos n\beta. \tag{33}$$

The longitudinal stresses only are considered in this paper. They are described by the expression:

$$\sigma_1=\frac{E}{1-\nu^2}(\varepsilon_1+\nu\varepsilon_2). \tag{34}$$

From the Presented Theory to the Ordinary Theory of Curved Pipes

We understand the term "ordinary theory of curved pipes" as a solution without regard to parameters λ and s ([1]). The accuracy of this solution is determinated by the number of terms in the series (10) ($n=2,3,4,\ldots$). The ordinary theory can be received as a particular case of our solution provided that $\lambda\to 0$. In this case, from (18) by applying L'Hopital's rule we get

$$\lim e|_{\lambda\to 0}=0. \tag{35}$$

Then according to (19) and (20) we have $a=1$; $s=0$. From (22) it follows that

$$\lim C_n|_{\substack{n=2\\ e\to 0}}=3/2. \tag{36}$$

If $n\geqslant 3$: $C_n=0$.
Under the above conditions the ordinary theory of curved pipes is obtained.

Results and Discussion

We received numerical results for the curved pipes parameter h ranging from 0.05 to 0.30. This range practically covers the main part of short-radius curved pipes.

The effect of the curved bar properties on the bending theory of curved pipes is estimated by comparison of our basic solution ($\lambda\neq 0$, $s\neq 0$) with the ordinary theory of curved pipes ($\lambda=0$, $s=0$) ([1]). Thus, the calculations are made for two values of the curvature parameter ($\lambda=0.8$ and $\lambda=0.5$).

To evaluate the separate influence of the neutral line displacement on numerical results we also developed a solution, in which the actual curvature of longitudinal fibers is considered only ($\lambda\neq 0$, $s=0$). This solution should be qualified as an intermediate variant of our basic theory. The results of the basic solution are compared also to this intermediate variant.

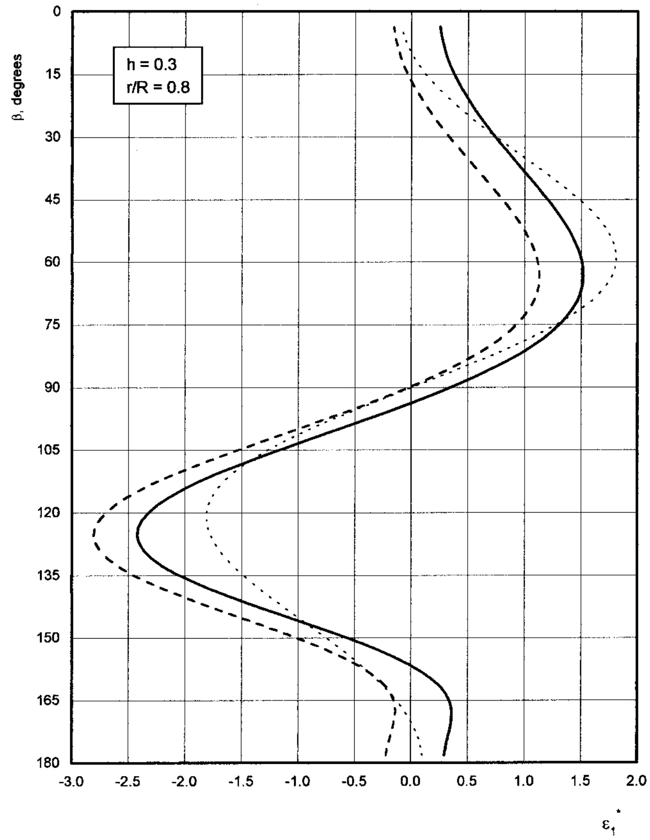

Fig. 3 Longitudinal strain distribution; (*a*) presented theory $\lambda\neq 0$, $s\neq 0$ (solid line), (*b*) intermediate variant $\lambda\neq 0$, $s=0$ (dashed line), (*c*) ordinary theory $\lambda=0$, $s=0$ (dotted line)

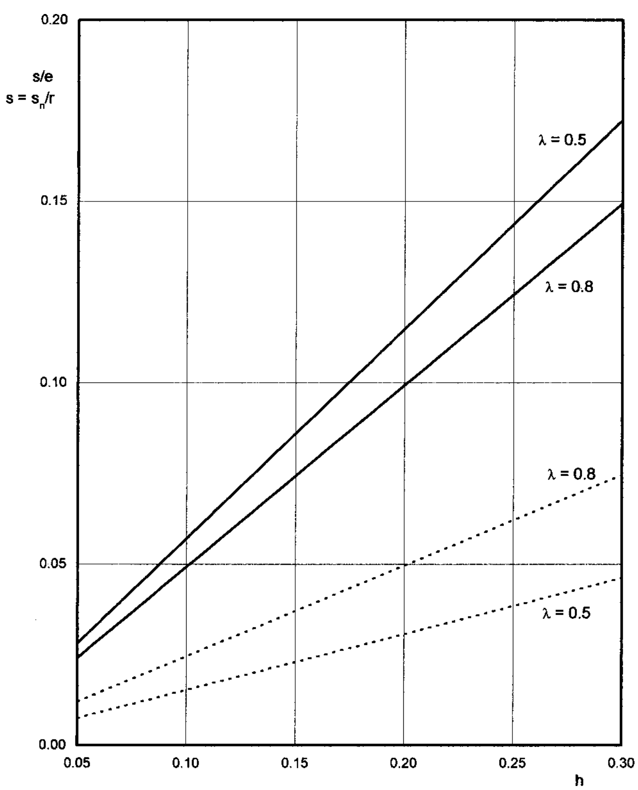

Fig. 2 Displacements of the neutral line of curved pipes; (*a*) s/e (solid line), (*b*) $s=s_n/r$ (dotted line)

The neutral line displacement (20) may be judged by the diagrams for function of the ratios s/e and $s=s_n/r$ from the curved pipe parameter h (Fig. 2). It follows from the diagrams that the neutral line displacement in a curved pipe is rather little in comparison with the displacement e in a rigid curved bar with a tubular cross section. However, it is shown further that the neutral line displacement if taken into account enables to revise the distribution and peak values of the strains.

In what follows the strains and stresses are presented as dimensionless ratios:

- for strains:

$$\varepsilon^*_{()}=\frac{\varepsilon_{(\,)}}{\kappa_0 r}; \tag{37}$$

- for stresses:

$$\sigma^*_{(\,)}=\frac{\sigma_{(\,)}}{E(\kappa_0 r)}. \tag{38}$$

Figure 3 shows the longitudinal strain distribution for a curved pipe with parameters $h=0.3$, $r/R=0.8$. The strain distribution is found: (*a*) under our basic solution, (*b*) under the intermediate variant of our theory, and (*c*) under the ordinary theory of curved pipes bending. The comparison shows that for the peak values of longitudinal strains the results of our basic theory are located between the results of the ordinary theory and our intermediate variant of the basic theory. The diagrams in Fig. 3 show that the neutral line displacement influences the longitudinal strains considerably.

The influence of the curvature parameter λ on the longitudinal strains distribution is reasonable. It is illustrated by the diagrams in Fig. 4 for a curved pipe with $h=0.3$. The calculations are made

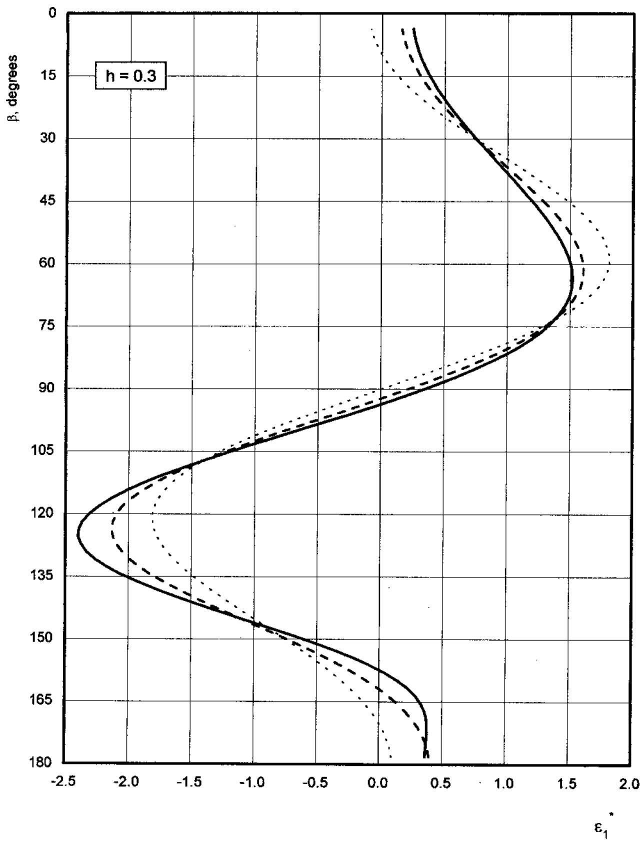

Fig. 4 Longitudinal strain distribution; (*a*) λ=0.8 (solid line), (*b*) λ=0.5 (dashed line), (*c*) ordinary theory λ=0, *s*=0 (dotted line)

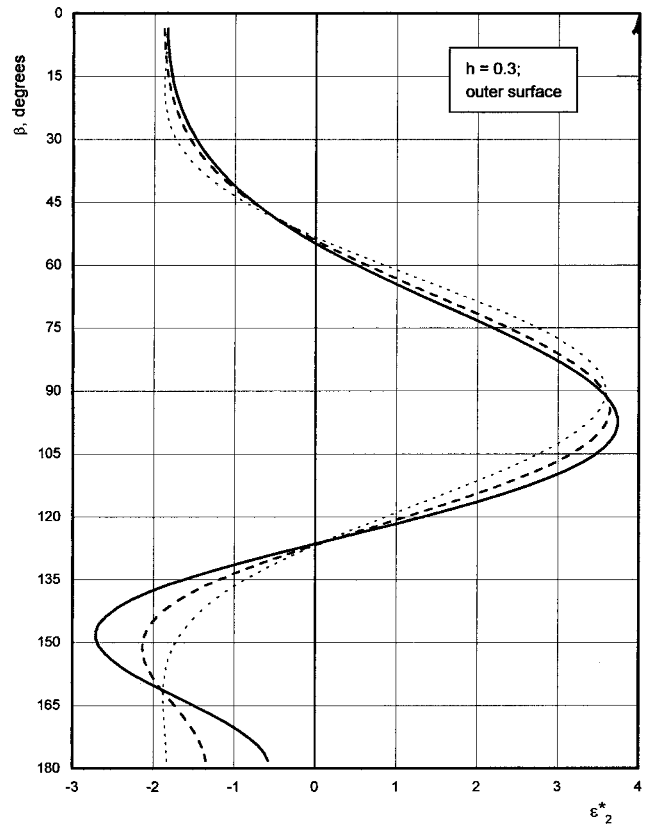

Fig. 5 Meridional bending strain distribution; (*a*) λ=0.8 (solid line), (*b*) λ=0.5 (dashed line), (*c*) ordinary theory λ=0, *s*=0 (dotted line)

under our basic theory and under the ordinary theory of curved pipes. Increase of the parameter λ causes consistent decrease of the longitudinal strains on the convex part of a curved pipe and increase of the strains on the concave part.

The divergences of peak values for the longitudinal strains calculated according to our basic theory for two values of parameter λ (0.8 and 0.5) and two values of h (0.05 and 0.30) are given in Table 1. Analysis of the table data shows that our theory essentially revises the peak values of longitudinal strains in comparison with both the ordinary theory and the variant which takes into account the actual curvature of longitudinal fibers only.

Meridional bending strain distributions under our basic solution and under the ordinary theory differ insignificantly on the most part of a curved pipe cross section. The exception is constituted by the concave part of cross section at $130\,\text{deg} \leqslant \beta \leqslant 180\,\text{deg}$ (see Fig. 5). For this part of cross section our theory presents essential revision in the distribution and peak values of the meridional bending strain.

Table 1 Differences (percent) in maximum values of the longitudinal strains compared to the presented basic theory

solution	sign of strains	$\lambda = 0.8$		$\lambda = 0.5$	
		$h = 0.05$	$h = 0.30$	$h = 0.05$	$h = 0.30$
$\lambda = 0$, $s = 0$	extension	+11	+20	+6	+13
	compression	-14	-26	-9	-15
$\lambda \neq 0$, $s = 0$	extension	-7	-25	-6	-15
	compression	+6	+16	+4	+11

The longitudinal stresses are compared with published theoretical and experimental data. Figure 6 presents diagrams of longitudinal stresses for the outer surface of a curved pipe with $h = 0.071527$, $r/R = 0.512$. The comparison shows that our solution is consistent with the experimental data received by Vissat and Del Buono [6]. In the same figure there is a diagram which presents the theoretical results obtained by Cheng and Thailer [3], in which parameter λ was taken into account only. The comparison shows that our solution gives the better approximation to the results of experiment (Fig. 6) for the peak values of longitudinal stresses.

The calculations under our basic theory and under the ordinary theory have shown that the rigidity factors of curved pipes do not practically depend on the parameters λ and s provided that these parameters are used together. In the given range of parameters h and λ the maximal divergence in the values of the rigidity factors is 1.7 percent.

The calculations under our technique for the given examples are executed by taking view of eight terms in initial expansion into a series (10) (to the 9th harmonic included). The calculations under the ordinary theory are executed including the 8th harmonic in (10). This way provided the high accuracy of calculations and reliability of the compared results.

Conclusions

• The presented theory of in-plane bending of curved pipes takes into account the both factors describing longitudinal strains in a curved bar:

- actual curvature of longitudinal fibers;
- displacement of the neutral line as related to the central line of a pipe.

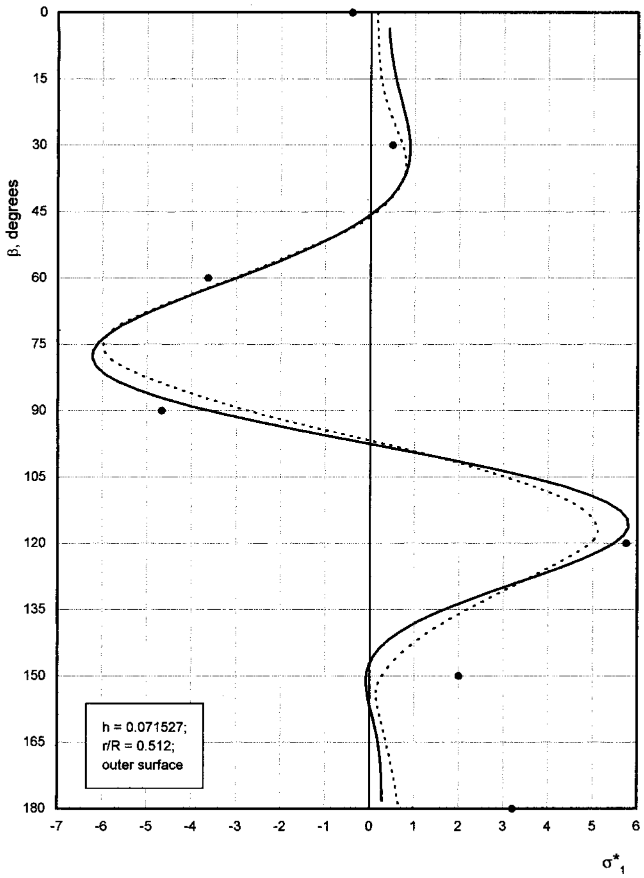

Fig. 6 Longitudinal stress distribution; (*a*) presented theory $\lambda \neq 0$, $s \neq 0$ (solid line), (*b*) Cheng and Thailer [3] $\lambda \neq 0$, $s = 0$ (dashed line), (*c*) experimental data of Vissat and Del Buono [6] (solid circles)

• The neutral line displacement being taken into account provides the conditions for pure bending of a curved pipe. The displacement is considered unknown and determined from the statics condition.

• The solution is developed using minimization of the total energy in the manner of Rayleigh-Ritz. Basic relations of the theory of elastic thin shells are also used.

•The solution is presented as the infinite set of linear equations. The formulas are given for the coefficients and free terms of the set of equations.

• The closed-form solution for integrals is obtained for the strain energy and neutral line displacement. In the expressions for integrals there are the parameters which characterize bending of curved rigid bars with a tubular cross section.

• The presented theory is applicable to pipes of any large curvature.

• It is shown that the ordinary theory of curved pipes can be obtained as a particular case of the presented solution.

• The formulas for the displacements, strains, stresses and the rigidity factor of curved pipes are obtained which include the parameters describing the large curvature of pipes.

• The obtained results are compared to:

- the ordinary theory of curved pipes;
- the solution which takes into account an actual curvature of fibers only;
- the published experimental data.

• The rigidity factor does not materially depend on the parameters describing bending of short-radius pipes provided that these parameters are used together.

• The neutral line displacement and the actual curvature of longitudinal fibers have provided the essential correction of the distribution and peak values of longitudinal strains in curved short-radius pipes under bending.

• The presented theory essentially revises the meridional bending strains distribution for the concave part of cross sections of curved pipes.

References

[1] Karman, Th., 1911, ''Über die Formänderung dünnwandiger Rohre, insbesondere federnder Ausgleichrohre,'' Z. Ver. Deut. Ing., **55**, pp. 1889–1895.

[2] Clark, R. A., and Reissner, E., 1951, ''Bending of Curved Tubes,'' *Advances in Applied Mechanics*, Vol. II, Academic Press, San Diego, pp. 93–122.

[3] Cheng, D. H., and Thailer, H. J., 1968, ''In-Plane Bending of Curved Circular Tubes,'' J. Eng. Ind., **90**, Series B, No. 4, pp. 666–670.

[4] Cheng, D. H., and Thailer, H. J., 1970, ''On Bending of Curved Circular Tubes,'' J. Eng. Ind., **92**, Series B, No. 1, pp. 62–66.

[5] Stasenko, I. V., and Rakhmanova, I. I., 1986, ''Analysis of Thin-Walled Pipes of the Large Curvature,'' *Strength Analyses*, Vol. 27, Mashinostroienie, Moscow, pp. 57–69. (in Russian).

[6] Vissat, P. L., and Del Buono, A. J., 1955, ''In Plane Bending Properties of Welding Elbows,'' Trans. ASME, **77**, pp. 161–175.

X. Markenscoff
Fellow ASME

L. Ni

Department of Mechanical and Aerospace Engineering,
University of California, San Diego,
La Jolla, CA 92093-0411

The Transient Motion of a Ramp-Core Supersonic Dislocation

The transient motion of a ramp-core dislocation spreading from $-\infty<x<\infty$ and jumping from rest to a supersonic speed in the x direction, is investigated by analysis on the complex transform plane. The new result of this analysis is that, instead of the Mach cone of the Volterra dislocation, there are two lines of discontinuity (of the stress) propagating in the $\pm z$ directions, inside of which there are arctan delta sequence ($\varepsilon\neq 0$) radiated supersonic fields, as well as subsonic fields. The lines of discontinuity arise at the tangent point of the Mach wavefront ($\varepsilon=0$) to the cylinder with radius $r=c_2 t$.
[DOI: 10.1115/1.1380678]

1 Introduction

The transient motion of a supersonic screw dislocation with spread ramp-like core starting from rest and jumping to a constant velocity with which it moves thereafter, is analyzed in detail. The analysis extends previous analysis by the authors (Markenscoff and Ni [1]) for subsonic motion starting from rest with constant velocity. Recently, Gumbsch and Gao [2] showed by a molecular dynamics simulation that dislocations can propagate supersonically if they are created as such. The present analysis complements this molecular dynamics simulation. Previously, general transient supersonic motion of Volterra dislocations had been analyzed by Callias and Markenscoff [3] and steady-state supersonic motion for Peierls dislocations by Weertman [4].

The new result of this analysis is that instead of the Mach cone of the Volterra dislocation there are two lines of discontinuity (of the stress) propagating in the $\pm z$ directions, inside of which there are arctan delta sequence ($\varepsilon\neq 0$) radiated supersonic fields, as well as subsonic fields. The lines of discontinuity arise at the tangent point of the Mach wavefront ($\varepsilon=0$) to the cylinder with radius $r=c_2 t$.

2 Governing Equations

The dislocation with ramp-like displacement-core function satisfies the differential equation for the antiplane strain field:

$$\frac{\partial^2 u}{\partial x^2}+\frac{\partial^2 u}{\partial z^2}=b^2\frac{\partial^2 u}{\partial t^2} \tag{1}$$

with boundary conditions

$$u(x,0,t)=\begin{cases}\dfrac{B}{2}\dfrac{1}{\pi}\left(\arctan\left[\dfrac{x}{\varepsilon}\right]+\dfrac{\pi}{\varepsilon}\right) & t<0\\ \dfrac{B}{2}\dfrac{1}{\pi}\left(\arctan\left[\dfrac{x-l(t)}{\varepsilon}\right]+\dfrac{\pi}{2}\right) & t\geqslant 0\end{cases} \tag{2}$$

where b is the shear wave slowness and B is the Burgers vector. By $x=l(t)$ is denoted the motion on the plane $z=0$.

The solution is obtained as before, by superposition of Problem I and Problem II, which has the solution (Markenscoff and Ni [1])

$$u(x,z,t)=f(x,z,t)*\frac{1}{\pi}\frac{\varepsilon}{\varepsilon^2+x^2}, \tag{3}$$

where $f(x,z,t)$ (Markenscoff [5]) is the solution of the classical Volterra dislocation with core $H(x-l(t))$, and $*$ denotes convolution. This solution is investigated in the sequel.

3 Analysis of the Supersonic Transient Motion

The solution of the Volterra dislocation jumping from rest to a supersonic speed is obtained by using Laplace transform in time and two-sided Laplace transform in space, analogously to Markenscoff [5] for subsonic motion. Following the same notation, we obtain the transform

$$\frac{\partial\hat{u}}{\partial z}(x,z,s)=\frac{B}{2}\frac{s}{2\pi i}\int_{Br}e^{s\lambda x}\frac{\beta}{s(\alpha+\lambda)}e^{-s\beta x}d\lambda, \tag{4}$$

where by α is denoted the dislocation's slowness. The inversion of the Bromwich contour is obtained by a Cagniard-de Hoop (C-H) technique as in Markenscoff [5]. It follows, from (4), that there is a pole at $\lambda=-\alpha$ if α is within the contour of integration. Considering the C-H contour, we see that, if

(i) $\dfrac{bx}{r}<\alpha<b$ there is no pole inside the contour (5)

(ii) $\alpha<\dfrac{bx}{r}$ there is a pole at $\lambda=-\alpha$. (6)

From (i) it follows that, in particular, there is no pole for x<0. Condition (ii) for the existence of a pole, which gives rise to a delta function in the solution, is written

$$x>\frac{\alpha z}{\sqrt{b^2-\alpha^2}} \tag{7}$$

where we consider only $z>0$. For $z<0$ the field is exactly symmetric. By inverting (4), the contribution of the pole is

$$\frac{\mathrm{B}}{2}\sqrt{b^2-\alpha^2}\,\delta(t-\alpha x-\sqrt{b^2-\alpha^2}z), \tag{8}$$

which gives rise to the Mach wavefronts on the line

$$z=\frac{-\alpha x}{\sqrt{b^2-\alpha^2}}+\frac{t}{\sqrt{b^2-\alpha^2}}. \tag{9}$$

Contributed by the Applied Mechanics Division of THE AMERICAN SOCIETY OF MECHANICAL ENGINEERS for publication in the ASME JOURNAL OF APPLIED MECHANICS. Manuscript received by the ASME Applied Mechanics Division, June 12, 2000; final revision, Dec. 14, 2000. Associate Editor: J. R. Barber. Discussion on the paper should be addressed to the Editor, Prof. Lewis T. Wheeler, Department of Mechanical Engineering, University of Houston, Houston, TX 77204-4792, and will be accepted until four months after final publication of the paper itself in the ASME JOURNAL OF APPLIED MECHANICS.

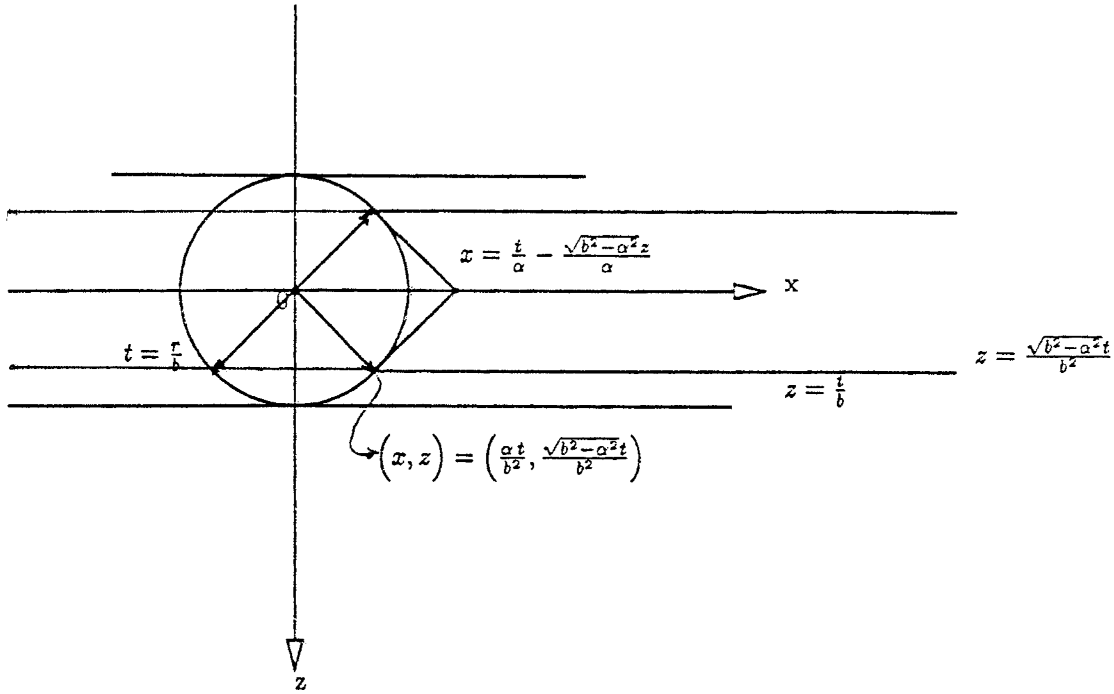

Fig. 1 Lines of discontinuity of the radiated field from a moving supersonic dislocation with ramp-like core

When $\alpha = x/r$, the contribution is half of the value (8).

It is easy to see that the Mach wave (see Fig. 1) meets the cylindrical wavefront $x^2+z^2=(t/b)^2$ at the point $(x,z)=(\alpha t/b^2, \sqrt{b^2-\alpha^2}/b^2 t)$ which lies on the line defined by $x = \alpha z/\sqrt{b^2-\alpha^2}$, i.e., for equality in (7).

The contribution to the solution of the ramp-dislocation from the pole at $\lambda=-\alpha$ is obtained by convolution of (8), i.e.,

$$\frac{\partial u}{\partial z} = \frac{\mathrm{B}}{2\pi}\sqrt{b^2-\alpha^2}\int_{\alpha z/\sqrt{b^2-\alpha^2}}^{\infty}\delta(t-\alpha\xi-\sqrt{b^2-\alpha^2}z)\,\frac{\varepsilon d\xi}{\varepsilon^2+(x-\xi)^2} \tag{10}$$

which yields

$$\frac{\partial u}{\partial z} = \frac{B}{2\pi}\sqrt{b^2-\alpha^2}\,\frac{\varepsilon}{\varepsilon^2+\left(x-\frac{t}{\alpha}+\frac{\sqrt{b^2-\alpha^2}}{\alpha}z\right)^2} \times H\left(t-\frac{b^2}{\sqrt{b^2-\alpha^2}}z\right). \tag{11}$$

The solution given by (11) is valid only for values of ξ in (10) that satisfy

$$\xi > \frac{\alpha z}{\sqrt{b^2-\alpha^2}} \tag{12}$$

since in order to have nonzero contribution, the zero of the delta function must be bigger than the lower limit, i.e.,

$$\xi = \frac{t}{\alpha} - \frac{\sqrt{b^2-\alpha^2}z}{\alpha} > \frac{\alpha z}{\sqrt{b^2-\alpha^2}} \tag{13}$$

inside which the solution exhibits the delta-sequence terms given by (11). Physically the meaning of it is that to the supersonic field will contribute only to those points (in time) of the spread core that lie on the Mach cone.

From (13) follows that

$$z < \frac{t\sqrt{b^2-\alpha^2}}{b^2} \tag{14}$$

which, by consideration of the symmetry in z, defines a strip (see Fig. 1),

$$\frac{-t\sqrt{b^2-\alpha^2}}{b^2} < z < \frac{t\sqrt{b^2-\alpha^2}}{b^2}. \tag{15}$$

We thus see that the lines $z=\pm t\sqrt{b^2-\alpha^2}/b^2$ separate a region in which the solution has a delta-sequence term given by (11) from a region for $z>t\sqrt{b^2-\alpha^2}/b^2$ (and $z<t\sqrt{b^2-\alpha^2}/b^2$, symmetrically) in which this term is absent.

The solution for $\partial u/\partial z(x,z,t)$ has, in addition to (11) which is due to the pole, the contribution from the convolution of the Volterra field which is contained within $t=rb$. This differs in the supersonic case $b>\alpha$ from the subsonic case $\alpha<b$ treated by Markenscoff and Ni [1], since in the evaluation of the convolution integrals by integration in the complex plane, some poles are now real. The convolution integral to be evaluated is given by Eq. (54) of Markenscoff and Ni [1], i.e., but now with $\alpha<b$

$$\int_{-l}^{l}\frac{G(\xi,z,t)}{\sqrt{l^2-\xi^2}(z^2+\xi^2)}\,\frac{\varepsilon}{\varepsilon^2+(x-\xi)^2}\,d\xi \tag{16}$$

where

$$G(x,z,t)=\frac{g_1(x,z,t)}{bg_2(x,z,t)}$$

$$g_1(x,z,t)=t^2[tx+\alpha(z^2-x^2)]+b^2x[\alpha r^2x-t(2z^2+x^2)]$$

$$g_2(x,z,t)=[\alpha x-t+\sqrt{b^2-\alpha^2}z][\alpha x-t-z\sqrt{b^2-\alpha^2}].$$

In order to evaluate (16) by integration in the complex plane, we find the poles of $G(\xi,x,t)/[(z^2+\xi^2)(\varepsilon^2+(x-\xi)^2)]$ which are

$$\text{(i)}\quad \xi=\pm zi,$$

$$\text{(ii)}\quad \xi=x\pm \varepsilon i,$$

$$\text{(iii) the zeros of } g_2(\xi,z,t):$$

$$\xi=\frac{t}{\alpha}\pm z\,\frac{\sqrt{b^2-\alpha^2}}{\alpha}.$$

Note that in the supersonic case, the poles (iii) are now real numbers, as contrasted with those of Eq. (56) of Markenscoff and Ni [1]. We then evaluate the residues as follows:
(i) From the poles $\xi=\pm zi$ the contribution to the solution $\partial u/\partial z\,(x,z,t)$ is

$$\frac{B}{2\pi}H(t-bz)\,\frac{b\varepsilon}{tz}\,\mathrm{Re}\left\{\frac{G(zi,z,t)}{\varepsilon^2+(x-zi)^2}\right\}=\frac{-BxzεH(t-bz)}{(x^2+(z+\varepsilon)^2)(x^2+(z-\varepsilon)^2)}. \tag{18}$$

(ii) From the poles $\xi=x\pm\varepsilon i$ the contribution to $\partial u/\partial z(x,z,t)$ is as in the subsonic case

$$\frac{\mathrm{B}}{2\pi}H(t-bz)\,\frac{1}{\sqrt{r_1r_2}}\,\mathrm{Re}\left\{\frac{G(x+\varepsilon i,z,t)}{z^2+(x+\varepsilon i)^2}\,e^{1/2(\theta_1-\theta_2)i}\right\} \tag{19}$$

where

$$r_1=[(l-x)^2+\varepsilon^2]^{1/2},\quad r_2=[(l+x)^2+\varepsilon^2]^{1/2},$$

$$l=[(t/b)^2-z^2]^{1/2}$$

$$\cos\frac{1}{2}(\theta_1-\theta_2)=\left[\frac{r_1r_2+l^2-x^2+\varepsilon^2}{2r_1r_2}\right]^{1/2},$$

$$\sin\frac{1}{2}(\theta_1-\theta_2)=\frac{\sqrt{2}\varepsilon x}{\sqrt{r_1r_2[r_1r_2+l^2-x^2+\varepsilon^2}}.$$

However, the value of (19) differs from its subsonic counterpart. We define

$$\frac{G(x+\varepsilon i,z,t)}{z^2+(x+\varepsilon i)^2}=\frac{1}{A_3}[R_3+M_3 i] \tag{20}$$

where

$$R_3+M_3 i\equiv g_1(x+\varepsilon i,z,t)[(z^2+x^2-\varepsilon^2)-2x\varepsilon i]\times[(\alpha(x-\varepsilon i)-t)^2-z^2(b^2-\alpha^2)]$$

$$A_3=b^2[x^2+(z+\varepsilon)^2][x^2+(z-\varepsilon)^2][(\alpha x-t+z\sqrt{b^2-\alpha^2})^2+\alpha^2\varepsilon^2]\cdot[(\alpha x-t-z\sqrt{b^2-\alpha^2})^2+\alpha^2\varepsilon^2].$$

By comparison to the subsonic case, we observe that $R_3=R_1$, $M_3=M_1$ where R_1 and M_1 are given in the Appendix of Markenscoff and Ni (2000).

We thus have for the contribution in (19):

$$\mathrm{Re}\left[\frac{G(x+\varepsilon i,z,t)}{z^2+(x+\varepsilon i)^2}\,e^{1/2(\theta_1-\theta_2)i}\right]=\frac{1}{A_3}\left[R_1\cos\frac{1}{2}(\theta_1-\theta_2)-M_1\sin\frac{1}{2}(\theta_1-\theta_2)\right]. \tag{21}$$

To $O(\varepsilon)$ Eq. (21) yields

$$\frac{\pi}{\alpha^2 b\sqrt{r_1r_2}}\,\frac{g_1(x,z,t)\left[\left(x-\frac{t}{\alpha}\right)^2-\frac{z^2D^2}{\alpha^2}\right]\cos\frac{1}{2}(\theta_1-\theta_2)}{(x^2+z^2)\left[\varepsilon^2+\left(x-\frac{t}{\alpha}+\frac{zD}{\alpha}\right)^2\right]\left[\varepsilon^2+\left(x-\frac{t}{\alpha}-\frac{zD}{\alpha}\right)^2\right]}$$

$$+\frac{\pi\sin\frac{1}{2}(\theta_1-\theta_2)}{\alpha zDb\sqrt{r_1r_2}}\,\frac{g_1(x,z,t)}{x^2+z^2}\left[\frac{\varepsilon}{\varepsilon^2+\left(x-\frac{t}{\alpha}-\frac{zD}{\alpha}\right)^2}-\frac{\varepsilon}{\varepsilon^2+\left(x-\frac{t}{\alpha}+\frac{zD}{\alpha}\right)^2}\right]$$

$$-\frac{\pi\sin\frac{1}{2}(\theta_1-\theta_2)}{\alpha zDb\sqrt{r_1r_2}}\,\frac{\left[\frac{\partial g_1}{\partial x}(x^2+z^2)-2xg_1\right]}{(x^2+z^2)^2}\times\left[\frac{\varepsilon\left(x-\frac{t}{\alpha}-\frac{zD}{\alpha}\right)}{\varepsilon^2+\left(x-\frac{t}{\alpha}-\frac{zD}{\alpha}\right)^2}-\frac{\varepsilon\left(x-\frac{t}{\alpha}+\frac{zD}{\alpha}\right)}{\varepsilon^2+\left(x-\frac{t}{\alpha}+\frac{zD}{\alpha}\right)^2}\right] \tag{22}$$

with

$$D=\sqrt{b^2-\alpha^2}.$$

(iii) We analyze the contribution from the poles $\xi=t/\alpha\pm z\sqrt{b^2-\alpha^2}/\alpha$, which unlike the subsonic case are now real and lie outside the branch cut interval $(l,-l)$, where l and $-l$ are branch points of the integrand in (16). Their contribution is

$$\frac{\pi}{2zbD}\,\frac{1}{\sqrt{r_1r_2}}\bigg|_{x=t/\alpha-zD/\alpha}\,\frac{g_1((t-zD)/\alpha,z,t)}{\left(z^2+\left(\frac{t}{\alpha}-\frac{zD}{\alpha}\right)^2\right)}\,\frac{\varepsilon^2}{\varepsilon^2+\left(x-\frac{t}{\alpha}+\frac{zD}{\alpha}\right)^2}$$

$$-\frac{\pi}{\alpha zbD}\,\frac{1}{\sqrt{r_1r_2}}\bigg|_{x\ t/\alpha+zD/\alpha}\,\frac{g_1\left(\frac{(t+zD)}{\alpha},z,t\right)}{\left(z^2+\left(x-\frac{t}{\alpha}+\frac{zD}{\alpha}\right)^2\right)}\times\frac{\varepsilon}{\varepsilon^2+\left(x-\frac{t}{\alpha}+\frac{zD}{\alpha}\right)^2}. \tag{23}$$

When $z\to tD/b^2$ the first term in (23)$\to 0$, since from (16),

$$\lim_{z\to tD/b^2} g_1\left(\frac{t-zD}{\alpha},z,t\right)=-\frac{zD^2}{\alpha}(tD-zb^2)\left[\left(\frac{t}{\alpha}-\frac{zD}{\alpha}\right)^2+z^2\right]\to 0$$

(in which case the pole coincides with the branch cut).

The total solution to $O(\varepsilon)$ is

$$\begin{aligned}\frac{\partial u}{\partial t}(x,z,t)=&\frac{B}{2\pi}\frac{DH(tD-b^2z)\varepsilon}{\varepsilon^2+\left(x-\frac{t}{\alpha}+\frac{\sqrt{b^2-\alpha^2}}{\alpha}z\right)^2}+\frac{B}{2\pi}H(t-bz)\Bigg\{\frac{-2x\varepsilon z}{[x^2+(z+\varepsilon)^2][x^2+(z-\varepsilon)^2]}+\frac{1}{\sqrt{r_1r_2}\alpha^2b}\frac{g_1(x_1t_1t)}{(x^2+z^2)}\\&\times\frac{\left[(x-t/\alpha)^2-\frac{z^2D^2}{\alpha^2}\right]\cos\theta}{\left[\varepsilon^2+\left(x-\frac{t}{\alpha}-\frac{zD}{\alpha}\right)^2\right]\left[\varepsilon^2+\left(x-\frac{t}{\alpha}+\frac{zD}{\alpha}\right)^2\right]}-\frac{1}{\alpha zDb}\left[\sin\theta F(x,z,t)-F\left(\frac{t}{\alpha}-\frac{zD}{\alpha},z,t\right)\right]\\&\times\frac{\varepsilon}{\varepsilon^2+\left(x\frac{t}{\alpha}+\frac{zD}{\alpha}\right)^2}+\frac{1}{\alpha zDb}\left[\sin\theta F(x,z,t)-F\left(\frac{t}{\alpha}+\frac{zD}{\alpha},z,t\right)\right]\frac{\varepsilon}{\varepsilon^2+\left(x-\frac{t}{\alpha}-\frac{zD}{\alpha}\right)^2}\\&+\frac{\sin\theta}{\sqrt{r_1r_2}\alpha zDb}\frac{\frac{\partial g_1}{\partial x}\cdot(x^2+z^2)-2xg_1}{(x^2+z^2)^2}\cdot\left[\frac{\varepsilon\left(x-\frac{t}{\alpha}-\frac{zD}{\alpha}\right)}{\varepsilon^2+\left(x-\frac{t}{\alpha}-\frac{zD}{\alpha}\right)^2}-\frac{\varepsilon\left(x-\frac{t}{\alpha}+\frac{zD}{\alpha}\right)}{\varepsilon^2+\left(x-\frac{t}{\alpha}+\frac{zD}{\alpha}\right)^2}\right]\Bigg\}\end{aligned}\tag{24}$$

where $\theta=\frac{1}{2}(\theta_1-\theta_2)$ and

$$F(x,z,t)=\frac{g_1(x,z,t)}{\sqrt{r_1r_2}(x^2+z^2)}.$$

We see from the above solution that in the limit as $\varepsilon\rightarrow 0$ there is no contribution outside the subsonic wavefront $t=rb$ except from the delta function which is the first term in (24), since, inside the circle, i.e., for $|x|<l$, as: $\varepsilon\rightarrow 0{:}\cos\theta\rightarrow 1,\sin\theta\rightarrow 0$ and

$$\frac{\partial u}{\partial z}\rightarrow\frac{\pi}{\alpha^2b\sqrt{\left(\frac{t}{b}\right)^2-z^2-x^2}}\frac{g_1(x,z,t)}{(x^2+z^2)\left[\left(x-\frac{t}{\alpha}\right)^2-z^2(b^2-\alpha^2)\right]}$$

and outside the circle, i.e., for $|x|>l$, as $\varepsilon\rightarrow 0$: $\cos\theta\rightarrow 0,\sin\theta\rightarrow 1$ and

$$\frac{\partial u}{\partial z}\rightarrow\frac{B}{2\pi}DH(tD-b^2z)\,\delta(t-\alpha x-\sqrt{b^2-\alpha^2}z)$$

which coincides with the Volterra dislocation solution (Callias and Markenscoff [3]).

The steady-state limit may be studied by setting $x\rightarrow X+T/\alpha$, $t\rightarrow t+T$ and letting $T\rightarrow\infty$. The wavefront $t=rb$ is now $(x+T/\alpha)^2+z^2=(t+T/b)^2$ and is centered at $(-T/\alpha)$ with radius $(t+T/b)^2$. As $T\rightarrow\infty$, the center$\rightarrow(-\infty,0)$ and the radius $\rightarrow\infty$. The lines $z=\pm t-\alpha x/\sqrt{b^2-\alpha^2}=\pm t-\alpha x/\sqrt{b^2-\alpha^2}$ remain the same, but as $X\rightarrow\infty$, the two lines approach $\pm$, respectively. The point $(x,z)=(\alpha t/b^2,\sqrt{b^2-\alpha^2}/b^2t)\rightarrow(\alpha(t+T)/b^2,\sqrt{b^2-\alpha^2}/b^2(t+T))\rightarrow(\infty,\infty)$ and thus only the delta-sequence fronts remain and they extend from the current position of the dislocation, all the way to infinity (as in Weertman [4]).

4. Conclusion

We have thus analyzed a ramp dislocation starting from rest and jumping to a supersonic speed. As a result of the transient motion, the radiated stress field consists of delta-sequence stresses around the two lines $x=t/\alpha\pm\sqrt{b^2-\alpha^2}/\alpha z$, confined within a strip $z=\pm t\sqrt{b^2-\alpha^2}/b^2$ and a radiated subsonic field between the wavefront $z\pm t/b$ and the lines $z=\pm t\sqrt{b^2-\alpha^2}/b^2$. In the steady-state limit, only the delta-sequence fronts remain. The lines of discontinuity at $z=t\sqrt{b^2-\alpha^2t}/b^2$ appear because of the point $(x,t)=(\alpha t/b^2,\sqrt{b^2-\alpha^2t}/b^2)$ (where the tangent meets the subsonic wavefront $r=c_2t$ having a special physical meaning in the solution of the Volterra dislocation (step function discontinuity). At this point, the Mach wavefront that starts at the current position of the dislocation $(t/\alpha,0)$ ends. The Mach wavefront, i.e., the tangent line from the dislocation to the circle with radius $r=c_2t$, can be considered as the envelope of the wavelets of radius c_2t emitted by the dislocation from every point on its path. Thus, the wavefront starts at the tangent point to the circle (with center at the origin and radius $r=c_2t$) and ends at the current position of the dislocation. As the core becomes spread, the effect of this tangent point is carried as a line of discontinuity.

Acknowledgment

This research was supported by the National Science Foundation, Grant Number CMS-9734939.

References

[1] Markenscoff, X., and Ni, L., 2001, ''The Transient Motion of a Dislocation with a Ramp-Like Core,'' J. Mech. Phys. Solids, in press.

[2] Gumbsch, P., and Gao, H., 1999, ''Dislocations Faster Than The Speed of Sound,'' Science, **283**, pp. 965–968.

[3] Callias, C., and Markenscoff, X., 1980, ''The Nonuniform Motion of a Supersonic Dislocation,'' Q. Appl. Math., **38**, pp. 323–330.

[4] Weertman, J., 1969, ''Dislocations in Uniform Motion on Slip or Climb Planes Having Periodic Forces,'' *Mathematical Theory Of Dislocations*, T. Mura, ed., ASME, New York, pp. 178–202.

[5] Markenscoff, X., 1980, ''The Transient Motion of a Nonuniformly Recurring Dislocation,'' J. Elast., **10**, pp. 193–201.

[6] Markenscoff, X., and Clifton, R. J., 1981, ''The Nonuniformly Moving Edge Dislocation,'' J. Mech. Phys. Solids, **29**, No. 3, pp. 253–262.

Journal of Applied Mechanics

Brief Notes

A Brief Note is a short paper that presents a specific solution of technical interest in mechanics but which does not necessarily contain new general methods or results. A Brief Note should not exceed 1500 words *or equivalent* (a typical one-column figure or table is equivalent to 250 words; a one line equation to 30 words). Brief Notes will be subject to the usual review procedures prior to publication. After approval such Notes will be published as soon as possible. The Notes should be submitted to the Editor of the JOURNAL OF APPLIED MECHANICS. Discussions on the Brief Notes should be addressed to the Editorial Department, ASME International, Three Park Avenue, New York, NY 10016-5990, or to the Editor of the JOURNAL OF APPLIED MECHANICS. Discussions on Brief Notes appearing in this issue will be accepted until two months after publication. Readers who need more time to prepare a Discussion should request an extension of the deadline from the Editorial Department.

The Contradicting Assumptions of Zero Transverse Normal Stress and Strain in the Thin Plate Theory: A Justification

K. Bhaskar and T. K. Varadan
Department of Aerospace Engineering, Indian Institute of Technology, Madras, Chennai 600 036, India

The need and validity of the contradicting assumptions of zero transverse normal stress and the corresponding strain in the classical plate theory are critically examined here. This is done by studying the relative magnitudes of these quantities with respect to other stresses and strains for a test problem amenable to an exact elasticity solution. [DOI: 10.1115/1.1352061]

Introduction

The thin plate theory ([1,2]) is a two-dimensional simplification of the three-dimensional problem based on the following assumptions:

(a) normals to the midplane of the undeformed plate remain normal to the midsurface after deformation, i.e., the transverse shear strains are negligible;
(b) normals to the midplane of the undeformed plate suffer no change in length during deformation, i.e., the transverse normal strain is negligible; and
(c) the transverse normal stress is negligible.

The second assumption is not consistent with the third assumption, since as per the three-dimensional constitutive law, the normal strain and the normal stress in any direction cannot be simultaneously zero (unless the problem is one of pure shear). The objective of this Note is to critically examine why these two contradicting assumptions are required in plate theory and to what extent they are reasonable; this is done in the light of an elasticity solution for a simple test case. A discussion of the need and validity of both these contradicting assumptions is not available, either in historical accounts of the development of the thin plate theory (for example, see [3]) or in references wherein the equations of three-dimensional elasticity are systematically reduced to a set of two-dimensional equations of various orders with the lowest order equations corresponding to the thin plate (see, for example, [4–6]).

Contributed by the Applied Mechanics Division of THE AMERICAN SOCIETY OF MECHANICAL ENGINEERS for publication in the ASME JOURNAL OF APPLIED MECHANICS. Manuscript received by the ASME Applied Mechanics Division, May 10, 1999; final revision, Nov. 6, 1999. Associate Editor: J. W. Ju.

The Elasticity Solution

The problem considered is that of an infinitely long slab of rectangular cross section undergoing cylindrical bending due to transverse sinusoidal loading (Fig. 1). The two longitudinal edges are assumed to be supported by shear diaphragms such that

$$\text{at } x=0,a: \quad w=0, \quad \sigma_x=0 \quad \text{for all } y \text{ and } z. \tag{1}$$

The Navier equations of equilibrium, for the plane strain problem, are

$$\begin{aligned}(2G+\lambda)u_{,xx}+Gu_{,zz}+(G+\lambda)w_{,xz}&=0\\(G+\lambda)u_{,xz}+(2G+\lambda)w_{,zz}+Gw_{,xx}&=0\end{aligned} \tag{2}$$

where G and λ are Lame's constants, dependent on the Young's modulus E and the Poisson's ratio μ.

The lateral surface conditions are

$$\begin{aligned}&\sigma_z=-q_o\sin\frac{\pi x}{a} \text{ and } \tau_{xz}=0 \text{ at } z=-h/2,\\&\qquad\qquad\text{for all } x \text{ and } y\\&\sigma_z=\tau_{xz}=0 \quad \text{at } z=h/2, \quad \text{for all } x \text{ and } y.\end{aligned} \tag{3}$$

The problem admits to a closed-form solution as follows. Corresponding to the sinusoidal load, the displacements can be assumed to vary harmonically with x as

$$u=U(z)\cos\left(\frac{\pi x}{a}\right) \tag{4}$$

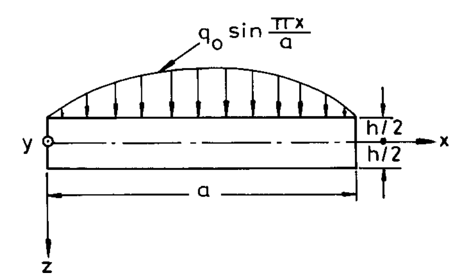

Fig. 1 The test problem

$$w = W(z)\sin\left(\frac{\pi x}{a}\right).$$

These variations satisfy the shear diaphragm conditions of Eq. (1) and reduce Eq. (2) to a set of ordinary differential equations as given by

$$\begin{aligned}&-(2G+\lambda)\beta^2 U + G U_{,zz} + (G+\lambda)\beta W_{,z} = 0\\ &-(G+\lambda)\beta U_{,z} + (2G+\lambda)W_{,zz} - G\beta^2 W = 0\end{aligned} \tag{5}$$

where $\beta = \pi/a$. The lateral surface conditions can also be expressed in terms of U and W. The solution for the resulting two-point boundary value problem is straightforward and is

$$\begin{aligned}U &= A\cosh\beta z + B\sinh\beta z + Cz\cosh\beta z + Dz\sinh\beta z\\ W &= \left[B - \frac{C(3-4\mu)}{\beta}\right]\cosh\beta z + \left[A - \frac{D(3-4\mu)}{\beta}\right]\sinh\beta z\\ &\quad + Dz\cosh\beta z + Cz\sinh\beta z\end{aligned} \tag{6}$$

where

$$D = \frac{q_o(1+\mu)\sinh\frac{\beta h}{2}}{E(\beta h + \sinh\beta h)} \qquad A = \frac{D\left(1-2\mu-\frac{\beta h}{2}\coth\frac{\beta h}{2}\right)}{\beta}$$

$$C = \frac{D\coth\frac{\beta h}{2}\left(\frac{\beta h}{2} + \sinh\frac{\beta h}{2}\cosh\frac{\beta h}{2}\right)}{\left(\frac{\beta h}{2} - \sinh\frac{\beta h}{2}\cosh\frac{\beta h}{2}\right)}$$

$$B = \frac{C\left(1-2\mu-\frac{\beta h}{2}\tanh\frac{\beta h}{2}\right)}{\beta}.$$

The Particular Case of a Thin Slab

To arrive at a comprehensive understanding of the behavior of the structure, especially as it becomes thinner and thinner, it is necessary to consider the components of the total strain energy due to bending, transverse shear and thickness-stretch (or contraction) separately. These denoted, respectively, as U_b, U_s, and U_t, are defined as

$$U_b = \frac{1}{2}\int \sigma_x\varepsilon_x dVol \qquad U_s = \frac{1}{2}\int \tau_{xz}\gamma_{xz} dVol$$
$$U_t = \frac{1}{2}\int \sigma_z\varepsilon_z dVol. \tag{7}$$

These, for the present problem, turn out to be

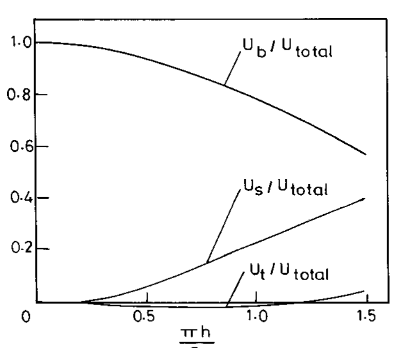

Fig. 2 Variation of strain energy components with respect to thickness

$$\begin{aligned}U_b = \frac{q_o^2 a^2}{384\pi E\Gamma}&[3(1-\mu-2\mu^2)(\sinh 4\beta h - 2\sinh 2\beta h)\\ &+12\beta h(1-\mu-2\mu^2)(\cosh 2\beta h - 1)\\ &-12(\beta h)^2(1-\mu-2\mu^2)\sinh 2\beta h + 8(\beta h)^3\{-10+2\mu\\ &+12\mu^2 + (7+\mu-6\mu^2)\cosh 2\beta h\}\\ &-8(\beta h)^4(1+\mu)\sinh 2\beta h + 16(\beta h)^5(1+\mu)]\end{aligned} \tag{8a}$$

$$\begin{aligned}U_s = \frac{q_o^2 a^2(1+\mu)}{192\pi E\Gamma}&[(3\sinh 4\beta h - 6\sinh 2\beta h)\\ &+12\beta h(\cosh 2\beta h - 1) - 12(\beta h)^2\sinh 2\beta h - 8(\beta h)^3\\ &\times(2+\cosh 2\beta h) + 8(\beta h)^4\sinh 2\beta h - 16(\beta h)^5]\end{aligned} \tag{8b}$$

$$\begin{aligned}U_t = \frac{q_o^2 a^2}{384\pi E\Gamma}&[3(5-\mu-6\mu^2)(\sinh 4\beta h - 2\sinh 2\beta h)\\ &+12\beta h(5-\mu-6\mu^2)(\cosh 2\beta h - 1)\\ &-12(\beta h)^2(5-\mu-6\mu^2)\sinh 2\beta h - 8(\beta h)^3(5-\mu-6\mu^2)\\ &\times(2+\cosh 2\beta h) - 8(\beta h)^4(1+\mu)\sinh 2\beta h\\ &+16(1+\mu)(\beta h)^5]\end{aligned} \tag{8c}$$

where $\Gamma = [\sinh^2\beta h - (\beta h)^2]^2$.

A plot of the three energy components versus the thickness parameter is as shown in Fig. 2. From this figure, it is clear that the bending action is more predominant compared to those of transverse shear and thickness-stretch as long as the thickness of the slab is small compared to the span; this is, of course, as can be expected. What is of greater interest is to find out how the ratios U_s/U_b, U_t/U_b, and U_t/U_s vary with the thickness. This is easily accomplished by obtaining the Taylor expansions corresponding to these ratios after substitution from Eqs. (8), as given by

$$\begin{aligned}U_s/U_b &= 2.82(h/a)^2 + 1.06(h/a)^4 + \dots\\ U_t/U_b &= -0.423(h/a)^2 + 2.86(h/a)^4 + \dots\\ U_t/U_s &= -0.150 + 1.07(h/a)^2 + \dots\end{aligned} \tag{9}$$

for $\mu=0.3$. Thus, for small thickness-to-span ratios (say, up to 1/20), both U_s/U_b and U_t/U_b grow nearly quadratically with h/a; further, U_t/U_s remains a constant for such thin plates with a value of 0.15 (i.e., $\mu/2$ for arbitrary μ).

Considering the limiting case of an extremely thin plate, i.e., as h/a tends to zero, it is immediately seen that both U_s/U_b and U_t/U_b tend to zero. This, then, is the starting point for the development of the thin plate theory. In other words, a "thin" plate is one for which the strain energy corresponding to transverse shear or thickness-stretch is zero. A look at Eq. (7) reveals that the energy components U_s and U_t can be made zero by neglecting either γ_{xz} or τ_{xz}, and either ε_z or σ_z. Since the shear stress and shear strain are directly proportional to each other, the neglect of the shear strain, by virtue of assumption (a) stated earlier, implies that the corresponding shear stress is also absent. As far as the other two assumptions are concerned, it is clear that only one of them would have been sufficient and the other appears to be an unnecessary, redundant constraint.

It is now necessary to examine which of these two assumptions—namely one that neglects ε_z and the one that neglects σ_z—is really reasonable. For this purpose, it is enough to consider the relative magnitudes of these quantities with respect to their in-plane counterparts. For the present problem, the maximum value of σ_z occurs on the loaded surface ($z=-h/2$) at midspan and is equal to $-q_o$. Comparing this with the value of $\sigma_{x\,\max}$, which occurs at the same point, one obtains, for the case of vanishing h/a,

$$\lim_{h/a\to 0}\left(\frac{\sigma_{z\ \max}}{\sigma_{x\ \max}}\right)=0. \tag{10}$$

Similarly, at the same point, one gets

$$\lim_{h/a\to 0}\left(\frac{\varepsilon_{z\ \max}}{\varepsilon_{x\ \max}}\right)=-\frac{\mu}{(1-\mu)}\cong -0.43 \quad \text{for } \mu=0.3. \tag{11}$$

Thus, *while σ_z does turn out to be negligible, ε_z is not really so*. However, it is ε_z that needs to be neglected to keep the thin plate theory simple, as explained below.

Justification of the Contradicting Assumptions of Thin Plate Theory

The displacement field of the thin plate theory, obtained by direct integration of the transverse shear strain and transverse normal strain which have been taken as zero, is

$$\begin{aligned} u(x,z)&=-zw_{,x} \\ w(x,z)&=w(x) \end{aligned} \tag{12}$$

where the special case of cylindrical bending is considered once again, for the sake of simplicity. If the assumption of zero ε_z is not employed, it is clear that w would also depend on z, and its variation with z has to be assumed to obtain a two-dimensional theory; such a theory would obviously be more complicated than the conventional thin plate theory. Thus, though not really negligible, ε_z has to be ignored from *the viewpoint of simplicity*.

Having thus justified the need for the zero-ε_z assumption, one may be curious to find out whether the zero-σ_z assumption in the thin plate theory can be dispensed with so as to avoid a violation of the material constitutive law. This question can be answered by comparison of a two-dimensional theory based on the assumptions of zero-ε_z and nonzero σ_z (to be designated as NPT—New Plate Theory), with the conventional thin plate theory based on neglect of both ε_z and σ_z (referred to as CPT). While a plane-stress reduced constitutive law as given by

$$\sigma_x=\frac{E}{(1-\mu^2)}\varepsilon_x \tag{13}$$

is used in CPT, the three-dimensional constitutive law given by

$$\sigma_x=2G\varepsilon_x+\lambda\varepsilon_x \tag{14}$$

is used in NPT. Thicknesswise integration would result in the following expressions for M_x:

$$\begin{aligned} &\text{CPT:}\quad M_x=-Dw_{,xx} \ \text{ where } \ D=\frac{Eh^3}{12(1-\mu^2)} \\ &\text{NPT:}\quad M_x=-D'w_{,xx} \ \text{ where } \ D'=\frac{(2G+\lambda)h^3}{12}=\frac{(1-\mu)^2D}{(1-2\mu)}. \end{aligned} \tag{15}$$

The equation of equilibrium for the case of cylindrical bending is given by

$$M_{x,xx}+q=0 \tag{16}$$

which is valid for both CPT and NPT. Substitution for M_x from Eq. (15) results in the following governing equations:

$$\begin{aligned} \text{CPT:}\quad Dw_{,xxxx}&=q \\ \text{NPT:}\quad D'w_{,xxxx}&=q. \end{aligned} \tag{17}$$

It can easily be verified that D' is greater than D for all possible values of μ, except when $\mu=0$ in which case both D' and D are equal. If one keeps in mind that CPT is known to yield a stiffer approximation of the three-dimensional structure and hence to lead to underestimates of deflections ([7]), then it is clear from Eq. (17) that NPT would only be worse. Thus, from the *viewpoint of accuracy*, the zero-σ_z assumption, though inconsistent with the zero-ε_z assumption, is necessary in the thin plate theory.

Conclusion

An exact elasticity solution has been presented for the simple case of cylindrical bending of an infinite strip. The magnitudes of various energy components, and of the transverse normal stress and the corresponding strain with respect to their in-plane counterparts, are studied. The relaxation of the zero-transverse-normal-stress and the zero-transverse-normal-strain assumptions in thin plate theory are critically examined. On the basis of these studies, one can conclude that:

(a) the transverse normal stress is certainly negligibly small compared to the in-plane stresses. However, the transverse normal strain is not negligible, but has magnitudes comparable to those of the in-plane strains;

(b) neglect of the transverse normal strain in thin plate theory is necessary only to effect simplicity, it cannot be justified otherwise.

(c) having reconciled to the above fact, one should not endeavour to adopt the three-dimensional constitutive law as being consistent with it rather than the plane-stress reduced law. This is because the resulting theory would then become more erroneous;

(d) finally, the assumption of zero-transverse-shear is quite reasonable for thin plates because the corresponding strain energy component does become negligibly small for a thin plate.

References

[1] Timoshenko, S. P., and Woinowsky-Krieger, S., 1959, *Theory of Plates and Shells*, McGraw-Hill, Tokyo.
[2] Varadan, T. K., and Bhaskar, K., 1999, *Analysis of Plates—Theory and Problems*, Narosa Publishing House, Delhi.
[3] Timoshenko, S. P., 1953, *History of Strength of Materials*, McGraw-Hill, New York.
[4] Epstein, P. S., 1942, ''On the Theory of Elastic Vibrations in Plates and Shells,'' J. Math. Phys., (Mass. Inst. Tech.), **21**, pp. 198–209.
[5] Iyengar, K. T. S., Chandrashekhara, K., and Sebastian, V. K., 1974, ''On the Analysis of Thick Rectangular Plates,'' Ing. Arch., **43**, pp. 317–330.
[6] Widera, O. E., 1970, ''An Asymptotic Theory for the Motion of Elastic Plates,'' Acta Mech., **9**, pp. 54–66.
[7] Srinivas, S., Rao, A. K., and Joga Rao, C. V., 1969, ''Flexure of Simply Supported Thick Homogeneous and Laminated Rectangular Plates,'' Z. Angew. Math. Mech., **49**, No. 8, pp. 449–458.

On Dynamics of Bar of Rectangular Cross Section

N. B. Rassoulova
Institute of Mathematics and Mechanics, Academy of Sciences of Azebaijan, 9F. Agayev st, Baku, Azerbaijan

The propagation of nonstationary waves in semi-infinite elastic rectangular bars is studied. It is assumed that two opposite lateral surfaces of the body are free of forces, while the two others are subjects to cross conditions. By introducing three new potential functions, the author succeeded in getting closed-form solutions in Laplace and Fourier transform parameters. Inversion of the transform solutions, carried out by an original method of inversion, is suggested herein. [DOI: 10.1115/1.1352063]

Contributed by the Applied Mechanics Division of THE AMERICAN SOCIETY OF MECHANICAL ENGINEERS for publication in the ASME JOURNAL OF APPLIED MECHANICS. Manuscript received and accepted by the ASME Applied Mechanics Division, Dec. 14, 1999; final revision, Oct. 19, 2000. Associate Editor: A. K. Mal.

Introduction

This paper deals with the three-dimensional problems of dynamics of elastic bodies for the semi-infinite rectangular bar. In contrast to the previous work ([1]) where this problem was considered only for mixed boundary conditions, we now investigate the solution for the case of free surfaces.

Statement and Solution of the Problem

We consider a semi-infinite rectangular prism occupying the space $-a \leqslant x \leqslant a$; $-b \leqslant y \leqslant b$; $z \geqslant 0$, where $2a$ and $2b$ are the sizes of cross section of the prism. At time $t=0$, the end-section of the prism is affected by the applied forces. The process taking place in an elastic prism initially in a nondeformed state, is described by a three-dimensional system of Lame equation which in vector form is as follows:

$$\rho \frac{\partial^2 \mathbf{U}}{\partial t^2} = (\lambda+\mu)\,\mathrm{graddiv}\,\mathbf{U} + \mu \Delta \mathbf{U} \qquad \mathbf{U}=\mathbf{U}(u,v,w) \tag{1}$$

where $\mathbf{U}$ is the displacement vector, and ρ is the density of material.

As is known from ([1]) the system (1) under the end-section conditions

$$\left.\begin{aligned} &\sigma_{zz}=\sigma_0(x,y)f(t)\\ &u=0\\ &v=0 \end{aligned}\right\} \quad \text{for } z=0 \tag{2}$$

and under initial zero data is reduced to a simpler form:

$$\begin{gathered} \mu q H_2 \psi_2 = (\lambda+2\mu) H_1 \varphi \\ H_2 \psi_1 = 0 \\ H_0 H_2 \psi_2 = -\frac{\sigma(x,y)}{\mu}\overline{f(p)} \end{gathered} \tag{3}$$

where

$$H_i = \frac{\partial^2}{\partial x^2} + \frac{\partial^2}{\partial y^2} - \left(\frac{p^2}{c_i^2} + q^2\right), \quad i=1,2$$

$$H_0 = \frac{\partial^2}{\partial x^2} + \frac{\partial^2}{\partial y^2} - q^2$$

are the Helmholtz operators; $c_1=\sqrt{(\lambda+2\mu)/\rho}$; $c_2=\sqrt{\mu/\rho}$; and the functions φ, ψ_1, and ψ_2 are related to twofold integral transforms (the Laplace transform with respect to t and the Fourier transform with respect to z) of the displacement functions by the following formulas:

$$\begin{aligned} \overline{u}_s &= \frac{\partial \varphi}{\partial x} + \frac{\partial \psi_1}{\partial y} - q\frac{\partial \psi_2}{\partial x} \\ \overline{v}_s &= \frac{\partial \varphi}{\partial y} - \frac{\partial \psi_1}{\partial x} - q\frac{\partial \psi_2}{\partial y} \\ \overline{w}_c &= q\varphi - \frac{\partial^2 \psi_2}{\partial x^2} - \frac{\partial^2 \psi_2}{\partial y^2} \end{aligned} \tag{4}$$

Here, the indices "s" and "c" indicate sin and cos Fourier transforms, and p and q are the parameters of Laplace and Fourier transforms, respectively.

Analogously, it can be proved, that the same system (1) for another variant of end-section conditions:

$$\left.\begin{aligned} &\sigma_{zx}=\tau_1(y)f(t)\\ &\sigma_{zy}=\tau_2(x)f(t)\\ &w=0 \end{aligned}\right\} \quad \text{on } z=0$$

corresponding to the tangent impact, is reduced to the following system:

$$\left.\begin{aligned} &(\lambda+2\mu)H_1\varphi = -\mu q H_2 \psi_2 \\ &H_0 H_2 \psi_2 = 0 \\ &H_2 \psi_1 = \frac{\overline{f(p)}}{\mu}\left[\int \tau_1(y)\,dy - \int \tau_2(x)\,dx\right] \end{aligned}\right\} \tag{5}$$

via the use of the following formulas:

$$\begin{aligned} \overline{u}_c &= \frac{\partial \varphi}{\partial x} + \frac{\partial \psi_1}{\partial y} + q\frac{\partial \psi_2}{\partial x}; \\ \overline{v}_c &= \frac{\partial \varphi}{\partial y} - \frac{\partial \psi_1}{\partial x} + q\frac{\partial \psi_2}{\partial y}; \\ \overline{w}_s &= -q\varphi - \frac{\partial^2 \psi_2}{\partial x^2} - \frac{\partial^2 \psi_2}{\partial y^2}. \end{aligned} \tag{6}$$

The systems (3) and (5) are simpler than the input system (1) and they easily yield to obtain solutions of the problem.

In the present paper we investigated the system (3), where $\sigma_0(x,y)$ is a function of axial forces, distributed at end section of the bar.

This system has to be integrated according to the lateral conditions, which are chosen here as follows:

- two opposite surfaces $x=\pm a$ are free of forces:

$$\sigma_{xx}=\sigma_{xy}=\sigma_{xz}=0 \tag{7}$$

- the other two lateral surfaces $y=\pm b$ assume one of the following variants of cross conditions:

$$\begin{aligned} &(a)\ \left.\begin{aligned} &\sigma_{yy}=0\\ &u=w=0 \end{aligned}\right\} \text{ on } y=\pm b \\ &(b)\ \left.\begin{aligned} &\sigma_{yx}=0\\ &\sigma_{yz}=0\\ &v=0 \end{aligned}\right\} \text{ on } y=\pm b. \end{aligned} \tag{8}$$

It is evident, that the solution of the considered problem exists only on the class (set) of functions with separated variables with respect to x and y. Taking into account this fact, the conditions (8) easily have been satisfied by choosing the corresponding solution in the following form:

$$\begin{aligned} \varphi &= \sum_k f_k(x)\cos\beta_k y \\ \psi_1 &= \sum_k l_k(x)\sin\beta_k y \\ \psi_2 &= \sum_k g_k(x)\cos\beta_k y \end{aligned} \tag{9}$$

where the parameter β_k is different in each variant:

$$(a)\quad \beta_k = \left(\frac{1}{2}+k\right)\frac{\pi}{b};$$

$$(b)\quad \beta_k = \frac{\pi k}{b}, \quad k=0,1,\ldots.$$

The functions $f_k(x)$, $l_k(x)$, and $g_k(x)$ can be determined from the system (3). Skipping the details, we arrive at the following solution:

$$f_k(x)=C_k\cosh\nu_{1k}x+\Omega_{1k}(x)$$
$$l_k(x)=l_k\sinh\nu_{2k}x \tag{10}$$
$$g_k(x)=A_k\cosh\nu_{2k}x+\Omega_{2k}(x)$$

Here $\Omega_{1k}(x)$ and $\Omega_{2k}(x)$ are particular solutions of the corresponding differential equations. It can be shown that for the simplest case when $\sigma_0(x,y)=\sigma_0=\text{const}$ or $\sigma_0(x,y)=\sigma_0(y)$ these particular solutions are as follows:

$$\Omega_{1k}=-\frac{\sigma_k\overline{f}(p)q}{(\lambda+2\mu)\nu_{1k}^2(\beta_k^2+q^2)};\quad \Omega_{2k}=-\frac{\sigma_k\overline{f}(p)}{\mu\nu_{2k}^2(\beta_k^2+q^2)} \tag{11}$$

where $\sigma_k(x)=1/2b\int_{-b}^{b}\sigma_o(x,y)\cos\beta_k y dy$ and $\nu_{ik}=\sqrt{p^2/c_i^2+q^2+\beta_k}$; $i=1,2$; $k=\overline{0,\infty}$.

Constants C_k, A_k, l_k are the solutions of the following linear algebraic system:

$$\begin{bmatrix}C_k\\A_k\\l_k\end{bmatrix}\times\mathbf{D}_k=\begin{bmatrix}d_1\\d_2\\d_3\end{bmatrix} \tag{12}$$

where the third-rank matrix $\mathbf{D}_k$ is as follows:

$$\mathbf{D}_k=\begin{bmatrix}[\nu_{1k}^2(\lambda+2\mu)-\lambda(\beta_k^2+q^2)]\cosh\nu_{1k}a & -2\mu q\nu_{2k}^2\cosh\nu_{2k}a & 2\mu\beta_k\nu_{2k}\cosh\nu_{2k}a\\ -2\beta_k\nu_{1k}\sinh\nu_{1k}a & -2\beta_k q\nu_{2k}\sinh\nu_{2k}a & -(\beta_k^2+\nu_{2k}^2)\sinh\nu_{2k}a\\ 2q\nu_{1k}\sinh\nu_{1k}a & -\nu_{2k}(q^2+\nu_{2k}^2-\beta_k^2)\sinh\nu_{2k}a & q\beta_k\sinh\nu_{2k}a\end{bmatrix} \tag{13}$$

and for constant Ω_{ik}

$$d_1=\lambda\Omega_{1k}(\beta_k^2+q^2),\quad d_2=0,\quad d_3=0.$$

Final solutions are presented in the form of (9) and considering the solution to the system (12), one can assert that the convergence of these series up to the third-order derivatives is evident.

Note, that if $\sigma_0(x,y)=\sigma_0=\text{const}$ and in the case (b), i.e., when the sides $y=\pm b$ are in contact with ideal smooth surface, the solution takes a simplest form:

$$f_0(x)=\frac{\lambda\sigma_0\overline{f}(p)\nu_{20}(q^2+\nu_{20}^2)q}{D_0\nu_{10}^2(\lambda+2\mu)}\sinh\nu_{20}a\cdot\cosh\nu_{10}x-\frac{\sigma_0 f(p)}{q\nu_{10}^2(\lambda+2\mu)} \tag{14}$$

$$g_0(x)=\frac{\lambda\sigma_0\overline{f}(p)q^2\sinh\nu_{10}a}{D_0\nu_{10}(\lambda+2\mu)}\cosh\nu_{20}x-\frac{\sigma_0 f(p)}{\mu q^2\nu_{20}^2} \tag{15}$$

$$l_k(x)=0,\quad k=\overline{0,\infty}$$

$$f_k(x)=g_k(x)=0,\quad k=\overline{1,\infty}$$

$$D_0=-[\nu_{10}^2(\lambda+2\mu)-\lambda q^2][q^2+\nu_{20}^2]\nu_{20}\cosh\nu_{10}a\cdot\sinh\nu_{20}a+4\mu q^2\nu_{10}\nu_{20}^2\cosh\nu_{20}a\cdot\sinh\nu_{10}a. \tag{16}$$

Thus, the problem is completely solved at transforms. Returning to real variables comprises a great difficulty. All existing methods are unpromising to find the inverse transforms to obtaining general solutions.

Only for the simplest solutions (14) and (15) can we use the "The Second Theorem of Expansion" ([2]) because as a whole, these functions are meromorphic in p complex plane. However, even in this case, this method does not reduce to the desired results, because it is impossible to obtain the roots of the equation $D_0(p)=0$ for arbitrary value of q.

Now, we propose the original method, which makes it possible to find the inverse functions, even for transforms of general solutions. For visualization purposes, we show this method for the simplest case of solution, (14) and (15), and construct graphs of certain quantities to verify the validity of the proposed method.

For simplicity, assume that $\overline{f}(p)=1/p$ (this corresponds to $f(t)=H(t)$, where H is the Heaviside function). Then according to (4), we can define the function $\dot{W}$ (the velocity of central axis along z):

$$\dot{\overline{W}}_c=-q^2\frac{\lambda\sigma_0}{\mu(\lambda+2\mu)}\cdot\left[\frac{q^2+\nu_{20}^2}{\nu_{20}^3}\cdot\frac{\sinh\nu_{20}a}{\cosh\nu_{20}a}\cdot\frac{1}{\nu_{10}^2}\cdot\frac{\cosh\nu_{10}x}{\cosh\nu_{10}a}-2\frac{\cosh\nu_{20}x}{\nu_{20}^2\cosh\nu_{20}a}\cdot\frac{\sinh\nu_{10}a}{\nu_{10}\cosh\nu_{10}a}\right]\times\frac{\nu_{20}^4}{D_0^*}-\frac{\sigma_0}{\lambda+2\mu}\cdot\frac{1}{\nu_{10}^2} \tag{17}$$

where

$$D_0^*=[\nu_{10}^2(\lambda+2\mu)-\lambda q^2][q^2+\nu_{20}^2]\nu_{20}\tanh\nu_{10}a-4\mu q^2\nu_{10}\nu_{20}^2\tanh\nu_{10}a.$$

Following [3], we can present ν_{20}^4/D_0^* in the form of the power series:

$$\frac{\nu_{20}^4}{D_0^*}=\sum_{n=1}^{\infty}e_n\frac{1}{\nu_{20}^n} \tag{18}$$

whose elements are transforms both in Laplace and in Fourier.

If we consider the solutions for the small values of t, it is sufficient to keep first few terms:

$$\frac{\nu_{20}^4}{D_0^*}\approx\frac{1}{\mu}\left(\frac{1}{\nu_{20}}-\frac{eq^2}{\nu_{20}^3}\right),\quad\text{where}\quad e=1-\frac{c_1-c_2}{2c_2}+\frac{\lambda}{\lambda+2\mu}.$$

Similarly, for the functions $\dot{\overline{U}}_s$ (the velocity of particles on a free surface along the ox-axis) we obtain

$$\dot{U}_s\big|_{x=\pm a}=-\frac{\lambda\sigma_0 q}{\mu(\lambda+2\mu)}\left[\frac{1}{\nu_{10}}\cdot\frac{\sinh\nu_{10}a}{\cosh\nu_{10}a}\cdot\frac{1}{\nu_{20}}\frac{\sinh\nu_{20}a}{\cosh\nu_{20}a}\right]\times\left(\frac{1}{\nu_{20}}-\frac{eq^2}{\nu_{20}^3}\right). \tag{19}$$

The inverse Laplace transform of the functions (17) and (19) (taking into account (18)), could be obtained as follows:

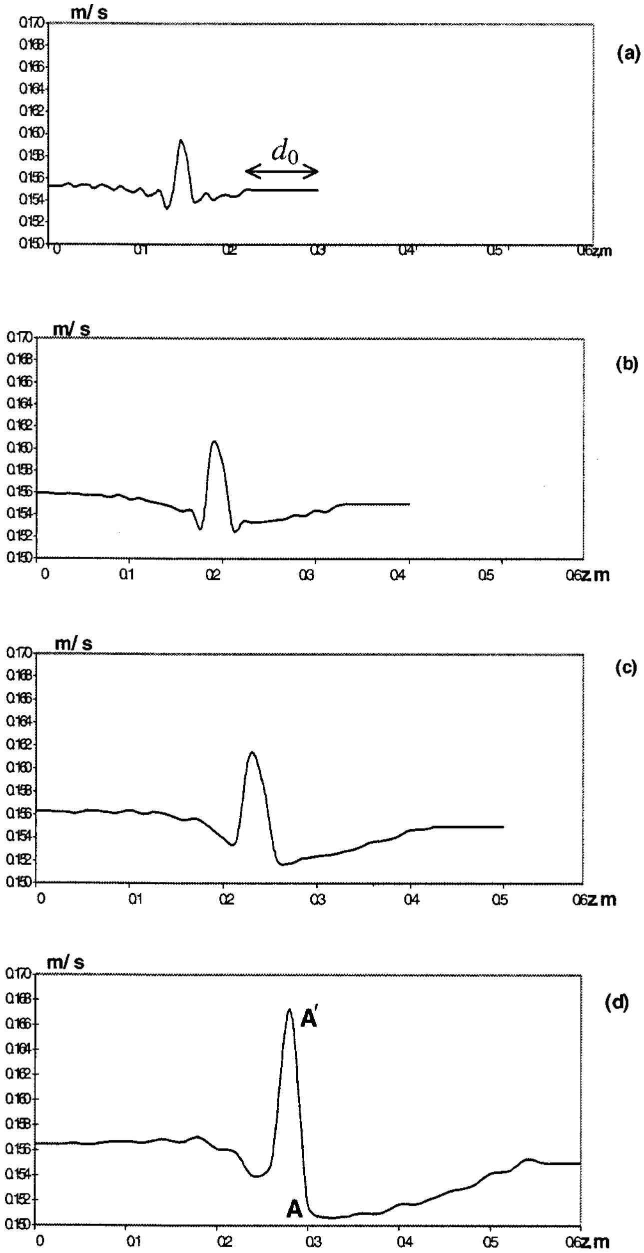

Fig. 1 Graphs of $\dot{W}$ at times: (*a*) $t=1.5\ a/c_1$, (*b*) $t=2\ a/c_1$, (*c*) $t=2.5\ a/c_1$, (*d*) $t=3\ a/c_1$

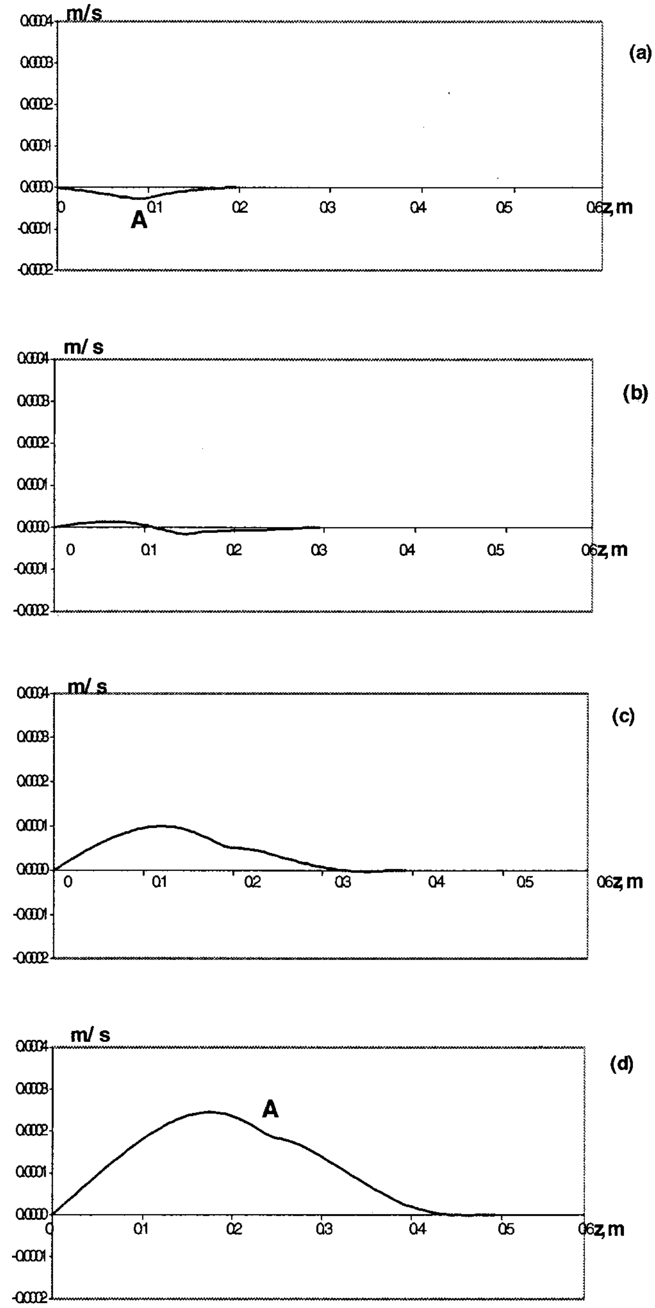

Fig. 2 Graphs of $\dot{U}$ at times: (*a*) $t=a/c_1$, (*b*) $t=1.5\ a/c_1$, (*c*) $t=2\ a/c_1$, (*d*) $t=2.5\ a/c_1$

$$(1)\quad \frac{q^2+\nu_{20}^2}{\nu_{20}^3}\cdot\frac{\sinh\nu_{20}a}{\cosh\nu_{20}a} \overset{L}{\leftrightarrow} c_2 a q\sin(qc_2t)-2\sum_k \frac{c_2}{\alpha}\,\frac{(q^2-\alpha_k^2)\sin(c_2t\sqrt{q^2+\alpha_k^2})}{\alpha_k^2\sqrt{q^2+\alpha_k^2}}$$

$$(2)\quad \frac{1}{\nu_{i0}^2}\cdot\frac{\cosh\nu_{il0}x}{\cosh\nu_{i0}a} \leftrightarrow_L \frac{c_i}{q}\sin(qc_it)-2\sum_m \frac{c_i}{\alpha}\times\frac{(-1)^m\cos(\alpha_m x)\sin(c_it\sqrt{q^2+\alpha_m^2})}{\alpha_m\sqrt{q^2+\alpha_m^2}},\quad i=1,2$$

$$(3)\quad \frac{\sinh\nu_{i0}a}{\nu_{i0}\cosh\nu_{i0}a} \overset{L}{\leftrightarrow} \frac{2c_i}{a}\sum_k \frac{\sin(c_it\sqrt{q^2+\alpha_k^2})}{\sqrt{q^2+\alpha_k^2}}\quad i=1,2$$

$$(4)\quad \frac{1}{\nu_{20}}\left[1-\frac{eq^2}{\nu_{20}^2}\right] \overset{L}{\leftrightarrow} c_2J_0(c_2qt)-\frac{e\sqrt{\pi}c_2^2tq}{\Gamma(3/2)}J_1(c_2qt)$$

$$\alpha_k=\left(\frac{1}{2}+k\right)\frac{\pi}{a};\quad k=\overline{0,\infty},\quad \nu_{i0}=\sqrt{\frac{p^2}{c_i^2}+q^2},\quad i=1,2.$$

And finally

$$\frac{\sigma_0}{(\lambda+2\mu)\nu_{10}^2} \overset{L,F}{\leftrightarrow} \frac{\sigma_0 c_1}{\lambda+2\mu} H\left(t-\frac{z}{c_1}\right). \qquad (*)$$

The calculations of $\dot{W}$ and $\dot{U}$ are made for the following values of parameters and time intervals. (Graphs are attached at the end Figs. 1–2.)

$$c_1 = 2c_2 = 6200 \text{ m/c}$$

$$\lambda = 2\mu = 1.5\times 10^{10} \text{ kg/m}^2$$

$$\sigma_0 = -2\times 10^6 \text{ kg/m}^2$$

$$a = 0.2 \text{ m}$$

$$t_1 = ka/c_1; \quad k = 1; 1.5; 2; 2.5 \ldots .$$

Discussion of the Results

Up to the moment $t = a/c_1$, the solutions on the oz-axis will be presented by the plane wave (*), representing longitudinal wave, propagating in the infinite elastic medium. Although this fact is known from physical considerations, it can be proved rigorously from the mathematical point of view.

The forepart of perturbations propagating with the velocity c_1 corresponds to the region where the reflected waves do not affect the behavior. Here the solution (*) takes place, and the width of the peak decreases according to the law:

$$d_0 = c_1 t - \sqrt{c_1^2 t^2 - a^2}.$$

Next to the forefront, there is a front of low-energy diffraction waves and a well, appearing as time progresses, between the forefront of waves and ''quasi-front'' AA' of the rising new wave. (Fig. 1) This wave can, without any doubt, only be the rod wave propagating with the velocity $c_3 = \sqrt{E/\rho}$. The back part of this wave will correspond, on average, to the solution given by the elementary theory of rods. The possible variations around the above solution can be related to the cross section inertia.

Simultaneously, in order to clearly demonstrate the advantage of exact theory over the elementary theory, the calculation for normal velocities of free surface particles $x = \pm a$ has also been carried out.

The results are shown in Fig. 2. The given graphs are more significant as compared to any arguments. The breakpoint A of those curves corresponds to the transverse shear wave front. Probably, a detailed investigation of the roots of equation $D_0 = 0$ for the higher values of time would show the possibility of diffraction wave degeneration (partly) into the Rayleigh wave concentrating the main energy of motion near the free surfaces.

Conclusions

1 The existence of three new potential functions (one longitudinal and two transverse) describing a three-dimensional motion of a linearly elastic rectangular bar has been proved. The system of the Lamé equations in these potential functions is simpler and is easily solved.

2 The method of inverse integral transform for low and finite values of time has been proposed. The validity of this method is proved once more by the logical results obtained.

References

[1] Rassoulova, N. B., 1997, ''Wave Propagation in Rectangular Prismatic Bars Subjected to Axial Impact,'' Izvestiya, Russian Academy of Sciences, Mekhanika Tverdogo Tela, No. 6, pp. 176–179.

[2] Ditkin, V. A. and Prudnikov, A. P., 1965, *Integral Transforms and the Operational Calculus*, Pergamon Press, New York.

[3] Doetsch, G., 1950, *Handbuch der Laplace-Transformation*, Vol. 2, Birkhauser Basel.

Hamilton Principle and Generalized Variational Principles of Linear Thermopiezoelectricity

Ji-Huan He

Shanghai Institute of Applied Mathematics and Mechanics, Shanghai University, Shanghai 200072, P. R. China

Via the semi-inverse method, a family of various variational principles is established for thermopiezoelectricity, including a Hamilton principle and a minimum complementary energy principle. [DOI: 10.1115/1.1352067]

Introduction

Recent interest in piezoelectric materials stems from their potential applications in intelligent structural systems. Chandrasekharaiah [1] proposed a generalized linear thermoelasticity theory for piezoelectric media, and He [2] applied the Lagrange multiplier method in search for a variational partner to the Chandrasekharaiah model. This revealed that the traditional approaches failed due to the variational crisis (some of multipliers become zero during the identification of the multipliers). Liu [3] obtained a unified variational principle for thermoelasticity. In this Note, applying the semi-inverse method (He [4,5]), we obtain two generalized variational principles for generalized linear thermopiezoelectricity. By constraining the obtained generalized functionals, two minimum energy principles are deduced, one of which is proved to be of Hamiltonian type.

Generalized Variational Principles

The essence of the semi-inverse method is to construct an energy-like functional with a certain unknown function, which can be identified step by step. An energy-like trial functional for the discussed problem can be constructed in the following form:

$$J(\sigma_{ij}, \gamma_{ij}, u_i, \theta, q_i, D_i, E_i, \Phi) = \int_{t^{(n-1)}}^{t^{(n)}} \int L dV dt + BI, \qquad (1)$$

where stress σ_{ij}, strain γ_{ij}, displacement u_i, temperature θ, heat flux q_i, electric displacement D_i, electric field E_i, and electric potential Φ are treated as independent variations, L is a trial Lagrangian and BI is the ''boundary'' integral, which are defined, respectively, as

$$L = (\sigma_{ij,j} + f_i) u_i + \tfrac{1}{2}\rho u_{i,t} u_{i,t} + F, \qquad (2)$$

$$BI = \sum_{k=1}^{7} \int_{t^{(n-1)}}^{t^{(n)}} \int_{A_k} G_k dA dt + \int_V G_8 dV. \qquad (3)$$

In the above expressions, F and G_i ($i=1$–8) are unknowns which can be determined in the manner described in the author's previous papers (He [2,4,5]). Using a sequence of manipulations, we ultimately obtain the Lagrangian in the form

Contributed by the Applied Mechanics Division of THE AMERICAN SOCIETY OF MECHANICAL ENGINEERS for publication in the JOURNAL OF APPLIED MECHANICS. Manuscript received by the ASME Applied Mechanics Division, May 23, 2000; final revision, Oct. 19, 2000. Associate Editor: M. J. Pindera.

$$L=(\sigma_{ij,j}+f_i)u_i+\tfrac{1}{2}\rho u_{i,t}u_{i,t}+\sigma_{ij}\gamma_{ij}-\tfrac{1}{2}\gamma_{ij}a_{ijkl}\gamma_{kl}$$
$$+\gamma_{ij}e_{mij}E_m+\gamma_{ij}b_{ij}\theta+\tfrac{1}{2}c\theta_0\theta^2+\theta c_iE_i-\theta t'q_{i,i}-\alpha\theta$$
$$+\tfrac{1}{2}(K_{ij}\tau+t')q_iq_j-\beta q_i-E_iD_i+\tfrac{1}{2}E_i\varepsilon_{ij}E_j+D_i\Phi_{,i}+g\Phi. \tag{4}$$

The unknowns appearing in the boundary integral *BI* can be written as follows:

$$G_1=-\sigma_{ij}n_j\overline{u_i},G_2=-u_i(\sigma_{ij}n_j-\overline{p_i}),G_3=\overline{\Phi}D_in_i,$$
$$G_4=\Phi(D_in_i-\overline{D_n}),G_5=-t'q_i(\theta-\overline{\theta}),$$
$$G_6=-t'\theta\overline{q_n},G_7=-t'Bi\,\theta(\tfrac{1}{2}\theta-\Theta),$$
$$-G_8=\tfrac{1}{2}[f_1u_i+(u_i-f_{2i})u_{i,t}]^{(n-1)}+\rho[u_i\tilde{u}_{i,t}]^{(n)}. \tag{5}$$

Here the bar (for example $\overline{u_i}$) indicates that the variable is prescribed on the boundary, f's are given functions of the coordinates x_i ($i=1$–3), $\tilde{u}_{i,t}$ is considered as a restricted variation, i.e., $\delta\tilde{u}_{i,t}=0$, the time t is semi-discrete, and the time difference is defined as $t'=t-t^{(n-1)}$, where the subscript n denotes nth time step, $n\geqslant 1$ and $t^{(0)}=0$. So we can obtain the analytical solution for $t\in[t^{(n-1)},t^{(n-1)}+t']$. The variables α and β in Eq. (4) are defined, respectively, as

$$\alpha=c\theta_0\theta^{(n-1)}+b_{ij}\gamma_{ij}^{(n-1)}+c_iE_i^{(n-1)}+t'\rho Q, \tag{6}$$

$$\beta=K_{ij}\tau q_i^{(n-1)}. \tag{7}$$

The definitions of the other variables in the above equations can be found in Chandrasekharaiah [1].

It is easy to prove that the stationary conditions of the obtained variational principle satisfy all the field equations and boundary/initial conditions. Further, it should be pointed out that the Euler equations with respect to θ and q_i read

$$c\theta_0\theta+b_{ij}\gamma_{ij}+c_iE_i-t'q_{i,i}=\alpha, \tag{8}$$

$$t'\theta_i+(K_{ij}\tau+t')q_i=\beta. \tag{9}$$

If the case $t'\to 0$, the above difference equations turn out to be the Fourier's laws for heat conduction:

$$c\theta_0\frac{\partial\theta}{\partial t}+b_{ij}\frac{\partial\gamma_{ij}}{\partial t}+c_i\frac{\partial E_i}{\partial t}=q_{i,i}+\rho Q, \tag{10}$$

$$\theta_{,i}=-K_{ij}\left(\tau\frac{\partial q_i}{\partial t}+q_i\right). \tag{11}$$

Equation (11) can be written in a more convenient form:

$$\tau\frac{\partial q_i}{\partial t}+q_i=-k_{ij}\theta_j, \tag{12}$$

where K_{ij} is the inverse of k_{ij}.

Next, we introduce a generalized thermo-strain-piezoelectric energy density defined as

$$\Pi=\tfrac{1}{2}\gamma_{ij}a_{ijkl}\gamma_{kl}-\gamma_{ij}e_{mij}E_m-\gamma_{ij}b_{ij}\theta$$
$$-\tfrac{1}{2}c\theta_0\theta^2-\theta c_iE_i-\tfrac{1}{2}E_i\varepsilon_{ij}E_j. \tag{13}$$

From (13), we have the following relations:

$$\frac{\partial\Pi}{\partial\gamma_{ij}}=\sigma_{ij},\quad \frac{\partial\Pi}{\partial E_m}=-D_m,\quad \frac{\partial\Pi}{\partial\theta}=-\rho S. \tag{14}$$

Constraining the generalized Lagrangian (4), we obtain the following Lagrangian with only two independent variations u_i and Φ:

$$\tilde{L}(u_i,\Phi)=\sigma_{ij}\gamma_{ij}-\Pi+g\Phi+\tfrac{1}{2}\rho u_{i,t}u_{i,t}. \tag{15}$$

We introduce a new variable Ω defined as

$$\Omega=\sigma_{ij}r_{ij}-\Pi, \tag{16}$$

and we call Ω the complementary energy density of thermopiezoelectricity. So we have the following functional:

$$\tilde{J}(u_i,\Phi)=\int_{t^{(n-1)}}^{t^{(n)}}\int\left(\Omega-g\Phi+\frac{1}{2}\rho u_{i,t}u_{i,t}\right)dVdt+BI, \tag{17}$$

which is proved to be a minimum principle, and we name it the minimum complementary energy principle of thermopiezoelectricity.

We can also begin with the following trial Lagrangian:

$$L_1=\sigma_{ij}(\gamma_{ij}-\tfrac{1}{2}u_{i,j}-\tfrac{1}{2}u_{j,i})+F. \tag{18}$$

Using the same sequence of manipulations as before, we can obtain the following generalized Lagrangian:

$$L_1=\tfrac{1}{2}\rho u_{i,t}u_{i,t}-\Pi+\sigma_{ij}(\gamma_{ij}-\tfrac{1}{2}u_{i,j}-\tfrac{1}{2}u_{j,i})+\theta(t'q_{i,i}+\alpha)$$
$$+q_i[\tfrac{1}{2}(K_{ij}\tau+t')q_j-\beta]-\Phi(D_{i,i}-g). \tag{19}$$

Constraining the Lagrangian (19) results in

$$\tilde{L}_1=T-\Pi, \tag{20}$$

where $T=\tfrac{1}{2}\rho u_{i,t}u_{i,t}$. Clearly, Eq. (20) has the form of a Hamiltonian.

Conclusions

In this Note, we have succeeded in obtaining a family of generalized variational principles for linear thermopiezoelectricity, from which various variational principles can be obtained by constraining the functional through the choice of field equations or boundary/initial conditions. All the obtained variational functionals can be reduced to the known variational principles of elasticity if the thermal and electrical effects are ignored. The present formulation provides a more comprehensive theoretical basis for finite element applications, and other modern numerical techniques.

Acknowledgments

The author thanks Prof. Marek-Jerzy Pindera and three unknown reviewers for their useful comments and suggestions. The work is supported by National Key Basic Research Special Fund of China (No. G1998020318).

References

[1] Chandrasekharaiah, D. S., 1998, "A Generalized Linear Thermo-Elasticity Theory for Piezoelectric Media," Acta Mech., **71**, pp. 39–49.
[2] He, J. H., 1999, "A Variational Principle for Thermo-Piezoelectricity Based on Chandrasekharaiah's Generalized Linear Theory," J. Univ. Shanghai Sci. Tech. **21**, No. 4, pp. 356–365.
[3] Liu, G. L., 1999, "A Unified Variational Theory for Coupled Thermoelasticity," Acta Mech. Sin., **31**, No. 2, pp. 165–172(in Chinese).
[4] He, J. H., 2000, "A Classical Variational Model for Micropolar Elastodynamics," Int. Nonlinear Sci. Numer. Simul. **1**, No. 2, pp. 133–138.
[5] He, J. H., 2000, "Generalized Hellinger-Reissner Principle," ASME J. Appl. Mech., **67**, No. 2, pp. 326–331.

Stability of Beams on Bi-Moduli Elastic Foundation

Z. H. Liu

L. Wang
e-mail: wanglei@sdu.edu.cn

Department of Civil Engineering, Shandong University,
Jinan 250061, P. R. China

L. Z. Pan
Shanghai Institute of Applied Mathematics and
Mechanics, Shanghai University, Shanghai 200000,
P. R. China

This paper adopts the newly structured δ function and displacement function. Using two adjacent transition points as two interval terminals while beams buckle makes the interval $[x_{i-1}, x_i]$. According to the Winkler's beam buckling theory on elastic foundation, we present the energy solutions of beams and then the exact solutions of buckling load of simple supported beams on bi-moduli elastic foundation. [DOI: 10.1115/1.1360181]

1 Introduction

The bi-moduli elastic foundation model assumes that when the foundation is compressed or tensioned, the reaction that the foundation gives its above construction is expressed by

$$P(x,y)=\begin{cases} K_1 W(x,y), & W\geqslant 0 \\ K_2 W(x,y), & W<0 \end{cases}$$

in which k_1, k_2 are the non-negative reaction coefficients. When k_1 equals to k_2, the bi-moduli elastic foundation model becomes the Winkler elastic foundation model. Because the variation of the tension and pressure reaction of the foundation leads to the nonlinear of governing equation, the mechanical problems of structures on bi-moduli elastic foundation becomes more complicated. Even if relatively simple conditions, it is very difficult to get the solutions of the nonlinear differential equations. In 1967, Tsai and Westmann first made the analysis of bending of beams on tensionless foundation (k_1 or k_2 is zero) ([1]). Since that, many scholars have always studied the bending of beams on tensionless foundation ([2]). In 1985, Adin first made the analysis of bending of beams on relatively common bi-moduli elastic foundation ([3]). At present, no one has presented the analysis of the beam stability on bi-moduli elastic foundation. In this paper, authors present the exact solutions of buckling load of simple supported beams on bi-moduli elastic foundation (See Fig. 1).

2 The Solution of the Stability of Beams on Bi-Moduli Elastic Foundation

If $k_1=k$ and $\alpha=k_2/k$, then the potential energy of beams is

$$\bar{\Pi}=\frac{1}{2}\int_0^1\left[EI(\bar{W}'')^2-\bar{P}(\bar{W}')^2+\frac{1+\alpha}{2}K\bar{W}^2+\frac{1-\alpha}{2}K\bar{W}|\bar{W}|\right]d\bar{x}. \tag{1}$$

Contributed by the Applied Mechanics Division of THE AMERICAN SOCIETY OF MECHANICAL ENGINEERS for publication in the ASME JOURNAL OF APPLIED MECHANICS. Manuscript received by the ASME Applied Mechanics Division, Feb. 3, 2000; final revision, Dec. 22, 2000. Associate Editor: S. Kyriakides.

Induct the following changes into (1):

$$x=\bar{x}/\bar{l},\quad W=\bar{W}/\bar{l},\quad \lambda=\bar{l}\sqrt[4]{K/EI},$$
$$P=\bar{P}/\sqrt{EIK},\quad \Pi=\bar{\Pi}\bar{l}/\sqrt{EIK}. \tag{2}$$

Then

$$\Pi=\frac{1}{2}\int_0^1\left[\frac{1}{\lambda^2}(W'')^2-P(W')^2+\frac{1+\alpha}{2}\lambda^2W^2+\frac{1-\alpha}{2}\lambda^2W|W|\right]dx. \tag{3}$$

The interval [0, 1] is divided into n small intervals: $[x_0,x_1],[x_1,x_2],\ldots,[x_{n-1},x_n]$. The displacement function made in the interval $[x_{i-1},x_i]$ is

$$W_i(x)=A_i\,\mathrm{Sin}\frac{x-x_{i-1}}{x_i-x_{i-1}}\pi\quad i=1,2,\cdots,n \tag{4}$$

$$W_i'(x)=\frac{\pi}{\Delta x_i}A_i\,\mathrm{Cos}\frac{x-x_{i-1}}{\Delta x_i}\quad i=1,2,\cdots,n. \tag{5}$$

Equation (4) should be subjected to the following conditions:

$$W_{i+1}'(x_i)=W_i'(x_i)\quad i=1,2,\cdots,n-1, \tag{6}$$

for (5) and (6) yield

$$-\frac{A_i}{\Delta x_i}=\frac{A_{i+1}}{\Delta x_{i+1}}\quad i=1,2,\cdots,n. \tag{7}$$

Then

$$\frac{A_1}{\Delta x_1}=\frac{(-1)^{2-1}A_2}{\Delta x_2}=\frac{(-1)^{3-1}A_3}{\Delta x_3}=\cdots=\frac{(-1)^{n-1}A_n}{\Delta x_n} \tag{8}$$

$$\frac{A_1+(-1)^{2-1}A_2+\cdots(-1)^{n-1}A_n}{\Delta x_1+\Delta x_2+\cdots+\Delta x_n}=\frac{(-1)^{i-1}A_i}{\Delta x_i}. \tag{9}$$

Thus

$$\Delta x_i=\frac{(-1)^{i-1}A_i}{\sum_{j=1}^{n}(-1)^{j-1}A_j}\quad i=1,2,\cdots,n, \tag{10}$$

for (10) yield

$$(-1)^{i-1}A_i=A\Delta x_i\quad i=1,2,\cdots,n. \tag{11}$$

Then

$$A_i^2=A^2(\Delta x_i)^2\quad i=1,2,\cdots,n \tag{12}$$

in which

$$\Delta x_i=x_i-x_{i-1}\quad i=1,2,\cdots,n$$
$$A=A_1-A_2+A_3-A_4+\cdots+(-1)^{n-1}A_n.$$

For (12), three following integral solutions are

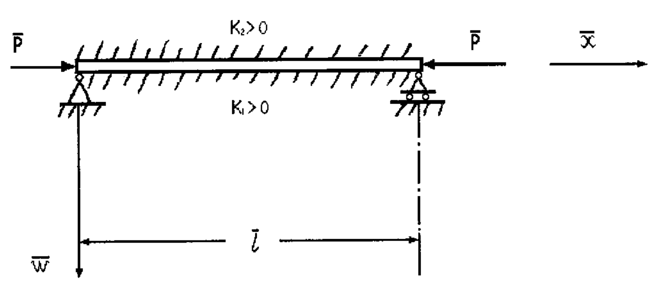

Fig. 1

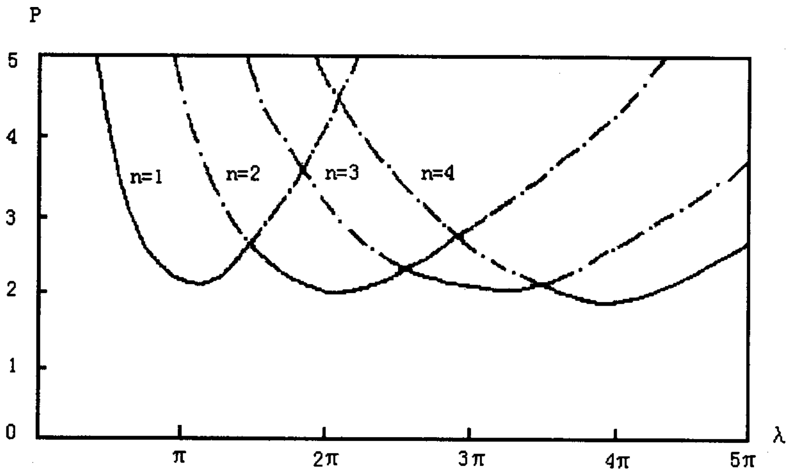

Fig. 2

$$\begin{cases} \int_{x_{i-1}}^{x_i} (W_i'')^2 dx = \frac{1}{2}\pi^4 A^2 (\Delta x_i)^{-1} \\ \int_{x_{i-1}}^{x_i} (W_i')^2 dx = \frac{1}{2}\pi^2 A^2 \Delta x_i \\ \int_{x_{i-1}}^{x_i} W_i^2 dx = \frac{1}{2} A^2 (\Delta x_i)^3 \quad i=1,2,\cdots,n \end{cases} . \tag{13}$$

In the interval $[x_{i-1}, x_i]$, Π is signed as Π_i,

$$\Pi_i = \frac{1}{2}\int_{x_{i-1}}^{x_i} \left[\frac{1}{\lambda^2}(W_i'')^2 - P(W_i')^2 + \lambda^2 \delta_i^4 W_i^2 \right] dx \quad i=1,2,\cdots,n \tag{14}$$

where

$$\delta_i = \alpha^{1+(-1)^i/8} \quad i=1,2,\cdots,n \tag{15}$$

$$\Pi = \sum_{i=1}^{n} \Pi_i \quad i=1,2,\cdots,n. \tag{16}$$

For (13), (14), and (16) yield

$$4\Pi = A^2 \left[\frac{\pi^2}{\lambda^2} \sum_{i=1}^{n} (\Delta x_i)^{-1} - \pi^2 P \sum_{i=1}^{n} \Delta x_i + \lambda^2 \sum_{i=1}^{n} \delta_i^4 (\Delta x_i)^3 \right] \tag{17}$$

For $\partial\Pi/\partial A_J = 0$ $j=1,2,\cdots,n$, and $\Sigma_{i=1}^n \Delta x_i = 1$, thus

$$P = \frac{\pi^2}{\lambda^2}\sum_{i=1}^{n} (\Delta x_i)^{-1} + \frac{\lambda^2}{\pi^2}\sum_{i=1}^{n} [\delta_i^4 (\Delta x_i)^3] \tag{18}$$

$$\frac{\partial P}{\partial \Delta x_i} = -\frac{\pi^2}{\lambda^2}(\Delta x_i)^{-2} + 3\frac{\lambda^2}{\pi^2}\delta_i^4 (\Delta x_i)^2 \quad i=1,2,\cdots,n. \tag{19}$$

To find the minimum of P, solve the equation $\partial P/\partial \Delta x_i = 0$, thus

$$\Delta x_i = \frac{\pi}{\sqrt[4]{3}\lambda \delta^i} \quad i=1,2,\cdots,n \tag{20}$$

$$\Delta x_i / \Delta x_1 = \delta_i^{-1} \quad i=1,2,\cdots,n. \tag{21}$$

For

$$\sum_{i=1}^{n} \Delta x_i = \sum_{i=1}^{n} [\Delta x_1 \delta_i^{-1}] = \Delta x_1 \sum_{i=1}^{n} \delta_i^{-1} = 1,$$

thus

$$\Delta x_1 = \frac{1}{\sum_{i=1}^{n} \delta_i^{-1}} \tag{22}$$

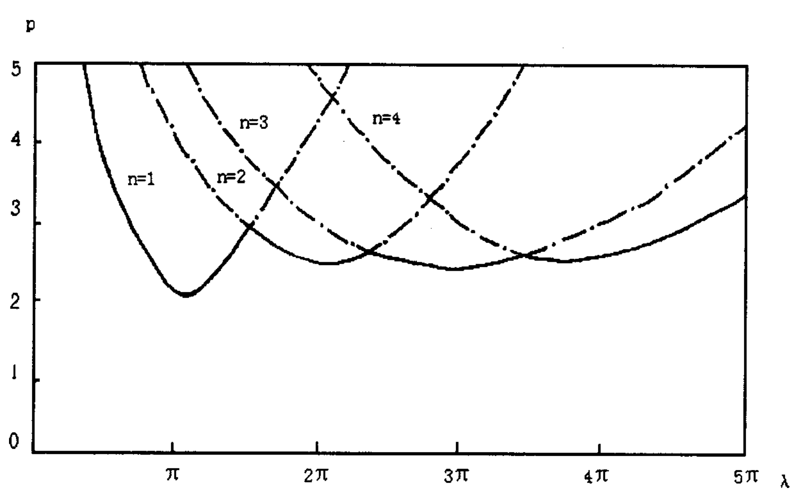

Fig. 3

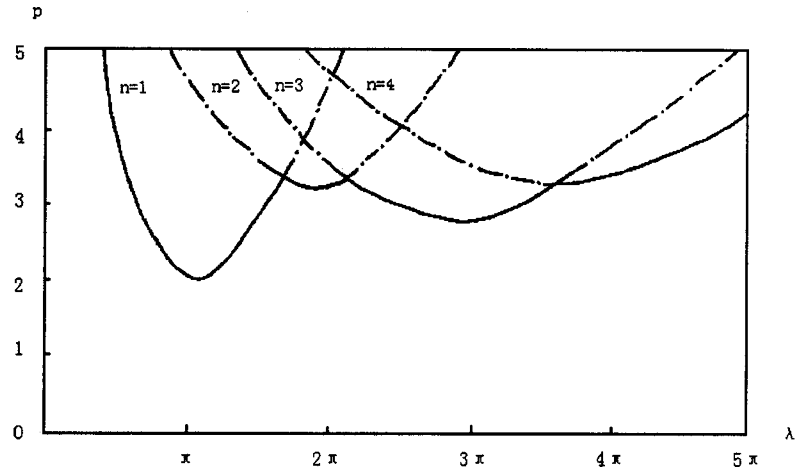

Fig. 4

$$\Delta x_i = \left[\delta_i \sum_{j=1}^{n} \delta_j^{-1} \right]^{-1}. \quad (23)$$

Substituting (23) into (18), thus

$$P = \frac{\pi^2}{\lambda^2} \left(\sum_{i=1}^{n} \delta_i \right) \left(\sum_{j=1}^{n} \delta_j^{-1} \right) + \frac{\lambda^2}{\pi^2} \left(\sum_{i=1}^{n} \delta_i \right) \left(\sum_{j=1}^{n} \delta_j^{-1} \right)^{-3}. \quad (24)$$

If n is an even number, then

$$P = \frac{n^2\pi^2}{\lambda^2} \frac{(1+\alpha^{1/4})(1+\alpha^{-1/4})}{4} + \frac{\lambda^2}{n^2\pi^2} \frac{4(1+\alpha^{1/4})}{(1+\alpha^{-1/4})^3} \quad (25)$$

for $\partial P/\partial\lambda = 0$, thus

$$\lambda = \tfrac{1}{2}(1+\alpha^{-1/4}) n\pi \quad (26)$$

$$P_{\min} = 2\alpha^{1/4}. \quad (27)$$

If n is an odd number, then

$$P = \frac{n^2\pi^2}{4\lambda^2} \left[(1+\alpha^{1/4}) + \frac{1}{n}(1-\alpha^{1/4}) \right] \cdot \left[(1+\alpha^{-1/4}) + \frac{1}{n}(1-\alpha^{-1/4}) \right] + \frac{\lambda^2}{n^2\pi^2} \left[(1+\alpha^{1/4}) + \frac{1}{n}(1-\alpha^{1/4}) \right] \cdot \left[(1+\alpha^{-1/4}) + \frac{1}{n}(1-\alpha^{-1/4}) \right]^{-3} \quad (28)$$

for $\partial P/\partial\lambda = 0$, thus

$$\lambda = \frac{1}{2} \left[(1+\alpha^{-1/4}) + \frac{1}{n}(1-\alpha^{-1/4}) \right] n\pi \quad (29)$$

$$P_{\min} = 2 \left[(1+\alpha^{1/4}) + \frac{1}{n}(1-\alpha^{1/4}) \right] \left[(1+\alpha^{-1/4}) + \frac{1}{n}(1-\alpha^{-1/4}) \right]^{-1}. \quad (30)$$

According to (25), (26), (27) or (28), (29), (30), the following curves are plotted. In Fig. 2, Fig. 3, and Fig. 4, the curves p-λ are shown for $\alpha=1$, 2 and 5 when the half-wave number n is 4. The solid line represents for the real curves p-λ. When λ exceeds the critical λ corresponding to the point of intersection of two adjacent curves, the half-wave number will be increased one.

3 Conclusions and Discussion

The dividing point of any two adjacent half-waves can be gotten by (22) and (23) when the buckling of beams on bi-moduli elastic foundation happens. Assume $\alpha=1$ in (25) and (28), then yields the equation of buckling load of beams on the Winkler foundation. The equation is

$$P = \frac{n^2\pi^2}{\lambda^2} + \frac{\lambda^2}{n^2\pi^2}.$$

And its curve p-λ is Fig. 2. Comparing Fig. 2 with Fig. 3 and Fig. 4, it can be gotten that more α increases, farther the minimum points of the curves p-λ deviate from the line $p=2$. The buckling of beams on bi-moduli elastic foundation first occurs along the direction of the least reaction coefficient of the foundation. So $\alpha \geqslant 1$ is adopted in (25) and (28). But the displacement function adopted by this paper does not adapt to the analysis of stability of simply supported beams on tensionless foundation, namely $\alpha \neq 0$ in (25) and (28). This special condition needs more study.

References

[1] Tsai, N. C., and Westmann, R. A., 1967, ‘‘Beams on Tensionless Foundation,’’ J. Eng. Mech., ASCE, **93**, No. EM5, pp. 1–12.
[2] Selvadurai, A. P. S., 1979, *Elastic Analysis of Soil-Foundation Interaction*, Elsevier, Amsterdam.
[3] Adin, M. A., Yankelevsky, D. Z., and Eisenberger, M., 1985, ‘‘Analysis of Beams on Bi-Moduli Elastic Foundation,’’ Comput. Methods Appl. Mech. Eng., **49**, pp. 319–330.

Period-Doubling Bifurcation and Non-Typical Route to Chaos of a Two-Degree-Of-Freedom Vibro-Impact System

G. L. Wen and J. H. Xie
Department of Applied Mechanics and Engineering,
Southwestern Jiaotong University, Chengdu 610031,
P. R. China

A nontypical route to chaos of a two-degree-of-freedom vibro-impact system is investigated. That is, the period-doubling bifurcations, and then the system turns out to the stable quasi-periodic response while the period 4-4 impact motion fails to be stable. Finally, the system converts into chaos through phrase locking of the corresponding four Hopf circles or through a finite number of times of torus-doubling. [DOI: 10.1115/1.1379035]

Contributed by the Applied Mechanics Division of THE AMERICAN SOCIETY OF MECHANICAL ENGINEERS for publication in the ASME JOURNAL OF APPLIED MECHANICS. Manuscript received by the ASME Applied Mechanics Division, Apr. 2, 2000; final revision, Dec. 5, 2000. Associate Editor: N.-C. Perkins.

Introduction

Vibro-impacting phenomena exist in many areas of applied mechanics and engineering. Because the noncontinuity property exists in the differential equations of vibro-impact systems, to investigate the Poincaré maps of vibro-impact systems is more suitable for the exhibition of complicated dynamic behaviors of the system than to do directly for the differential equations of the motions (see Shaw and Shaw [1], Luo and Xie [2], and Xie, [3]). Unfortunately, the Poincaré maps of vibro-impact systems can only be written as implicit forms. Therefore, some enormous difficulties exist unavoidably in the study of dynamic behavior of vibro-impact systems, especially for multiple-degree-of-freedom vibro-impact systems. Even though a large amount of results on the dynamics of one-degree-of-freedom vibro-impact system have been presented, there is still more work to be done in multiple-degree-of-freedom vibro-impact systems. The existence of quasi-periodic impact motions of a two-degree-of-freedom vibro-impact system similar to the one herein was still recently investigated by Luo and Xie (see [2]).

It is well known that the routes to chaos from period-doubling cascades and from a finite number of times of torus-doubling both are typical. In this brief note, after the period-doubling bifurcation of the two-degree-of-freedom vibro-impact system aforesaid is verified by analytical method, we briefly reported a nontypical route to chaos for the multiparameter vibro-impact system. That is, the period-doubling cascades occur cease after two times of period-doubling bifurcations, and then the system turns out to the stable quasi-periodic response while the period 4-4 impact motion fails to be stable. Finally, after the simultaneously appearing four Hopf circles fail to stable, the system converts into chaos directly through phrase locking of the corresponding four Hopf circles or through a finite number of times of torus-doubling.

However, though it is perhaps easy to investigate by theoretical analysis the process of period-doubling cascade for some simple map systems, few proper analytical methods could be employed to investigate the whole process of period-doubling cascades of some quite complex dynamic system such as multi-degree-of-freedom vibro-impact systems so far. Usually, one may take it for granted a route from period-doubling cascades to chaos existing in a very complex system after the arduous analyses of one or two of period-doubling bifurcations and a seemly reasonable plot of period-doubling bifurcation cascades are made. According to the results presented this brief note, it is very possible for those complicated vibro-impact systems with multiple degree-of-freedom that the long period motions, quasi-periodic responses, and chaotic responses are quite easily be confused each other.

Analysis of Period-Doubling Bifurcation of the System

The mechanical model of a two-degree-of-freedom vibro-impact system with a gap B is shown in Fig. 1. The mass M_1 impacts against a rigid surface when its displacement X_1 equals the gap B. The impact is described by a coefficient of restitution R, and it is assumed that the duration of impact is negligible compared to the period of the force.

Between two consecutive impacts, for $X_1<B$, the equations of motion of the vibro-impact system with proportional damping of the Rayleigh type are written in nondimensional form

$$\begin{cases} \begin{bmatrix} 1 & 0 \\ 0 & \mu_m \end{bmatrix}\begin{Bmatrix} \ddot{x}_1 \\ \ddot{x}_2 \end{Bmatrix}+\begin{bmatrix} 2\zeta & -2\zeta \\ -2\zeta & 2\zeta(1+\mu_c) \end{bmatrix}\begin{Bmatrix} \dot{x}_1 \\ \dot{x}_2 \end{Bmatrix} \\ \quad +\begin{bmatrix} 1 & -1 \\ -1 & 1+\mu_k \end{bmatrix}\begin{Bmatrix} x_1 \\ x_2 \end{Bmatrix}=\begin{Bmatrix} 1-f_2 \\ f_2 \end{Bmatrix}\sin(\omega t+\tau), \quad (x_1<b) \\ \dot{x}_{1+}=-R\dot{x}_{1-}, \quad (x_1=b) \end{cases} \tag{1}$$

where the nondimensional quantities are in forms

$$\mu_m=\frac{M_2}{M_1}, \quad \mu_k=\frac{K_2}{K_1}, \quad \mu_c=\mu_k, \quad f_2=\frac{P_2}{P_1+P_2},$$

$$\omega=\Omega\sqrt{\frac{M_1}{K_1}}, \quad \zeta=\frac{C_1}{2\sqrt{K_1M_1}}, \quad t=T\sqrt{\frac{K_1}{M_1}}, \quad b=\frac{BK_1}{P_1+P_2},$$

$$x_i=\frac{X_iK_1}{P_1+P_2}, \quad \dot{x}_{1+}=\frac{\dot{X}_{1+}K_1}{P_1+P_2}, \quad \dot{x}_{1-}=\frac{\dot{X}_{1-}K_1}{P_1+P_2} \quad i=1,2.$$

In Eq. (1), a dot denotes differentiation with respect to the nondimensional time t, the phase angle τ is used only to make a suitable choice for the origin of time in the calculation between two consecutive impacts, $\dot{x}_{1+}$ and $\dot{x}_{1-}$ represent the impacting mass velocities of approach and departure, respectively.

Choosing a Poincaré section $\sigma\subset R^4\times S$, where $\sigma=(x_1,\dot{x}_1,x_2,\dot{x}_2,\theta)\in R^4\times S$, $x_1=b$, $\dot{x}_1=\dot{x}_{1+}$, we can establish the Poincaré map of the system (see [2]) and express it briefly as

$$X'=\tilde{f}(v,X) \tag{2}$$

where $\theta=\omega t$, $\tilde{f}=(\tilde{f}_1,\tilde{f}_2,\tilde{f}_3,\tilde{f}_4)^T$, $X\in R^4$, $X=X^*+\Delta X$, $X'=X^*+\Delta X'$, $v\in R^1$. $X^*=(\dot{x}_{1+},x_{20},\dot{x}_{20},\tau_0)^T$ is a fixed point in the hyperplane σ. ΔX and $\Delta X'$ are the disturbed vectors of X, X', respectively. $v=\omega$ is the bifurcation parameter.

With a change of variables, the map (2) is given by

$$\Delta X'=\tilde{f}(v,X)-X^*\overset{\text{Def}}{=}f(v,\Delta X). \tag{3}$$

Map (3) is C^∞. Suppose that there exists fixed point X^* for v in some neighborhood of the critical parameter values $v=v_c$, at which $Df_{\Delta X}(v,0)$ satisfies the following hypotheses:

H1 $Df_{\Delta X}(v,0)$ has an eigenvalue $\lambda_1(v_c)=-1$, and the other eigenvalues stay inside the unit circle;

H2 $\mathbf{d}|\lambda_1(v)|/\mathbf{d}v|_{v=v_c}>0$.

Subject to the hypotheses H1 and H2, the fixed point X^*, which is stable for $v<v_c$, becomes unstable for $v>v_c$, whereas there may exist period-doubling bifurcation in the map (2) for $v=v_c$.

To determine the existence of period-doubling bifurcation in the four dimensional map (3), a center manifold reduction (see, for example, [4]) and a normal form technique (see [5,6]) are applied to reduce the Poincaré map (3) to a normal form, as follows:

$$x'=g(\mu,x)=-x+N(\mu,x)=-x+n_{11}\mu x+n_{03}x^3+\cdots \tag{4}$$

where $\mu=v-v_c$. Let $g^2(\mu,x)=g(\mu,g(\mu,x))$. It follows that the period-two points of Eq. (4) satisfy

$$g^2(\mu,x)-x=0. \tag{5}$$

Supposing now

$$n_{11}\cdot n_{03}\neq 0, \tag{6}$$

one can easily obtain by the implicit function theorem that

$$\mu=\mu(x)=-\frac{n_{03}}{n_{11}}x^2+O(x^2). \tag{7}$$

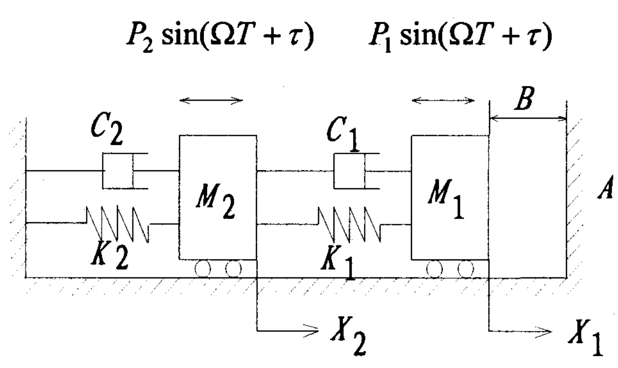

Fig. 1 The mechanics model

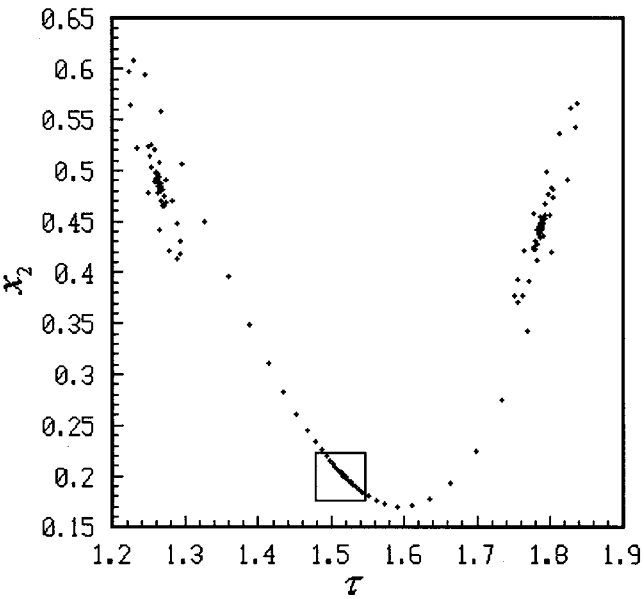

Fig. 2 ***v*=0.75, stable period 2 fixed points**

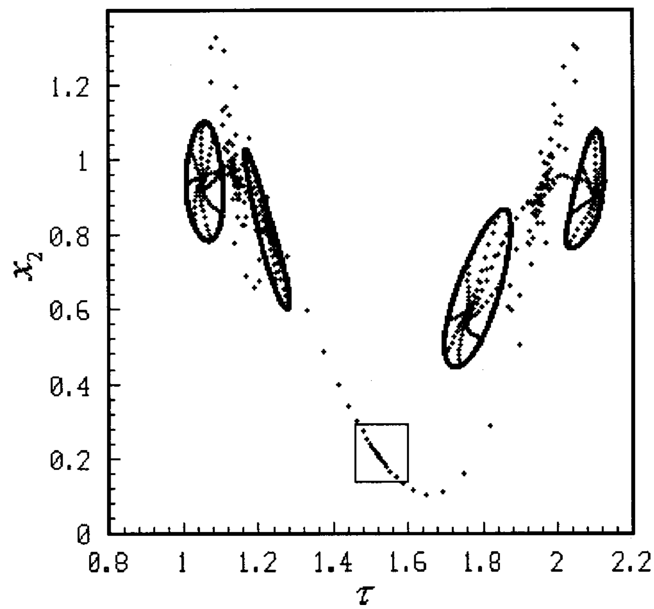

Fig. 4 ***v*=0.7563, four stable Hopf circles**

In other words, the implicit function theorem guarantees the existence of period-doubling bifurcation of map (2) for v in a neighborhood of v_c (corresponding to μ in a neighborhood of zero) when (6) holds.

The stability of the theoretical fixed point and the period-two points may be determined, respectively, from

$$\begin{cases} \left.\dfrac{\partial g}{\partial x}\right|_{x=0,\mu=\mu} = -1 + n_{11}\mu + O(\mu) \\ \left.\dfrac{\partial g^2}{\partial x}\right|_{x=x,\mu=\mu(x)} = 1 + 4n_{11}\mu + O(\mu) \end{cases} . \tag{8}$$

Nontypical Routes to Chaos

In this section the interesting dynamic characters of the vibro-impact system given in Fig. 1 involve a sort of a nontypical route to chaos.

(1) The system with parameters: $\mu_m=2$, $\mu_k=6.1$, $f_2=0$, $\zeta=0$, $b=1.6$, $R=0.82$ has been chosen for analysis. ω is taken as the bifurcation parameter; that is, $v=\omega$. When v is at $v_c \approx 0.745716$, find that the eigenvalues of $Df_{\Delta X}(v,0)$ in (3) $\lambda_1 = -1.000003$, $\lambda_2=-0.893354$ $\lambda_{3,4}=-0.183694 \pm i0.835633$. Then, with v increases through v_c on the interval $v \in [0.744, 0.751]$, $\lambda_1(v)$ will cross the unit circle and the other eigenvalues will still stay inside the unit circle. v_c is a period-doubling bifurcation critical value.

The map (3) satisfying the hypotheses H1 is reduced to the normal form (4). It then follows that $n_{11}=-0.572016$, $n_{03}=0.009147$, and a stable supercritical period-doubling bifurcation occurs. Numerical simulations of original four-dimensional map (2) are carried out for determining dynamics near the bifurcation value v_c. The dynamic behavior of the vibro-impact system is shown in the projected Poincaré section in Figs. 2–6. The Poin-

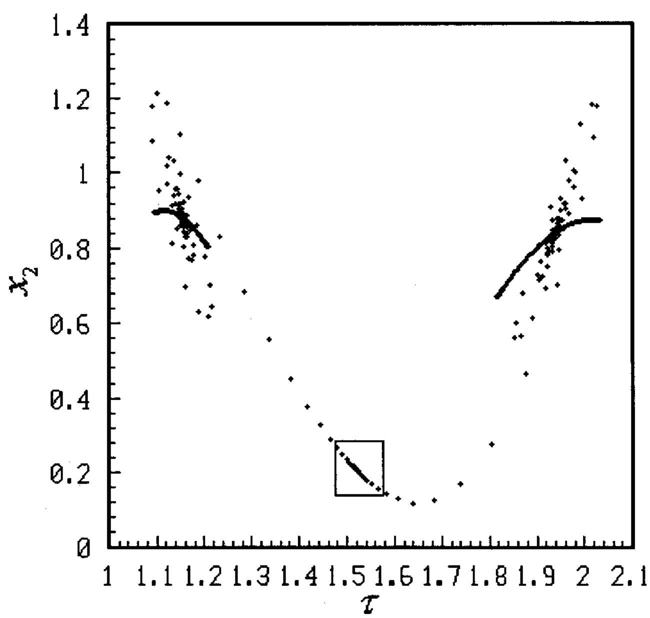

Fig. 3 ***v*=0.7554, stable period 4 fixed points**

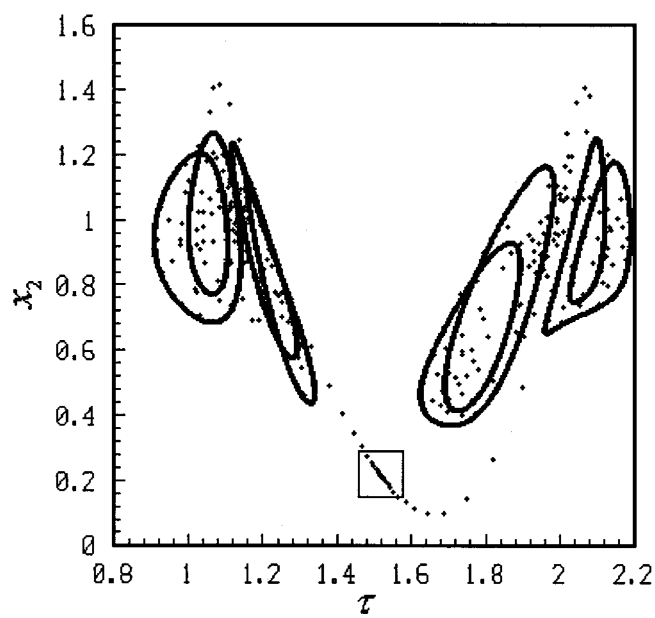

Fig. 5 ***v*=0.75685, four stable 2*T*-torus**

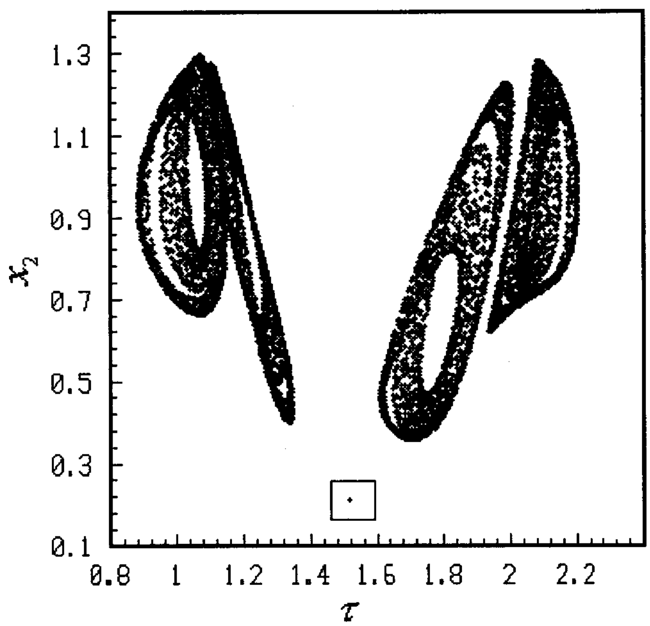

Fig. 6 ***v*=0.75705, chaos**

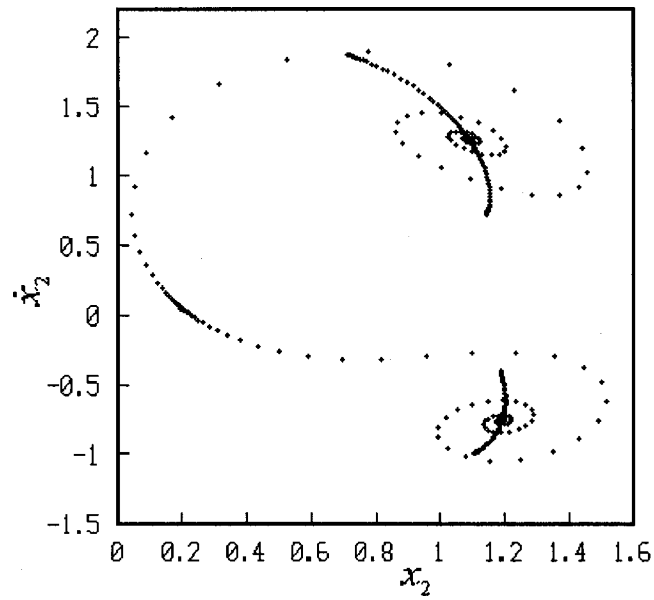

Fig. 8 ***v*=0.754, stable period 4 fixed points**

caré section is taken in the form σ, which will be four-dimensional. Here, the numerical results is projected to the (τ,x_2)-plane, which is called the projected Poincaré section, but the other the projected Poincaré sections are not shown herein for the sake of succinctness. The theoretical fixed point of four-dimensional map (4) corresponds to the 1-1 periodic impact motion of the system (1). We take it as an initial map point in numerical simulations and denote its location by □. The vibro-impact system (1) exhibits stable 1-1 orbits as $v \in [0.744,0.745676)$. As v passes through v_c, there exists a family of stable period-two fixed points (i.e., stable period 2-2 impact motion) bifurcating from the theoretical fixed point. As an example, the theoretical fixed point corresponding to $v=0.75$ is taken as initial map point, and it is attracted to the stable period 2 fixed points after 1500 impacts, as shown in Fig. 2. The result is in agreement with the one obtained by the analytical treatment in Section 2. As v keeps on increasing, find stable period-four points shown in Fig. 3. After then, it is surprising that the period-doubling cascade stops and four Hopf circles appear simultaneously by the Hopf bifurcations of the corresponding period-four points as seen in Fig. 4. As the values of v moves further away from v_c, the system evolutes to chaos (in Fig. 6) through a finite number of times of torus-doubling process "4 Hopf circles (in Fig. 4)$\rightarrow 4\times 2T$ torus (in Fig. 5)$\rightarrow 4\times 4T$ torus$\rightarrow 4\times 8T$ torus$\rightarrow$the breaking of $4\times 8T$ torus$\rightarrow$Chaos (in Fig. 6)". With further increase in the value of v, the system will be drawn out from chaotic motions, and stable quasi-periodic impacts occur, which is represented as the more complex torus. Finally, transition again to chaos through once torus-doubling bifurcation of the complex torus occurs.

(2) Consider another family of system parameters: $\mu_m=2$, $\mu_k=6$, $f_2=0$, $\zeta=0$, $b=1.5$, $R=0.7$. $v=\omega$ is still taken as the bifur-

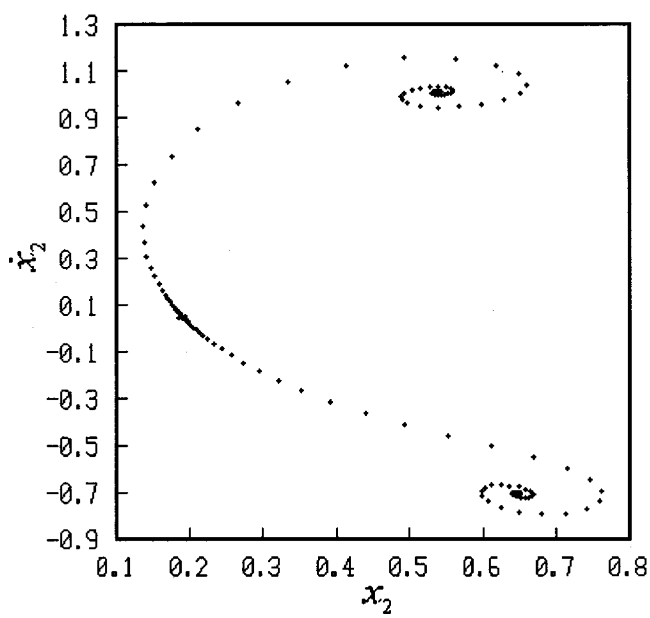

Fig. 7 ***v*=0.7515, stable period 2 fixed points**

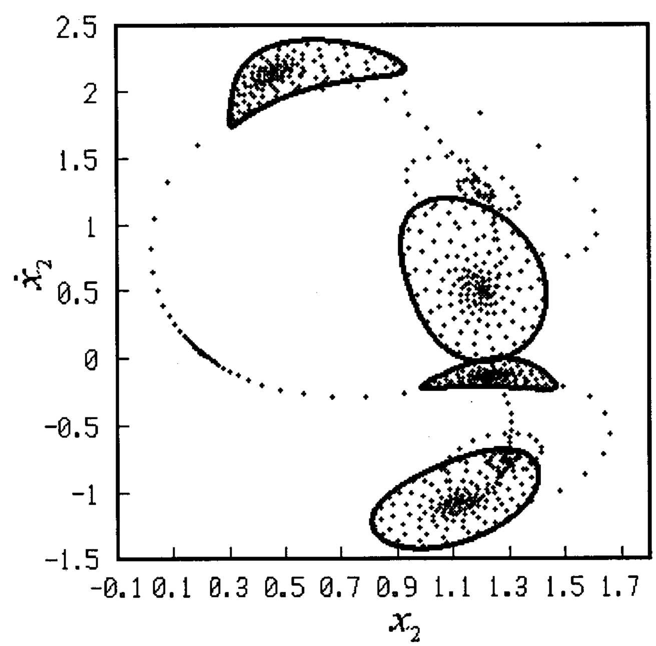

Fig. 9 ***v*=0.7552, four stable Hopf circles**

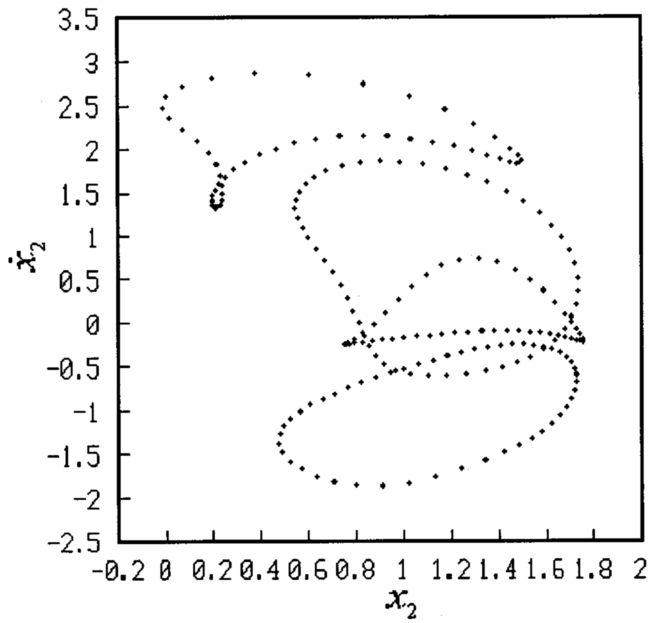

Fig. 10 $v = 0.755965$, **phase locking**

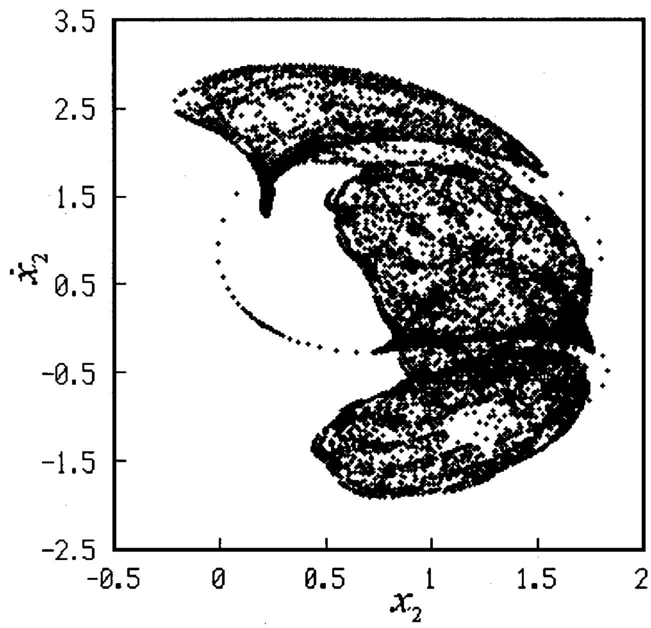

Fig. 11 $v = 0.755971$, **chaos**

cation parameter. When v is at $v_c \approx 0.7444904$, the eigenvalues of $Df_{\Delta X}(v,0)$ is $\lambda_1 = -1.000001$, $\lambda_2 = -0.8505967$ $\lambda_{3,4} = -0.148746 \pm i0.732957$. With v increases through v_c, a stable supercritical period-doubling bifurcation occurs. The dynamic evolution of the vibro-impact system (1) is shown in Figs. 7–11, in which the phrase locking in Fig. 10 is obtained by ignoring the first 500 impacts among 5000 impacts. It is remarkably mentioned the fate of the simultaneously appearing four Hopf circles differs from that of the first family of system parameters.

Conclusions and Discussion

The dynamic responses of the two-degree-of-freedom vibro-impact system in Fig. 1 have been considered in this note. If the bifurcation plots (v, τ_2) of this system under the two families of parameters was presented out respectively, one can find surprisingly the plots very alike to those usual period-doubling bifurcation cascades plots emerging in well-known classical systems such as $F_\mu(x) = \mu x(1-x)$. As a matter of fact, the real dynamic evolution of the vibro-impact system, however, is different at all to only from period-doubling bifurcation cascades to chaos. The significance of the nontypical route to chaos presented in this brief note is just located in the information of easily confusing long period motions, quasi-periodic responses, and chaotic responses in complicated multiparameter vibro-impact systems.

Acknowledgment

This research is supported by a grant from the National Natural Science Foundation of P. R. China No 10072051.

References

[1] Shaw, J., and Shaw, S. W., 1989, "The Onset of Chaos in a Two-degree-Freedom Impacting System," ASME J. Appl. Mech., **56**, pp. 168–174.
[2] Luo, G. W., and Xie, J. H., 1998, "Hopf Bifurcation of a Two-Degree-of-Freedom Vibrato Impact System," J. Sound Vib., **213**, No. 3, pp. 391–408.
[3] Xie, J. H., 1996, "Codimension Two Bifurcations and Hopf Bifurcations of an Impacting Vibrating System," Appl. Math. Mech., **17**, pp. 65–75.
[4] Car, J., 1981, *Applications of Center Manifold Theory* (Applied Mathematical Sciences 35), Springer-Verlag, New York, pp. 33–36.
[5] Iooss, G., 1987, *Forms normales d'applications: Caractérisation globale et méthode de calcul*, Universite de Nice, Nice, France.
[6] Elphick, C., Tirapegui, E., Brachet, M., Coullet, P., Iooss, G., 1987, "A Simple Global Characterization for Normal Forms of Singular Vector Fields," Physica D, **29**, pp. 95–127.

Analysis of Anisotropic Beams: An Analytic Approach

V. Rovenski

O. Rand
Associate Professor

Faculty of Aerospace Engineering, Technion-ITT,
Haifa 32000, Israel

An analytic solution for the elastic response of anisotropic composite beams of rectangular cross section is presented. The formulation is based on the expression of the stress tensor components as trigonometric series and exponential functions. The ability to predict the elastic response and the corresponding elastic coupling mechanisms is well demonstrated and discussed.
[DOI: 10.1115/1.1360183]

Introduction

For the last three decades, the analysis of composite beams has been the focal point of many research efforts, and the rapidly growing interest in this area during the last decade testify for its potential in a vast range of engineering applications.

One of the classical approaches to the analysis of anisotropic beams has been presented by Lekhnitskii [1], who expressed the stress functions and the stress tensor in terms of complex potentials, developed a rigorous derivation of the associated governing equations and boundary conditions, and presented analytic solu-

Contributed by the Applied Mechanics Division of THE AMERICAN SOCIETY OF MECHANICAL ENGINEERS for publication in the ASME JOURNAL OF APPLIED MECHANICS. Manuscript received by the ASME Applied Mechanics Division, Apr. 20, 2000; final revision, Nov. 8, 2000. Associate Editor: M.-J. Pindera.

tions for some specific cases. In this note, an exact solution for generic anisotropic beams is derived and discussed in terms of Lekhnitskii's formulation.

The linear problem may be divided into smaller subproblems and classified with respect to three main categories. The *first* category deals the nature of the applied loads. Here, it is convenient to obtain first the solution for the case where the stresses do not vary along the length of the beam, and subsequently extend it to the general case of nonuniformly distributed surface loads. The *second* aspect for which classification of the problem is required is the number of laminae. The basic level with that respect contains the case of a single lamina (i.e., a homogeneous beam). Such a solution may be extended for cases of two or more laminae using interlaminar compatibility equations, see also Rand and Rovenski [2]. The *third* aspect of classification is the shape of a section. Since the present methodology is closely related to the solution of Dirichlet problem for the domain occupied by lamina, it is first convenient to apply the analysis to rectangular cross section.

The present approach employs analytic techniques and does not include numerical approximations (such as predetermined shape functions, iterative schemes, numerical integration and/or differentiation, etc.). Subsequently, the model is free of simplified assumptions regarding the solution, and therefore all global and minor effects and details (including all stress and strain components) are simultaneously kept. For that reason the accuracy of the present approach is well analytically established. For other analysis techniques, the reader is referred to Savoia and Reddy [3], Whitney [4], and Makeev and Armanios [5].

The core solution presented in this note is focused on the case of a homogeneous beam where the loads create stresses which do not vary along its span. The associated complex potentials, the stress functions, the stress and the strain vectors, and the displacements are presented as trigonometric series, the coefficients of which are the solutions of a linear system of algebraic equations. The method may handle both tip and surface loads. The ability to predict the elastic coupling mechanisms is also presented. The generality of the core solution enables a direct extension of the method to several cases that include laminate beams, spanwise dependent loads, polar anisotropy, and additional solid and thin-walled cross section geometries. The analytic derivation and the illustrative examples have been carried out using MAPLE symbolic manipulations software.

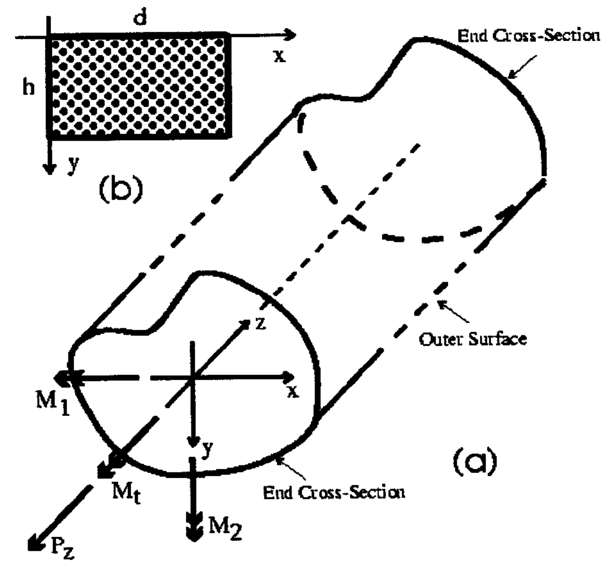

Fig. 1 Composite beam notation; (*a*) general view, (*b*) a rectangular cross section

Formulation of the Problem

Consider an uniform composite beam (i.e., a solid slender structure having two kind of boundaries: the two end cross sections and the outer cylindrical surface), as shown in Fig. 1(a). In the present note, the case of a rectangular cross section of width d and height h will be under discussion, and for the sake of convenience, the origin of the Cartesian coordinate system is placed at the corner of the rectangular $\Pi=\{0\leqslant x\leqslant d,\ 0\leqslant y\leqslant h\}$, see Fig. 1($b$). The material possesses anisotropy which is obtained by a rotation of orthotropic material by the angle $-t$ about the y-axis, and therefore, the $x-z$ planes exhibit elastic symmetry. Due to the above defined anisotropy, the constitutive relations $\varepsilon=[a]\boldsymbol{\sigma}$ are defined using a symmetric compliance matrix $[a]=\{a_{ij}\}_{1\leqslant i,\, j\leqslant 6}$, containing 13 nonzero constants nine of which are independent. $\boldsymbol{\sigma}=\{\sigma_x,\sigma_y,\sigma_z,\tau_{yz},\tau_{xz},\tau_{xy}\}^{\mathsf{T}}$, and $\varepsilon=\{\varepsilon_x,\varepsilon_y,\varepsilon_z,\gamma_{yz},\gamma_{xz},\gamma_{xy}\}^{\mathsf{T}}$ are the stress and the strain vectors, respectively.

The end loads are assumed to be given only by their residuals: tip moments $\mathbf{M}=\{M_1,M_2,M_t\}$ (about the $-x$, y, and $-z$ directions), and an axial force P_z (in the $-z$ direction), see Fig. 1(a). In addition, distributed loads $\mathbf{F_s}=\{\overline{X},\overline{Y},\overline{Z}\}$ (per unit area) along the outer surface of the beam and body forces $\mathbf{F_b}=\{X,Y,Z\}$ (per unit volume) are applied. For simplicity we assume below $\mathbf{F}_b=\mathbf{0}$. To comply with the basic assumption that states that the stresses do not vary along the beam, the loads are limited to the case where they are not functions of z and they create no force or moment residual,

$$\int_{\partial\Pi}\{\overline{X},\overline{Y},\overline{Z},\tilde{x}\overline{Y}-\tilde{y}\overline{X},\tilde{x}\overline{Z},\tilde{y}\overline{Z}\}ds=\mathbf{0}, \tag{1}$$

where $\tilde{x}=x-d/2$ and $\tilde{y}=y-h/2$. The above described loading leads to a state where the beam curvature components $k_1=-u_{,zz}$ and $k_2=-v_{,zz}$, the axial strain $\varepsilon_0=w_{,z}(d/2,h/2)$ and the twist $\theta=1/2(v_{,x}-u_{,y})_{,z}(d/2,h/2)$, are all constants. The curvature characteristics and the axial strain are related to the tip and surface loads by the equalities[1]

$$\begin{cases} k_1I_1=a_{33}M_2 \\ \qquad +\displaystyle\int_{\partial\Pi}\left[\frac{1}{2}(a_{13}\tilde{x}^2-a_{23}\tilde{y}^2)\overline{X}+a_{23}\tilde{x}\tilde{y}\overline{Y}+\frac{1}{2}a_{35}\tilde{x}\tilde{y}\overline{Z}\right]ds, \\ \varepsilon_0hd=a_{33}P_z \\ \qquad +\displaystyle\int_{\partial\Pi}(a_{13}\tilde{x}\overline{X}+a_{23}\tilde{y}\overline{Y}+a_{35}\tilde{x}\overline{Z})ds, \\ k_2I_1=a_{33}M_1-\dfrac{a_{35}}{2}M_t \\ \qquad +\displaystyle\int_{\partial\Pi}\left[a_{13}\tilde{x}\tilde{y}\overline{X}+\frac{1}{2}(a_{23}\tilde{y}^2-a_{13}\tilde{x}^2)\overline{Y}+\frac{1}{2}a_{35}\tilde{x}\tilde{y}\overline{Z}\right]ds, \end{cases} \tag{2}$$

where $I_1=1/12dh^3$, $I_2=1/12hd^3$ are the principal moments of inertia of Π. The twist can be derived using the solution of the linear system as will be shown in what follows.

The derivation of the displacements u,v,w in the x,y,z directions, respectively, is aimed towards the determination of the *warping* functions U, V, and W of x, y for a given set of k_1, k_2, ε_0, and θ. The *stress functions* F and Ψ are defined so that equilibrium equations are satisfied identically. They are linear combinations (with known coefficients μ_k,λ_k) of the *complex potentials* $\Phi_k(z_k)=P_k(z_k)+\mathbf{i}Q_k(z_k)$, $k=1,2,3$, and analytic functions of the complex variables $z_k=x_k+\mathbf{i}y_k=x+\mu_k y$ in the rectangles $\Pi_k=\{0\leqslant x_k\leqslant d,\ 0\leqslant y_k\leqslant h\beta_k\}$. Here $\mu_k,\overline{\mu_k}$ are six roots of the

[1]These formulas in absence of force projection Z are given in Lekhnitskii [1].

polynomial $l_6(\mu)$ associated with the compatibility equations, depending on t and on the reduced elastic constants $b_{ij}=a_{ij}-a_{i3}a_{3j}/a_{33}$ $(i,j=1,2,4,5,6)$, see Lekhnitskii [1]. For the cases considered in the present note (and for the materials discussed in Makeev and Armanios [5]) $\mu_k=\mathbf{i}\beta_k$, $(\beta_k>0)$, and $\lambda_k=\mathbf{i}v_k$ are purely imaginary. In the isotropic case, $\beta_k=1$, $\lambda_k=0$.

The stresses, strains, and displacements may be expressed in terms of complex potentials as well. The stresses have to satisfy the 12 boundary conditions

$$
\begin{aligned}
\{\sigma_x,\tau_{xy},\tau_{xz}\}(0,y)&=-\{\overline{X}_3,\overline{Y}_3,\overline{Z}_3\}(y),\\
\{\sigma_x,\tau_{xy},\tau_{xz}\}(d,y)&=\{\overline{X}_4,\overline{Y}_4,\overline{Z}_4\}(y),\\
\{\tau_{xy},\sigma_y,\tau_{yz}\}(x,0)&=-\{\overline{X}_1,\overline{Y}_1,\overline{Z}_1\}(x),\\
\{\tau_{xy},\sigma_y,\tau_{yz}\}(x,h)&=\{\overline{X}_2,\overline{Y}_2,\overline{Z}_2\}(x),
\end{aligned}
\tag{3}
$$

from which the complex potentials can be found. Here $\overline{X}_i,\overline{Y}_i,\overline{Z}_i$, $1\leqslant i\leqslant 4$ are the distributed surface loads along the edges of the rectangular cross section.

Method of Solution

Each of harmonic functions P_k (and Q_k) is uniquely determined in Π_k by its boundary values, as a sum of four harmonic functions. We represent these boundary values as the standard Fourier series with coefficients $\{A_{kn},B_{kn},C_{kn},D_{kn}\}$. For example,

$$
\begin{aligned}
P_3(x,y_3)=\sum_{n=1}^{\infty}&\left\{\left(A_{3n}\sinh\left(\frac{\pi n y_3}{d}\right)-B_{3n}\sinh\left(\frac{\pi n(y_3-h\beta_3)}{d}\right)\right)\right.\\
&\times\sin\left(\frac{\pi n x}{d}\right)+\left(C_{3n}\sinh\left(\frac{\pi n x}{h\beta_3}\right)\right.\\
&\left.\left.-D_{3n}\sinh\left(\frac{\pi n(x-d)}{h\beta_3}\right)\right)\sin\left(\frac{\pi n y_3}{h\beta_3}\right)\right\},
\end{aligned}
\tag{4}
$$

where $y_3=y\beta_3$. Hence the stresses are expressed as 12 terms series. For example,

$$
\begin{aligned}
\tau_{xz}=\tilde{\tau}_{xz}+\frac{f\tilde{y}}{2b_{55}}+2\pi\sum_{n=1}^{\infty}&\left\{\left[-A_{1n}\cosh\left(\frac{\pi n y\beta_1}{d}\right)v_1\beta_1\right.\right.\\
&+B_{1n}\cosh\left(\frac{\pi n(y-h)\beta_1}{d}\right)v_1\beta_1-A_{2n}\cosh\left(\frac{\pi n y\beta_2}{d}\right)v_2\beta_2\\
&+B_{2n}\cosh\left(\frac{\pi n(y-h)\beta_2}{d}\right)v_2\beta_2+A_{3n}\cosh\left(\frac{\pi n y\beta_3}{d}\right)\beta_3\\
&\left.-B_{3n}\cosh\left(\frac{\pi n(y-h)\beta_3}{d}\right)\beta_3\right]\frac{n}{d}\sin\left(\frac{\pi n x}{d}\right)\\
&+\left[-C_{1n}\sinh\left(\frac{\pi n x}{h\beta_1}\right)v_1+D_{1n}\sinh\left(\frac{\pi n(x-d)}{h\beta_1}\right)v_1\right.\\
&-C_{2n}\sinh\left(\frac{\pi n x}{h\beta_2}\right)v_2+D_{2n}\sinh\left(\frac{\pi n(x-d)}{h\beta_2}\right)v_2\\
&\left.\left.+C_{3n}\sinh\left(\frac{\pi n x}{h\beta_3}\right)-D_{3n}\sinh\left(\frac{\pi n(x-d)}{h\beta_3}\right)\right]\frac{n}{h}\cos\left(\frac{\pi n y}{h}\right)\right\},
\end{aligned}
\tag{5}
$$

where $\overline{\tau}_{xz}=1/h\int_0^h\overline{Z}_4dy$ and $f=-2\theta-a_{35}/a_{33}k_2$. Therefore, using the boundary conditions (5), we define the 12 series of linear equations with the unknowns $\{A_{kn},B_{kn},C_{kn},D_{kn}\}$, see details in Rovenski and Rand [6]. For example, $\tau_{xz}(0,y)=-\overline{Z}_3(y)$, $\tau_{xy}(0,y)=-Y_3(y)$ yield

$$
\begin{aligned}
v_1D_{1n}\sinh\left(\frac{\pi n d}{h\beta_1}\right)&+v_2D_{2n}\sinh\left(\frac{\pi n d}{h\beta_2}\right)-D_{3n}\sinh\left(\frac{\pi n d}{h\beta_3}\right)\\
&=f\frac{h^2((-1)^n-1)}{2\pi^3n^3b_{55}}+\frac{hZ_{3n}}{2n\pi},\\
\frac{h}{d}\sum_{j=1}^{\infty}\frac{j}{n}&[\beta_1(A_{1j}-(-1)^nB_{1j})H^1_{jn}+\beta_2(A_{2j}-(-1)^nB_{2j})H^2_{jn}\\
&+\beta_3v_3(A_{3j}-(-1)^nB_{3j})H^3_{jn}]-D_{1n}\cosh\left(\frac{\pi n d}{h\beta_1}\right)-D_{2n}\\
&\times\cosh\left(\frac{\pi n d}{h\beta_2}\right)-v_3D_{3n}\cosh\left(\frac{\pi n d}{h\beta_3}\right)+C_{1n}+C_{2n}+v_3C_{3n}\\
&=\overline{\tau}_{xy}\frac{h((-1)^n-1)}{n^2\pi^2}-\frac{hY_{3n}}{2n\pi},
\end{aligned}
\tag{6}
$$

where $\overline{\tau}_{xy}=1/d\int_0^d\overline{X}_2dx$, $H^i_{jn}=-2d^2n(-1)^n\sinh(\pi h_j\beta_i/d)/\pi(h^2j^2\beta_i^2+d^2n^2)$, and the surface loads $\overline{Z}_3,\overline{Y}_3$ are represented as series

$$
\overline{Z}_3=-\overline{\tau}_{xz}+\sum_{n=1}^{\infty}Z_{3n}\cos\left(\frac{\pi n y}{h}\right),\quad \overline{Y}_3=\sum_{n=1}^{\infty}Y_{3n}\sin\left(\frac{\pi n y}{h}\right).
\tag{7}
$$

By truncating the infinite series using m terms only, we write the above linear system of equations in a matrix form as

$$
M\overline{x}=-\frac{f}{2}\overline{V}+\tilde{V},
\tag{8}
$$

where the vector $\overline{x}$ contains $12m$ variables $\{A_{kn},B_{kn},C_{kn},D_{kn}\}$, $\underline{M}$ is a square matrix (generally nonsingular). Note that $\overline{V}=0$ when $\mathbf{M}=\mathbf{0}$, $P_z=0$, and $\tilde{V}=0$ when $\mathbf{F_s}=\mathbf{0}$. The known vectors $M^{-1}\overline{V}$ and $M^{-1}\tilde{V}$ are expressed in terms of the coefficients $\{\overline{A}_{kn},\overline{B}_{kn},\overline{C}_{kn},\overline{D}_{kn}\}$ and $\{\tilde{A}_{kn},\tilde{B}_{kn},\tilde{C}_{kn},\tilde{D}_{kn}\}$. In other words, $\{A_{kn},B_{kn},C_{kn},D_{kn}\}=-f/2\{\overline{A}_{kn},\overline{B}_{kn},\overline{C}_{kn},\overline{D}_{kn}\}+\{\tilde{A}_{kn},\tilde{B}_{kn},\tilde{C}_{kn},\tilde{D}_{kn}\}$ hold. Hence, the stress functions are expressed as

$$
\Psi=-\frac{f}{2}\overline{\Psi}+\tilde{\Psi}+\Psi_0,\quad F=-\frac{f}{2}\overline{F}+\tilde{F}+F_0,
\tag{9}
$$

where Ψ_0,F_0 are known functions. In a similar form, the stresses, the strains, and the displacements are expressed.

The proper integration of the stress components over the cross-sectional area yields

$$
M_t=-\frac{f}{2}\overline{C}+\tilde{C}.
\tag{10}
$$

The quantities $\overline{C}=(I_2/b_{44})+(I_1/b_{55})+\int\int_{\Pi}(\tilde{x}\overline{\tau}_{yz}-\tilde{y}\overline{\tau}_{xz})$, $\tilde{C}=\int\int_{\Pi}(\tilde{x}\tilde{\tau}_{yz}-\tilde{y}\tilde{\tau}_{xz})$ in (10) may be expressed as series as well. For obvious reasons, the quantity $\overline{C}$ (integral of the stress function Ψ in case $f=-2$ and $\mathbf{F_s}=\mathbf{0}$) may be referred to as the *torsional rigidity*, see also Lekhnitskii [1]. Once $\overline{C}$, $\tilde{C}$, and k_2 are calculated, f and the twist θ may be determined in terms of the applied moments and surface loads. One may verify that $\overline{A}_{kn}=\overline{B}_{kn}$, $\overline{C}_{kn}=\overline{D}_{kn}$ hold, moreover, $\overline{A}_{kn}=\overline{B}_{kn}=\overline{C}_{kn}=\overline{D}_{kn}=0$ hold for even n. Therefore, in the absence of external surface loads the number of equations is considerably smaller.

It should be emphasized that the present approach offers a generic solution methodology for orthotropic material. Note that the application of the general formulation presented in Lekhnitskii [1] was confined to special rectangular orthotropic configuration (i.e., the case where the angle of rotation is zero) in which the stress function $F=0$ and the stress function Ψ satisfies the following PDE:

$$a_{44}\Psi_{,xx}+a_{55}\Psi_{,yy}=f. \quad (11)$$

Therefore, the Fourier series in Lekhnitskii [1] are applied to simpler cases. The following example shows the above capability of the present methodology.

Example 1. An Orthotropic Beam. To solve the special orthotropic configuration case by the present approach, we let $t=0$ (or 90 deg) and $\mathbf{F_s}=\mathbf{0}$. Then $\lambda_k=0$, and $\beta_3=\sqrt{a_{44}/a_{55}}$. Examination of the system (8) shows that $A_{kn}=B_{kn}=C_{kn}=D_{kn}=0$, $k=1,2$, and

$$\begin{aligned}A_{3n}=B_{3n}&=-\frac{fd^2((-1)^2-1)}{2\pi^3n^3a_{44}\sinh\left(\dfrac{\pi nh\beta_3}{d}\right)},\\ C_{3n}=D_{3n}&=-\frac{fh^2((-1)^n-1)}{2\pi^3n^3a_{55}\sinh\left(\dfrac{\pi nd}{h\beta_3}\right)}.\end{aligned} \quad (12)$$

Hence $F=0$, and Ψ has the following form (equivalent to solution in Lekhnitskii's [1]):

$$\begin{aligned}\Psi=&f\frac{x(x-d)}{4a_{44}}\\ &-\frac{fd^2}{\pi^3a_{44}}\sum_{n=1,3,5,\ldots}^{\infty}\frac{1}{n^3}\frac{\sinh\left(\dfrac{\pi ny\beta_3}{d}\right)-\sinh\left(\dfrac{\pi n(y-h)\beta_3}{d}\right)}{\sinh\left(\dfrac{\pi nh\beta_3}{d}\right)}\\ &\times\sin\left(\frac{\pi nx}{d}\right)+f\frac{y(y-h)}{4a_{55}}-\frac{fh^2}{\pi^3a_{55}}\sum_{n=1,3,5,\ldots}^{\infty}\frac{1}{n^3}\\ &\times\frac{\sinh\left(\dfrac{\pi nx}{h\beta_3}\right)-\sinh\left(\dfrac{\pi n(x-d)}{h\beta_3}\right)}{\sinh\left(\dfrac{\pi nd}{h\beta_3}\right)}\sinh\left(\frac{\pi ny}{h}\right).\end{aligned} \quad (13)$$

For isotropic beam one obtains $a_{44}=a_{55}$, $a_{35}=0$, $f=-2\theta$, $\beta_k=1$, $v_k=0$ (for all t), while (12), (13) are still applicable.

Solution Implementation

The solution contains two main stages. *First* the initial data (i.e., engineering constants, shape parameters, lay-up angle, and surface loads) is used to carry out the following steps: (1) calculation of the reduced elastic constants; (2) determination of the compatibility equations polynomials roots; (3) solution of the boundary equations (a linear system). In the *second* stage, the end loads (tip axial force, bending, and torsional tip moments) are used for (4) calculation of the deformation measures k_1, k_2, ε_0 and θ; (5) series representation of the stress functions, the stress and the strain vectors, the displacements.

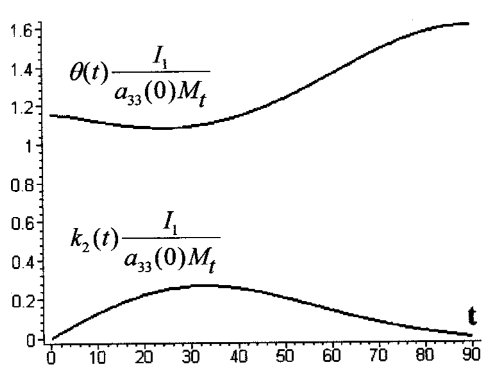

Fig. 2 The twist, θ, and the bending curvature k_2, as functions of the layup angle, t, due to torsional moment

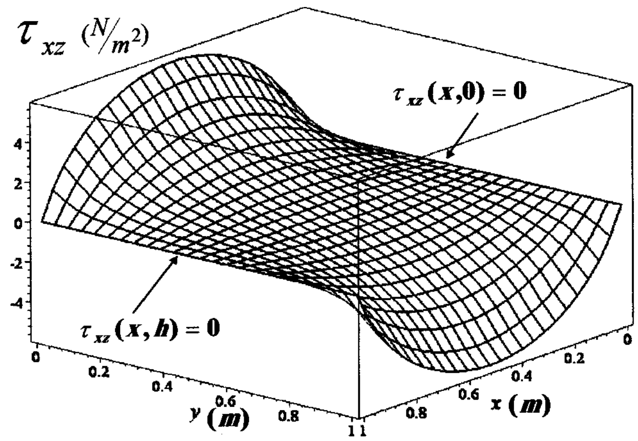

Fig. 3 The stress component τ_{xz} (M_t=1 N/m)

In the examples presented in this note, a homogeneous beam with $h=d=1m$, made of graphite/epoxy orthotropic material of the following characteristics is used:

$$\begin{aligned}&E_3=129.1\cdot10^9\ \text{N/m}^2,\quad E_1=E_2=9.4\cdot10^9\ \text{N/m}^2,\\ &G_{23}=4.3\cdot10^9\ \text{N/m}^2,\quad G_{13}=5.5\cdot10^9\ \text{N/m}^2,\\ &G_{12}=2.5\cdot10^9\ \text{N/m}^2,\quad v_{12}=0.5,\quad v_{13}=v_{23}=0.02.\end{aligned} \quad (14)$$

Here we transformed the data of Rand [7] when the axes are replaced according to the rule: $X\to -Z$, $Y\to Z$, $Z\to -Y$.

Steps 1–2. For $t=15$ deg we calculate matrices $\{a_{ij}\}$ and $\{b_{ij}\}$. The roots of the polynomial l_6 and the coefficients v_k are obtained as

$$\begin{aligned}&\beta_1=1.80,\quad \beta_2=0.661,\quad \beta_3=1.49,\\ &v_1=2.71,\quad v_2=0.0573,\quad v_3=1.40.\end{aligned} \quad (15)$$

Step 3. The linear system of equations is solved for the unknowns $\{A_{kn},B_{kn},C_{kn},D_{kn}\}$, see Section 2. The inverse matrix M^{-1} and the vectors $M^{-1}V, M^{-1}\tilde{V}$ are determined. Then, $\bar{C}$ and $\tilde{C}$ are calculated. For the present case, $m=4$ was found to be sufficient for determining the value of the torsional rigidity of $0.861\cdot10^9$ N/m^2.

Step 4. Assuming that $M_t=1$ N·m, $M_1=M_2=P_z=0$ and $\mathbf{F_s}=\mathbf{0}$, (2) is used to derive the curvatures $k_1=0$, $k_2=0.23\cdot10^{-9}$/m and the axial strain $\varepsilon_0=0$. Then, using the torsional rigidity (see Step 3), and (10), we derive $f=-2.32\cdot10^{-9}$/m and the twist $\theta=1.40\cdot10^{-9}$/m. By varying the angle t, the function $\theta(t)$ and $k_2(t)$ are derived and presented in Fig. 2 in a nondimensional form. k_2 represents the induced elastic coupling (i.e., the bending due to the torsional moment).

Step 5. At this stage, the expressions in the form of truncated series (with the coefficients obtained in Steps 3,4) for the stress functions, the stress and the strain vectors, and for the displacement components are used. Due to the relatively lengthy expressions for functions, stresses, displacements, and warping functions, only graphical results are provided in Figs. 3–4 (these illustrative examples have been obtained for $m=14$).

The convergence properties of the present methodology are demonstrated by Fig. 5 in terms of the ratio of the twist and the stresses $\tau_{yz}(d/4,h/4), \tau_{xy}(d/4,h/4)$ for $m=2,4,\ldots,16$ to the limit value. As shown, the global quantity, θ converges rapidly, and the large stress components converge faster than the small ones.

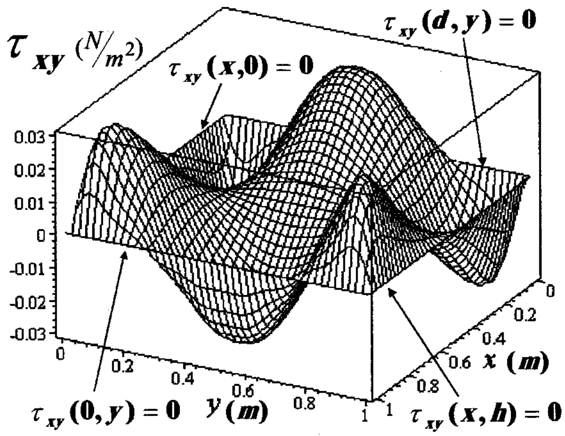

Fig. 4 The stress component τ_{xy} (M_t=1 N/m)

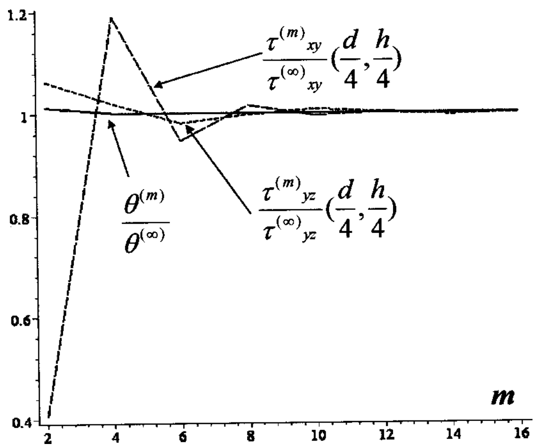

Fig. 5 Convergence path as a function of the number of terms, m, (t=15 deg torsional moment)

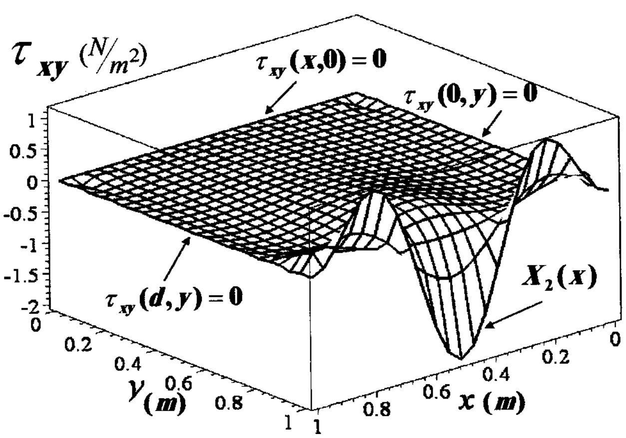

Fig. 6 The stress component τ_{xy} for $\bar{X}_2=\cos(2\pi x/d)-\cos(4\pi x/d)$

Remark 1. For the case considered here, the three stress components $\sigma_x, \sigma_y, \tau_{xy}$ are significantly smaller then the other stress components (see Figs. 3, 4). This fact was the basis for the analytic solutions presented by Rand [7,8]. Accordingly, by assuming $\sigma_x=\sigma_y=\tau_{xy}=0$, the strain-stress relations may be simplified to

$$\varepsilon_z=a_{33}\sigma_z+a_{35}\tau_{xz}, \quad \gamma_{yz}=a_{44}\tau_{yz}, \quad \gamma_{xz}=a_{35}\varepsilon_z+a_{55}\tau_{xz}. \tag{16}$$

The derivation in Rand [8] shows that for this case $k_1=0$, $k_2=-M_t/I_1a_{35}$ (identical to the present results), and in addition

$$\theta=\frac{M_t}{2I_1a_{33}}\left[\frac{1}{r_z}(a_{33}a_{55}-a_{35}^2)+\frac{1}{2}a_{35}^2\right], \tag{17}$$

where

$$r_z=2-\frac{192}{q\pi^4}\sum_{n=0}^{\infty}\frac{(-1)^n}{(2n+1)^4}\tanh(\bar{m}q)\left[\frac{\sin(\bar{m})}{\bar{m}}-\cos(\bar{m})\right], \tag{18}$$

and $\bar{m}=(2n+1)/2\pi$, $q=d/h\sqrt{a_{33}a_{55}-a_{35}^2/a_{33}a_{44}}$. The above expressions correlate perfectly and are practically identical to the results presented in Fig. 2.

Continuing series of examples, and assuming that the only external load is $\bar{X}$ which acts along the face $y=h$, as $\bar{X}_2=\cos(2\pi x/d)-\cos(4\pi x/d)$, we obtain $\tilde{C}=-0.97\cdot 10^{-18}$ N/m, $\theta=0.11\cdot 10^{-26}$/m, $k_1=0.71\cdot 10^{-12}$/m, $k_2=\varepsilon_0=0$. The solution τ_{xy} is presented in Fig. 6.

References

[1] Lekhnitskii, S. G., 1981, *Theory of Elasticity of an Anisotropic Elastic Body*, Mir Publishers, Moscow.

[2] Rand, O., and Rovenski, V., 2000, "A Closed Form Solution for Laminated Composite Beams," *Proceedings of the American Helicopter Society 56th Annual Forum*, Virginia, May, No. 00015.

[3] Savoia, M., and Reddy, J. N., 1992, "A Variational Approach to Three-Dimensional Elasticity Solutions of Laminated Composite Beams," J. Appl. Mech., **59**, pp. S166–S175.

[4] Whitney, J. M., 1985, "Elasticity Analysis of Orthotropic Beams Under Concentrated Loads," Compos. Sci. Technol., **22**, pp. 167–184.

[5] Makeev, A., and Armanios, E. A., 1999, "A Simple Elasticity Solution for Predicting Interlaminar Stresses in Laminated Composites," J. Am. Helicopter Soc., **44**, No. 2, pp. 94–100.

[6] Rovenski, V., and Rand, O., 2000, "Analysis of Laminated Composite Beams—An Analytic Approach," *Proceedings of the 40th Israel Annual Conference on Aerospace Sciences*, Tel-Aviv, Feb., pp. 467–478.

[7] Rand, O., 1994, "Nonlinear Analysis of Orthotropic Beams of Solid Cross-Sections," Composite Structures, **29**, pp. 27–45.

[8] Rand, O., 1998, "Fundamental Closed-Form Solutions for Solid and Thin-Walled Composite Beams Including a Complete Out-of-Plane Warping Model," Int. J. Solids Struct., **35**, No. 21, pp. 2775–2793.

A Restudy of the Paradox on an Elastic Wedge Based on the Hamiltonian System

W. A. Yao and C. Xu
State Key Laboratory of Structural Analysis of Industrial Equipment, Dalian University of Technology, Dalian 116023, P. R. China

In this paper, the paradox on the elastic wedge is restudied under the Hamiltonian system. This research shows that a special paradox in Euclidean space under the Lagrange system is just the Jordan form solutions in symplectic space under the Hamiltonian system, so they can be solved directly and rationally by normal mathematical physics methods. [DOI: 10.1115/1.1360184]

Contributed by the Applied Mechanics Division of THE AMERICAN SOCIETY OF MECHANICAL ENGINEERS for publication in the ASME JOURNAL OF APPLIED MECHANICS. Manuscript received by the ASME Applied Mechanics Division, May 5, 2000; final revision, Dec. 5, 2000. Associate Editor: A. K. Mal.

Introduction

For an elastic wedge subjected to tractions proportional to $r^{\mu-1}(\mu\geqslant 1)$ on the surfaces, the classical solution becomes infinite when the vertex angle and constant μ satisfy certain definite relationships. Dempsey [1], Ting [2], and Wang [3] have given solution of this paradox in special case. Ding et al. [4] recently restudied the paradox, and discovered the secondary paradox. All of these methods above are limited in the Euclidean space, the information on the characteristics of the paradox is incomplete. Looking from the analogy theory between computational structural mechanics and optimal control ([5]), the Hamiltonian system theory can be introduced into the theory of elasticity ([6]), so the powerful methods, such as the separation of variables, etc., can be applied directly ([7]).

Hamiltonian System in Polar Coordinate

In a polar coordinate system (r,θ), let an elastic wedge of vertex angle 2α occupy the region $0\leqslant R_1\leqslant r\leqslant R_2<\infty,\ -\alpha\leqslant\theta\leqslant\alpha$. We denote by u, v the radial and circumferential displacement, and by $\sigma_r,\ \sigma_\theta,\ \tau_{r\theta}$ the stress components. By introducing variables

$$\xi=\ln r,\quad r=\exp(\xi);\quad S_r=r\sigma_r,\quad S_\theta=r\sigma_\theta,\quad S_{r\theta}=r\tau_{r\theta}\tag{1}$$

the Hellinger-Reissner variational principle (see, e.g., [8]) can be rewritten as

$$\delta\int_{-\alpha}^{\alpha}\int_{\ln R_1}^{\ln R_2}\left\{S_r\frac{\partial u}{\partial\xi}+S_\theta\left(u+\frac{\partial v}{\partial\theta}\right)+S_{r\theta}\left(\frac{\partial v}{\partial\xi}-v+\frac{\partial u}{\partial\theta}\right)\right.$$
$$\left.-\frac{1}{2E}\left[S_r^2+S_\theta^2-2\nu S_rS_\theta+2(1+\nu)S_{r\theta}^2\right]\right\}d\xi d\theta=0.\tag{2}$$

Now a dot denotes the differential with respect to ξ. Maximizing (2) with respect to S_θ gives

$$S_\theta=\nu S_r+E(u+\partial v/\partial\theta).\tag{3}$$

The substituting of Eq. (3) in Eq. (2) then yields

$$\delta\int_{-\alpha}^{\alpha}\int_{\ln R_1}^{\ln R_2}\left\{S_r\dot{u}+S_{r\theta}\dot{v}+\nu S_r\left(u+\frac{\partial v}{\partial\theta}\right)+S_{r\theta}\left(\frac{\partial u}{\partial\theta}-v\right)\right.$$
$$\left.+\frac{E}{2}\left(u+\frac{\partial v}{\partial\theta}\right)^2-\frac{1}{2E}\left[(1-\nu^2)S_r^2+2(1+\nu)S_{r\theta}^2\right]\right\}d\xi d\theta=0.\tag{4}$$

The dual variables of u, v are $S_r,\ S_{r\theta}$, respectively, and together they constitute the state function-vector $\mathbf{v}=\{u,v,S_r,S_{r\theta}\}^T$ in symplectic space. Expanding the variational Eq. (4) gives dual equations

$$\dot{\mathbf{v}}=\mathbf{H}\mathbf{v};$$

where

$$\mathbf{H}=\begin{bmatrix}-\nu & -\nu\partial/\partial\theta & (1-\nu^2)/E & 0\\ -\partial/\partial\theta & 1 & 0 & 2(1+\nu)/E\\ E & E\partial/\partial\theta & \nu & -\partial/\partial\theta\\ -E\partial/\partial\theta & -E\partial^2/\partial\theta^2 & -\nu\partial/\partial\theta & -1\end{bmatrix}.\tag{5}$$

Besides, the free boundary conditions on the surfaces $\theta=\pm\alpha$ are

$$\nu S_r+E(u+\partial v/\partial\theta)=0,\quad S_{r\theta}=0;\quad \text{when}\quad \theta=\pm\alpha.\tag{6}$$

The dual Eqs. (5) with the boundary conditions (6) can be solved by the method of separation of variables:

$$\mathbf{v}=\exp(\mu\xi)\boldsymbol{\Psi}(\theta)=r^\mu\{\overline{u}(\theta),\ \overline{v}(\theta),\ \overline{S}_r(\theta),\ \overline{S}_{r\theta}(\theta)\}^T\tag{7}$$

where μ is the eigenvalue, $\boldsymbol{\Psi}$ is eigenfunction vector depending only on θ. $\boldsymbol{\Psi}$ must satisfy equation

$$\mathbf{H}\boldsymbol{\Psi}=\mu\boldsymbol{\Psi}\tag{8}$$

and the boundary conditions (6).

In this paper, we will only discuss symmetric deformations. The symmetric boundary conditions are

$$v=0,\quad S_{r\theta}=0\quad \text{when}\quad \theta=0.\tag{9}$$

For convenience, let

$$\begin{gathered}s(\mu,\alpha)=\sin 2\mu\alpha+\mu\sin 2\alpha;\\ s_1(\mu,\alpha)=\partial s(\mu,\alpha)/\partial\mu=2\alpha\cos 2\mu\alpha+\sin 2\alpha\end{gathered}\tag{10}$$

$$\begin{gathered}\widetilde{A}_1(\mu,\alpha)=-\mu\cos 2\alpha-\cos 2\mu\alpha;\\ \widetilde{A}_2(\mu,\alpha)=-2\mu\alpha\sin 2\alpha-(\cos 2\alpha+\cos 2\mu\alpha)/(1-\mu)\end{gathered}\tag{11}$$

By solving Eq. (8) with boundary conditions (6) and (9), the nonzero eigenvalue equation can be given as $s(\mu,\alpha)=0$, that is, when $s(\mu,\alpha)=0$ and $s_1(\mu,\alpha)\neq 0$, μ is a single eigenvalue; when $s(\mu,\alpha)=s_1(\mu,\alpha)=0$, μ is a double eigenvalue.

An Elastic Wedge Subjected to Tractions Proportional to $r^{\mu-1}(\mu\geqslant 1)$

On the surface $\theta=\alpha$, we assume the load as

$$\begin{gathered}\nu S_r+E(u+\partial v/\partial\theta)=pr^\mu=p\exp(\mu\xi),\\ S_{r\theta}=qr^\mu=q\exp(\mu\xi)\quad \text{when}\quad \theta=\alpha.\end{gathered}\tag{12}$$

And on the other surface $\theta=-\alpha$, the load is symmetric with (12). Due to the fact that the load on surfaces $\theta=\pm\alpha$ is proportional to $\exp(\mu\xi)$, the original problem can be solved by the method of separation of variables, see Eq. (7). So boundary conditions (12) can be rewritten as

$$\nu\overline{S}_r+E(\overline{u}+d\overline{v}/d\theta)=p,\quad \overline{S}_{r\theta}=q\quad \text{when}\quad \theta=\alpha.\tag{13}$$

(a) *When μ isn't the eigenvalue*. To solve Eq. (8) with conditions (9), we can give its general solution as

$$\boldsymbol{\Psi}_\mu^{(0)}=\begin{cases}[-(1+\nu)A_1\cos(1+\mu)\theta+(3-\nu-\mu-\nu\mu)A\\ \quad\times\cos(1-\mu)\theta]/E\mu\\ [(1+\nu)A_1\sin(1+\mu)\theta-(3-\nu+\mu+\nu\mu)A\\ \quad\times\sin(1-\mu)\theta]/E\mu\\ -A_1\cos(1+\mu)\theta+(3-\mu)A\cos(1-\mu)\theta\\ A_1\sin(1+\mu)\theta+(1-\mu)A\sin(1-\mu)\theta\end{cases}\tag{14}$$

the substitution of (14) into the boundary conditions (13) results in equations

$$\begin{cases}A_1\cos(1+\mu)\alpha+(1+\mu)A\cos(1-\mu)\alpha=p\\ A_1\sin(1+\mu)\alpha+(1-\mu)A\sin(1-\mu)\alpha=q\end{cases}.\tag{15}$$

The solution of (15) is

$$\begin{cases}A_1=[-p(1-\mu)\sin(1-\mu)\alpha+q(1+\mu)\\ \quad\times\cos(1-\mu)\alpha]/s(\mu,\alpha)\\ A=[p\sin(1+\mu)\alpha-q\cos(1+\mu)\alpha]/s(\mu,\alpha)\cdot\\ \quad\equiv\widetilde{A}(\mu,\alpha)/s(\mu,\alpha)\end{cases}\tag{16}$$

So we can give the classical solution $\mathbf{v}_\mu^{(0)}=r^\mu\boldsymbol{\Psi}_\mu^{(0)}$ of a wedge subjected to traditions proportional to $r^{\mu-1}$. It is the same as the results of Dempsey [1], etc.

(b) *When $\mu(\neq 1)$ is a single eigenvalue*. In this case, due to the vanishing of the determinant of (15), no solution exists in general, and so initial paradox occurs. However, the eigenfunction vector for μ exists. Substituting (14) into free boundary conditions (6), we can give as

$$\begin{cases} A_1 \cos(1+\mu)\alpha+(1+\mu)A\cos(1-\mu)\alpha=0 \\ A_1 \sin(1+\mu)\alpha+(1-\mu)A\sin(1-\mu)\alpha=0 \end{cases}. \tag{17}$$

Because μ is an eigenvalue $[s(\mu,\alpha)=0]$, nontrivial solutions of (17) is $A_1=\tilde{A}_1(\mu,\alpha)A$. For simplicity, let $A=1$ and $A_1=\tilde{A}_1(\mu,\alpha)$ in expression (14), we can write the eigenfunction vector $\tilde{\mathbf{\Psi}}_\mu^{(0)}$ for eigenvalue μ. With the load eigenvalue being equal to natural eigenvalue, its solution must be a Jordan form one. The governing equation for the Jordan form solution is

$$\mathbf{H}\mathbf{\Psi}_\mu^{(1)}=\mu\mathbf{\Psi}_\mu^{(1)}+A\tilde{\mathbf{\Psi}}_\mu^{(0)} \tag{18}$$

where A is a constant. According to (18), we can give the first-order Jordan form general solution

$$\mathbf{\Psi}_\mu^{(1)}=\{\overline{u}^{(1)},\ \overline{v}^{(1)},\ \overline{S}_r^{(1)},\ \overline{S}_{r\theta}^{(1)}\}^T \tag{19}$$

where

$$\begin{aligned}\overline{u}^{(1)}=\frac{1}{E\mu}\bigg\{&-(1+\nu)A_2\cos(1+\mu)\theta+(1+\nu)\tilde{A}_1A\theta\sin(1+\mu)\theta \\ &+\frac{1+\nu}{\mu}\tilde{A}_1A\cos(1+\mu)\theta+(3-\mu-\nu-\nu\mu)A\theta\sin(1 \\ &-\mu)\theta-\frac{3-6\mu+\mu^2-\nu+2\nu\mu+\nu\mu^2}{\mu(1-\mu)}A\cos(1-\mu)\theta\bigg\}\end{aligned} \tag{20a}$$

$$\begin{aligned}\tilde{v}^{(1)}=\frac{1}{E\mu}\bigg\{&(1+\nu)A_2\sin(1+\mu)\theta+(1+\nu)\tilde{A}_1A\theta\cos(1+\mu)\theta \\ &-\frac{1+\nu}{\mu}\tilde{A}_1A\sin(1+\mu)\theta+(3+\mu-\nu+\nu\mu)A\theta\cos(1 \\ &-\mu)\theta+\frac{3-6\mu-\mu^2-\nu+2\nu\mu-\nu\mu^2}{\mu(1-\mu)}A\sin(1-\mu)\theta\bigg\}\end{aligned} \tag{20b}$$

$$\begin{aligned}\overline{S}_r^{(1)}=&-A_2\cos(1+\mu)\theta+\tilde{A}_1A\theta\sin(1+\mu)\theta \\ &+(3-\mu)A\theta\sin(1-\mu)\theta+\frac{2}{1-\mu}A\cos(1-\mu)\theta\end{aligned} \tag{20c}$$

$$\begin{aligned}\overline{S}_{r\theta}^{(1)}=&A_2\sin(1+\mu)\theta+\tilde{A}_1A\theta\cos(1+\mu)\theta \\ &-(1-\mu)A\theta\cos(1-\mu)\theta.\end{aligned} \tag{20d}$$

Substituting (20) into (13) and using relationship $s(\mu,\alpha)=0$, we can give

$$\begin{cases} A_2\cos(1+\mu)\alpha+2A\alpha\sin(1-\mu)\alpha+\dfrac{2}{1-\mu}A \\ \quad\times\cos(1-\mu)\alpha=p \\ A_2\sin(1+\mu)\alpha-2A\alpha\cos(1-\mu)\alpha=q. \end{cases} \tag{21}$$

Its solution is

$$\begin{aligned}A_2=\frac{2}{s_1(\mu,\alpha)}\bigg\{&p\alpha\cos(1-\mu)\alpha+q\bigg[\alpha\sin(1-\mu)\alpha \\ &+\frac{\cos(1-\mu)\alpha}{1-\mu}\bigg]\bigg\};\quad A=\frac{\tilde{A}(\mu,\alpha)}{s_1(\mu,\alpha)}.\end{aligned} \tag{22}$$

So the solution for the initial paradox can be solved as

$$\begin{aligned}\mathbf{v}_\mu^{(1)}&=\exp(\mu\xi)[\mathbf{\Psi}_\mu^{(1)}+A\xi\tilde{\mathbf{\Psi}}_\mu^{(0)}+C_0\tilde{\mathbf{\Psi}}_\mu^{(0)}] \\ &=r^\mu[\mathbf{\Psi}_\mu^{(1)}+A\ln r\tilde{\mathbf{\Psi}}_\mu^{(0)}+C_0\tilde{\mathbf{\Psi}}_\mu^{(0)}]\end{aligned} \tag{23}$$

where constants A_2 and A are defined upon (22). C_0 is an arbitrary constant. The solution (23) is the same as the result of Ding et al. [4].

(c) *When μ is a double eigenvalue*. In this case, due to the vanishing of the determinant of (21), no solution exists, and so secondary paradox occurs. Because μ is a double eigenvalue, nontrivial solutions $A_2=\tilde{A}_2(\mu,\alpha)A$ of the homogeneous equations for (21) exist. For simplicity, let $A=1$ and $A_2=\tilde{A}_2(\mu,\alpha)$ in expressions (20), we can write the first-order Jordan form eigenfunction vector $\tilde{\mathbf{\Psi}}_\mu^{(1)}$.

Because load eigenvalue is equal to a double natural eigenvalue, its solution must be of the second-order Jordan form. Its governing equation is $\mathbf{H}\mathbf{\Psi}_\mu^{(2)}=\mu\mathbf{\Psi}_\mu^{(2)}+A\tilde{\mathbf{\Psi}}_\mu^{(1)}$. To solve these equations with conditions (9), we can give a second-order Jordan form general solution as

$$\mathbf{\Psi}_\mu^{(2)}=\{\overline{u}^{(2)},\ \overline{v}^{(2)},\ \overline{S}_r^{(2)},\ \overline{S}_{r\theta}^{(2)}\}^T \tag{24}$$

where

$$\begin{aligned}\overline{u}^{(2)}=\frac{1}{E\mu}\bigg\{&-(1+\nu)A_3\cos(1+\mu)\theta+(1+\nu)\tilde{A}_2A\theta\sin(1+\mu)\theta \\ &+\frac{1+\nu}{\mu}\tilde{A}_2A\cos(1+\mu)\theta+\frac{1+\nu}{2}\tilde{A}_1A\theta^2\cos(1+\mu)\theta \\ &-\frac{1+\nu}{\mu}\tilde{A}_1A\theta\sin(1+\mu)\theta-\frac{1+\nu}{\mu^2}\tilde{A}_1A\cos(1+\mu)\theta \\ &-\frac{3-\mu-\nu-\nu\mu}{2}A\theta^2\cos(1-\mu)\theta \\ &-\frac{3-6\mu+\mu^2-\nu(1-2\mu-\mu^2)}{\mu(1-\mu)}A\theta\sin(1-\mu)\theta \\ &+\frac{3-9\mu+9\mu^2-\mu^3-\nu(1-3\mu+3\mu^2+\mu^3)}{\mu^2(1-\mu)^2} \\ &\times A\cos(1-\mu)\theta\bigg\}\end{aligned} \tag{25a}$$

$$\begin{aligned}\overline{v}^{(2)}=\frac{1}{E\mu}\bigg\{&(1+\nu)A_3\sin(1+\mu)\theta+(1+\nu)\tilde{A}_2A\theta\cos(1+\mu)\theta \\ &-\frac{1+\nu}{\mu}\tilde{A}_2A\sin(1+\mu)\theta-\frac{1+\nu}{2}\tilde{A}_1A\theta^2\sin(1+\mu)\theta \\ &-\frac{1+\nu}{\mu}\tilde{A}_1A\theta\cos(1+\mu)\theta+\frac{1+\nu}{\mu^2}\tilde{A}_1A\sin(1+\mu)\theta \\ &+\frac{3+\mu-\nu+\nu\mu}{2}A\theta^2\sin(1-\mu)\theta \\ &-\frac{3-6\mu-\mu^2-\nu(1-\mu)^2}{\mu(1-\mu)}A\theta\cos(1-\mu)\theta \\ &-\frac{3-9\mu+9\mu^2+\mu^3-\nu(1-\mu)^3}{\mu^2(1-\mu)^2}A\sin(1-\mu)\theta\bigg\}\end{aligned} \tag{25b}$$

$$\overline{S}_r^{(2)}=-A_3\cos(1+\mu)\theta+\tilde{A}_2A\theta\sin(1+\mu)\theta+\frac{1}{2}\tilde{A}_1A\theta^2\cos(1+\mu)\theta-\frac{1}{2}(3-\mu)A\theta^2\cos(1-\mu)\theta+\frac{2}{1-\mu}A\theta\sin(1-\mu)\theta+\frac{2}{(1-\mu)^2}A\cos(1-\mu)\theta \quad (25c)$$

$$\overline{S}_{r\theta}^{(2)}=A_3\sin(1+\mu)\theta+\tilde{A}_2A\theta\cos(1+\mu)\theta-[\tilde{A}_1\sin(1+\mu)\theta+(1-\mu)\sin(1-\mu)\theta]A\theta^2/2. \quad (25d)$$

Substituting (25) into (13) and using relationships $s(\mu,\alpha)=s_1(\mu,\alpha)=0$, we can solve

$$\begin{cases} A_3=\dfrac{1}{\mu\sin 2\alpha}\left\{p\left[\sin(1-\mu)\alpha+\dfrac{\cos(1-\mu)\alpha}{(1-\mu)\alpha}\right]-q\left[\cos(1-\mu)\alpha-\dfrac{\sin(1-\mu)\alpha}{(1-\mu)\alpha}-\dfrac{\cos(1-\mu)\alpha}{(1-\mu)^2\alpha^2}\right]\right\}. \\ A=\tilde{A}(\mu,\alpha)/(2\mu\alpha^2\sin 2\alpha) \end{cases} \quad (26)$$

So the solution for the secondary paradox can be given as

$$\mathbf{v}_\mu^{(2)}=r^\mu\left\{\mathbf{\Psi}_\mu^{(2)}+A\ln r\tilde{\mathbf{\Psi}}_\mu^{(1)}+\frac{1}{2}A\ln^2 r\tilde{\mathbf{\Psi}}_\mu^{(0)}+C_0[\tilde{\mathbf{\Psi}}_\mu^{(1)}+\ln r\tilde{\mathbf{\Psi}}_\mu^{(0)}]+C_1\tilde{\mathbf{\Psi}}_\mu^{(0)}\right\}. \quad (27)$$

It is the same as the result of Ding et al. [4].

Conclusion

This approach is different from the traditional semi-inverse solutions and it gives rationally all solutions of the paradox, and its result reveals that such a special paradox in Euclidean space is just the Jordan form solution in symplectic space. For a wedge subjected to tractions proportional to $r^{\mu-1}(\mu\geqslant 1)$ on the surfaces, the following conclusion can be drawn: (1) the paradox does not exist when μ is not the eigenvalue; (2) the initial paradox occurs when μ is a single eigenvalue, and its solution is one which is composed of the first-order Jordan form; (3) the secondary paradox occurs when μ is a double eigenvalue, and its solution is one which is composed of the second-order Jordan form.

References

[1] Dempsey, J. P., 1981, ‘‘The Wedge Subjected to Tractions: A Paradox Resolved,’’ J. Elast., **11**, No. 1, pp. 1–10.
[2] Ting, T. C. T., 1984, ‘‘The Wedge Subjected to Tractions: A Paradox Reexamined,’’ J. Elast., **14**, pp. 235–247.
[3] Wang, M. Z., 1986, ‘‘The Wedge Subjected to General Tractions: A Paradox Resolved,’’ Acta Mech. Sin., **18**, No. 3, pp. 242–252 (in Chinese).
[4] Ding, H. J., Peng, N. L., and Li, Y., 1998, ‘‘The Wedge Subjected to Tractions Proportional to r^n: A Paradox Resolved,’’ Int. J. Solids and Structures, **35**, No. 20, pp. 2695–2714.
[5] Zhong, W. X., and Zhong, X. X., 1990, ‘‘Computational Structural Mechanics, Optimal Control and Semi-analytical Method for PDE,’’ Computers and Structures, **37**, No. 6, pp. 993–1004.
[6] Zhong, W. X., 1995, *A New Systematic Methodology for Theory of Elasticity*, Dalian University of Technology Press, Dalian, China (in Chinese).
[7] Zhong, W. X., and Yao, W. A., 1997, ‘‘The Saint-Venant Solutions of Multilayered Composite Plates,’’ Advances in Structural Engineering, **1**, No. 2, pp. 127–133.
[8] Hu, H. C., 1981, *Variational Principle of Elasticity and Its Application* Science Press, Beijing, China (in Chinese).

Chaotic Motion of a Symmetric Gyro Subjected to a Harmonic Base Excitation

X. Tong
Lucent Technologies, 480 Red Hill Road, Middletown, NJ 07724

N. Mrad
Structures, Materials, and Propulsion Laboratory, Institute for Aerospace Research, National Research Council Canada, 1500 Montreal Road, Building M-3, Ottawa, Ontario K1A 0R6, Canada

Chaotic motion of a symmetric gyro subjected to a harmonic base excitation is investigated in this note. The Melnikov method is applied to show that the system possesses a Smale horse when it is subjected to small excitation. The transition from regular motion to chaotic motion is investigated through numerical integration in conjunction with Poincaré map. It is shown that as the spin velocity increases, the chaotic motion turns into a regular motion.

[DOI: 10.1115/1.1379036]

Introduction

In recent years, several researchers have conducted studies investigating the chaotic motion in rigid-body systems ([1–6]). Recently, Ge et al. [7] conducted a detailed study evaluating the nonlinear behavior of a symmetric heavy gyroscope mounted on a vibrating base. In their study, the chaotic motion of the system with linear damping was investigated by using a variety of techniques, such as the Melnikov method, Poincaré map, power spectrum analysis, and Liapunov exponents.

In this note, the motion of a symmetric gyro (Fig. 1) subjected to a harmonic vertical base excitation is studied, with particular emphasis on its nonlinear dynamic behavior without taking into account the damping effect. The symmetric gyro can be used to model a variety of physical systems, ranging from a child's top to a modern gyroscopic navigational instrument. The Melnikov method is applied to predict the transversal intersections of stable and unstable manifolds for the system when subjected to small base excitation. The transition from regular motion to chaotic motion is investigated through numerical integration in conjunction with the Poincaré map. The effect of the gyro's spin velocity on its global motion is also investigated. It is shown that the gyro's spin velocity has a significant effect on dynamic behavior of the system.

Equations of Motion

Consider a symmetric gyro mounted on a harmonically oscillating base, as shown in Fig. 1. The motion of the gyro can be described using Euler's angles θ (nutation), ϕ (precession), and ψ (spin). The Lagrangian of the gyro system can be written as

$$L=\frac{1}{2}I_1(\dot{\theta}^2+\dot{\phi}^2\sin^2\theta)+\frac{1}{2}I_3(\dot{\phi}^2\cos\theta+\dot{\psi}^2)^2-Mg(l+\overline{l}\sin\omega t)\cos\theta \quad (1)$$

Contributed by the Applied Mechanics Division of THE AMERICAN SOCIETY OF MECHANICAL ENGINEERS for publication in the ASME JOURNAL OF APPLIED MECHANICS. Manuscript received by the ASME Applied Mechanics Division, July 22, 1997; final revision, Feb. 25, 2001. Associate Editor: A. A. Ferri.

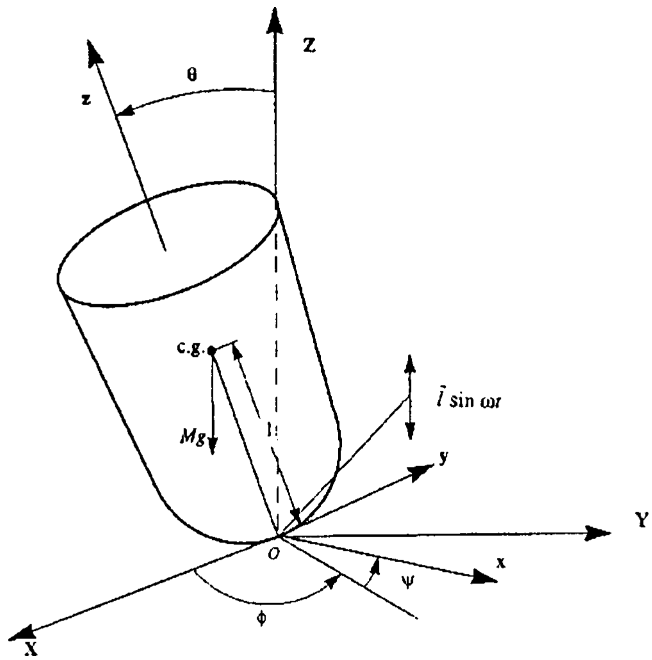

Fig. 1 A symmetric gyro subjected to a harmonic base excitation

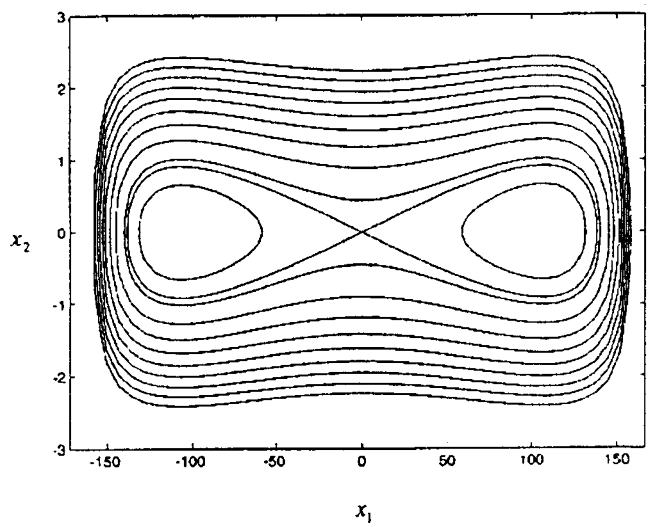

Fig. 2 The phase plane of a symmetric gyro

where I_1 and I_3 are the polar and equatorial moments of inertia of the symmetric gyro, Mg is the gravity force, l is the distance between the center of gravity and point O, $\bar{l}$ and ω are the amplitude and frequency of the base excitation, respectively.

Letting

$$x_1=\theta \quad \text{and} \quad x_2=\frac{p_\theta}{I_1}=\frac{1}{I_1}\frac{\partial L}{\partial \dot{\theta}} \tag{2a}$$

$$\gamma=\frac{p_\phi}{I_1}=\frac{1}{I_1}\frac{\partial L}{\partial \dot{\phi}} \quad \text{and} \quad \delta=\frac{p_\psi}{I_1}=\frac{1}{I_1}\frac{\partial L}{\partial \dot{\psi}}, \tag{2b}$$

the normalized canonical Equations of Motion (EOM) of the gyro employing the time invariant generalized angular momenta γ and δ can be written as

$$\dot{x}_1=x_2 \tag{3a}$$

$$\dot{x}_2=-\frac{(\gamma-\delta\cos x_1)(\delta-\gamma\cos x_1)}{\sin^3 x_1}+F\sin x_1+\varepsilon\bar{F}\sin\omega t\sin x_1 \tag{3b}$$

where

$$F=\frac{Mgl}{I_1} \quad \varepsilon\bar{F}=\frac{Mg\bar{l}}{I_1}. \tag{4}$$

Application of the Melnikov Method

For the symmetric gyro of Fig. 1, without base excitation ($\varepsilon=0$), the normalized canonical EOM (3) can be reduced to

$$\dot{x}_1=x_2 \tag{5a}$$

$$\dot{x}_2=-\frac{(\gamma-\delta\cos x_1)(\delta-\gamma\cos x_1)}{\sin^3 x_1}+F\sin x_1 \tag{5b}$$

for which the normalized time invariant Hamiltonian can be expressed as

$$h=\frac{H}{I_1}=\frac{x_2^2}{2}+\frac{(\gamma-\delta\cos x_1)^2}{2\sin^2 x_1}+\upsilon\frac{\delta^2}{2}+F\cos x_1 \tag{6}$$

where $\upsilon=I_1/I_3$. Although the right-hand side of Eq. (5b) appears to be singular at $x_1=0$ where $\gamma=\delta$, a careful application of l'Hopital's rule reveals that it is regular at that point; namely, when $x_1=0$, $x_2=0$. The above system representation is one of few rigid-body systems for which analytical solutions were found (e.g., see [8]). For $0<\gamma<2\sqrt{Mgl/I_1}$ and $\gamma=\delta$, the vertically spinning state ($x_1=0$, $x_2=0$) of the gyro is unstable (saddle). The homoclinic orbit (separatrix) connecting the saddle to itself (Fig. 2) is given by [8] as

$$\cos x_1=1-b\sec^2\left(\frac{\sqrt{ab}}{2}t\right) \tag{7}$$

where

$$b=2-\gamma^2/a \quad \gamma=\delta \quad a=2Mgl/I_1.$$

However, for the symmetric gyro subjected to a small base excitation ($\varepsilon\neq0$), the highly degenerate homoclinic orbit is expected to break and perhaps to intersect transversely. In such a case, Eq. (6) can be viewed as a Hamiltonian with a time variant perturbation,

$$\dot{\mathbf{x}}=\mathbf{f}(\mathbf{x})+\varepsilon\mathbf{g}(\mathbf{x},t) \tag{8}$$

where

$$\mathbf{x}=(x_1,x_2)$$

$$\mathbf{f}(x)=(x_2,-(\gamma-\delta\cos x_1)(\delta-\gamma\cos x_1)/\sin^3 x_1+F\sin x_1)$$

$$\mathbf{g}(x,t)=(0,\bar{F}\sin\omega t\sin x_1). \tag{9}$$

The existence of the transversal intersections of homoclinic orbits implies complex dynamic behavior in the sense of the Smale horseshoe and provides a necessary condition for chaotic motion to occur. Due to Melnikov [9], analytical technique exists for detecting the transversal intersections of homoclinic orbits in the Poincaré map of a perturbed system. The detection of these transversal intersection is accomplished by calculating the appropriate Melnikov integral, which is the first-order (in the perturbation parameter ε) measure of the distance between the stable and unstable manifolds associated with the saddle point on the Poincaré map. A convenient form of the Melnikov method for computation purposes is expressed as ([10])

$$M(t_0)=\int_{-\infty}^{\infty}\mathbf{f}(\mathbf{q}^0(t))\wedge\mathbf{g}(\mathbf{q}^0(t),t+t_0)dt \tag{10}$$

where the wedge product is of the type $\mathbf{f}\wedge\mathbf{g}=f_1g_2-f_2g_1$, and t is time. The homoclinic orbit of the unperturbed symmetric gyro system is then given by

$$\mathbf{q}^0(t)=\left(\cos^{-1}[1-b\sec^2(\sqrt{ab}t/2)],\right.$$
$$\left.\times\frac{b\sqrt{ab}\sec^2(\sqrt{ab}t/2)\tanh(\sqrt{ab}t/2)}{\sqrt{1-(1-b\sec^2(\sqrt{ab}t/2))^2}}\right). \qquad (11)$$

By substituting Eqs. (9) and (11) into (10), The Melnikov integral is reduced to

$$M(t_0)=\int_{-\infty}^{\infty}\bar{F}b\sqrt{ab}\sec^2\left(\frac{\sqrt{ab}}{2}t\right)\tanh\left(\frac{\sqrt{ab}}{2}t\right)\sin\omega(t+t_0)dt$$
$$=\int_{-\infty}^{\infty}\bar{F}b\sqrt{ab}\sec^2\left(\frac{\sqrt{ab}}{2}t\right)\tanh\left(\frac{\sqrt{ab}}{2}t\right)$$
$$\times(\sin\omega t\cos\omega t_0+\cos\omega t\sin\omega t_0)dt. \qquad (12)$$

Since the odd part of the above integral is zero, the Melnikov function $M(t_0)$ can be simply reduced to

$$M(t_0)=\left\{\int_{-\infty}^{\infty}\bar{F}b\sqrt{ab}\sec^2\left(\frac{\sqrt{ab}}{2}t\right)\tanh\left(\frac{\sqrt{ab}}{2}t\right)\sin\omega t dt\right\}$$
$$\times\cos\omega t_0. \qquad (13)$$

The integral in Eq. (13) can be evaluated by the residual method, to yield

$$M(t_0)=\frac{1}{2}\bar{F}b\sqrt{ab}\cosh\left(\frac{\pi\omega}{2}\right)\cos\omega t_0$$
$$=\frac{1}{4}\frac{\bar{F}}{F}(\sqrt{4F-\gamma^2})^3\cosh\left(\frac{\pi\omega}{2}\right)\cos\omega t_0. \qquad (14)$$

It can be deduced from (14) that the Melnikov function has simple zeros. Thus the motion of the symmetric gyro subjected to small base excitation is chaotic in the sense that the system possesses a Smale horseshoe.

Numerical Analysis

To investigate the transition from regular motion to chaotic motion as the amplitude of the base excitation is varied, the perturbed EOM (8) is integrated numerically for 14 different initial conditions. Throughout this analysis, computations were performed for

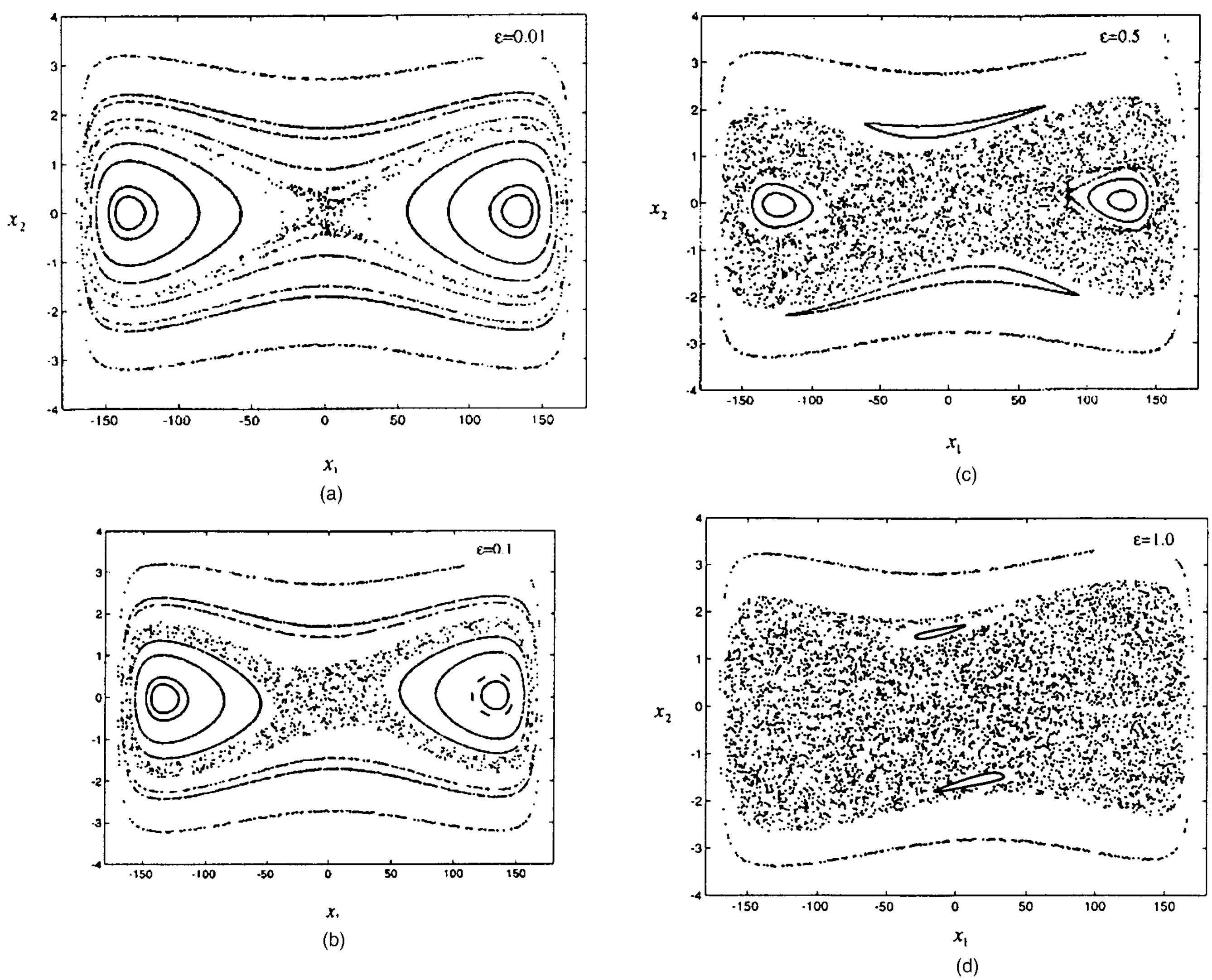

Fig. 3 (*a*) The Poincaré map of a symmetric gyro (ε=0.01); (*b*) the Poincaré map of a symmetric gyro (ε=0.1); (*c*) the Poincaré map of a symmetric gyro (ε=0.5); (*d*) the Poincaré map of a symmetric gyro (ε=1.0)

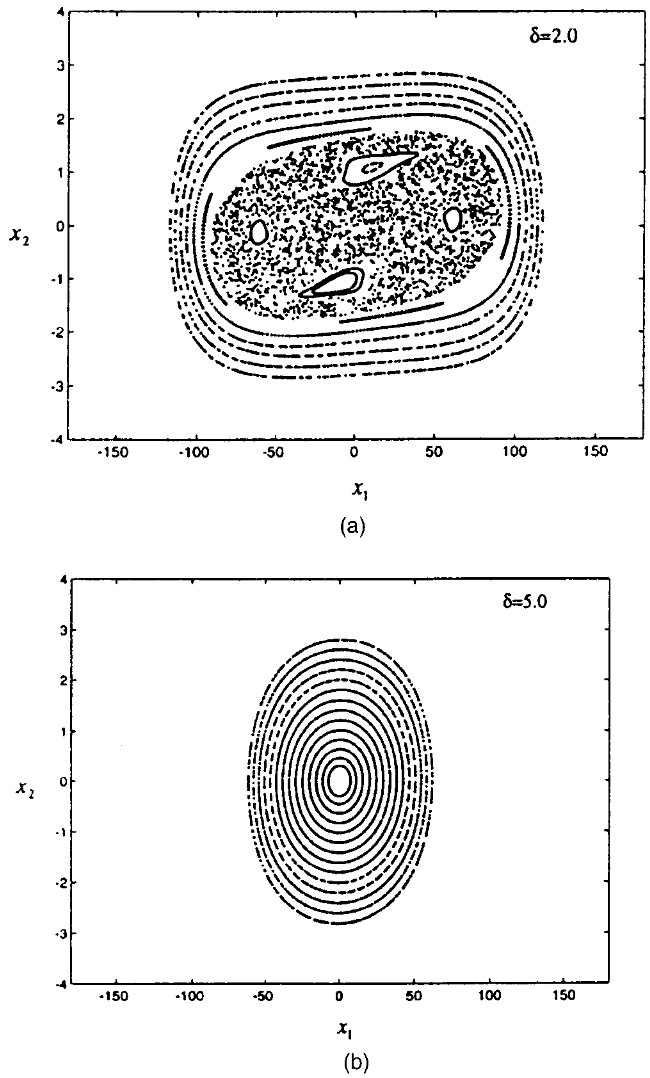

Fig. 4 **(*a*) The Poincaré map of a symmetric gyro (δ=2.0 and ε=1.0); (*b*) the Poincaré map of a symmetric gyro (δ=5.0 and ε=1.0)**

a symmetric gyro with the following parameters: $\gamma=\delta=0.3$, $F=1.0$, and $\omega=1.0$. Results are presented on Poincaré maps that were generated by looking at the system stroboscopically with a period $T=2\pi/\omega$. The two observed different types of motion on Poincaré maps, regular and chaotic, are readily distinguished. For regular motion, successive points describe smooth curves or separate points. For chaotic motion, the points fill an area on the Poincaré map in an apparently random manner.

For a fairly small perturbation ($\varepsilon=0.01$), Fig. 3(*a*), one observes that the Poincaré map is covered by resonant and nonresonant quasi-periodic trajectories. For a resonant quasi-periodic trajectory, successive points in Poincaré map trace a simple curve which covers only a fraction of the interval from $x_1=0$ to $x_1=180$ deg. For a nonresonant quasi-periodic trajectory, successive points in Poincaré map covers all values of x_1 between 0 and 180 deg. This result agrees with the celebrated KAM theorem (after Kolmogorov, Arnold, and Moser) ([11]). This theorem states that for a sufficiently small perturbation, most of periodic and quasi-periodic motions existing in the unperturbed system, will be slightly distorted but still preserved. In addition, it is observed that a small region that is close to the separatrix is covered by chaotic trajectories. This feature corroborates the results obtained in the previous section by means of the Melnikov method.

If the amplitude of the perturbation is increased by small amounts ($\varepsilon=0.1$ and $\varepsilon=0.5$), as shown in Figs. 3(*b*) and 3(*c*), one can observe that on the Poincaré map some regions are covered by regular trajectories and some by chaotic ones. If the amplitude is further increased to a relative large value, as shown in Fig. 3(*d*) ($\varepsilon=1.0$), one observes that the whole Poincaré map is covered by chaotic trajectories except for few islands. This result indicates that an onset of global chaos has occurred.

It is important to realize under what conditions a nonlinear system will become chaotic but more important to realize how chaotic motion can be prevented. To investigate the effect of the gyro's spin velocity on the various dynamic behavior of the system, the amplitude and frequency of the base excitation, ($F=\omega=1.0$), and the amplitude of the perturbation ($\varepsilon=1.0$) were fixed, and the parameter $\gamma=\delta=(I_3/I_1)\omega_3$ (ω_3 is the gyro's spin velocity) is varied. As δ is increased from 0.3 to 2.0, one can observe from Fig. 4(*a*) that more and more chaotic motion has disappeared. As δ is further increased to 5.0, Fig. 4(*b*), the whole Poincaré map is covered by regular motion. These results indicate that the gyro's spin velocity has a significant effect on the gyro's dynamic behavior, i.e., a chaotic motion will turn into a regular motion as the spin velocity increases. This can be explained by the fact that for $F=1.0$, the homoclinic orbit does not exist in the unperturbed system for $\delta>2.0$. This finding has practical importance for the design of gyroscope instruments. For instance, it is desirable to set the gyro in more stable spinning state by simply giving higher initial spinning velocity.

References

[1] Kozlov, V. V., 1976, "Splitting of Separatrices in the Perturbed Euler-Poinsot Problem," Moscow Univ. Math. Mech. Bull., **31**, pp. 55–59.

[2] Galgoni, L., Giogilli, A., and Strlcyn, J. M., 1981, "Chaotic Motions and Transition to Stochasticity in the Classical Problem of Heavy Rigid Body With Fixed Point," Nuovo Cimento B, **61B**, pp. 1–20.

[3] Holmes, P. J., and Marsden, J. E., 1983, "Melnikov's Method and Arnold Diffusion for Hamiltonian Systems on Lie Groups," Indiana Univ. Math. J., **32**, pp. 273–309.

[4] Tong, X., and Rimrott, F. P. J., 1993, "Chaotic Attitude Motion of Gyrostat Satellites in a Central Force Field," Nonlinear Dynamics, **4**, pp. 269–291.

[5] Tong, X., and Tabarrok, B., 1997, "Bifurcation of Self-Excited Rigid Bodies Subject to Small Perturbation Torques," AIAA Journal of Guidance, Control and Dynamics, **20**, pp. 123–128.

[6] Tong, X., Tabarrok, B., and Rimrott, F. P. J., 1995, "Chaotic Motion of an Asymmetric Gyrostat in the Gravitational Field," Int. J. Non-Linear Mech., **30**, pp. 191–203.

[7] Ge, Z. M., Chen, H. K., and Chen, H. H., 1996, "The Regular and Chaotic Motions of a Symmetric Heavy Gyroscope With Harmonic Excitation," J. Sound Vib., **198**, pp. 131–147.

[8] Goldstein, H., 1980, *Classical Mechanics*, 2nd Ed., Addison-Wesley, Reading, MA.

[9] Melnikov, V. K., 1963, "On the Stability of the Center for Time Periodic Perturbations," Transactions of Moscow Mathematical Society, **12**, pp. 1–57.

[10] Guckenheimer, J., and Holmes, P. J., 1985, *Nonlinear Oscillators, Dynamical Systems and Bifurcations of Vector Fields*, 2nd Ed., Springer-Verlag, New York.

[11] Lichtenberg, A. J., and Liberman, M. A., 1992, *Regular and Stochastic Motion*, 2nd Ed., Springer-Verlag, New York.

Journal of Applied Mechanics

Discussion

Discussion: "Combinations for the Free-Vibration Behavior of Anisotropic Rectangular Plates Under General Edge Conditions" (Narita, Y., 2000, ASME J. Appl. Mech., 67, pp. 568–573)

C. W. Bert
Perkinson Chair Professor, School of Aerospace and Mechanical Engineering, The University of Oklahoma, Norman, OK 73019-1052. Life Fellow ASME

The author is to be commended for his new approach to the important problem of calculation of natural frequencies for anisotropic plates. However, two comments are in order.

First, the paper lists only three classical boundary conditions: simply supported, clamped, and free. Actually, there is a fourth one: guided or sliding (Bert and Malik [1]). For this boundary condition, the effective shear force and the bending slope are both zero. Exact natural frequency results were given for a variety of such cases of isotropic plates in [1].

The second comment is that, although the Ritz method is an upper bound solution, it converges rather slowly in the case of anisotropic plates. For design purposes, a lower bound to a frequency is often more important than an upper bound. The convergence of the Ritz method, a Fourier series method (Whitney [2]), and the differential quadrature method were studied by Bert et al. [3] for free vibration of simply supported plates of highly anisotropic material ($E_L/E_T=25$, compared to 15.4 in the present paper). The latter two methods provided lower bounds.

References

[1] Bert, C. W., and Malik, M., 1994, "Frequency Equations and Modes of Free Vibrations of Rectangular Plates With Various Edge Conditions," Proc. Inst. Mech. Eng., Part C: J. Mech. Eng. Sci. **208C**, pp. 307–319.
[2] Whitney, J. M., "Free Vibrations of Anisotropic Rectangular Plates," 1972, J. Acoust. Soc. Am. **52**, pp. 448–449.
[3] Bert, C. W., Wang, X., and Striz, A. G., 1994, "Convergence of the DQ Method in the Analysis of Anisotropic Plates," J. Sound Vib. **170**, pp. 140–144.

Closure to "Discussion of 'Combinations for the Free-Vibration Behavior of Anisotropic Rectangular Plates Under General Edge Conditions'" (2001, ASME J. Appl. Mech. 68, p. 685)

Y. Narita
Department of Mechanical Engineering, Hokkaido Institute of Technology, 7-15 Maeda, Teine-ku, Sapporo, 006-8585, Japan
e-mail: narita@hit.ac.jp

Although the main idea of the paper is an introduction of the Polya counting theory to an engineering counting problem that may be encountered in applied mechanics, this author equally appreciates the interest shown by Professor Bert in the proposed Ritz method to calculate natural frequencies of anisotropic plates with arbitrary boundary conditions. Professor Bert raised two constructive comments that are answered in order.

The first comment is that the present author took up only three classical boundary conditions (i.e., free, simply supported, and clamped edges) in numerical examples and did not consider the fourth boundary condition of a guided or sliding edge with zero effective shear force and bending moment. The function (20) in the x and y-direction ([1]) is not applicable in its direct form to the fourth boundary condition but it is widely accepted that the fourth condition is not as important as the first three ones. It may be possible to apply the present function to the fourth boundary condition by adding a constant term to give a constant displacement caused by the guided or sliding edge and also constraining the slope at the edge.

The second comment, which is more important, is on convergence rates of the present solution applied to anisotropic plates. Before commenting on that, I have to make it clear that the caption in Table 2 of [1] was erroneous. The convergence result in the table was for a specially orthotropic square plate. (i.e., anisotropic plate with a fiber orientation angle $\theta=0$ deg), not for skew orthotropic square plates ($\theta=30$ deg). This was obvious that the converged values in Table 2 are in exact agreement with those of specially orthotropic plates in Table 5 of [1].

Professor Bert stated that "it (Ritz method) converges rather slowly in the case of anisotropic plates." I agree that the Ritz method tends to give slower convergence for anisotropic plates than for isotropic and specially orthotropic plates, but this tendency is also found for other methods and the important question is how slow the solution becomes. To see this, another test is conducted here to observe convergence rates of the present method for highly anisotropic material.

$$Q_{11}/Q_{22}=25,\ Q_{12}/Q_{22}=0.25 \quad \text{and} \quad Q_{66}/Q_{22}=0.5$$

Table 1 Convergence of frequency parameters Ω of diagonally orthotropic square plates (θ=45 deg, Q_{11}/Q_{22}=25, Q_{12}/Q_{22}=0.25, and Q_{66}/Q_{22}=0.5)

B.C.	Num.of terms	1st	2nd	3rd	4th
FFFF	6x6	18.90	24.70	43.30	59.60
	8x8	18.82	24.60	42.67	58.79
	10x10	18.82	24.60	42.65	58.71
	12x12	18.82	24.60	42.65	58.70
	14x14	18.83	24.60	42.65	58.70
SSSS	4x4	53.87	95.06	165.5	178.1
	6x6	52.91	91.58	143.6	156.0
	8x8	52.46	91.55	142.4	154.4
	10x10	52.19	91.54	142.3	153.8
	12x12	52.01	91.54	142.3	153.3
	14x14	51.89	91.54	142.3	153.0
	16x16	51.80	91.54	142.2	152.8
CCCC	6x6	91.31	145.8	208.2	217.0
	8x8	91.24	145.8	208.0	216.3
	10x10	91.22	145.8	208.0	216.2
	12x12	91.22	145.8	208.0	216.2
	14x14	91.22	145.8	208.0	216.2
CFFF	6x6	5.947	18.28	35.78	43.23
	8x8	5.919	18.11	35.25	42.93
	10x10	5.904	18.05	35.12	42.90
	12x12	5.898	18.03	35.08	42.89
	14x14	5.898	18.03	35.08	42.89

used in reference [2]. This material has stronger anisotropy (E_L/E_T=25) than that (E_L/E_T=15.4) used in ([1]).

Table 1 presents convergence test results of diagonally orthotropic square plates (θ=45 deg) with such material for boundary conditions of FFFF (free plate). SSSS (simply supported plate), CCCC (clamped plate), and CFFF (cantilever plate). Frequency parameters

$$\Omega=\omega a^2(\rho h/D_0)^{1/2} \quad \text{with a reference stiffness } D_0 = E_T h^2/12(1-v_{LT}v_{TL}) \tag{1}$$

are presented with four significant figures for the number of terms $M\times N=6\times 6\sim 14\times 14$ ($4\times 4\sim 16\times 16$ for SSSS) in Eq. (15) of [1], and underlined figures are converged values within the range of our significant figures. It is seen that two extreme cases of the FFFF (totally free plate with only natural boundary conditions) and the CCCC (the most constrained plate with only geometrical boundary conditions) plates do yield fast convergence, while the SSSS plate with both natural and geometrical boundary conditions does slower convergence, particularly for the fundamental mode.

The convergence behaviors of some different solutions are compared for the fundamental frequency of the SSSS plate in reference [2]. The present values are converted to their frequency parameter

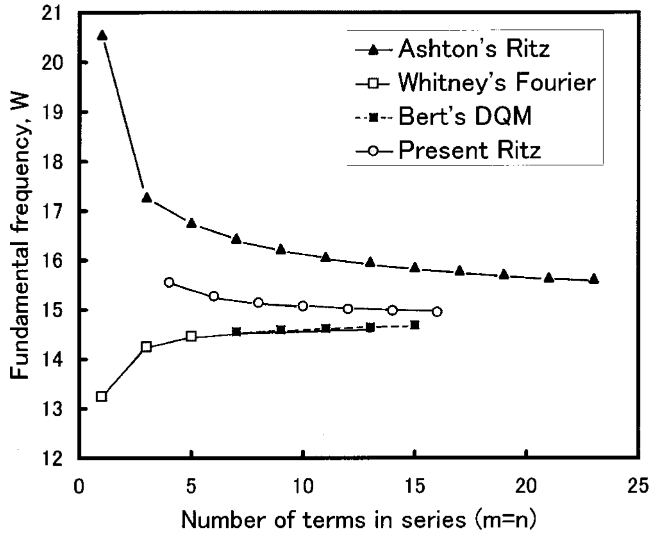

Fig. 1 Convergence of the fundamental frequency parameter $W=\Omega b^2(\rho/(Q_{22}h^2))^{1/2}$ by Ashton's Ritz method. Whiteney's Fourier, Bert's DQM, and the present Ritz method. (Data are replotted from Fig. 4 in [2].)

$$W=\omega b^2(\rho/Q_{22}h^2)^{1/2} \tag{2}$$

and are shown in Fig. 1 with those presented in Fig. 4 of [2]. It is observed that the present Ritz method gives much better upper bound than the Ritz result of Ashton and approaches closely to the lower bound of the Fourier analysis and DQ method. This figure therefore indicates that the convergence rate of the Ritz method is rather dependent on the choice of displacement functions.

The present author has an opinion that use of the Ritz method with (modified) polynomial functions yields very accurate upper bounds with advantages in applying to arbitrary boundary conditions and in computation time, when it is used with the following points in mind ([3]).

- The first few terms of the polynomial (say, ten) give rapid convergence of the solution, but the use of higher order polynomials (say, 20 or more terms) tends to make the eigenvalue equation numerically unstable, unless it is somehow modified.
- The plate region considered should have a regular plan, such as rectangular and elliptical plates. For plates of irregular geometry, e.g., with cutouts or L-shaped plates, the solution accuracy deteriorates.

In summary, the Ritz method with modified polynomials is a valuable and recommendable approach. The only problem is that because it is very easy to use and guarantees good accuracy, one cannot escape this easiness and does not create new methodology.

References

[1] Narita, Y., 2000, "Combinations for the Free-Vibration Behaviors of Anisotropic Rectangular Plates Under General Edge Conditions," ASME J. Appl. Mech., **67**, pp. 568–573.

[2] Bert, C. W., Wang, X., and Striz, A. G., "Convergence of the DQ Method in the Analysis of Anisotropic Plates," J. Sound Vib., **170**, pp. 140–144.

[3] Narita, Y., 1995, "Series and Ritz-Type Buckling Analysis," *Buckling and Postbuckling of Composite Plates*, G. J. Turvey and I. H. Marshall, eds., Chapman and Hall, London, p. 56.

Discussion: "Common Errors on Mapping of Nonelliptic Curves in Anisotropic Elasticity" (Ting, T. C. T., 2000, ASME J. Appl. Mech., 67, pp. 655–657)

C. Q. Ru
Department of Mechanical Engineering, University of Alberta, Edmonton, AB T6G 2GB, Canada
e-mail: c.ru@ualberta.ca

Professor Ting's paper ([1]) clearly clarifies several simple but important concepts on conformal mapping techniques applied to anisotropic plane elasticity. Here, I would like to add my own comments on these interesting issues.

(1) First, it should be stated that conformal mapping techniques, combined with the Stroh's method, have been successfully applied in some important cases to anisotropic elasticity with nonelliptical curves. An example is the Eshelby's problem for an inclusion of arbitrary shape in an anisotropic medium ([2]), or in a piezoelectric medium [3], of the same material constants. As stated by Prof. Ting in [1], and also by some other authors elsewhere, because a point z on Γ will be transformed, under three different mappings $w_\alpha(\xi)$ $(\alpha=1,2,3)$, to three different points ξ_α on the unit circle in ζ-plane, the transformed boundary conditions on the unit circle in the ζ-plane will contain three unknown Stroh's functions which take values at three different points. Therefore, unless the boundary conditions are decoupled for the three Stroh's functions, one cannot solve the transformed boundary value problem in the ζ-plane. The key fact associated with the problem studied in [2] is that the three interface conditions (in complex form) for an arbitrarily shaped inclusion, surrounded by an anisotropic medium of the same material constants, can be written in a decoupled form in which the three unknown Stroh's functions are completely decoupled to each other. It is this fact that allows one to apply conformal mapping techniques to each of the three Stroh's functions and the associated curve independently of the other two. For a similar result for piezoelectric materials, see [3].

The second key result of ([2]) is that for each of the three closed curves Γ_α $(\alpha=1,2,3)$ (that is Γ^α defined in [1]), one can construct an auxiliary function $D_\alpha(z)$ which satisfies the condition

$$\overline{z}=D_\alpha(z), \quad z\in\Gamma_\alpha \tag{1}$$

and is analytic and single-valued in the exterior of the curve Γ_α, except at infinity where $D_\alpha(z)$ tends to a polynomial $P_\alpha(z)$. As shown in [2] (and [3] for piezoelectric materials), with aid of these auxiliary functions, the techniques of analytic continuation can be applied to the inclusion of arbitrary shape to get an analytic solution for the Stroh's functions.

The above key result (which has been questioned by someone!) can be shown, clearly and rigorously, as follows. Assume that the exterior of Γ_α is mapped onto the exterior of the unit circle in the ξ-plane by a polynomial conformal mapping

$$z=w_\alpha(\xi)=\lambda_\alpha\xi+\sum_{k=0}^{N} c_{\alpha k}\xi^{-k}, \quad \alpha=1,2,3 \tag{2}$$

where λ_α is a real number, $c_{\alpha k}$ are some complex constants, and N is a finite integer. It is emphasized that the definition of the conformal mapping (2) implies that it has a unique inverse conformal mapping $w_\alpha^{-1}(z)$ which is well defined on the exterior of the curve Γ_α and maps the exterior of the curve Γ_α (without any branch cut!) on to the exterior of the unit circle. Evidently, this means that the inverse mapping $w_\alpha^{-1}(z)$ is analytic, single-valued and nonzero in the exterior of the curve Γ_α. This is just part of the definition (2)—not any further "proof" is needed. Here, similar to all other conformal mapping methods, the inverse mapping $w_\alpha^{-1}(z)$ is treated as the known, and we need not discuss how to construct an explicit expression for the inverse mapping $w_\alpha^{-1}(z)$ from the single-valued branches of the multivalued inverse function of (2). In particular, all branch points of the inverse function of (2) fall inside the interior of the curve Γ_α in the z-plane, or inside the interior of the unit circle in the ξ-plane. For example, for a hypotrochoidal curve, it is readily seen from (A11) of [4] that all singularity points of the conformal mapping (at which the derivative of the mapping function vanishes, as described by the condition (3) or (6) of [1]) fall inside the interior of the unit circle in the ξ-plane and thus do not trouble the single-valued inverse mapping for the exterior.

Based on these facts, it is easily verified that the desired function $D_\alpha(z)$ is given by

$$D_\alpha(z)=\overline{w_\alpha}\left(\frac{1}{w_\alpha^{-1}(z)}\right)=\frac{\lambda_\alpha}{w_\alpha^{-1}(z)}+\sum_{k=0}^{N}\overline{c_{\alpha k}}[w_\alpha^{-1}(z)]^k \tag{3}$$

where $w_\alpha^{-1}(z)$ is the (unique) inverse mapping of the polynomial mapping (2). First, $D_\alpha(z)$ given by (3) meets the condition (1) on the curve Γ_α. Second, because $w_\alpha^{-1}(z)$ is analytic, single-valued and nonzero outside the curve Γ_α, $1/w_\alpha^{-1}(z)$ and $[w_\alpha^{-1}(z)]^k$ (k is any integer not larger than N) are analytic and single-valued outside the curve Γ_α. Thus, $D_\alpha(z)$ given by the right-hand side of (3) is obviously analytic and single-valued in the exterior of the curve Γ_α, except at infinity where $D_\alpha(z)$ tends to a polynomial of degree N. Therefore, the auxiliary function $D_\alpha(z)$ complying with the conditions (1) can be constructed by (3) in terms of the associated polynomial mapping which maps the exterior to the curve Γ_α onto the exterior of the unit circle. Similar auxiliary functions have been applied to isotropic elasticity [4] and piezoelectric materials [3].

(2) Finally, as stated in [1], the mapping (15) of [1], although provides a one-to-one mapping for the boundaries, does not always offer a one-to-one mapping for the exteriors of the boundaries. Regarding this issue, as stated in [2,3], the boundary correspondence principle of conformal mappings for exterior domains ([5]) can be used to identify the conditions under which a one-to-one mapping for the boundaries automatically offers a one-to-one mapping for the exteriors. For instance, for an elliptical boundary Γ, because the right-hand side of (15) of [1] is analytic outside the unit circle and has a simple pole (of degree one) at infinity in the ξ-plane, it follows from the boundary correspondence principle [5] that the expression (15) of [1] provides a one-to-one conformal mapping between the exterior of the curve Γ_α and the exterior of the unit circle in the ξ-plane, not any pointwise verification is needed. I believe that this comment offers a valuable insight to this interesting issue.

References

[1] Ting, T. C. T., 2000, "Common Errors on Mapping of Nonelliptic Curves in Anisotropic Elasticity," ASME J. Appl. Mech., **67**, pp. 655–657.
[2] Ru, C. Q., 2001, "Analytic Solution for an Inclusion of Arbitrary Shape in an Anisotropic Plane or Half-Plane" (submitted for publication).
[3] Ru, C. Q., 2000, "Eshelby's Problem for Two-Dimensional Piezoelectric Inclusions of Arbitrary Shape," Proc. R. Soc. London, Ser. A, **A456**, pp. 1051–1068.
[4] Ru, C. Q., 1999, "Analytic Solution for Eshelby's Problem of an Inclusion of Arbitrary Shape in a Plane or Half-Plane," ASME J. Appl. Mech., **66**, pp. 315–322.
[5] Ivanov, V. I., and Trubetakov, M. K., 1995, *Handbook of Conformal Mapping With Computer-Aided Visualization*, CRC Press, Boca Raton, FL.

Closure to "Discussion of 'Combinations for the Free-Vibration Behavior of Anisotropic Rectangular Plates Under General Edge Conditions'" (2001, ASME J. Appl. Mech., 68, p. 687)

T. C. T. Ting
Department of Civil and Materials Engineering,
University of Illinois at Chicago, 842 Taylor Street, M/C 246, Chicago, IL 60607-7023
e-mail: tting@uic.edu

Contrary to what Professor Ru stated in his first sentence, the paper did not discuss "conformal mapping" techniques applied to anisotropic plane elasticity. The paper discussed "mapping" in anisotropic elasticity. As emphasized in Section 4 of the paper, mapping in anisotropic elasticity is not conformal. Many papers that dealt with mapping in anisotropic elasticity used the word conformal mapping indiscriminately.

I have presented clearly what I wanted to say in the paper. I have no further comments.

Journal of Applied Mechanics

Errata

Erratum: "Explicit Equations of Motion for Mechanical Systems With Nonideal Constraints" [ASME J. Appl. Mech., 68, pp. 462–467]

F. E. Udwadia and R. E. Kalaba

In this paper, item (S2) of Section 3, page 464, should read

2 $\phi(q,t)=0$, $\psi(q,\dot{q},t)=0$, with $\phi(q_0,0)=0$, $\dot{\phi}(q_0,0)=0$, and $\psi(q_0,\dot{q}_0,0)=0$.